Structural characterization of the rescue mechanism of proteins synthesis in bacteria

Gaetano d'Urso

UNIVERSITÉ DE RENNES 1

THESE DE DOCTORAT DE

L'UNIVERSITE DE RENNES 1

ECOLE DOCTORALE N° 605
Biologie Santé
Spécialité: Biologie Moléculaire et Structurale, Biochimie

Par
Gaetano D'URSO

Structural characterization of the rescue mechanism of protein synthesis in bacteria

Thèse présentée et soutenue à Rennes, le 20 Octobre 2022

Unité de recherche : Institut de Génétique et Développement de Rennes, UMR CNRS 6290

Rapporteurs avant soutenance :

Emmanuelle Schmitt	Directrice de recherche CNRS UMR 7654, Ecole Polytechnique, Palaiseau
Stefano Marzi	Directeur de recherches CNRS UPR 9002 ARN, IBMC, Strasbourg

Composition du Jury :

Président :	Luc Paillard	Professeur des Universités, IGDR, Université de Rennes 1
Examinateurs :	Irmgard Maria Sinning	Group leader, Heidelberg University, Biochemistry Center, Germany
	Emmanuelle Schmitt	Directrice de recherche CNRS UMR 7654, Ecole Polytechnique, Palaiseau
	Stefano Marzi	Directeur de recherches CNRS UPR 9002 ARN, IBMC, Strasbourg
Dir. de thèse :	Reynald Gillet	Professeur des Universités, IGDR, Université de Rennes 1
Co-dir. de thèse :	Emmanuel Giudice	Maitre de conférences, IGDR, Université de Rennes 1

Table of contents

I INTRODUCTION

I - INTRODUCTION

I INTRODUCTION

1. The bacterial ribosome

1.1 From DNA to proteins: the role played by the ribosomes in the central dogma of molecular biology

The idea that DNA could contain the information needed to determine the sequence of proteins started to become popular in 1954 when it was first proposed by George Gamow (Gamow, 1954) after the discovery of DNA structure in 1953 by Watson and Crick (Watson and Crick, 1953). The relationship DNA – RNA – protein, called central dogma, describes the flow of the genetic information from DNA to the proteins through two main steps:

I. *Transcription* of DNA into mRNA (messenger RNA);

II. *Translation* of mRNA in amino acid sequence (protein).

Thanks to this mechanism, cells can maintain and protect the genetic information while synthetizing the building blocks essential to their survival and the development of the organism of which they are part.

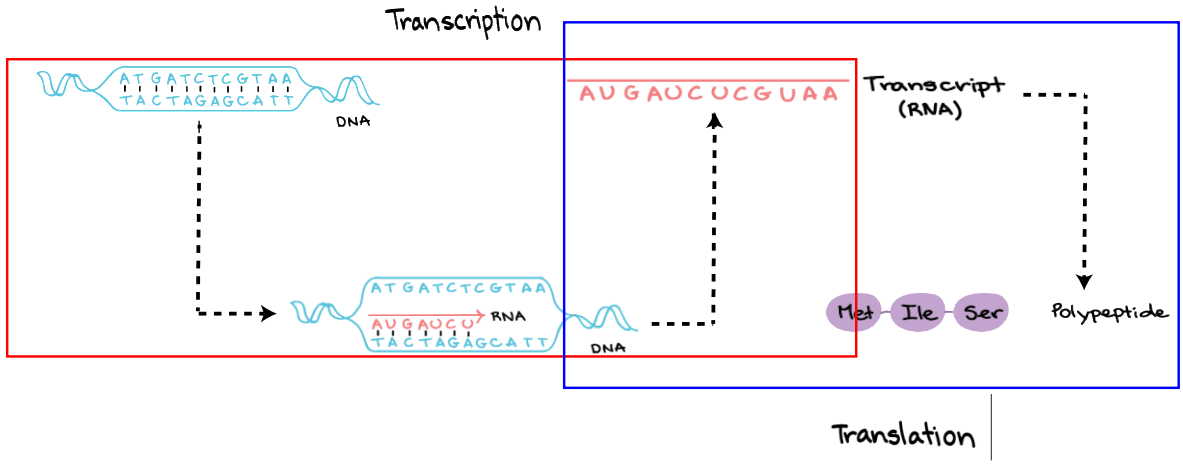

Figure 1: The central dogma of molecular biology. The double stranded DNA is in light blue, the single stranded mRNA in red and the polypeptide in violet.

The four letters code which allows the storage of the genetic information in the DNA, is read and used to produce an mRNA molecule. The mRNA strand is based on the same alphabet as the DNA, except for the thymine (T) which is substituted by uracile (U). In bacteria, the RNA transcript can be readily used as a mature mRNA. In eukaryotes, the primary RNA transcript has to go through a process called splicing where some parts of the mRNA transcript may be removed while some caps are generally added to the extremities to reach its mature form. The place where

transcription takes place also differs. Eukaryotes have a nucleus, where chromosomes are stored, but protein synthesis is a cytoplasmic process. So, for the translation to occur, the mRNA produced in eukaryotes must be exported into the cytosol. Prokaryotic cells lack a nucleus, so transcription and translation are both carried out in the cytosol. Once the mRNA molecule is matured into its final version, it is ready to be translated into proteins. The nucleotide sequence of the mRNA is read in groups of three bases called codons. The 20 amino acids are encoded by 61 codons, plus a "start" codon and three "stop" codons (Table 1). For this reason, the genetic code is called degenerated or redundant.

Table 1: The genetic code. Each amino acid is associated to their respective codons. In green the "start" codon; in red the "stop" codons.

	U		C		A		G		
	UUU		UCU		UAU		UGU		U
	UUC	Phe	UCC		UAC	Tyr	UGC	Cys	C
U	UUA		UCA	Ser	UAA	STOP	UGA	STOP	A
	UUG	Leu	UCG		UAG	STOP	UGG	Trp	G
	CUU		CCU		CAU		CGU		U
	CUC		CCC		CAC	His	CGC		C
C	CUA	Leu	CCA	Pro	CAA		CGA	Arg	A
	CUG		CCG		CAG	Gln	CGG		G
	AUU		ACU		AAU		AGU		U
	AUC	Ile	ACC		AAC	Asn	AGC	Ser	C
A	AUA		ACA	Thr	AAA		AGA		A
	AUG	Met	ACG		AAG	Lys	AGG	Arg	G
	GUU		GCU		GAU		GGU		U
	GUC		GCC		GAC	Asp	GGC		C
G	GUA	Val	GCA	Ala	GAA		GGA	Gly	A
	GUG		GCG		GAG	Glu	GGG		G

1.2 The bacterial ribosome

The translation process is performed by a molecular complex known as ribosome. Ribosomes are macromolecular machines present in all cells, whose role in the

central dogma is to read the information carried by the mRNA molecule and synthesize the corresponding polypeptide chain that will next fold into a specific shape to form a particular protein. Based on the organism they belong to, ribosomes are around 200 Å – 300 Å (20 – 30 nm) in diameter, with a molecular mass going from 2,3 MDa in prokaryotes to 4,3 MDa in eukaryotes, and an rRNA-to-protein ratio close to 65% (Melnikov et al., 2012a). Only mitochondrial ribosomes present an inverse ratio, with more proteins than rRNA (Lightowlers et al., 2014). In general, ribosomal proteins do not have catalytic activity, acting mostly as a scaffold essential to enhance the ability of the rRNA portion in forming the peptide bond between amino acids, as well as to ensure the proper mRNA folding. For that reason we can also refer to the ribosome as a ribozyme, RNA molecules being the ones able to catalyze biological reactions. Structurally speaking, a ribosome is composed of a small subunit and a large subunit, whose name is derived from their sedimentation rates expressed in Svedberg (S). The prokaryotic ribosome is called 70S and consists of a 30S (small) subunit and a 50S (large) subunit. During the present Ph.D., I focused my attention on the *Escherichia coli* ribosome which 30S subunit (0,8 MDa) is composed of 21 proteins and a 16S rRNA molecule of 1542 bases, while the 50S subunit (1,5 MDa) presents 31 proteins and two rRNA molecules: a 23S of 2904 nucleotides and a 5S of 120 nucleotides (Alberts, Bruce et al., 2002; Garret, Grishman, 2009). In comparison the eukaryotes have a larger 80S ribosome, consisting of a 40S (small) subunit and a 60S (large) subunit. In this case the 40S subunit is composed of 33 proteins and an 18S rRNA of 1900 bases, while the 60S subunit presents 49 proteins, a 28S rRNA of 4700 nucleotides, a 5.8S rRNA of 160 nucleotides and a 5S rRNA nof 120 nucleotides, although variations in the number of bases may exist depending on the organism (Alberts, Bruce et al., 2002; Ben-Shem et al., 2011; Klinge et al., 2011). The ribosomes of the three domains of life (Archaea, Bacteria, and Eucarya) differ in their protein composition. For that reason, a nomenclature was established in which, for each protein, the prefix “u“ stands for ubiquitous (present in both the domains), “b“ is used for proteins present in bacteria only (*i.e.* without homologs in archaea and eukaryotes), while “e“ and “a“ are used respectively for eukaryotes and archaea proteins (Table 2, Table 3) (Ban et al., 2014).

Table 2: The nomenclature of 50S bacterial proteins.
The proteins highlited in orange are only present in bacteria while the ones in light blue are universals.

Large Subunit			
New Name	**Old Bacteria Name**	**Old Yeast Name**	**Old Human Name**
uL1	L1	L1	L10A
uL2	L2	L2	L8
uL3	L3	L3	L3
uL4	L4	L4	L4
uL5	L5	L11	L11
uL6	L6	L9	L9
bL9	L9	-	-
uL10	L10	P0	P0
uL11	L11	L12	L12
bL12	L7/L12	-	-
uL13	L13	L16	L13A
uL14	L14	L23	L23
uL15	L15	L28	L27A
uL16	L16	L10	L10
bL17	L17	-	-
uL18	L18	L5	L5
bL19	L19	-	-
bL20	L20	-	-
bL21	L21	-	-
uL22	L22	L17	L17
uL23	L23	L25	L23A
uL24	L24	L26	L26
bL25	L25	-	-
bL27	L27	-	-
bL28	L28	-	-
uL29	L29	L35	L35
uL30	L30	L7	L7
bL31	L31	-	-
bL32	L32	-	-
bL33	L33	-	-
bL34	L34	-	-
bL35	L35	-	-
bL36	L36	-	-

Table 3: Thenomenclature of 30S bacterial proteins. The proteins highlited in orange are only present in bacteria while the ones in light blue are universals.

Small Subunit			
New Name	**Old Bacteria Name**	**Old Yeast Name**	**Old Human Name**
bS1	S1	-	-
uS2	S2	S0	SA
uS3	S3	S3	S3
uS4	S4	S9	S9
uS5	S5	S2	S2
bS6	S6	-	-
uS7	S7	S5	S5
uS8	S8	S22	S15A
uS9	S9	S16	S16
uS10	S10	S20	S20
uS11	S11	S14	S14
uS12	S12	S23	S23
uS13	S13	S18	S18
uS14	S14	S29	S29
uS15	S15	S13	S13
bS16	S16	-	-
uS17	S17	S11	S11
bS18	S18	-	-
uS19	S19	S15	S15
bS20	S20	-	-
bS21	S21	-	-
bTHX	THX	-	-

1.2.1 The Bacterial ribosome small subunit

As previously described, the *E. coli* 30S subunit is composed of a 16S rRNA of 1540 nucleotides encoded by the *rrsA* gene, and 21 proteins, 6 of them specific for bacteria. Due to the particular 3D folding of the 16S rRNA the 30S structure can be described by four distinct domains: the flexible and mobile head is connected to the central body, which in turn presents a shoulder on the left and a platform on the right

(Figure 2) (Wimberly et al., 2000a). The associated proteins are distributed mostly on the external surface, while those placed toward the inner surface allow the formation of contact points with the 50S subunit. Structurally speaking, the 30S proteins show one or more globular domains with a long extension, mostly composed of basic amino acids. It has been shown that these extensions (α-helices, loops, etc.) are in close contact with the rRNA, and they play an important role in the stabilization of the rRNA folding during the 30S biogenesis, by neutralizing the charge repulsion of its backbone (Wimberly et al., 2000). The 16S rRNA structure, on the other hand, is an arrangement of helical, or pseudo-helical, elements in the three-dimensional space. We can distinguish more than 50 double helices connected by single stranded loops. These secondary structures give life to different types of helix-helix packing that contribute to the formation of four domains. Among them, we distinguish three compact domains, such as the 5' domain (5'), the central domain (C) and 3' major domain (3'M), as well as an extended one called 3' minor domain (3'm) (Figure 2) (Wimberly et al., 2000a).

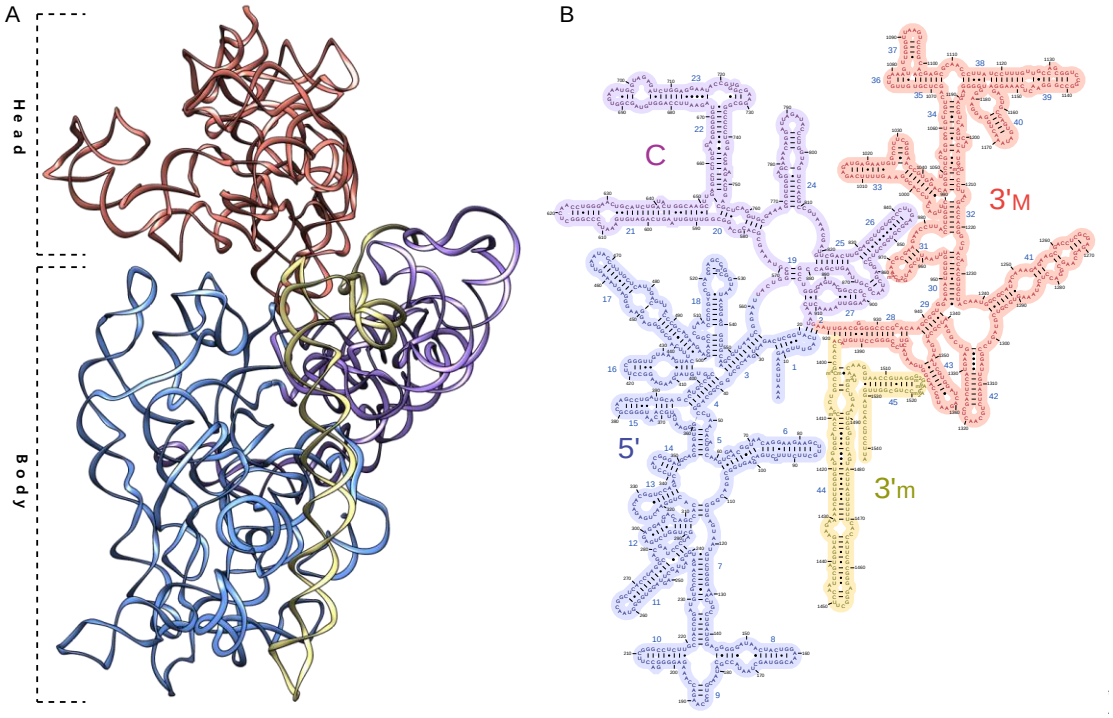

Figure 2: Structure and organization of the 30S subunit 16S rRNA from T. thermophilus. A) Three-dimensional folding of the rRNA in which we highlight the head and the body of the subunit as well as the four structural domains. The 5' domain is in cornflower blue, the central domain is in medium purple, the 3' mejor domain si in salmon and the 3' minor domain is in khaki. B) Secondary structure organization of the rRNA. The color code is the same as for the panel A (Center for molecular biology).

Functionally speaking, the 30S subunit plays a fundamental role during translation because it discriminates the different tRNAs entering the A-site, thus ensuring the decoding of the information brought by the mRNA into a polypeptide sequence. The three conserved bases G530, A1492 and A1493 belonging to Decoding Center (DC) play a central role during the process (Carter et al., 2000). In concert with the 50S, the small subunit ensures the translocation of the different tRNAs and their associated codons within the A, P and E sites (Figure 3). The 3' end of the 16S plays an important role in binding the mRNA during the translation initiation: its 6/8 nucleotides portion, called anti-Shine – Dalgarno (anti-SD), matches the 5' end of the mRNA known as Shine – Dalgarno sequence (SD). This interaction is essential not only for the binding of the mRNA to the small subunit, but also for the correct positioning of the "start" codon in the P site (Shine and Dalgarno, 1974).

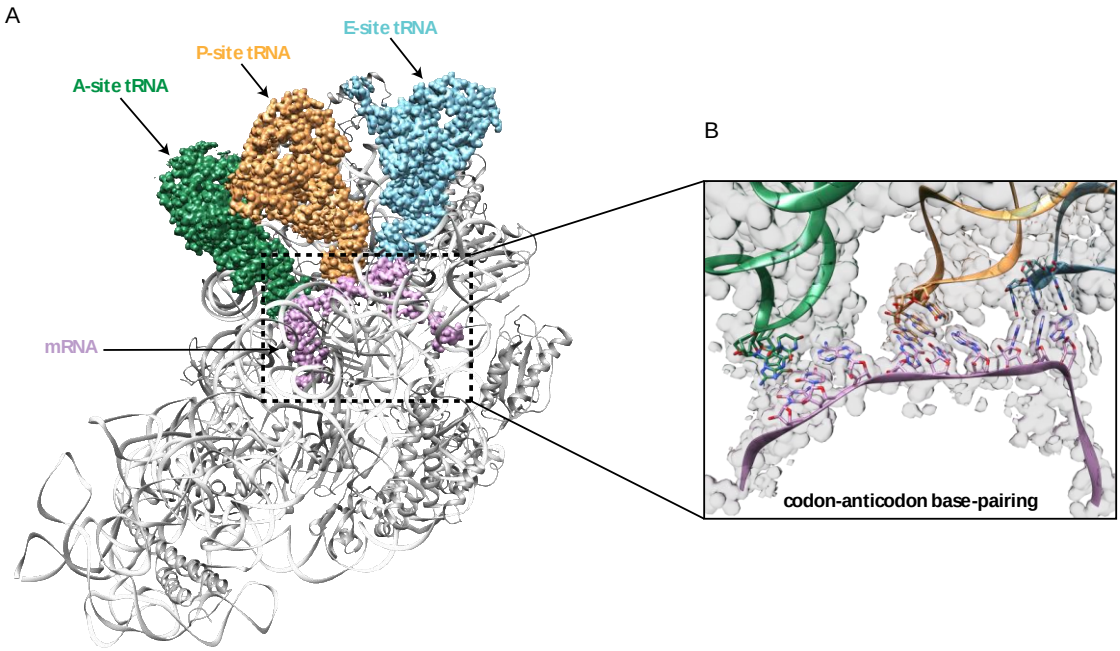

Figure 3: 30S representation during translation. A) 30S subunit bound to a mRNA (pink) and three tRNA in the A (green), P (orange) and E (cyan) sites. The 16S and proteins are represented in light grey. B) Focus on the codon–anticodon recognition (PDB: 6GSK. Rozov et al., 2010).

1.2.2 The 50S large subunit

E. coli 50S subunit is composed of a 23S rRNA of 2900 nucleotides coded by the *rrl* gene, a 5S rRNA of 120 nucleotides coded by the *rrf* gene and 33 proteins, 15 of them specific for bacteria (Ban et al., 2000). The folding of both 23S and 5S gives life

to a subunit that consists of 6 rRNA domains (Figure 4). In particular, most of the nucleotides forming domain I are involved in the building of protein exit tunnel walls, while domain II is the largest 50S domain and is characterized by the presence of three protrusions. One of them is formed by the helix H42 and H44 binding the ribosomal protein bL12 and interacting with the elongation factors. Domain IV represents most of the interface with the 30S subunit and, for that reason, is not stabilized by many ribosomal proteins. Domain V is involved with the peptidyl transfer activity of the ribosome (Garret and Rodriguez-Fonseca, 1996; Niessen et al., 2000). In addition, one of its regions, formed by helix 75, represents the binding site for uL1 essential in controlling tRNA release from the E site. Domain VI is the smallest 23S domain and its importance derives from the presence of the sarcin-ricin loop (SRL), essential for the binding of several translation factors (Szewczak and Moore, 1995; Correll et al., 1998; Ban et al., 2000). Finally, the 5S rRNA represents the domain VII of the 50S subunit (Figure 4). As for the small subunit, the 33 ribosomal proteins are dispersed all over the rRNA, and are mostly present on the external surface and absent from the region that faces the 30S subunit. The overall structure and secondary structure elements for the 50S proteins are quite similar to that of the 30S subunit, with long extension penetrating the RNA elements. The primary role of these proteins is, once again, to neutralize the charge repulsion of the rRNA backbone and stabilize the 3D structure of the subunit.

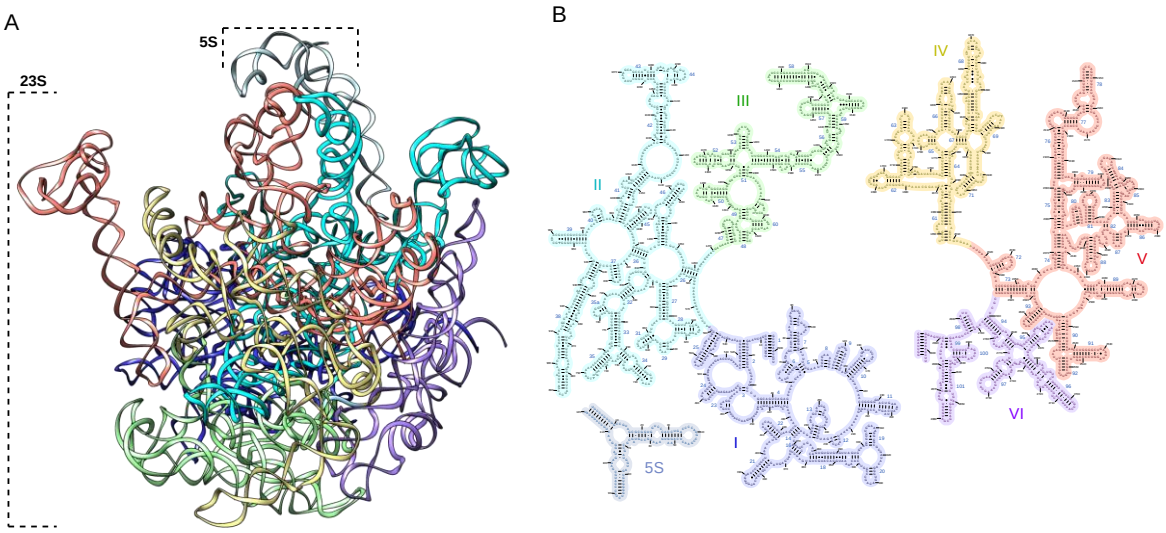

Figure 4: Structure and organization of the 50S subunit 23S and 5S rRNA. A) Three-dimensional folding of the rRNA in which we highlight the six domains and the 5S. Domain I is medium blue, domain II is cyan, domain III is light green, domain IV si khaki, domain V is salmon, domain VI is medium purple, and the 5S is light grgey. B) Secodary structure organization of the rRNA. The color code is the same as for the panel A (Center for molecular biology).

The bottom of the 50S subunit is characterized by the presence of six proteins forming the exit portion of the polypeptide channel, a tunnel where the nascent peptide goes out from the ribosome. The proteins at that surface may play an important role during the protein secretion because they can take contact with membrane elements (Ban et al., 2000). In addition, sequence-specific interaction between these proteins and the nascent polypeptide sequence (effector sequences) are essential for translation regulation. While the 30S ensures the decoding of the information brought by the mRNA, the 50S subunit is responsible of the peptidic transfer, the passage of the nascent peptide from the P/E-site tRNA to the A/P-site tRNA catalyzed by the peptidic transfer center (PTC) (Figure 5).

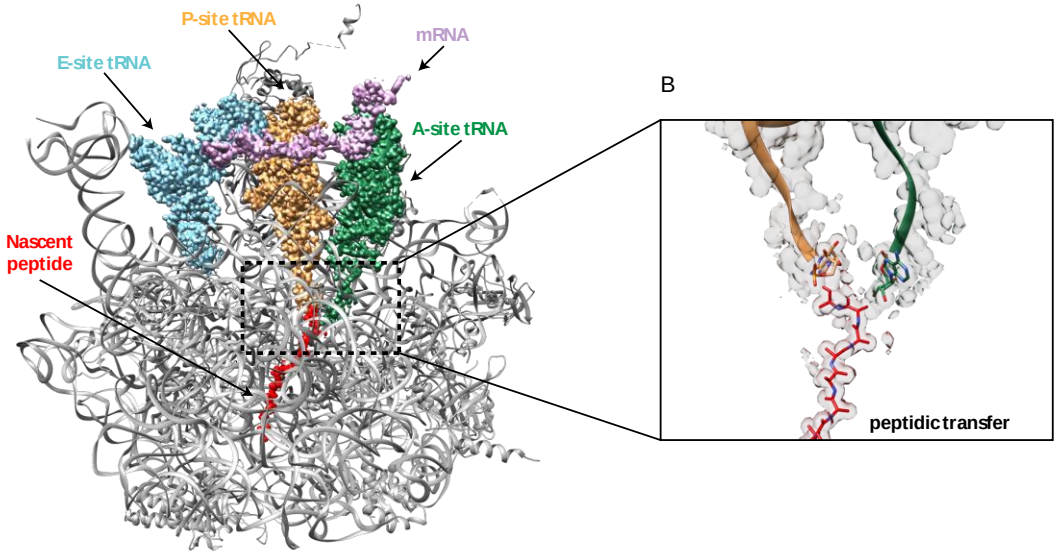

Figure 5: 50S representation during translation. A) 50S subunit bound to three tRNA in the A (green), P (orange) and E (cyan) site, a mRNA (pink) and a short nascent peptide (red). The 23S, 5S and proteins are represented in light grey. B) Focus on the peptidic transfer (PDB: 6GSK. Rozov et al., 2010; 4V5H. Seidelt et al., 2009).

1.2.3 The 70S

The assembly of the large subunit (50S) on the small one (30S) gives life to the complete structure of the ribosome (70S) which, as a whole, represents the largest ribonucleoprotein particle and accomplishes the protein synthesis in all living cells (Maguire and Zimmermann, 2001; Schmeing and Ramakrishnan, 2009). Following its assembly, it is possible to distinguish the formation of three fundamental morphological elements essential to accomplish the translation. These are the three tRNA recognition and binding sites, *i.e.* the A-site (aminoacyl-tRNA), P-site (peptidyl-tRNA) and E-site (exit). Starting from the A site, all the tRNAs will transit within the

ribosome until they are expelled from the E site, in a manner faithful to the information coded inside the mRNA (see 2 The bacterial protein synthesis).

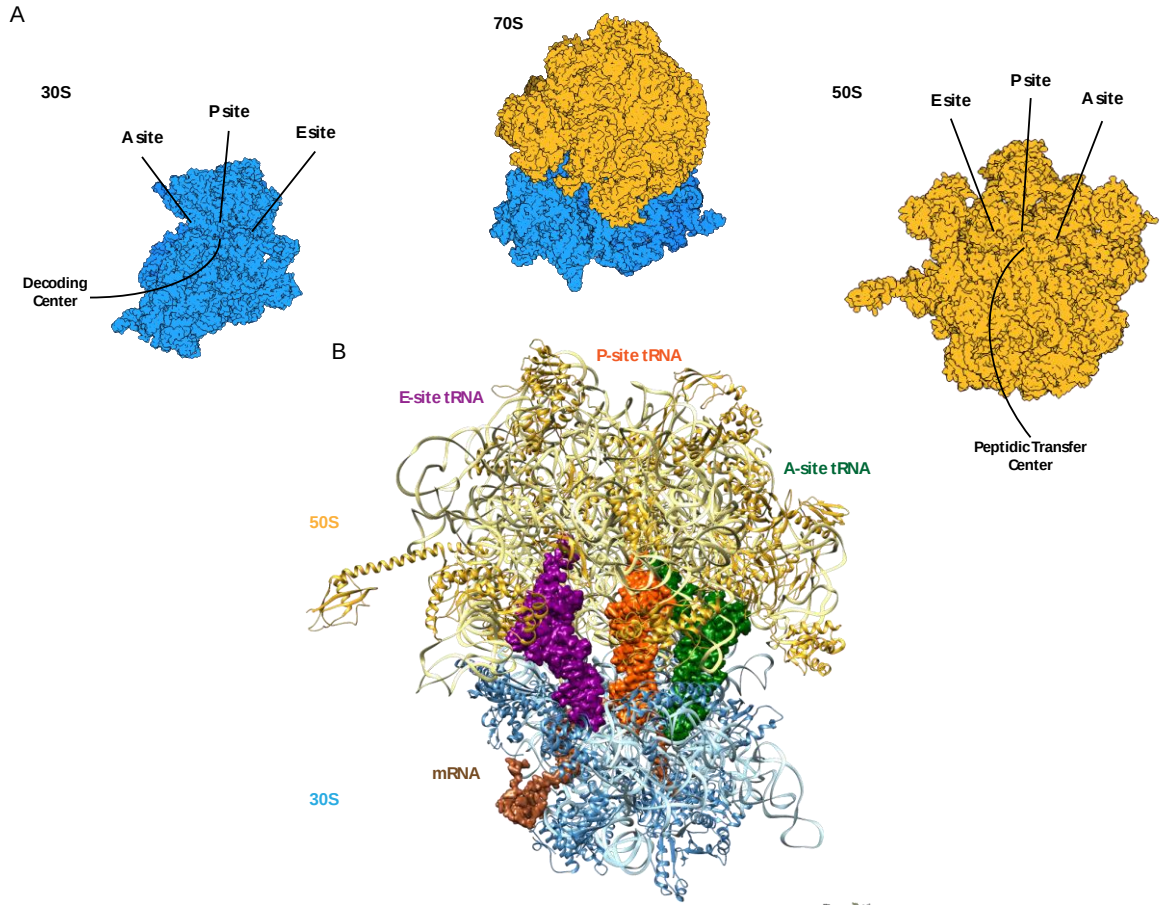

Figure 6: 70S representation. A) Schematic representation of the 30S (left, dodger blue), the 50S (right, goldenrod) and the 70S (middle, both colour). The tRNA's binding sitesand the catalytic sites are highlighted on the two subunits. B) Atomic model of the 70S ribosome with three tRNAs (A-site green, P-site orange, E-site purple) and a mRNA (brown). The 50S rRNAs are in khaki while the large subunit proteins are in golden. The 30S rRNA is in light blue, while the small subunit proteins are in sky blue (PDB: 4V4Y. Yusupova et al., 2009).

The formation of the complete ribonucleoprotein is the result of the assembly of the two subunits which are held together thanks to a series of "bridges" that occur between the two surfaces of contact. These contacts can rearrange or break during the different conformational changes that the ribosome undergoes during translation (Yusupov et al., 2001; Valle et al., 2003; Spahn et al., 2004; Schuwirth et al., 2005). The intersubunit bridges occur mostly between rRNA helices, thus they are mostly rRNA-rRNA contacts. However, in some cases, these interactions also involve rRNA-protein or protein-protein contacts (Liu and Fredrick, 2016).

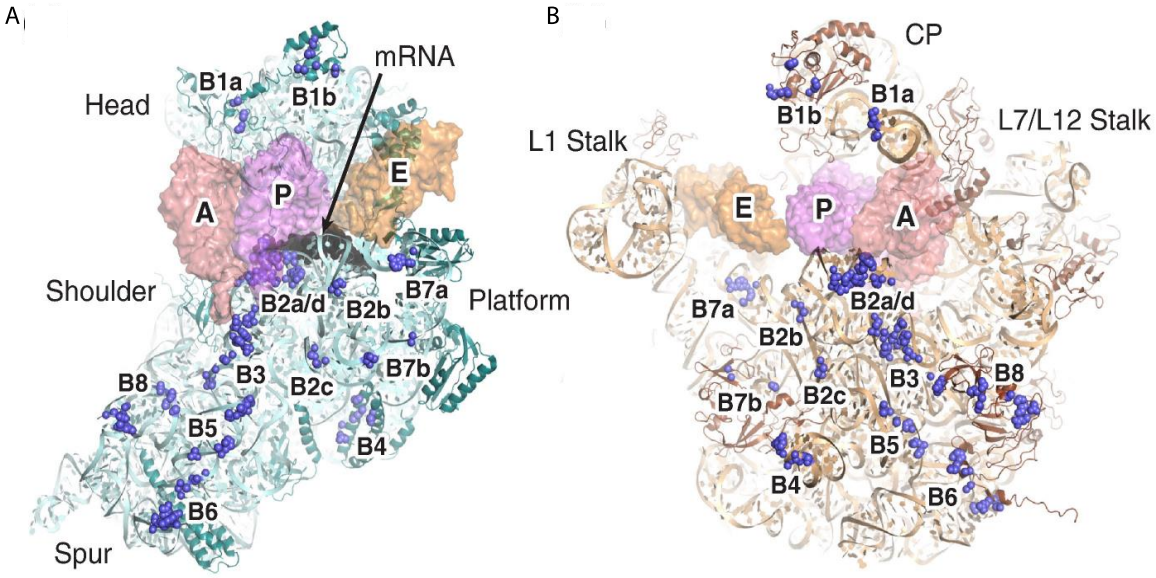

Figure 7: The Ribosome Intersubunit bridges. A) Schematic representation of the contact zones present on the 30S subunit (light blue). B) Schematic representation of the contact zones present on the 50S subunit (gold). In both the structures The A-site tRNA (red), P-site tRNA (pink) and E-site tRNA (orange) are shown on both subunits. The bridges between the two subunits are highlighted in blue (Liu and Fredrick, 2016).

The B1 bridge ensures the connection between the 30S head and the 50S central protuberance through two main points of contact: the B1a and the B1b bridges. The first one involves the uS13 protein and helix H38 of the 23S, while the second one occurs between uS13 and the 50S proteins uL5 and bL31 (Liu and Fredrick, 2016). The B2 bridge is formed by different contacts in a large zone of the 30S platform. In particular, the B2a/d is formed by the 23S helix H69 and several 16S elements, such as the helix h44, the loop of the helix h24 and the loop of the helix h45. Since it is close to the decoding center, its rearrangement during the A-site tRNA codon – anticodon selection is essential to ensure the correct base pairing between the mRNA and the aa-tRNA (Ogle and Ramakrishnan, 2005; Jenner et al., 2010; Satpati et al., 2014; Liu et Friedrick, 2016). The B2b is formed by contacts between the 16S helix h24 and 23S helix H68. This interaction involves also the helix h45 and the helix H71 in the absence of an A-site tRNA (Fischer et al., 2015). The B2c bridge is a tripartite interaction involving the 16S helices h24/h27 and the 23S helix H67. The B3 bridge is formed by the 16S helix h44 and the 23S helix H71 but, sometimes, additional bridge contacts involve also the 50S protein uL14 in presence of Mg^{2+} ions. B4 is based on an rRNA – protein interaction that involves the 23S helix H34 and the 16S protein uS15. The presence of this bridge is essential for optimal subunit

association and translation activity (Komoda et al., 2006). The bridges B5 and B6 both involve the 16S helix h44 that interacts with the 23S helix H62 (bridge B5) and the 50S protein bL9 (bridge B6). The B7 bridge connects the 30S platform to the 23S protuberance. As for B1, we can distinguish two contact zones: B1a and B1b. B1a involves the 16S helix h23 and the 23S helix H68, while B1b is a three-element contact formed by the helices h23/h24 and the 50S protein bL12. Finally, the B8 bridge is formed by the 16S helix h14 and the 50S proteins bL9 and uL14 (Liu and Friedrick, 2016). The bridges described above are, of course, formed at the end of the initiation, during the subunits joining, where some elements placed at their interface undergo several conformational changes. (Harms et al., 2001; Schuwirth et al., 2005; Liu and Friedrick, 2016). The subunits are capable of forming a 70S particle even in absence of initiation factors, in a way that only depends on Mg^{2+} concentrations (Tissieres and Watson, 1958). High Mg^{2+} levels promote subunits association, while low Mg^{2+} concentrations favor their dissociation. Obviously, the bridges undergo several rearrangements, associated with the conformational changes of the ribosome observed during the translation cycle, and are fully disrupted during ribosome recycling.

During translation, the nascent polypeptide chain goes through an exit tunnel that crosses the 50S subunit before emerging from the ribosome. The tunnel length is ~100 Å from the PTC to the exit, while its diameter varies from 28 Å at the exit to 10 Å in its initial part (Nissen et al., 2000). Structurally speacking, most of its surface consists of the 23S domains I to V, except for the proteins uL4, uL22 and uL23 (Nissen et al., 2000; Voss et al., 2006). Since in its narrowest segment the tunnel has a diameter comparable to that of an α-helix, the protein folding occurs mostly at the exit and at the surface of the ribosome. Altought the tunnel is primarily made of rRNA, the presence of hydrophilic groups avoids the interactions that could occur during the passage of the aminoacidic chain (Nissen et al., 2000). Once the nascent chain emerges from the ribosome exit channel, the ribosome itself, molecular chaperons and other factors assist the folding in a correct tertiari structure essential for its function.

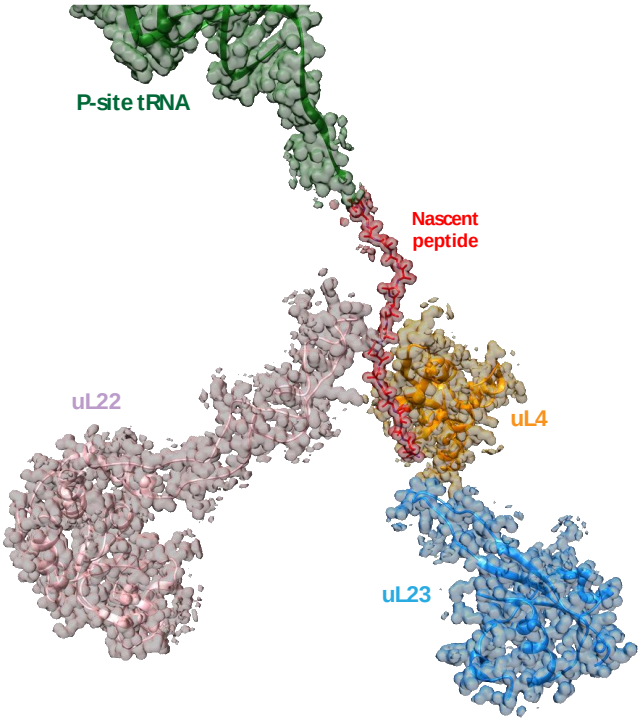

Figure 8: Proteins involved in the formation of the 50S exit channel. The P-site tRNA is green, the nascent peptide is red, uL4 orange, uL22 pink and uL23 blue.

When the polypeptide chain emerges from the exit channel, the Trigger Factor (TF) anchors the ribosome through the uL23 protein and starts the protein folding based on the amino acids sequence (Rodnina and Wintermayer, 2016). While most of the proteins do not need any further interventions by other chaperones, about 30% of the other cytosolic proteins need the assistance of HSP70 (DnaK) and HSP60 (GroEL), two ATP-dependent chaperons, to complete their folding (Kramer et al., 2009; Castanié-Cornet et al., 2014). Polypeptides of membrane proteins bringing specific signals are recognized by the signal recognition particle (SRP) as they exit the ribosome and are targeted to the cytoplasmatic membrane (Lurikin and Sinning, 2004; Bornemann et al., 2014). In bacteria, since the first amino acid incorporated in the nascent peptide during translation is an N-formyl methionine, the enzymes peptide deformylase (PDF) and methionine aminopeptidase (MAP) provide the deformylation and the removal of the first methionine, respectively. These modifications are important for the stability and function of many proteins (Bornemann et al., 2014).

2 The bacterial protein synthesis

The whole process is highly dynamic but, to simplify its narration, it can be divided in four main phases: **initiation**, **elongation**, **termination** and **ribosome recycling**. All along this process, the ribosome forms several transient complexes with different factors, bringing life to stable intermediates that can reveal how this machine navigates through the different conformations.

2.1 Translation initiation

Translation initiation represents the rate-limiting step of protein production. This phase results in the assembly of the 70S initiation complex (70S*IC)* during which the mRNA start codon is placed into the 30S P site, allowing the correct positioning of the $tRNA^{fMet}$ CAU anticodon directly into the P site and the assembly of the two ribosomal subunits. In the subsequent steps, all the other codon – anticodon base pairings take place in the A site.

2.1.1 The mRNA translation initiation regions (TIRs)

Apart from the ribosomal subunits, a key role in translation initiation is played by the mRNA translation initiation region (TIR), a 5' end region that contains several elements essential for the formation of the 30S initiation complex 30S*IC*.

One of these elements is the Shine-Dalgarno (SD) sequence (or ribosome binding site (RBS)), a region placed several nucleotides upstream of the start codon, and which is complementary to the 3' end of the 16S (Shine and Dalgarno, 1974). The base pairing between the SD and the anti-SD of the 16S forms a duplex that confers to the nascent 30S*IC* an increased chance to bring the mRNA start codon into the P site and to give life to productive 30S – mRNA complexes (Gualerzi and Pon, 2015). However, a large number of transcripts lack a 5' UTR region in their TIRs and, by consequence, an SD element. They are named leaderless mRNAs. In that case, other mechanisms ensure the 30S*IC* formation, such as the intervention of the bS1 protein.

The next important characteristic is the AUG codon, the most common start codon in *E. coli* (present in the 83% of the mRNAs) that codes for a methionine (Hecht et al., 2017). The GUG (14%) and UUG (3%) codons can also alternatively fulfil this function (Hecht et al., 2017). These three codons are characterized by the presence

of a central uracyl, which is therefore a discriminating feature in initiation codon recognition (Gualerzi et Pon, 2015). The AUG codon is not only important for the translation initiation of canonical mRNAs but also essential for the translation of leaderless mRNAs (Brock et al., 2008).

2.1.2 Formation of the initiation complex

As aforementioned, in bacteria, the translation initiation starts with the formation of the 30S*IC* when the AUG start codon joins the 30S P site and is by consequence recognized by the complementary anticodon of the $tRNA^{fMet}$. In addition, three important proteins called initiation factors (IFs) IF1, IF2 and IF3 intervene during this step to ensure the fidelity of the process. So far three different initiation mechanisms have been described (Figure 9) (Yamamoto et al., 2016).

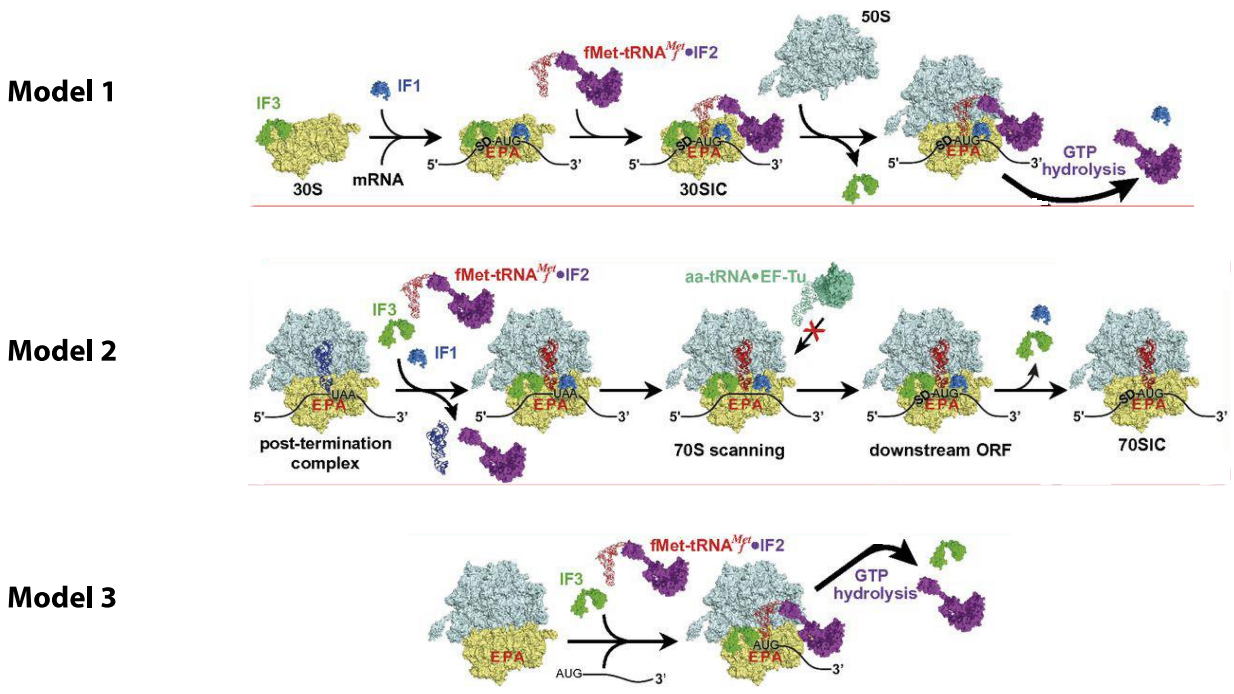

Figure 9: Scheme representing the three different model for the translation initiation, from Yamamoto et al., 2016. 30S is in yellow, 50S is in light blue, IF1 is in blue, IF2 is in purple, IF3 is in green, tRNA is in pink. Model 1: translation starts with the formation of the 30SIC. Model 2: translation starts at the end of the same process, with the shifting of the start codon into P site once again. Model 3: translation initiaition for mRNA macking of SD sequence.

- ***Model 1:*** IF3 binds the 30S E site, avoiding the binding of the 50S (Figure 9, Model 1). At the same time, the mRNA binds the 30S, placing the start codon into the P site while IF1 occupies the A site in order to hamper the binding of

aminoacylated tRNA. The binding of the IF2•GTP-tRNA^{fMet} tripartite complex allows the initiator tRNA anticodon to pair with the P-site start codon, resulting in the 30S*IC*. IF3 is then released, allowing the binding of the 50S subunit and the formation of the so-called 70S initiation complex (70S*IC*). After GTP hydrolysis, IF1 leaves the 70S*IC* and is followed by IF2 roughly 60ms later (Caban et al., 2017; Keledhonkar et al. 2020). This results in the formation of the elongation competent 70S (70SEC) with the mRNA and initiator tRNA properly positioned.

- ***Model 2:*** this second mechanism is called "70S-scanning initiation" (Figure 9, Model 2). Once the 70S has finished the reading of an open reading frame (ORF), the two subunits remain associated. IF1, IF2•GTP-tRNA^{fMet} and IF3 arrive on the ribosome. IF1 and IF2 occupy the A and E sites respectively and prevent the entrance of tRNAs. This allows the ribosome to scan the mRNA until a new start codon is positioned within the P site. IF1 and IF3 then leave the ribosome, the tRNA^{fMet} recognizes the START codon allowing the release of IF2 and a new 70*IC* is formed (Yamamoto et al., 2016).
- ***Model 3:*** this model is proposed for the leaderless mRNAs (Figure 9, Model 3) (Moll et al., 2004; Udagawa et al., 2004). In this case the initiation uses already assembled 70S. However, bS1 and uS2 are not required for mRNA recruitment and binding. IF3 and IF2•GTP-tRNA^{fMet} are always present and play the same role as during the canonical initiation, but IF1 is dispensable as it can interfere with the initiation in these conditions (Moll et al., 2004; Udagawa et al., 2004).

In this scenario, regardless of the model in which the process takes place, the tRNA^{fMet} anticodon will be paired to the start codon within the P site. At this point elongation can start.

2.2 Translation elongation

During translation elongation, a series of fundamental reactions take place and are repeated cyclically. These are, in order, the decoding, the peptide bond formation and the translocation. Elongation starts when the ORF's second codon, in the ribosome A site, is sampled by an aa-tRNA and ends when the ribosome reaches a stop codon. During this phase, the sequential addition of amino acids (carried by their respective tRNAs) to the nascent polypeptide chain occurs. The entire mechanism is

assisted by the elongation factor thermo unstable (EF-Tu) and the elongation factor G (EF-G).

2.2.1 The decoding

The decoding consists of the ability of the entire machinery to translate the information brought by the mRNA in the form of codons in a nascent polypeptide chain. This process occurs in the A site where the ribosome selects the correct tRNA based on the ability of its anticodon to form base pairs with the mRNA codon (Figure 10).

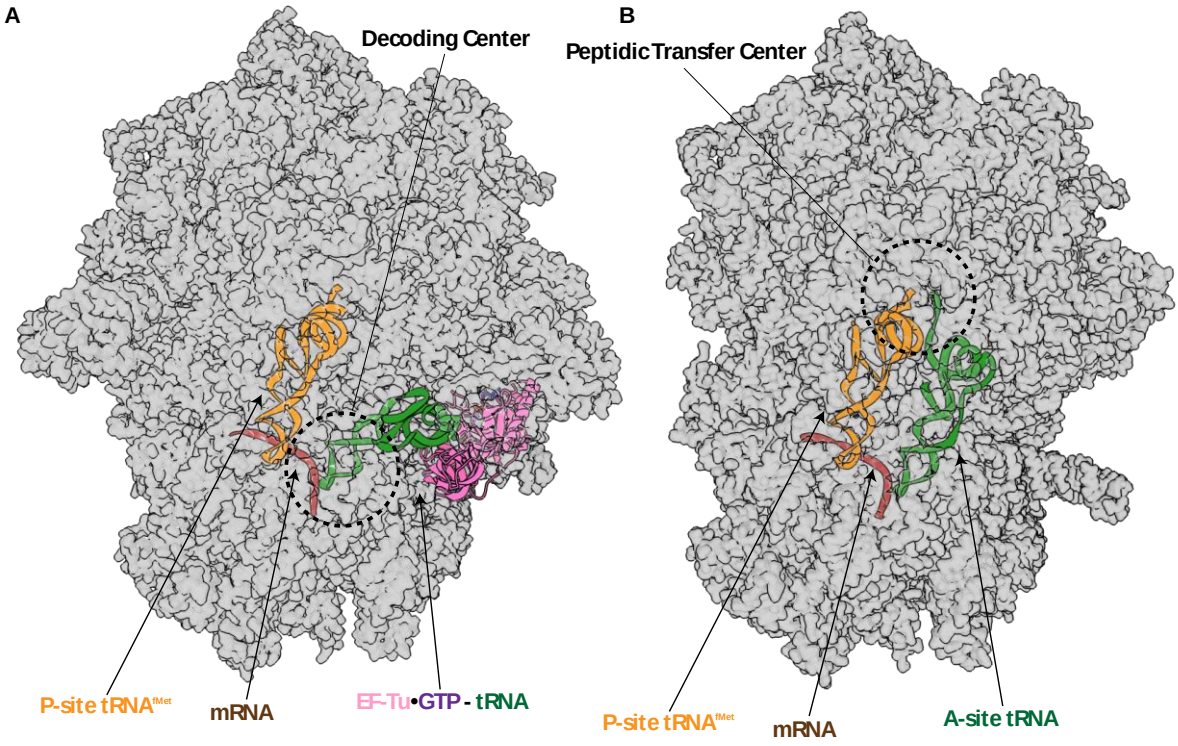

Figure 10: Representation of the pre-accommodated (A) and accommodated (B) tRNA in the ribosome A site. P-site tRNA ^{fMet} is orange, the tRNA in the process of being accommodated is green, the mRNA is brown, EF-Tu is pink, the GTP is violet, the 70S density is light grey. PDB: (A) 5WFS, (B) 7K00.

Before the tRNA comes to the ribosome, it needs to be aminoacylated by a specific aminoacyl-tRNA synthetase (aaRS), a ligase that catalyzes the binding of the specific amino acid to the 3' end of the respective tRNA, in a two-step mechanism (Figure 11):

1) In the first step, the aaRS binds the specific amino acid in presence of an ATP molecule. This brings life to an aaRS-amino acid-AMP complex after the release of a pyrophosphate;
2) In the second step, the specific tRNA binds the aaRS-amino acid-AMP complex through a covalent bond with the amino acid. The reaction is catalyzed by releasing the AMP molecule and results in the formation of the aaRS-amino acid-tRNA complex. After that, the aa-tRNA is released (Rajendran et al., 2018).

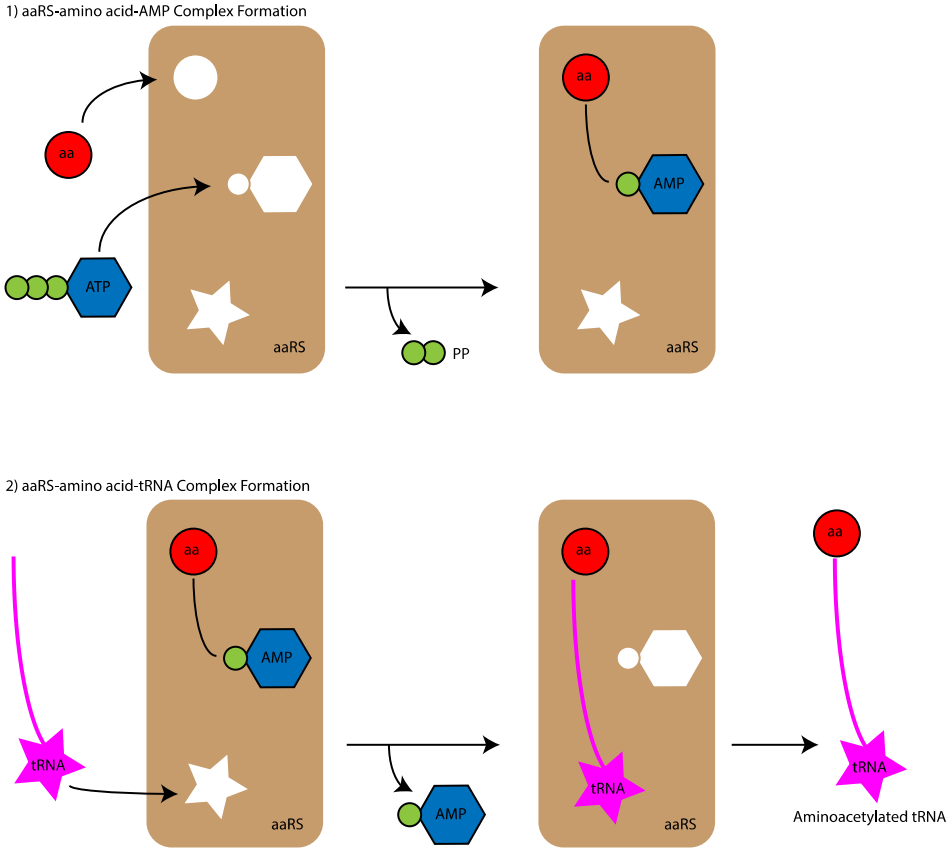

Figure 11: Schematic representation of the aminoacylation process catalyzed by aaRS. aaRS is light brown, the amino acid is red, the ATP/AMP is in blue and light green, pyrophospate is light green, the tRNA is magenta.

Once the ester bond between the tRNA universally conserved 3'-CCA sequence and the carboxylic acid moiety of the corresponding amino acid is formed, the aminoacylated tRNA is taken in charge by EF-Tu to form a ternary complex aa-tRNA-EF-Tu•GTP ready to bind the ribosome. The initial phase of tRNA selection and binding to the ribosome is very rapid and independent from the mRNA codon within the A site. The 50S protein bL12 assists the aa-tRNA-EF-Tu•GTP complex

recruitment by interacting with the D-loop of EF-Tu (Wieden et al., 2001; Blanchard et al., 2004; Diaconu et al., 2005). The tRNA is first positioned into the A site in a pre-accommodated conformation to sample the codon-anticodon interaction, the crucial step of translation that links the mRNA genetic information with the amino acid sequence of a protein (Schmeing et al., 2009). The overall process of base pairing is controlled by three universally conserved bases of the 16S rRNA decoding center: G530, A1492 and A1493. These three nucleotides interact with the tRNA only if the Watson-Crick geometry of the codon-anticodon base pairing is correct (Figure 12 A) (Nissen et al., 2001; Ogle et al., 2005; Voorhees and Ramakrishnan, 2013).

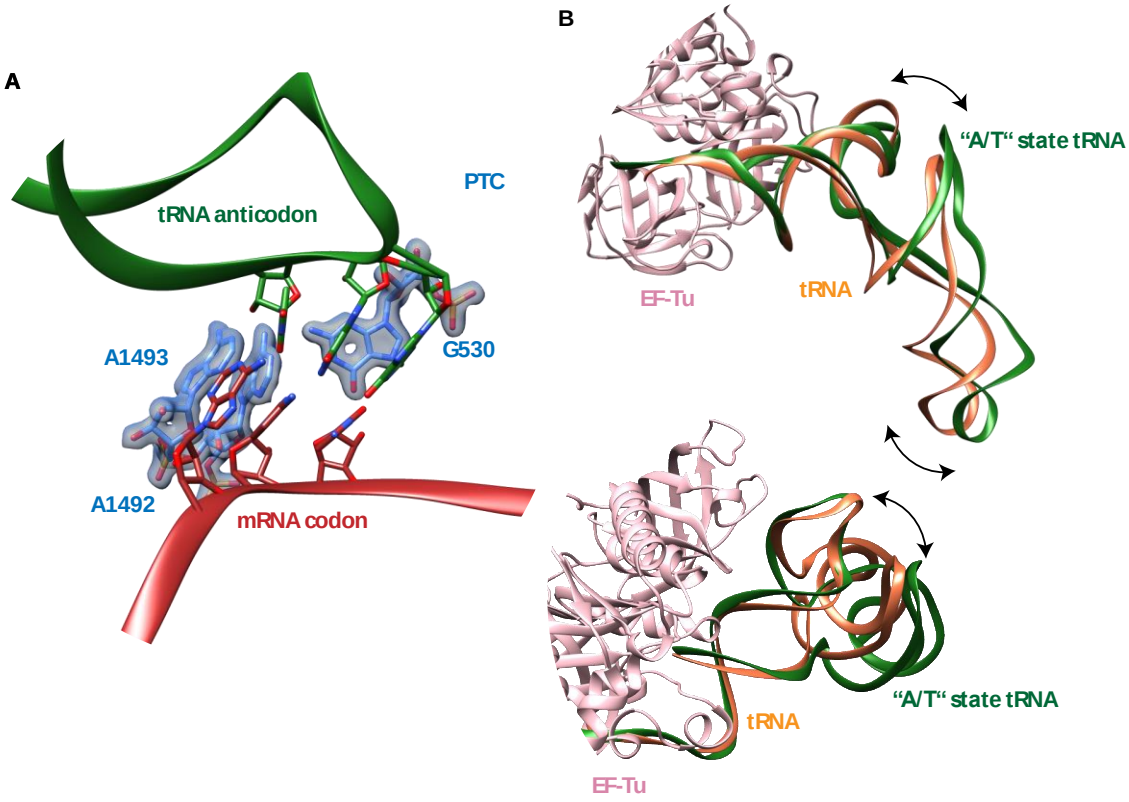

Figure 12: (A) PTC during decoding. The aa-tRNA is green, the mRNa is red, the PTC is blue. (B) "A/T" conformation of the aa-tRNA. EF-Tu is pink, "A/T" state aa-tRNA is green. An accomodated tRNA (orange) is shown for comparison (PDB: 1TTT (Nissen et al., 1995), 4V5G (Schmeing et al., 2009)).

In addition to the codon-anticodon recognition, the tRNA body is also fundamental in decoding. Indeed, during the binding of the ternary complex, the aa-tRNA adopts the so called "A/T" conformation (Figure 12 B) (Stark et al., 1997; Valle et al., 2002). The codon recognition triggers a conformational change in the 30S subunit that brings the shoulder domain in contact with EF-Tu•GTP. The interaction causes a shift of some regions into EF-Tu•GTP domain II, thus triggering the breaking of the interactions between the tRNA 3' end and the elongation factor and a distortion of the aa-tRNA

acceptor arm. By consequence, this process causes rearrangements into the domain I (GTP binding domain) of EF-Tu where, together with the intervention of the sarcin-ricin loop (SRL) of the 30S, the GTP hydrolysis occurs. Following the GTP hydrolysis, EF-Tu undergoes a series of domains rearrangements that disrupt the interaction with both the 30S and the aa-tRNA. This results in the dissociation of the factor from the ribosome and the complete accommodation of the aa-tRNA into the peptidic-transfer center (PTC) of the A site in a conformation called “A/A“ (Berchtold et al., 1993). The GDP is then exchanged with a new GTP and EF-Tu is recycled and can once again bind a aa-tRNA. This process is assisted by the elongation factor thermo stable (EF-Ts) which, by consequence, regulates the relative abundance of EF-Tu in its active form (EF-Tu•GTP) (Burnett et al., 2013).

2.2.2 The peptidyl transfer

The crucial step of protein synthesis is the formation of the peptidic bond between the α-amino group of the aa-tRNA and the aminoacyl ester of the peptidyl tRNA present in the P site. Once the A site is occupied by an aa-tRNA, a series of conformational changes occur in the 23S rRNA, allowing the exposure of the peptidyl tRNA ester for the reaction (Schmeing et al., 2005). Several catalytic mechanisms have been proposed. Biochemical studies suggest that the reaction is catalyzed by entropic effects alone, consistent with the fact that no important effects on the rate of peptide bond formation have been reported for mutations on the 23S. Thus, rRNA groups do not play a direct role in catalysis, although differences have been reported in the mechanism of the ribosome and in solution (Satterthwait and Jencks, 1974; Sievers et al., 2004; Sharma et al., 2005; Seila et al., 2005; Kingery et al., 2008).

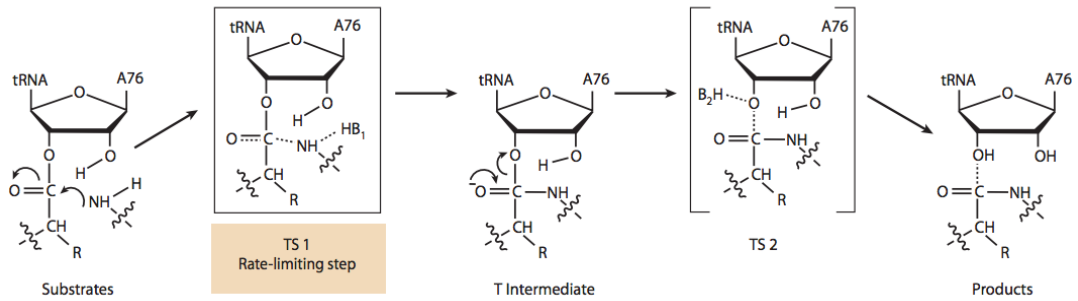

Figure 13: Schematic representation of the peptidic transfer (Voorhees and Ramakrishnan, 2013).

In detail, several analyses suggest that the two-step mechanism brings to the formation of an early transition state (TS1, Figure 13) represented by a zwitterionic tetrahedral intermediate during the rate-limiting step of the reaction, the zwitterionic tetrahedral intermediate is then deprotonated to give life to a second transition state (TS2, Figure 13) before the formation of the final product (Figure 13) (Lang et al, 2008; Rodnina, 2013).

2.2.3 The translocation

After the formation of a new peptide bond, the ribosome hosts a deacetylated tRNA into the P site and a new peptidyl tRNA straddling the A and P sites. For this cycle to repeat, the tRNAs already present within the ribosome need to move one position to free the A site and make it accessible to the next aa-tRNA. This “shifting“ step is called translocation (Figure 14). In particular, the A- and P-site tRNAs move, respectively, to the P and E site while, at the same time, the mRNA moves by one codon. The main actor involved in this tRNAs ballet within the ribosome is the elongation factor G (EF-G) coupled with a GTP molecule (Achenbach and Nierhaus, 2015). The binding of this factor allows the shifting of the two tRNAs and the mRNA anticodon by one position passing through an intermediate state characterized by an A/P tRNA and a P/E tRNA (Semenkov et al., 2000; Pan et al., 2007; Walker et al., 2008; Holtkamp et al., 2014). This hybrid state is accompanied by a series of movements of the ribosome itself to assist the transition from the previous to the next step. More precisely, the EF-G•GTP binding induces a rotation (ratcheted) of the 30S head relative to the 50S subunit of 7° (Figure 15) (Achenbach and Nierhaus, 2015). The fulcrum of this rotation is represented by the B3 bridge between the two subunits (Liu and Fredrick, 2013).

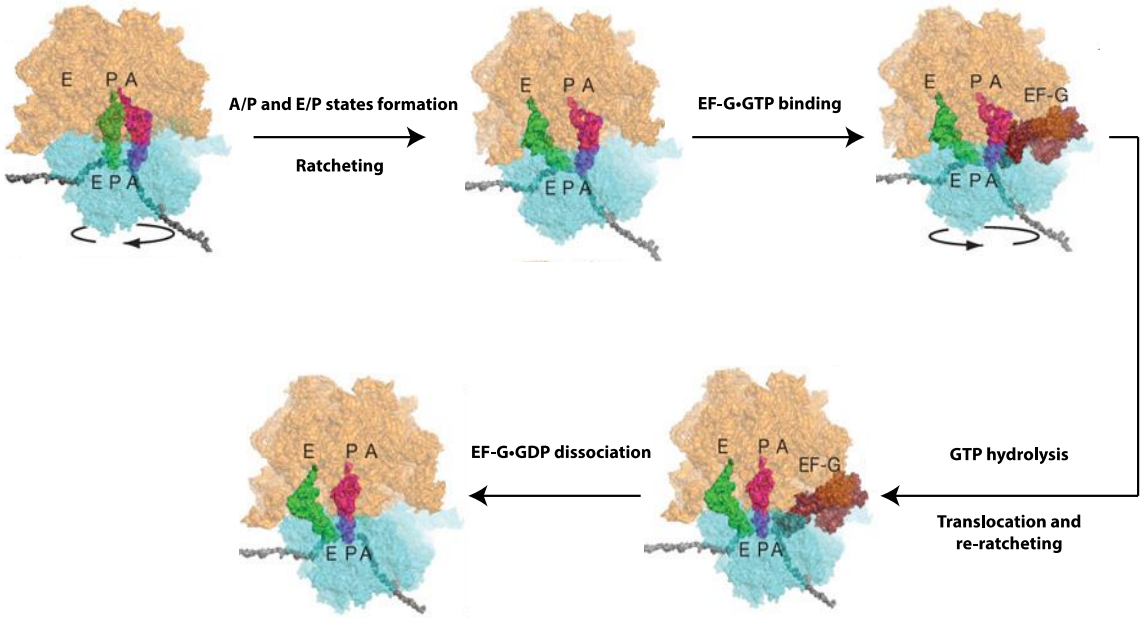

Figure 14: Representation of the translocation process adapted from Schmeing and Ramakrishnan, 2009. After peptidic bond formation the two tRNAs shift in a hybrid state to which EF-G•GTP binds. After GTP hydrolyses, the tRNAs move to the P and E site respectively. The 30S head undergoes a revers ratcheting motion and the EF-G•GDP dissociates from the ribosome (Shmeing and Ramakrishnan, 2009).

The ribosome undergoes this conformational change very quickly and independently of translocation, although it is of fundamental importance in this process (Horan and Noller, 2007; Qin et al., 2014; Sharma et al., 2016). A second movement occurs, at the level of 30S head which, this time, undergoes a counter-clockwise rotation (swivel) with respect to its body of approximately 18°, in the same direction as the tRNAs shifting (Figure 15) (Achenbach and Nierhaus, 2015).

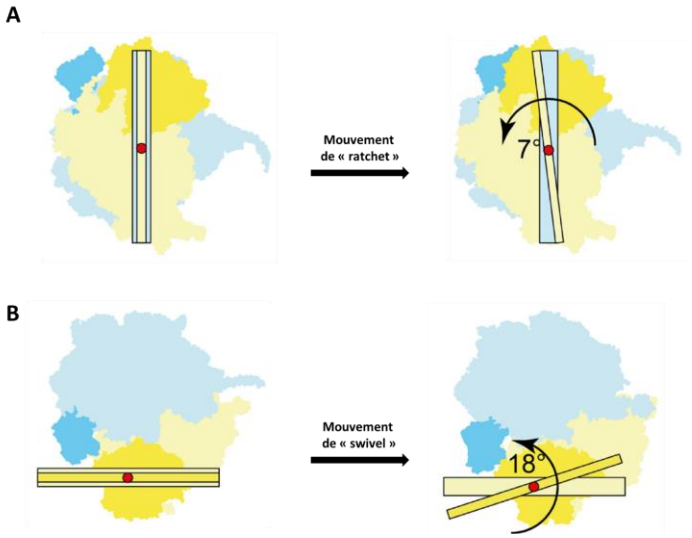

Figure 15: Movement of the 30S head during transolcation adapted from Achenbach and Nierhaus, 2015

These movements are very important during translocation because in the pre-translocation state a natural “constriction“ between the head and the platform of the small subunit could inhibit the tRNA transit from the P to E site (Voorhees and Ramakrishnan, 2013). In parallel with the double rotation of the 30S head, the L1 stalk on the 50S bends by ~ 60 Å towards the E site covering, and stabilizes the tRNA at P/E position (Figure 16) (Noller et al., 2017). At the same time, once EF-G•GTP has joined the ribosome by contacting its binding site on the 50S, the tip of the domain IV takes contact with the codon-anticodon base pairing and favorizes the displacement of the tRNA from the A to the P site, while the deacetylated tRNA is displaced to the E site (Noeller et al., 2017). Finally, after GTP hydrolysis and P_i release, the tRNAs move into the final P and E sites together with a reverse rotation of the head (Noller et al., 2017). The EF-G•GDP is released from the ribosome and, as a result, the ribosome advances by one codon while the A site is freed and available to host a new aa-tRNA.

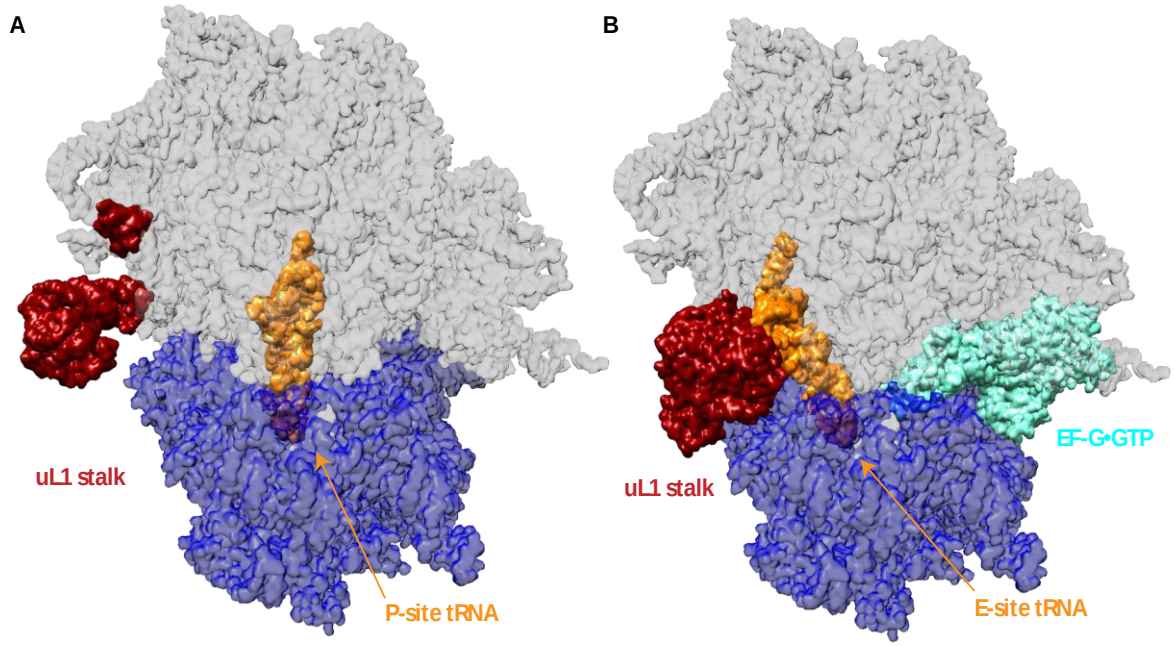

Figure 16: Movement of L1 stalk during translocation (Noeller et al., 2017). 50S is grey, 30S is blue, EF-G•GTP is in aquamarine, tRNA is orange, L1 stalk is red. PDB: 4V9H, 4V9D.

2.3 Translation termination and ribosome recycling

The elongation cycle, and all its sub-steps described above, continues until a so-called “stop“ codon is found within the ribosome A-site, signaling the end of the coding portion of the mRNA transcript. This signal initiates the process of translation termination and ribosome recycling during which the newly synthesised peptide is released while the two ribosomal subunits dissociate to be ready for a new translation cycle (Dunkle and Cate, 2010). The two main factors involved in this process are two class I release factors RF1 and RF2 (Schmeing and Ramakrishnan, 2009).

2.3.1 The “stop“ codon recognition

The genetic code possesses three termination codons: UAA, UAG and UGA (Table 1). These three codons are not recognized by a new entering tRNA but by the factors cited above. In particular, whereas the UAA “stop” codon is recognized by both factors, UAG and UGA are recognized only by RF1 and RF2, respectively (Schmeing and Ramakrishnan, 2009). The ability of these factors to bind the ribosome once the “stop“ codon reaches the A site involves some conserved elements present in both RF1/RF2 and the 16S.

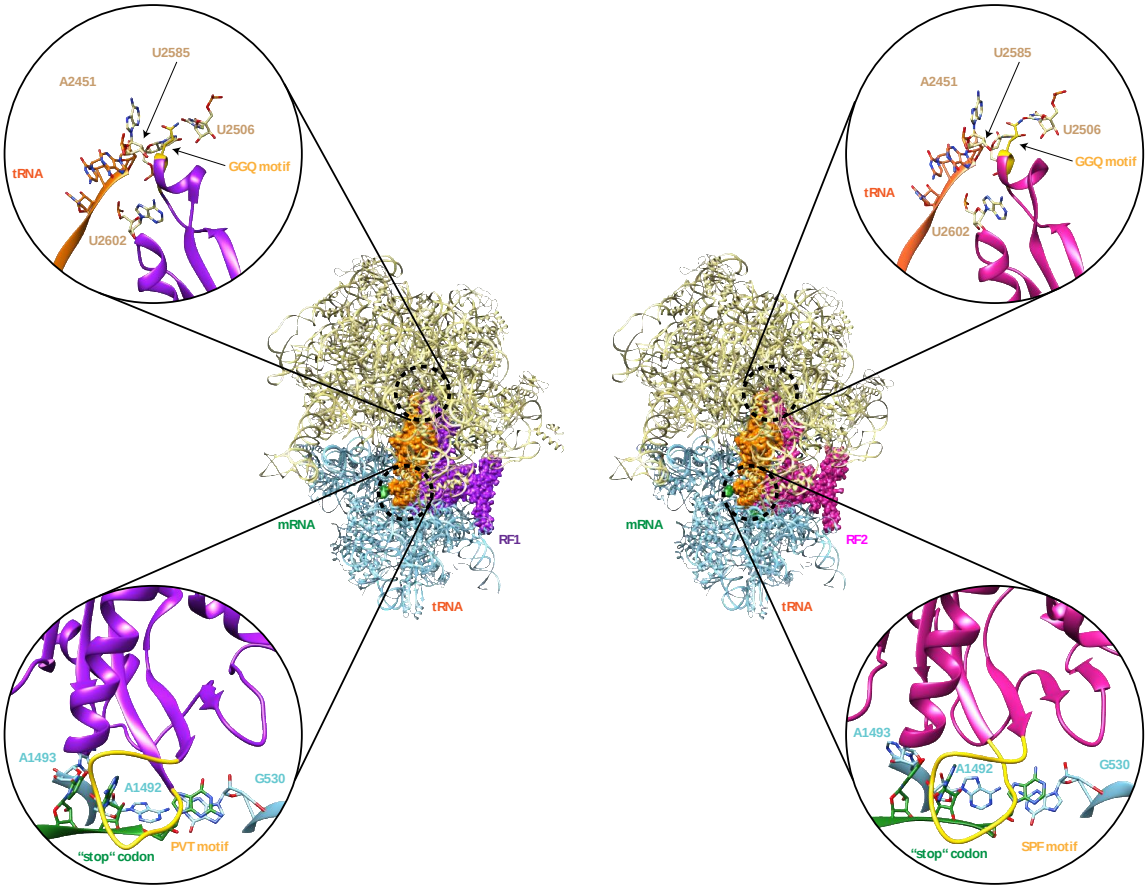

Figure 17: RF1 and RF2 whithin the ribosome. Top panels, close-up on the bindig of the GGQ motif to the PTC. Middle panel, representation of the ribosome in complex with a tRNA and either RF1 (left) or RF2 (right). Bottom panels, close-up close-up on the interaction between the "stop" codon, the 16S and the RF1's PVT (left) or RF2's SPF (right) motifs. 50S is khaki, 30S is sky blue, tRNA is orange, mRNA is green, RF1 is purple, RF2 is magenta, PVT, SPF and GGQ are gold. PDB: 4V7P, 4V67 (Korostelev et al., 2008).

In particular, the decoding center (DC) residues G530, A1492 and A1493 play an important role in the recognition of "stop" codons, undergoing a series of conformational changes and forming important interactions during this step (Figure 17, bottom panels) (Loh and Song, 2010). On the other hand, the tripeptide motifs PVT in RF1 and SPF in RF2 give specificity for "stop" codons UAG and UGA respectively (Figure 17, bottom panels) (Loh and Song, 2010). While the first nucleotide of the "stop" codon (U) is recognized by both RF1 and RF2 thanks to a particular packing of the PVT and SPF motifs, RF1 only establishes hydrogen bonds if an A is present at the second position whereas RF2 can accommodate either an A or a G. The third nucleotide of the "stop" codon position stacks on 16S G530, which favorise A and G rather than C or U (Loh and Song, 2010).

2.3.2 The hydrolysis of the nascent peptide

In parallel, the GGQ motif of RF1/RF2 is positioned into the peptidyl-transfer center (PTC) with a particular conformation only possible thanks to the presence of the two glycine residues (Gly238 and Gly239) (Figure 17, top panels) (Laurbeg et al., 2008; Korostelev et al., 2008; Weixlbaumer et al., 2008). The accommodation of the GGQ motif within the PTC induces a conformational change in U2585 which moves away from the ester bond of peptidyl-tRNA, now exposed to a nucleophilic attack by a molecule of water (Figure 18).

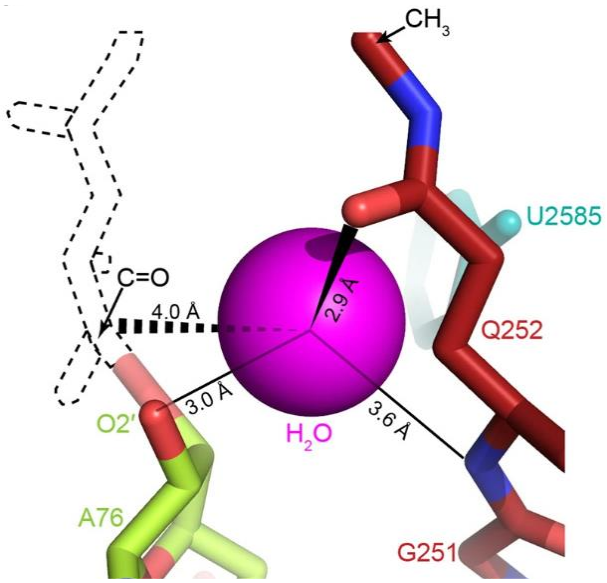

Figure 18: The catalytic pocket of the PTC during translation termination (Adapted from Zeng and Jin, 2018). The water molecule is magenta, tRNA is green, 23S is cyan, RF is red, nascent peptid is with dashed lines.

At the same time, the GGQ Gln240 makes a hydrogen bond through its main chain with the 3'-OH of deacetylated P-site tRNA A76 (Laurbeg et al., 2008; Korostelev, 2011; Zeng and Jin, 2018). The "stop codon" recognition and the nascent peptide hydrolysis are two events extremely cooperative. However, the mechanism under the coordination remains elusive. Several studies propose that the binding of RF1/RF2 to the ribosome causes conformational changes in the 16S and 23S. These rearrangements induce another conformational change in the release factors and the accommodation the GGQ motif into the PTC (Loh and Song, 2010).

2.3.3 RFs liberation and ribosome recycling

In addition to the class I release factors RF1/RF2, another factor, called released factor 3 (RF3) and belonging to class II, intervenes during translation termination (Zavialov et al., 2001, 2002; Pallesen et al., 2013, Koutmou et al., 2014; Peske et al., 2014; Shi and Joseph, 2016). Once the neo-synthesised peptide is released, the RF1/RF2 need to move away from the ribosome, and this task is accomplished by RF3. This class II factor is normally free into the cytoplasm and binds GTP or GDP with the same affinity (Koutmou et al., 2014). In its GDP-binding state, it presents a high affinity for ribosome termination complexes. In this state, RF3 binds the RF1/2-tRNA-70S complex and the GDP moiety is exchanged with a GTP. The 30S head undergoes a ratchet motion that results in the ejection of RF1/2. At this point, RF3 hydrolyses the GTP molecule and leaves the ribosome (Peske et al., 2014).

However, ribosomes still contain tRNA and mRNA. To be reused for the next round of translation, the ribosome needs to be freed and the two subunits dissociated. Subunits dissociation is catalyzed by the ribosome recycling factor (RRF) together with EF-G (Rodnina, 2018). First, RRF binds the A site, stabilizing the ratcheted state of the 30S, with the tRNA in a P/E site conformation (Gao et al., 2005; Dunkle et al., 2011). EF-G•GTP binds to the ribosome, hydrolyses its GTP and pushes on RRF. This disrupts the B2a intersubunit bridge and results in the subunits separation (Schuwirth et al., 2005; Rodnina, 2018). The 30S still carries tRNA and the mRNA with it. IF3 is responsible for tRNA dissociation while the mRNA spontaneously

leaves the small subunits (Rodnina, 2018). The 30S-IF3 complex is then ready to undergo another translation cycle.

All the translation steps are summarized in Figure 19 (Schmeing and Ramakrishnan, 2009).

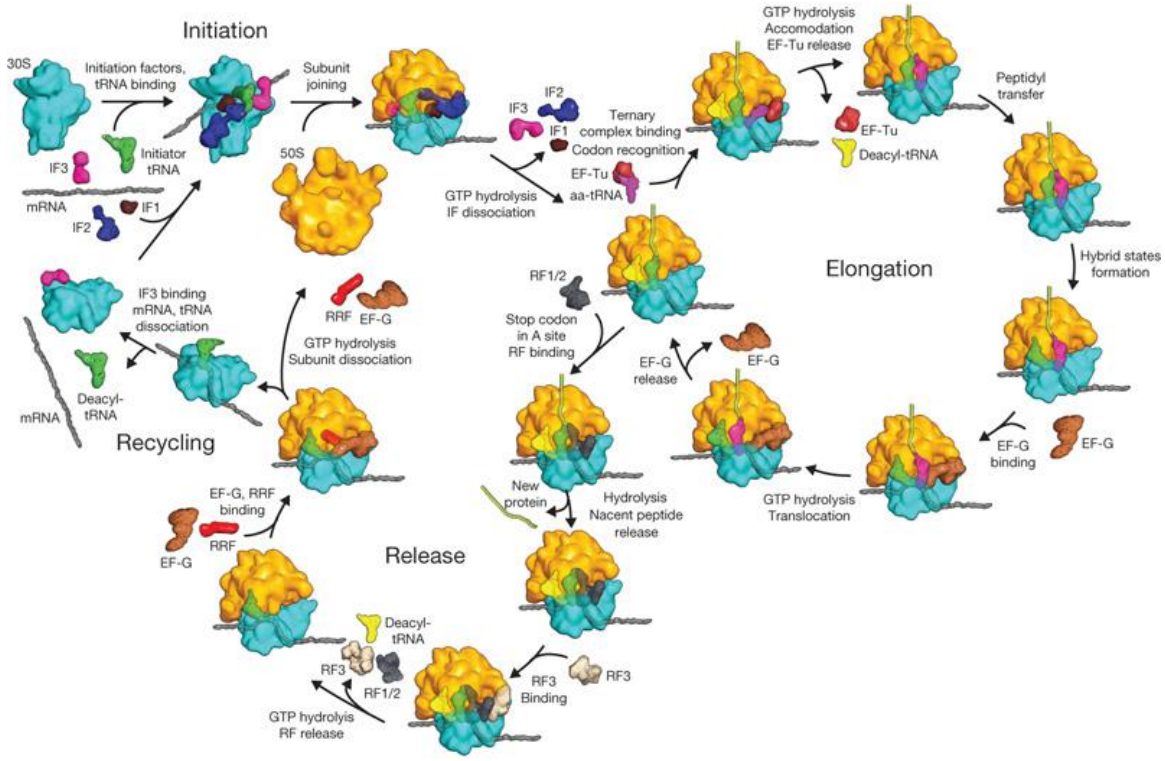

Figure 19: Schematic representation of bacterial translation from Schmeing and Ramakrishnan, 2009.

3 Quality control of bacterial translation

The success of a translation cycle depends on the ribosome's ability to translate, with high fidelity, the information contained in an mRNA into an amino acids chain. As consequence, mRNAs themselves not only have to preserve a high fidelity in the information they carry but, in addition, they have to exhibit high integrity throughout their sequence. However, mRNAs are subjected to constant changes and modifications that could potentially have adverse consequences on translation. mRNAs biogenesis is a very complicated process that involves highly elaborate molecular machines. A misprocessing in mRNA synthesis and maturation can lead to truncated transcripts (Frischmayer et al., 2002; van Hoof et al., 2002). Truncated transcripts often lack a "stop" codon, causing an inability to recruit the release factors RF1/2, release the neo-synthesised peptide, and recycle the subunits. The mRNAs are also susceptible to chemical insults that can interfere with the codon-anticodon

recognition. These situations are very frequent in bacteria, causing the accumulation of non-functional ribosomes and the production of truncated, eventually toxic proteins. Taken together, these phenomena contribute to cell death. As a result, bacteria evolved a series of translation quality control processes to detect errors in protein synthesis and ensure cell survival. The main rescue system present in bacteria is *trans*-translation, mediated by the transfer-messenger RNA (tmRNA) and the small basic protein SmpB (Guyomar, D'Urso et al., 2021). Other rescue mechanisms are based on the intervention of the alternative rescue factors A and B ArfA and ArfB (Keiler, 2015; Himeno et al., 2015; Huter et al., 2017).

3.1 Ribosome stalling causes

Bacteria present a large network of factors dedicated to ribosome rescue, which ensures cell survival despite ribosome stalling. One of the most common causes of ribosome stalling is when ribosomes reach the 3'-end of a so-called "non-stop" mRNA. Another situation where problematic events can occur is when ribosomes pause before reaching the "stop" codon. In this case we refer to "no-go" mRNAs.

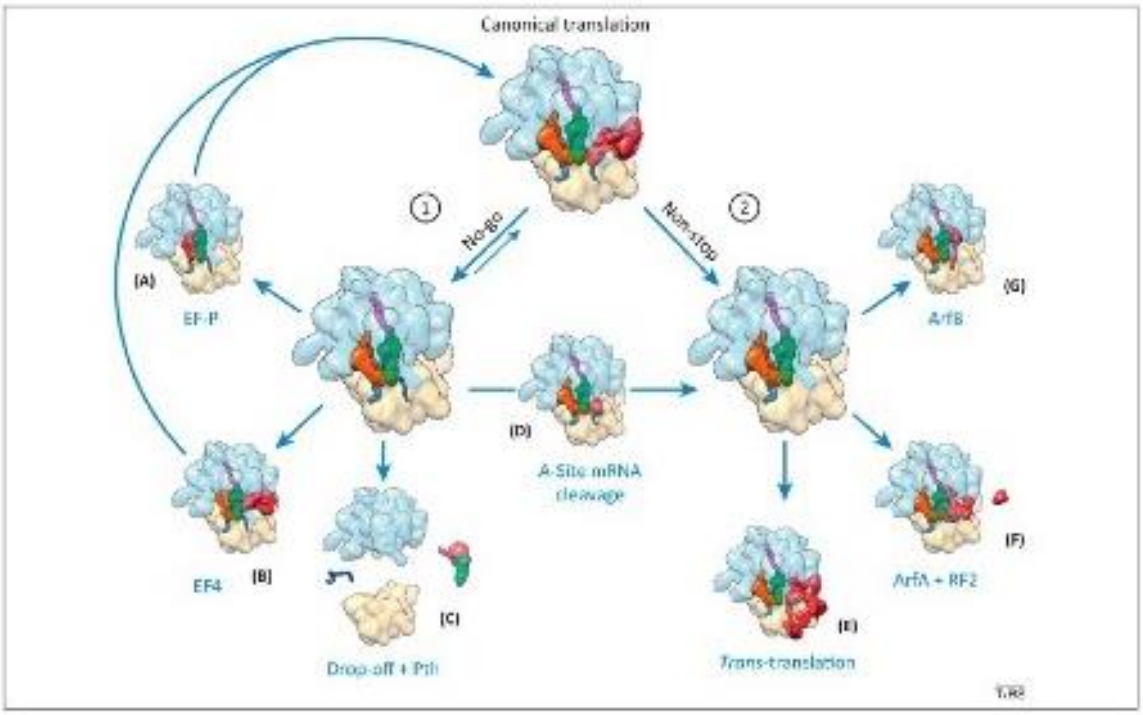

Figure 19: Schematic representation of bacterial rescue systems during ribosome stalling on defective mRNAs (Giudice and Gillet, 2013)

The "non-stop" mRNAs are the product of exonucleolytic degradation of the 3'-end of the transcript or endonucleolytic cleavage by RNases. Both processes induce a

truncation of the mRNA sequence that results in the loss of the “stop” codon and the ribosome stalling at the mRNA 3’-end (Inada, 2020). Other mechanisms can generate truncated mRNAs, such as mutations causing the disappearance of the “stop” codon, oxydative stress, frame-shifting, tRNAs suppressors intervention (Abo et al., 2002a; Ueda et al., 2002; Hayes and Sauer, 2003a; Poulsen et al., 2012). In this case, this first line of defense is represented by the *trans*-translation mechanism that relies on two important partners: the tmRNA and the SmpB protein (Giudice and Gillet, 2013). Alternatively, two alternative rescue factors are present in bacteria based on ArfA (together with RF2) or ArfB (Chadani et al., 2012; Kurita et al., 2014; James et al., 2016; Huter et al., 2017).

The “no-go” mRNAs present a “stop” codon at 3’-end but, on the other hand, they are characterized by roadblocks along their sequence that cause the ribosome to stall within the open reading frame (ORF). The phenomenon can be caused by the presence of secondary structure elements on the mRNA, rare codons, the presence of SD-like sequences, the binding of deacetylated tRNAs, presence of antibiotics (*e.g.* aminoglycosides), specific peptide sequences in the exit tunnel or the lack of some translation factors (Roche and Sauer, 2002; Abo et al., 2002a; Hayes et al., 2002; Wendrich et al., 2002; Li et al., 2008; Li et al., 2012; Guydoh et al., 2017; Ikeuchi et al., 2019). These situations can lead the stalled ribosome to different rescue possibilities. The first solution is the “drop-off“ mechanism based on the spontaneous detachment of the tRNAs. Another possibility is represented by the intervention of the elongation factor 4 (EF4) and the elongation factor P (EF-P) (Qin et al., 2006; Connel et al., 2008; Hummels et al., 2020). EF4 is a conserved bacterial factor that catalyzes the tRNA back-translocation from P and E site to A and P site, respectively (Qin et al., 2006). Then, EF-P enters the ribosome by the E site and binds to a site located between the P and E sites (Blaha et al., 2009). Its N-terminal domain is positioned close to the aminoacyl acceptor stem of a P-site tRNA and, in this way, it favorizes the formation of the peptide bond during elongation, especially on proline-rich sequences (Buskirk and Green, 2013; Ude et al., 2013; Hummels et al., 2020). Finally, the “no-go“ mRNA can also be cleaved in the A site thanks to the activity of the 3’➔5’ exonuclease RNase II, becoming so a “non-stop“ mRNA (Garza-Sanchez et al., 2009).

In the course of this Ph.D. thesis, our efforts were particularly focused on the biochemical and structural study of *trans*-translation, the main bacterial rescue system for ribosome stalling on “non-stop” mRNAs, to obtain a detailed description of the mechanism at a molecular level.

3.2 The *trans*-translation rescue mechanism

The biological importance of rescuing “non-stop” translation complexes is highlighted by the fact that three different mechanisms have evolved in several bacterial species to ensure cell survival (Giudice and Gillet, 2013). Among them, the most important is *trans*-translation whose central components, essential in orchestrating this sophisticated ballet, are the transfer-messenger RNA (tmRNA) and its partner the small basic protein B (SmpB) (Hayes and Keiler, 2010; Barends et al., 2011, Giudice and Gillet, 2013). This complex, together with other translation factors, ensures the ejection of the aberrant mRNA, the tagging of the truncated polypeptide and ribosome recycling. In this paragraph we describe, in the attached reviews, the actors involved in this process, the molecular detail of the mechanism as derived from our recent structural cryo-EM studies, as well as the current and future prospects for developing a new generation of *trans*-translation inhibitors (D’Urso et al., 2022; Campos-Silva et al., 2022).

3.2.1 Review: *"Trans-Translation Is an Appealing Target for the Development of New Antimicrobal Compounds"*

microorganisms

MDPI

Review

Trans-Translation Is an Appealing Target for the Development of New Antimicrobial Compounds

Rodrigo Campos-Silva [1,2], Gaetano D'Urso [1], Olivier Delalande [1], Emmanuel Giudice [1], Alexandre José Macedo [2] and Reynald Gillet [1,*]

[1] CNRS, Institut de Génétique et Développement de Rennes (IGDR) UMR6290, University of Rennes, 35000 Rennes, France; camposrdrg@gmail.com (R.C.-S.); gaetano.durso@univ-rennes1.fr (G.D.); olivier.delalande@univ-rennes1.fr (O.D.); emmanuel.giudice@univ-rennes1.fr (E.G.)

[2] Programa de Pós-Graduação em Ciências Farmacêuticas, Faculdade de Farmácia and Centro de Biotecnologia, Universidade Federal do Rio Grande do Sul, Porto Alegre 90610-000, Brazil; alexandre.macedo@ufrgs.br

* Correspondence: reynald.gillet@univ-rennes1.fr; Tel.: +33-02-2323-4507

Abstract: Because of the ever-increasing multidrug resistance in microorganisms, it is crucial that we find and develop new antibiotics, especially molecules with different targets and mechanisms of action than those of the antibiotics in use today. Translation is a fundamental process that uses a large portion of the cell's energy, and the ribosome is already the target of more than half of the antibiotics in clinical use. However, this process is highly regulated, and its quality control machinery is actively studied as a possible target for new inhibitors. In bacteria, ribosomal stalling is a frequent event that jeopardizes bacterial wellness, and the most severe form occurs when ribosomes stall at the 3′-end of mRNA molecules devoid of a stop codon. *Trans*-translation is the principal and most sophisticated quality control mechanism for solving this problem, which would otherwise result in inefficient or even toxic protein synthesis. It is based on the complex made by tmRNA and SmpB, and because *trans*-translation is absent in eukaryotes, but necessary for bacterial fitness or survival, it is an exciting and realistic target for new antibiotics. Here, we describe the current and future prospects for developing what we hope will be a novel generation of *trans*-translation inhibitors.

Keywords: antibiotics; ribosome; SmpB; tmRNA; *trans*-translation

Citation: Campos-Silva, R.; D'Urso, G.; Delalande, O.; Giudice, E.; Macedo, A.J.; Gillet, R. *Trans*-Translation Is an Appealing Target for the Development of New Antimicrobial Compounds. *Microorganisms* **2022**, *10*, 3. https://doi.org/10.3390/microorganisms10010003

Academic Editor: José Marques Andrade

Received: 24 November 2021
Accepted: 16 December 2021
Published: 21 December 2021

1. Introduction

Protein synthesis, or translation, is a fundamental biological process that occurs on ribonucleoprotein nanomachines named ribosomes. The bacterial ribosome is, therefore, a major antibiotic target, and many types of inhibitors can stop bacterial growth by binding its functional centers and interfering with the ribosome's ability to synthesize proteins [1]. However, bacteria have evolved a wide set of mechanisms to resist the inhibitory effect of antibiotics, including those that target the ribosome. Indeed, resistance mechanisms have been identified for nearly every antibiotic currently in clinical use. Combined with the fact that pharmaceutical companies have not developed more than a few antibiotics recently, infections that are treatable now will probably, once again, become life threatening [2].

It is generally accepted that among the most important bacteria to target, those in the ESKAPE pathogens group (*Enterococcus faecium*, *Staphylococcus aureus*, *Klebsiella pneumoniae*, *Acinetobacter baumannii*, *Pseudomonas aeruginosa*, and *Enterobacter* spp.) are of enormous interest when it comes to drug discovery [3,4]. They are the leading cause of nosocomial infections throughout the world, and most are multidrug-resistant isolates [5]. The World Health Organization (WHO) regularly issues global reports on antimicrobial resistance (AMR) surveillance [6], and the topic has ranked in the top 10 global health issues over the past few years [4,7].

To combat this crisis, we need new antibiotics, and, most importantly, we need new classes of antibiotics with novel mechanisms of action [8]. To do this, we must first identify

new molecular processes that can be targeted. Ideally, these should be conserved among pathogenic bacteria; indispensable to the survival, or at least to the fitness, of the bacteria; sufficiently specific, so that they can distinguish between bacterial species and minimize microbiotal damage; not targeted by current antibiotics; absent in eukaryotes to limit toxicity. In fact, *trans*-translation, the primary quality control mechanism for rescuing stalled ribosomes in bacteria, appears to be a perfect candidate, allowing us to target this key cellular process in a totally new way. Here, we discuss the potential of targeting this pathway with novel antimicrobial compounds.

2. Ribosomal Stalling: From No-Go to Non-Stop

Several phenomena can cause the production of aberrant mRNA molecules that lead to the accumulation of stalled ribosomes in bacteria. The most frequently observed are spontaneous mutations in their corresponding genes, as well as transcription defects after the RNA polymerase prematurely terminates transcription, or does not correctly transcribe the stop codon [9]. Other phenomena include mRNA degradation, caused by either endo- or 3′–5′ exo-ribonucleases, or by environmental stresses that result in chemical and physical damage [10]. "Non-stop" situations (readthrough) can also occur when a canonical stop codon is translated in the presence of non-sense suppressor tRNA [11,12], aberrant frameshifts [13], or translational error-inducing drugs [14]. In bacteria, translation initiation mainly relies on the binding of the ribosomal binding site, the Shine–Dalgarno (SD) sequence to the 3′-end of 16S ribosomal RNA. This, therefore, means that translation can start before transcription is actually complete, and that non-stop events, such as degradation, can occur both before translation starts or while the ribosome advances along the mRNA [15]. It must be noted that another type of defective translation event can also appear during certain stressful conditions (e.g., starvation), which, during translation, slow or stop ribosomes upstream from the stop codon. Due to the presence of a stop codon, this situation is called "no-go" instead of "non-stop." Even though this process could eventually be reversed, it is problematic if it occurs for too long, as endonucleases, such as RelE (the toxin component of the type II RelE–RelB toxin–antitoxin system), will cut the mRNA within the ribosomal A site to facilitate tmRNA-mediated rescue, and conserve the energy and nutrients being used to combat stress [16]. The "no-go" then becomes "non-stop," and triggers the same quality control mechanisms for ribosomal release. In all of these cases, the rescue of non-stop ribosomes is essential in most or all bacteria [17], suggesting that interference with non-stop quality control mechanisms is surely a promising antibiotic development path.

3. *Trans*-Translation Components Are Major Targets for Interference

Despite the recent discovery of several back-up systems (see [18], for a complete review), *trans*-translation is the principal and most sophisticated quality control mechanism for avoiding inefficient protein synthesis on stalled non-stop bacterial ribosomes. It mainly relies on the complex between tmRNA and SmpB, the two main actors in the process.

3.1. Transfer-Messenger RNA (tmRNA)

Having both transfer and messenger RNA functions, tmRNAs are chimeric RNA molecules that are typically 260 to 420 nucleotides in length (363 nts in *Escherichia coli*). The *ssrA* gene, which encodes tmRNA, has been found in nearly all bacterial genomes [19]. tmRNA is always first transcribed as a precursor, and it is subsequently processed at its CCA 5′- and 3′-ends [20–23]. The number of tmRNA molecules per cell has been estimated to be 500–700, roughly 5% of the total number of ribosomes, as estimated from the ratio of tmRNA-to-5S ribosomal RNA [24,25]. As with classical tRNA, the T-loop undergoes some base modifications, with the TrmA enzyme catalyzing 5-methyluridine and TruB enabling pseudouridine production [26,27]. The classic mature tmRNA is composed of a tRNA-like domain (TLD), a messenger-like domain (MLD), and a large, halo-shaped pseudoknot (PK) ring (Figure 1).

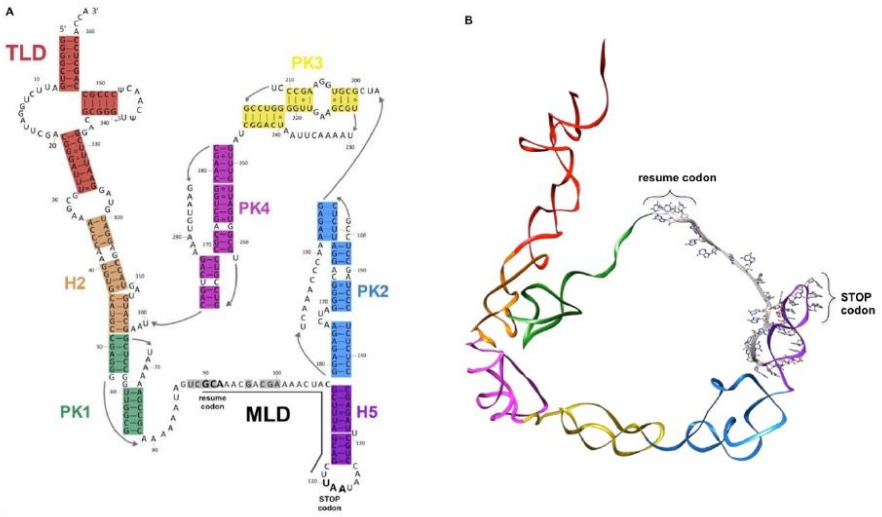

Figure 1. tmRNA. (**A**) Organization of the secondary structure of *Escherichia coli* tmRNA. The internal open reading frame is underlined. (**B**) 3D structure of the *E. coli* tmRNA molecule. In both panels, the tRNA-like domain (TLD, red) is followed by helix H2 (orange). The pseudoknot ring is composed of PK1 (dark green), PK2 (steel blue), PK3 (yellow), PK4 (magenta), helix H5 (purple), and the mRNA-like domain (MLD, grey). The resume and stop codons are indicated.

The TLD portion plays the same role as in classical tRNA; the acceptor stem is always recognized and aminoacylated by alanine tRNA synthetase (AlaRS) after recognition of a G3:U base pair, a motif also present in canonical $tRNA^{Ala}$ [28–30]. The domain displays a classical T-loop, and a small D-loop without a stem. It is also devoid of an anticodon loop, since no codon will need to be recognized within the vacant decoding site of a stalled ribosome [20,26,31]. In fact, this ostensible problem is overcome by SmpB; when interacting with the TLD region, it mimics codon–anticodon recognition and allows tmRNA to accommodate into the ribosomal A site (see below). The MLD is the RNA portion that contains the internal open reading frame (ORF) of tmRNA, which encodes the aminoacidic sequence A*ANDENYALAA in *E. coli*, with the first A* being carried by the TLD. This sequence is added to the stalled protein during *trans*-translation. The tag sequence displays strong phylogenetic conservation, with the consensus sequence A*AN----ALAA. The final three alanines (AxAA) are crucial, allowing for specific recognition of the tagged protein by proteases. The nature of the RNA sequence upstream from the resume codon allows for the correct placement of the codon into the decoding center. Accordingly, mutations in this region can lead to reading frameshifts or a loss of tmRNA function [32–34]. In fact, the structural elements that precede the resume codon, rather than the sequence itself, are important for the reinitiation of translation [35–39]. Once the ORF is completely translated, the tagged peptide is specifically degraded by several proteases. In addition to this classical single-chain conformation, tmRNA also exists (in alpha-proteobacteria, cyanobacteria, and some beta-proteobacteria lineages) as a two-piece molecule, a formation caused by a circular gene permutation that splits it into two molecules [40,41]. In this case, the TLD, MLD, and PK1 are similar to those of "one-piece" tmRNA, but the loop containing the tag reading frame is broken, and there are fewer pseudoknots [42].

3.2. SmpB

SmpB is a small, basic protein of ~160 amino acids, encoded by the *smpB* gene. In the *E. coli* genome, it is located just upstream from the *ssrA* gene that codes for tmRNA [43]. SmpB binds to tmRNA with high affinity, and is its most important partner during ribosome rescue. In fact, in its absence, tmRNA can no longer accommodate its TLD portion into the vacant A site [44–47]. A comparison between the SmpB proteins in the various ESKAPE bacteria reveals that the six proteins conserve the same fold, but the sequence and length of the C-terminal tail differs, especially in *S. aureus*, *A. baumannii*, and *E. cloacae* (Figure 2).

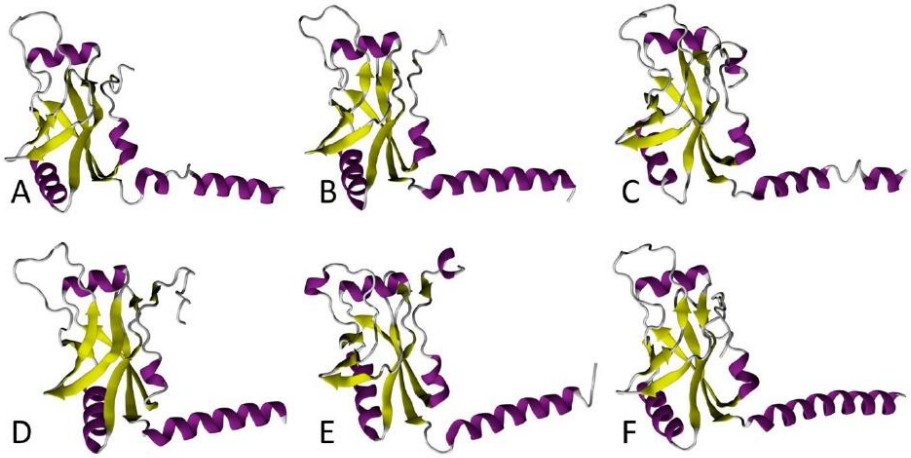

Figure 2. Comparison between 3D models of SmpB in ESKAPE bacteria. In each conformation, the tmRNA TLD contact region is on the left side, and the helix-shaped C-terminal end is shown to the right. The α-helices and β-strands are purple and yellow, respectively. These models of *Enterococcus faecium* (**A**), *Staphylococcus aureus* (**B**), *Klebsiella pneumoniae* (**C**), *Acinetobacter baumannii* (**D**), *Pseudomonas aeruginosa* (**E**), and *Enterobacter cloacae* (**F**) were all computed with the I-TASSER program using *E. coli* SmpB as the structural template (PDB 7ACJ).

The SmpB body is arranged in an oligonucleotide/oligosaccharide binding (OB) domain that folds in a classical fashion into a β-barrel made up of six antiparallel β-strands, which is also typical of other RNA-binding proteins, such as IF1 or bS1 [48–50]. By interacting with the tmRNA TLD, SmpB mimics the missing D-loop and anticodon stem–loop present in classical tRNA [51,52]. The interesting shape assumed by the tmRNA–SmpB complex is important for its entry into the ribosome, as it simulates the codon–anticodon pairing, which then promotes the reactivity of a cognate tRNA. Of the ~160 amino acids, the last 30 C-terminal residues form a tail, which is unstructured in solution, but folds into an α-helix during *trans*-translation. This C-terminal tail is rich in positively charged side-chain residues, essential for contacts with the tmRNA helix H5, as well as for interactions with the negatively charged nucleotides within the decoding site of the 30S ribosomal subunit [53–57]. Indeed, by inserting into the mRNA entry channel, the C-terminal tail is instrumental in selecting the stalled ribosomes with empty mRNA entry channels. The recent cryo-electron microscopy (cryo-EM) structures of *E. coli* tmRNA–SmpB bound to a stalled ribosome [56,57], and the previous crystallographic study of *trans*-translation in *Thermus thermophilus* [58], both show that, just as in canonical translation, the presence of the protein in the decoding center induces reorientation of nucleotides A1492 and A1493 in helix 44. Besides its main RNA-binding site on the TLD, SmpB also has a secondary RNA-binding site, which later binds the MLD to ensure that the resume codon is correctly

positioned in the ribosomal A site [56]. These results confirm the long-predicted importance of SmpB in the *trans*-translation partnership [53,55,59].

4. The Molecular Process of *Trans*-Translation

During *trans*-translation (Figure 3), the tmRNA–SmpB complex is first brought to the ribosome with EF-Tu•GTP. Stalled ribosomes are selected by SmpB, whose C-terminal tail probes the mRNA entrance channel [58]. In this pre-accommodation state, GTP hydrolysis in EF-Tu is favored, as are conformational changes in the ribosomal subunits, and this induces the accommodation of tmRNA–SmpB into the vacant ribosomal A site. After transpeptidation occurs between the stalled incomplete peptide and the tmRNA alanine, a swap between the tmRNA MLD and the non-stop mRNA allows translation to resume. The C-terminal tail of SmpB, which was involved in ribosomal vacant A site recognition, then rotates by 60° to allow the MLD to move into the mRNA channel, as well as to allow ejection of the problematic mRNA. The ribosome translates the MLD until it reaches the stop codon, after which the stalled ribosomes are recycled (see [60], for the structural details of the process). The incomplete peptides are tagged with a signal sequence that results in quick proteolysis. Two AAA+ proteolytic enzymes (ATPases associated with various cellular activities), ClpXP and ClpAP, are able to degrade the tagged proteins by converting ATP hydrolysis energy into mechanical work [61]. FtsH, a hexameric protease anchored to the internal side of the cytoplasmic membrane, is also involved in degrading a small subset of tagged proteins present in the inner membrane [43]. On the other hand, the energy-independent protease Tsp takes over the tmRNA-tagged substrates in the periplasm [62]. The problematic mRNAs are degraded by RNase R [63]. This enzyme, of 92 kDa, belongs to the RNase II superfamily, a group of exoribonucleases able to degrade the RNA molecules in the 3′ → 5′ direction [64], as well as digest various RNA substrates [65,66]. However, the details of how the ribonuclease works with the complex to promptly recognize and handle problematic mRNA is still unclear.

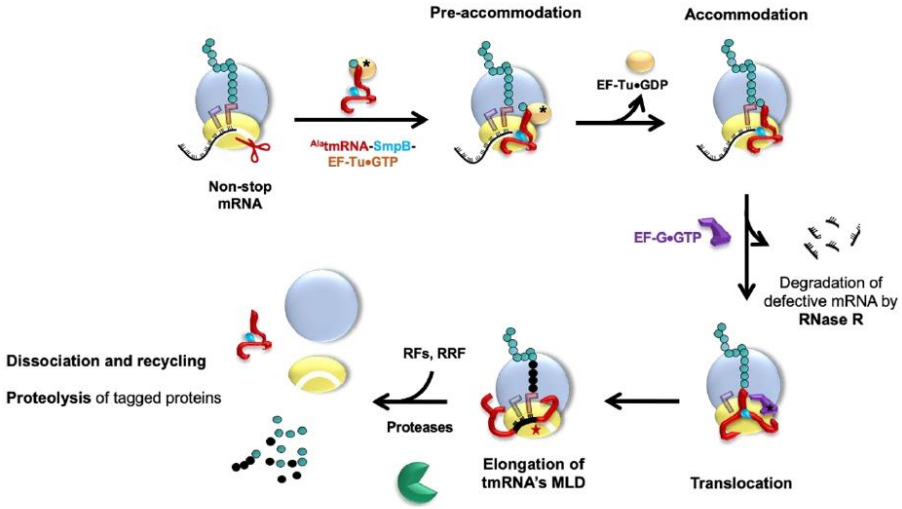

Figure 3. The complete *trans*-translation quality control cycle. **Pre-accommodation state:** tmRNA associates with its partner SmpB to form a complex. Elongation factor EF-Tu•GTP binds to ^{Ala}tmRNA–SmpB, thereby forming the quaternary complex needed to rescue the ribosome stalled on a non-stop mRNA. To recognize these ribosomes, this quaternary complex enters the vacant ribosomal A site. There, SmpB mimics a codon–anticodon pairing while its C-terminal tail inserts into the mRNA channel.

The EF-Tu•GDP is then released after GTP hydrolysis. **Accommodation**: The ^{Ala}tmRNA–SmpB complex is accommodated into the A site, triggering the peptidyl transfer reaction. **Translocation:** Thanks to GTP hydrolysis, EF-G•GTP helps shift the tmRNA–SmpB into the P site. EF-G•GDP is released, and the non-stop mRNA is ejected then degraded by RNase R. **Elongation**: The tmRNA open reading frame is placed into the A site, and new tRNAs arrive at the ribosome to resume translation. **Termination**: The tmRNA–SmpB complex moves towards the E site, and the TLD and SmpB are promptly ejected. Translation of the MLD continues until translation of the tmRNA-encoded tag is terminated at the stop codon with the help of the release factors (RFs). The ribosomal subunits are then dissociated by the ribosome recycling factor (RRF), and the nascent peptide is degraded by ClpXP/ClpAP/FtsH/Tsp proteases. All of the components are now recycled and ready for a new round.

5. *Trans*-Translation as a Target for New Antimicrobial Compounds

Considering that *trans*-translation is absent in eukaryotes, tmRNA–SmpB is an especially promising target for novel antibiotics. Obviously, when it is essential to the survival of pathogenic bacteria, the *trans*-translation machinery is an excellent specific target for use in developing molecules to kill bacteria directly [35,67,68]. When non-lethal, because alternative rescue factors can take over the rescue process, deletion of tmRNA and/or SmpB induces various phenotypes, including loss of virulence or loss of antibiotic tolerance [69–72]. These hypersensitive mutants are not viable in the presence of low doses of some protein synthesis inhibitors (chloramphenicol, lincomycin, spiramycin, tylosin, erythromycin, and spectinomycin) that do not otherwise significantly affect the growth of wild-type cells [69,70,73]. Strikingly, mutants deleted for tmRNA are also more sensitive to antibiotics that do not target translation than wild-type cells, such as inhibitors of cell wall synthesis. This is probably because these drugs stress the bacteria, and this is handled more efficiently when *trans*-translation is active [74]. In all of these cases, it is possible that *trans*-translation inhibitors could be used in combination with already commercialized antibiotics, in order to diminish their minimal inhibitory concentration (MIC) in pathogens, or even to reenable the use of antibiotics no longer used because of resistance. Finally, *trans*-translation is also important for persister survival, as well as tolerance to a variety of antibiotics and stresses [75]. Despite the enormous potential and extensive research into how it works and how this pathway can be targeted for treatments against bacterial infection, there are currently no drugs on the market that use this mechanism. Since this review focuses on *trans*-translation, we will only discuss the possible strategies for specifically impairing that process via targeting tmRNA, SmpB, and/or the ribosome itself. However, we must mention that a global strategy should not overlook the possibility of altering the activity of supporting actors, such as the highly conserved aminoacyl-tRNA synthetase (AlaRS) enzyme, serine protease ClpP, or ribonuclease RNase R.

6. Antibiotics Targeting *Trans*-Translation: Are We There Yet?

6.1. Oxadiazole Compounds

In 2013, based on a luciferase assay, Keiler's group performed a high-throughput screening assay on a library of 663,000 candidate compounds. This led to the identification of 1,3,4-oxadiazole and tetrazol-based compounds as broad-spectrum antibiotics that specifically inhibited the pathway [67]. The most promising compound was the oxadiazole KKL-35 (Figure 4), which displays an antibiotic effect against very distantly related bacteria, suggesting that it may have antibiotic activity against a broad spectrum of species, thus paving the way for the development of the first class of small molecules inhibiting *trans*-translation. How KKL-35 targets *trans*-translation could not be easily identified. KKL-35 binds poorly to tmRNA and SmpB, suggesting that the compound probably affects a later step in the quality control process. Indeed, later biochemical experiments, using *Mycobacterium smegmatis* and *Staphylococcus aureus* cells, highlighted KKL-2098, an analog of KKL-35 that incorporates a photoreactive azide group and a terminal alkyne moiety. KKL-2098 targets helix 89 of 23S rRNA, but in a region not targeted by conventional antibiotics. It

binds to a pocket adjacent to the peptidyl transfer center (PTC), without inhibiting canonical translation [68,76]. More recently, this result was confirmed by cryo-EM (EMDB with the accession code EMD-20121). Despite a rather low occupancy, KKL-2098, cross-linked to a non-stop ribosome, binds near the PTC and significantly alters the conformation of the ribosomal protein bL27. This suggests that 1,3,4-oxadiazoles may, at least in part, inhibit *trans*-translation by preventing tmRNA–SmpB binding at the A site, or by interfering with the translocation of the complex from the A to the P site [77]. In another oxadiazole example, a *Bacillus subtilis* proteomic response library was used to show that KKL-35 and other oxadiazole derivatives induce responses that are similar to those of ionophores, which disturb metal homeostasis, and to other agents, causing oxidative stress responses. This activity could be linked to the importance of *trans*-translation in cells undergoing oxidative stress [78].

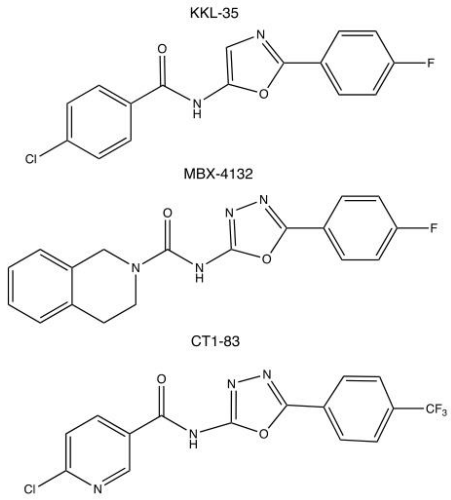

Figure 4. Chemical structures of the experimental oxadiazole compounds KKL-35, MBX-4132, and CT1-83.

In 2017, our group developed a new double-fluorescence reporter system for the simultaneous and specific quantification of bacterial *trans*-translation, as well as proteolysis, in *E. coli* [79]. However, when we tested KKL-35, we did not observe any significant changes in fluorescence levels, despite its strong antibiotic activity, suggesting that *trans*-translation is not its only target, or that the molecule is rapidly metabolized (certainly due to amide bond fragility, see below) and the resulting products of degradation act on another target in *E. coli*. These data were supported by the fact that the inhibitory activity of KKL-35 is similar in both a Δ*arfA* strain (in which *trans*-translation is essential) and in a Δ*ssrA* strain deprived of *trans*-translation. Furthermore, in the human pathogen *Legionella pneumophila* (which causes Legionnaires' disease), the antibiotic activity of KKL-35 is not related to the specific inhibition of *trans*-translation, as it remained active against *L. pneumophila* mutants expressing an alternate ribosome-rescue system and lacking tmRNA [80].

Because the characterization of a new antibiotic target in living cells can be slow, difficult, and treacherous (as shown with KKL-35), we recently constructed a system to detect *trans*-translation in vitro [81]. It is based on an engineered tmRNA variant that reassembles green fluorescent protein (GFP) when *trans*-translation is active. This system is, thus, adapted for the high-throughput screening of chemical compounds by fluorescence, and the limited number of reaction components allows for the direct detection of the relevant targets of *trans*-translation, which are as follows: tmRNA, SmpB, and the ribosome itself.

Based on this simple system, we demonstrated that several 1,3,4-oxadiazole compounds do, indeed, inhibit *trans*-translation in vitro, though only moderately [81,82]. In KKL-35, replacing the benzene of the chloro-aryl moiety with a pyridine group (compound CT1-83, see Figure 4) results in much stronger inhibition of *trans*-translation.

However, because of the rapid hydrolysis of the amide bond of KKL-35 in liver microsomes, it cannot be used in animals. A recent structure–activity relationship (SAR) program thus led to the development of a new uriedo-oxadiazole derivate, MBX-4132 (Figure 4). This compound is much more stable and not significantly less potent, able to inhibit *trans*-translation both in vitro and in vivo, and clears multidrug-resistant *Neisseria gonorrhoeae* in infected mice [77]. While the oxadiazole strategy has been deeply studied, its cellular targets and mode of action remain uncertain, which justifies further investigation, as well as the continued search for other molecules.

6.2. Pyrazinamide

In 2011, it was proposed that pyrazinamide (PZA), a mainstay of anti-tuberculosis combination therapy [83], inhibits *trans*-translation [84]. Using proteomic studies, pyrazinoic acid (POA), the hydrolyzed and active form of PZA, was shown to bind to the ribosomal protein S1, encoded by the *rpsA* gene [84]. Interestingly, POA only inhibits *trans*-translation and not canonical translation, and this inhibition depends strictly on wild-type *M. tuberculosis* S1. Crystal structures of the S1–POA complex revealed that the residues Lys303, Phe307, Phe310, and Arg357 in the S1 domain directly interact with POA, and that mutations on these locations blocked the interaction with the drug, and diminished the binding between S1 and tmRNA [85]. However, the action of PZA on S1 and *trans*-translation in *M. tuberculosis* was called into question, and experiments suggest that this drug directly targets a critical player in the metabolism of coenzyme A instead [86]. A recent study seems to confirm this hypothesis, since no measurable binding between POA and S1 could be recovered, despite the use of a wide panel of biophysical methods, including nuclear magnetic resonance (NMR) spectroscopy, isothermal titration calorimetry (ITC), microscale thermophoresis (MST), and electrophoretic mobility shift assays (EMSA) [87].

6.3. Peptides and Oligonucleotides

Peptide aptamers (PA) are combinatorial proteins that consist of a stable scaffold protein and random amino acids designed to bind to specific targets, in order to disrupt their activity [88]. In a recent study into the ways to vaccinate and protect zebrafish against infection, PAs were developed to target SmpB in *Aeromonas veronii* [89]. These opportunistic bacteria depend on *trans*-translation for virulence, and they are commonly found in aquaculture, where they cause wound infection, diarrhea, and septicemia [90]. The aptamers directed against SmpB were selected from a PA library, and the leading aptamer PA-1 (sequence: GGVTFLVNTYPNGVQSRAGG) was shown to specifically target SmpB, and to knockdown its functioning. When PA-1 was introduced into *A. veronii*, the engineered strain was much less virulent and could be used as a potential attenuated live vaccine, thereby providing a novel strategy for preventing *A. veronii* infection [89]. A second aptamer PA-2 (sequence: IGQEWGLGVRGPLSAK) was demonstrated to interact not only with SmpB, but also with the alternative rescue factor ArfA, resulting in the dysfunction of both rescue factors [91]. Considering the expected conservation of the fold in SmpB (see Figure 2), PA-1 and PA-2 could theoretically target a wide range of different bacteria.

Another peptide strategy involves using a peptide that mimics the SmpB C-terminal tail to compete with endogenous SmpB for binding in the vacant ribosomal A site, thus preventing tmRNA recruitment and, in turn, inhibiting *trans*-translation. We showed that the peptide that corresponds to the C-terminal extremity of *E. coli* SmpB (sequence: GKKQHDKRSDIKEREWQVDKARIMKNAHR) acts as a potent *trans*-translation inhibitor in vivo [79].

Finally, the most obvious strategy is to use antisense oligonucleotides directed towards the genes encoding SmpB or tmRNA (*ssrA* gene), or towards the mature tmRNA itself.

This approach is already in use in vitro by various laboratories, often as an internal control, with an antisense oligonucleotide targeting the tmRNA MLD and, thereby, very efficiently inhibiting *trans*-translation (for an example, see [92]).

7. Conclusions

Although *trans*-translation was discovered more than 25 years ago, and has been studied carefully ever since, with several attempts made to develop molecules to target it, the only chemical family that has displayed potential activity derives from 1,3,4-oxadiazole compounds. The recent development of sensitive and selective high-throughput screening assays that target ESKAPE pathogenic bacteria will undoubtedly help us to find new scaffolds that specifically target ribosome rescue [92]. Current studies work from scratch, by screening pharmacologically active small molecules from large chemical or natural product libraries [93], or are based on rational drug design, attempting to target the interactions between tmRNA, SmpB, and the ribosome (Figure 5), as recently described in cryo-EM structural studies [56,57]. Among the interactions discussed, the most promising targets may be the TLD–SmpB interface (in order to inhibit the tmRNA–SmpB interaction before the complex enters the ribosome); the mechanism of stalled ribosome recognition (to block or compete with SmpB C-terminal tail insertion into the empty mRNA channel); the SmpB–MLD binding site, which allows resume codon registration during translocation (to impede protein tagging). The possible specific integration of such molecules within pathogenic bacteria would be an extraordinary tool in the fight against multiresistance. There is no doubt that the groundwork already laid will soon respond to this increasingly urgent antibiotic resistance emergency.

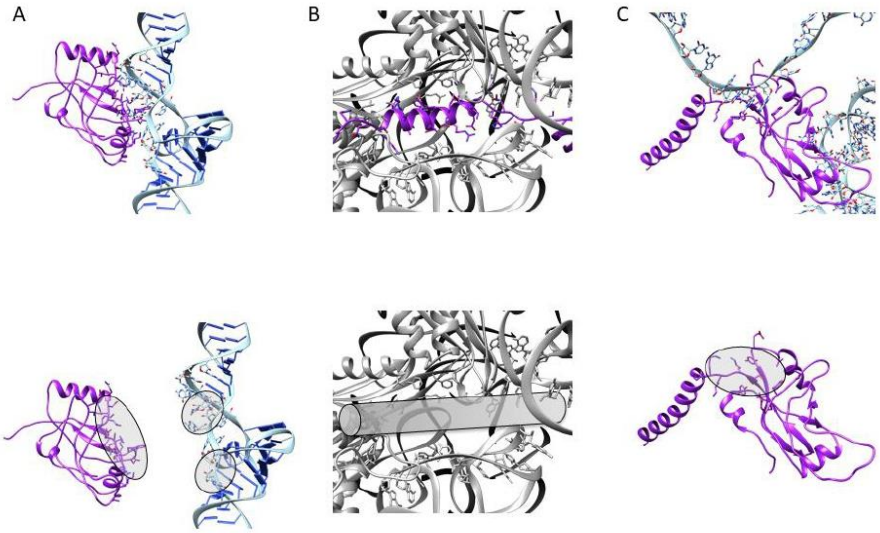

Figure 5. Potential anti-*trans*-translation targets. To interfere with *trans*-translation, one can (**A**) inhibit the tmRNA–SmpB interaction by targeting the binding sites of either partner; (**B**) compete with the SmpB C-terminal tail for stalled ribosome recognition; (**C**) alter the tagging process by targeting the binding site between SmpB and the MLD.

Author Contributions: R.C.-S., G.D. and R.G. wrote the first draft of the manuscript. R.C.-S., G.D., O.D., E.G., A.J.M. and R.G. participated in manuscript revision and approved its final version. All authors have read and agreed to the published version of the manuscript.

Funding: This research was funded by the Centre National de la Recherche Scientifique (UMR CNRS 6290), the University of Rennes 1, the Agence Nationale pour la Recherche as part of the RIBOTARGET 18-JAM2-0005-03 project under the JPI AMR framework. Funding was also received from the CAPES-COFECUB program (RCD), the European Union's ERASMUS+ program (GU), and the Britanny Region (GU). The APC was funded by CNRS.

Institutional Review Board Statement: Not applicable.

Informed Consent Statement: Not applicable.

Data Availability Statement: Not applicable.

Acknowledgments: We thank Juliana Berland for insightful comments on the manuscript.

Conflicts of Interest: Reynald Gillet is a co-inventor of the screening system described here (patent application #EP/2018/063780).

References

1. Vázquez-Laslop, N.; Mankin, A.S. Context-specific action of ribosomal antibiotics. *Annu. Rev. Microbiol.* **2018**, *72*, 185–207. [CrossRef]
2. Ero, R.; Yan, X.F.; Gao, Y.G. Ribosome protection proteins—"New" players in the global arms race with antibiotic-resistant pathogens. *Int. J. Mol. Sci.* **2021**, *22*, 5356. [CrossRef] [PubMed]
3. Rice, L.B. Federal funding for the study of antimicrobial resistance in nosocomial pathogens: No ESKAPE. *J. Infect. Dis.* **2008**, *197*, 1079–1081. [CrossRef] [PubMed]
4. Tacconelli, E.; Carrara, E.; Savoldi, A.; Harbarth, S.; Mendelson, M.; Monnet, D.L.; Pulcini, C.; Kahlmeter, G.; Kluytmans, J.; Carmeli, Y.; et al. Discovery, research, and development of new antibiotics: The WHO priority list of antibiotic-resistant bacteria and tuberculosis. *Lancet Infect. Dis.* **2018**, *18*, 318–327. [CrossRef]
5. Santajit, S.; Indrawattana, N. Mechanisms of antimicrobial resistance in ESKAPE pathogens. *BioMed Res. Int.* **2016**, *2016*, 2475067. [CrossRef]
6. Prestinaci, F.; Pezzotti, P.; Pantosti, A. Antimicrobial resistance: A global multifaceted phenomenon. *Pathog. Glob. Health* **2015**, *109*, 309–318. [CrossRef]
7. Kakkar, A.K.; Shafiq, N.; Singh, G.; Ray, P.; Gautam, V.; Agarwal, R.; Muralidharan, J.; Arora, P. Antimicrobial stewardship programs in resource constrained environments: Understanding and addressing the need of the systems. *Front. Public Health* **2020**, *8*, 140. [CrossRef]
8. Tyers, M.; Wright, G.D. Drug combinations: A strategy to extend the life of antibiotics in the 21st century. *Nat. Rev. Microbiol.* **2019**, *17*, 141–155. [CrossRef]
9. Janssen, B.D.; Diner, E.J.; Hayes, C.S. Analysis of aminoacyl- and peptidyl-tRNAs by gel electrophoresis. *Bact. Regul. RNA* **2012**, *905*, 291–309. [CrossRef]
10. Doma, M.K.; Parker, R. RNA quality control in eukaryotes. *Cell* **2007**, *131*, 660–668. [CrossRef] [PubMed]
11. Collier, J.; Binet, E.; Bouloc, P. Competition between SsrA tagging and translational termination at weak stop codons in *Escherichia coli*. *Mol. Microbiol.* **2002**, *45*, 745–754. [CrossRef] [PubMed]
12. Ueda, K.; Yamamoto, Y.; Ogawa, K.; Abo, T.; Inokuchi, H.; Aiba, H. Bacterial SsrA system plays a role in coping with unwanted translational readthrough caused by suppressor tRNAs. *Genes Cells* **2002**, *7*, 509–519. [CrossRef] [PubMed]
13. Hayes, C.S.; Sauer, R.T. Cleavage of the a site mRNA codon during ribosome pausing provides a mechanism for translational quality control. *Mol. Cell* **2003**, *12*, 903–911. [CrossRef]
14. Abo, T.; Ueda, K.; Sunohara, T.; Ogawa, K.; Aiba, H. SsrA-mediated protein tagging in the presence of miscoding drugs and its physiological role in *Escherichia coli*. *Genes Cells* **2002**, *7*, 629–638. [CrossRef]
15. Laursen, B.S.; Sørensen, H.P.; Mortensen, K.K.; Sperling-Petersen, H.U. Initiation of protein synthesis in bacteria. *Microbiol. Mol. Biol. Rev.* **2005**, *69*, 101–123. [CrossRef]
16. Pedersen, K.; Zavialov, A.V.; Pavlov, M.Y.; Elf, J.; Gerdes, K.; Ehrenberg, M. The bacterial toxin RelE displays codon-specific cleavage of mRNAs in the ribosomal A site. *Cell* **2003**, *112*, 131–140. [CrossRef]
17. Keiler, K.C.; Feaga, H.A. Resolving nonstop translation complexes is a matter of life or death. *J. Bacteriol.* **2014**, *196*, 2123–2130. [CrossRef]
18. Müller, C.; Crowe-McAuliffe, C.; Wilson, D.N. Ribosome rescue pathways in bacteria. *Front. Microbiol.* **2021**, *12*, 652980. [CrossRef]
19. Gueneau de Novoa, P.; Williams, K.P. The tmRNA website: Reductive evolution of tmRNA in plastids and other endosymbionts. *Nucleic Acids Res.* **2004**, *32*, D104–D108. [CrossRef]
20. Komine, Y.; Kitabatake, M.; Yokogawa, T.; Nishikawa, K.; Inokuchi, H. A tRNA-like structure is present in 10Sa RNA, a small stable RNA from Escherichia coli. *Proc. Natl. Acad. Sci. USA* **1994**, *91*, 9223–9227. [CrossRef]
21. Li, Z.; Pandit, S.; Deutscher, M.P. 3′ Exoribonucleolytic trimming is a common feature of the maturation of small, stable RNAs in *Escherichia coli*. *Proc. Natl. Acad. Sci. USA* **1998**, *95*, 2856–2861. [CrossRef] [PubMed]

22. Lin-Chao, S.; Wei, C.L.; Lin, Y.T. RNase E is required for the maturation of ssrA RNA and normal ssrA RNA peptide-tagging activity. *Proc. Natl. Acad. Sci. USA* **1999**, *96*, 12406–12411. [CrossRef] [PubMed]
23. Gimple, O.; Schön, A. In vitro and in vivo processing of Cyanelle tmRNA by RNase P. *Biol. Chem.* **2001**, *382*, 1421–1429. [CrossRef]
24. Lee, S.Y.; Bailey, S.C.; Apirion, D. Small stable RNAs from *Escherichia coli*: Evidence for the existence of new molecules and for a new ribonucleoprotein particle containing 6S RNA. *J. Bacteriol.* **1978**, *133*, 1015–1023. [CrossRef]
25. Moore, S.D.; Sauer, R.T. Ribosome rescue: tmRNA tagging activity and capacity in *Escherichia coli*. *Mol. Microbiol.* **2005**, *58*, 456–466. [CrossRef]
26. Felden, B.; Hanawa, K.; Atkins, J.F.; Himeno, H.; Muto, A.; Gesteland, R.F.; McCloskey, J.A.; Crain, P.F. Presence and location of modified nucleotides in *Escherichia coli* tmRNA: Structural mimicry with tRNA acceptor branches. *EMBO J.* **1998**, *17*, 3188–3196. [CrossRef]
27. Ranaei-Siadat, E.; Fabret, C.; Seijo, B.; Dardel, F.; Grosjean, H.; Nonin-Lecomte, S. RNA-methyltransferase TrmA is a dual-specific enzyme responsible for C5-methylation of uridine in both tmRNA and tRNA. *RNA Biol.* **2013**, *10*, 572–578. [CrossRef]
28. Hou, Y.M.; Schimmel, P. A simple structural feature is a major determinant of the identity of a transfer RNA. *Nat. Cell Biol.* **1988**, *333*, 140–145. [CrossRef]
29. Schimmel, P.; Ribas de Pouplana, L. Footprints of aminoacyl-tRNA synthetases are everywhere. *Trends Biochem. Sci.* **2000**, *25*, 207–209. [CrossRef]
30. Ribas de Pouplana, L.; Schimmel, P. Aminoacyl-tRNA synthetases: Potential markers of genetic code development. *Trends Biochem. Sci.* **2001**, *26*, 591–596. [CrossRef]
31. Nameki, N.; Tadaki, T.; Himeno, H.; Muto, A. Three of four pseudoknots in tmRNA are interchangeable and are substitutable with single-stranded RNAs. *FEBS Lett.* **2000**, *470*, 345–349. [CrossRef]
32. Williams, K.P.; Martindale, K.A.; Bartel, D.P. Resuming translation on tmRNA: A unique mode of determining a reading frame. *EMBO J.* **1999**, *18*, 5423–5433. [CrossRef] [PubMed]
33. Lee, S.; Ishii, M.; Tadaki, T.; Muto, A.; Himeno, H. Determinants on tmRNA for initiating efficient and precise *trans*-translation: Some mutations upstream of the tag-encoding sequence of *Escherichia coli* tmRNA shift the initiation point of *trans*-translation in vitro. *RNA* **2001**, *7*, 999–1012. [CrossRef] [PubMed]
34. Miller, M.R.; Healey, D.W.; Robison, S.G.; Dewey, J.D.; Buskirk, A.R. The role of upstream sequences in selecting the reading frame on tmRNA. *BMC Biol.* **2008**, *6*, 29, Published 30 June 2008. [CrossRef]
35. Thibonnier, M.; Thiberge, J.M.; De Reuse, H. *Trans*-translation in *Helicobacter pylori*: Essentiality of ribosome rescue and requirement of protein tagging for stress resistance and competence. *PLoS ONE* **2008**, *3*, e3810. [CrossRef] [PubMed]
36. Kieft, J.S. Viral IRES RNA structures and ribosome interactions. *Trends Biochem. Sci.* **2008**, *33*, 274–283. [CrossRef]
37. Yang, C.; Glover, J.R. The SmpB-tmRNA tagging system plays important roles in *Streptomyces coelicolor* growth and development. *PLoS ONE* **2009**, *4*, e4459. [CrossRef] [PubMed]
38. Barends, S.; Zehl, M.; Bialek, S.; De Waal, E.; A Traag, B.; Willemse, J.; Jensen, O.N.; Vijgenboom, E.; Van Wezel, G.P. Transfer–messenger RNA controls the translation of cell-cycle and stress proteins in *Streptomyces*. *EMBO Rep.* **2010**, *11*, 119–125. [CrossRef]
39. Katz, A.; Elgamal, S.; Rajkovic, A.; Ibba, M. Non-canonical roles of tRNAs and tRNA mimics in bacterial cell biology. *Mol. Microbiol.* **2016**, *101*, 545–558. [CrossRef]
40. Keiler, K.C.; Shapiro, L.; Williams, K.P. tmRNAs that encode proteolysis-inducing tags are found in all known bacterial genomes: A two-piece tmRNA functions in *Caulobacter*. *Proc. Natl. Acad. Sci. USA* **2000**, *97*, 7778–7783. [CrossRef] [PubMed]
41. Sharkady, S.M.; Williams, K.P. A third lineage with two-piece tmRNA. *Nucleic Acids Res.* **2004**, *32*, 4531–4538. [CrossRef]
42. Gaudin, C.; Zhou, X.; Williams, K.P.; Felden, B. Two-piece tmRNA in cyanobacteria and its structural analysis. *Nucleic Acids Res.* **2002**, *30*, 2018–2024. [CrossRef] [PubMed]
43. Moore, S.D.; Sauer, R.T. The tmRNA system for translational surveillance and ribosome rescue. *Annu. Rev. Biochem.* **2007**, *76*, 101–124. [CrossRef]
44. Karzai, A.W.; Susskind, M.M.; Sauer, R. SmpB, a unique RNA-binding protein essential for the peptide-tagging activity of SsrA (tmRNA). *EMBO J.* **1999**, *18*, 3793–3799. [CrossRef]
45. Hanawa-Suetsugu, K.; Takagi, M.; Inokuchi, H.; Himeno, H.; Muto, A. SmpB functions in various steps of *trans*-translation. *Nucleic Acids Res.* **2002**, *30*, 1620–1629. [CrossRef]
46. Shimizu, Y.; Ueda, T. The role of SmpB protein in *trans*-translation. *FEBS Lett.* **2002**, *514*, 74–77. [CrossRef]
47. Wower, J.; Zwieb, C.W.; Hoffman, D.W.; Wower, I.K. SmpB: A protein that binds to double-stranded segments in tmRNA and tRNA. *Biochemistry* **2002**, *41*, 8826–8836. [CrossRef] [PubMed]
48. Bycroft, M.; Hubbard, T.J.; Proctor, M.; Freund, S.M.; Murzin, A.G. The solution structure of the S1 RNA binding domain: A member of an ancient nucleic acid–binding fold. *Cell* **1997**, *88*, 235–242. [CrossRef]
49. Dong, G.; Nowakowski, J.; Hoffman, D.W. Structure of small protein B: The protein component of the tmRNA–SmpB system for ribosome rescue. *EMBO J.* **2002**, *21*, 1845–1854. [CrossRef] [PubMed]
50. Someya, T.; Nameki, N.; Hosoi, H.; Suzuki, S.; Hatanaka, H.; Fujii, M.; Terada, T.; Shirouzu, M.; Inoue, Y.; Shibata, T.; et al. Solution structure of a tmRNA-binding protein, SmpB, from *Thermus thermophilus*. *FEBS Lett.* **2003**, *535*, 94–100. [CrossRef]
51. Gutmann, S.; Haebel, P.W.; Metzinger, L.; Sutter, M.; Felden, B.; Ban, N. Crystal structure of the transfer-RNA domain of transfer-messenger RNA in complex with SmpB. *Nature* **2003**, *424*, 699–703. [CrossRef]

52. Bessho, Y.; Shibata, R.; Sekine, S.; Murayama, K.; Higashijima, K.; Hori-Takemoto, C.; Shirouzu, M.; Kuramitsu, S.; Yokoyama, S. Structural basis for functional mimicry of long-variable-arm tRNA by transfer-messenger RNA. *Proc. Natl. Acad. Sci. USA* **2007**, *104*, 8293–8298. [CrossRef]
53. Kaur, S.; Gillet, R.; Li, W.; Gursky, R.; Frank, J. Cryo-EM visualization of transfer messenger RNA with two SmpBs in a stalled ribosome. *Proc. Natl. Acad. Sci. USA* **2006**, *103*, 16484–16489. [CrossRef] [PubMed]
54. Kurita, D.; Sasaki, R.; Muto, A.; Himeno, H. Interaction of SmpB with ribosome from directed hydroxyl radical probing. *Nucleic Acids Res.* **2007**, *35*, 7248–7255. [CrossRef] [PubMed]
55. Nonin-Lecomte, S.; Germain-Amiot, N.; Gillet, R.; Hallier, M.; Ponchon, L.; Dardel, F.; Felden, B. Ribosome hijacking: A role for small protein B during *trans* -translation. *EMBO Rep.* **2009**, *10*, 160–165. [CrossRef]
56. Rae, C.D.; Gordiyenko, Y.; Ramakrishnan, V. How a circularized tmRNA moves through the ribosome. *Science* **2019**, *363*, 740–744. [CrossRef] [PubMed]
57. Guyomar, C.; D'Urso, G.; Chat, S.; Giudice, E.; Gillet, R. Structures of tmRNA and SmpB as they transit through the ribosome. *Nat. Commun.* **2021**, *12*, 4909. [CrossRef]
58. Neubauer, C.; Gillet, R.; Kelley, A.C.; Ramakrishnan, V. Decoding in the absence of a codon by tmRNA and SmpB in the Ribosome. *Science* **2012**, *335*, 1366–1369. [CrossRef]
59. Kurita, D.; Muto, A.; Himeno, H. Role of the C-terminal tail of SmpB in the early stage of *trans*-translation. *RNA* **2010**, *16*, 980–990. [CrossRef] [PubMed]
60. D'Urso, G.; Guyomar, C.; Chat, S.; Giudice, E.; Gillet, R. Insights into the ribosomal *trans*-translation rescue system: Lessons from recent structural studies. *FEBS J.* 2022; *in press*.
61. Fei, X.; Bell, T.A.; Barkow, S.R.; Baker, T.A.; Sauer, R.T. Structural basis of ClpXP recognition and unfolding of ssrA-tagged substrates. *eLife* **2020**, *9*, e61496. [CrossRef] [PubMed]
62. Karzai, A.W.; Roche, E.D.; Sauer, R.T. The SsrA–SmpB system for protein tagging, directed degradation and ribosome rescue. *Nat. Struct. Biol.* **2000**, *7*, 449–455. [CrossRef]
63. Richards, J.; Mehta, P.; Karzai, A.W. RNase R degrades non-stop mRNAs selectively in an SmpB-tmRNA-dependent manner. *Mol. Microbiol.* **2006**, *62*, 1700–1712. [CrossRef]
64. Cheng, Z.-F.; Deutscher, M.P. Purification and characterization of the *Escherichia coli* exoribonuclease RNase R. Comparison with RNase II. *J. Biol. Chem.* **2002**, *277*, 21624–21629. [CrossRef] [PubMed]
65. Matos, R.G.; Pobre, V.; Reis, F.P.; Malecki, M.; Andrade, J.M.; Arraiano, C.M. Structure and degradation mechanisms of 3′ to 5′ exoribonucleases. In *Ribonucleases. Nucleic Acids and Molecular Biology*; Nicholson, A., Ed.; Springer: Berlin/Heidelberg, Germany, 2011; pp. 192–222. [CrossRef]
66. Saramago, M.; Bárria, C.; Dos Santos, R.F.; Silva, I.; Pobre, V.; Domingues, S.; Andrade, J.; Viegas, S.; Arraiano, C.M. The role of RNases in the regulation of small RNAs. *Curr. Opin. Microbiol.* **2014**, *18*, 105–115. [CrossRef]
67. Ramadoss, N.S.; Alumasa, J.N.; Cheng, L.; Wang, Y.; Li, S.; Chambers, B.S.; Chang, H.; Chatterjee, A.K.; Brinker, A.; Engels, I.H.; et al. Small molecule inhibitors of *trans*-translation have broad-spectrum antibiotic activity. *Proc. Natl. Acad. Sci. USA* **2013**, *110*, 10282–10287. [CrossRef]
68. Huang, Y.; Alumasa, J.N.; Callaghan, L.T.; Baugh, R.S.; Rae, C.D.; Keiler, K.C.; McGillivray, S.M. A Small-molecule inhibitor of *trans*-translation synergistically interacts with cathelicidin antimicrobial peptides to impair survival of *Staphylococcus aureus*. *Antimicrob. Agents Chemother.* **2019**, *63*, e02362-18. [CrossRef] [PubMed]
69. De la Cruz, J.; Vioque, A. Increased sensitivity to protein synthesis inhibitors in cells lacking tmRNA. *RNA* **2001**, *7*, 1708–1716.
70. Vioque, A.; de la Cruz, J. *Trans*-translation and protein synthesis inhibitors. *FEMS Microbiol. Lett.* **2003**, *218*, 9–14. [CrossRef] [PubMed]
71. Feaga, H.A.; Viollier, P.; Keiler, K.C. Release of nonstop ribosomes is essential. *mBio* **2014**, *5*, e01916-14. [CrossRef]
72. Giudice, E.; Macé, K.; Gillet, R. *Trans*-translation exposed: Understanding the structures and functions of tmRNA-SmpB. *Front. Microbiol.* **2014**, *5*, 113. [CrossRef]
73. Andini, N.; Nash, K.A. Expression of tmRNA in mycobacteria is increased by antimicrobial agents that target the ribosome. *FEMS Microbiol. Lett.* **2011**, *322*, 172–179. [CrossRef] [PubMed]
74. Luidalepp, H.; Hallier, M.; Felden, B.; Tenson, T. tmRNA decreases the bactericidal activity of aminoglycosides and the susceptibility to inhibitors of cell wall synthesis. *RNA Biol.* **2005**, *2*, 70–74. [CrossRef] [PubMed]
75. Li, J.; Ji, L.; Shi, W.; Xie, J.; Zhang, Y. *Trans*-translation mediates tolerance to multiple antibiotics and stresses in *Escherichia coli*. *J. Antimicrob. Chemother.* **2013**, *68*, 2477–2481. [CrossRef] [PubMed]
76. Alumasa, J.N.; Manzanillo, P.S.; Peterson, N.D.; Lundrigan, T.; Baughn, A.D.; Cox, J.S.; Keiler, K.C. Ribosome rescue inhibitors kill actively growing and nonreplicating persister *Mycobacterium tuberculosis* cells. *ACS Infect. Dis.* **2017**, *3*, 634–644. [CrossRef]
77. Aron, Z.D.; Mehrani, A.; Hoffer, E.D.; Connolly, K.L.; Srinivas, P.; Torhan, M.C.; Alumasa, J.N.; Cabrera, M.; Hosangadi, D.; Barbor, J.S.; et al. *Trans*-translation inhibitors bind to a novel site on the ribosome and clear *Neisseria gonorrhoeae* in vivo. *Nat. Commun.* **2021**, *12*, 1779. [CrossRef]
78. Senges, C.H.R.; Stepanek, J.J.; Wenzel, M.; Raatschen, N.; Ay, Ü.; Märtens, Y.; Prochnow, P.; Hernández, M.V.; Yayci, A.; Schubert, B.; et al. Comparison of proteomic responses as global approach to antibiotic mechanism of action elucidation. *Antimicrob. Agents Chemother.* **2020**, *65*, e01373-20. [CrossRef]

79. Macé, K.; Demay, F.; Guyomar, C.; Georgeault, S.; Giudice, E.; Goude, R.; Trautwetter, A.; Ermel, G.; Blanco, C.; Gillet, R. A genetic tool to quantify *trans*-translation activity in vivo. *J. Mol. Biol.* **2017**, *429*, 3617–3625. [CrossRef] [PubMed]
80. Brunel, R.; Descours, G.; Durieux, I.; Doublet, P.; Jarraud, S.; Charpentier, X. KKL-35 exhibits potent antibiotic activity against *Legionella* species independently of *trans*-translation inhibition. *Antimicrob. Agents Chemother.* **2018**, *62*, e01459-17. [CrossRef]
81. Guyomar, C.; Thépaut, M.; Nonin-Lecomte, S.; Méreau, A.; Goude, R.; Gillet, R. Reassembling green fluorescent protein for in vitro evaluation of *trans*-translation. *Nucleic Acids Res.* **2020**, *48*, e22. [CrossRef]
82. Tresse, C.; Radigue, R.; Gomes Von Borowski, R.; Thepaut, M.; Le, H.H.; Demay, F.; Georgeault, S.; Dhalluin, A.; Trautwetter, A.; Ermel, G.; et al. Synthesis and evaluation of 1,3,4-oxadiazole derivatives for development as broad-spectrum antibiotics. *Bioorganic Med. Chem.* **2019**, *27*, 115097. [CrossRef]
83. Cole, S.T. Microbiology. Pyrazinamide—Old TB drug finds new target. *Science* **2011**, *333*, 1583–1584. [CrossRef]
84. Shi, W.; Zhang, X.; Jiang, X.; Yuan, H.; Lee, J.S.; Barry, C.E.; Wang, H.; Zhang, W.; Zhang, Y. Pyrazinamide inhibits *trans*-translation in *Mycobacterium tuberculosis*. *Science* **2011**, *333*, 1630–1632. [CrossRef] [PubMed]
85. Yang, J.; Liu, Y.; Bi, J.; Cai, Q.; Liao, X.; Li, W.; Guo, C.; Zhang, Q.; Lin, T.; Zhao, Y.; et al. Structural basis for targeting the ribosomal protein S1 of *Mycobacterium tuberculosis by* pyrazinamide. *Mol. Microbiol.* **2015**, *95*, 791–803. [CrossRef] [PubMed]
86. Dillon, N.A.; Peterson, N.D.; Feaga, H.A.; Keiler, K.C.; Baughn, A.D. Anti-tubercular activity of pyrazinamide is independent of *trans*-translation and RpsA. *Sci. Rep.* **2017**, *7*, 6135. [CrossRef] [PubMed]
87. Vallejos-Sánchez, K.; Lopez, J.M.; Antiparra, R.; Toscano, E.; Saavedra, H.; Kirwan, D.E.; Amzel, L.M.; Gilman, R.H.; Maruenda, H.; Sheen, P.; et al. *Mycobacterium tuberculosis* ribosomal protein S1 (RpsA) and variants with truncated C-terminal end show absence of interaction with pyrazinoic acid. *Sci. Rep.* **2020**, *10*, 8356. [CrossRef] [PubMed]
88. Reverdatto, S.; Burz, D.S.; Shekhtman, A. Peptide aptamers: Development and applications. *Curr. Top. Med. Chem.* **2015**, *15*, 1082–1101. [CrossRef]
89. Liu, P.; Huang, D.; Hu, X.; Tang, Y.; Ma, X.; Yan, R.; Han, Q.; Guo, J.; Zhang, Y.; Sun, Q.; et al. Targeting inhibition of SmpB by peptide aptamer attenuates the virulence to protect zebrafish against *Aeromonas veronii* infection. *Front. Microbiol.* **2017**, *8*, 1766. [CrossRef]
90. Li, Y.; Liu, Y.; Zhou, Z.; Huang, H.; Ren, Y.; Zhang, Y.; Li, G.; Zhou, Z.; Wang, L. Complete genome sequence of *Aeromonas veronii* Strain B565. *J. Bacteriol.* **2011**, *193*, 3389–3390. [CrossRef]
91. Liu, P.; Chen, Y.; Wang, D.; Tang, Y.; Tang, H.; Song, H.; Sun, Q.; Zhang, Y.; Liu, Z. Genetic selection of peptide aptamers that interact and inhibit both small protein B and alternative ribosome-rescue factor A of *Aeromonas veronii* C4. *Front. Microbiol.* **2016**, *7*, 1228. [CrossRef]
92. Thépaut, M.; Campos-Silva, R.; Renard, E.; Barloy-Hubler, F.; Ennifar, E.; Boujard, D.; Gillet, R. Safe and easy in vitro evaluation of tmRNA-SmpB-mediated *trans*-translation from ESKAPE pathogenic bacteria. *RNA* **2021**, *27*, 1390–1399. [CrossRef]
93. Wilson, B.A.P.; Thornburg, C.C.; Henrich, C.J.; Grkovic, T.; O'Keefe, B.R. Creating and screening natural product libraries. *Nat. Prod. Rep.* **2020**, *37*, 893–918. [CrossRef] [PubMed]

3.2.2 Review: *"Insights into the ribosomal trans-translation rescue system: lessons from recent structural studies"*

The FEBS Journal

FEBS PRESS science publishing by scientists

STRUCTURAL SNAPSHOT

Insights into the ribosomal *trans*-translation rescue system: lessons from recent structural studies

Gaetano D'Urso, Charlotte Guyomar, Sophie Chat, Emmanuel Giudice and Reynald Gillet

Institut de Génétique et Développement de Rennes (IGDR), CNRS, Univ. Rennes, France

Keywords
cryo-EM; ribosome; SmpB; tmRNA; *trans*-translation

Correspondence
R. Gillet, Univ. Rennes, CNRS, Institut de Génétique et Développement de Rennes (IGDR) UMR6290, 35000 Rennes, France
Tel: +33 (0)2 23 23 45 07
E-mail: reynald.gillet@univ-rennes1.fr

(Received 6 October 2021, revised 27 December 2021, accepted 10 January 2022)

doi:10.1111/febs.16349

The arrest of protein synthesis caused when ribosomes stall on an mRNA lacking a stop codon is a deadly risk for all cells. In bacteria, this situation is remedied by the *trans*-translation quality control system. *Trans*-translation occurs because of the synergistic action of two main partners, transfer-messenger RNA (tmRNA) and small protein B (SmpB). These act in complex to monitor protein synthesis, intervening when necessary to rescue stalled ribosomes. During this process, incomplete nascent peptides are tagged for destruction, problematic mRNAs are degraded and the previously stalled ribosomes are recycled. In this 'Structural Snapshot' article, we describe the mechanism at the molecular level, a view updated after the most recent structural studies using cryo-electron microscopy.

Introduction

Protein synthesis, or translation, is carried out by the ribonucleoprotein nanomachines called ribosomes. They read the information contained within mRNA and catalyse polypeptide chains synthesis by forming peptide bonds between the amino-acids corresponding to each three-base triplet, or codon. To ensure that the genetic information is accurately translated, multiple quality control mechanisms are needed. One of the most critical outcomes of inefficient protein synthesis occurs when ribosomes stall along the mRNA molecule, something which notably occurs during translation of 'non-stop' mRNA transcripts lacking a termination codon. The absence of a stop codon prevents translation termination, so ribosomes accumulate on the defective mRNA and form stalled polysomal chains that are no longer productive [1], thus undermining bacterial cell vitality. In addition, the translation of defective mRNA results in the production of truncated proteins which are potentially toxic for the cell. This phenomenon occurs frequently, for instance in *Escherichia coli* where ~ 2–4% of the translating ribosomes stall on a defective mRNA and need to be rescued [2]. To tackle the problem of 'non-stop' stalling, all bacteria firstly use the same rescue system, *trans*-translation. This system is based on the synergy of transfer-messenger RNA (tmRNA), a chimeric molecule 260 to 420 nucleotides long (e.g. 363 nucleotides in *E. coli*) and its partner small protein B (SmpB) [3]. tmRNA is composed of a large pseudoknot ring (PK); a tRNA-like domain (TLD) and a messenger-like domain (MLD) that contains an internal ORF devoid of a N-formylmethionine start codon (Fig. 1A). The tmRNA molecule begins by being transcribed as a non-mature precursor, which is then processed at its 5′ and 3'-ends, while nucleotides in the T-loop are modified at least twice [4–7]. Thanks to the recognition of a

Abbreviations
Arf, alternative ribosome-rescue factor; cryo-EM, cryo-electron microscopy; DC, decoding centre; MLD, messenger-like domain; OB, oligonucleotide/oligosaccharide-binding; PK, pseudoknot; PTC, peptidyl transferase centre; RF, release factor; RNase R, ribonuclease R; RQC, ribosome-associated quality control; SmpB, small protein B; TLD, tRNA-like domain; tmRNA, transfer-messenger RNA.

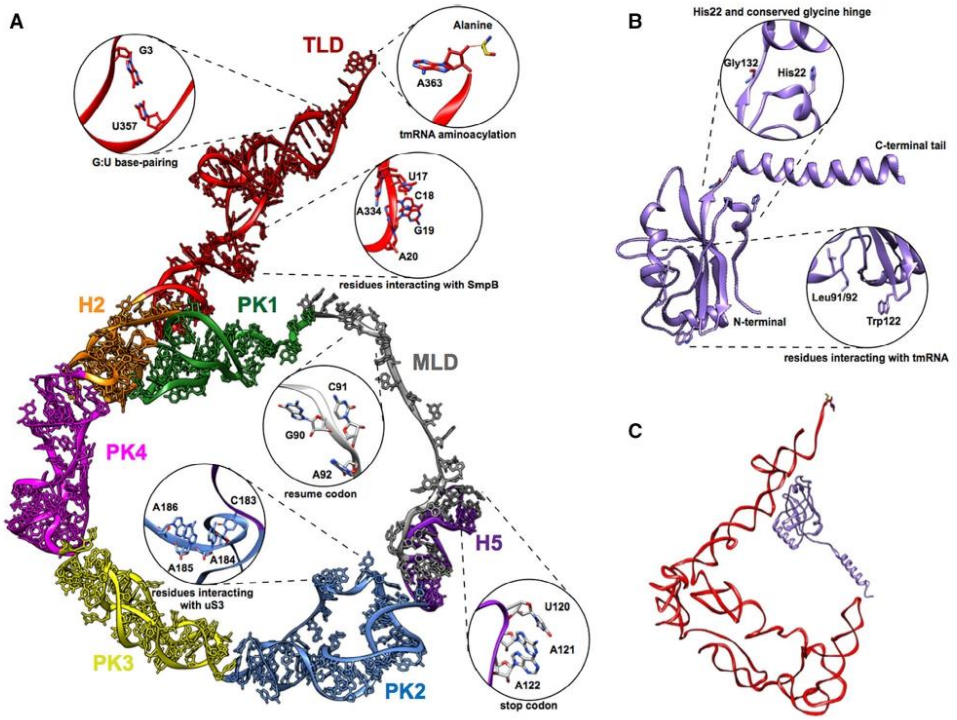

Fig. 1. Elements in the *trans*-translation rescue system (A) 3D structure of a tmRNA molecule. The transfer-like domain (TLD) is red, while helix H2 is orange. This is followed by the pseudoknot ring, made up of the four pseudoknots PK1 (dark green), PK2 (steel blue), PK3 (yellow) and PK4 (magenta). The MLD is grey and the helix H5 is purple. The resume codon, stop codon, conserved G-U base pair, tmRNA aminoacylatoin and the residues interacting with SmpB and uS3 are highlighted. (B) 3D structure of SmpB (purple). The residues interacting with the tmRNA, His22 and the conserved Gly132 are highlighted. (C) 3D structure of the tmRNA-SmpB complex when bound to the ribosome during unlocking of the stalled ribosome. SmpB (purple) binds to the TLD's D-loop in tmRNA (red). All structural figures were done using UCSF chimera [63].

G3 : U base-pair as occurs in canonical $tRNA^{Ala}$, the TLD is always aminoacylated by alanine tRNA synthetase (AlaRS) [5]. The MLD encodes for the consensus sequence AN–[–]$_n$–ALAA (e.g. ANDENYALAA in *E. coli*) followed by a termination codon, allowing specific recognition of tagged proteins by proteases. The proteases involved in degrading tmRNA-tagged proteins are ClpXP/ClpAP, FtsH and Tsp. During that process much, if not all, of the MLD's sequence conservation is important for recognition by cellular proteases and/or adaptor proteins [8]. The tmRNA partner SmpB is a small basic protein of ~ 160 amino acids. Its body is folded into an oligonucleotide/oligosaccharide-binding (OB) fold domain, while the last 30 residues form a tail unstructured in solution but which folds as an α-helix within the ribosome (Fig. 1B). SmpB is tmRNA's most important associate, binding it with high affinity (~ 20 to 50 nM) [9,10], in a molar ratio of 1 : 1 [11,12] (Fig. 1C). The other major actor in *trans*-translation is Ribonuclease R (RNase R), a 3′→5′ exoribonuclease in the RNase II superfamily involved in degrading truncated non-stop mRNA [13]. During the rescue process (Fig. 2), the tmRNA TLD is bound to SmpB and accommodated into the vacant ribosomal A site. After transpeptidation occurs between the stalled incomplete peptide and the tmRNA alanine, a swap between the tmRNA messenger-like domain (MLD) and the original problematic mRNA allows translation to resume [14,15]. The ribosome translates the information on the

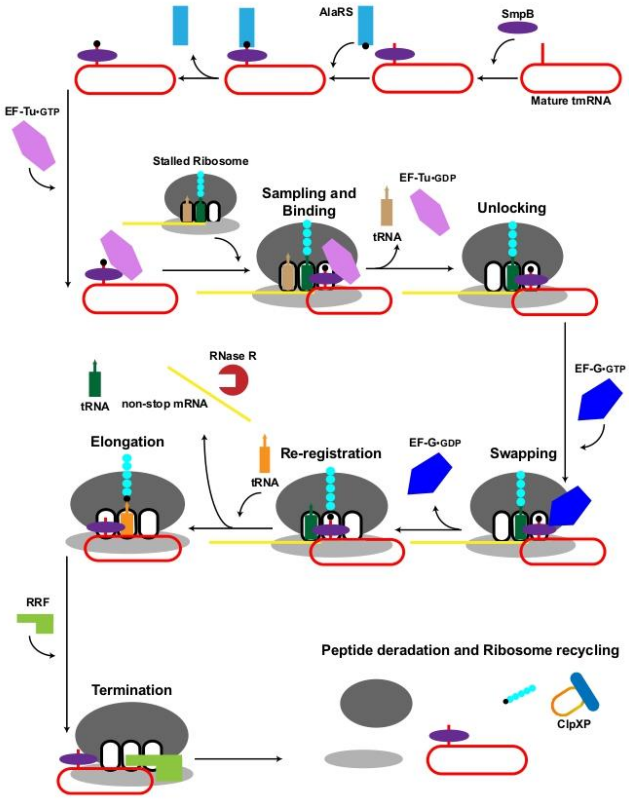

Fig. 2. The complete *trans*-translation quality control cycle. Ribosome sampling, binding and unlocking: Mature tmRNA associates with its partner SmpB to form a complex. AlaRS charges the complex with an alanine, and the enzyme is released. EF-Tu•GTP binds to tmRNA-SmpB to form the quaternary complex needed to rescue the ribosome stalled on a non-stop mRNA. To recognize these ribosomes the quaternary complex enters the ribosomal A site. There, SmpB mimics a codon-anticodon pairing, while its C-terminal tail is inserted in the mRNA channel. If the tail fits in the empty mRNA channel the elongation factor EF-Tu•GDP is released after GTP hydrolysis. The Ala-tmRNA-SmpB complex is then accommodated into the A site, triggering the peptidyl transfer reaction. mRNA swapping and re-registration: EF-G•GTP helps shift the tmRNA-SmpB into the P site thanks to hydrolysis of its GTP. EF-G•GDP is released, and the non-stop mRNA is ejected and then degraded by RNase R. The tmRNA's ORF is placed into the A site and new tRNAs arrive at the ribosome to resume translation. Elongation, termination, peptide degradation and ribosome recycling: The tmRNA-SmpB complex moves towards the E site and the TLD and SmpB are promptly ejected, while the translation of the MLD continues until the ribosome reaches the MLD's stop codon. The ribosome subunits are then dissociated by the Ribosome Recycling Factor RRF and the nascent peptide is degraded by ClpXP/ClpAP/FtsH/Tsp proteases. All of the components are recycled and ready for a new round.

tmRNA's ORF, just until it reaches the stop codon. The stalled ribosome is then recycled naturally into free subunits, while the incomplete peptides are tagged with a signal sequence that results in proteolysis. The problematic mRNAs meet the same fate, as they are degraded by RNase R (for a recent complete review, see reference [3]).

Remarkably, *trans*-translation is present in nearly all bacteria [16], and it is their main mechanism to start afresh, preventing cell death. Some bacteria also have back-up rescue processes based on the alternative ribosome-rescue factors A and B (ArfA and ArfB) [17,18] or using ribosome-associated quality control (RQC) pathways mediated by RqcH and RqcP [3,19].

Recent studies have also reported alternative systems based on ArfT in *Francisella tularensis* and on BrfA in *Bacillus subtilis* [20,21]. However, these backup mechanisms are imperfect as none of them is able to accomplish with specificity the three outcomes of *trans*-translation, that is, not only ribosome recycling but also protein and RNA targeted degradation. This is likely why *trans*-translation predominates and why, if some bacteria use only *trans*-translation, none use only ArfA or ArfB [22]. Therefore, and despite their physiological importance [18,23], one can expect that even when these are present, they are not enough to ensure steady and prolonged cell fitness, particularly in the presence of stress, this highlights the great importance of *trans*-translation for bacterial survival.

Based on the most recent data produced by cryo-electron microscopy (cryo-EM) [24,25], we focus here on the structural foundation for the perfect synchronicity seen between the various partners of *trans*-translation.

The carefully choreographed ballet of *trans*-translation

We can divide *trans*-translation into different stages based on both the similarities and differences between it and canonical translation. The first 'ribosome sampling, binding and unlocking' step covers the identification of stalled ribosomes and transpeptidation of the stalled incomplete polypeptide on the tmRNA TLD. Next, in 'mRNA swapping and re-registration', the MLD elongates and problematic mRNA is degraded. Finally, in 'peptide degradation and ribosome recycling', tagged peptides are released and degraded, and the ribosomes are recycled.

Ribosome sampling, binding and unlocking

We can further separate this step into two consecutive states related to canonical translation: pre-accommodation and accommodation. During pre-accommodation, the quaternary complex (tmRNA–SmpB–EF-Tu•GTP) recognizes and enters the stalled ribosome [26]. This process involves several coordinated actions (Fig. 3). The acceptor and T-arms of tmRNA's alanylated TLD are bound to EF-Tu in its GTP state, while the TLD elbow region formed by the D and variable loops is in close contact with the body of SmpB. Stalled ribosomes are selected by SmpB, which uses its C-terminal tail to probe the occupancy of the ribosomal mRNA channel inside and downstream from the decoding site (Fig. 3A-B). If the channel is already occupied by an mRNA, SmpB cannot

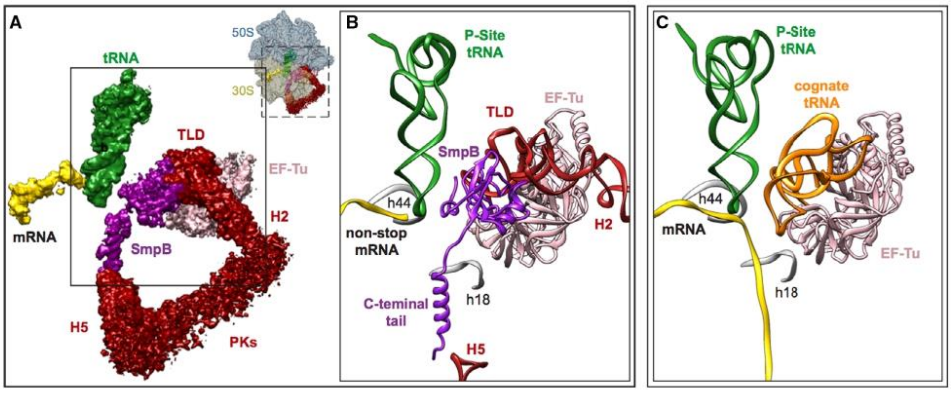

Fig. 3. Highlight on the interactions between the main *trans*-translation actors and the stalled ribosome during the initial binding step (A) Overview of the *trans*-translating ribosome and focus on the characteristic spatial arrangements of EF-Tu, tmRNA, SmpB, P-Site tRNA and non-stop mRNA (PDB 7ABZ, EMDB EMD-11710). The 50S subunit is light blue, the 30S is grey, EF-Tu is pink, tmRNA is red, SmpB is magenta, the P-Site tRNA is green and non-stop mRNA is yellow. The map is contoured at 2 σ and only for the regions within 2 Å of the non-stop mRNA, P-site tRNA, tmRNA and SmpB. (B) Details of the interactions between the tmRNA tRNA-like domain (TLD), the H5 helix, SmpB and EF-Tu. The P-Site tRNA, mRNA and the decoding centre (16S rRNA helices h18 and h44) are also shown. (C) Comparison with the pre-accommodation state of a cognate tRNA (orange) in the 30S closed conformation (PDB 6WD9, EMDB EMD-21628) with a long mRNA (modelled from PDB 6BY1). The TLD mimics the Acceptor- and T-arms of Trna, while the core of SmpB mimics the anticodon stem of tRNA during initial codon selection. SmpB long C-terminal tail folds in the mRNA channel whose entrance is closed by the tip of helix H5. This ensures that the complex does not interfere with canonical translation. All structural figures were done using UCSF chimera [63].

insert its tail, and this is how *trans*-translation avoids interfering with canonical translation (Fig. 3C). On the other hand, if it is available, the C-terminal tail extends along the mRNA path and forms an α-helix whose extremity is in contact with the tmRNA helix H5. This specific interaction is surely instrumental for the complete recognition of the empty A site and downstream mRNA channel which would otherwise be impossible in the presence of a full-length mRNA. Additionally, the binding of PK2, which anchors H5 at the entrance to the mRNA channel, seems to be the more important interaction for positioning of the MLD into the channel. During this step, SmpB mimics a codon-anticodon interaction, as if a correct tRNA-mRNA interaction was occurring. Once on the ribosome, EF-Tu contacts the 50S subunit, further stabilizing the entire complex. The 30S subunit is in a closed conformation that resembles that of the equivalent ternary complex tRNA–EF-Tu•GTP [12,27,28]. The L-shaped TLD forms a 120°-angle, while the CCA 3′-end of the acceptor stem is in the same conformation as observed in canonical tRNA [12,25,29,30]. Just upstream from the TLD acceptor stem, the helix H2 lies between the two ribosomal subunits, allowing the MLD, helix H5 and the pseudoknots to form a 'PK ring' surrounding the 30S 'beak' [24–26,31,32]. At this point, the only contact between the PK ring and the ribosome occurs through PK2 and H5: PK2 is in close contact with the uS3 RNA-binding domain, while helix H5 crowds the groove formed by uS3, uS4 and uS5 at the entrance of the mRNA channel. Inside the Ribosome decoding centre, the 16S nucleotide A1492 remains within helix h44, while A1493 is partially flipped out towards the major groove because of its interaction with the SmpB well-conserved residue His22 (Fig. 4A-C). This conformation is different from that of canonical decoding in which the binding of mRNA and cognate tRNA in the A site induces A1492 and A1493 to flip out of the internal loop of h44 and interact, respectively, with the first and second base pairs of the codon-anticodon helix (Fig. 4D-E) [33].

As observed during canonical translation, the B1a bridge is open, and the B1b/c bridges are closed [34–36]. This pre-accommodation state favours GTP hydrolysis in EF-Tu as well as conformational changes in the ribosomal subunits, inducing accommodation (Fig. 5). The EF-Tu•GDP complex is then released from the ribosome, and SmpB moves more deeply into the A site. As compared with pre-accommodation, the

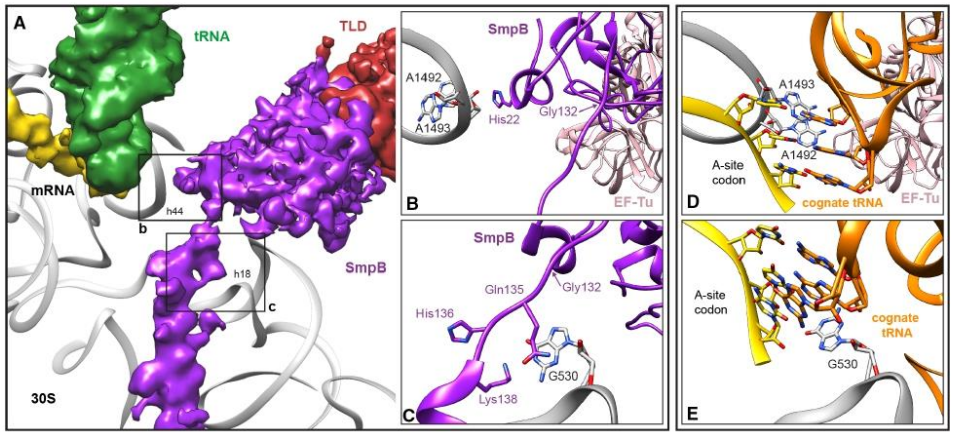

Fig. 4. Interaction of SmpB with the decoding centre (DC) during the binding step. (A) Overview of the DC during the binding of the tmRNA-SmpB-EF-Tu•GTP quaternary complex to the stalled ribosome (PDB 7ABZ, EMDB EMD-11710). (B) Close-up view of the interactions between the first -helix of SmpB and nucleotides A1492 and A1493 of 16S rRNA. (C) Close-up view of the interactions between SmpB C-terminal tail and G530 of 16S rRNA. Residues and nucleotides within 4 Å of each other are indicated. The position of the conserved Gly132 is also indicated. (D) Comparison with interactions observed between mRNA, cognate tRNA and nucleotides A1492 and A1493 of 16S rRNA during the pre-accommodation state of a cognate tRNA (PDB 6WD9, EMDB EMD-21628). (E) Same as (D) but with the nucleotide G530. The 16S rRNA is grey, SmpB is magenta, tRNA is green and non-stop mRNA is yellow. The map is contoured at 2 and only for the regions within 2 Å of the non-stop mRNA, P-site tRNA, tmRNA and SmpB. All structural figures were done using UCSF chimera [63].

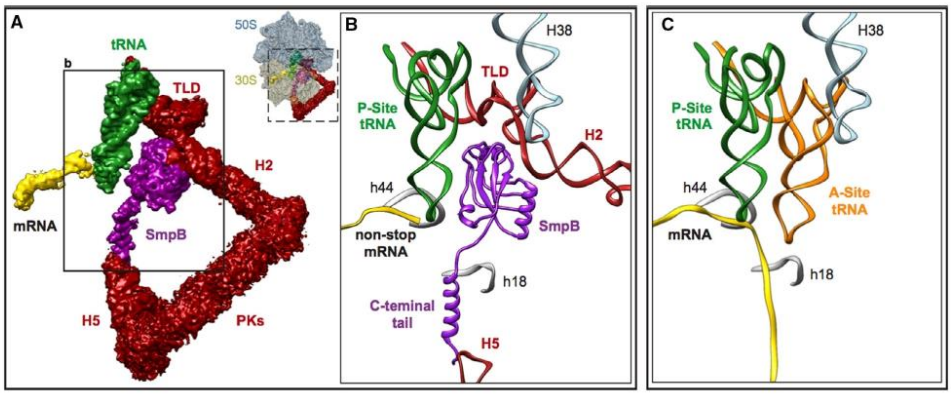

Fig. 5. Highlight on the interactions between the main *trans*-translation actors and the stalled ribosome during the unlocking step (A) Overview of the *trans*-translating ribosome and focus on the characteristic spatial arrangements of tmRNA, SmpB, P-Site tRNA and non-stop mRNA inside the ribosome (PDB 7AC7, EMDB EMD-11713). The 50S subunit is light blue, the 30S is grey, tmRNA is red, SmpB is magenta, the P-Site tRNA is green and non-stop mRNA is yellow. The map is contoured at 2 and only for the regions within 2 Å of the non-stop mRNA, P-site tRNA, tmRNA and SmpB. (B) Details of the interactions between the tmRNA tRNA-like domain (TLD), the H5 helix, SmpB and the P-Site tRNA. The mRNA, 23S rRNA helix H38 and 16S rRNA helices h18 and h44 are also shown. (C) Comparison with the structure of a cognate tRNA (orange) accommodated in the A site (PDB 7K00, EMDB EMD-22586) in the presence of a long non-truncated mRNA (modelled from PDB 6BY1). The TLD perfectly mimics the Acceptor- and T-arms of A-Site tRNA within the peptidyl-transferase centre (PTC). The core of SmpB rotates to replace the codon-anticodon interactions observed during canonical translation. SmpB long C-terminal tail still occupies the mRNA channel and its interactions with helix H5 are reinforced before re-registration starts. All structural figures were done using UCSF chimera [63].

PK ring is now larger and the MLD portion is unfolded—with the exception of a hairpin between U88 and A100 whose presence was earlier confirmed by biochemical assays [37]—meaning that it is ready to enter the mRNA path. The TLD region switches into the peptidyl transferase centre (PTC), accommodated in the same way as correct tRNA [38]. The TLD's T-loop interacts with both uL16 and 23S rRNA helices H38 and H89, while the D-loop is still in contact with SmpB although the protein rotated by ~ 30°. The SmpB C-terminal tail remains folded into a helix within the mRNA channel. In the decoding centre, A1493 is now completely outside and forms π-stacking with H22, while its partner A1492 is in an intermediate conformation, partially flipped out of helix 44 (Fig. 6) in a scenario that resembles a ribosome with a vacant A site during canonical translation [39]. The interaction between PK2 and uS3 is maintained, while helix H5 blocks the mRNA entrance channel completely, in close contact with uS3, uS4, uS5 and the extremity of the SmpB C-terminal tail. Unlocking then occurs once the truncated peptide is displaced from the P-site tRNA to the tmRNA alanine during transpeptidation. This reaction is accompanied by a partial rotation of the 30S head relative to the 50S subunit [24,25,40]: the small and large subunits rotate by 8–10° with respect to each other, while the head undergoes a simultaneous rotation of 5–7° with respect to the body [41,42]. These movements induce a shift of both tmRNA and tRNA into intermediate A/P and P/E binding states respectively. EF-G then enters the ribosome, tmRNA is translocated into the P site, and the stalled tRNA passes through the E site and is ejected from the ribosome (Fig. 7). Here, the presence of EF-G is associated with classical large-scale conformational changes of the small 30S subunit (ref [43]), including a ~ 5° rotation of the body/platform domains, while the head is swivelled by an additional ~ 19°. However, during *trans*-translation, this step is characterized by a unique additional 12° tilt movement around an axis that is approximately parallel to the mRNA, around the A- and P-site codons. These rotational head movements link TLD translocation to MLD loading, showcasing how the elements move within the ribosome [44]. B1a and B1b bridges between the two ribosomal subunits open, thereby allowing the tmRNA helix H2 to slide between these subunits (see below). After GTP hydrolysis, the EF-G•GDP complex dissociates from the ribosome, and the subunits return to their initial state.

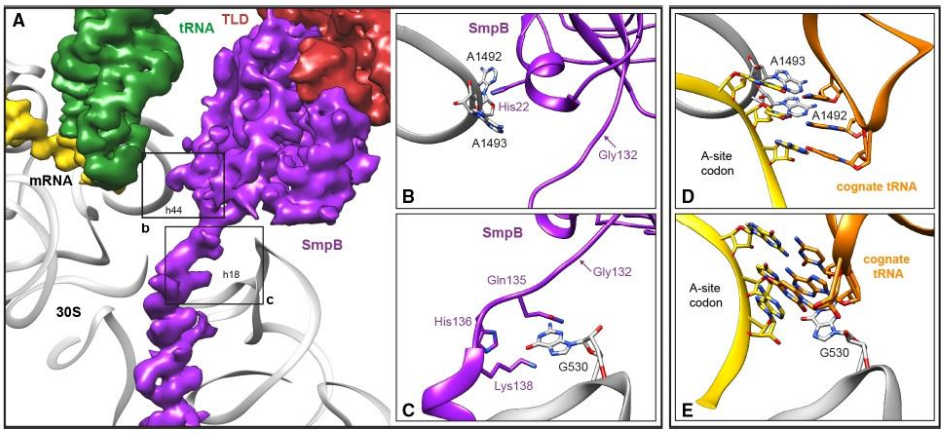

Fig. 6. Interaction of SmpB with the decoding centre (DC) during the unlocking step. (A) Overview of the DC during the binding of the tmRNA-SmpB-EF-Tu•GTP quaternary complex to the stalled ribosome (PDB 7AC7, EMDB EMD-11713). (B) Close-up view of the interactions between the first -helix of SmpB and nucleotides A1492 and A1493 of 16S rRNA. (C) Close-up view of the interactions between SmpB C-terminal tail and G530 of 16S rRNA. Residues and nucleotides within 4 Å of each other are indicated. The position of the conserved Gly132 is also indicated. (D) Comparison with interactions observed between mRNA, cognate tRNA and nucleotides A1492 and A1493 of 16S rRNA a translating ribosome with tRNAs in the A and P sites (PDB 7K00, EMDB EMD-22586. (E) Same as (D) but with the nucleotide G530. The 16S rRNA is grey, SmpB is magenta, tRNA is green and non-stop mRNA is yellow. The map is contoured at 2 and only for the regions within 2 Å of the non-stop mRNA, P-site tRNA, tmRNA and SmpB. All structural figures were done using UCSF chimera [63].

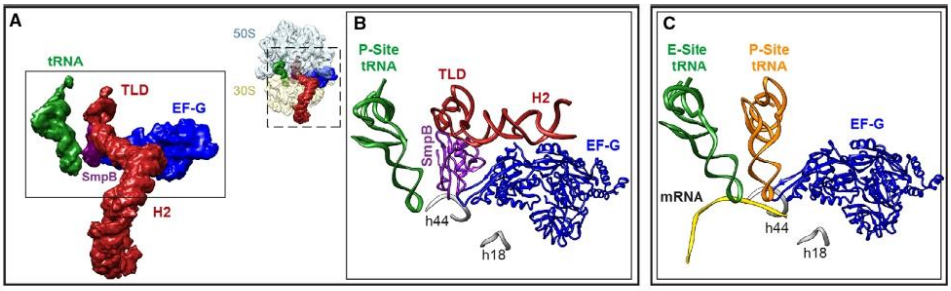

Fig. 7. Highlight on the interactions between the main *trans*-translation actors and the ribosome during the swapping (A) Overview of the *trans*-translating ribosome and focus on the characteristic spatial arrangements of tmRNA, SmpB, E-Site tRNA and EF-G inside the ribosome (PDB 4V6T, EMDB EMD-5386). The 50S subunit is light blue, the 30S is grey, tmRNA is red, SmpB is magenta, the E-Site tRNA is green, EF-G is blue. (B) Details of the interactions between the tmRNA tRNA-like domain (TLD), SmpB, EF-G and the E-Site tRNA. 16S rRNA helices h18 and h44 are also shown. Note that the map resolution did not permit to build an atomic model of SmpB C-terminal tail. (C) Comparison with the structure of a P-site tRNA (orange) (PDB 7K52, EMDB: EMD-22671). All structural figures were done using UCSF chimera [63].

As the release of non-stop ribosomes is essential for cell survival, and the main rescue system for this is *trans*-translation, it has to be noted that this process is a very appealing target in the development of new antimicrobial compounds [45,46], especially since it is absent in eukaryotes [47]. Impairing any of the specific interactions that occur between SmpB, tmRNA and the ribosome is therefore a promising strategy for killing pathogenic bacteria or for making them extremely sensitive to existing antibiotics. For instance, a recent cryo-EM structural study performed in the absence of a tmRNA-SmpB complex suggests that the acylaminooxadiazoles bind ribosomes near the peptidyl transferase centre, in a position that would clash with

tmRNA in the A site, thereby inhibiting *trans*-translation by preventing tmRNA-SmpB binding described here, or else by interfering with the translocation of the complex from the A to the P site [48]. Moreover, it changes the conformation of ribosomal protein bL27 which, in this position would not be able to participate in the peptidyl transferase reaction when tmRNA is presented in the A site.

mRNA swapping and re-registration

While the TLD-SmpB complex is transferred to the P site in a translocation state related to canonical translation, the problematic non-stop mRNA and the MLD are swapped. In this new state, the PK ring completely changes its conformation so that the MLD can enter the mRNA channel in an unusual initiation mechanism (Fig. 8). To do this, the MLD must first pass through the 30S latch (or A-site latch), a physical barrier present between the head (helix 34) and body (guanosine 530) of the 16S rRNA when the small subunit is in a closed conformation [24,44]. Successful loading of the MLD into the path occurs when bridges B1a and B1b open, which is only possible after the 30S head undergoes a rotation of 21° and a tilt of 3° [44]. Helix H5 moves away from uS4 and uS5 to free up the mRNA channel and to permit the MLD to enter. MLD loading is accomplished during the backward movements repositioning the 30S head: by staying associated with S3, the MLD is directly guided through the opened latch into the mRNA path [44]. The nucleotides forming the tip of the helix are stabilized by uS2, while the beginning of the helix and the end of the ORF interact with uS3, uS4 and uS5. SmpB's body is still interacting strongly with the TLD, but the C-terminal tail goes through an important conformational change during this translocation step. Indeed, in

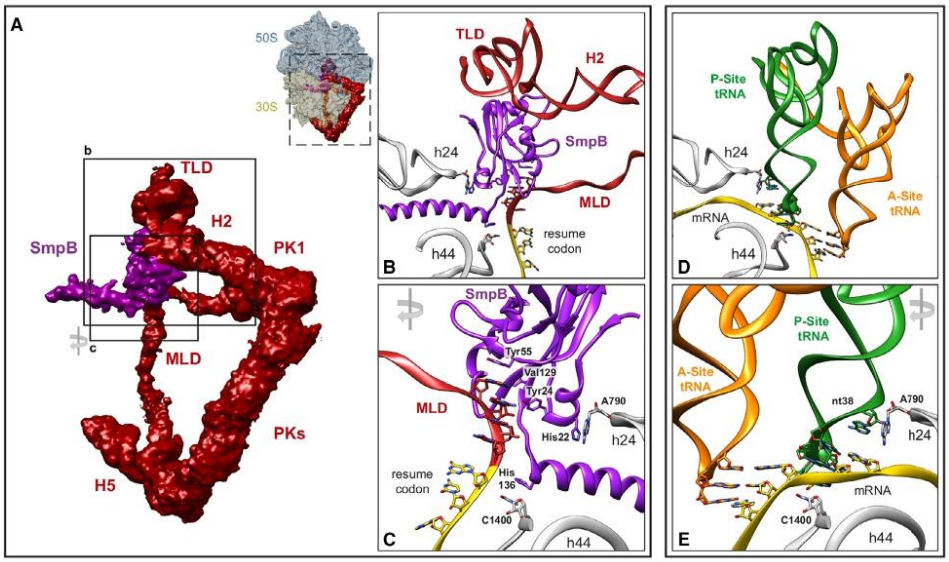

Fig. 8. Highlight on the interactions between the main *trans*-translation actors and the ribosome during the re-registration step (A) Overview of the *trans*-translating ribosome and focus on the characteristic spatial arrangements of tmRNA and SmpB inside the ribosome (PDB 7ACJ, EMD-11717). The 50S subunit is light blue, the 30S is grey, tmRNA is red and SmpB is magenta. The map is contoured at 2 σ and only for the regions within 2 Å of tmRNA and SmpB. (B) Details of the interactions between tRNA-like domain (TLD) and messenger-like domain (MLD) of tmRNA and SmpB and the mRNA exit channel (16S helices h24 and h44). The position of the resume codon (yellow) is highlighted. (C) Close-up view on the interactions between SmpB Tyr24, Tyr55 and Val129 and the four nucleotides upstream the resume codon. The view is rotated by 180°. (D–E) Comparison with the structure of a translating ribosome (PDB 7K00, EMDB EMD-22586) with a long non-truncated mRNA (modelled from PDB 6BY1). The SmpB C-terminal tail occupies the mRNA exit channel and its globular body stacks with A790 and C1400 of 16 rRNA, just like a P-Site tRNA. As a result, the resume codon is correctly placed into the vacant A site. All structural figures were done using UCSF chimera [63].

order for the MLD to enter the mRNA channel and the A site, the tail of the protein must liberate the space it had previously occupied. This portion of the protein, therefore, undergoes a large 62° rotation, flipping over to the other side of the mRNA path within the E site. These data confirm that the highly conserved Glycine 132 acts as a flexible hinge that enables movement of the C-terminal tail, thus permitting proper positioning and establishment of the tmRNA open reading frame (ORF) as the surrogate template [49]. The non-stop mRNA is then released and degraded by RNase R. Re-registration occurs when the resume codon is precisely positioned into the decoding centre. This is made possible by direct interactions between SmpB Tyr24, Tyr55 and Val129 and the four nucleotides just upstream from the MLD resume codon (Fig. 8), thereby ensuring greater control of the sequence and limiting the frame-shift risks [50–53]. Translation then re-registers on the tmRNA's internal ORF, and a new aminoacyl-tRNA complex binds to the resume codon.

Peptide degradation and ribosome recycling

Based on recent structural studies and our knowledge in the field of canonical translation, it is pretty clear how the translation of the entire MLD must continue. The tmRNA-SmpB complex should shift towards the E site and then leave the ribosome in such a way that the truncated peptide is transferred on the next tRNAs that are encoded by the following ORF codons, right up until the stop codon is reached. Surprisingly, there have been no reports of tmRNA-SmpB in the E site, and instead, the complex seems to move past that site to arrive directly at the solvent side of the ribosome [24]. Indeed, the risk of clashing with the ribosome in the E site makes it unlikely that the complex would remain stable in this step. After the post-E site move, the MLD will then have to stretch along the mRNA path [54,55] and the H5 helix will have to unfold, certainly helped by the helicase properties of the ribosomal proteins uS2, uS4 and uS5. Indeed, these interactions are certainly linked to the helicase activity of these ribosomal proteins, already observed in the presence of structured mRNA molecules [56–59]. Although the later steps of *trans*-translation, that is translation and termination, have not yet been visualized in atomic detail, they are presumed to be canonical. Once the stop codon reaches the decoding centre, RF1 or RF2 release factors enter into the A site, freeing the tagged peptide so it can then be degraded by proteases. However, the release of tmRNA from the 30S could be more complicated due to its large structure wrapping around the 30S. The rescue process ends with the recycling of the ribosome (Fig. 9 and Movie S1).

Conclusion

The recent high-resolution cryo-EM structures have yielded a better understanding of how *trans*-translation occurs, revealing why this fascinating process does not interfere with canonical translation but also how it tricks the ribosome into continuing its catalytic activities on such a highly unusual substrate. Ten years ago, we still thought of SmpB as the simple 'handyman of tmRNA' [60]. However, the studies showcase the crucial role played by SmpB during each and every step of tmRNA quality control. Indeed, its work begins early and outside the ribosome, when it binds to the TLD of tmRNA, protecting it from degradation [9] and enhancing the efficiency of alanylation [10,61,62]. It is then not just instrumental but in fact mandatory to tmRNA for recognizing and binding stalled ribosomes.

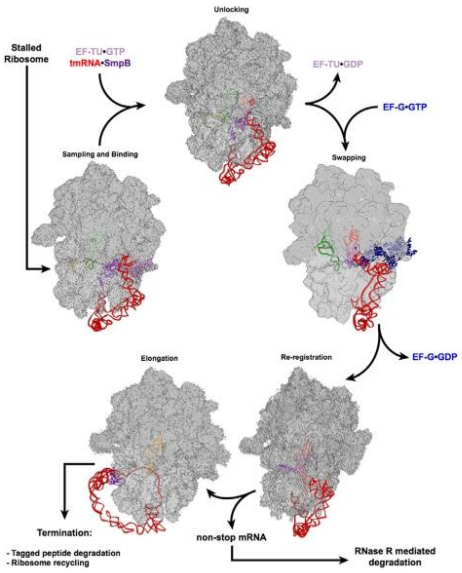

Fig. 9. Structural overview of *trans*-translation. The steps structurally described are: the non-stop stalled ribosome binding (PDB 7ABZ, EMDB EMD-11710); unlocking (PDB 7AC7, EMD-11713); swapping (PDB 4V6T, EMD-5386); re-registration (PDB 7ACJ, EMD-11717) and elongation (PDB 6Q9A, EMD-4478). tmRNA is red, SmpB is purple, P-site tRNA is green, non-stop mRNA is yellow, EF-Tu is pink, EF-G is blue and the ribosome is grey. All structural figures were done using UCSF chimera [63].

To achieve this, SmpB mimics a codon-anticodon pairing within the vacant ribosomal A site and extends its C-terminal tail downstream into the mRNA channel, thereby establishing specific interactions with the ribosome. In the next step of translocation, the protein goes through an important conformational change, mimicking the interactions of a tRNA anticodon loop in the P site. This allows for the correct positioning of the MLD resume codon as well as the ejection of non-stop mRNA. SmpB continues to accompany tmRNA during the subsequent rounds of translation of the MLD, protecting tmRNA as its TLD emerges from the ribosome [11]. In fact, SmpB is more like a 'conductor' of the *trans*-translation symphony orchestra organized to overcome stalled ribosomes, as it is involved throughout the entire quality control process.

Acknowledgements

The authors gratefully acknowledge aid from the Agence Nationale pour la Recherche as part of the RIBOTARGET 18-JAM2-0005-03 project under the JPI AMR framework. Funding was also received from the French Direction Générale de l'Armement (CG), the Université de Rennes 1 (CG), the European Union's ERASMUS+ program (GU) and the Région Bretagne (GU). We thank Juliana Berland for her insightful comments on the manuscript.

Conflict of interest

The authors declare no conflict of interest.

Author contributions

GU and RG wrote the first draft of the manuscript. All authors participated in manuscript revision and approved its final version.

Data availability statement

All the structures described are available in PDB/EMDB repository ressources.

References

1 Cougot N, Molza A-E, Delesques J, Giudice E, Cavalier A, Rolland J-P, et al. Visualizing compaction of polysomes in bacteria. *J Mol Biol*. 2014;**426**:377–88.
2 Ito K, Chadani Y, Nakamori K, Chiba S, Akiyama Y, Abo T. Nascentome analysis uncovers futile protein synthesis in Escherichia coli. *PLoS One*. 2011;**6**:e28413.
3 Müller C, Crowe-McAuliffe C, Wilson DN. Ribosome rescue pathways in bacteria. *Front Microbiol*. 2021;**12**:652980.
4 Gimple O, Schön A. *In vitro* and *in vivo* processing of cyanelle tmRNA by RNase P. *Biol Chem*. 2001;**382**:1421–9.
5 Komine Y, Kitabatake M, Yokogawa T, Nishikawa K, Inokuchi H. A tRNA-like structure is present in 10Sa RNA, a small stable RNA from Escherichia coli. *Proc Natl Acad Sci USA*. 1994;**91**:9223–7.
6 Li Z, Pandit S, Deutscher MP. 3' exoribonucleolytic trimming is a common feature of the maturation of small, stable RNAs in Escherichia coli. *Proc Natl Acad Sci USA*. 1998;**95**:2856–61.
7 Lin-Chao S, Wei C-L, Lin Y-T. RNase E is required for the maturation of ssrA RNA and normal ssrA RNA peptide-tagging activity. *PNAS*. 1999;**96**:12406–11.
8 Moore SD, Sauer RT. The tmRNA system for translational surveillance and ribosome rescue. *Annu Rev Biochem*. 2007;**76**:101–24.
9 Karzai AW, Susskind MM, Sauer RT. SmpB, a unique RNA-binding protein essential for the peptide-tagging activity of SsrA (tmRNA). *EMBO J*. 1999;**18**:3793–9.
10 Barends S, Karzai AW, Sauer RT, Wower J, Kraal B. Simultaneous and functional binding of SmpB and EF-Tu·GTP to the alanyl acceptor arm of tmRNA 11Edited by J. Doudna. *J Mol Biol*. 2001;**314**:9–21.
11 Bugaeva EY, Shpanchenko OV, Felden B, Isaksson LA, Dontsova OA. One SmpB molecule accompanies tmRNA during its passage through the ribosomes. *FEBS Lett*. 2008;**582**:1532–6.
12 Neubauer C, Gillet R, Kelley AC, Ramakrishnan V. Decoding in the absence of a codon by tmRNA and SmpB in the ribosome. *Science*. 2012;**335**:1366–9.
13 Richards J, Mehta P, Karzai AW. RNase R degrades non-stop mRNAs selectively in an SmpB-tmRNA-dependent manner. *Mol Microbiol*. 2006;**62**:1700–12.
14 Keiler KC, Waller PR, Sauer RT. Role of a peptide tagging system in degradation of proteins synthesized from damaged messenger RNA. *Science*. 1996;**271**:990–3.
15 Bessho Y, Shibata R, Sekine S, Murayama K, Higashijima K, Hori-Takemoto C, et al. Structural basis for functional mimicry of long-variable-arm tRNA by transfer-messenger RNA. *Proc Natl Acad Sci USA*. 2007;**104**:8293–8.
16 Hudson CM, Williams KP. The tmRNA website. *Nucleic Acids Res*. 2015;**43**:D138–40.
17 Shimizu Y. ArfA recruits RF2 into stalled ribosomes. *J Mol Biol*. 2012;**423**:624–31.
18 Chadani Y, Ono K, Kutsukake K, Abo T. Escherichia coli YaeJ protein mediates a novel ribosome-rescue pathway distinct from SsrA- and ArfA-mediated pathways. *Mol Microbiol*. 2011;**80**:772–85.

19 Lytvynenko I, Paternoga H, Thrun A, Balke A, Müller TA, Chiang CH, et al. Alanine Tails Signal Proteolysis in Bacterial Ribosome-Associated Quality Control. *Cell*. 2019;**178**:76–90.e22.
20 Goralski TDP, Kirimanjeswara GS, Keiler KC. A new mechanism for ribosome rescue can recruit RF1 or RF2 to nonstop ribosomes. *MBio*. 2018;**9**:e02436–18.
21 Shimokawa-Chiba N, Müller C, Fujiwara K, Beckert B, Ito K, Wilson DN, et al. Release factor-dependent ribosome rescue by BrfA in the Gram-positive bacterium Bacillus subtilis. *Nat Commun*. 2019;**10**:5397.
22 Keiler KC, Feaga HA. Resolving nonstop translation complexes is a matter of life or death. *J Bacteriol*. 2014;**196**:2123–30.
23 Chadani Y, Ono K, Ozawa S, Takahashi Y, Takai K, Nanamiya H, et al. Ribosome rescue by Escherichia coli ArfA (YhdL) in the absence of trans-translation system. *Mol Microbiol*. 2010;**78**:796–808.
24 Rae CD, Gordiyenko Y, Ramakrishnan V. How a circularized tmRNA moves through the ribosome. *Science*. 2019;**363**:740–4.
25 Guyomar C, D'Urso G, Chat S, Giudice E, Gillet R. Structures of tmRNA and SmpB as they transit through the ribosome. *Nat Commun*. 2021;**12**:4909.
26 Valle M, Gillet R, Kaur S, Henne A, Ramakrishnan V, Frank J. Visualizing tmRNA entry into a stalled ribosome. *Science*. 2003;**300**:127–30.
27 Schmeing TM, Ramakrishnan V. What recent ribosome structures have revealed about the mechanism of translation. *Nature*. 2009;**461**:1234–42.
28 Voorhees RM, Ramakrishnan V. Structural basis of the translational elongation cycle. *Annu Rev Biochem*. 2013;**82**:203–36.
29 Stagg SM, Frazer-Abel AA, Hagerman PJ, Harvey SC. Structural studies of the tRNA domain of tmRNA. *J Mol Biol*. 2001;**309**:727–35.
30 Gutmann S, Haebel PW, Metzinger L, Sutter M, Felden B, Ban N. Crystal structure of the transfer-RNA domain of transfer-messenger RNA in complex with SmpB. *Nature*. 2003;**424**:699–703.
31 Weis F, Bron P, Giudice E, Rolland J-P, Thomas D, Felden B, et al. tmRNA-SmpB: a journey to the centre of the bacterial ribosome. *EMBO J*. 2010;**29**:3810–8.
32 Fu J, Hashem Y, Wower I, Lei J, Liao HY, Zwieb C, et al. Visualizing the transfer-messenger RNA as the ribosome resumes translation. *EMBO J*. 2010;**29**:3819–25.
33 Ogle JM, Brodersen DE, Clemons WM, Tarry MJ, Carter AP, Ramakrishnan V. Recognition of cognate transfer RNA by the 30S ribosomal subunit. *Science*. 2001;**292**:897–902.
34 Pape T, Wintermeyer W, Rodnina MV. Complete kinetic mechanism of elongation factor Tu-dependent binding of aminoacyl-tRNA to the A site of the E. coli ribosome. *EMBO J*. 1998;**17**:7490–7.
35 Rodnina MV, Wintermeyer W. Fidelity of aminoacyl-tRNA selection on the ribosome: kinetic and structural mechanisms. *Annu Rev Biochem*. 2001;**70**:415–35.
36 Ogle JM, Murphy FV, Tarry MJ, Ramakrishnan V. Selection of tRNA by the ribosome requires a transition from an open to a closed form. *Cell*. 2002;**111**:721–32.
37 Felden B, Himeno H, Muto A, McCutcheon JP, Atkins JF, Gesteland RF. Probing the structure of the Escherichia coli 10Sa RNA (tmRNA). *RNA*. 1997;**3**:89–103.
38 Cheng K, Ivanova N, Scheres SHW, Pavlov MY, Carazo JM, Hebert H, et al. tmRNA.SmpB complex mimics native aminoacyl-tRNAs in the A site of stalled ribosomes. *J Struct Biol*. 2010;**169**:342–8.
39 James NR, Brown A, Gordiyenko Y, Ramakrishnan V. Translational termination without a stop codon. *Science*. 2016;**354**:1437–40.
40 Giudice E, Mace K, Gillet R. Trans-translation exposed: understanding the structures and functions of tmRNA-SmpB. *Front Microbiol*. 2014;**5**:113.
41 Ermolenko DN, Majumdar ZK, Hickerson RP, Spiegel PC, Clegg RM, Noller HF. Observation of intersubunit movement of the ribosome in solution using FRET. *J Mol Biol*. 2007;**370**:530–40.
42 Mohan S, Donohue JP, Noller HF. Molecular mechanics of 30S subunit head rotation. *Proc Natl Acad Sci USA*. 2014;**111**:13325–30.
43 Guo Z, Noller HF. Rotation of the head of the 30S ribosomal subunit during mRNA translocation. *Proc Natl Acad Sci USA*. 2012;**109**:20391–4.
44 Ramrath DJF, Yamamoto H, Rother K, Wittek D, Pech M, Mielke T, et al. The complex of tmRNA-SmpB and EF-G on translocating ribosomes. *Nature*. 2012;**485**:526–9.
45 Feaga HA, Viollier PH, Keiler KC. Release of nonstop ribosomes is essential. *MBio*. 2014;**5**:e01916.
46 Campos-Silva R, D'Urso G, Delalande O, Giudice E, Macedo AJ, Gillet R. Trans-translation is an appealing target for the development of new antimicrobial compounds. *Microorganisms*. 2021;**10**:3.
47 Thepaut M, Campos-Silva R, Renard E, Barloy-Hubler F, Ennifar E, Boujard D, et al. Safe and easy *in vitro* evaluation of tmRNA-SmpB-mediated trans-translation from ESKAPE pathogenic bacteria. *RNA*. 2021;**11**:1399.
48 Aron ZD, Mehrani A, Hoffer ED, Connolly KL, Srinivas P, Torhan MC, et al. trans-Translation inhibitors bind to a novel site on the ribosome and clear Neisseria gonorrhoeae *in vivo*. *Nat Commun*. 2021;**12**:1799.
49 Camenares D, Dulebohn DP, Svetlanov A, Karzai AW. Active and Accurate trans-translation requires distinct determinants in the C-terminal tail of SmpB protein and the mRNA-like domain of transfer messenger RNA (tmRNA) *♦. *J Biol Chem*. 2013;**288**:30527–42.

50 Konno T, Kurita D, Takada K, Muto A, Himeno H. A functional interaction of SmpB with tmRNA for determination of the resuming point of trans-translation. *RNA*. 2007;**13**:1723–31.
51 Miller MR, Healey DW, Robison SG, Dewey JD, Buskirk AR. The role of upstream sequences in selecting the reading frame on tmRNA. *BMC Biol*. 2008;**6**:29.
52 Watts T, Cazier D, Healey D, Buskirk A. SmpB contributes to reading frame selection in the translation of transfer-messenger RNA. *J Mol Biol*. 2009;**391**:275–81.
53 Kucukelbir A, Sigworth FJ, Tagare HD. Quantifying the local resolution of cryo-EM density maps. *Nat Methods*. 2014;**11**:63–5.
54 Wower IK, Zwieb C, Wower J. Transfer-messenger RNA unfolds as it transits the ribosome. *RNA*. 2005;**11**:668–73.
55 Bugaeva EY, Surkov S, Golovin AV, Ofverstedt L-G, Skoglund U, Isaksson LA, et al. Structural features of the tmRNA-ribosome interaction. *RNA*. 2009;**15**:2312–20.
56 Takyar S, Hickerson RP, Noller HF. mRNA helicase activity of the ribosome. *Cell*. 2005;**120**:49–58.
57 Qu X, Wen J-D, Lancaster L, Noller HF, Bustamante C, Tinoco I. The ribosome uses two active mechanisms to unwind messenger RNA during translation. *Nature*. 2011;**475**:118–21.
58 Zhang Y, Hong S, Ruangprasert A, Skiniotis G, Dunham CM. Alternative Mode of E-Site tRNA Binding in the Presence of a Downstream mRNA Stem Loop at the Entrance Channel. *Structure*. 2018;**26**:437–445.e3.
59 Amiri H, Noller HF. Structural evidence for product stabilization by the ribosomal mRNA helicase. *RNA*. 2019;**25**:364–75.
60 Felden B, Gillet R. SmpB as the handyman of tmRNA during trans-translation. *RNA Biol*. 2011;**8**:440–9.
61 Shimizu Y, Ueda T. The role of SmpB protein in trans-translation. *FEBS Lett*. 2002;**514**:74–7.
62 Hanawa-Suetsugu K, Takagi M, Inokuchi H, Himeno H, Muto A. SmpB functions in various steps of trans-translation. *Nucleic Acids Res*. 2002;**30**:1620–9.
63 Pettersen EF, Goddard TD, Huang CC, Couch GS, Greenblatt DM, Meng EC, et al. UCSF Chimera–a visualization system for exploratory research and analysis. *J Comput Chem*. 2004;**25**:1605–12.

Supporting information

Additional supporting information may be found online in the Supporting Information section at the end of the article.

Movie S1. Movie of ribosomal trans-translation.

3.3 The alternatives to *trans*-translation

The *ssrA* and *smpB* genes coding, respectively, for tmRNA and SmpB have been found in all bacteria and they are essential to cell survival in different species, bringing defects in virulence and/or cell cycle control (Huang et al., 2000; Keiler and Shapiro, 2003; Thibonnier et al., 2008; Mann et al., 2012; Svetlanov et al., 2012; Fey et al., 2013; Ramadoss et al., 2013; Personne and Parish, 2014). In some other bacteria the deletion of *trans*-translation genes has only mild consequences on cell survival, such as defects in the response to different stresses or an increased susceptibility to antibiotics (Abo et al., 2002; Munavar et al., 2005; Shin et al., 2007). This evidence suggested the presence of other accessory mechanisms that would allow for cell survival in the absence of the main translation rescue system. Two other mechanisms have been highlighted for the nonstop mRNA decay (NSD), each of which is based on alternative ribosome-rescue factors (Arfs) able to recognize and bind a vacant A site. The first mechanism involves the ArfA factor together with RF2, while the second is only based on the action of ArfB (Chadani et al., 2012; Kurita et al., 2014; Huter et al, 2017; Inada, 2020). An additional rescue system, called Ribosome-Associated Quality Control has also been recently described in bacteria (Lytvynenko et al., 2019)

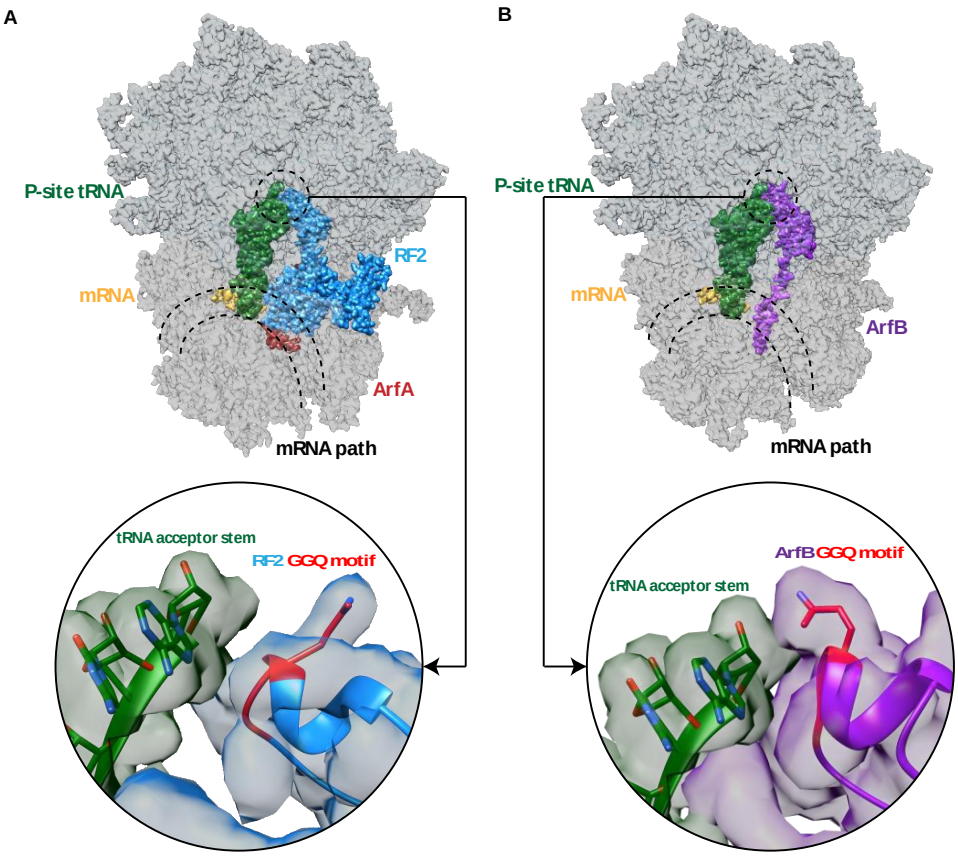

Figure 20: The two Arf factors. Top: representation of a stalled ribosome with the ArfA-RF2 complex (A) and ArfB (B). Bottom: focus on the interaction between the P-site tRNA and the GGQ motif in RF2 (A) and ArfB (B). tRNA is green, mRNA is yellow, ArfA is red, ArfB is purple, RF2 is cyan. PDB: 5MGP, 4V95.

3.3.1 The alternative ribosome-rescue factor A (ArfA)

The importance of this backup system for *trans*-translation has been demonstrated when studies on double mutant bacteria, lacking both *ssrA* and *arfA* genes, showed the lethality of these simultaneous deletions (Chadani et al., 2010). Furthermore, ArfA activity is finely tuned by the presence or the absence of tmRNA. The mRNA transcript of the *arfA* gene presents a stem-loop that acts as a substrate for RNase III cleavage (Chadani et al., 2011; Garzza-Sanchez et al., 2011). When tmRNA is present, the truncated protein coming from the cleaved transcript is tagged by tmRNA for degradation. In the absence of tmRNA, the short ArfA is not tagged and it can play its role in ribosome rescue (Chadani et al., 2011; Garzza-Sanchez et al., 2011). As with SmpB, the C-terminal tail of ArfA acts as a probe which identifies the absence of mRNA in the entry channel. After that, it binds close to the DC and recruits RF2 on the ribosome (Shimizu, 2012). The rescue mechanism of ArfA is based on peptidyl-tRNA hydrolysis, which means that it frees the ribosome by hydrolyzing the peptidic bond between the P-site tRNA and the nascent peptide. However, this factor lacks a GGQ motif, essential for this task. For this reason, ArfA, once it is accommodated within the A site, recruits RF2 to accomplish this function (Chadani et al., 2012; James et al., 2016; Demo et al., 2017; Huter et al., 2017b; Ma et al., 2017; Zeng et al., 2017).

3.3.2 The alternative ribosome-rescue factor B (ArfB)

Different from ArfA, the ArfB factor is able to rescue the ribosome independently from the presence of tmRNA•SmpB and ArfA•RF2 complexes. As previously described for AfrA and SmpB, ArfB also presents a C-terminal tail, disordered in solution, that acts as a probe to detect vacant mRNA entry channel and to bind an empty A site (Gagnon et al., 2012). On the other hand, the N-terminal tail contains the conserved GGQ motif essential to hydrolyze the bond between the nascent peptide and the peptidyl-tRNA (Kogure et al., 2014). Thanks to that, ArfB can act alone to rescue the ribosomes (Chadani et al., 2011; Handa et al., 2011). In addition, although ArfB is

preferentially recruited on stalled ribosomes, it mantains some rescue activity on ribosomes containing an mRNA that extends into A site (Handa et al., 2011).

3.3.3 The Bacterial Ribosome-Associated Quality Control

Recently, in bacteria, a new rescue system known as RQC has been described for the first time in *B. subtilis* (Lytvynenko et al., 2019). While this mechanism is well described in eukaryotes, many aspects remain obscure within bacterial cells. This process, to occur, needs the separation of ribosomal subunits by a recently described factor known as MutS2, bringing to a large ribosomal subunit in complex with the peptidyl-tRNA-nascent chain (Muller et al., 2021; Cerullo, Filbeck et al., 2022). The main actor involved in this process is called RqcH, a NEMF-family protein that binds the large subunit and extend the nascent peptide with an alanine chain (Udagawa et al., 2021). For the tailing process, another factor called RqcP is needed (Crowe-McAuliffe et al., 2021; Filbeck et al., 2021). How the process in bacteria is terminated is still unknown. Based on recent cryo-EM studies, we can hypothesize the following mechanism: after MutS2 subunits separation, RqcP recognizes and binds the peptidyl-tRNA-nascent chain preparing the system for the first alanine adding. RqcH bound to an alanine-tRNA^{Ala} binds to the empty A site with the subsequent peptidyl transfer among the two tRNA. The P-site tRNA moves towards the E site bound to RqcP and is then released. At the same time, The A/P-site-tRNA bringing the nascent peptidic chain moves within the P site, freeing the A site for the next alanine-tRNA^{Ala} bound to RqcH. The tailing process continues until the dissociation of the chain with an unknown mechanism (Crowe-McAuliffe et al., 2021). However, several questions are still open about this elegant mechanism, also involved in ribosome rescue.

4 The cryo-transmission electron microscopy (cryo-TEM)

4.1 Introduction

Biological macromolecules rarely work alone and understanding their structural organization is one of the fundamental features required to understand the mechanistic details underlying their functioning. For that reason, structural biology was developed to study the architecture and the dynamical properties of molecular assemblies to provide fundamental insights into their functional framework and physiological roles. At the dawn of the structural study of biological molecules, one of the most widely used techniques was X-ray crystallography. This technique, which made possible for the first time the study of the spatial organization of the atoms of a molecule, is nevertheless strongly limited by the ability of proteins or other macromolecules to form crystals, as well as by the large amounts of high-purity samples to be used. In addition, the structures obtained from crystals correspond to a somehow “unnatural” conformation, *i.e.* an ensemble of biological molecules packed in a way that thermodynamically favors the formation of the crystal. While the X-ray crystallography allows obtaining very precise data (or high-resolution structures) even for large molecular systems (such as ribosomes, viral capsid or DNA origami) the expression, purification, and crystallization of membrane proteins and large and dynamical molecular complexes are often particularly difficult. A second technique used in structural analysis is the nuclear magnetic resonance (NMR). Although NMR does not require the inclusion of samples in crystals, the analysis requires a large quantity of samples and is only applicable to small biological systems (the current size limit of protein NMR is ~35kDa with an upper limit of ~100kDa). In addition, the samples need to be enriched with isotopes because it greatly enhances the spectrometer sensitivity and allows for site-specific interrogation of structures and intermolecular contacts. To overcome the limitations and restraints of these techniques, in particular, relative to their application on big complexes, membrane proteins, and dynamical assemblies for which different conformations and states exist, cryo-transmission electron microscopy, or simply cryo-electron microscopy (cryo-EM), has been developed, emerging as the technique that allows studying challenging systems not yet structurally characterized.

4.1.1 From optic to cryo-electron microscopy

In 1878 Abbe proved that the resolution of an image acquired with a microscope (in which the light source is represented by photons) depends on the wavelength of the particle used to image a sample. In particular, in a classical optic microscope, photons have a wavelength between 400 nm and 700 nm. Since the smallest detectable distance separating two points cannot be less than half of the wavelenght used, in the case of photons they do not allow the detection of details below 200 nm. The interest in finding a light source with shorter wavelength came, therefore, from the need to observe smaller and smaller objects and describe them at the atomic level. Thanks to two main discoveries by de Broglie and Busch, who respectively described in 1924 the properties of the electron wave and in 1926 the effect of a magnetic coil on an electron beam, electrons (wavelength of ~0,004 nm) began to be considered as a potential light source for imaging extremely small objects. Starting from these assumptions Knoll and Ruska from the Techincal University of Berlin, successfully built in 1931 the first electron microscope. From this time onwards, different observation techniques using electron have been developed, first and foremost transmission electron microscopy (TEM) and scanning electron microscopy (SEM). Unlike SEM in which images are produced by raster scanning the sample surface with a focused electron beam of high energy, for TEM a beam of electrons is produced and transmitted through an ultra-thin sample. Then, unscattered and scattered electrons passing through the sample are focused and hit the camera placed under the sample, at the bottom of the microscope, to produce the image. Three major bottlenecks, however, needed to be overcome to use this technique to image high-resolution features of biological samples. First of all, biological molecules are dependent on their aqueous environment and if we want to get truthfully images of these molecules, in their physiological state, we need to preserve this environment. Secondly, the sample needs to be preserved from radiation damage caused by high-energy electrons. Finally, the sample needs to be preserved from the ultra-high vacuum of the TEM microscope. To overcome these problems, a breakthrough came when samples started to be rapidly vitrified in their hydrated state by plunging into a temperature and humidity-controlled environment (Dubochet et al., 1982a/b; Dubochet et al., 1981; Lepault et al., 1982, 1983; Adrian et al., 1984; Vogel et al., 1986; Bellare et al., 1988; Almgren et al; 1996; Nogales, 2016). The electron microscopy analysis of vitrified samples preserved in amorphous ice gave rise to the

emergence of cryo-electron microscopy (cryo-EM), which has now become one of the mainstream structural biology techniques. This technique also presents the advantage of instanteously “freezing” the molecule, limitating the vibration of the atoms and allowing for high-resolution observation.

4.2 The origin of the image contrast

4.2.1 The scattering

Scattering is the physical phenomenon that occurs when an electron hits an object. In particular, it consists of the deviation of the trajectory followed by the moving particles as a result of the disuniformities present in the medium it passes through. Considering the corpuscular nature of the electrons, three different scenarios can occur when they interact with the sample within the microscope column:

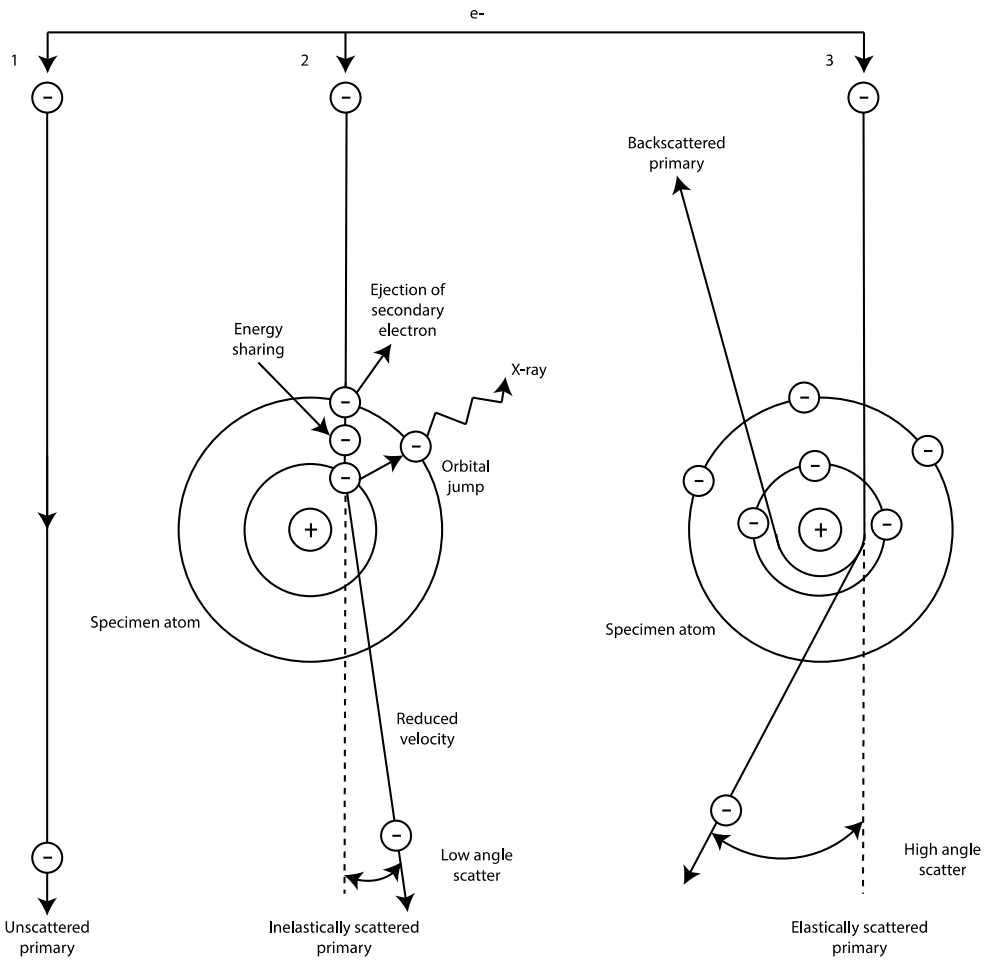

Figure 21: Schematic representation of the different scenario that an electron can experience during the interaction with an atom within a microscope.

1 In the first possible scenario, the incident electron does not interact with any of the atoms in the sample, thus preserving its motion unchanged. In this case, we are talking about unscattered primary electrons (Figure 21, 1);
2 In the second case, the incident electron interacts with an atom of the specimen, thus transferring part of its energy to it. As a result, the incident electron will emerge from the sample with a lowered energy value and at a different angle. Here we refer to these electrons as inelastically scattered primary electrons (Figure 21, 2);
3 In the last possible case the incident electron interacts with an atom within the sample but no energy transfer takes place. Although the trajectory of the emerging electron deviates from the incident trajectory, the amount of energy remains identical to the initial one. We refer to these electrons as elastically scattered primary electrons (Figure 21, 3).

All these three phenomena occur when observing a sample using TEM and, as a result, the three different types of electrons emerging from the sample will contribute to the final image formation.

4.2.2 Amplitude and phase contrast

Within a TEM we can distinguish between two types of contrast that, together contribute to the image formation: the amplitude contrast and the phase contrast.

As we have already seen, as long as the path of the incident electron within the microscope column is not disturbed by any dense object, it will continue straight ahead until it reaches the detector. In this case, no information is transferred into the final image (Figure 21, 1). Imagine now that a dense object is placed between the incident electron beam and the detector. In this case, all the electrons scattered through the sample will be collected by the magnetic lenses and their trajectory will be bent to be focused on the detector plane. The electron scattered at very high angles will not be focused on the image plane and are usually removed by the aperture of the lens. However, because of their lower energy, the remaining scattered electrons will be more easily bent by the magnetic lens, and as a result, focused into a point placed higher than the real image plane. The formation of images on different planes, finally, leads to a blurred image as a whole. These electrons, therefore, need to be blocked in their path by specific elements present in the microscope column called energy filters, to prevent them from contributing to the

image formation (Figure 21, 2). The same fate awaits the backscattered electrons which, due to their nature, will not reach the detector (Figure 21, 3). Thus, the final image will be the combination of unscattered electrons (in the less dense region of the sample) and those few scattered electrons not eliminated on their way to the detector (in the dense regions). Within the final image, this different electron combination will be visible as areas of different contrast. Darker areas with higher contrast are due to scattered electrons and lighter areas with lower contrast are due to unscattered electrons. This difference in chromatic intensity constitutes the amplitude contrast, which is nothing more than a phenomenon due to the removal of some electrons before they reach the image plane.

To understand phase contrast, one must consider the incident electron as a plane wave, a kind of array in which each element within it is characterized by a specific value of amplitude (A) and phase (φ). The amplitude of the plane wave will always be the same, while the phase varies according to the position of the wave in space as it travels along the microscope column. When a plane wave interacts with the different scattering centers (atoms, residues, secondary structures, etc.) of the sample, it will physically produce a series of ripples which will induce a slowing down of the phase variation along the wave path. Each ripple along the plane wave will interfere with the other, generating constructive or destructive interference. The constructive interference of the phase ripples will form further plane waves emerging from the specimen which will continue to propagate along the column until they reach the detector, interfering with the other emerging plane wave at different scattering angles at the detector surface, carrying each one the information derived from the interactions with the different scattering centers within the specimen. As can be seen, the scattering phenomenon that gives rise to phase contrast involves a decomposition of the information present in the sample, which is then combined to form the 2D projection of the sample onto the detector. Since the scattering phenomenon results in a decomposition of the information present in the sample, it can be seen as the physical process underlying the Fourier transform.

4.2.3 Plane wave propagation and phase shift

The interaction between a plane wave and the different scattering centers within a sample generates a series of wavefronts, each of which represents the

decomposition of the complex information contained in the sample. The components scattered at different scattering angles, inside the microscope, will be focused by the lens on the back focal plane where the Fourier transform of the complex wave relative to the initial object is formed (Figure 22, A). However, what is described corresponds to an ideal microscope. As explained before, not all waves will reach the detector and contribute to the formation of the final image. To better understand what happens during a plane wave propagation and, at the same time, to see what information is visible in the final image, we represent plane waves through the so-called Argand diagram, where the waves are represented as vector quantities characterized by a module A and an angle given by the φ (Figure 22, B).

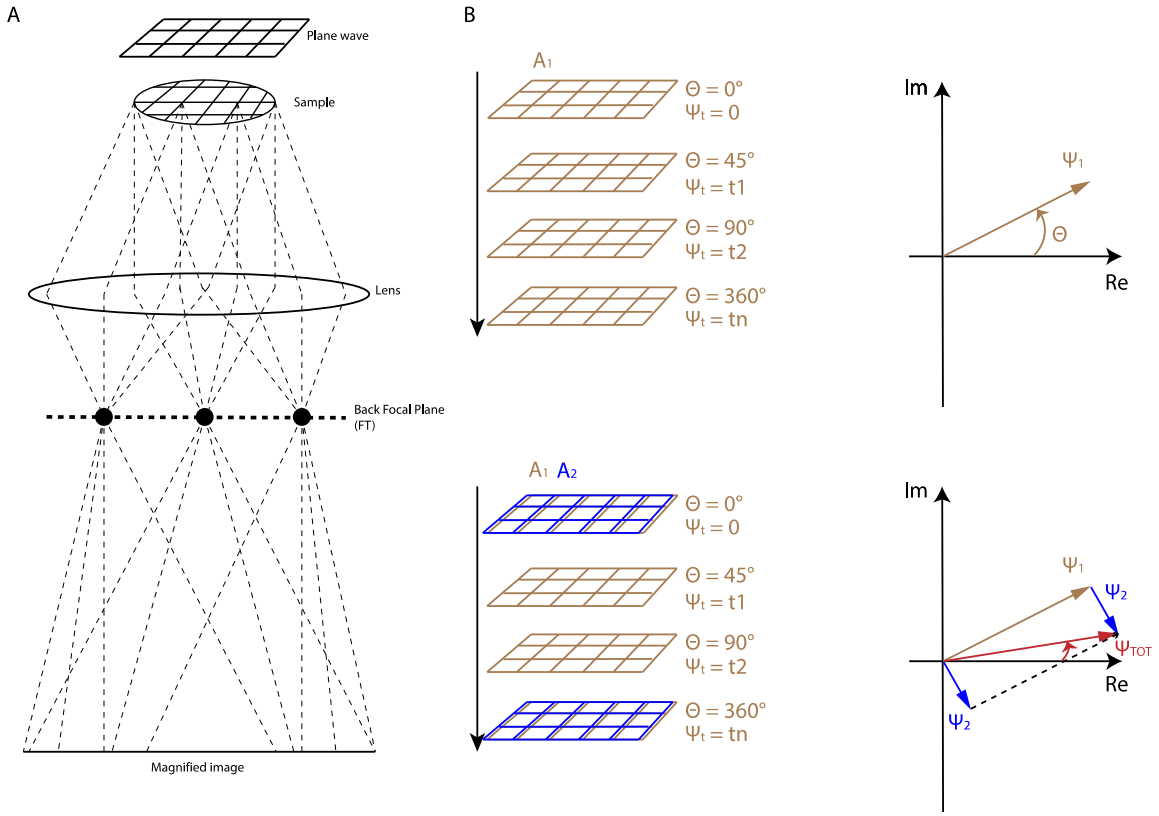

Figure 22: Representation of the plane wave propagation and thir interaction with the sample. A) Scattering of the plane wave and components propagation. B) Representation of the plane waves on an Argand diagram.

The wave function ψ_t at time t = 1 on an Argan diagram is represented as a vector of module A = 1 and angle Θ = 45° (Figure 22, B top). Let's suppose that, in the same space, is present a second plane wave (blue) this time characterized by an A = ¼ and a Θ = 275° (Figure 22, B bottom). To understand how these two plane waves, following the scattering with the sample, will encounter interference and thus contribute to the final image, we apply the sum between vectors within the Argand

diagram. The sum vector will then be represented by the wave function ψ_{TOT} (red), which, in practical terms, indicates the probability that the information carried by the plane wave will be transferred into the final image. From this example, we can easily deduce that what plays a fundamental role in the transmission of the information into the final image is the angle described between the two vectors, representing the two plane waves characterized by different phase values. This angle is called phase shift. Indeed, if the angle described by the two vectors is 0°, the phase shift will be 0°. The sum vector will have a modulus (amplitude) bigger than the modulus of the individual vectors. In this case, the two waves are “in phase“. For phase shifts different from 0°, the sum vector modulus will be always smaller than the modulus of one of the two vectors. As a consequence, the probability that the information is transferred into the image will be lower. In this case, the waves are “out of phase“.

4.2.4 The contrast transfer function (CTF)

Each of the Fourier components capable to reach the detector, whether unscattered or scattered, will contribute differently to the formation of the final image. Let’s now imagine that a plane wave is interacting with our sample. Part of the plane wave will be unscattered (ψ_1), characterized by a certain value of amplitude and a phase of φ = 45°. A second component, instead, will be scattered (ψ_2), emerging from the sample with a phase value different from that of the unscattered component. To understand what the phase shift between the scattered and unscattered components amounts to, let’s consider what happens when an X-ray interacts with the electron cloud of an atom. The oscillating electric field of the X-ray beam (which represents the incident electron beam of the microscope and, by consequence, the unscattered component), when it interacts with an electron in the atom, will transfer part of its energy to the latter, thereby inducing its oscillation. An oscillating electric charge, in turn, generates an electric field that spreads outwards. The direction in which the electric field generated by the electron (scattered component) emerges will be characterised by a particular angle respect to the direction of the incident electric field. This angle will be, therefore, the phase shift. In general, the oscillation of the incident electric field is equal to the resonance frequency of the electron. In this case, the two electric fields are exactly 90° out of phase with each other. In other words, the second electric field will emerge with a 90° phase shift. In addition, another difference that contributes to the phase shift depends from the fact that compared to the unscattered component,

the scattered component follows a longer path before reaching the detector. Because of this, the scattered component presents an additional phase shift defined by Δ*l*. Coming back to our example, let's assume that the difference in the path for the scattered component is a quarter of the wavelength at which these components propagate, so Δ*l* = λ/4. Then, the total phase shift between the two components will be equal to φShift = 90° + λ/4 = 180° (Figure 23, A, B top). In addition, due to the interaction with the sample, the amplitude of the scattered component is smaller than the unscattered component.

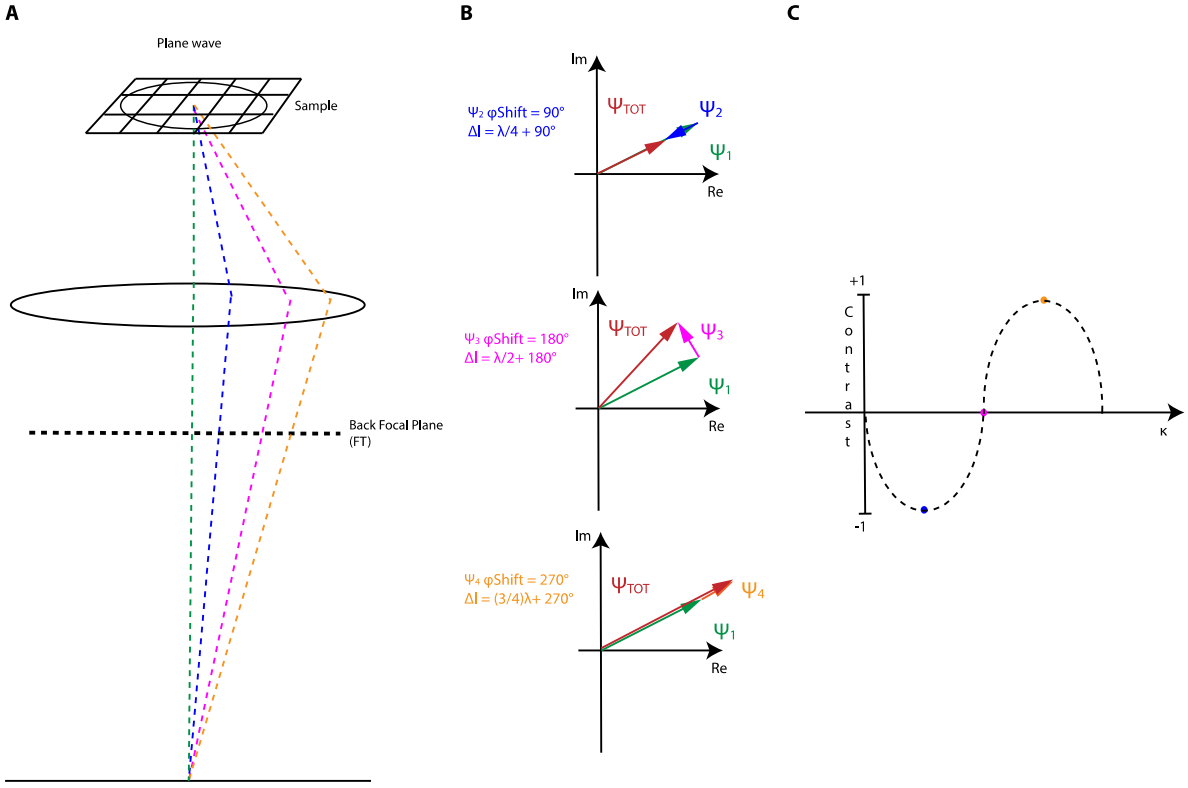

Figure 23: The phase shift during the scattering. A) Representation of the different components at different phase shifts. B) Sums of the scattered components vectors on the Argand diagram. C) CTF curve.

Representing what we said in an Argand diagram, we see that the two vectors representing the two components point in opposite directions. The sum vector ψ_{TOT} will have a lower modulus (and, therefore, amplitude) than that of the unscattered component. We can say that, at the detector level, the scattered component will contribute the most to decreasing the amplitude value (amount of signal transmitted in the image) of the unscattered component. To better understand, for practical purposes, the amount of information transmitted into the final image, it is possible to represent this situation in another diagram called the frequency-contrast plot, on the

x-axis of which we have the spatial frequencies (κ) and on the y-axis the contrast values oscillating between +1 and -1. The scattered component, by maximally decreasing the amount of information transferred within the final image, contributes to its formation in a negatively. Within this plot, this contribution is represented with a point of ordinate -1. As for the abscissa, it will not be very high because, the scattering angle is relatively low, which means that the scattering centers are placed at a great distance between each other (Figure 23, C). The greater the distance between the centers, the less detailed the information transmitted within the final image. This information is at a low spatial frequency (κ) or at low resolution. We now consider two other scattered components whose different length in path will be, respectively, $\Delta l = \lambda/2$ for ψ_3 and $\Delta l = 3\lambda/4$ for ψ_4. By consequence, the total phase shifts are ψ_3 φShift = 90° + λ/2 = 270° and ψ_4 φShift = 90° + 3λ/4 = 360° (Figure 23, B middle and bottom). In the first case, the sum vector (ψ_{TOT}) presents a modulus (amplitude) almost equal to that of the unscattered vector. Since the unscattered vector has a zero contribution to the formation of the image, being of modulus almost identical to ψ_1, the component ψ_3 will give a negligible contribution to the formation of the final image. This, on the frequency-contrast plot results in a point of ordinate 0 but with a high abscissa κ, since the component scatters at higher angles. The opposite situation to that of ψ_2 is observed for ψ_4. In this case, the vector has a greater modulus than that of the unscattered component, thus contributing positively to the transfer of information within the final image. In the frequency-contrast plot, this component is represented with a point of maximum contrast (ordinate of +1) and higher spatial frequency (Figure 23, C). Proceeding in this way for each of the scattered components at different angles, we create a characteristic pattern of points that give rise to the so-called contrast transfer function (CTF). The CTF tells us how much phase contrast is transferred within the final image as a function of the angle (spatial frequencies) at which the different components emerge from the sample.

4.2.5 The defocalization and CTF correction

The points where the CTF crosses the x-axis correspond to areas in which the information related to those particular scattering centers is lost since the contrast value associated with them is equal to 0. To recover the information lost in such a way as to obtain images that, when added together, give the most realistic and

detailed representation of the starting sample, it is necessary to vary their contribution within the CTF. One way to do this is to play on the phase shift between scattered and unscattered components. The element of the total phase shift that can be varied is given by the difference in the path length of the components before reaching the detector, i.e. the Δ*l.* The length of the distance traveled by a component can be made to vary by playing on the strength of the magnetic lenses of the microscope necessary to focus (bend) these waves on the image plane. In this case, the more current flows through the lens, the greater its ability to bend the trajectory of the electron which, as a result, will be focused into a point higher than the image plane. On the contrary, by decreasing the amount of current flowing through the lens, its focusing power will decrease and, consequently, the components will be focused on a point lower than the real image plane. In the first case, the image that is formed will be over-focused and the path of the scattered components will be shorter than the one followed to reach the real image plane. In the second case, the components will travel a greater distance, forming a defocused image. Both over-focused and defocused images present information coming from different components than those present within the “focused“ image.

By Varying the defocus value (ie the Δ*l)*, one modifies the phase shift modifying the CTF which will now present values other than 0 where previously the wave functions intersected the x-axis.

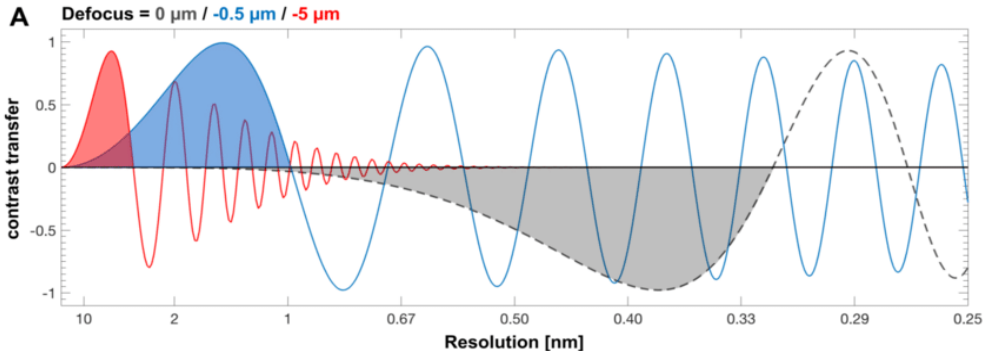

Figure 24: Different CTF curves based on different defocus value adapted from Bauerlein, 2018.

As we can see from Figure 24, a defocus of 0 µm (focused image) is characterized by a CTF (dotted line) with an important loss of information at low spatial frequencies, i.e. information coming from scattering centers placed at a great distance from each other that give information related to elements with a lack of details (shape of the sample). Increasing instead the defocus value (blue and red lines), the CTF

undergoes a shift and presents a higher oscillation. Here the information at low spatial frequencies is recovered but, as we move towards high spatial frequencies (high-resolution information) the information is increasingly fragmented due to the high oscillation. For each component that contributes positively to the image formation, there will be one immediately next to it that contributes negatively, canceling each other out. In addition, there is a flattening of the components at higher spatial frequencies, a phenomenon due to the partial spatial and temporal coherence of the electron beam. Since the high-resolution information is fragmented and confused, it will be difficult to capture details of the sample from an image with high defocus values. By combining images taken at different defocus values it is possible to obtain a more homogeneous range of information for a complete and realistic description of the specimen. However, a problem remains as the components that contribute positively and negatively to the formation of the image cancel each other. To compensate for this loss of information one can either exclude the negative component or, more efficiently, flip the phases of these components by multiplying their amplitude by -1. By acquiring images at different defocus values and by correcting the CTF with phase flipping, most of the components scattered by the different scattering centers of the sample can be contained within the final images and the loss of information is minimized.

4.3 The cryo-EM for single particles analysis

The cryo-EM technique makes possible the study and the observation of hydrated and frozen biological molecules, in a state close to their native state, to preserve the conformation assumed during the physiological processes in which they are involved. This goal is pursued through three major stages: sample preparation, image acquisition, and image processing. In the following chapter, we describe step-by-step the basic principles of the main image analysis approach used for our research purposes, known as single particle analysis (SPA) (Figure 26). In SPA the 3D information of the sample is trapped as 2D projections of the single particles within images. With this approach, the specimen is embedded in a thin film of vitreous ice near liquid nitrogen temperature and imaged under a limited electron beam exposure to minimize the radiation damage. In these conditions, images have a low signal-to-noise ratio (SNR), sufficient however to determine the orientation of particles' 2D projections. Once orientations are known, images belonging to the same particle

view are averaged together and used to retrieve a 3D map. As a result, the SPA requires the acquisition of hundred of thousands or even millions of 2D projections representing the different orientations of the particles to allow for the reconstruction of an electron density map with a high enough resolution for model building.

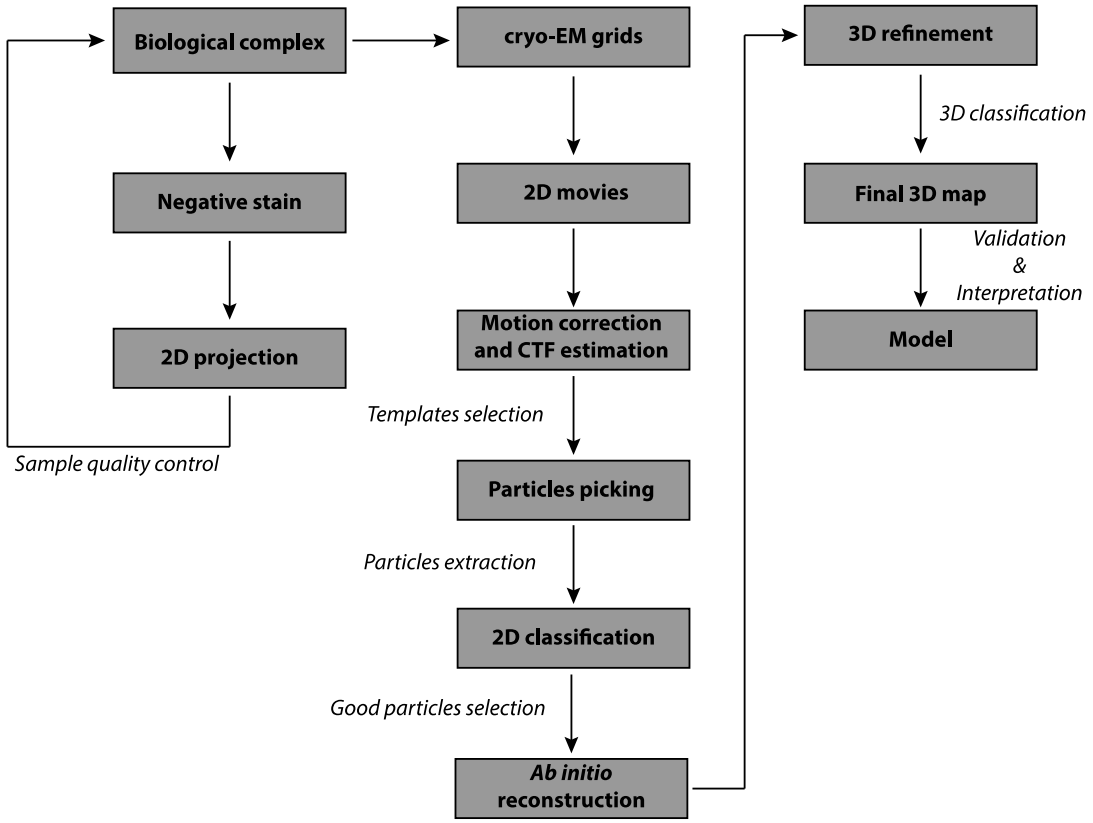

Figure 25: Scheme representing the cryo-EM single particles analysis from sample preparation to final model building.

4.3.1 Sample preparation

One of the major advantages of SPA is that it only requires small quantities of sample (hundreds of pmols/µl) and small volumes per grid (2-4 µl). In addition, purity is not the most important requirement because the presence of some contaminants can be ignored during the image analysis. In this case, to obtain a reasonable amount of particles of interest it may be necessary to acquire more images. However, because of the low signal-to-noise ratio, SPA needs that thousands of identical images (corresponding to the same view of a particle) images to be averaged together, so the ideal specimen should be as homogenous as possible. Eventually, for samples with high heterogeneity, the structural or compositional variation can be fixed by using, respectively, mild chemical cross-linking to reduce

intrinsic flexibility or the appropriate purification method (Kastner et al., 2008; Thompson et al., 2016). Apart from the biological issues, one of the most important steps in the sample preparation is the choice of the right grid and support. Grids in cryo-EM (and in EM in general) are commonly made of copper or gold. The mesh lattice (commonly 200 or 300 mesh) is coated with a carbon film that can be continuous (especially for negative staining) or “holey“. In cryo-EM analysis, holey carbon films are preferred because they ensure a reduced noise from the background as the sample is imaged suspended in vitreous ice holes. To facilitate the automatic image acquisition, the commercially available grids present a regular pattern of holes with different sizes and spacing. The grid surface is hydrophobic and it is often necessary to make this surface hydrophilic, so that the sample can spread along the whole surface. In this case, the grid hydrophilization is carried out through the so-called “glow discharge“ during which a plasma, generated through the ionization of a gas (air, argon, oxygen, or combinations), hit the grid surface rendering it hydrophilic (Gan et al., 2008).

Before the vitrification procedure, the quality of the sample is traditionally assessed using negative staining EM, to check the concentration, the purity and the integrity of the sample at room temperature. To do so, the specimen is adsorbed on a grid covered with a thin carbon film. The sample is then stained with a heavy metal salt solution (typically uranyl acetate at 1%) and blotted to ensure that only a thin layer of the stained sample remains. This process rapidly dehydrates particles on the grids and envelops them in a shell of heavy metal atoms that generates a high amplitude contrast. This technique can generate images for 3D reconstruction however, the dehydration of the sample, the use of a continuous carbon film that generates preferred orientation, and the grain size of the stain limitate the resolution and the quality of the images (Ohi et al., 2004; Booth et al., 2011).

To be observed in their “native” conformation, the biological samples, indeed, must be preserved in their aqueous environment before they can be placed in the electron microscope. However in the aqueous or cellular environment, biological macromolecules are highly dynamic, In addition, because the electrons must not interact with anything but the sample a high vacuum needs to be maintained within the microscope column. As a result, aqueous biological samples must be stabilized and protected before they can be imaged. For years, researchers wondered if

freezing the sample could preserve it in its native state, protected from vacuum and radiation damage. However, when water freezes, it gradually forms crystals that expand causing molecular damage and denaturation. To solve this problem, one approach was to cool the sample rapidly, before ice crystals have the time to form. In 1981, the Dubouchet group showed that pure water could be frozen in a “vitreous“ non-crystalline state by plunging it into liquid ethane once it was spread on an EM grid (Dubouchet et McDowall, 1981). A few years later, macromolecules were added to a water solution showing that they could be preserved in a frozen hydratated state (Adrina et al., 1984). Plunge freezing has become the standard technique to observe samples in a hydrated state with an electron microscope. The temperature for water vitrification needs to drop faster than 10^5 K/s. For that reason, the cryogen used for vitrification has to have a freezing point below the temperature needed for vitrification, a high thermal conductivity to rapidly cool the sample, and also a high boiling point to prevent vapor formation between the sample and the cryogen (Bellare et al, 1999). Nitrogen cannot be used for this purpose because it has a low thermal conductivity that allows for the formation of crystalline ice. The most commonly used cryogens are propane and ethane, whose transition from the gaseous to the liquid state is ensured by cooling it with liquid nitrogen. Because of the flammable nature of those gas, liquefaction is performed with many precautions, by gently releasing the compressed gas inside a special container cooled and surrounded by liquid nitrogen (Figure 25, B). These containers are part of a system, called plunge freezer that, together, allows performing the entire freezing process (Figure 25, A). The plunge freezing follows three consecutive steps: first of all, 2/4 µl of sample are applied on a hydrophilic cryo-EM grid; then the excess of liquid is blotted until only a thin layer of sample remains, and finally the grid is rapidly plunged into the cryogen (Dobro et al., 2010). The grid is stored in a grid box surrounded by liquid nitrogen before it is loaded into the cryo-holder.

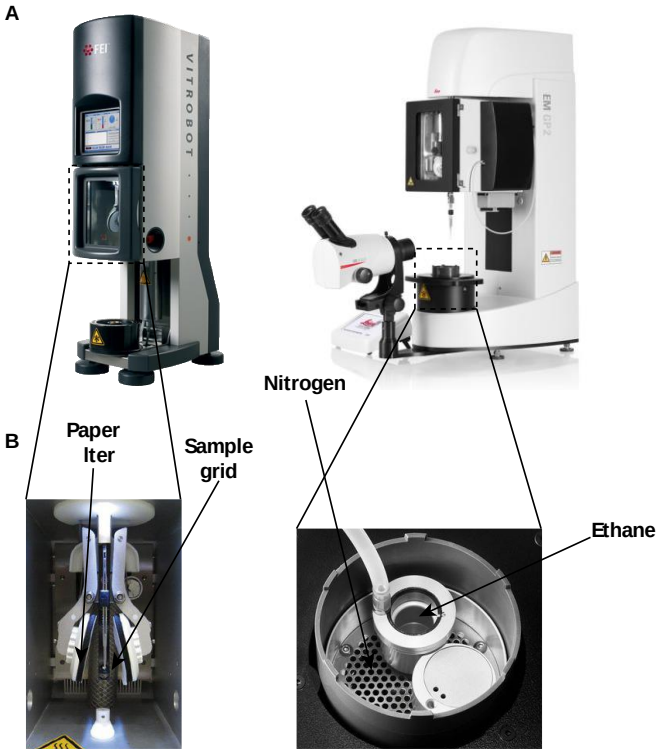

Figure 26: Plunge freezer systems used for sample vitrification. A) Left: Vitrobot Mark IV. Right: EM GP2 Leica. B) Left: Focus on the blotting chamber of the Vitrobot Mark IV. Right: Focus on the cryogenic chamber of the EM GP2.

During this process, it is important to get the best ice thickness for the image acquisition. Here, several factors play a crucial role, such as the size of the particles and their shape, the nature of the particles-solvent interactions, and the duration and type of blotting used. Thicker ice provides more stability to the sample under the electron beam. However, particles could not be easy to see because of the reduced SNR. On the other hand, if too much sample is blotted away, the ice can be too much thin and it coluld break during the interaction with the beam. In addition, a thin ice layer can induce preferential particle orientations, denaturation (due to the exposure of particles to an extended air/water interface), and the displacement of the specimen toward the grid edges (Lepper et al, 2010). In practice, temperature, humidity, and blotting conditions must be optimized for each sample.

Once the grid is ready to be observed, it is loaded within the electron microscope using a cryo-holder. The cryo-holder is a critical element for the image acquisition because it ensures the transfer of hydrated frozen grids within the microscope column by keeping the temperature stable and avoiding any external contamination.

The grid is loaded inside a pre-cooled cryo-station that allows the transfer from the grid box to the cryo-holder.

4.3.2 Image acquisition

As we have already explained in previous sections, during a cryo-EM session images must be taken at different defocus to produce sufficient phase contrast based on the interference of scattered and unscattered components. Two elements within the electron microscope are essential for a good cryo-EM data collection session: the electron source and the electron detector.

The electron source (or electron gun) of an electron microscope accelerates electrons through the microscope column. There are two kinds of electron guns: the thermionic source and the field-emission gun (FEG). The thermionic source produces electrons when heated. At high temperatures, electrons have sufficient energy to leave the surface of the source and be accelerated all along the microscope column. The material of the source must have a high melting point, for that reason, the materials used for a thermoionic source are either tungsten, cerium hexaboride (CeB_6) or lanthanum hexaboride (LaB_6). CeB6 and LaB6 filaments are often preferred since they have a much longer lifespan, are brighter, and with a smaller energy width, meaning that the electrons emitted from these filaments are more monochromatic, have higher resolution, and produces better SNR pictures. As for the FEG source, it produces electrons when a large electric potential is applied between the source and the anode. In practice, for all applications that require a bright and coherent electron source, FEG is the best (William and Carter, 2009).

When we image a specimen, the dose of electrons used to acquire an image must not be very high to avoid radiation damage to the sample and thus preserve the most important details at higher resolution. For this reason, due to the low electron dose used, the images obtained are rather noisy (Low SNR). Therefore one needs a good detector that can record most of the electrons arriving on its surface without inducing an additional degradation of the image, i.e. without adding more noise. For a detector, the rate of signal degradation during the acquisition is expressed with the detective quantum efficiency (DQE). Mathematically, this parameter is given by the ratio between the square of the SNR of the output image and the square of the SNR of the input image ($DQE = SNR^2_O/SNR^2_I$) (McMullan et al., 2014). Among the different recording devices, we mention photographic films, charged coupled devices

(CCD) and direct electron detectors (DED). The first devices used in cryo-EM were photographic films, characterized by a large field of view and very small pixels set by the silver halide grain size. However their use introduces contamination of the microscope column caused by the presence of water in the emulsion and, in addition, they need to be developed and digitized resulting in a very large time-consuming acquisition (Thompson et al., 2016). CCD cameras present a scintillator that emits photons when an electron hits it. The photons are then converted into a digital signal. In practice, a CCD presents an array of photosensitive elements where the charge accumulates (Sander et al., 2005; Booth et al., 2006). This charge is then transferred and digitized in an image after being amplified. The CCD cameras allowed the development of automated image acquisition, even if some inconveniences make their DQE inferior to that of films (Thompson et al., 2016). Nowadays the detectors of choice for high-resolution acquisition are the DEDs (Faruqi and Henderson, 2007; Bai et al., 2015). DEDs detectors (such as CMOS) detect incident electrons passing through a semiconductor layer where they deposit energy. To reduce the backscattering of some electrons when they pass through the support matrix (that produces noise), the thickness of this support became thinner and thinner. One of the most important benefits of DEDs is the ability to acquire multiple frames, where the electron dose hitting the sample is spread and used to create a movie. An additional advantage is that DEDs, in particular CMOS, have significantly improved the DQE, similar to photographic films. In this way, each frame acquired during a single exposure can be aligned to the others to correct the mechanical drift of the particles induced by the electron beam (Li et al., 2013; Scheres, 2014; Rubinstein et al., 2015).

4.3.3 Image processing

Based on the advantages coming from the technologies developed over the years, data collection for SPA is more straightforward nowadays. Although most of the success of a cryo-EM session depends on the quality of the sample and the grid, once a suitable region of the specimen has been identified, one tries to get as many good-quality images as possible. The information present within the images needs to be oversampled to avoid loss of resolution, in particular at high spatial frequencies. In this way the image data set coming from a cryo-EM session will present as much information as possible about the orientations, structural details and dynamism of the

sample, as these elements are needed for a complete description at the atomic level. In SPA we try to determine the atomic model of a monodisperse macromolecular assembly through 2D projections of a 3D density. The processing of the recorded images represents a significant part of the entire workflow in SPA. Several software packages have been developed over the years, for a successful interpretation of the images and reconstruction of the final 3D density map, such as EMAN2, FREALIGN, RELION, cryoSPARC, etc (Tang et al., 2007; Grigorieff, 2007; Scheres, 2012; Punjani, 2017). However, the image analysis workflow is roughly the same, whichever software is preferred.

First of all the movies coming from the detector are aligned together to correct the drift induced by the physical interaction between the sample and the electron beam, as well as some vibrations caused by the cryo-holder. Each frame doesn't contain enough signal to be used for SPA and they need to be summed before being processed. However, if not corrected, the motions between the frames will blur the images and limit the resolution. The relative rotations and translations of the particles are calculated and then corrected by aligning each frame against a common reference. From small particles, where the SNR is very low, the movement is calculated by taking into account all neighboring particles on the same field of view (Li et al., 2013; Scheres, 2014). The recorded movies are affected also by optical configuration inaccuracies of the electron microscope that, adding up with the noise, result in distorted 2D projection of particles and an unreliable representation of the specimen. These aberrations present within the images determine and alter the pattern and shape of the CTF. The CTF is modeled not only on the phenomena that occur between the scattered and unscattered electrons, but it also depends on the acceleration voltage, spherical aberration, defocus, astigmatism and amplitude contrast (Frank, 1996; Cheng et al., 2015). Defocus and astigmatism are approximate or totally unknown and must be calculated from the data. This is accomplished by calculating a theoretical CTF that can approximate the Thon rings of the power spectra of the micrographs (Thon, 1966; Mindell and Grigorieff, 2003). Once the theoretical and the experimental CTFs fit together, the parameters of the latter are approximated as those of the experimental curve derived from the images. In this way, all the parameters that characterize the final image (i.e. the experimental CTF) are known and can be used for the following steps.

Once that pre-treatment is done, particles in different orientations can be identified within images. In the early stages of picking, when we still don't know a lot about the particle shape, a manual approach is preferred. The picked particles can then be fed to an algorithm (either template or deep-learning based), which predicts the particle coordinates in the whole micrograph's dataset. The auto-picked particles are then extracted, keeping only a small box around the particle of interest. After which ones need to identify the most suitable particles for high-resolution reconstruction. Indeed the algorithms often select false positives as a result of the presence of high contrast artifacts (Figure 27). To only select suitable particles for the next rounds of analysis and to assign the angular distribution to the different particles views in the sample, the dataset is aligned and grouped in a homogenous subset via a 2D classification step. The goal of this clustering is to assign to each of the different classes *K*, established by the operator, all the 2D projections representing the different particle orientations. In practice, all images are aligned and compared to *K* templates and assigned to the one they most resemble in an iteratively (Figure 27).

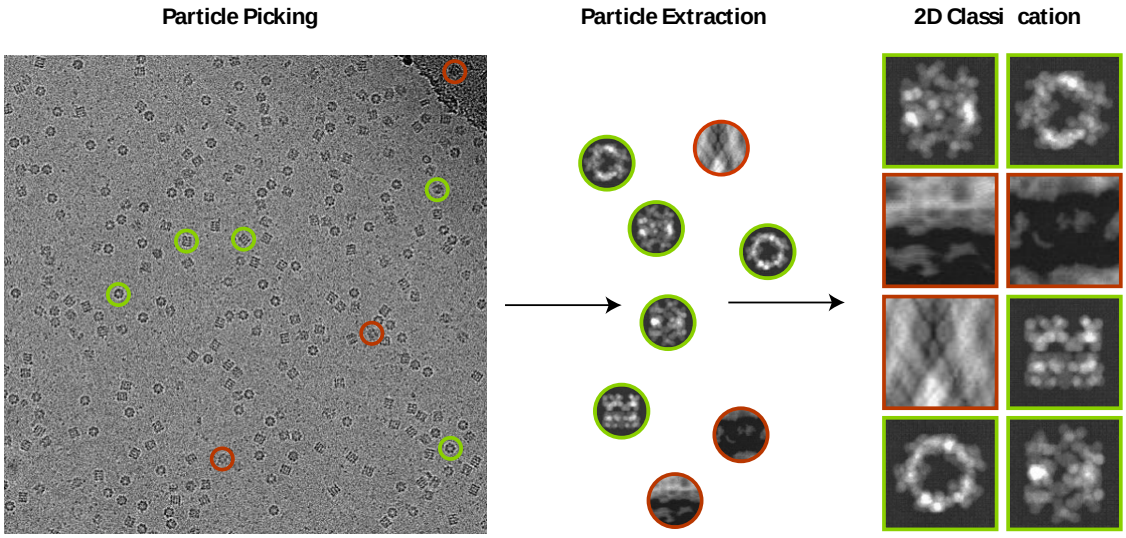

Figure 27: Picking, extraction and classification of particles from a micrographs. Automated picking algorithms pick both good (green) and bad (red) particles (left). All the particles are then extracted within a box (middle) and classified (right). From classification we can select good classes from the entire dataset.

At this point, once the 2D projections of the different particle views have been clustered in homogenous classes, a first *ab initio* 3D volume must be calculated if no reasonable templates are available. The reconstruction of a 3D *ab initio* density map requires the determination of the orientation (three Euler angles) and the origin (two translations) parameters for each 2D particle projection. Unfortunately, at this stage,

no prior knowledge is present about these parameters. A method for assigning orientation to 2D projections is based on the central slice theorem or Fourier slice theorem which considers the Fourier transform of every single projection (Crowther et al., 1970; van Heel, 1987; Bracewell, 2000). Since the 2D Fourier transform of a 3D object represents an intermediate section of the 3D transform of the object, two 2D Fourier transforms of the same 3D volume must intersect along a common line of amplitude and phase values according to a particular angle (Figure 28). The common line of amplitude and phase values of the 2D projections Fourier transforms is nothing but the 1D Fourier transform along a particular direction given by the angle Θ.

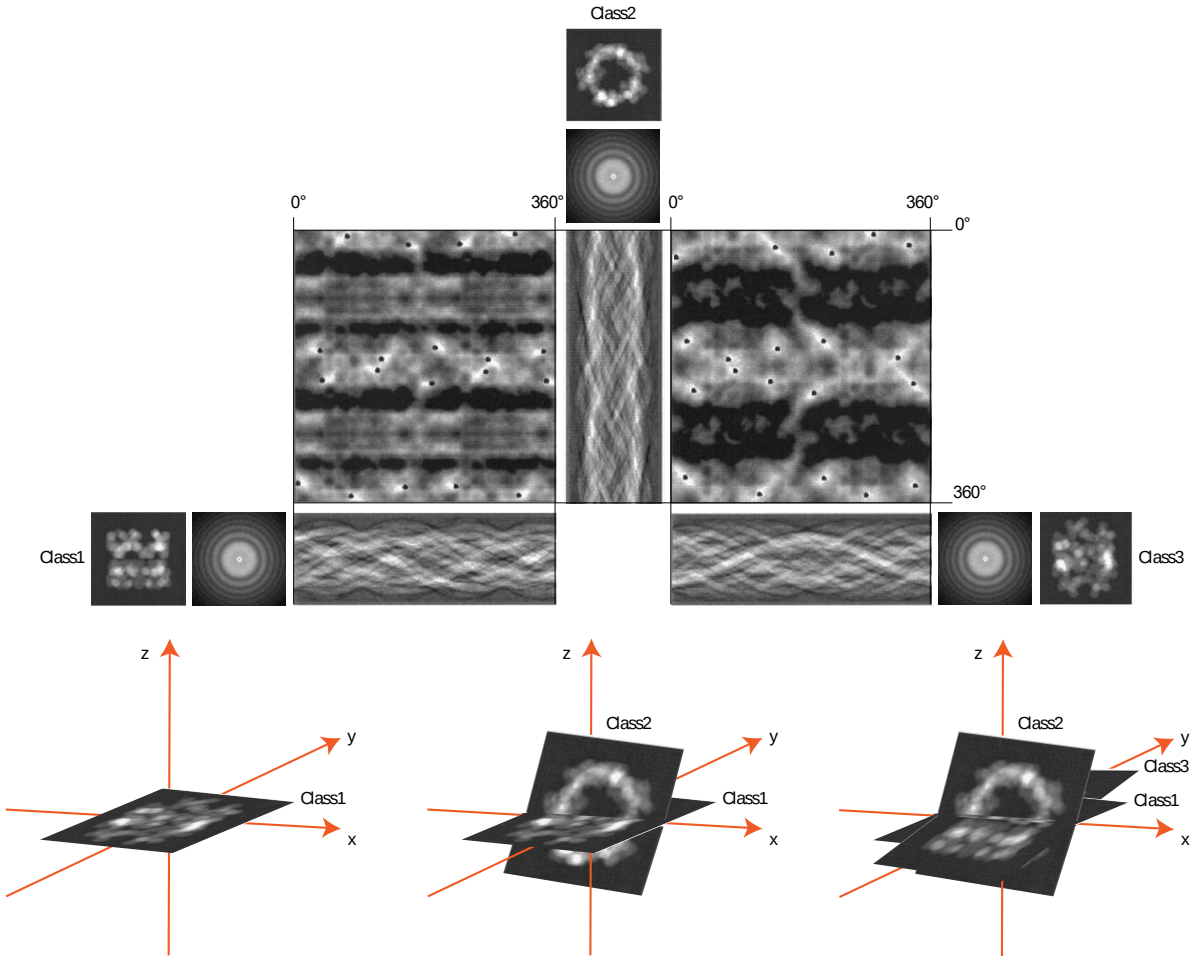

Figure 28: Central slice theorem or Fourier slice theorem. Schematic representation of the method used for the ab-initio model reconstruction starting from 2D projection classes.

Given that we have access to the power spectrum of two 2D projections for which we need to find the relative orientation of one with respect to the other, we calculate the 1D Fourier transforms along all possible directions that branch off from the center, and we use these values to build a sinogram (van Heel, 1987; Bracewell, 2000).

Within the sinogram the maxima, given by common values between the two power spectra of the 2D projections, will represent the line along which the two projections intersect, thus establishing their relative orientation (Figure 28, top). This procedure is repeated for each of the selected 2D classes (ie the particle view) generated during the previous classification (Figure 28, bottom). At the end, the *ab initio* 3D volume is nothing else than the 3D inverse Fourier transform of the power spectra relative to each particle orientation in space. However, the success of the 3D angular search strongly depends on the quality of the data. So it is important that the classes generated during 2D classification represent homogeneous particle views. After we obtained an initial volume, the model has to be refined before getting the final 3D density map. During refinement the back projections are calculated, i.e. the 2D projections of particle views derived from the *ab initio* volume. The back projections are then used to modify the orientation parameters of the experimental 2D projections to find the best match between the experimental data and the claculated structure. Recursively, the different experimental views are re-classified with respect to the back projections and then re-oriented in a more precise way with new orientation parameters. This iterative procedure allows for the optimization of the orientation assignment and results in a more accurate model characterized by the presence of more structural details. The final resolution of the refined volume is given by the Fourier shell correlation curve (FSC). The FSC is obtained by calculating the correlation coefficient, in the resolution shell, extracted from the Fourier transform of two volumes generate from the two halves of the dataset. The spatial frequency value at which the FSC crosses the 0.143 value on the y-axis represents the resolution of the map (Harauz and van Heel, 1986). The resolution, however, tells us the average quality of the reconstruction along the entire volume obtained without taking into account the peculiarities present in a macromolecular assembly. Many biological molecules, for instance, are characterized by an intrinsic heterogeneity given by the presence of flexible and dynamic portions. The quality of the flexible regions is generally blurred and it is very hard to get information about their atomic organization. The interpretation of structural characteristics in these areas is very poor and not relevant on a biological point of view. To deal with the structure heterogeneity, particle projections are re-classified but in three dimensions. The user sets a number (*K*) of 3D templates and the 2D particle images are aligned to all the 3D templates to find the best matching one. Once the best alignment for all

projections is found, several 3D volumes are generated each of them representing the conformational heterogeneity present in the sample. If any residual variability in the recostructions is still detectable, another 3D classification can be run with a higher number of classes until each final reconstruction reflect a homogeneous subset of particles. Each of the final 3D volumes will represent a final map reflecting the conformational variability of the particle within the sample. Finally, the EM map needs to be interpreted and validated before building an atomic model. The interpretation of the results, and by consequence the ability to reconstruct the atomic model, depends on the final resolution, the identification of different conformational states and the availability of a crystallographic or reasonably good homology model to fit inside the volume. A high-resolution 3D density EM map allows a *de novo* reconstruction of the proteins or nucleic acid, making also possible the detection of multiple conformational changes at atomic resolution with respect to a crystallographic structure. So, the availability of high-resolution maps of different functional states of our molecules renders the cryo-EM a unique technique to study the real dynamicity of biological complexes.

II - Section 1:

Cryo-EM study of the *trans*-translation mechanism

1.1. Contex of study

Protein synthesis is a complex and fascinating process. Given its importance for the survival of every living organism, cells possess several rescue systems to ensure their proper functioning. These processes are put in place when one or more ribosomes are unable to complete the translation process, as when they are faced with an mRNA that lacks a stop codon. When such an mRNA molecule is translated, no termination signal will be present in the ribosomal A site and consequently, because of the inability to terminate the process, the ribosome stuck on the mRNA. This situation is very costly for the cell and will, in the long run, inhibit the entire protein synthesis. Furthermore, the protein synthesized from these defective mRNAs can be toxic to the cell. To avoid this situation and allow the restoration of the canonical normal, bacterial cells have an ancestral mechanism called *trans*-translation. As reported in Campos Da Silva et al., 2022 and D'Urso et al., 2022, the main players involved in this process are tmRNA and SmpB, as well as the RNase R ribonuclease. In a complex ballet, these actors allow the recycling of the ribosome, the tagging of the neosynthesised peptide for degradation, and the subsequent degradation of the aberrant messenger by RNase R. Although over the years several biochemical and structural studies have been carried out to understand how the different actors work and interact during this process, several aspects were yet to be characterized such as the atomic interactions at the base of this process, or how the RNase R participate to *trans*-translation and interacts with the other actors. During this doctorate, I applied myself to answer these questions and better characterize this molecular mechanism. In particular, using cryo-EM analysis, we have been able to describe three key steps that make up this process: pre-accommodation, accommodation and translocation. For each of these stages, we reconstructed high-resolution atomic model, and even identified an additional conformational intermediate of the translocation step. Together, these structures shed light on the transit of the tmRNA-SmpB complex within a ribosome stalled on a non-stop mRNA, from their arrival with the elongation factor-thermo unstable (EF-Tu) until the positioning of the tmRNA transfer-like domain (TLD) within the P site. In addition, our near atomic description of the process allowed us to identify salient elements at the basis of its operation, describe the conformational changes of the ribosome and understand why *trans*-translation does not interfere with canonical translation. Since *trans*-translation is vital for many bacteria, required for the virulence of other species

and absent from eukaryotes, it is a promising new target to develop new antimicrobial compounds. As such, our results will also be instrumental in helping the structure-based design of *trans*-translation inhibitors.

However, this first description lacks information regarding the involvement of two secondary factors: RNase R, a 3' exoribonuclease known to specifically degrade the non-stop mRNAs, and the ribosomal protein bS1 which helps the binding and unfolding of the mRNA during the initiation step of translation but also influences *trans*-translation *in vivo* and *in vitro*. The following chapter recounts our structural study of *trans*-translation (Section 1) as well as what we have done so far to characterize the roles of both RNase R and bS1 (Section 2 and 3 respectively).

1.2 Articles: *"Structures of tmRNA and SmpB as they transit through the ribosome"*

nature COMMUNICATIONS

ARTICLE

https://doi.org/10.1038/s41467-021-24881-4 OPEN

Structures of tmRNA and SmpB as they transit through the ribosome

Charlotte Guyomar[1,2], Gaetano D'Urso[1,2], Sophie Chat[1], Emmanuel Giudice[1✉] & Reynald Gillet[1✉]

In bacteria, *trans*-translation is the main rescue system, freeing ribosomes stalled on defective messenger RNAs. This mechanism is driven by small protein B (SmpB) and transfer-messenger RNA (tmRNA), a hybrid RNA known to have both a tRNA-like and an mRNA-like domain. Here we present four cryo-EM structures of the ribosome during *trans*-translation at resolutions from 3.0 to 3.4 Å. These include the high-resolution structure of the whole pre-accommodated state, as well as structures of the accommodated state, the translocated state, and a translocation intermediate. Together, they shed light on the movements of the tmRNA-SmpB complex in the ribosome, from its delivery by the elongation factor EF-Tu to its passage through the ribosomal A and P sites after the opening of the B1 bridges. Additionally, we describe the interactions between the tmRNA-SmpB complex and the ribosome. These explain why the process does not interfere with canonical translation.

[1] Univ. Rennes, CNRS, Institut de Génétique et Développement de Rennes (IGDR) UMR 6290, Rennes, France. [2] These authors contributed equally: Charlotte Guyomar, Gaetano d'Urso. ✉email: emmanuel.giudice@univ-rennes1.fr; reynald.gillet@univ-rennes1.fr

In bacteria, ribosomes frequently stall on messenger RNAs (mRNAs) that lack a termination codon, leading to the accumulation of non-productive translation complexes. These complexes are composed of chains of polysomes that are in turn made up of stalled ribosomes, incomplete peptidyl-tRNAs and problematic mRNAs. Depending on where the first ribosome gets stuck, these defective events are defined either as 'non-stop' or 'no-go': non-stop if occurring at the 3′-end of a problematic mRNA lacking a stop codon, or no-go if it occurs before encountering a stop codon (for a review, see Giudice and Gillet[1]). Because stalling results in the build-up of non-productive polysomes as well as a potential synthesis of toxic polypeptides, cell viability and survival depends on rescuing the trapped ribosomes[2].

While *trans*-translation is the main rescue system for freeing stalled ribosomes in bacteria, the mechanism is absent in eukaryotes, making it a particularly attractive target when developing new antibiotics[2,3]. The process is driven by two principal players, transfer-messenger RNA (tmRNA) and small protein B (SmpB). tmRNA is a hybrid RNA molecule that is highly structured. It folds into several domains, including a tRNA-like domain (TLD), which is associated with SmpB, and an mRNA-like domain (MLD), which has an internal open reading frame. The TLD resembles the upper part of tRNA, and SmpB mimics tRNA's anticodon stem-loop[4]. Because the TLD's third base pair is a G·U wobble specifically recognized by alanyl-tRNA synthetase (AlaRS), tmRNA is always charged with an alanine[5]. Aminoacylation allows the elongation factor Tu (EF-Tu·GTP) to bring the alanyl-tmRNA-SmpB complex into the stalled ribosome, similarly to how a canonical tRNA is delivered. The second key domain of tmRNA is the MLD, whose internal open reading frame encodes for a tag, which is added to the stuck incomplete peptide so that it is specifically recognized by proteases[6]. The rest of the tmRNA is composed of four pseudoknots (PKs) (PK1 to PK4) and several RNA helices (Supplementary Fig. 1). When tmRNA travels through the ribosome, canonical translation resumes on the MLD, and the ribosomal subunits are finally released when the stop codon is reached. The non-stop mRNAs are degraded by RNase R[7], and several proteases degrade the incomplete peptides[8,9].

The early steps of *trans*-translation can be subdivided into three main processes. The first is the pre-accommodation step (PRE-ACC), when the quaternary complex made by alanylated tmRNA, SmpB, EF-Tu and GTP binds to the A site of stalled ribosomes. In the accommodation step (ACC), EF-Tu hydrolyses GTP and disassociates from the complex, causing the aminoacyl-tmRNA end to swing into the peptidyl transferase centre (PTC). The stalled peptide is then transferred to the alanine residue on tmRNA, and in the third translocation step (TRANS), EF-G catalyses the shifting of the tmRNA-SmpB complex from the A to the P site. The problematic mRNA is released, and the tmRNA resume codon enters the A site to be decoded.

Various structural analyses have been done that have greatly contributed to understanding how tmRNA-SmpB moves through the ribosome to perform *trans*-translation. Among these, the first cryo-electron microscopy (cryo-EM) studies described the PRE-ACC, ACC and TRANS steps, but unfortunately these were poorly resolved (with resolutions not better than 14 Å)[10–14]. The crystal structure of a truncated tmRNA associated with SmpB and EF-Tu and bound to the ribosome was then resolved at 3.2 Å. This showed how, during the PRE-ACC step, SmpB recognizes stalled ribosomes and facilitates decoding in the absence of an mRNA codon in the A site. However that structure does not include the PK ring, which should contain the MLD, the PKs and the H5 stem-loop[15]. At 8.3 Å, a cryo-EM structure of the *Escherichia coli* ribosome in complex with tmRNA-SmpB and EF-G allowed us to better understand re-registration on the MLD[16]. More recently, three high-resolution structures of *trans*-translation intermediates were also published[17], and these provide more details on how the circularized tmRNA-SmpB complex moves through the ribosome. However, no high-resolution structure of the PRE-ACC step in full-length tmRNA has been published, so there has been no detailed molecular description of how the $tmRNA^{ala}$-SmpB-EF-Tu complex loads on the ribosome. This step is particularly interesting since, unlike in canonical translation, ribosome recognition only occurs in the absence of codon–anticodon base pairing. The major role played by SmpB and tmRNA interactions during pre-accommodation and how this affects the subsequent transition to the ACC and TRANS states was unclear.

Here we show four cryo-EM structures of *trans*-translating ribosomes at resolutions from 3.0 to 3.4 Å (Fig. 1, Supplementary Figs. 2–4 and Supplementary Table 1). The ribosomes from *E. coli*, stalled on a small non-stop mRNA with Phe-$tRNA^{Phe}$ in the P site, are mixed with aminoacylated tmRNA, EF-Tu·GTP and SmpB, and the complexes are examined alone or in the presence of kirromycin, an antibiotic that prevents EF-Tu·GDP release, to identify the PRE-ACC (Fig. 1a) and ACC (Fig. 1b) states. In a third experiment, in the presence of elongation factor G (EF-G), we identify two different translocation states. The first 'TRANS' state is just after the translocation of tmRNA-SmpB from the A to the P site (Fig. 1c), while the 'TRANS*' state (Fig. 1d) occurs after TRANS but just before the tmRNA-SmpB complex exits the P site. Our structures provide insight into the mechanism by which tmRNA-SmpB navigates into the ribosome to perform *trans*-translation.

Results

Pre-accommodation step. The first structure we present is of the PRE-ACC state. It features a stalled ribosome, a truncated mRNA, and the tmRNA-SmpB-EF-Tu·GDP quaternary complex bound to the A site (Fig. 1a). This is the first high-resolution structure that shows the entire quaternary complex, including tmRNA's PK ring, H2 helix and H5 stem-loop. The complex is quite dynamic and the PK ring is flexible, resulting in a local resolution that fluctuates between 3.5 and 10 Å. However, the tips of the H5 stem-loop and SmpB C-terminal tail are seen ~3.5 Å, PK2 is ~4.5 Å and the interfaces between tmRNA, SmpB and EF-Tu are ~5.5 Å, which allows for the molecular description of specific interactions.

The TLD/EF-Tu interactions are similar to those observed in the previously published crystal structure of a *Thermus thermophilus* ribosome bound to a complex containing a tmRNA fragment, SmpB, EF-Tu·GDP and kirromycin[15] (Supplementary Fig. 5), although tmRNA-SmpB binds the ribosome slightly differently in this structure (see below). It also confirms that only one SmpB protein is bound to the TLD during pre-translocation[18]. While the EF-Tu switch 1 loop is too flexible to be modelled, densities are observed for the GDP and kirromycin (Supplementary Fig. 6), so it is clear that EF-Tu is in its GDP-bound state after GTP[19,20]. The TLD is partly positioned in what is known as the 'A/T' state, which allows the simultaneous interactions of tmRNA-SmpB with the decoding centre (DC) and EF-Tu with the 50S subunit[21]. As expected[22,23], we confirm that the large open L-shaped TLD forms an angle of ~120°, allowing the SmpB-bound tmRNA to mimic the functioning of a canonical tRNA. The conformations of the 3′-CCA end, the acceptor arm, and the T-arm portion also resemble those of the PRE-ACC state of aminoacyl-tRNA (Supplementary Fig. 7). While the acceptor and T-arms of the TLD are in close contact with EF-Tu (Supplementary Fig. 6), the TLD elbow region (formed by the D

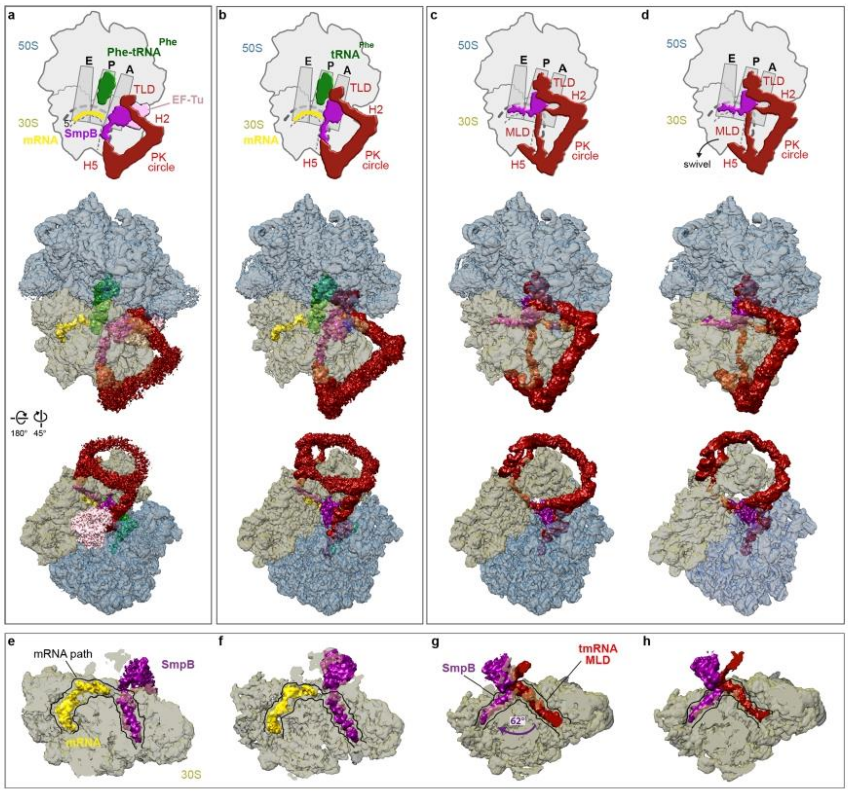

Fig. 1 High-resolution structures of four consecutive *trans*-translation states. Shown are the **a** pre-accommodation (PRE-ACC), **b** accommodation (ACC), **c** translocation (TRANS) and **d** intermediate post-translocation (TRANS*) complexes. Top, schematic representations of the complexes showing the ribosomal 50S (blue) and 30S (khaki) subunits, non-stop mRNA (yellow), P-site $tRNA^{phe}$ (green), elongation factor EF-Tu (pink), SmpB (purple) and tmRNA (red). Also indicated are the ribosome's A, P and E sites, and the tmRNA structural domains: the H2 helix, H5 stem-loop, pseudoknot (PK) ring, mRNA-like domain (MLD) and tRNA-like domain (TLD). Middle, electron density maps contoured at 2.5 σ, where sigma refers to the variance in the map. Bottom, the same density maps rotated by 180° around the *Y*-axis and 45° around the *X*-axis. **e**–**h** Cross-sections of the 30S subunits in the same states as (**a**–**d**), respectively, showing the SmpB C-terminal tail, non-stop mRNA and the MLD in the mRNA channel.

and variable loops) is in close contact with the SmpB body (Supplementary Fig. 8a). As a result, the Trp122 residue of SmpB is inserted into the hydrophobic pocket formed by A15, U17 and A334 (Supplementary Fig. 9a, left). The highly conserved nucleotide G19, known to prevent tmRNA-SmpB binding when mutated to C[24], is tightly packed at the surface of one of SmpB's hydrophobic patches (Leu91 and Leu92) of SmpB, and it is maintained there by its stacking with C18 (Supplementary Fig. 9b, left). The H2 helix points out of the ribosome between the two subunits, while the MLD, H5 stem-loop and the four PKs are tightly packed into an elliptic ring of 81 × 97 Å around the beak of the 30S small subunit (Fig. 1a). The PK ring is quite flexible, resulting in a lower resolution than everywhere else in the ribosome except for the H5 stem-loop and PK2, which is the only PK in close contact with the ribosome (Fig. 2). PK2's nucleotides C183 to A185 interact with residues Arg72, Pro73 and Ile77, which belong to the type II K-homology (KH2) RNA-binding domain of uS3 (Fig. 2b). The H5 stem-loop is well-defined and interacts with the uS3, uS4 and uS5 proteins involved in the helicase activity of the ribosome[25,26] (Fig. 2a). Its nucleotides G114 and C115 are stabilized by residues Arg132 and Arg136 of the uS3 C-terminal domain. U119 interacts with uS4 residue Arg47. U120, the stop codon's first nucleotide, lies on top of uS5 residue Ile60, while its second, A121, is at the interface between uS3 and uS5 (Fig. 2c). Interestingly, most of these interactions are similar to those previously described for structured mRNAs[27,28]. However, compared to those mRNAs, the H5 stem-loop mostly differs in how it interacts with uS5. Indeed, as the tmRNA is not yet engaged in the mRNA channel, there are no interactions with Arg20, Phe33, or Val56, and instead the tip of the stem-loop rests on top of the α1 helix residues Ile60 and Gln61.

Despite its high flexibility, the MLD is folded and quite dense, resting between the shoulder and beak of the 30S subunit, parallel to the mRNA path. SmpB lies on the DC, and its core mimics the cognate codon–anticodon base pairs[15]. In the DC, A1492 is stacked on the 16S rRNA h44 helix, while A1493 is in an intermediate state, shifted toward the major groove because of its interaction with SmpB's His22 (Fig. 3). This conformation is different from that of canonical decoding[29,30], but similar to the published high-resolution structure of an empty *E. coli*

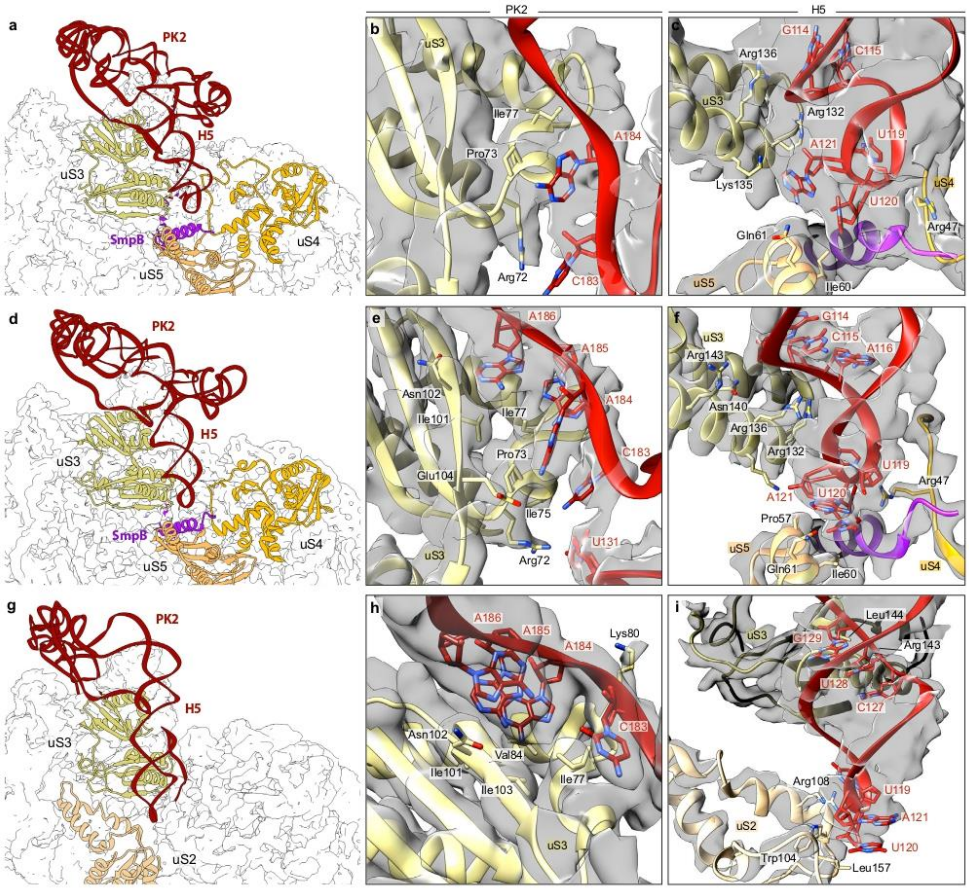

Fig. 2 The H5 and PK2 domains of tmRNA interact with the uS2, uS3, uS4 and uS5 proteins on the small ribosomal subunit. Shown are the **a**–**c** pre-accommodation state, **d**–**f** accommodation state, and **g**–**i** translocation state. Left column, overview of the interactions between tmRNA (red), SmpB (purple), and the ribosomal proteins uS2 (tan), uS3 (khaki) uS4 (gold) and uS5 (sandy brown). To highlight the motion of the H5 stem-loop during translocation, all structures are aligned on uS3. Middle, close-up of the interactions between the PK2 pseudoknot and uS3's KH2 RNA-binding domain. Right, close-up of the interactions between the H5 stem-loop and SmpB, uS3, uS4 and uS5. Residues and nucleotides within 4 Å of each other are indicated, and the cryo-electron density map is displayed.

ribosome[31] (Supplementary Fig. 10). Our structure also slightly differs from the crystal structure of a tmRNA fragment, SmpB and EF-Tu of *Thermus Thermophilus* bound to a ribosome[15] (Supplementary Fig. 10a, g). Since the main difference between the two complexes comes from our inclusion of the PK ring, we hypothesize that H5 stalling at the entrance channel slows down the movement of the complex. The interaction between H5 and the SmpB C-terminal tail (see below) would therefore result in the stabilization of an earlier stage of pre-accommodation, explaining the difference in SmpB position/conformation (Supplementary Fig. 5) and why A1493 is not yet flipped out. The beginning of the SmpB C-terminal tail is mostly unstructured, but the Gln135, His136 and Lys138 residues tightly interact with the conserved 16S rRNA G530 residue (Fig. 3a and Supplementary Fig. 11).

Interactions between tmRNA-SmpB and the 30S subunit lead to the closure of 30S, similarly to what occurs with cognate tRNA binding[32] (Supplementary Fig. 12). This closed conformation increases GTP hydrolysis, explaining why tmRNA-SmpB can be efficiently accommodated in the PTC even without cognate codon–anticodon pairing. The rest of the SmpB C-terminal tail is folded into an α-helix that occupies the mRNA path downstream from the stalled mRNA (Fig. 1e), and it is stabilized there by its interaction with 16S rRNA. Specifically, SmpB's Arg139 interacts with the C1195 nucleotide of the h34 helix, while Lys138 and Arg145 interact with the tip of the h18 helix at C528, G529 and A535 (Fig. 4). The tail is also further maintained by its interaction with the first two β-sheets of uS5, in particular, the residues Arg20 and Phe33 (which stack with SmpB's Trp147) and Phe31 (which interacts with Lys143).

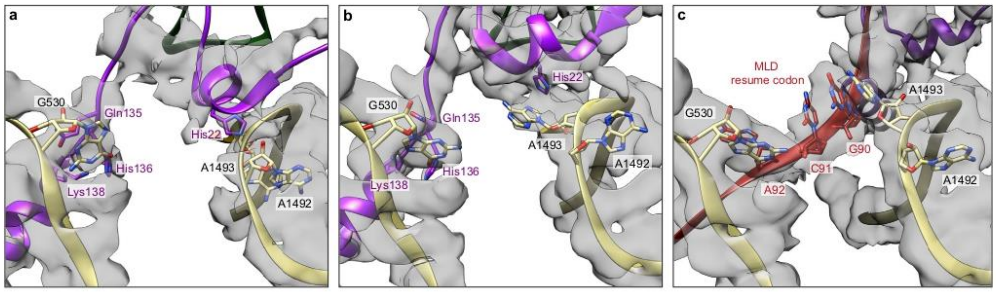

Fig. 3 Detailed view of the decoding centre during *trans*-translation. Close-up of the interactions between SmpB (purple) and the conserved nucleotides G530, A1492 and A1493 of the 16S rRNA (khaki) in the **a** pre-accommodation and **b** accommodation states. **c** Interactions between tmRNA's resume codon (red) and the same nucleotides during the translocation state. Residues and nucleotides within 4 Å of each other are indicated, and the cryo-electron density map is displayed.

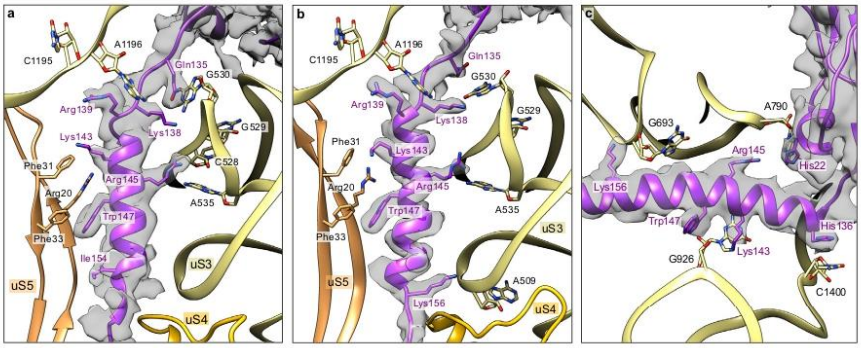

Fig. 4 Interactions between SmpB's C-terminal tail and the 30S small ribosomal subunit. Each panel details the contacts that stabilize the C-terminal tail of SmpB in the mRNA channel during the **a** pre-accommodation, **b** accommodation, and **c** translocation states. SmpB is purple, 16S rRNA is khaki, and the ribosomal proteins uS4 and uS5 are gold and sandy brown, respectively. Residues and nucleotides within 4 Å of each other are indicated, and the cryo-electron density map of SmpB is displayed.

The SmpB C-terminal tail also engages in a previously unseen interaction with the tmRNA H5 stem-loop. Indeed, the tmRNA nucleotides U119, U120 and U121 interact with SmpB residues Lys156 and Asn157 (Fig. 5).

Accommodation step. The second structure we present here is of the ACC state, which occurs after the release of the EF-Tu·GDP complex and the accommodation of the TLD in the PTC (Fig. 1b). The structure resolution is 3.1 Å (Supplementary Fig. 2), with local resolutions fluctuating between 3 and 10 Å. Unsurprisingly, the PK ring is the least well-resolved part of the complex. The H5 stem-loop, TLD, SmpB and some parts of PK2 are observed at resolutions better than 3.5 Å, allowing for detailed molecular description of the interactions between tmRNA, SmpB and the ribosome. In contrast with the structure recently described by Rae et al.[17], our structure also includes a $tRNA^{Phe}$ in the P site, and no tRNA in the E site.

When compared to the PRE-ACC state, the PK ring is in the same position around the beak, but is now larger (96 × 128 Å). As the H5 stem-loop moves towards the ribosome (Fig. 2d and Supplementary Fig. 13), PK2 interacts more closely with the KH2 RNA-binding domain of uS3 (Fig. 2e), confirming previous data by Rae et al.[17]. Indeed, the hydrophobic patch formed between uS3's third α-helix (residues Pro73 to Ile77) and its third β-sheet (residues Ile101 to Glu104) stabilizes PK2 nucleotides C183 to A186 (Fig. 2e), while uS3's Arg72 forms an ionic interaction with U131. The PKs are better outlined here than in the PRE-ACC state (Supplementary Fig. 3), which suggests that at this point they are more relaxed and stable. The MLD is mostly stretched, and presents a single dense region at its centre that is compatible with the presence of a previously described hairpin between nucleotides U88 and A100[33], a pairing which may protect the resume codon until it is used (Supplementary Fig. 14). The TLD acceptor arm swings into the PTC and interacts with the 50S subunit (Fig. 1b). After analysing the PTC density, we concluded that the transfer of the P-site tRNA phenylalanine to the incoming tmRNA alanine had already occurred (Supplementary Fig. 15). The N-terminal arm of bL27, known to play a critical role in tRNA substrate stabilization during the peptidyl transfer reaction[34–37], is well-resolved, which allowed us to build a complete atomic model. It extends into the PTC, where it contacts both the P-site $tRNA^{Phe}$ and the TLD (Supplementary Fig. 15). Interestingly, it was recently suggested that a rotated conformation of bL27 is preferred when non-stop ribosomes are bound by KKL-2098, a newly proposed *trans*-translation inhibitor[38]. The N-terminal arm is usually quite flexible but it is particularly well-resolved in the current ACC conformation. This may imply that *trans*-translation specifically requires the N terminus of bL27 to be oriented towards the PTC. It would

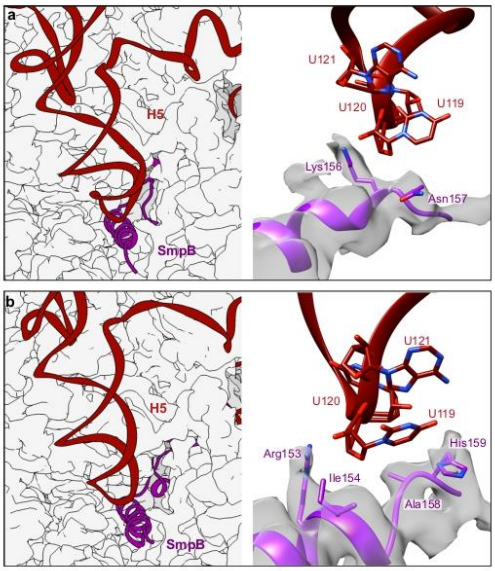

Fig. 5 Detailed view of the interactions between the C-terminal tail of SmpB and the H5 stem-loop of tmRNA. Left: position of the H5 stem-loop at the entrance of the mRNA channel. Right: focus on the residues involved in the interactions between SmpB and H5 during the **a** pre-accommodation and **b** accommodation states. SmpB is purple, tmRNA is red and the surface of the ribosomal small subunit is light grey. Residues and nucleotides within 4 Å of each other are indicated, and the cryo-electron density map of SmpB is displayed.

explain why KKL-2098 stabilisation of the rotated orientation of bL27 impedes *trans*-translation but not canonical translation.

The TLD T-arm mimics tRNA and interacts with uL16 and the 23S rRNA helices H38 and H89 (Supplementary Fig. 16). The contacts between the TLD D-loop and SmpB are maintained during this state, but the body is rotated to allow for TLD accommodation on the A site (Supplementary Fig. 8b). This results in a further insertion of Trp122 into the previously discussed hydrophobic pocket, where it interacts strongly with tmRNA nucleotides A334 and U17 (Supplementary Fig. 9a, middle). The tmRNA conserved nucleotide G19 stays at the surface of SmpB (Supplementary Fig. 9b, middle). In the DC, interactions with the conserved 16S rRNA nucleotides G530 and C1054 are also maintained and even reinforced, with Lys138 binding with G530, and His136 interacting with both C1397 and G530 (Fig. 3b and Supplementary Fig. 11b). In addition, the conserved nucleotide A1492 is now in an intermediate state inside the 16S rRNA h44 helix, whereas A1493 is outside and completely flipped, stacking on the SmpB's residue His22 (Fig. 3b). This conformation is very similar to the structure of a translating *E. coli* ribosome with no tRNA in the A site[39] (Supplementary Fig. 10b, e, as well as what is seen in the previous structure from Rae et al.[17], although the His22 position differs (Supplementary Fig. 10b, h). The tmRNA H5 stem-loop still interacts with helicases uS4 and uS5, and it is even more tightly packed on the C-terminal domain of uS3 (Fig. 2f). The interactions with uS3 residues Arg132, Lys135 and Arg136 and uS4 residue Arg47 are maintained, while new interactions are observed with uS3 Arg72, Asn140 and Arg143. However, both uS3 Arg131 and uS4 Arg44, which were previously shown to be critical for helicase activity[25], point away from the helix. SmpB's C-terminal tail has the same position and folding as are observed during the PRE-ACC state (Fig. 1f), and maintains the same interactions with uS5 ribosomal protein and 16S rRNA, with the addition of an interaction between Lys156 and A509 (Fig. 5b). However, tmRNA's H5 loop interacts even more tightly with the extremity of the C-terminal tail of SmpB. Arg153 and His159 interact with the phosphate groups between U119, U120 and A121, while Ile154 and Ala158 join with uS5 to form a hydrophobic pocket in which U120 resides (Fig. 5b).

Translocation step. A third experiment in the presence of EF-G permitted us to visualize two different states, which occur after the translocation of tmRNA-SmpB to the P site. The first of the resulting structures shows the translocation state (TRANS) resolved at a resolution of 3.2 Å (Fig. 1c and Supplementary Fig. 2), and is consistent with the previously described TRANS conformation[12,14,17]. The local resolution of the TLD and SmpB C-terminal tail is ~3.25 Å, the rest of SmpB and the MLD are ~3.5 Å, and the resolution of the H5 stem-loop and PK2 fluctuates between 3.75 and 5 Å. The map's resolution allowed us to build a robust and detailed atomic model that includes crucial portions of the MLD. The tmRNA PK ring is now fully distorted but remains well-outlined (Supplementary Fig. 3), with a distance of about 130 Å between PK1 and the top of the H5 stem-loop. PK1 is pulled between the two subunits and lies on the tip of the H38 helix of the 23S rRNA, while the tmRNA H2 helix interacts with uS19. PK2 still strongly interacts with uS3's KH2 RNA-binding domain (Fig. 2g) while the pulling on the MLD moves the H5 stem-loop away from uS4 and uS5 (Supplementary Fig. 13). The tip of the helix (nucleotides U119, U120 and A121) now interacts with uS2's Trp104, Arg108 and Leu157, while C127, U128 and G129 interact with uS3's Arg143 and Leu144 (Fig. 2i). The MLD is stretched and inserted into the mRNA channel (Fig. 1g). It interacts with the helicases uS3, uS4 and uS5 in a way that resembles the binding of structured mRNAs (Supplementary Fig. 17)[27,28]. The contacts observed during the PRE-ACC and ACC steps are maintained. However, the MLD also interacts with the uS3 α5 helix (Gln123, Arg126 and Arg127) and β5 sheet (Ile162, Arg164, Glu166) and lies on the surface of uS5 (Phe31, Glu55 and Val56). The tmRNA nucleotide A97 interacts with Arg131 and is stacked on uS5 Val56, which puts it right at the centre of the proximal helicase active site[40]. The first resume codon's G90 nucleotide is stacked on the conserved 16S rRNA nucleotide A1493, while A1492 remains inside the 16S rRNA's helix h44 (Fig. 3c and Supplementary Fig. 10c, i). G530 interacts with the third resume codon's nucleotide A92 (Fig. 3c), which is, however, not yet in a conformation compatible with the codon–anticodon interaction observed during canonical translation[30] (Supplementary Fig. 10c, f). This precise positioning is made possible by direct interactions between the four nucleotides just upstream from the MLD resume codon and SmpB, as previously suggested by biochemical and structural studies[17,41–43] (Fig. 6). Indeed, SmpB's Tyr55 and Tyr24 residues are instrumental in correctly positioning the tmRNA resume codon in the A site. Tyr55 stacks with tmRNA's A86 and serves as the foundation for the stacking of the four bases upstream from the resume codon. Tyr24 lies between tmRNA's A86 and G87, and by forming weak hydrogen bonds with both, it might serve as a secondary checkpoint, ensuring a finer control of the sequence and limiting the risk of frameshifting.

The TLD has moved to the P site and continues to interact strongly with the SmpB body (Supplementary Fig. 8c). SmpB's Trp122 residue is still deeply embedded in its hydrophobic pocket

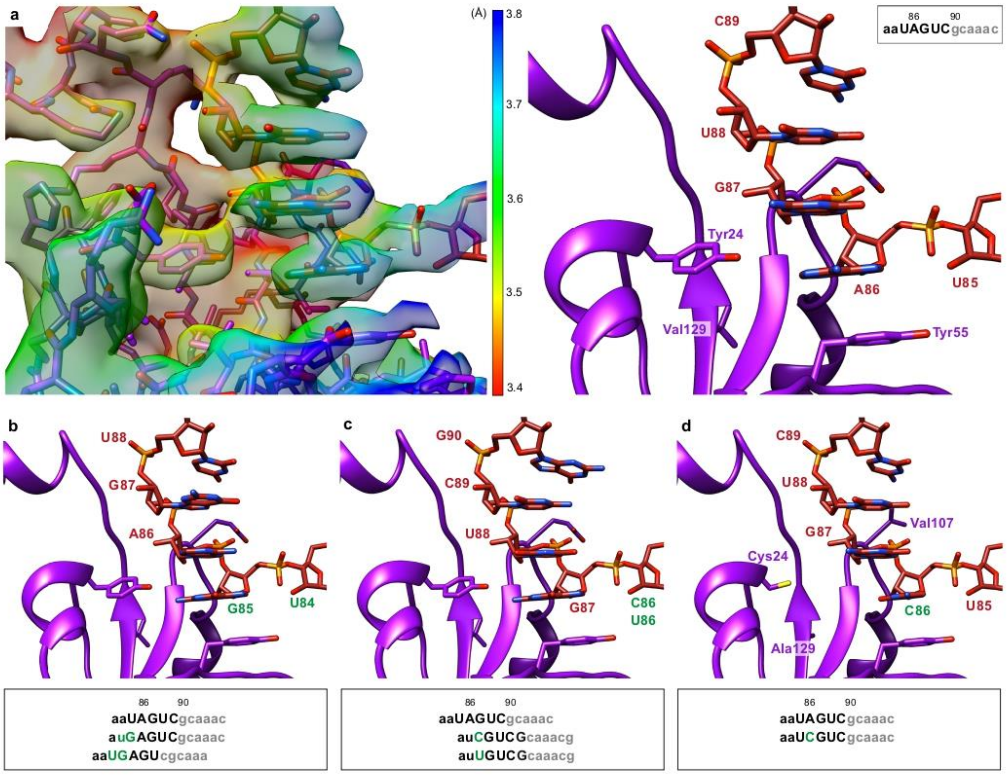

Fig. 6 The structure of translocated tmRNA reveals how the right resume codon is selected. a Left, focus on the interactions between SmpB (purple) and the four nucleotides just upstream of the tmRNA (red) resume codon. The cryo-electron density map is displayed and coloured according to the local resolutions as computed with ResMap[74]. Right, same but without the map. For clarity, cartoon representation is used for SmpB and only the four residues involved in the codon selection are shown. **b** An A84U/U85G double mutation in tmRNA maintains a high level of *trans*-translation but also promotes -1 frameshifting[41]. **c** Mutation of tmRNA's highly conserved A86 nucleotide into a pyrimidine nucleotide lowers the stacking interaction with SmpB Tyr55 and results in a +1 frameshift[41,42]. **d** An SmpB triple mutant (Y24C, E107V and V129A) can partially reverse the effect of the tmRNA A86C mutation, allowing for both +1 frameshifting and in-frame re-registration[43]. The boxes show part of the MLD sequence, with the wild-type sequence repeated at the top for reference. The first two codons are grey, the mutated nucleotides are green and the five nucleotides presented in the figure are in capital letters. Where appropriate, the sequences of the mutants are shifted to highlight the frameshifts caused by the mutations.

(Supplementary Fig. 9a, right), while the tmRNA G19 nucleotide is tightly packed at the surface of the first β-sheet of SmpB (Supplementary Fig. 9b, right). During translocation, the SmpB C-terminal tail rotates by 62° to make the DC available to the MLD resume codon. It retains its helical structure and binds the mRNA channel in the E site (Fig. 1g), where it is stabilized through different interactions with 16S rRNA (Fig. 4c). It is noteworthy that the two conserved histidines His22 and His136, which were involved in the DC during the PRE-ACC and ACC states, have in fact a dual purpose, as they now also help position the tmRNA-SmpB complex in the P site. Indeed, His22 now stacks with 16S rRNA's nucleotide A790, while SmpB's His136 is instrumental in positioning the tail through new stacking interactions with 16S rRNA C1400 (Fig. 4c). In doing so, SmpB mimics the way in which a P-site tRNA anticodon loop interacts with both mRNA and 16S rRNA (Fig. 7).

The SmpB C-terminal tail is further stabilized in the mRNA path by a series of interactions that occur between the charged residues Lys143, Arg145 and Lys156 and the 16S rRNA phosphates G926, A790 and G693, respectively (Fig. 4c). Arg139 is also instrumental, as it forms hydrogen bonds with both C1399 and G1401 (Fig. 4c and Supplementary Fig. 11c). This strong anchoring of the SmpB C-terminal tail into the mRNA exit tunnel is essential as it enables the truncated mRNA to be ejected from the ribosome. As previously described[16], the translocation process is assisted by the swivel of the 30S subunit's head (Supplementary Movie 1), which allows the tmRNA H2 helix to cross the B1a bridge. However, there is no EF-G in our structure, and we observed only a moderate swivel, with a head-to-body rotation of 5.7° and a head tilt of 3.7° (Supplementary Table 2).

New intermediate translocation step yields insights into tmRNA-SmpB movement within the ribosome. Another population obtained from the same dataset allowed us to identify

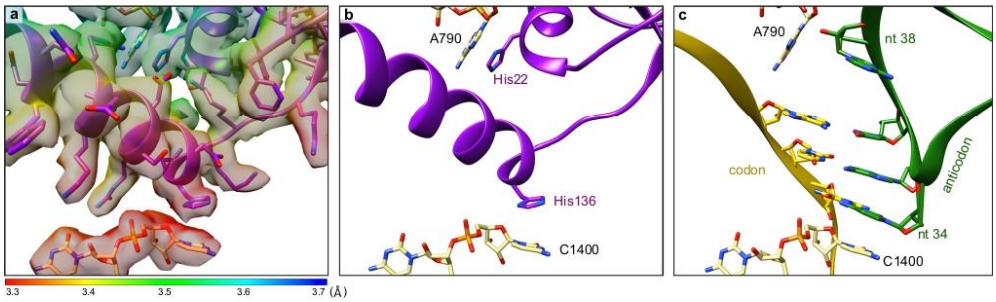

Fig. 7 SmpB mimics the interactions of a tRNA anticodon loop in the P site. a Focus on the interactions between SmpB and the 16S rRNA P-site in the translocation state. The cryo-electron density map is displayed and coloured according to the local resolutions as computed with ResMap[74]. **b** Same as (**a**), but without the map. For clarity, cartoon representation is used for SmpB and only His22 and His126 are shown. **c** Comparison with a P-site tRNA[30] (PDB code 7K00). The SmpB C-terminal tail occupies the mRNA path, replacing the codon-anticodon interaction. SmpB also reproduces the anticodon loop interactions with the 16S rRNA. The stacking interaction between His22 and A790 replaces the interaction usually observed with the sugar of tRNA's nucleotide (nt) 38. Meanwhile, His136 replaces the anticodon's nucleotide 34, stacking on the C1400 rRNA nucleotide. SmpB is purple, tRNA is green, mRNA is yellow and 16S rRNA is khaki.

a new intermediate state, which we named 'TRANS*' (Fig. 1d). Seen at a resolution of 3.4 Å (Supplementary Fig. 2), it occurs after TRANS and just before tmRNA-SmpB exits the P site.

In canonical translation, before translocation, the two ribosomal subunits spontaneously rotate by 8–10° with respect to each other, in a ratchet-like motion. This moves the tRNAs into the hybrid A/P and P/E states (in these states, the first letter refers to the position of the tRNA on the 30S subunit and the second to its position on the 50S)[44]. The 30S head domain also undergoes a partial (5–7°) forward rotation with respect to its body[45]. EF-G binding then triggers a swivel, a larger ~21° rotation and moderate ~3° tilt of the 30S head[16,46]. This clears the way for the translocation of tRNA between the P and E sites on the small subunit, a path that would otherwise be constricted by rRNA nucleotides in the head and platform regions[47]. In the TRANS* structure, the rotation of the 30S head is rather large (~14°), but still less than that observed in the presence of EF-G·GDP and tRNAs[48,49], EF-G·GDP and tmRNA[16], or with a frameshift-prone tRNA[50] (Supplementary Table 2). This surely reflects a back-swivelling motion of the 30S head after the release of EF-G. The presence of the TLD in the P/P state clearly shows that TRANS* is a post-translocational intermediate state. Interestingly, the ~12° head tilt is much larger than in any other structure except that of the tmRNA-SmpB-EF-G complex on the ribosome[16]. This demonstrates that the presence of tmRNA-SmpB in the P site is sufficient to strongly tilt the head, and this prompted us to revisit how tmRNA-SmpB passes the ribosomal bridges[51] (Fig. 8).

In the PRE-ACC state, the tip of the 50S helix H38 is unstructured. The B1a bridge is wide open, but the B1b/c bridges are closed (Fig. 8a). In the ACC state, the tmRNA H2 helix follows the movement of the TLD and is inserted between the two ribosomal subunits. The H38 helix of the 50S is well-ordered, and all three B1 bridges are closed[13] (Fig. 8b). Next, in TRANS, the tmRNA H2 helix moves towards the other side of B1a as B1b begins to open (Fig. 8c). The TRANS* state displays a much larger 30S head rotation and tilt (+8° each) (Fig. 8d). While the TLD-SmpB complex is mostly unaffected by this movement, the tmRNA H2 helix is slightly bent, and the entire PK ring rotates along with the head. This results in a destabilisation of the MLD at the entrance of the mRNA channel (Supplementary Fig. 18). Furthermore, the B1b and B1c bridges are now wide open, unlike during canonical translation (Supplementary Movie 1). We hypothesize that the head's large tilt is due to its interaction with the tmRNA H2 and PK1 conserved domains, and that this movement is instrumental in helping tmRNA to pass the intersubunit bridges on its way towards the E site. However we could not detect structures showing SmpB and/or the TLD in the E site. In fact, Rae et al.[17] recently suggested that a stable E-site intermediate was unlikely, due to induced clashes with the ribosome. We can therefore assume that tmRNA-SmpB just transits through quickly. Indeed, in our TRANS* structure the SmpB C-terminal tail is still tightly interacting with the ribosome in the mRNA path (Fig. 1h). As the tmRNA-SmpB complex continues to travel towards the E site, the C-terminal tail will either have to move along the mRNA path (between uS7, uS11 and bS21 and the 16S rRNA helices H28 and H45), tightly anchoring SmpB in the E site, or else the tail will have to stay in place, forcing SmpB to fold on itself. Together with the observation of a large opening between the two ribosomal subunits in the TRANS* conformation, this suggests that the TLD and SmpB are promptly ejected from the E site as translation continues on the MLD. The complex would then reach the post-E conformation described by Rae et al.[17].

Discussion

In this study, we present four cryo-EM structures of the *trans*-translation machinery, confirming previous structural data but also providing details of the interactions between tmRNA, SmpB and the ribosome throughout the process of *trans*-translation. These shed light on how the tmRNA-SmpB complex recognizes stalled ribosomes, how it selects the codon needed to resume translation of the tag and how it crosses the various ribosomal bridges without interfering with canonical translation.

One significant finding is that the SmpB C-terminal tail is not the only sensor used by *trans*-translation for stalled ribosomes detection. Indeed, in both the pre-accommodation and accommodation structures, the tmRNA H5 stem-loop plays a crucial role, interacting with the end of the SmpB C-terminal tail and closing off access to the mRNA channel. The positions of both the C-terminal tail and the stem-loop are incompatible with a ribosome undergoing canonical translation, because a steric clash would occur with a non-truncated mRNA (Fig. 9). This conclusion is further supported by the observation that although the deletion of the last five SmpB residues has no effect on tmRNA-mediated tagging, the tagging is severely reduced with the deletion of two additional residues (Met155 and Ile154) or by their

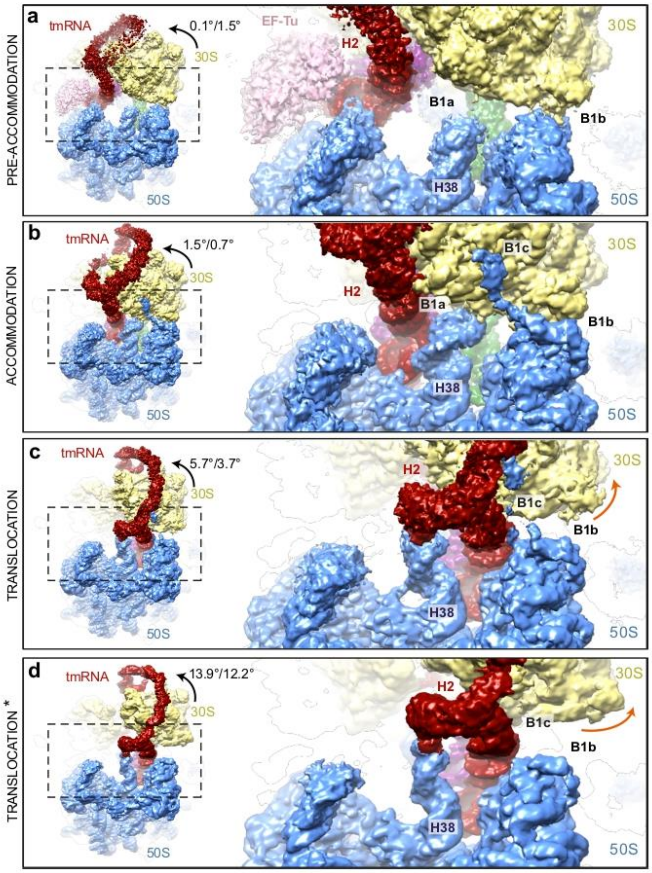

Fig. 8 Transit of tmRNA through the B1a, B1b, and B1c bridges during *trans*-translation. Close-up view of the opening and closing of bridges B1a, B1b and B1c during **a** pre-accommodation, **b** accommodation, **c** translocation and **d** intermediate translocation (TRANS*) states. The 50S ribosomal subunit is blue, 30S is khaki, elongation factor EF-Tu is pink, tmRNA is red, SmpB is purple and $tRNA^{phe}$ is green. The tmRNA helix H2 and the 50S helix H38 are also labelled. Black arrows indicate the degree of rotation and tilt of the 30S head measured with respect to its body, as per Nguyen and Whitford[87]. Orange arrows highlight the opening of bridges B1b and B1c. All maps are contoured at 2.5 σ, where sigma represents variance in the map.

simultaneous mutation into negatively charged residues[52]. The SmpB residue Ile154 seems to be of particular importance, as its mutation into proline is sufficient to impede tmRNA tagging[53]. The fact that Met155 and Ile154 mutations impair tagging but not binding suggest that these residues are mandatory for the correct positioning of the resume codon within the DC. As the H5 stem-loop interacts with SmpB exactly in this region (Fig. 5), we hypothesize that the contact between H5 and the C-terminal tail provide a second anchoring point (the first being the SmpB–TLD interaction) and this facilitates the correct positioning of the resume codon during translocation. We also confirmed that the tmRNA H5, PK2 and MLD domains make numerous contacts with the uS3, uS4 and uS5 proteins at the entrance of the mRNA channel. These three proteins are known to be instrumental in ribosome helicase activity[25]. In the PRE-ACC and ACC states, the H5 stem-loop strongly interacts with residues in the uS3 α6 helix, uS4 α1-α2 linker and uS5 α1 helix (Supplementary Fig. 17a, b). Interestingly, this mostly involves the same positively charged residues that have been shown to interact with structured mRNAs[27,28]. These notably include uS3 residues Arg132 and Lys135, and uS4 Arg47, all of which are known to be critical for helicase activity[25]. While H5 lies on the distal helical active site, it is not inserted deep enough in the mRNA channel to reach the proximal active site[40]. This may explain why the H5 stem-loop remains highly structured at these early stages. However, because of its strong interaction with the 30S, H5 could play the role of a fulcrum, helping with the mechanical unfolding and correct positioning of the MLD in the mRNA channel during translocation. In the TRANS state, H5 is flipped towards uS2 and replaced by the single-stranded portion of the MLD in a manner resembling the binding of structured mRNAs[27,28] (Supplementary Fig. 17c, d). The backbone of the single-stranded portion of the MLD is extended and straightened, and SmpB helps properly place the resume codon in the A site. This brings the tmRNA

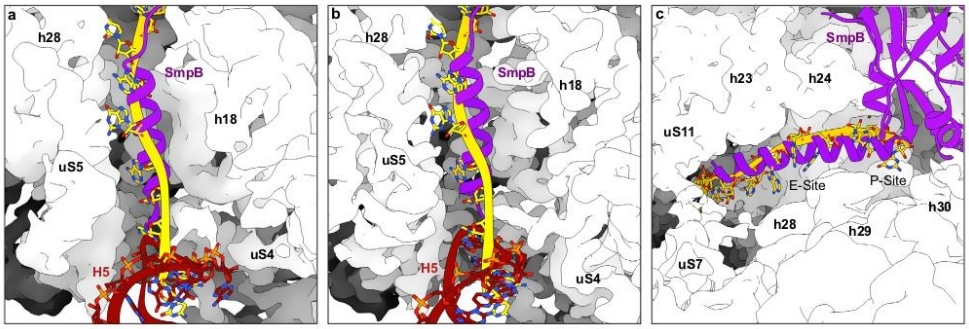

Fig. 9 Close-up of the mRNA path during *trans*-translation. In the **a** pre-accommodation and **b** accommodation states, the C-terminal tail of SmpB (purple) occupies the mRNA channel, while the H5 stem-loop of tmRNA (red) closes the entrance. Both domains would clash with a canonical mRNA (yellow, PDB code 6ZTJ[88]), forcing the selection of stalled ribosomes. **c** After translocation, the C-terminal tail is rotated by 62° and deeply inserted into the mRNA exit tunnel. There again, it clashes with the mRNA (PDB code 7JT1[89]), resulting in the ejection of the non-stop mRNA from the ribosome. The cryo-electron density map of the 30S small subunit is shown as a white surface.

nucleotide A97 (the 11th nucleotide when counting from the P site) to the centre of the helicase proximal active site, while part of the MLD interacts downstream with the distal active site. This confirms that the uS3 protein favors binding of extended single-strand mRNAs at the entrance of the tunnel, and is consistent with the hypothesis that product stabilization plays a role in the unwinding of structured mRNAs by the ribosomal helicase[28,40]. While the H5 helix is yet to be unfolded, the comparison between the TRANS and TRANS* states also provides some information on the helicase mechanism (Supplementary Fig. 18). Indeed, the most apparent difference between these two states is an extra 8° of both rotation and tilt of the 30S head in TRANS* (Supplementary Table 2). Although this state is not as well-resolved as TRANS, the PK2, H5 and MLD domains remain quite well-defined, except for a small portion of the single-stranded MLD right in the proximal helicase active site. This suggests that the forward head rotation and tilt lengthen the mRNA channel and destabilize the MLD. The canonical translation could then resume, allowing for the unfolding of H5 (which contains a large portion of the tagging sequence, see Supplementary Fig. 1) during the ensuing steps. Together, our structures confirm the involvement of the positively charged residues of uS3 and uS4 in both the basic mRNA-binding activity of the ribosome as well as its helicase activity, and they are consistent with the recent tandem model for the ribosomal helicase[40].

During translocation, SmpB also plays a major role in ensuring that the resume codon is correctly positioned within the DC. Our TRANS structure unambiguously shows how SmpB binds to the four nucleotides just upstream of the MLD resume codon (Fig. 6). The two residues, Tyr24 and Tyr55, are of particular importance in this interaction. First, the residue at position 55 is always an aromatic amino acid[54], and it serves as the foundation for the stacking of the four bases upstream of the resume codon. Because the stacking of amino acids is more stable on purines than on pyrimidines[55], tmRNA has evolved to strongly favour purine at position 86 and pyrimidine at position 85 to avoid −1 frameshifting[56]. Second, the highly conserved Tyr24 lies between the two tmRNA nucleotides A86 and G87. By forming weak hydrogen bonds with both, it certainly serves as a secondary checkpoint to ensure a finer control of the sequence and to limit the risks of frameshifting. Indeed, the steric repulsion between tyrosine's hydroxyl group and guanine's amine group explains the clear preference for A over G at position 86, while the possibility of forming a hydrogen bond between the same hydroxyl group and the N3 explains the slight preference for purine instead of pyrimidine at position 87[56]. Taken together, these observations explain why the A84U/U85G double mutation not only maintains a high level of *trans*-translation, but also promotes −1 frameshifting[41] (Fig. 6b), as well as why the mutation of A86C and A86U in tmRNA impedes *trans*-translation and promotes a +1 frameshifting of the MLD[41,42] (Fig. 6c). Our TRANS structure also help us to understand how the triple mutation of Y24C, E107V and V129A in SmpB can partially reverse the effects of the A86C mutation of tmRNA (Fig. 6d). Indeed, by simultaneously altering the sequence checkpoint (mutation Y24C), the shape of the binding pocket (mutation V129A) and the positioning of the tmRNA backbone (mutation E107V), the triple mutation facilitates the shifting of the MLD at the surface of SmpB, allowing for both in-frame and +1 frame re-registration[43].

While passing through the ribosome, the SmpB C-terminal tail remains folded in an α-helix. However, it is always tightly fixed inside the mRNA channel thanks to its positively charged residues (Fig. 4). Among these, the conserved DKR motif (Asp137, Lys138, Arg139) at the base of the C-terminal tail is of particular interest. Indeed, while single mutations in this motif have only a marginal effect, the substitution of alanine for all three residues completely abolishes *trans*-translation[52,53]. Interestingly, we observed that these residues work together to stabilize SmpB in the DC, with Asp137 binding to C1397, Lys138 to G530 and Arg139 to A1196 (Supplementary Fig. 11a, b). These interactions are completed by Lys134 (which binds to C1054), Gln135 (which stacks with G530) and His136 (which plays a central role, binding both G530 and C1397). Contrary to what was described by Rae et al.[17], we only observed a moderate stacking interaction between His22 and A1493, and no stacking of His136 and G530. This certainly explains why *trans*-translation is much less sensitive than canonical translation to DC mutations[53]. After translocation to the P site, the SmpB C-terminal tail rotates by 62° and occupies both the P- an E-site parts of the mRNA path. In this way, SmpB can forcefully eject the non-stop mRNA from the ribosome. While Rae et al.[17] emphasized the role of SmpB's Gly132 conserved residue in this rotation, the nature of the interaction that

correctly positions SmpB in the P site was not clear. Our structure shows that this is made possible not only by the charged residues of the C-terminal tail, but also by the two histidines His22 and His136, which mimic the interactions of a tRNA stem-loop with the 16 rRNA.

Our structures also allow for a better understanding of the molecular basis of tmRNA-SmpB interactions throughout *trans*-translation. Among the different contacts formed between the two partners (Supplementary Fig 8), it is worth noting the continuous stacking of tmRNA nucleotide G19 on the conserved hydrophobic patch (Leu90, Leu91, Leu92) on the surface of SmpB, as it has been reported that a G19C mutation in tmRNA abolishes *trans*-translation[24]. Decreasing the stacking interaction between C18, G19 and the SmpB surface also affects the binding of Trp122 in its hydrophobic pocket and destabilizes the entire tmRNA-SmpB complex, effectively preventing *trans*-translation.

To conclude, *trans*-translation is an appealing antibiotic target since it is essential for fitness and vital to many pathogens, yet absent in eukaryotes. Our structures give a better understanding of how *trans*-translation occurs, but they also showcase its differences and similarities with canonical translation, and confirm the fact that it does not interfere with that process. We hope that our detailed description of the interactions between the accommodated tmRNA-SmpB and the ribosome, as well as the newly described interface between the MLD and SmpB in the TRANS conformation, might be useful to develop the recently proposed anti-*trans*-translation strategies[38,57–59].

Methods

Ribosome purification. Ribosomes were purified from the *E. coli* strain MG1655. When the culture reached an OD_{600} of 0.8, the cells were pelleted, resuspended in FP buffer (20 mM Tris-HCl pH 7.5, 50 mM MgOAc, 100 mM NH_4Cl, 0.5 mM EDTA and 1 mM DTT), then lysed in a French press. The lysate was then clarified by centrifugation at 20,000 × *g* for 45 min at 4 °C. Next, the supernatant was layered 1:1 (v:v) over a high-salt sucrose cushion buffer (10 mM Tris-HCl pH 7.5, 10 mM MgOAc, 500 mM NH_4Cl, 0.5 mM EDTA, 1.1 M sucrose and 1 mM DTT). After ultracentrifugation at 92,000 × *g* for 20 h at 4 °C, the resulting ribosome pellets were resuspended in 1 mL of 'Ribo_A' buffer (10 mM Tris-HCl pH 7.5, 10 mM $MgCl_2$, 50 mM NH_4Cl, 0.5 mM EDTA and 1 mM DTT). To isolate the 70S ribosomes from 30S and 50S ribosomal subunits, the ribosomes were centrifuged at 95,000 × *g* for 18 h at 4 °C through a 10–45% (w/w) linear sucrose gradient in Ribo_A buffer. The different gradients were fractionated before determining the A_{260} absorbance profiles. Fractions corresponding to the 70S peak were mixed and diluted in Ribo_A buffer for a final ultracentrifugation at 92,000 × *g* for 20 h at 4 °C. The ribosomal pellets were resuspended in Ribo_A buffer, then stored at −80 °C.

RNA purification. The tmRNAs were purified in native conditions as previously described[60]. We used a synthetic non-stop mRNA (Thermo Fisher Scientific) with the sequence 5′-AGGAGGUGAGGU**UUU**-3′ (the Shine–Dalgarno sequence is underlined and the phenylalanine codon is bold). Phenylalanine-specific *E. coli* tRNA was purchased from Sigma. The *E. coli* $tRNA^{Ala}$ was transcribed in vitro from the plasmid pUC19-ala-tRNA using a MEGAscript T7 transcription kit (Thermo Fisher Scientific)[61]. Before transcription, the plasmid was linearized by BstNI restriction enzymes, purified with purified phenol/alcohol/chloroform, then precipitated using 3 M sodium acetate.

Protein purification. To generate an SmpB with a His-tagged C-terminus, the *E. coli smpB* gene was cloned between the NdeI and XhoI restriction sites in pET22b (+) vector. The protein was expressed in *E. coli* BL21(DE3)Δ*ssrA* cells[62] and purified as previously described[58]. T7 expression system was used to overexpress his-tagged AlaRS, his-tagged phenylalanyl-tRNA synthetase (PheRS) and his-tagged elongation factor EF-Tu in *E. coli* BL21(DE3) strain. These were then isolated using a HisTrap HP column (GE Healthcare) as previously described[63]. His-tagged EF-G was overexpressed from pQE60 vector in *E. coli* BL21/pREP4. This overexpression was induced by 1 mM IPTG at an OD_{600} of 0.6 over 3 h at 37 °C. The cells were lysed in a French press and the lysate was applied to a HisTrap HP column equilibrated with 'EF-G-I buffer' (50 mM NaH_2PO_4/Na_2HPO_4 pH 8, 300 mM NaCl and 20 mM imidazole). The column was washed in that buffer and the protein eluted with a linear gradient of imidazole going from 20 to 300 mM. The elution fractions were concentrated with an Amicon Ultra-15 filter (Sigma) in 'EF-G-II buffer' (10 mM HEPES-KOH pH 7.5, 500 mM KCl, 0.5 mM EDTA and 10% glycerol) then stored at −20 °C. To avoid ribosomal degradation in vitro, the plasmid pABA-RNR_D280N was used to express the his-tagged RNase R mutated on its catalytic site[64] in *E. coli* BL21(DE3) cells. After lysis in a French press in 'RNR-FP buffer' (50 mM NaH_2PO_4/Na_2HPO_4 pH 8, 300 mM NaCl and 10 mM imidazole), the lysate was filtered and applied to a HisTrap HP equilibrated with the same buffer. The column was then washed with an 'RNR-A buffer' (50 mM NaH_2PO_4/Na_2HPO_4 pH 8, 300 mM NaCl and 20 mM imidazole) and an 'RNR-B buffer' (50 mM NaH_2PO_4/Na_2HPO_4 pH 8, 1 M NaCl and 20 mM imidazole). The mutated RNase R was eluted in RNR-A buffer with a linear gradient of imidazole from 20 to 500 mM. The fractions corresponding to the mutated RNase R were concentrated using an Amicon Ultra-15 in 'RNR-C buffer' (10 mM HEPES-KOH pH 7.5, 500 mM KCl, 0.5 mM EDTA and 50% glycerol), then stored at −20 °C.

Preparation of ribosomal complexes. In order to obtain the most *trans*-translation states from the A to P sites in the ribosome, three different complexes were prepared. These were all obtained using *E. coli* components, to which we added RNase R (a known partner of *trans*-translation) in order to reproduce native conditions as closely as possible.

For the first complex, we incubated 50 pmol phenylalanine-tRNA (phe-tRNA) for 2 min at 80 °C. This was followed by a second incubation at room temperature for 30 min in 'Buffer I' (10 mM HEPES-KOH pH 7.5, 5 mM $MgCl_2$ and 20 mM NH_4Cl). Next, 250 pmol EF-Tu·GDP were activated into EF-Tu·GTP immediately before it was incubated with 2 mM GTP in 'Buffer II' (62.5 mM HEPES-KOH pH 7.5, 9 mM $MgCl_2$ and 75 mM NH_4Cl) for 15 min at 37 °C. Aminoacylation of tmRNA was performed by mixing 125 pmol tmRNA, 250 pmol EF-Tu·GTP, 125 pmol SmpB, 190 pmol AlaRS, 2 mM ATP, 30 µM alanine and Buffer II. We then blocked the ribosome on non-stop mRNA by mixing 25 pmol *E. coli* 70S, 50 pmol non-stop mRNA and 100 pmol folded phe-tRNA in 'Buffer III' (5 mM HEPES-KOH pH 7.5, 9 mM MgOAc, 50 mM KCl, 10 mM NH_4Cl and 1 mM DTT) for 15 min at 37 °C. Finally, the complex was created by mixing the blocked ribosomes with the aminoacylated tmRNA supplemented by 100 pmol SmpB and 250 µM kirromycin to trap EF-Tu in its GDP-bound conformation. This prevents the release of tmRNA, and was done as previously described[15] for 15 min at 37 °C. We then added 250 pmol RNAse R for an additional 10 min.

The second complex was obtained exactly like the first, but without EF-Tu. For the third complex, phe-tRNA and alanine-tRNA (ala-tRNA) were folded as described above. After the folding step, either 50 pmol ala-tRNA or 20 pmol phe-tRNA was aminoacylated by mixing 2 mM ATP, 30 µM of the corresponding amino acid, 80 pmol of the corresponding aminoacyl-tRNA synthetase, and Buffer II. In parallel, tmRNAs were also aminoacylated and ribosomes blocked as described above, this time using 50 pmol phe-tRNA. The complex was completed by incubating the stalled ribosomes, the aminoacylated tmRNA and EF-G (at a 1:3 ratio between the ribosome and EF-G) for 10 min at 37 °C, after which ala-$tRNA^{ala}$ was added and the mix was left to incubate for 15 min in order to translocate the tmRNA in the ribosome.

Electron microscopy. After adjusting concentrations to 100 nM in Buffer III, samples were directly applied to glow-discharged holey carbon films (Quantifoil 2/2 µm). These grids were then flash-frozen in liquid ethane using a Vitrobot Mark III (FEI), then transferred to a Cs-corrected Titan Krios electron microscope (FEI) operating at 300 kV and equipped with an FEG electron source. Images were automatically recorded using SerialEM[65] under low-dose conditions on a K2 direct electron detector (Gatan) using a defocus range of −1 to −3 µm, a nominal magnification of ×105,000, and a final pixel size of 1.1 Å (complex 1), or a defocus range of −0.7 to −2 µm, a nominal magnification of ×130,000, and a final pixel size of 1.04 Å (complexes 2 and 3). Movies were corrected for the effects of drift and beam-induced motion using MotionCor2 software[66]. Contrast transfer function (CTF) parameters were estimated using Gctf software[67]. Electron micrographs showing signs of drift or astigmatism were discarded, and for complexes 1 through 3, this resulted in respective datasets of 3143, 10,484 and 11,433 images. Particles were semi-automatically selected in Cryosparc[68] and subjected to two rounds of 2D classification in order to discard defective particles. This resulted in 59,016 (dataset 1), 373,247 (dataset 2) and 207,135 particles (dataset 3). All subsequent data processing was performed in RELION[69,70]. Further 3-D autorefinements with a soft circular mask (diameter 380 Å) produced initial cryo-EM reconstructions for the three datasets at overall resolutions of 4.27, 3.84 and 3.24 Å, respectively. To improve the homogeneity, datasets 2 and 3 were then sorted into ten subsets using the 3D classification function. The classes that were clearly homogenous 70S ribosomes were selected, resulting in the retention of 238,808 (dataset 2) and 174,863 particles (dataset 3) for the next round of analysis.

After CTF refinement and particle polishing, the 'shiny' particles from all datasets were subjected to a second round of 3D auto-refinement. We then subtracted the signal of the ribosome from the datasets, using a soft mask (voxel values of 0 inside, 1 outside, extended by 6 pixels with a soft edge of 6 pixels) generated from the previous refinement run. The subtracted datasets were then sorted by a 3D classification without alignment[71]. Various numbers of classes were tested in order to split the datasets into as many 3D classes as possible while still keeping the groups homogeneous. This allowed for the separation of particles containing the tmRNA-SmpB complexes while limiting the bias induced by masking each factor separately. As a result, dataset 1 was separated into three classes: pre-accommodated ternary complexes (18,452 particles); poorly resolved accommodated tmRNA-SmpB complexes without EF-Tu and stalled ribosomes

without the tmRNA-SmpB complex. Dataset 2 was separated into five classes, with only one containing the tmRNA-SmpB complex accommodated in the A site (86,622 particles), and the rest having different conformations of stalled ribosomes and junk particles. Dataset 3 was also processed into five classes, separated between the tmRNA-SmpB complex accommodated in the A site (62,156 particles); two distinctive conformations of the tmRNA-SmpB complex translocated into the P site (with 14,192 particles in TRANS and 11,059 particles in TRANS*); stalled ribosomes (1 class) and junk (1 class). The particles from datasets 2 and 3 corresponding to the accommodated state were merged together and subjected to another round of 3D classification with signal subtraction of the empty ribosomes. After sorting the particles into four classes, one class of 36,069 particles was finally selected. We finally reverted to the original non-subtracted particles, and each step (PRE-ACC, ACC, TRANS, TRANS*) was reconstructed separately. The pixel size was then accessed by comparison with the atomic model of the *E. coli* mature 70S subunit[31] (PDB 4YBB) and adjusted to 1.074 (instead of 1.1 Å/pixel) for dataset 1. Further 3D auto-refinement and post-processing (with the adjusted pixel size) yielded maps with overall resolutions of 3.2 Å (PRE-ACC), 3.1 Å (ACC), 3.2 Å (TRANS) and 3.4 Å (TRANS*) based on RELION's gold-standard Fourier shell correlation calculation[72,73]. Local resolutions were estimated using Resmap[74], and map quality was analysed using Phenix mtriage software[75]. These consensus maps were then used as a basis for multi-body refinement[76,77] into three separate maps of the ribosomal large subunit, the body of the small subunit and the head of the small subunit, while including overlapping parts of the tmRNA-SmpB complex in each. The corresponding masks were made using a 30 Å low-pass filtered version of the consensus map and 12 Å soft-edges to define the solvent region boundary and to ensure that all the bodies overlapped. The resulting density maps were then sharpened using Phenix[78], and used with the consensus maps for building and refinement of the models.

Model building and refinement. UCSF-Chimera[79] was used to rigid-body fit the crystal structure (2.1 Å) of the *E. coli* (PDB 4YBB) mature 70S subunit[31] into the cryo-EM maps, with each protein and RNA treated separately. Atomic coordinates for ET-Tu were taken from PDB code 5AFI[80], while tmRNA and SmpB coordinates were modelled from 4V8Q[15] (PRE-ACC), 6Q97[17] (ACC) and 6Q98[17] (TRANS and TRANS*). All models were manually adjusted in the multi-body maps using COOT[81], with the exception of the MLD and PKs, which were first adjusted with MDFF[82] as follows. The system was set up in vacuo and subjected to energy minimization for 5000 steps (50 ps) to relax any steric clashes. To fit the atoms into the EM density, a production run of 100,000 steps was performed. The forces applied to the atoms were scaled by a factor of 0.3, and to prevent overfitting, harmonic restraints were applied so that the secondary structure using a force constant of 200 kcal mol^{-1} rad^{-2}. Default values were used to restrain the hydrogen bonds, cis-peptide bonds and chiral centres. All steps were performed using VMD[83], NAMD2[84] and the CHARMM36[85] force fields. Once the structure was complete, Mg^{2+} ions were manually added in COOT using the 'unmodelled blobs' function and a threshold of 5.5 RMSD. The atomic models were further improved by real space refinement against their respective consensus maps using Phenix. After a first refinement, outliers were manually corrected in COOT and the structure underwent a final refinement in Phenix, which produced the structures presented here. Models were evaluated with MolProbity[86–89] and the remaining analysis and the illustrations were done using UCSF-Chimera[79].

Reporting summary. Further information on research design is available in the Nature Research Reporting Summary linked to this article.

Data availability

All of the data supporting the findings of this study are available within the paper and in the Supplementary Materials. The atomic coordinates and electron density maps have been deposited in the EMDB and PDB under the following accession codes, respectively: EMD-11710 and 7ABZ (pre-accommodated state); EMD-11713 and 7AC7 (accommodated state); EMD-11717 and 7ACJ (translocated state) and EMD-11718 and 7ACR (post-translocated intermediate state).

Received: 17 September 2020; Accepted: 13 July 2021;
Published online: 13 August 2021

References

1. Giudice, E. & Gillet, R. The task force that rescues stalled ribosomes in bacteria. *Trends Biochem Sci.* **38**, 403–411 (2013).
2. Keiler, K. C. & Feaga, H. A. Resolving nonstop translation complexes is a matter of life or death. *J. Bacteriol.* **196**, 2123–2130 (2014).
3. Buskirk, A. R. & Green, R. Ribosome pausing, arrest and rescue in bacteria and eukaryotes. Philos Trans R Soc Lond B Biol Sci. **372**, 20160183 (2017).
4. Bessho, Y. et al. Structural basis for functional mimicry of long-variable-arm tRNA by transfer-messenger RNA. *Proc. Natl Acad. Sci. U.S.A.* **104**, 8293–8298 (2007).
5. Komine, Y., Kitabatake, M., Yokogawa, T., Nishikawa, K. & Inokuchi, H. A tRNA-like structure is present in 10Sa RNA, a small stable RNA from Escherichia coli. *Proc. Natl Acad. Sci. U.S.A.* **91**, 9223–9227 (1994).
6. Tu, G. F., Reid, G. E., Zhang, J. G., Moritz, R. L. & Simpson, R. J. C-terminal extension of truncated recombinant proteins in Escherichia coli with a 10Sa RNA decapeptide. *J. Biol. Chem.* **270**, 9322–9326 (1995).
7. Richards, J., Mehta, P. & Karzai, A. W. RNase R degrades non-stop mRNAs selectively in an SmpB-tmRNA-dependent manner. *Mol. Microbiol.* **62**, 1700–1712 (2006).
8. Karzai, A. W., Roche, E. D. & Sauer, R. T. The SsrA-SmpB system for protein tagging, directed degradation and ribosome rescue. *Nat. Struct. Biol.* **7**, 449–455 (2000).
9. Janssen, B. D. & Hayes, C. S. The tmRNA ribosome-rescue system. *Adv. Protein Chem. Struct. Biol.* **86**, 151–191 (2012).
10. Valle, M. et al. Visualizing tmRNA entry into a stalled ribosome. *Science* **300**, 127–130 (2003).
11. Weis, F. et al. Accommodation of tmRNA-SmpB into stalled ribosomes: a cryo-EM study. *RNA* **16**, 299–306 (2010).
12. Weis, F. et al. tmRNA-SmpB: a journey to the centre of the bacterial ribosome. *EMBO J.* **29**, 3810–3818 (2010).
13. Kaur, S., Gillet, R., Li, W., Gursky, R. & Frank, J. Cryo-EM visualization of transfer messenger RNA with two SmpBs in a stalled ribosome. *Proc. Natl Acad. Sci. U.S.A.* **103**, 16484–16489 (2006).
14. Fu, J. et al. Visualizing the transfer-messenger RNA as the ribosome resumes translation. *EMBO J.* **29**, 3819–3825 (2010).
15. Neubauer, C., Gillet, R., Kelley, A. C. & Ramakrishnan, V. Decoding in the absence of a codon by tmRNA and SmpB in the ribosome. *Science* **335**, 1366–1369 (2012).
16. Ramrath, D. J. F. et al. The complex of tmRNA-SmpB and EF-G on translocating ribosomes. *Nature* **485**, 526–529 (2012).
17. Rae, C. D., Gordiyenko, Y. & Ramakrishnan, V. How a circularized tmRNA moves through the ribosome. *Science* **363**, 740–744 (2019).
18. Bugaeva, E. Y., Shpanchenko, O. V., Felden, B., Isaksson, L. A. & Dontsova, O. A. One SmpB molecule accompanies tmRNA during its passage through the ribosomes. *FEBS Lett.* **582**, 1532–1536 (2008).
19. Schuette, J.-C. et al. GTPase activation of elongation factor EF-Tu by the ribosome during decoding. *EMBO J.* **28**, 755–765 (2009).
20. Loveland, A. B., Demo, G. & Korostelev, A. A. Cryo-EM of elongating ribosome with EF-Tu•GTP elucidates tRNA proofreading. *Nature* **584**, 640–645 (2020).
21. Voorhees, R. M. & Ramakrishnan, V. Structural basis of the translational elongation cycle. *Annu. Rev. Biochem.* **82**, 203–236 (2013).
22. Gutmann, S. et al. Crystal structure of the transfer-RNA domain of transfer-messenger RNA in complex with SmpB. *Nature* **424**, 699–703 (2003).
23. Stagg, S. M., Frazer-Abel, A. A., Hagerman, P. J. & Harvey, S. C. Structural studies of the tRNA domain of tmRNA. *J. Mol. Biol.* **309**, 727–735 (2001).
24. Hanawa-Suetsugu, K., Takagi, M., Inokuchi, H., Himeno, H. & Muto, A. SmpB functions in various steps of trans-translation. *Nucleic Acids Res.* **30**, 1620–1629 (2002).
25. Takyar, S., Hickerson, R. P. & Noller, H. F. mRNA helicase activity of the ribosome. *Cell* **120**, 49–58 (2005).
26. Qu, X. et al. The ribosome uses two active mechanisms to unwind messenger RNA during translation. *Nature* **475**, 118–121 (2011).
27. Zhang, Y., Hong, S., Ruangprasert, A., Skiniotis, G. & Dunham, C. M. Alternative mode of E-site tRNA binding in the presence of a downstream mRNA stem loop at the entrance channel. *Structure* **26**, 437–445.e3 (2018).
28. Amiri, H. & Noller, H. F. Structural evidence for product stabilization by the ribosomal mRNA helicase. *RNA* **25**, 364–375 (2019).
29. Ogle, J. M. et al. Recognition of cognate transfer RNA by the 30S ribosomal subunit. *Science* **292**, 897–902 (2001).
30. Watson, Z. L. et al. Structure of the bacterial ribosome at 2 Å resolution. *Elife* **9**, e60482 (2020).
31. Noeske, J. et al. High-resolution structure of the Escherichia coli ribosome. *Nat. Struct. Mol. Biol.* **22**, 336–341 (2015).
32. Ogle, J. M., Murphy, F. V., Tarry, M. J. & Ramakrishnan, V. Selection of tRNA by the ribosome requires a transition from an open to a closed form. *Cell* **111**, 721–732 (2002).
33. Felden, B. et al. Probing the structure of the Escherichia coli 10Sa RNA (tmRNA). *RNA* **3**, 89–103 (1997).
34. Wang, H. et al. Crystal structure of ribosomal protein L27 from Thermus thermophilus HB8. *Protein Sci.* **13**, 2806–2810 (2004).
35. Maguire, B. A., Beniaminov, A. D., Ramu, H., Mankin, A. S. & Zimmermann, R. A. A protein component at the heart of an RNA machine: the importance

of protein l27 for the function of the bacterial ribosome. *Mol. Cell* **20**, 427–435 (2005).
36. Trobro, S. & Aqvist, J. Role of ribosomal protein L27 in peptidyl transfer. *Biochemistry* **47**, 4898–4906 (2008).
37. Voorhees, R. M., Weixlbaumer, A., Loakes, D., Kelley, A. C. & Ramakrishnan, V. Insights into substrate stabilization from snapshots of the peptidyl transferase center of the intact 70S ribosome. *Nat. Struct. Mol. Biol.* **16**, 528–533 (2009).
38. Aron, Z. D. et al. trans-Translation inhibitors bind to a novel site on the ribosome and clear Neisseria gonorrhoeae in vivo. *Nat. Commun.* **12**, 1799 (2021).
39. James, N. R., Brown, A., Gordiyenko, Y. & Ramakrishnan, V. Translational termination without a stop codon. *Science* **354**, 1437–1440 (2016).
40. Amiri, H. & Noller, H. F. A tandem active site model for the ribosomal helicase. *FEBS Lett.* **593**, 1009–1019 (2019).
41. Konno, T., Kurita, D., Takada, K., Muto, A. & Himeno, H. A functional interaction of SmpB with tmRNA for determination of the resuming point of trans-translation. *RNA* **13**, 1723–1731 (2007).
42. Miller, M. R., Healey, D. W., Robison, S. G., Dewey, J. D. & Buskirk, A. R. The role of upstream sequences in selecting the reading frame on tmRNA. *BMC Biol.* **6**, 29 (2008).
43. Watts, T., Cazier, D., Healey, D. & Buskirk, A. SmpB contributes to reading frame selection in the translation of transfer-messenger RNA. *J. Mol. Biol.* **391**, 275–281 (2009).
44. Ermolenko, D. N. et al. Observation of intersubunit movement of the ribosome in solution using FRET. *J. Mol. Biol.* **370**, 530–540 (2007).
45. Mohan, S., Donohue, J. P. & Noller, H. F. Molecular mechanics of 30S subunit head rotation. *Proc. Natl Acad. Sci. U.S.A.* **111**, 13325–13330 (2014).
46. Guo, Z. & Noller, H. F. Rotation of the head of the 30S ribosomal subunit during mRNA translocation. *Proc. Natl Acad. Sci. U.S.A.* **109**, 20391–20394 (2012).
47. Ling, C. & Ermolenko, D. N. Structural insights into ribosome translocation. *Wiley Interdiscip. Rev. RNA* **7**, 620–636 (2016).
48. Ramrath, D. J. F. et al. Visualization of two transfer RNAs trapped in transit during elongation factor G-mediated translocation. *Proc. Natl Acad. Sci. U.S.A.* **110**, 20964–20969 (2013).
49. Zhou, J., Lancaster, L., Donohue, J. P. & Noller, H. F. How the ribosome hands the A-site tRNA to the P site during EF-G-catalyzed translocation. *Science* **345**, 1188–1191 (2014).
50. Hong, S. et al. Mechanism of tRNA-mediated +1 ribosomal frameshifting. *Proc. Natl Acad. Sci. U.S.A.* **115**, 11226–11231 (2018).
51. Liu, Q. & Fredrick, K. Intersubunit bridges of the bacterial ribosome. *J. Mol. Biol.* **428**, 2146–2164 (2016).
52. Sundermeier, T. R., Dulebohn, D. P., Cho, H. J. & Karzai, A. W. A previously uncharacterized role for small protein B (SmpB) in transfer messenger RNA-mediated trans-translation. *PNAS* **102**, 2316–2321 (2005).
53. Miller, M. R. et al. The role of SmpB and the ribosomal decoding center in licensing tmRNA entry into stalled ribosomes. *RNA* **17**, 1727–1736 (2011).
54. Hudson, C. M. & Williams, K. P. The tmRNA website. *Nucleic Acids Res.* **43**, D138–D140 (2015).
55. Wilson, K. A., Holland, D. J. & Wetmore, S. D. Topology of RNA-protein nucleobase-amino acid π-π interactions and comparison to analogous DNA-protein π-π contacts. *RNA* **22**, 696–708 (2016).
56. Williams, K. P., Martindale, K. A. & Bartel, D. P. Resuming translation on tmRNA: a unique mode of determining a reading frame. *EMBO J.* **18**, 5423–5433 (1999).
57. Tresse, C. et al. Synthesis and evaluation of 1,3,4-oxadiazole derivatives for development as broad-spectrum antibiotics. *Bioorg. Med Chem.* **27**, 115097 (2019).
58. Guyomar, C. et al. Reassembling green fluorescent protein for in vitro evaluation of trans-translation. *Nucleic Acids Res.* **48**, e22 (2020).
59. Thépaut, M. et al. Safe and easy evaluation of tmRNA-SmpB-mediated trans-translation in ESKAPE pathogenic bacteria. *bioRxiv*, https://doi.org/10.1101/2020.12.16.423090 (2020).
60. Ranaei-Siadat, E. et al. In vivo tmRNA protection by SmpB and pre-ribosome binding conformation in solution. *RNA* **20**, 1607–1620 (2014).
61. Gillet, R. & Felden, B. Transfer RNA(Ala) recognizes transfer-messenger RNA with specificity; a functional complex prior to entering the ribosome? *EMBO J.* **20**, 2966–2976 (2001).
62. Cougot, N. et al. Visualizing compaction of polysomes in bacteria. *J. Mol. Biol.* **426**, 377–388 (2014).
63. Shimizu, Y. et al. Cell-free translation reconstituted with purified components. *Nat. Biotechnol.* **19**, 751–755 (2001).
64. Matos, R. G., Barbas, A. & Arraiano, C. M. RNase R mutants elucidate the catalysis of structured RNA: RNA-binding domains select the RNAs targeted for degradation. *Biochem. J.* **423**, 291–301 (2009).
65. Mastronarde, D. N. Automated electron microscope tomography using robust prediction of specimen movements. *J. Struct. Biol.* **152**, 36–51 (2005).
66. Zheng, S. Q. et al. MotionCor2: anisotropic correction of beam-induced motion for improved cryo-electron microscopy. *Nat. Methods* **14**, 331–332 (2017).
67. Zhang, K. Gctf: Real-time CTF determination and correction. *J. Struct. Biol.* **193**, 1–12 (2016).
68. Punjani, A., Rubinstein, J. L., Fleet, D. J. & Brubaker, M. A. cryoSPARC: algorithms for rapid unsupervised cryo-EM structure determination. *Nat. Methods* **14**, 290–296 (2017).
69. Scheres, S. H. W. RELION: implementation of a Bayesian approach to cryo-EM structure determination. *J. Struct. Biol.* **180**, 519–530 (2012).
70. Zivanov, J. et al. New tools for automated high-resolution cryo-EM structure determination in RELION-3. *Elife* **7**, e42166 (2018).
71. Bai, X., Rajendra, E., Yang, G., Shi, Y. & Scheres, S. H. W. Sampling the conformational space of the catalytic subunit of human γ-secretase. *Elife* **4**, e11182 (2015).
72. van Heel, M. & Stöffler-Meilicke, M. Characteristic views of E. coli and B. stearothermophilus 30S ribosomal subunits in the electron microscope. *EMBO J.* **4**, 2389–2395 (1985).
73. Scheres, S. H. W. & Chen, S. Prevention of overfitting in cryo-EM structure determination. *Nat. Methods* **9**, 853–854 (2012).
74. Kucukelbir, A., Sigworth, F. J. & Tagare, H. D. Quantifying the local resolution of cryo-EM density maps. *Nat. Methods* **11**, 63–65 (2014).
75. Afonine, P. V. et al. New tools for the analysis and validation of cryo-EM maps and atomic models. *Acta Crystallogr. D. Struct. Biol.* **74**, 814–840 (2018).
76. Nakane, T., Kimanius, D., Lindahl, E. & Scheres, S. H. Characterisation of molecular motions in cryo-EM single-particle data by multi-body refinement in RELION. *eLife* **7**, e36861 (2018).
77. Nakane, T. & Scheres, S. H. W. Multi-body refinement of Cryo-EM images in RELION. *Methods Mol. Biol.* **2215**, 145–160 (2021).
78. Afonine, P. V. et al. Real-space refinement in PHENIX for cryo-EM and crystallography. *Acta Crystallogr. D. Struct. Biol.* **74**, 531–544 (2018).
79. Pettersen, E. F. et al. UCSF Chimera—a visualization system for exploratory research and analysis. *J. Comput. Chem.* **25**, 1605–1612 (2004).
80. Fischer, N. et al. Structure of the E. coli ribosome-EF-Tu complex at <3 Å resolution by Cs-corrected cryo-EM. *Nature* **520**, 567–570 (2015).
81. Casañal, A., Lohkamp, B. & Emsley, P. Current developments in Coot for macromolecular model building of Electron Cryo-microscopy and Crystallographic Data. *Protein Sci.* **29**, 1069–1078 (2020).
82. Trabuco, L. G., Villa, E., Mitra, K., Frank, J. & Schulten, K. Flexible fitting of atomic structures into electron microscopy maps using molecular dynamics. *Structure* **16**, 673–683 (2008).
83. Humphrey, W., Dalke, A. & Schulten, K. VMD: visual molecular dynamics. *J. Mol. Graph* 14, 33–38, 27–28 (1996).
84. Phillips, J. C. et al. Scalable molecular dynamics on CPU and GPU architectures with NAMD. *J. Chem. Phys.* **153**, 044130 (2020).
85. Huang, J. & MacKerell, A. D. CHARMM36 all-atom additive protein force field: validation based on comparison to NMR data. *J. Comput. Chem.* **34**, 2135–2145 (2013).
86. Williams, C. J. et al. MolProbity: more and better reference data for improved all-atom structure validation. *Protein Sci.* **27**, 293–315 (2018).
87. Nguyen, K. & Whitford, P. C. Steric interactions lead to collective tilting motion in the ribosome during mRNA–tRNA translocation. *Nat. Commun.* **7**, 10586 (2016).
88. Webster, M. W. et al. Structural basis of transcription-translation coupling and collision in bacteria. *Science* **369**, 1355–1359 (2020).
89. Carbone, C. E., Demo, G., Madireddy, R., Svidritskiy, E. & Korostelev, A. A. ArfB can displace mRNA to rescue stalled ribosomes. *Nat. Commun.* **11**, 5552 (2020).

Acknowledgements

This article is in memory of Professor Brice Felden. The authors gratefully acknowledge aid from the Agence Nationale pour la Recherche as part of the RIBOTARGET 18-JAM2-0005-03 project under the JPI AMR framework. Funding was also received from the French Direction Générale de l'Armement (C.G.), the Université de Rennes 1 (C.G.) and the European Union's ERASMUS+ program (G.U.), as well as from the Région Bretagne (G.U.). Thanks are also due for electron microscope use at the Centre de Microscopie et d'Imagerie de Rennes (MRic), the EMBL Heidelberg Cryo-Electron Microscopy Service Platform and the Integrated Structural Biology platform of the Strasbourg Instruct-ERIC center IGBMC-CBI supported by FRISBI (ANR-10-INBS-0005-001). We thank Juliana Berland and Felix Weis for their comments on the manuscript.

Author contributions

C.G. performed the biochemical experiments and analysis. S.C. and C.G. performed the cryo-EM experiments. G.U. and E.G. performed the image analysis and model building. R.G. and E.G. supervised the project. All authors participated in writing the manuscript and approved its final version.

Competing interests

The authors declare no competing interests.

Additional information

Supplementary information The online version contains supplementary material available at https://doi.org/10.1038/s41467-021-24881-4.

Correspondence and requests for materials should be addressed to E.G. or R.G.

Peer review information *Nature Communications* thanks Chris Rae and other, anonymous, reviewers for their contributions to the peer review of this work. Peer review reports are available.

Reprints and permission information is available at http://www.nature.com/reprints

Publisher's note Springer Nature remains neutral with regard to jurisdictional claims in published maps and institutional affiliations.

Supplementary Figures

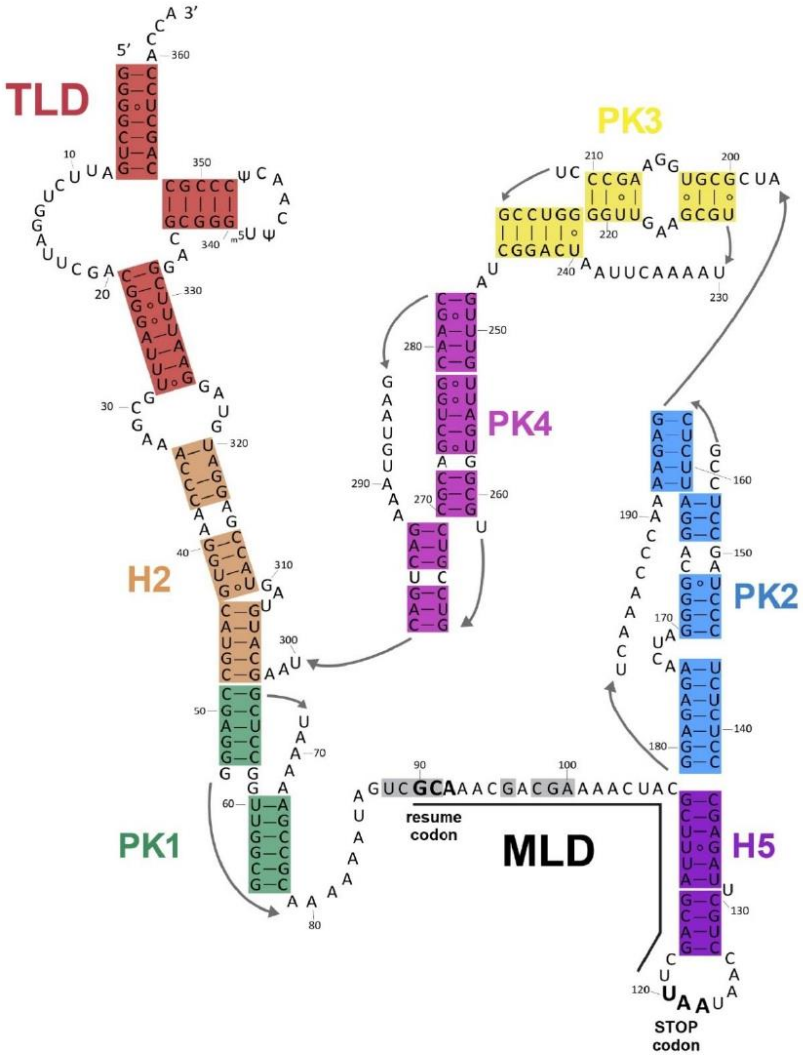

Supplementary Figure 1. Secondary structure of *Escherichia coli* tmRNA. To highlight the different structural domains, the helices in the tRNA-like domain (TLD) are red, the H2 helix is orange, the H5 stem-loop is purple, and the four pseudoknots (PK1 to PK4) are green, light blue, yellow, and pink, respectively. The mRNA-like domain (MLD) is underlined in black, with the putative transient central hairpin highlighted in grey. The resume codon (positions 90 to 92) and the stop codons (positions 120 to 122) are indicated. The grey arrows indicate the connection between consecutive nucleotides, and nucleotides are numbered in increments of ten.

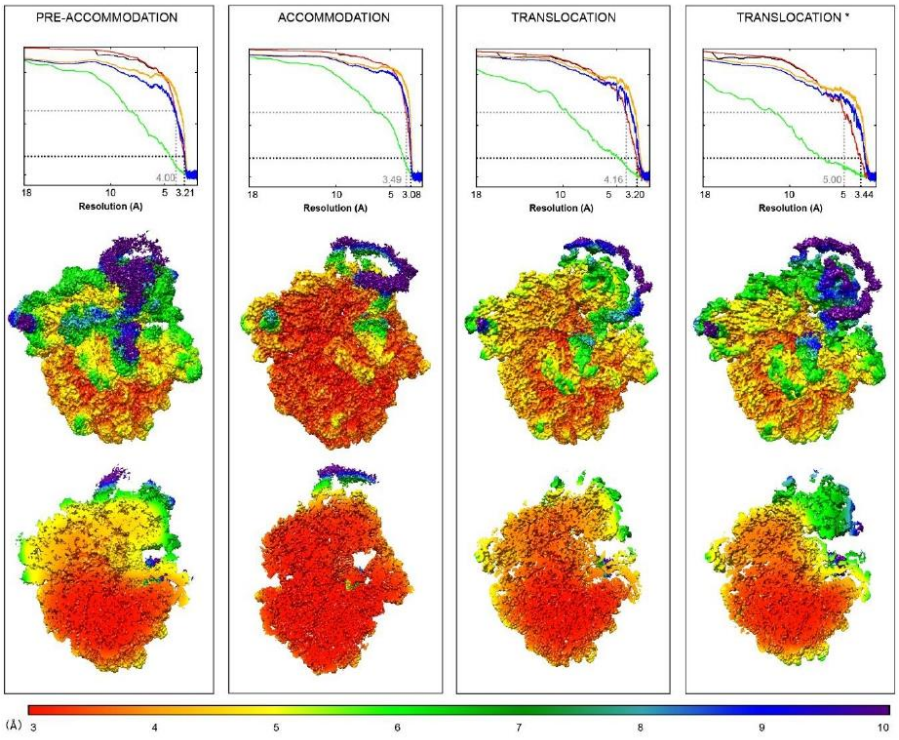

Supplementary Figure 2. Evaluating map quality for the consensus density maps. *Top*, Fourier shell correlation (FSC) curves calculated between the unmasked (green), masked (red), or solvent-corrected (black) half-maps, and between the atomic model and the unmasked (orange) or masked (blue) consensus-sharpened maps. Dashed lines indicate *FSC* = 0.143 (black) and 0.5 (grey). Corresponding resolutions calculated for the solvent-corrected half-maps are indicated. *Middle,* Front view of the consensus-sharpened density maps, which are coloured according to the local resolutions as computed with ResMap[1]. *Bottom*, Same as middle view, but sliced halfway through the maps.

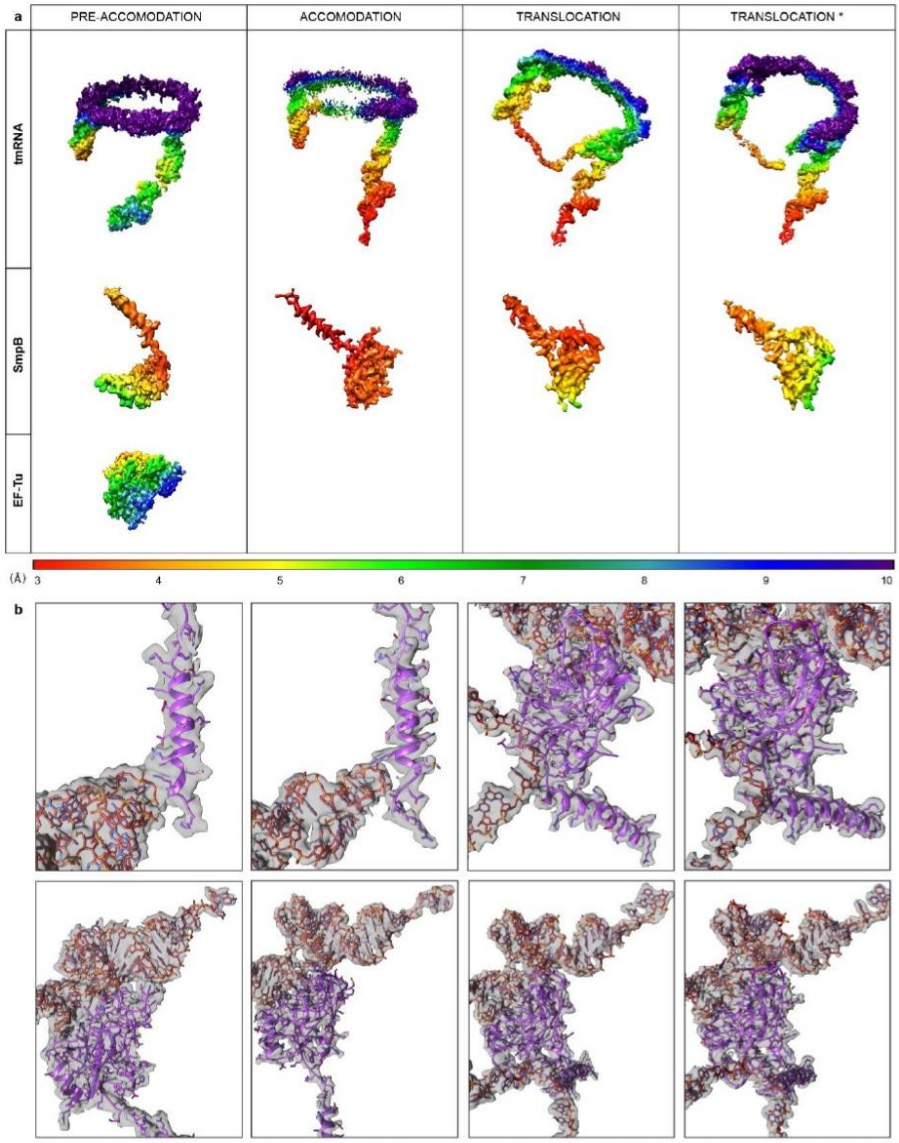

Supplementary Figure 3. Local resolutions of each of the individual components of the *trans*-translation complex. (a) Consensus-sharpened maps of tmRNA, SmpB, and EF-Tu are coloured according to the local resolutions as computed with ResMap[1]. **(b)** A representative sample of the maps showing the densities along with the models of SmpB, the tip of H5, the TLD, and the MLD.

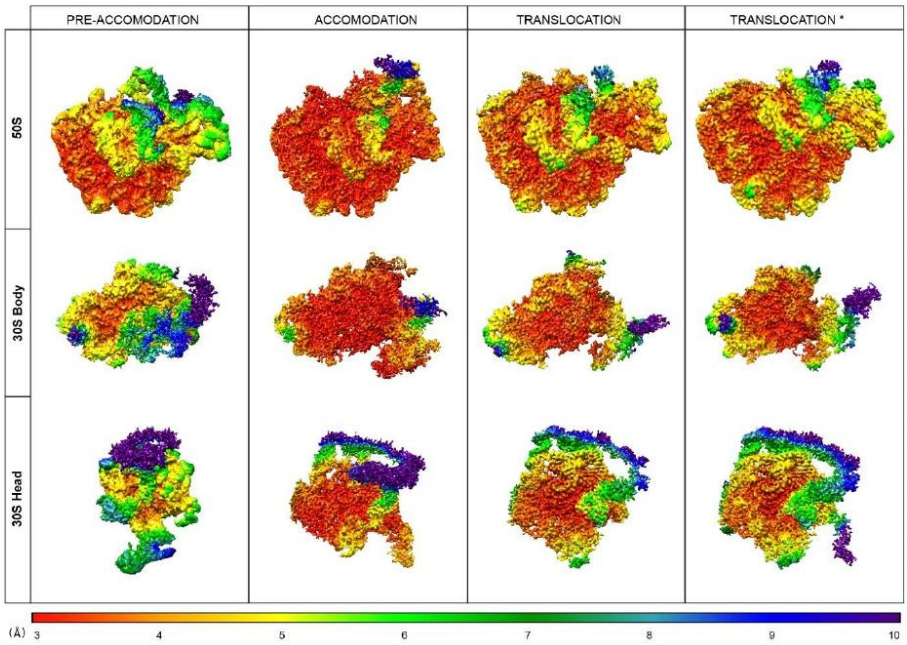

Supplementary Figure 4. Evaluating map quality for multi-body refinement. Sharpened-density maps of the large ribosomal subunit, small ribosomal subunit body, and small ribosomal subunit head regions are coloured here according to the local resolutions as computed with ResMap[1].

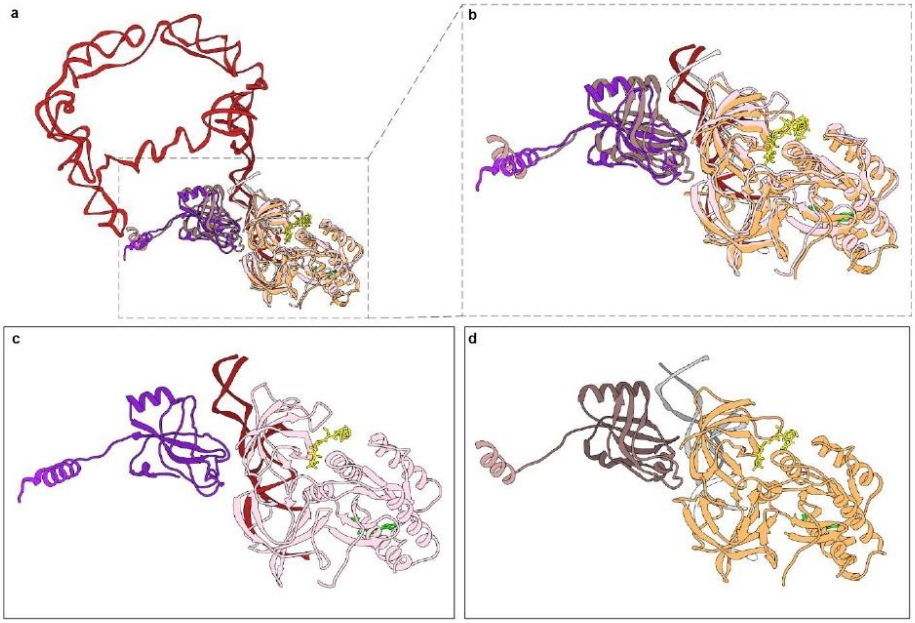

Supplementary Figure 5. Structural comparison between the Ala-tmRNA-SmpB-EF-Tu·GDP quaternary complex observed in the pre-accommodation state and a crystal structure of Ala-tmRNAΔ^{m}·SmpB·EF-Tu·GDP. (a) Global view of the overlay of our structure (tmRNA is red, SmpB is purple, and EF-Tu is light pink) and the structure published by Neubauer *et al.*[2] (PDB code 4V8Q, with tmRNA grey, SmpB dark pink, and EF-Tu orange) obtained after rigid-body fitting their atomic model (including the ribosome) into our electron density map. The RMSD between the two complexes calculated for the P and Cα is 3.23 Å, with SmpB (Cα-RMDS^{SmpB} = 4.1 Å) accounting for the biggest difference between the two structures. In both, GDP is green and kirromycin is yellow. **(b)** Close-up of the shared areas of the two structures, which are then shown separately in **(c)** and **(d)**.

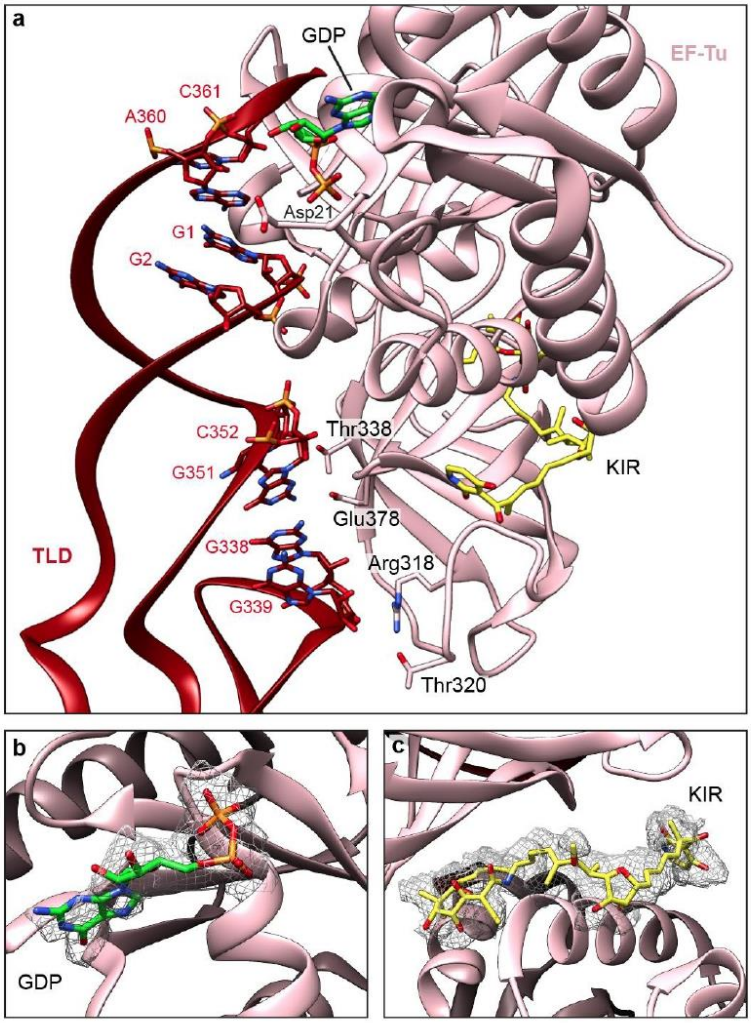

Supplementary Figure 6. Interactions between EF-Tu and the tRNA-like domain (TLD) of tmRNA**. (a)** Details of the contacts between the TLD (red) and EF-Tu (pink). All residues and nucleotides within 4 Å of each other are indicated. **(b-c)** Focus on the densities of **(b)** GDP (green) and **(c)** kirromycin (KIR, yellow). The cryo-electron density maps of the GDP and KIR are shown as grey meshes.

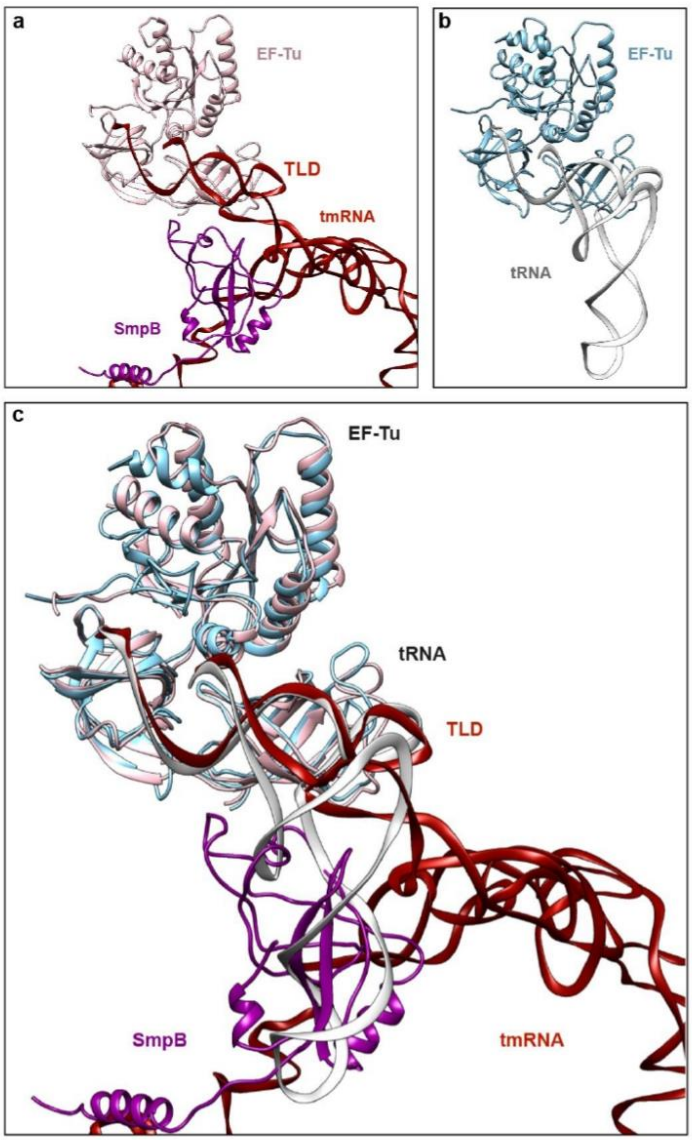

Supplementary Figure 7. Structural comparison between the tmRNA-SmpB-EF-Tu·GDP quaternary complex and a canonical tRNA-EF-Tu·GDP ternary complex. **(a)** Overview of the tmRNA-SmpB-EF-Tu·GDP quaternary complex. The tmRNA is red, SmpB is purple, and EF-Tu is pink. **(b)** Overview of the canonical tRNA-EF-Tu·GDP ternary complex[3] (PDB code 4V5L). EF-Tu is light blue and tRNA is white. **(c)** Overlaying the two structures highlights the similarities between the TLD and the upper part of the tRNA, while also showing that SmpB replaces the tRNA anticodon stem-loop.

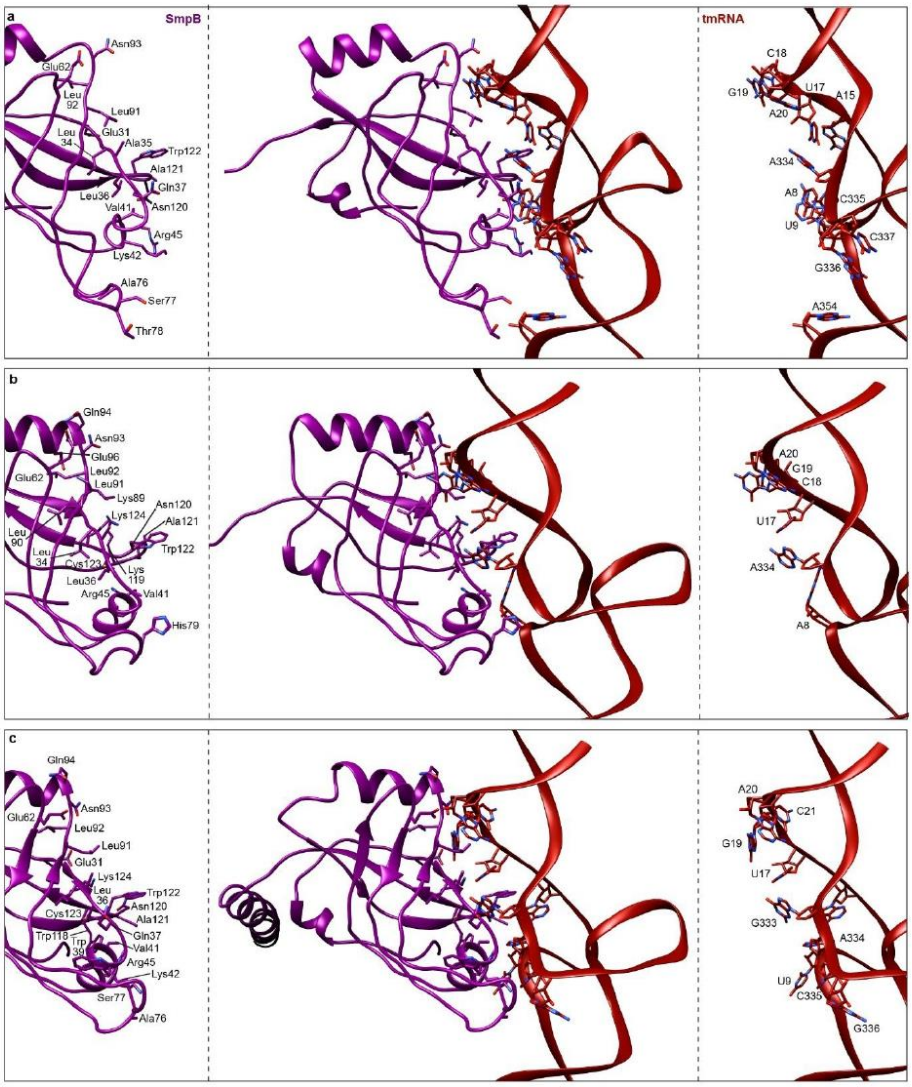

Supplementary Figure 8. Details of the interactions between the SmpB body and the tmRNA TLD during *trans*-translation. Shown are the **(a)** pre-accommodation, **(b)** accommodation, and **(c)** translocation states. *Left*, Focus on the SmpB residues that are within 4 Å of the TLD. *Middle*, Overview of the interaction between SmpB (purple) and the tmRNA TLD (red). *Right*, Focus on the TLD nucleotides within 4 Å of SmpB.

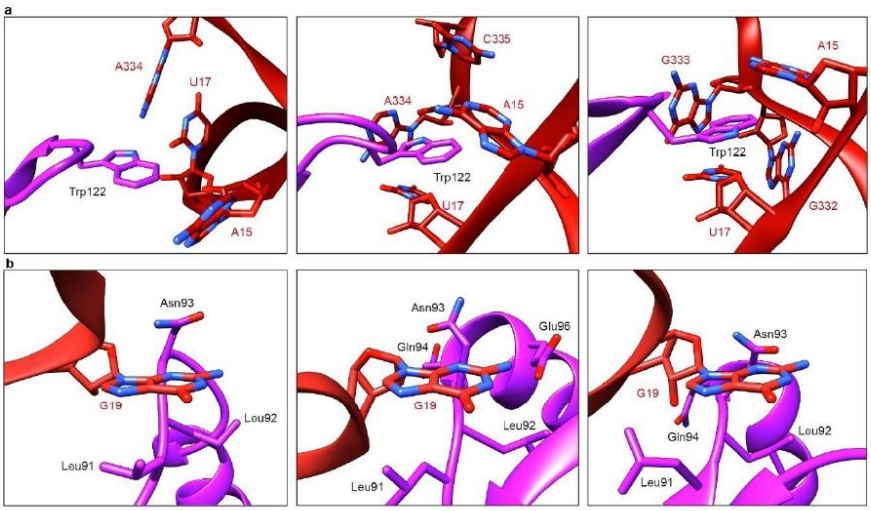

Supplementary Figure 9. Crucial interactions between tmRNA and SmpB are maintained throughout the *trans*-translation process. (a) SmpB's Trp122 is deeply embedded in a hydrophobic pocket delimited by tmRNA's U17 and A334. **(b)** The G19 nucleotide of tmRNA is tightly packed on the hydrophobic surface of SmpB. Shown are *left,* pre-accommodation; *middle,* accommodation; and *right,* translocation states. SmpB is purple, tmRNA is red, residues and nucleotides within 4 Å of each other are indicated

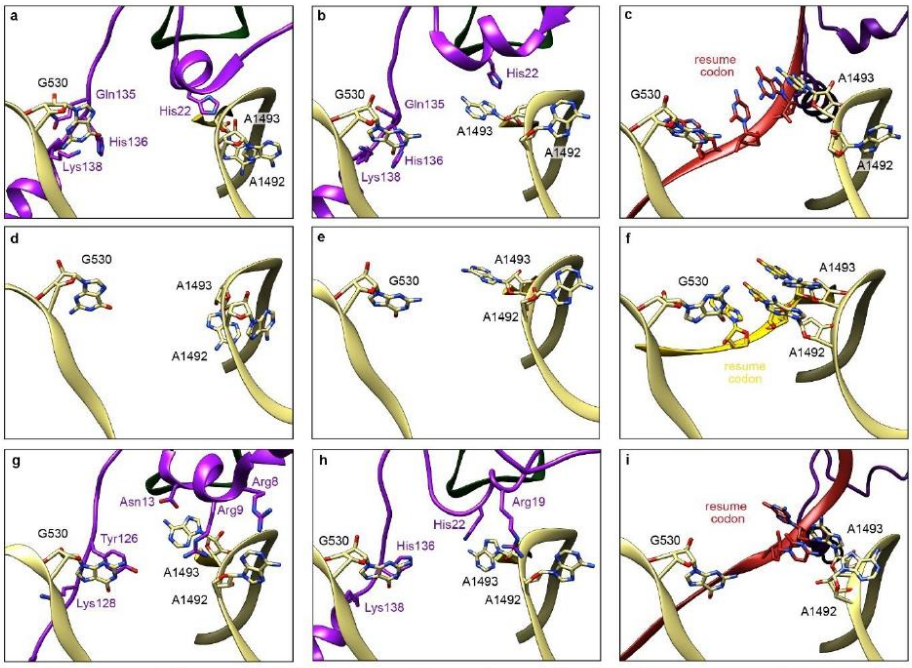

Supplementary Figure 10. Different conformation of the decoding centre. Close-up of the decoding centre (DC) in our **(a)** pre-accommodation, **(b)** accommodation, and **(c)** translocation states. **(d)** The DC of an empty *E. coli* ribosome[4] (PDB code 4YBB). **(e)** The DC of an *E. coli* ribosome with a tRNA in the P site, but an empty A site[5] (PDB code 5MDZ). **(f)** The DC in an *E. coli* ribosome with cognate tRNAs in the A and P sites[6] (PDB code 7K00). **(g)** The DC in a crystal structure of a complex containing a tmRNA fragment, SmpB, and EF-Tu bound to the *T. thermophilus* ribosome[2] (PDB code 4V8Q). **(h)** The DC in the accommodation state (PDB code 6Q97) described by Rae *et al.*[7] **(i)** Same as (h) but for the translocation state (PDB code 6Q98). In all panels, SmpB is purple, tmRNA is red, and the 16S rRNA is khaki. All residues and nucleotides that are within 4 Å of each other are indicated.

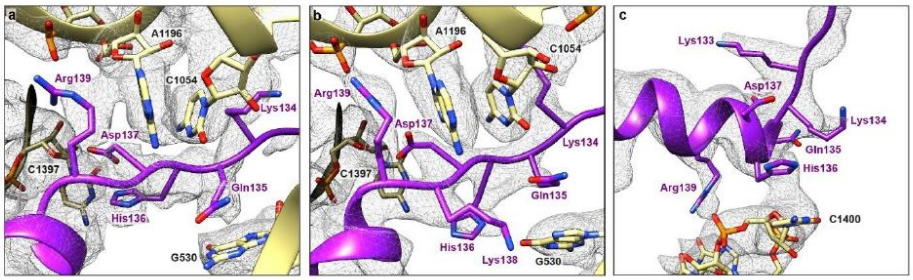

Supplementary Figure 11. Close-up of the region surrounding SmpB's His136. (a) In the pre-accommodation state, Lys134 and Arg139 both interact with the 16S rRNA and flank the stacked nucleotides C1054 and A1196. His136 and Asp137 form hydrogen bonds with C1397, and Gln135 is staked on G530. **(b)** These interactions are retained and even reinforced during the accommodation state, with Lys138 bonding with G530 and His136 interacting with both C1397 and G530. **(c)** His136 takes on a more crucial role during the translocation state. Its strong staking on C1440 as well as the hydrogen bonds formed between Arg139 and both C1399 and G1401 combine to place the SmpB C-terminal tail in the mRNA exit tunnel.

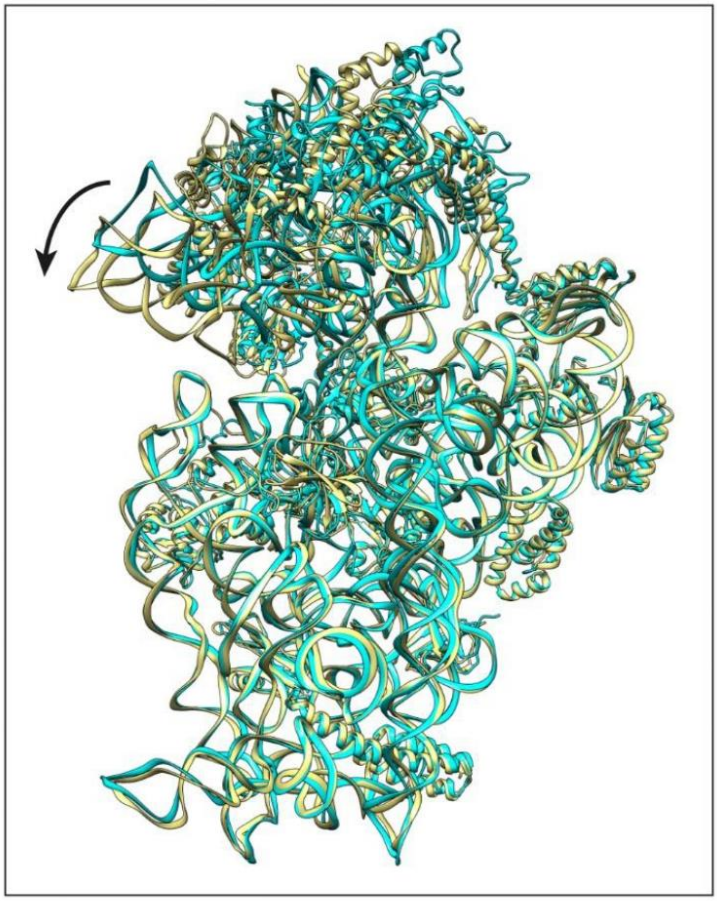

Supplementary Figure 12. Movement of the 30S subunit head during Ala-tmRNA·SmpB·EF-Tu·GDP pre-accommodation. Comparison between the 30S subunit in the pre-accommodation state (khaki) and that of an empty ribosome[8] (cyan; PDB code 4V4Q). The black arrow highlights the fact that when the quaternary complex made up of alanylated tmRNA, SmpB, EF-Tu, and GTP is bound, the small subunit head closes as if a cognate tRNA has been decoded.

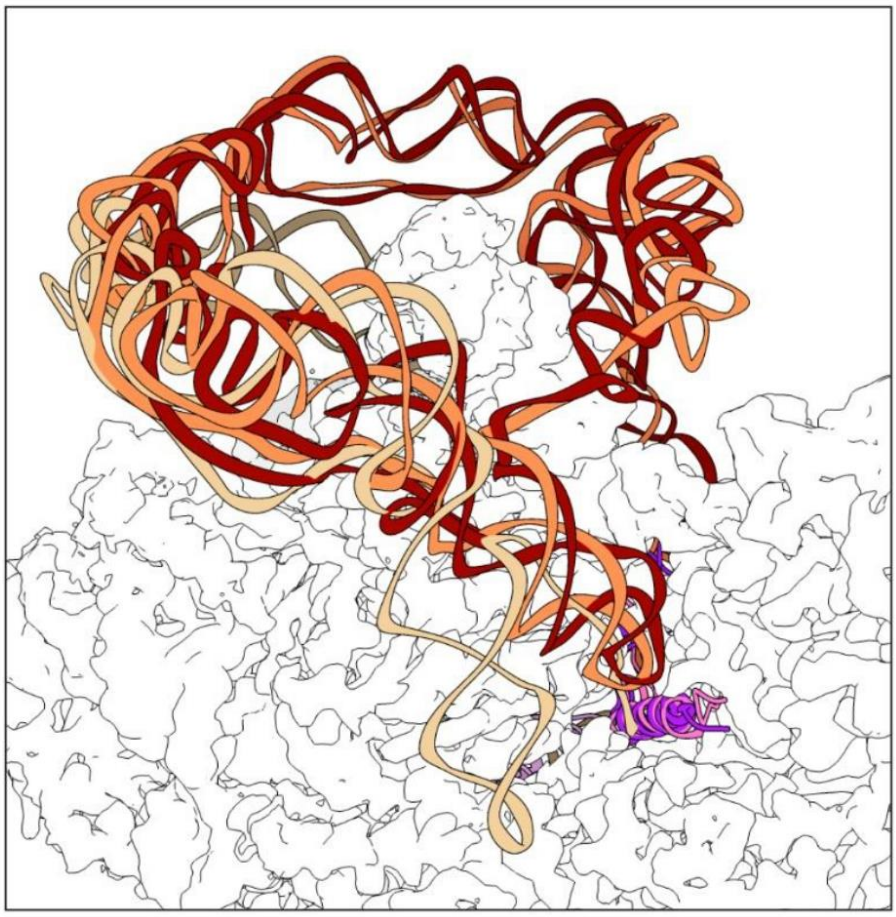

Supplementary Figure 13. Movement of the tmRNA pseudoknot ring and H5 stem-loop during *trans*-translation. Overlay of the atomic structures of the tmRNA-SmpB complex in the pre-accommodation state (tmRNA is red, SmpB is purple); the accommodation state (tmRNA is orange, SmpB is pink); and the translocation state (tmRNA is beige and SmpB is hidden behind the 30S head). The cryo-electron density map of 30S is shown as a white surface.

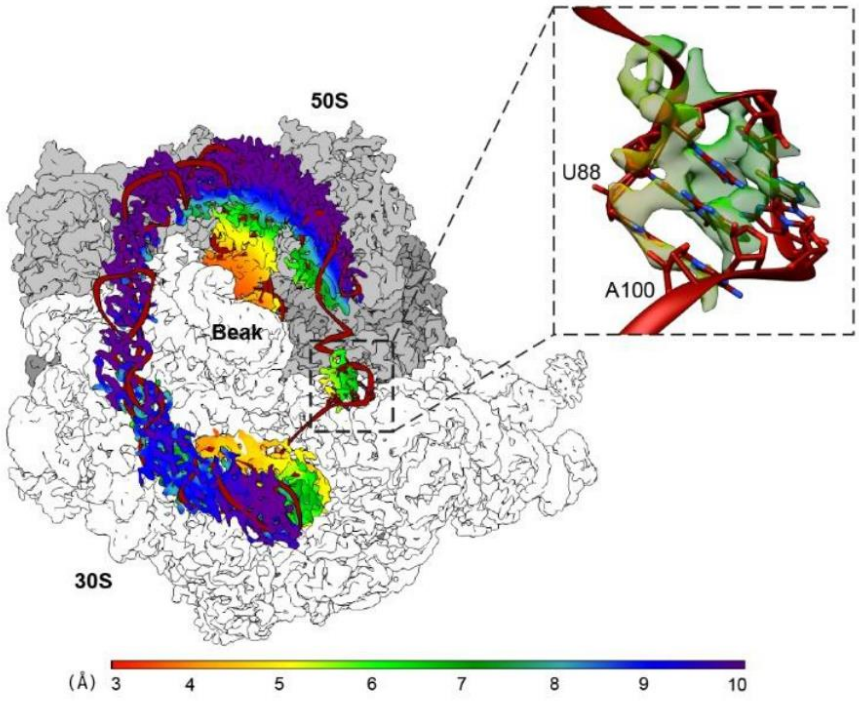

Supplementary Figure 14. In the accommodation state, the cryo-EM density confirms the presence of a hairpin in the tmRNA MLD. The zoom shows the dense region in the middle of the MLD, which is compatible with the presence of a hairpin between A88 and U100[9]. The 50S subunit is grey, the 30S is white, the tmRNA is red, and the cryo-electron density map around the MLD is shaded according to the local resolution as computed using ResMap[1].

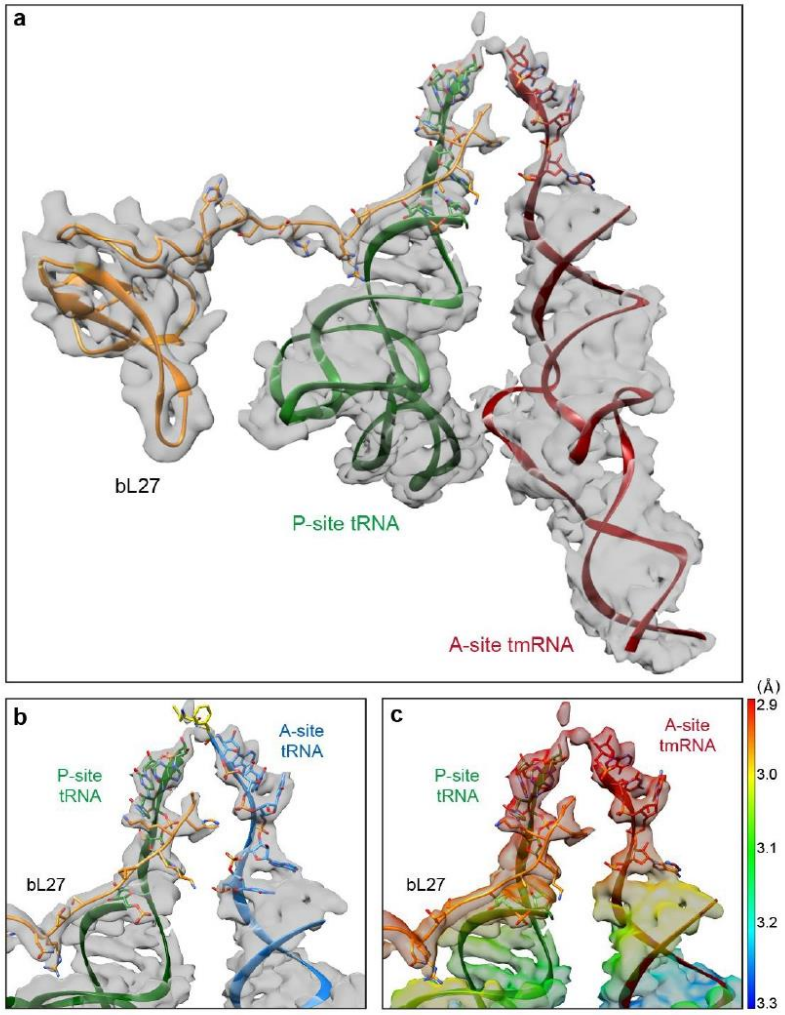

Supplementary Figure 15. Focus on the peptidyl transfer centre (PTC) during the accommodation state. (a) General view of the interaction between the ribosomal protein bL27 (orange), the P-site deacylated $tRNA^{Phe}$ (green), and the dipeptidyl-tmRNA (red). The electron density map is shown in grey. **(b)** Close-up of the PTC in the post-catalysis state of canonical translation[10] (PDB code 1VY5) rigid-body fitted in our electron density map (grey). Here the dipeptidyl-tRNA is blue, the newly synthesized dipeptide is yellow, and the other colours are the same as in the other panels. **(c)** Close-up of the accommodation state. The electron density map is coloured according to the local resolutions as computed with ResMap[1] The TLD closely resembles an aminoacylated tRNA, and the flexible N-terminal arm of bL27 is in the same conformation as during canonical translation.

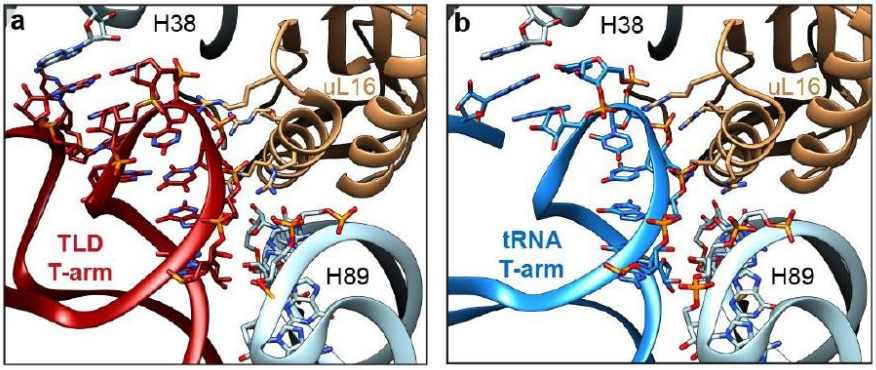

Supplementary Figure 16. Structural comparison between the T-arms of tmRNA and tRNA in the A site. (a) Close-up of the interaction between the tmRNA T-arm and the 50S ribosomal subunit. **(b)** Same, but for the tRNA T-arm[6] (PDB code 7K00). The tmRNA is red, tRNA is blue, uL16 is brown, and the 16S rRNA is light blue. To highlight the similarities between the two structures, the residues and nucleotides that are within 4 Å of each other are indicated.

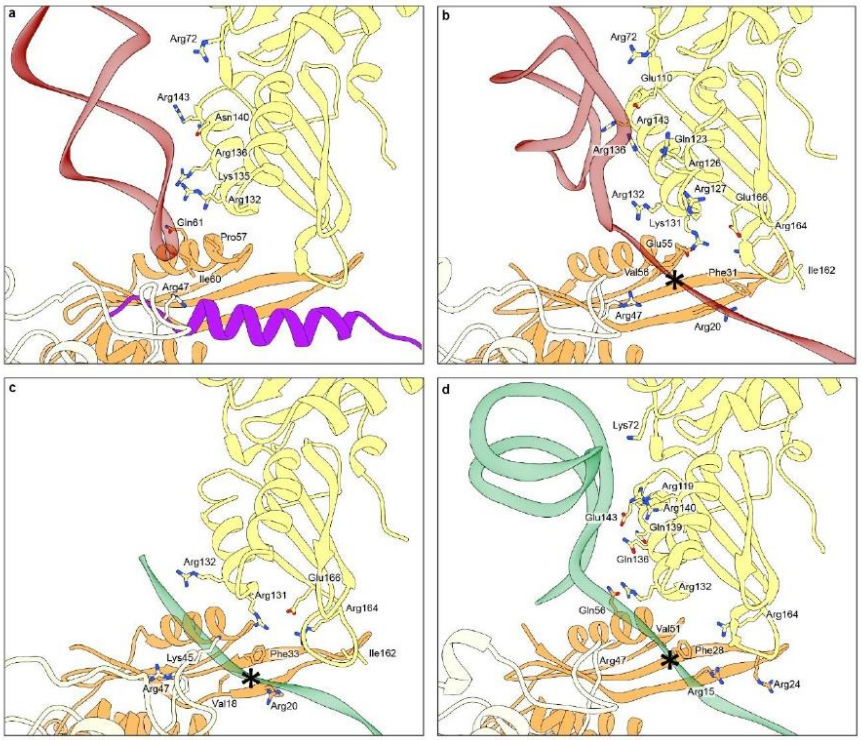

Supplementary Figure 17. Insight into the mechanism of action of the ribosomal helicase during *trans*-translation. (a) Close-up of the interactions between the H5 stem-loop and the ribosomal proteins uS3, uS4, and uS5 in the accommodation state. **(b)** Same, but for the translocation state. **(c)** Same, but for the single-stranded portion of a hairpin-containing mRNA[11] (PDB code 6BY1) **(d)** Same, but for the dnaX mRNA stem-loop bound to the *Thermus thermophilus* ribosome[12] (PDB code 5UQ7). SmpB is purple, tmRNA is red, mRNAs are green, and the ribosomal proteins uS3, uS4, and uS5 are khaki, orange, and white, respectively. The helicase residues within 4 Å of tmRNA or mRNAs are indicated. The stars represent the position of the proximal helicase active site, 11 nucleotides away from the P site[13]. To facilitate the comparison, all four structures are aligned on uS5.

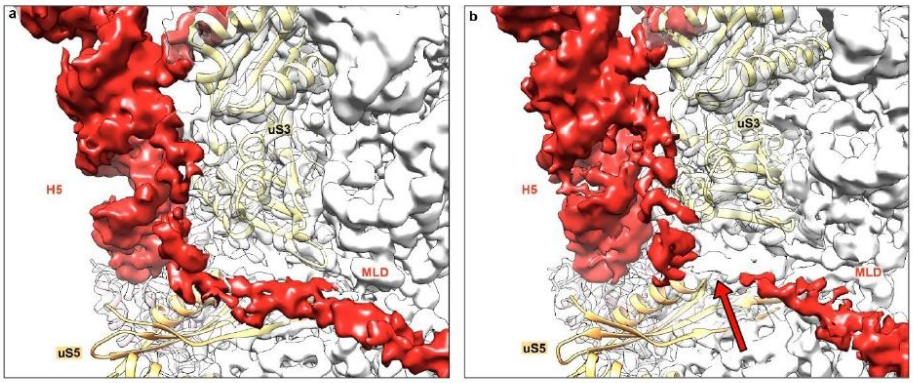

Supplementary Figure 18. Insight into the mechanism of action of the ribosomal helicase during the translocation steps. Close-up of the H5 stem-loop and MLD at the entrance of the mRNA channel in the **(a)** TRANS state and **(b)** TRANS* state. The electron density map of tmRNA is red and the 30S is white or transparent to allow for the localisation of the ribosomal protein uS3 and uS5 (khaki and orange, respectively). The arrow signals that in the TRANS* map, the MLD density is missing in the region of the proximal helicase active site[13].

Supplementary Tables

Supplementary Table 1. Cryo-EM data collection, refinement, and validation statistics.

	#1 PRE-ACC (EMD-11710) (PDB 7ABZ)	#2 ACC (EMD-11713) (PDB 7AC7)	#3 TRANS (EMDB-11717) (PDB 7ACJ)	#4 TRANS* (EMDB-11718) (PDB 7ACR)
Data collection and processing				
Magnification	105k	130k	130k	130k
Voltage (kV)	300	300	300	300
Electron exposure (e–/Å^2)	35	29	29	29
Defocus range (μm)	-1 to -3	-0.7 to -2	-0.7 to -2	-0.7 to -2
Pixel size (Å)	1.1 (fitted to 1.074)	1.04	1.04	1.04
Symmetry imposed	none	none	none	None
Micrographs collected (no.)	4,343	22,350	11,812	11,812
Micrographs used (no.)	3,143	21,917	11,433	11,433
Initial particle images (no.)	59,016	580,382	207,135	207,135
Final particle images (no.)	18,452	36,069	14,192	11,059
Map resolution (Å)				
FSC threshold: 0.143	3.21	3.08	3.20	3.44
FSC threshold: 0.5	4.00	3.49	4.16	5.00
Map resolution range (Å)	2.9-17.6	2.9-14.4	2.9-12.3	3.0-15.2
Refinement				
Initial models used (PDB code)	4YBB, 5AFI, 4V8Q	4YBB, 6Q97	4YBB, 6Q98	4YBB, 6Q98
Model resolution (Å)				
FSC threshold: 0.143	3.1	2.8	2.8	2.9
Map sharpening				
B factor (Å^2)	-42	-35	-24	-25
Model composition				
Non-hydrogen atoms	157,237	154,880	151,798	151,662
Protein residues	6,311	5,975	5,864	5,858
Nucleotide	5,017	5,017	4,920	4,920
Ligands	194	443	310	214
B factors mean (Å^2)				
Protein	111.73	98.05	117.32	147.69
Nucleotide	156.02	124.93	138.48	170.65
Ligand	93.89	72.87	84.93	92.48
RMS deviations				
Bond lengths (Å)	0.002	0.002	0.003	0.005
Bond angles (°)	0.648	0.494	0.567	0.594
Validation				
MolProbity score	2.15	1.71	1.99	2.01
Clashscore	16.22	10.27	13.20	14.14
Poor rotamers (%)	0.54	0.37	0.58	0.48
Ramachandran plot				
Favoured (%)	93.30	96.98	94.75	94.90
Allowed (%)	6.49	2.92	5.09	4.96
Disallowed (%)	0.21	0.10	0.16	0.14

Supplementary Table 2. 30S-head-to-body and 30S-body-to-50S rotations in ribosomal complexes.

Refs.	PDB ID	Body rotation (°)	Head rotation (°)	Head tilt (°)	tmRNA-SmpB location	tRNA location	Factors	Antibiotics	Organism	Resolution (Å)
Jenner et al. (2009)[14]	4V6F	0 / 1.3	0 / -0.5	0 / 0.7	-	A,P,E	-	-	Eco	3.1
PRE	7ABZ	0.3	0.1	1.5	pre A	P,E	EF-Tu·GDP	Kir	Eco	3.2#
ACC	7AC7	-1.3	1.5	0.7	A	P	-	-	Eco	3.1#
TRANS	7ACJ	-1.8	5.7	3.7	P	-	-	-	Eco	3.2#
TRANS*	7ACR	-1.2	13.9	12.2	P	-	-	-	Eco	3.4#
Carbone et al. (2020)[15]	7JT1	0.5	0.0	0.7	-	P	ArfB-1, ArfB-2	-	Eco	3.30#
Amiri and Noller (2019)[11]	6BY1	1.8 / 1.3	-0.1 / -0.3	1.0 / 1.0	-	A,P and A,P,E	Hairpin-containing mRNA	-	Eco	3.94
Fischer et al. (2015)[16]	5AFI	0.9	-0.8	0.3	-	pre A	EF-Tu·GDP	Kir	Eco	2.9
Watson et al. (2020)[6]	7K00	0.6	-0.2	0.6	-	A/P/E	-	Par	Eco	1.98#
Pulk et al. (2013)[17]	4V9O	2.8 / 3.8 / 4.0 / 6.7	6.1 / 7.1 / 5.3 / 11.4	0.8 / 0.2 / 2.1 / 3.3	-	-	EF-G·GDPCP	Vio	Eco	2.9
Noeske et al. (2015)[4]	4YBB	-0.6 /5.5	7.0 / 10.3	2.2 / 0.9	-	-	-	-	Eco	2.1
James et al. (2016)[5]	5MDZ	-1.8	1.5	1.6	-	P	-	-	Eco	3.1
Ramrath et al. (2013)[18]	4V7B	3.2	17.8	3.1	-	ap/P, pe/E	EF-G·GDP	Fus	Eco	6.8#
Ramrath et al. (2012)[19]	4V6T	6.0	17.0	11.5	P	E	EF-G	Fus	Eco	8.3#
Dunkle et al. (2011)[20]	4V9D	-0.1 / 8.9	0.2 / 3.5	0.6 / 0.9	-	P/E and P respectively	-	-	Eco	3.0
Li et al. (2015)[21]	3J9Z	-1.9	1.6	2.1	-	P,E	EF-G·GTP	-	Eco	3.6#
Li et al. (2015)[21]	3JA1	8.3	5.6	1.2	-	P/E	EF-G·GTP		Eco	3.6#
Rae et al. (2019)[7]	6Q97	-1.5	1.9	1.0	A	E**	-	-	Eco	3.9#
Rae et al. (2019)[7]	6Q98	-1.4	5.1	4.0	P	-	-	-	Eco	4.3#
Rae et al. (2019)[7]	6Q9A	-1.9	1.7	1.5	past E	P	-	-	Eco	3.7#
Rae et al. (2019)[7]	6Q95	-0.9	2.3	1.0	A	P,E	-	-	Tth	3.7#
Neubauer et al. (2012)[2]	4V8Q	-0.1	0.7	0.5	A*	P,E	EF-Tu·GDP	Kir	Tth	3.1
Zhou et al. (2014)[22]	4W29	3.0 / 3.0	20.1 / 20.4	3.2 / 2.8	-	AP/AP,pe/E	EF-G·GDP	Fus	Tth	3.80
Schuwirth et al. (2005)[8]	4V4Q	-1.5 / -2.6	15.4 / 6.7	1.1 / 2.6	-	-	-	-	Tth	3.46
Polikanov et al. (2014)[10]	1VY5	-0.9 / 1.0	0.9 / -0.5	0.6 / 0.9	-	A,P,E	-	-	Tth	2.55
Voorhees et al. (2010)[3]	4V5L	0.6	-1.0	0.4	-	A,P,E	EF-Tu·GDPCP		Tth	3.10
Hong et al. (2018)[23]	5VPP	-0.8 / 0.3	19.0 / 19.2	3.3 / 3.0		e*/E			Tth	3.9

Calculations are based on Nguyen and Whitford[24], and we used the same structure (PDB 4V6F) as the reference configuration[14] (see first line). For the movements, when multiple ribosomes are present in the asymmetric unit, all values are shown. Key: Fus, fusidic acid; Kir, kirromycin; Par, paromomycin; Vio, viomycin; Eco, *Escherichia coli*; Tth, *Thermus thermophilus*; *, only an engineered TLD is present; **, P-site fMet-NH-tRNA is present in the atomic model but not in the cryo-EM map; and #, structure derived from cryo-EM.

Supplementary Table 3. Bacterial strains, plasmids, and synthetic sequences.

Strain name	Description	Source
E. coli MG1655	Strain used for ribosome purification	CGSC (The Coli Genetic Stock Center)
E. coli BL21(DE3)*ΔssrA*	Strain used to purify SmpB protein	[25]

Plasmid name	Description	Source
pUC19-ala-tRNA	Plasmid to produce Alanine specific tRNA	[26]
pQE30-AlaRS	Plasmid to express and purify alanyl-tRNA synthetase	[27]
pQE30-PheRS	Plasmid to express and purify phenylalanyl-tRNA synthetase	[27]
pQE60-EF-G	Plasmid to express and purify EF-G	[27]
pABA-RNR_D280N	Plasmid to express and purify the mutated RNase R (D280N)	[28]

DNA name	Description	Sequence	Source
non-stop mRNA	Small non-stop mRNA to stall ribosomes	5′-AGGAGGUGAGGUUUU-3′	Thermo Fisher Scientific
tRNA-phe	Phenylalanine-specific tRNA isolated from E. coli MRE 600		Sigma
Forward_SmpB-N*de*I	Primer#1	5′-TCACGACGCATATGACGAAG	[29]
Reverse_SmpB-X*ho*I	Primer#2	5′-ACTCGAGACGGTGGGCGTTTTTC	[29]

Supplementary References

1. Kucukelbir, A., Sigworth, F. J. & Tagare, H. D. Quantifying the local resolution of cryo-EM density maps. *Nat. Methods* **11**, 63–65 (2014).
2. Neubauer, C., Gillet, R., Kelley, A. C. & Ramakrishnan, V. Decoding in the absence of a codon by tmRNA and SmpB in the ribosome. *Science* **335**, 1366–1369 (2012).
3. Voorhees, R. M., Schmeing, T. M., Kelley, A. C. & Ramakrishnan, V. The Mechanism for Activation of GTP Hydrolysis on the Ribosome. *Science* **330**, 835–838 (2010).
4. Noeske, J. et al. High-resolution structure of the Escherichia coli ribosome. *Nat. Struct. Mol. Biol.* **22**, 336–341 (2015).
5. James, N. R., Brown, A., Gordiyenko, Y. & Ramakrishnan, V. Translational termination without a stop codon. *Science* **354**, 1437–1440 (2016).
6. Watson, Z. L. et al. Structure of the bacterial ribosome at 2 Å resolution. *Elife* **9**, (2020).
7. Rae, C. D., Gordiyenko, Y. & Ramakrishnan, V. How a circularized tmRNA moves through the ribosome. *Science* **363**, 740–744 (2019).
8. Schuwirth, B. S. et al. Structures of the bacterial ribosome at 3.5 A resolution. *Science* **310**, 827–834 (2005).
9. Felden, B. et al. Probing the structure of the Escherichia coli 10Sa RNA (tmRNA). *RNA* **3**, 89–103 (1997).
10. Polikanov, Y. S., Steitz, T. A. & Innis, C. A. A proton wire to couple aminoacyl-tRNA accommodation and peptide-bond formation on the ribosome. *Nat. Struct. Mol. Biol.* **21**, 787–793 (2014).
11. Amiri, H. & Noller, H. F. Structural evidence for product stabilization by the ribosomal mRNA helicase. *RNA* **25**, 364–375 (2019).
12. Zhang, Y., Hong, S., Ruangprasert, A., Skiniotis, G. & Dunham, C. M. Alternative Mode of E-Site tRNA Binding in the Presence of a Downstream mRNA Stem Loop at the Entrance Channel. *Structure* **26**, 437-445.e3 (2018).
13. Amiri, H. & Noller, H. F. A tandem active site model for the ribosomal helicase. *FEBS Lett.* **593**, 1009–1019 (2019).

14. Jenner, L. B., Demeshkina, N., Yusupova, G. & Yusupov, M. Structural aspects of messenger RNA reading frame maintenance by the ribosome. *Nat. Struct. Mol. Biol.* **17**, 555–560 (2010).

15. Carbone, C. E., Demo, G., Madireddy, R., Svidritskiy, E. & Korostelev, A. A. ArfB can displace mRNA to rescue stalled ribosomes. *Nat. Comm.* **11**, 5552 (2020).

16. Fischer, N. et al. Structure of the E. coli ribosome-EF-Tu complex at <3 Å resolution by Cs-corrected cryo-EM. *Nature* **520**, 567–570 (2015).

17. Pulk, A. & Cate, J. H. D. Control of ribosomal subunit rotation by elongation factor G. *Science* **340**, 1235970 (2013).

18. Ramrath, D. J. F. et al. Visualization of two transfer RNAs trapped in transit during elongation factor G-mediated translocation. *Proc Natl. Acad. Sci. U.S.A.* **110**, 20964–20969 (2013).

19. Ramrath, D. J. F. et al. The complex of tmRNA-SmpB and EF-G on translocating ribosomes. *Nature* **485**, 526–529 (2012).

20. Dunkle, J. A. et al. Structures of the bacterial ribosome in classical and hybrid states of tRNA binding. *Science* **332**, 981–984 (2011).

21. Li, W. et al. Activation of GTP hydrolysis in mRNA-tRNA translocation by elongation factor G. *Sci. Adv.* **1**, (2015).

22. Zhou, J., Lancaster, L., Donohue, J. P. & Noller, H. F. How the ribosome hands the A-site tRNA to the P site during EF-G-catalyzed translocation. *Science* **345**, 1188–1191 (2014).

23. Hong, S. et al. Mechanism of tRNA-mediated +1 ribosomal frameshifting. *Proc. Natl. Acad. Sci. U.S.A.* **115**, 11226–11231 (2018).

24. Nguyen, K. & Whitford, P. C. Steric interactions lead to collective tilting motion in the ribosome during mRNA–tRNA translocation. *Nat. Comm.* **7**, 10586 (2016).

25. Cougot, N. et al. Visualizing compaction of polysomes in bacteria. *J. Mol. Biol.* **426**, 377–388 (2014).

26. Gillet, R. & Felden, B. Transfer RNA(Ala) recognizes transfer-messenger RNA with specificity; a functional complex prior to entering the ribosome? *EMBO J.* **20**, 2966–2976 (2001).

27. Shimizu, Y. et al. Cell-free translation reconstituted with purified components. *Nat. Biotechnol.* **19**, 751–755 (2001).

28. Matos, R. G., Barbas, A. & Arraiano, C. M. RNase R mutants elucidate the catalysis of structured RNA: RNA-binding domains select the RNAs targeted for degradation. *Biochem. J.* **423**, 291–301 (2009).
29. Guyomar, C. et al. Reassembling green fluorescent protein for in vitro evaluation of trans-translation. *Nucleic Acids Res.* **48**, e22 (2020).

1.3 Conclusion and perspectives

This work has given life to four high-resolution density maps of a ribosome during different stages of *trans*-translation. The results obtained have made possible to describe more precisely the intriguing ballet performed by the tmRNA – SmpB complex during the pre-accommodation, accommodation and two different states of translocation stages. Our unique structural knowledge of *trans*-translation (Rae et al., 2019; Guyomar et al. 2021) allowed us to select, among the interactions susceptible to be targeted to alter the process, the most promising ones (Fig. 7). These are: *i)* the interfaces between tmRNA and SmpB; *ii)* the mechanism of stalled ribosome recognition by SmpB; *iii)* the tmRNA-SmpB ribosomal binding site which allows resume codon registration during translocation. With the help of Dr. O. Delalande, an expert in molecular simulation and drug design who recently join our group, in collaboration with Prof. P. Dallemagne (UR 4258 CERMN) and with the help of Dr. Stéphane Teletchea (UFIP, UMR 6286 CNRS Nantes), our team is now using HTS virtual screening to explore these molecular interfaces in ESKAPE bacteria. Our structural data will also be instrumental to establish the quantitative structure-activity relationship (QSAR) of the hit compounds discovered by wet biochemistry and to rationalize the chemical optimization of our molecules.

III - Section 2:

Cryo-EM study of the association of the RNase R to the ribosome

2.1 Context of study

Although the results reported in the previous section give us a detailed picture of what happens during the rescue of a stalled ribosome, much remains to be done to get a full description of the whole process and the different actors involved. More particularly, we know that a third key player involved in this mechanism is RNase R, the key ribonuclease that degrades the non-stop mRNA (see Introduction, paragraph 3.2 - D'Urso et al., 2021 and Campos – Da silva et al., 2022). Several biochemical studies suggest that this ribonuclease associates with the tmRNA and SmpB during the growth of a bacterial cell, thus forming a tripartite complex, which is maintained during *trans*-translation as it reaches the ribosomal platform. However, no structure of RNase R during *trans*-translation or even alone is currently known.

During this Ph.D. I investigated the interaction of RNase R, first on a stalled ribosome and then in the context of a *trans*-translating ribosome with tmRNA and SmpB. We have also worked to understand the role of the three key players in a more complex system represented by disomes.

2.2 The RNase R

The RNase R (ribonuclease R) is a 95kDa 3'-5' exoribonuclease encoded by the *rnr* gene, belonging to the RNB superfamily. It presents 60% sequence homology with RNase II, another member of the RNB family, as well as several structural similarities, although the latter is smaller in size than the former (Deutscher and Li, 2000; Zuo and Deutscher, 2001a/b; Cheng and Deutscher, 2002; Li and Deutscher, 2004; Condon, 2007). We can distinguish four conserved domains between RNase R and RNase II: moving from the N- to the C-terminal end we find two cold shock domains (CSD1 and CSD2), the central catalytic RNB domain and the S1 domain. In addition, RNase R has two other domains: the "Helix-Turn-Helix" (HTH) domain at the N-terminal extremity and the K-rich domain at the C-terminal end (Figure 29, Figure 30) (Ge et al., 2010). The only atomic structure available was obtained in 2017 by X-ray crystallography and lacks the two highly flexible HTH and K-rich domains (Figure 30 A) (Chu et al., 2017).

Figure 29: The schematic comparison between the RNase II (top) and RNase R (bottom). N-terminal domain is in blue, CSD1/2 are in green, RNB is purple, S1 is orange, HTH is light green and K-rich is red (Adapted from Giudice et al., 2014)

In contrast to other ribonucleases, RNase R has a ribonuclease and an additional helicase activity. The two activities are apparently independent of each other, but they occur in a region close to the same catalytic channel (Awano et al., 2010; Hossain et al., 2015). In particular, the helicase activity is accomplished by the two CSD domains which include “Walker A” and a “Walker B” motifs. These motifs allow ATP binding in the presence of RNA. While ATP hydrolysis is not required, the presence of ATP is essential for the helicase activity to take place (Awano et al., 2010; Hossain et al., 2015).

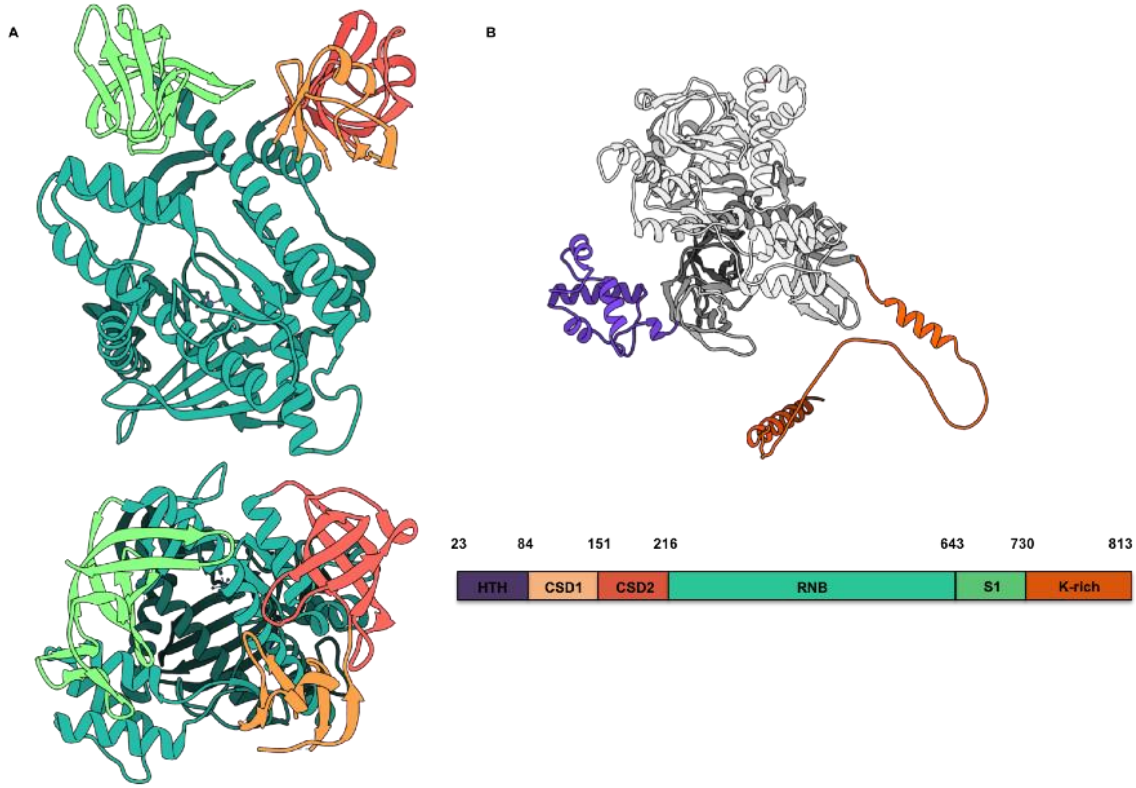

Figure 30: RNase R structure. A) Side (above) and top (below) view of the RNase R crystal structure (PDB: 5XGU, Chu et al., 2017). B) Complete model of the RNase R modelled with Alphafold with the HTH domain in purple and the K-rich doamin in orange.

The most important feature of RNase R is its ability to degrade double-stranded RNA. For this to be possible, the target RNA molecule must have a 3' single-stranded extension of at least seven nucleotides (Cheng and Deutscher, 2005). Based on the structure shown in Figure 30A and on the ability to degrade double-stranded RNA molecules, two different mechanisms have been proposed: in the first case the 3' extension of the substrate enters through the channel formed by the CSDs and S1 domains (Figure 30 A, bottom); in the second case the 3' extension enters through the channel formed between the CSD domains and the RNB catalytic domain (Chu et al., 2017). From a functional point of view, thanks to its particular activity, RNase R is involved in several physiological mechanisms within bacterial cells, acting on a wide range of substrates such as rRNA, tRNA, tmRNA and sncRNA (Arraiano et al., 2010; Saramago et al., 2014; Domingues et al., 2015; Wellner et al., 2018). In the case of *trans*-translation, in addition to digesting non-stop mRNAs, it is also involved in the maturation of tmRNA under cold stress (Cairrao et al., 2003). Similarly, it is involved in the metabolism of 16S and 23S rRNAs and, in association with YbeY, it is also capable of eliminating non-translating ribosomes associated into polysomes chains by binding to the 30S subunit (Jacob et al., 2013). The expression and half-life of RNase R depend strongly on the different growth phases of the bacterial cell, as well as on environmental conditions or the presence of *trans*-translation players. At 10°C, the expression is about eight times higher than that of RNase II, whereas, under normal growth conditions, the protein is very unstable during the exponential phase and loses its catalytic activity. However, in the stationary phase, RNase R is highly stable and functional (Andrade et al., 2006; Chen and Deutscher, 2010). These differences have been linked to the acetylation of the residue K544. In the exponential phase, the acetylation of K544 allows the tmRNA-SmpB complex to interact with the C-terminal portion of RNase R, allowing it to attract the Lon and HslUV proteases that, degrade the protease by attacking its N-terminal end. In the stationary phase, the absence of acetylation due to the non-production of the YfiQ enzyme prevents the mechanism described above (Figure 31) (Liang and Deustcher, 2012; Domingues et al., 2015).

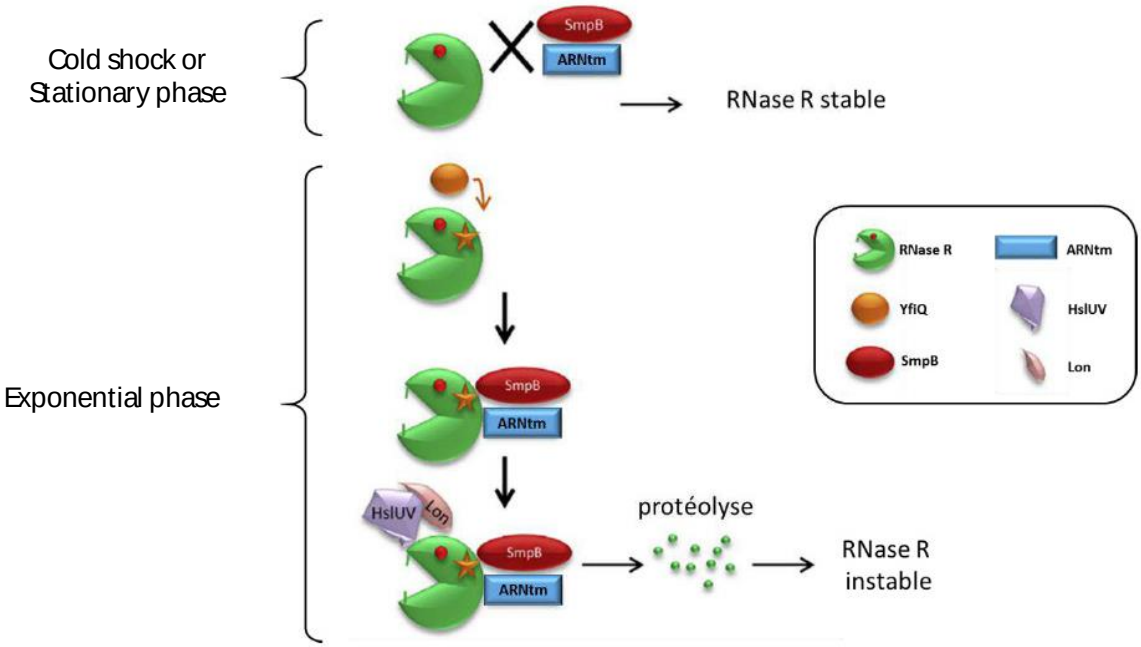

Figure 31: Schematic representation of RNase R expression, adapted from Domingues et al., 2015. RNase R is green, tmRNA is cyan, SmpB is red, YfiQ is orange, Lon is pink and HslUV is violet. The acetylation is represented with a star.

However, as reported before, the degradation of non-stop mRNAs during *trans*-translation depends on the presence of the tmRNA-SmpB complex. In addition, the specificity of degradation during this mechanism also depends on the segment 726 - 744 of the K-rich domain, as well as the Q278 residue whose mutation renders the ribonuclease inactive (Richards et al., 2006; Ge et al., 2010; Liang and Deutscher, 2013).

Understanding the mechanism of action of the RNase R and describing the molecular interactions that occur during *trans*-translation is of paramount importance for several reasons. Firstly, among the different known exoribonucleases, RNase R is the only one present in mycoplasmas. In addition, *Salmonella thyphymurium* strains with a deletion for RNase R are more sensitive to antibiotics that target canonical translation (Saramago et al., 2014). For these reasons, these studies show that this enzyme may be a potential target for the development of new antibacterial agents.

2.3 Materials and methods

All the factors necessary to conduct this study, as well as the *in vitro* complex formation, were obtained as explained in "Materials and methods" of the manuscript Guyomar, D'Urso et al., 2021 in Section 1. The only difference is due to the use, for part of the experiments, of *E. coli* ribosomes carrying a streptavidin tag purified with the same protocol, from the Rpst5998 strain, for which the culture was supplemented with 1% kanamycin. The purification process for RNase R is explained in the next paragraph.

2.3.1 RNase R purification

The *E. coli* strain BL21(DE3) was transformed with the plasmid pET15b-RNR_D280R containing the gene encoding the RNase R protein mutated within the RNB domain (D280N) and tagged at the C-ter extremity with a six-histidine sequence. An overnight preculture was launched using LB culture medium supplemented with ampicillin (100 µg/mL) at 37°C under agitation. 2L of LB medium were inoculated with a starting OD_{600nm} of 0.05. Cells were grown at 37°C until the exponential phase was reached at OD_{600nm} = 0.6. From this point, 4h of induction were performed by addition of IPTG with a final concentration of 1 mM. Subsequently, cells were centrifuged, washed with 0.9% NaCl saline, pelleted, and stored at -80°C overnight. The pellet was thawed and resuspended in a lysis buffer (HEPES-KOH 20mM, KCl 300 mM, $MgCl_2$ 2mM, PMSF 0,5 mM, Imidazole 10mM, DTT 1mM, pH 8). Cells were then lysed with French press, incubated on ice under stirring for 30 minutes in presence of 50 U/mL of Benzonase ® (Merck millipore), and then centrifuged. The supernatant was filtered and applied to a HisTrap HP™ column (1 mL, Cytiva) (Figure 32, 1) previously equilibrated with an equilibration buffer (HEPES-KOH 20mM, KCl 300 mM, $MgCl_2$ 2mM, Imidazole 10mM, DTT 1mM, pH 8). The sample was washed with 10 mL of washing buffer (HEPES-KOH 20mM, KCl 1M, $MgCl_2$ 2mM, Imidazole 10mM, DTT 1mM, pH 8) and then eluted with a 0%-100% imidazole gradient in elution buffer (HEPES-KOH 20mM, KCl 300mM, $MgCl_2$ 2mM, Imidazole 500mM, DTT 1mM, pH 8). The fractions corresponding to the elution peak were deposited on a 12% SDS-PAGE gel and those of interest pooled together and passed on a series of 3 HiTrap® desalting columns with Sephadex G-25 resin (5 mL, Cytiva) (Figure 32, 2), previously equilibrated with Concentration buffer (HEPES-KOH 10mM, KCl 100mM, $MgCl_2$ 1mM, EDTA 0,5mM, DTT 1mM, pH 7,5) to eliminate

the imidazole. The fractions of interest were then concentrated on Amicon® 50kDa (Merck millipore), previously equilibrated with the concentration buffer added with 0.01% Tween 20. 10% glycerol was then added for conservation and the final sample was then dosed, aliquoted and stored at -80°C.

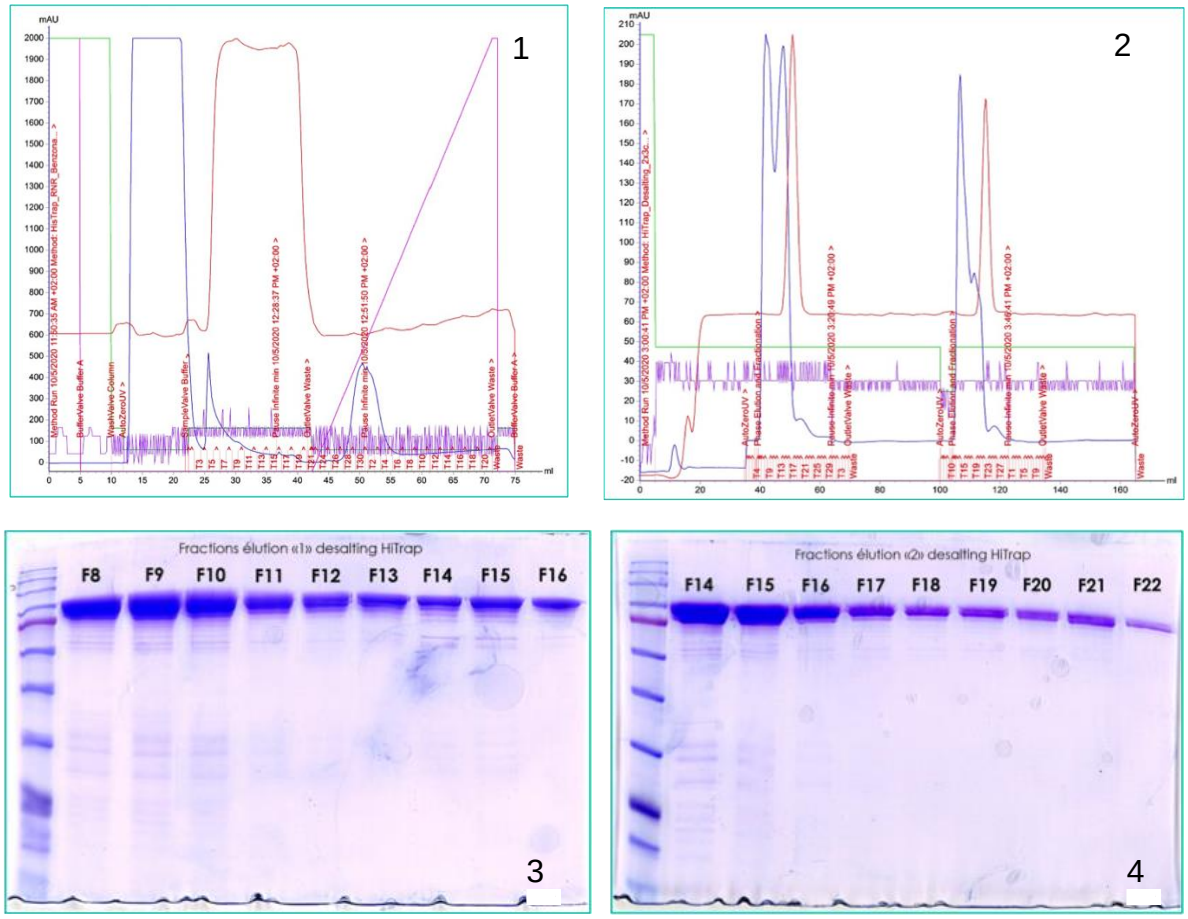

Figure 32: RNase R purification. 1) HisTrap chromatogram. 2) Desalting chromatogram. 3) and 4) SDS-PAGE gel of the fractions after buffer exchange through desalting columns.

2.3.2 PCR product for disome formation

For disomes stalling, we designed a DNA sequence using the first 60 nucleotides coming from the *E. coli* gene encoding for EF-Tu (*tufA*). The length of the transcript was chosen according to what has been reported in previous studies (Ingolia et al., 2019, Olson et al., 2020). We also added a Shine-Dalgarno sequence appropriately spaced from the start codon using of a 7 nucleotides spacer. The plasmid pUC19 was used for amplification and production and the insertion was performed between the restriction sites BamH I and Hind III. The entire construct was subsequently fabricated by GenScript Biotech. The plasmid carrying the sequence of interest was

subjected to PCR to amplify the insert. The PCR product was then purified and used for the formation of our complex, after being transcribed into the corresponding non-stop mRNA (non-stop mRNA_60) within the PURExpress® In Vitro Protein Synthesis Kit (NEB).

2.3.3 Macromolecular complexes formation

2.3.3.1 Stalled ribosome + RNase R

100 pmol of tRNA-Phe (See Guyomar, D'Urso et al., 2021 – Materials and Methods) were incubated 2 minutes at 80°C and then 30 minutes at room temperature to promote folding. Next, 50 pmol of Strep-Tagged ribosomes were stalled in the presence of 100 pmol of non-stop mRNA (See Guyomar, D'Urso et al., 2021 – Materials and Methodes) and 100 pmol of tRNA-Phe, previously folded, in Buffer III (HEPES-KOH 5mM, KCl 50mM, MgOAc 9mM, NH_4Cl 10mM, DTT 1mM, pH 7,5) and incubated 15 min at 37°C. Finally, the complex was made by adding 1 nmol of RNase R to the stalled ribosomes, adjusting the concentrations of Mg^{2+} and KCL accordingly. The complex was then incubated 10 min at 37°C. To eliminate the excess of unbound RNase R, the complex was passed on a StrepTrap HP column (1mL, Cytiva) (Figure 33, 1) previously equilibrated with Buffer III. The elution was performed using the same buffer supplemented with 2.5 mM d-Desthiobiotin. The fractions corresponding to the elution peak were concentrated on Amicon® 100 kDa. The concentrated sample was deposited on 12% SDS-PAGE gel to check for the presence of the ribosome-bound protein (Figure 33, 2). Having verified the formation of the complex, the same sample was used at a concentration of 120 nM to prepare cryo-EM grids.

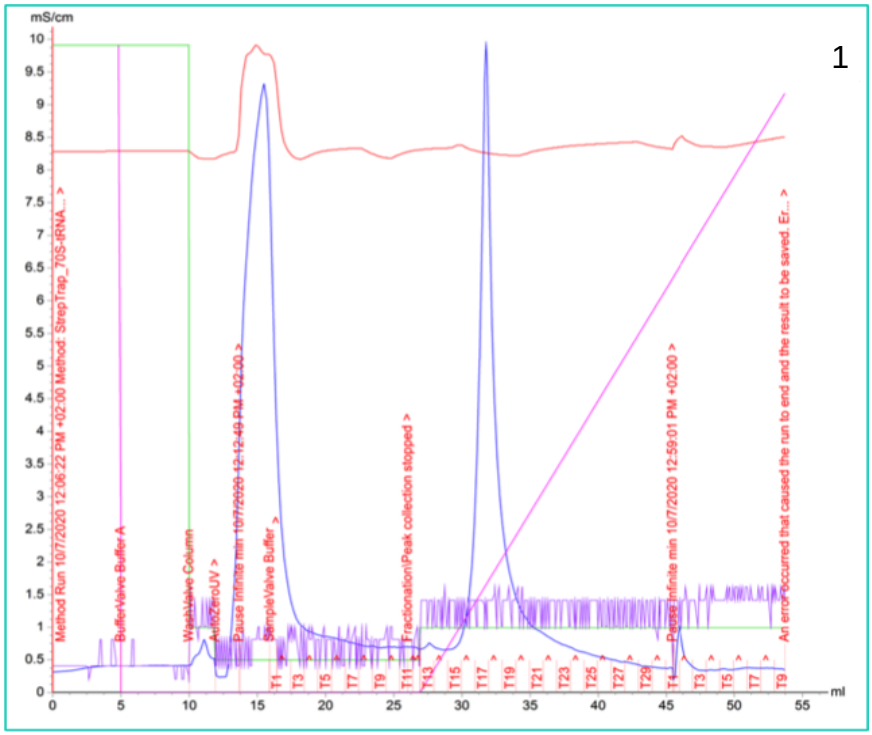

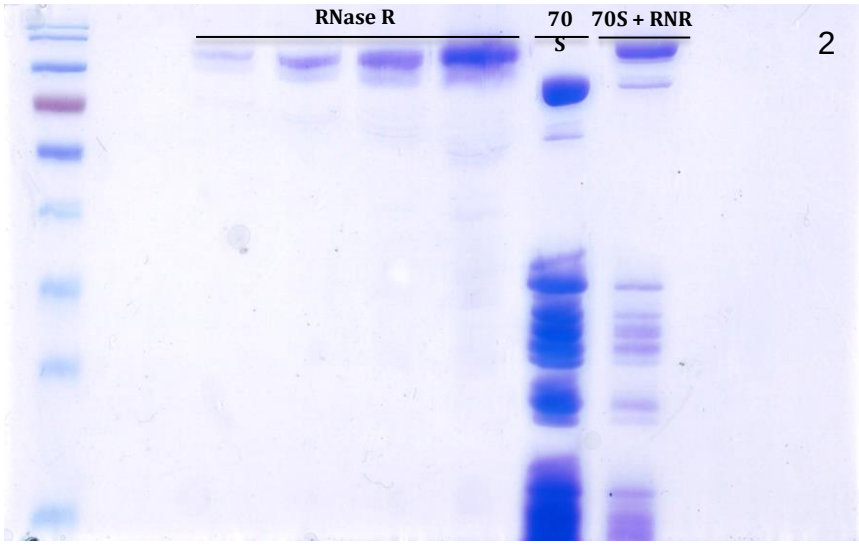

Figure 33: Stalled ribosome + RNase R purification. 1) StrepTrap Chromatogram. 2) SDS-PAGE gel used to control the presence of the RNase R on the ribosome after the purification of the complex. The first four tracks correspond to different RNase R concentrations; the fifth track corresponds to a ribosome; the sixth is for the complex.

2.3.3.2 Stalled ribosome + RNaseR + tmRNA-SmpB

After folding of 60 pmol of tRNA-Phe, 300 pmol of tmRNA were aminoacylated and incubated for 30 minutes at 37°C in the presence of 300 pmol of SmpB, 600 pmol of AlaRS, 30µM of alanine, and 2mM of ATP in buffer II (HEPES-KOH 62,5 mM, $MgCl_2$ 9mM, NH_4Cl 75 mM, pH 7,5). 60 pmol of ribosomes were then stalled as described above. At this point, the solution containing the blocked ribosomes was divided into two sets of 30 pmol each. 150 pmol of aminoacylated tmRNA-SmpB were added to

one set (Cplx I), while 300 pmol of RNase R were added to the other (Cplx II), to assess whether the order in which the elements are added affected the final complex. Both sets were incubated for 10 minutes at 37°C and, after, Cplx II was purified as previously described. At this point, the final complexes were formed. Cplx I was placed in the presence of 300 pmol of RNase R, while Cplx II was mixed with 150 pmol of tmRNA-SmpB. Once again the complexes were incubated for 10 minutes at 37°C. The complexes were then diluted at 120 nM for cryo-EM analysis.

2.3.3.3 Stalled disomes + tmRNA-SmpB

For the reconstitution of the stalled disomes we used the PURExpress® In Vitro Protein Synthesis Kit (NEB). We used a volume equal to 10 reactions, as reported by the manufacturer. Each reaction was supplemented with 2µL of PCR product and 2µL of mini anti-ssrA, the latter to block the activity of the tmRNA present within the reaction mixture. At this point, the reactions were incubated for 20 minutes at 37° C. The reactions were then deposited on a sucrose gradient 10%-40% prepared in Ribo_A Buffer (Tris-HCl 10mM, $MgCl_2$ 10mM, NH_4Cl 50mM, EDTA 0.5mM , DTT 1mM, pH 7,5), to purify the disomes from the rest of the elements present in the reaction. The reactions were centrifuged with the SW28 rotor at 22000 rpm for 16 hours at 4°C. The gradient was aliquoted in fractions of 500 µL and those corresponding to the disome peak were combined and concentrated on a sucrose cushion in Ribo_B Buffer (Tris-HCl 10mM, MgOAc 10mM, NH_4Cl 500mM, EDTA 0,5mM, Sucrose 1,1 M, DTT 1mM, pH 7,5). The disomes were centrifuged with the 70-Ti rotor at 30000 rpm 20 hours at 4°C. The supernatant was gently discarded and the pellet was resuspended for at least 6 hours in 30 µL of Buffer II. The disomes were dose and aliquoted. 100 pmol of tmRNA were aminoacylated in the presence of 100 pmol of SmpB, 200 pmol of AlaRS, 30µM of alanine, 2mM of ATP in buffer II (HEPES-KOH 62,5 mM, $MgCl_2$ 9mM, NH_4Cl 75 mM, pH 7,5) and incubated for 30 minutes at 37°C. The so-formed complex was then added to 10 pmol of disomes and incubated for 10 minutes at 37°C. In the end, disomes were diluted to 50 mM for cryo-EM analysis.

2.3.4 Cryo-EM grids preparation

After the preparation of the complexes from the various purified elements, these were directly deposited on grids and immediately frozen. For the monosome complexes, we used Quantifoil® R3.5/1 grids (Cu 200m), ionized for 30 seconds at 10mA with glow-discharge (Leica, EM ACE 600), while for disomes we used C-Flat® R4/2 grids (Cu 200m). The monosome samples were then frozen with the Vitrobot™ (Thermofisher Scientific), while disomes were vitrified with the automatic plunge freezer EM GP (Leica). In both cases, 2,5 µL of sample are deposited on the grid. After 20 seconds of contact, the excess of volume was blotted for 3.5 seconds, using two paper discs (Vitrobot™), in the case of monosomes and for 2 seconds using one paper disc, in the case of disomes. The temperature of the ethane (around -180°C) and the cooling speed (-3000°C/second) prevent the formation of crystalline ice so that the sample is trapped in a thin amorphous ice layer. The temperature of the plunge freezer systems chamber was maintained at 22°C in the presence of a saturated atmosphere with 100% humidity, in order to avoid any evaporation of the sample, which could induce changes in the concentration of particles and salts in the suspension medium.

2.3.5 Image acquisition with Tecnai G2 Sphera

The screening of the samples was done with our in-house Tecnai G2 Sphera microscope (MRic-TEM platform, Rennes) with a LaB6 electron source accelerated to 200 kV. The Grids were placed on a Simple Origin Model 205 Grid Cryo Transfer holder and images were acquired with a TVIPS TemCam-XF416(ES) camera characterized by a pixel size of 1,72 Å and an image size of 4096x4096 pixels. Four images were taken for each hole with a defocus range from -2.6 µm to -3.4 µm. Disomes images were binned 2x to speed up the calculations during the treatment.

2.3.6 Image acquisition with Titan Krios

Only the complex formed by the stalled ribosome + RNase R underwent high-resolution acquisition at the EMBL Imagin Center in Heidelberg. Images were acquired with a Titan Krios G3 300 kV equipped with a X-FEG electron source, a SelectriX energy filter, a Gatan Quantum K3 direct electron detector camera, Volta phase plate and the SerialEM software for automated data acquisition. The image pixel size was 0.822 Å with a defocus range between -0.75 µm and -1.5 µm and a

total dose of 33.48 e/Å. The movies acquired on the Tecnai G2 Sphera and on the Titan Krios were then treated in the same way as explained in the following section 2.4.3.

2.4 Results and discussion

2.4.1 Low-resolution analysis of "Stalled ribosome + RNase R" complex

To characterize the third major player involved in *trans*-translation, *i.e*., RNase R, we first sought to investigate its ability to recognize and bind ribosomes stalled on non-stop mRNAs. After the *in vitro* complex formation, (see section 2.3 Materials and methods) and before observing the sample with cryo-EM, we first sought to biochemically verify that the RNase R binds to the ribosomes. The complex was purified through chromatography by taking advantage of the presence of the streptavidin tag on ribosomes. The fractions corresponding to the elution peak were then pooled and deposited on gel where it was possible to ascertain the presence of both the ribosomes and RNase R (Fig 33). Having ascertained the ability of RNase R to recognize and bind a stalled ribosome, we then moved on to low-resolution characterization of this complex by cryo-EM.

494 movies were acquired with our local microscope (see section 2.3.5) and were imported into cryoSPARC and immediately subjected to motion correction and CTF estimation. 62.269 particles were extracted from the movies and then organized into 250 classes through 2D Classification. About 10.000 particles corresponding to the best classes were selected and used to obtain a first *ab initio* density map. To slightly improve the resolution, the *ab initio* density map was finally subjected to a round of refinement, resulting in a final map with a 12.59 Å resolution.

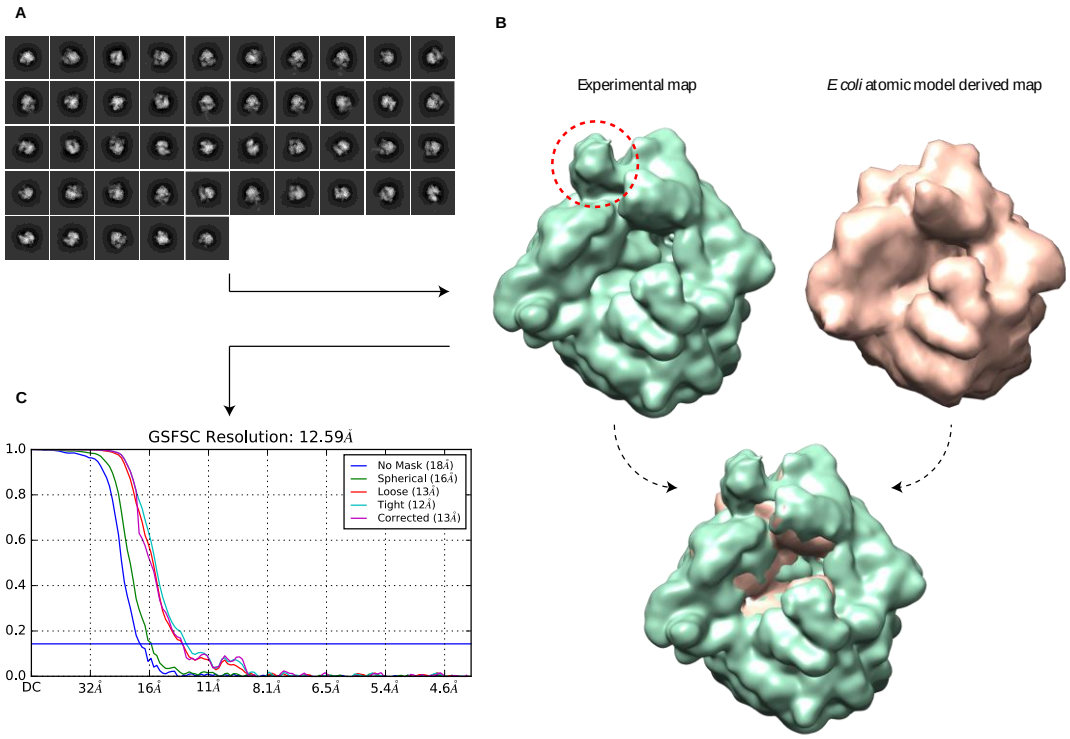

Figure 34: cryoSPARC image analysis of the "Stalled ribosome + RNase R" complex after low-resolution acquisition. A) 2D classification after particles extraction. B) Comparison between the model coming from 2D classes and a classical E. coli 70S. C) GSFSC resolution plot of the map generated in cryoSPARC

The comparison of this preliminary map with the density map of an *E. coli* ribosome, obtained in the same condition, brought out the presence of a protuberance straddling the head and the body of the small subunit near the uS3, uS4 and uS5 proteins, where the mRNA entry channel is localized, as reported in previous studies (Malecki et al., 2014; Venaktaraman et al., 2014). As the presence of RNase R anchored to the stalled ribosomes was confirmed by SD PAGE, we concluded that the observed protuberance was the RNAse R. Although the result was at a rather low resolution, it was sufficient to note that the RNase R binds the ribosome on the same region as the tmRNA's helix H5 and PK2 pseudoknot during the *trans*-translation process (see Guyomar, D'Urso et al., 2021).

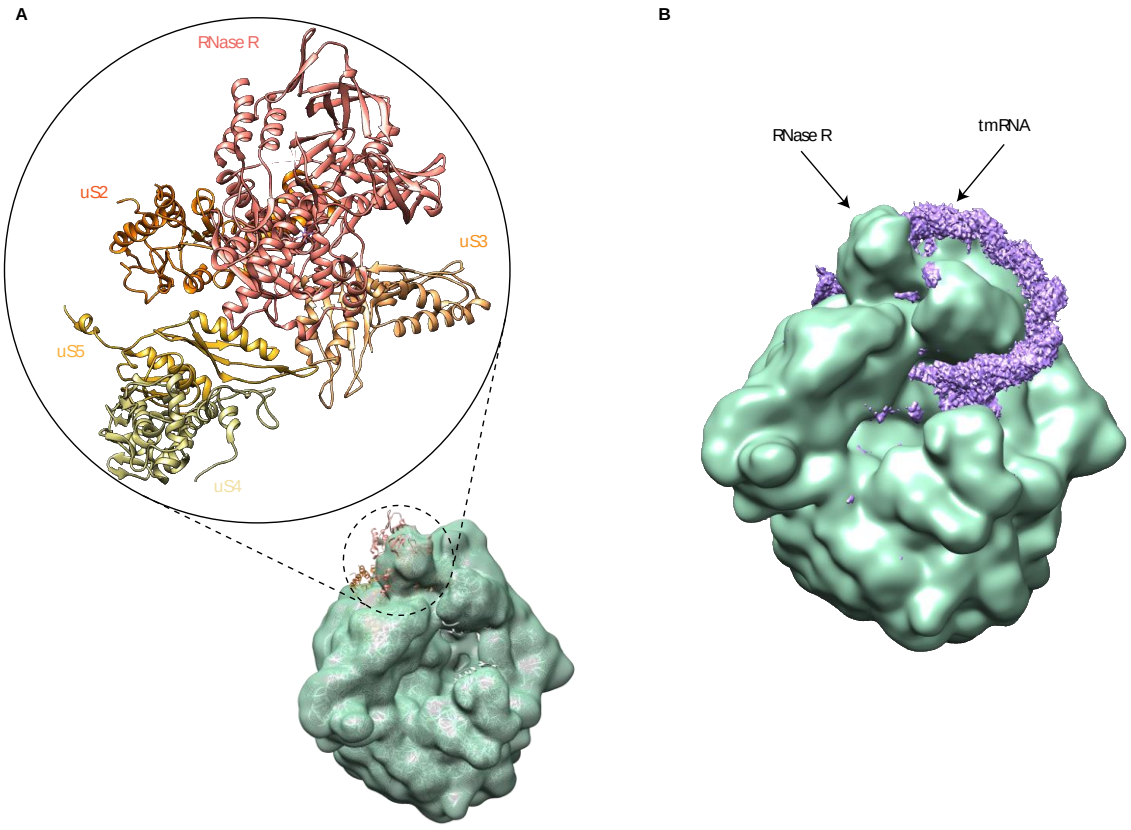

Figure 35: Analysis of the "Stalled ribosome + RNase R" low-resolution density map. A) Focus on the proteins flanking the binding area of the RNase R. The RNase R is salmon, uS2 is orange, uS3 is gold, uS4 is khaki, uS5 is gold. B) Comparison between our density map with the RNase R and the tmRNA density. The Rnase R and the H5 and PK2 domain of the tmRNA bind to the same area of the ribosome.

That result suggests that a sharp competition could exist between RNase R and the tmRNA-SmpB complex to bind a stalled ribosome in the course of *trans*-translation, in contrast to what was shown by Richards et al. and Venkaktraman et al. in which they showed, in a different way, that the recruitment of the RNase R depends on the activity of tmRNA-SmpB complex or SmpB alone (Richards et al., 2006; Venaktaraman et al., 2014). Since the two main players bind the small subunit on the same zone, straddling the mRNA entry channel, the fact that they could arrive together and coexist on a stalled ribosome (Karzai and Sauer, 2001; Liang and Deutscher, 2010), is quite questionable and needs to be proven.

Given the absence of tmRNA-SmpB complex on this map, it is important to remember that RNase R has many other activities within the cells. For example, it is involved in 16S rRNA maturation (Deutscher, 2009; Purusharth et al., 2007) as well as in the removal of defective and unmatured 70S ribosomes. By associating with the

endonuclease YbeY, RNase R degrades these ribosomes, alone or within a polysome (Jacob et al., 2013). Therefore, at this stage, we cannot exclude that what we observed was related to these activities and not to *trans*-translation.
To answer these questions and to see if indeed what previous studies have suggested can be confirmed, we continued our investigation by trying to understand the behavior of RNase R in the presence of the tmRNA-SmpB complex on a stalled ribosome.

2.4.2 Low-resolution analysis of "Stalled ribosome + RNase R + tmRNA-SmpB" complex

Taking into account the preliminary results obtained from the observation of the first complex, the next step was to investigate the behavior of the protein simultaneously with tmRNA and SmpB. Since we hypothesize a spatial competition between the tmRNA-SmpB complex and RNase R, we first investigated the possibility of temporal regulation for the whole system. To do so, two complexes were made in which the addition of RNase R and tmRNA-SmpB occurred alternatively (see 2.3.3.2 Stalled ribosome + RNase R + tmRNA-SmpB). Starting with a stalled ribosome, the reaction was split into two. On one side we added RNase R (Cplx I), while on the other side we added tmRNA-SmpB suitably aminoacylated (Cplx II). At this point, part of both samples was observed in cryo-EM to make sure that the complex was formed.

We then added tmRNA-SmpB to the first complex (Cplx I) and RNAse R to the second complex (Cplx II). As before, the two complexes were analyzed by cryo-EM. For Cplx I, from the 592 movies acquired, 53.746 particles were used to reconstruct the final map while, for Cplx II, from the 690 movies acquired, 62.231 particles were used for the final reconstruction. From the comparison of the two final complexes, it can be observed that in both cases the mass corresponding to RNase R is absent, while the density corresponding to the tmRNA-SmpB complex can be easily recognized (Figure 36). Based on what we have seen, in Cplx I the addition of tmRNA and SmpB induced a displacement of the previously bound RNase R that was well anchored to the ribosome, whereas, in the second case (Cplx II), the presence of tmRNA prevent the interaction of the RNase R with the ribosome. This clearly shows that both actors bind the 30S surface near the mRNA entry channel but

tmRNA-SmpB affinity is much stronger to the point that it can eject the RNase R from its binding site.

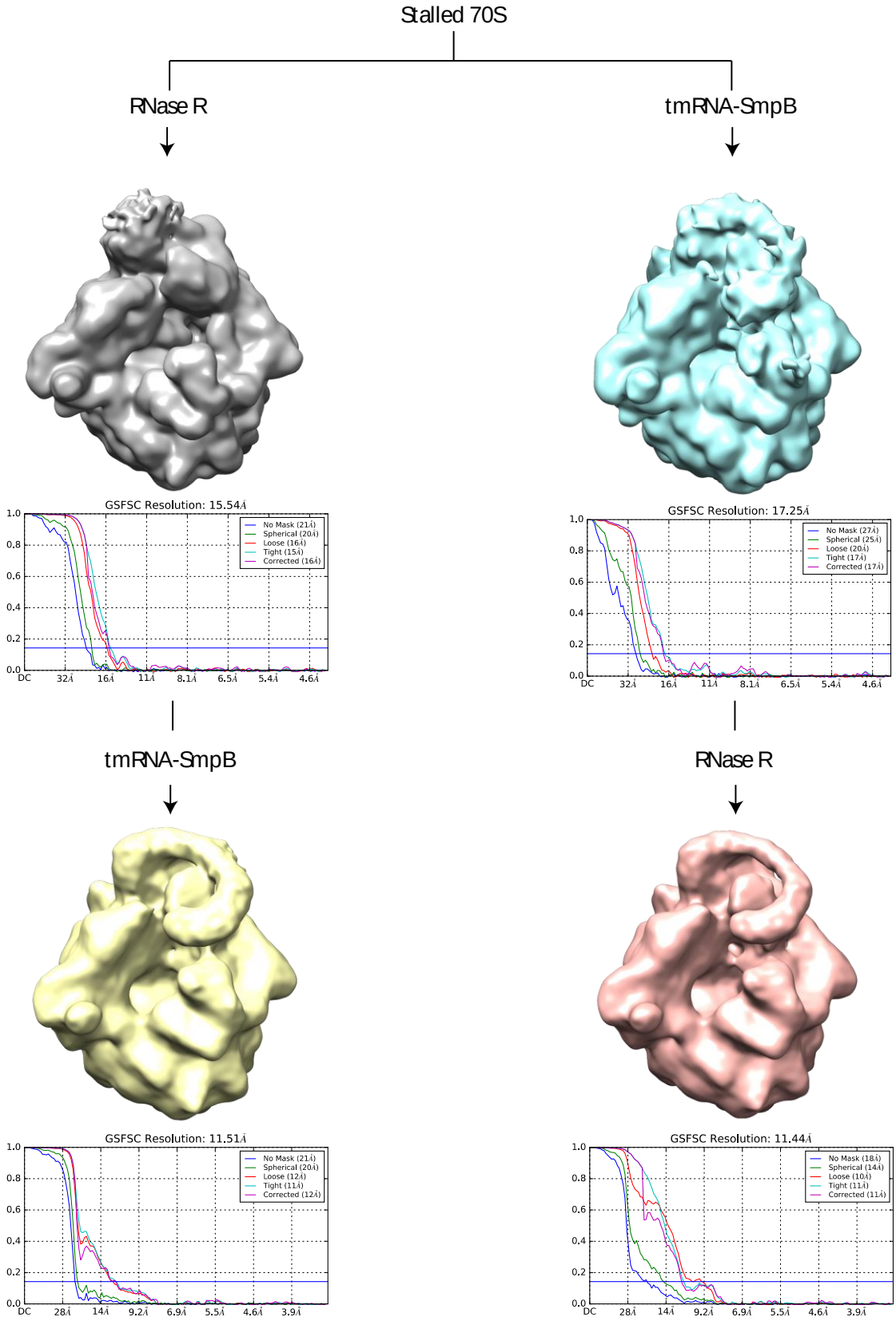

Figure 36: Schematic representation of the low-resolution study of RNase R and tmRNA-SmpB binding to a stalled ribosome. Each density map present the the GSFSC

In particular, in presence of the tmRNA-SmpB complex, the position normally occupied by the RNase R is now occupied by helix H5 and PK2. As suggested by Venkataraman and colleagues (2014), the H5 helix of the tmRNA would cause conformational changes in the small 30S subunit required for RNase R recruitment. Thus, it is reasonable to assume that RNase R occupies a different position on the ribosome surface when it interacts in the context of *trans*-translation. Furthermore, it was also described that the length and position of the ORF of the tmRNA plays a crucial role in the recruitment of the RNase R during *trans*-translation (Venkataraman et al., 2014), suggesting that it would bind nearby. In particular, mutation of the last two adenine codons (which are in the H5 helix) of the tmRNA tagging sequence into two aspartic acids is sufficient to disrupt the recruitment of RNase R on the *trans*-translating ribosome. We first hypothesized that a binding site could be slightly above EF-Tu, directly in contact with the MLD, close to the A-Site uS12 protein. This protein has been described to interact with the RNase R via the highly conserved Asp88 (Strader et al., 2013). The RNase R would then be located near the 3' end of the mRNA, which is consistent with its 3' - 5' exoribonuclease activity. However, no other extra density appears to be present in our map. In addition, the access to the 3' end of mRNA from this area would be highly complex (if not impossible) given the presence of tmRNA and the subsequent expulsion of the same mRNA by SmpB. On this basis, the only hypothesis that we could formulate is that both RNase R and tmRNA-SmpB arrive simultaneously during *trans*-translation, carrying out their activity on two separate but consecutive ribosomes, stalled on the same non-stop mRNA. To test this hypothesis, the next step was to study RNase R, tmRNA, and SmpB on a more complex system, formed by two ribosomes stalled on the same non-stop mRNA. On the other hand, we also decided to conduct a high-resolution study of the "Stalled ribosome + RNase R" complex to describe for the first time the molecular interactions that take place between these two partners.

2.4.3 High-resolution analysis of the “Stalled ribosome + RNase R“ complex

The high-resolution study was conducted on a Titan Krios G3 microscope at the EMBL Imaging Center in Heidelberg. The 48-hour acquisition time allowed us to obtain 22.810 movies with a pixel size of 0.822 Å. The image analysis was conducted with cryoSPARC (v2.15.0) and RELION (3.1-beta-commit). Movies were imported into cryoSPARC where they were first subjected to Motion correction and CTF estimation. After the pretreatment, 881.222 particles were extracted and subjected to two rounds of 2D classification. At this point, 802.832 particles were selected and used to obtain a first preliminary 3D density map with a resolution of 2.67 Å.

From this point on, all subsequent steps were carried out in RELION. The preliminary *ab initio* model was used to generate a first density map immediately subjected to 3D classification to separate the dataset into different conformations assumed by the ribosome and eliminate those junk particles still present. From the 10 classes generated, 529.307 particles were selected, representing a somewhat stable ribosome with albeit some mobility at the level of the small subunit head. At this point, a mask around the small subunit was created in such a way as to focus our attention increasingly on the density relative to RNase R, which turns out to be highly dynamic and not very well defined as a result of its high flexibility. Thanks to the mask, we subtracted much of the ribosome-related signal, and the remaining signal was organized into 10 classes once again. 4 classes containing 376.655 particles were selected on the basis of the presence of the tRNA within the P site, which is essential for the stabilization of the entire complex. However, the signal related to RNase R was still highly blurred and not well defined. Similarly, a smaller mask was created only around the protein of interest, subtracting the remaining part of the small subunit. From the 5 classes obtained, none of them turned out to be defined to such an extent that elements of secondary structure can be observed.

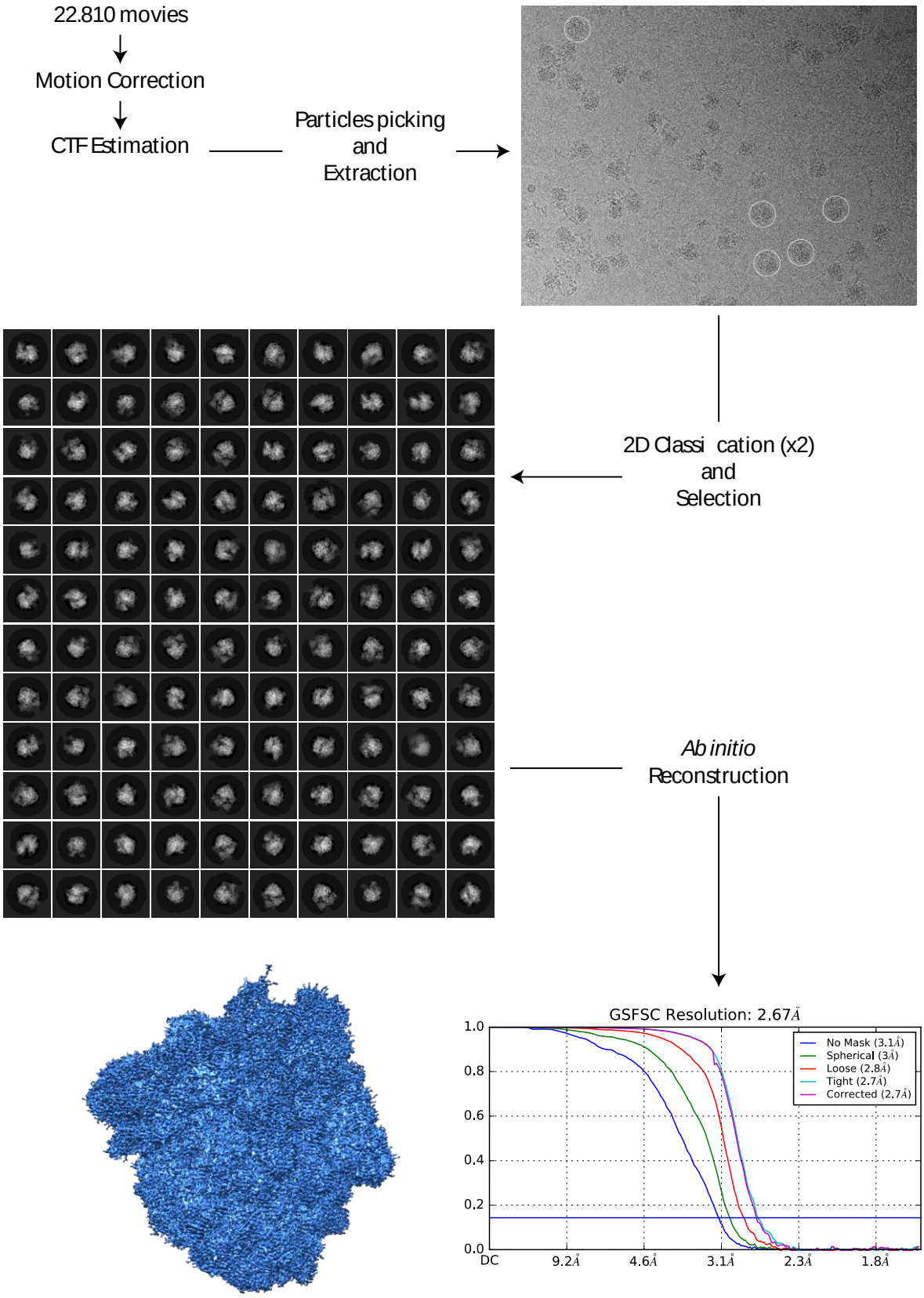

Figure 37: Schematic representation of the high-resolution study of the "Stalled ribosome + RNase R" complex in cryoSPARC including the particle picking, the 2D classification and the final map with its GSFSC resolution plot.

Since we thought that the problem could be due to the relatively small contribution of the RNase R to the signal (with respect to the ribosome) even when performing 3D classification with signal substraction, we tried to focus only on the protein, but using a 2D classification. Starting from the electron density map obtained after the second round of 3D classification, we created a spherical mask with a diameter of 100 Å centered on the RNase, to only consider the signal inside it. After properly centering all the images on the newly created mask, we performed a 2D classification with alignment on the remaining RNase R signal both in RELION and in cryoSPARC. In both cases, the classification was performed two times keeping 273.860 particles in RELION and 123.130 particles in cryoSPARC. The selected particles were then used to generate an electron density map. In both cases, unfortunately, we were unable to obtain enough information (15.37 Å RELION, 5.12 Å cryoSPARC) to reconstruct a model for the RNase R and produce a molecular description of the contacts occurring during the interaction with the ribosome. The protein appears to be highly dynamic although well anchored to the ribosome. This dynamism may be an intrinsic property of the RNase R since the N- (Helix-Turn-Helix) and C-terminal (K-rich) domains (Figure 30 A) were not resolved into crystallographic structure (Chu et al., 2017). However, other studies suggest instead that this dynamism derives essentially from the weakness of the interactions with the ribosome (Malecki et al., 2014), in particular if we consider that the protein could be stabilized by binding an RNA strand.

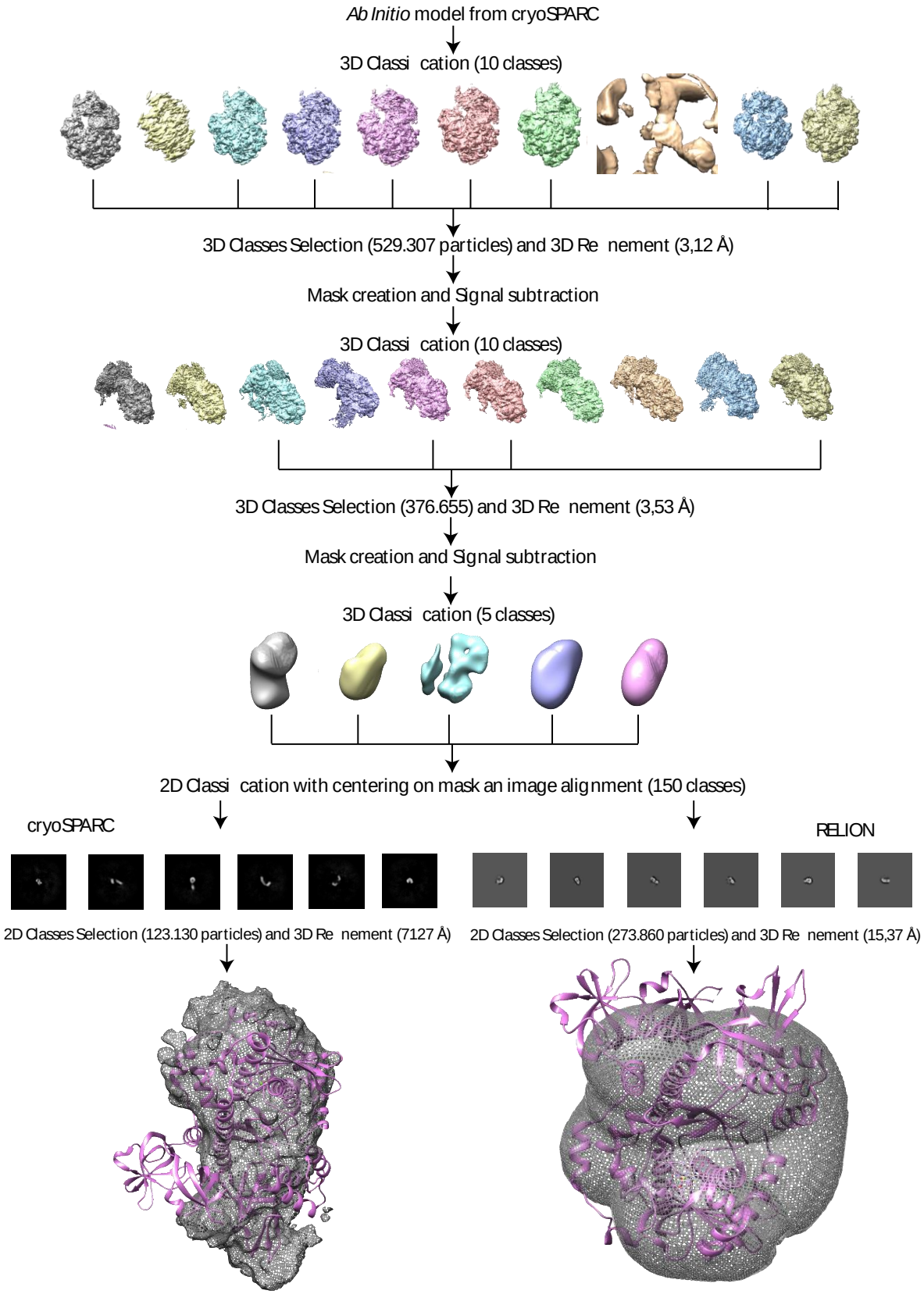

Figure 38: Schematic representation of the high-resolution study of the "Stalled ribosome + RNase R" complex in RELION. Here we report the several 3D classifications with signal subraction and, in the end, the maps of the RNase R obtained after 2D reclassification in cryoSPARC and RELION.

In our study, the presence of the stalled ribosome-bound RNase R was confirmed both biochemically and structurally. If the protein had presented a very weak interaction, much of it would have disappeared during the passage of the complex on a chromatographic column, thus making it impossible to ascertain its presence on either SDS-PAGE gel or cryo-EM grid. The very poorly defined signal and the difficulties found during the electron density map reconstruction can thus be explained by the dinamicity of the protein at the surface of the ribosome and by its intrinsic flexibility, especially for the domains located at the extremity of the sequence (Figure 30 B). Indeed, if one of these two domains were the element in interaction with the ribosome, the central body of the protein could assume different conformations, by hovering just above the 30S surface. This will give rise to a lot of heterogeneity that will be very hard to account in structural studies. However, we do not want to say that this protein cannot be studied from a structural point of view, as atomic models have been reconstructed of many other highly dynamic factors. In this case, we are only at the beginning of the characterization of the RNase R in cryo-EM, and many other tests are in the pipeline. A possible solution to this problem might be to use an mRNA that is sufficiently long to protrude from the entry channel. In this case, the binding of the mRNA may help to anchor the protein and limit its conformational space at the surface of the SSU. Another solution might be implemented during sample preparation, before grid preparation, by increasing the concentration of cross-linking agents such as glutaraldehyde. The risk, in this case, would be to induce the formation of non-specific interactions between the RNase R and the ribosome. In any case, the team currently tests various strategies in order to obtain soon a first description of RNase R during its interaction with a stalled ribosome.

2.4.4 Low-resolution study of the “Stalled disomes + tmRNA-SmpB“ complex

During protein synthesis, a single mRNA molecule can be translated by several ribosomes at the same time, each producing a single copy of the protein encoded by that transcript. In this way, several ribosomes are attached to a single mRNA molecule, forming a characteristic "pearl necklace" called polyribosomes or polysomes. As for canonical translation, we can imagine that a similar situation arises

during *trans*-translation when several ribosomes are translating the same non-stop mRNA molecule. When the first ribosome stalled at the 3' end of the messenger it jams all the others, which finish by colliding into each other (at least in the absence of rescue machinery). In this scenario, the first ribosome would present an empty A-site and a P-site tRNA carrying the nascent polypeptide chain, while the following translating ribosomes (with occupied A, P and E site) will collide on it. Considering that RNase R and the tmRNA are competing for the same binding site, and that no additional interactions were observed between tmRNA and other elements of the *trans*-translating ribosome (ie bS1), one can wonder if the RNase R could be present the second stalled (collided) ribosome. To get a more exhaustive description of the *trans*-translation process on one hand, and try to answer this question on the other hand, we decided to study *trans*-translation on a more complex system based on two ribosomes stalled on the same non-stop mRNA molecule, commonly called disomes.

The first step of this study was to design a non-stop mRNA molecule long enough to accommodate two ribosomes at the same time. While on one hand this transcript had to be longer than the one needed for a single ribosome, on the other hand the length had to be such that three or more ribosomes could be bound, in order to promote the formation of disome (by forbidding the formation of more complex structures such as trisomes or polysomes) and make the image analysis easier by limiting the diversity of the sample. We thought that this would probably help for the study of *trans*-translation partners by making the system as simple as possible and reducing the number of potential targets for the protein.

Based on ribosome profiling studies, focused on sequencing of short mRNA fragments physically enclosed by the ribosome and shielded from nuclease digestion, we determined that the ideal length of our transcript had to be around 60 nucleotides (Guydosh and Green, 2014; Lareau et al., 2014; Matsuo et al., 2017; Ingolia et al., 2019, Olson et al., 2020). In particular, we chose the first 60 nucleotides of the *tufA* gene that encodes for *E. coli* EF-Tu, one of the proteins most commonly found within the bacterial cell. The sequence was then appropriately complemented at the 5' end with the promoter sequence for the T7 polymerase, followed by a Shine-Dalgarno sequence and a 7-base spacer upstream the start codon.

A

>ref|NC_000913.3|:c3471506-3469966 Escherichia coli str. K-12 substr. MG1655,complete genome

GTGTCTAAAGAAAAATTTGAACGTACAAAACCGCACGTTAACGTTGGTACTATCGGCCA (60 bases)

B

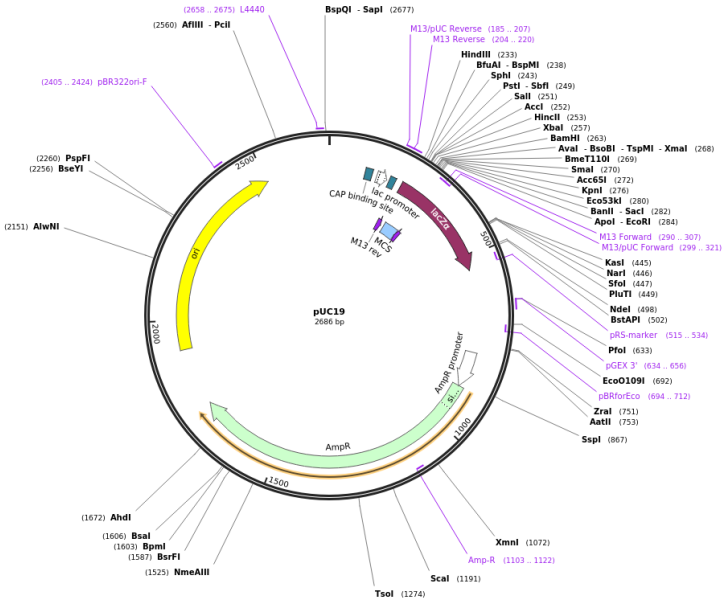

C

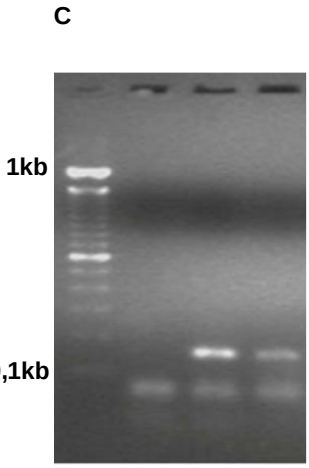

Figure 39: Production of the non-stop mRNA for disomes. A) The first 60 nucleotides used for the mRNA production coming from the EF-Tu gene. In red the starting codon B) The vector in which we inserted our sequence. C) The PCR product purified used for the mRNA production.

Next, the sequence was inserted within the pUC19 vector for the storage and the subsequent PCR product production. The stalled disomes were then produced using the PURExpress kit containing all the factors needed for the transcription of the PCR product and the subsequent stalling. In addition, the reaction mixture was supplemented with a RNA molecule (mini-anti ssrA) complementary to the MLD portion of the tmRNA, to block the tmRNA present in the kit.

Using a 10-40% sucrose gradient, the disomes were separated from the remaining ribosome species present within the reaction, as well as from smaller molecules. In particular, we observed that two types of disomes came out: the first type where two ribosomes lay on the same mRNA strand spaced from each other, the second type where the two ribosomes were collided with each other (Fig. 40, 2). These two species were quite distinct within the gradient, with the first migrating less than the latter. This may be due to the fact that, given the distance between the two ribosomes for the first type, they might move independently, resulting in their density

to be intermediate between that of a single ribosome and that of two collided ribosomes.

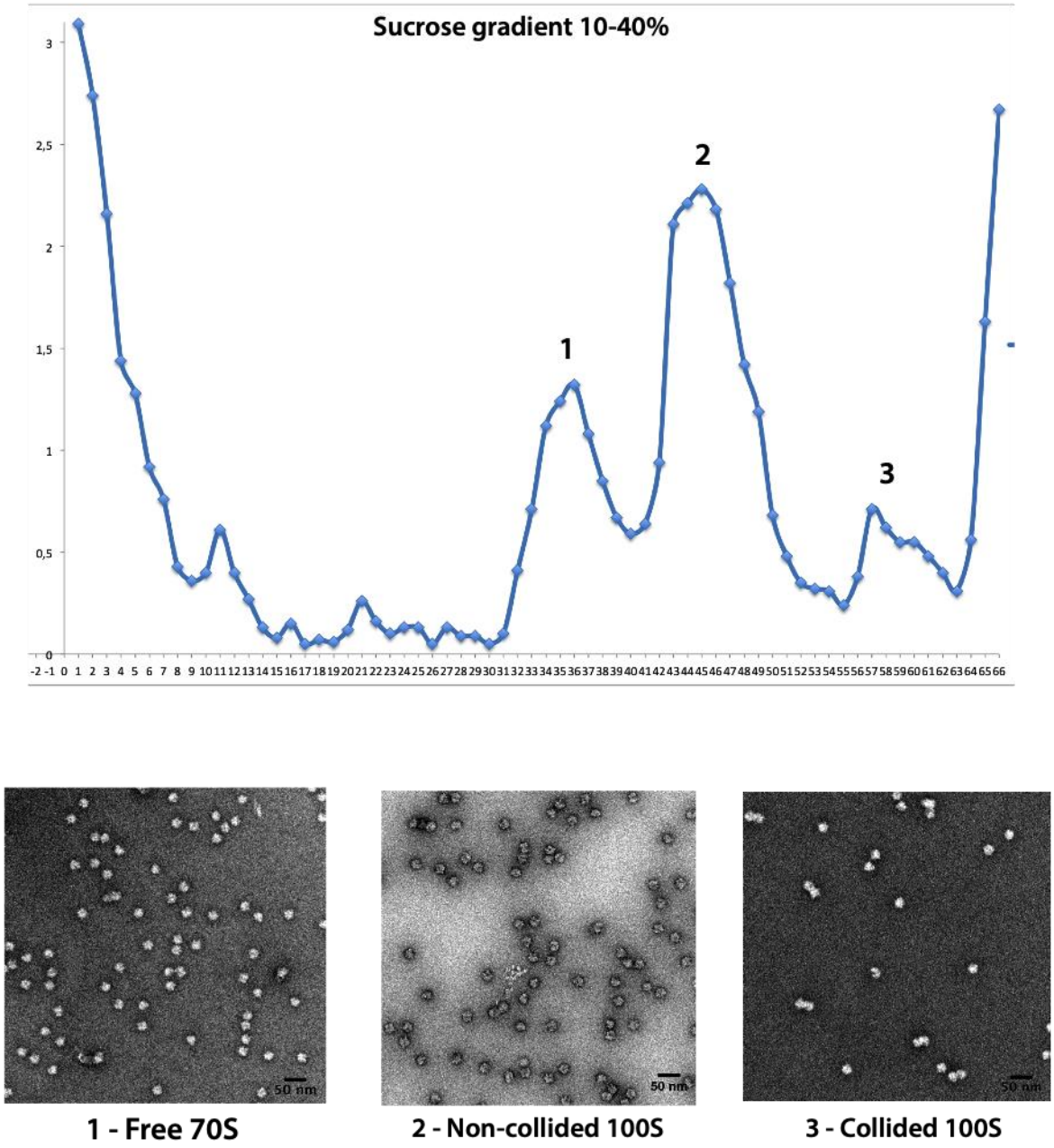

Figure 40: The sucrose gradient profile used for disomes purification. For the three identified peacks the characterization of the sample using negative staining EM is also shown.

As a consequence, the first type disomes are positioned on the 10-40% sucrose gradient exactly between free ribosomes and collided disomes. As the non-collided disomes were not useful to our study, we used the collided one in the following steps of our experiment. After the fractions of interest were picked and concentrated on sucrose cushion, the sample was re-suspended to the volume suitable for complex formation. At this stage we added tmRNA-SmpB (see 2.3 Materials and Methods). The reaction was finally diluted to the proper concentration for grids preparation.

2.4.4.1 Data processing and results of *E. coli* disomes during *trans*-translation

2.5µL of the sample at 100 µM were applied on C-flat 4/2 200 mesh holy carbon grids and immediately vitrified in liquid ethane using a Vitrobot Mark III with a blotting time of 2 s. 1881 movies were collected using our in-house microscope by binning the pixel size at 3.444 Å (Figure 41). In this case movies were binned to speed up the calculation during the image analysis. Indeed, such astuteness allows us to use a box size of less than 520 pixels without impacting the quality of the reconstruction, as we are only interested, at this stage, in observing whether the theorized complex was successfully assembled. Particles were at first manually picked by centering the box in between the two ribosomal particles. Then, the extracted particles were used as a template for the automated picking in cryoSPARC. Several rounds of 2D classification allowed us to only select classes belonging to disomes, leaving behind anything that corresponds to isolated ribosomes (which may result from the separation of a ribosome from the non-stop mRNA during the purification process) (Figure 41).

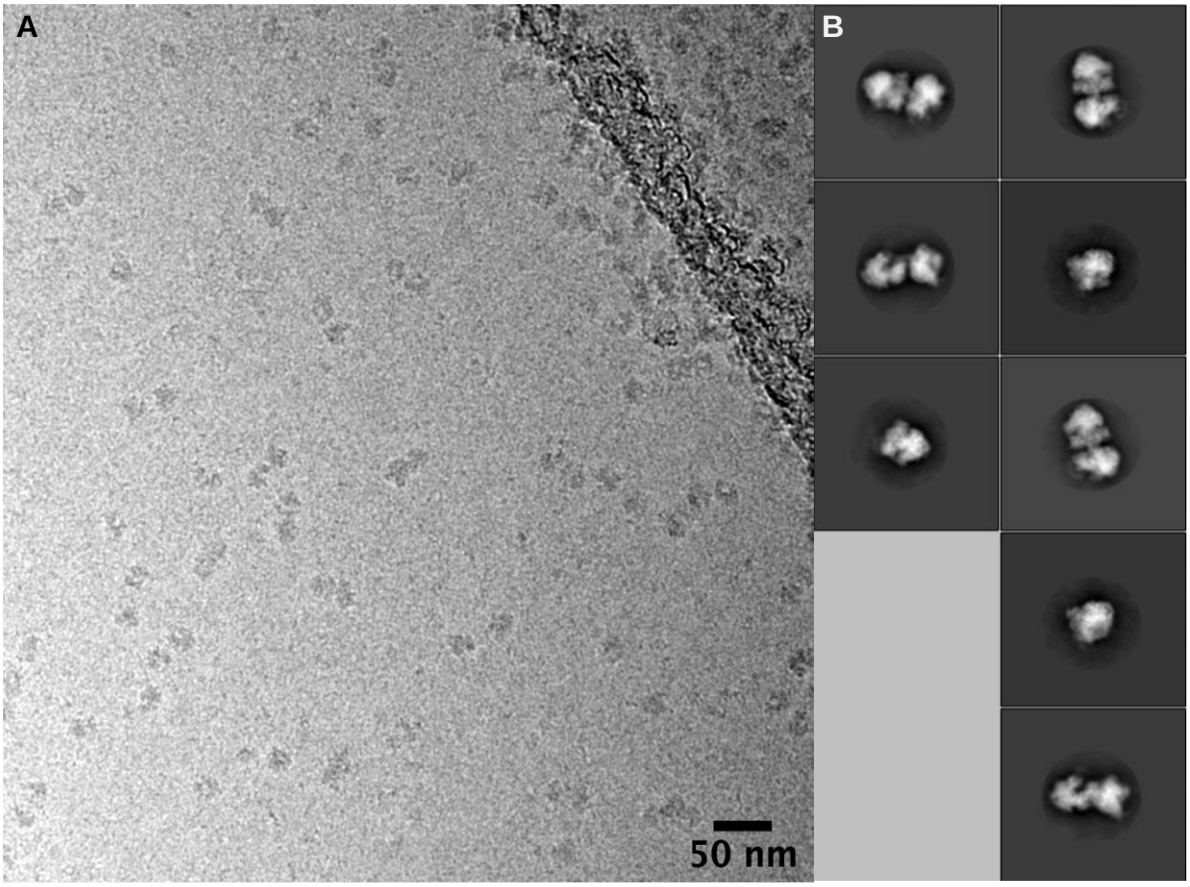

Figure 41: Example of the disomes observed A) Movie acquired with our in-house cryo microscope. B) 2D classes selected for the reconstruction.

20836 particles were used for an *ab-initio* reconstruction, generating 3 different models to split the dataset in different classes corresponding to trash particles, collided empty disomes and *trans*-translating collided disomes. At the end, we selected the reconstruction for the *trans*-translating collided disomes, which corresponded to 7072 particles. Next, we refined the map. The selected refined volume, representing our final model, had a final resolution of 17.22 Å (Figure 42).

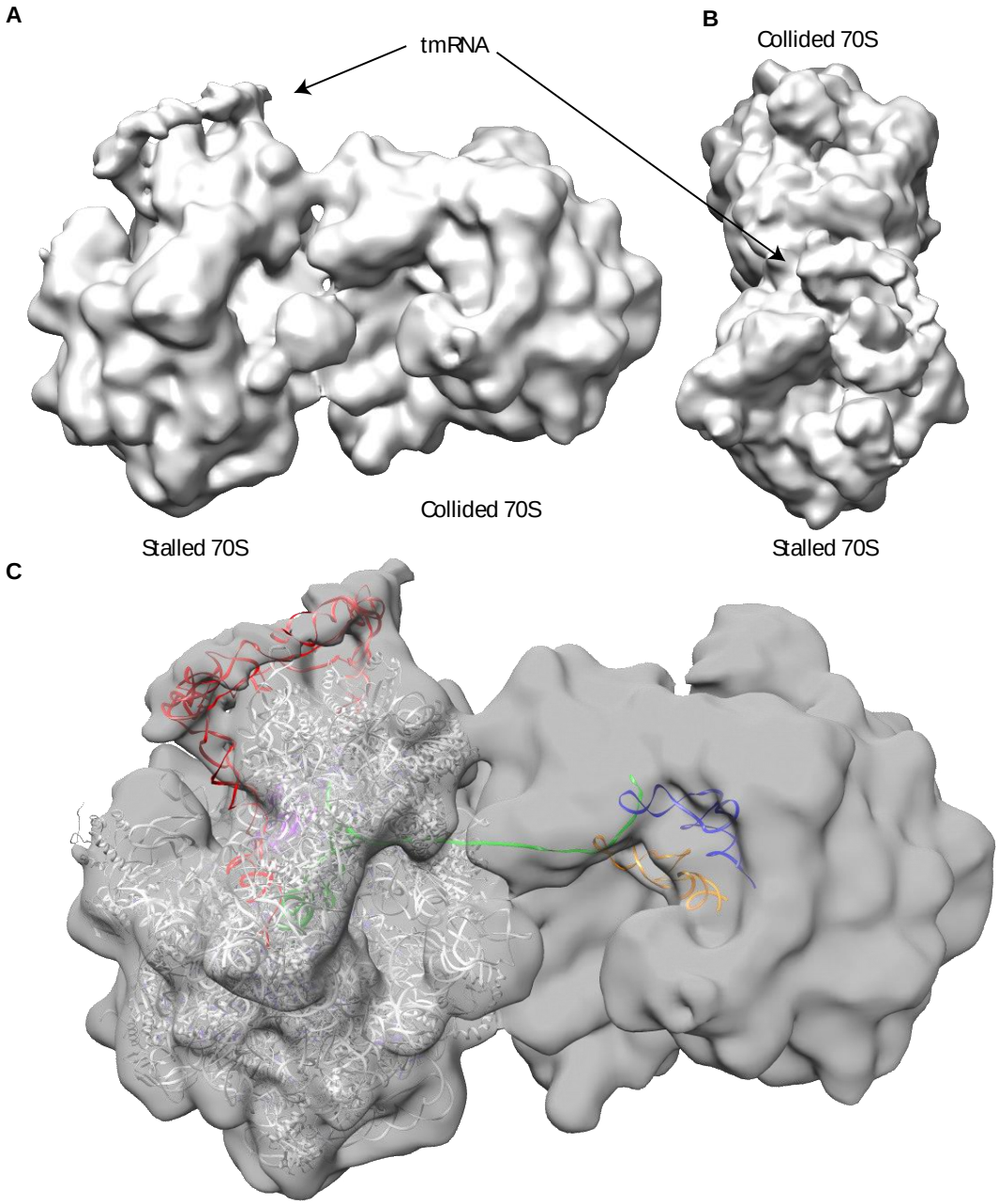

Figure 42: 3D density map of our trans-translating disome in complex with tmRNA and SmpB. A) Side view of the density map. B) Top view of the density map. C) Atomic model of the trans-translated ribosome (Guyomar, D'Urso et al., 2021; PDB: 7AC7) fitted within the trans-translating 70S and A -, P- site tRNA and mRNA fitted within the collided 70S coming (Saito et al., 2022; PDB: 7QG8). The stalled ribosome is white, the tmRNA is red, the SmpB is purple, the A-site tRNA is orange, the P-site tRNA is blue, and the mRNA is green.

From the resulting 3D reconstruction we can see the presence of the tmRNA-SmpB complex within the A site of the stalled ribosome. To perform its function on a stalled ribosome, the tmRNA-SmpB complex needs an empty A-site, free from any potential

mRNA portion. This confirms that, during disome formation, the stalled ribosome has effectively reached the end of the non-stop mRNA. The collided ribosome is rotated with respect to the stalled one, and the two SSU are making extensive contact with each other (Figure 42 A, B). By comparing our map with the structures of isolated ribosomes undergoing *trans*-translation (Guyomar, D'Urso et al., 2021; PDB: 7AC7), we conclude saying that the conformation assumed by the tmRNA corresponds to the accommodation state, with the TLD portion fully inserted into the A site, the peptidyl-tRNA in the P site and the MLD portion still folded within the ring of pseudoknots (Figure 42 C). On the other hand, the collided ribosome shows two tRNAs, one in the A site and the other in the P site, confirming that both ribosomes were translating the information contained into the non-stop mRNA. The conformation of the disomes we are looking at does not correspond to any form of hibernation.

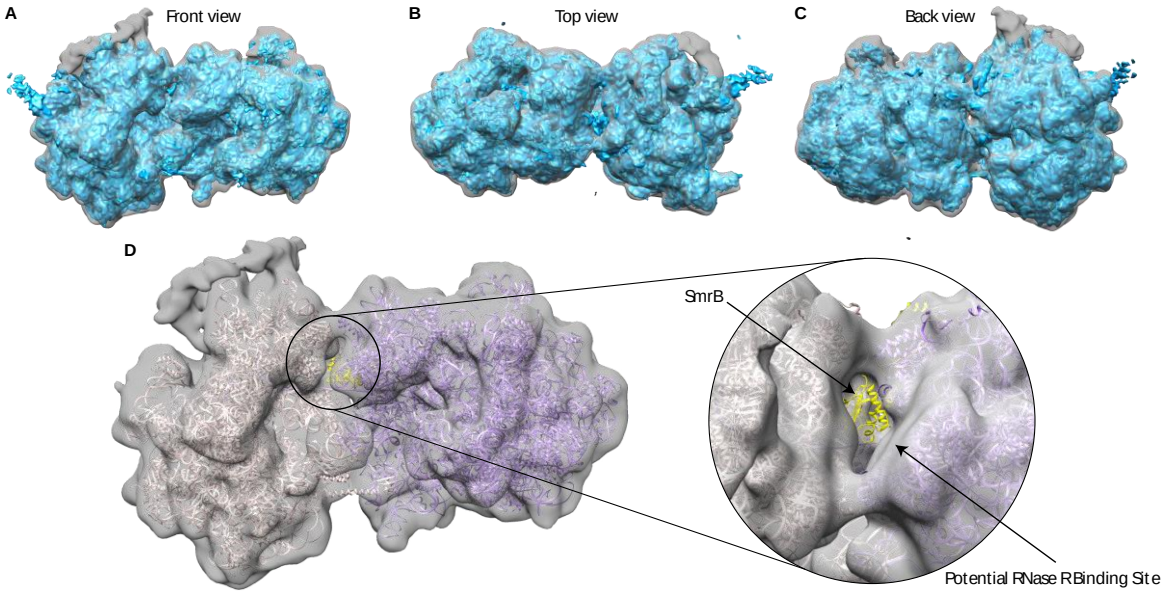

Figure 43: Comparison between our data and other stalled ribosomes. A) Front view, B) top view and C) back views of the superposition between our map (grey) and the map of an E Coli Disome stalled on the arrest peptide VemPl of stalled (pink) and collided (purple) ribosomes from Saito et al. fitted in our density map (grey). In yellow the atomic model of the SmrB rescue factor that cleaves mRNA upstream of the stalled ribosome (Saito et al., 2022; PDB: 7QGN, 7QG8).

The experimental data we obtained were likewise compared with those derived from a recent work by Saito and co-workers (Saito et al., 2022) in which they shed light on the activity of the SmrB factor, implicated in the detection and rescue of ribosome

collision following the stalling on arrest peptide. As clearly visible on the superposition of our and their map (Figure 43 A, B and C), the two structures appear to be nearly identical. This shows that there are no structural differences between collided disomes obtained from non-stop mRNA or arrest-peptide encoding mRNA. Based on what we have observed from our previous study of RNase R, it appears that, if the protein binds the collided ribosome, it will be placed exactly at the interface between the two SSU (Figure 43 D). This position may not be very accessible but, interestingly, it corresponds roughly to the binding site of SmrB, whose activity is to cleave the defective mRNA strand at the interface between the two stalled ribosomes in order to free them and to promote *trans*-translation.

Looking at these evidences, one possible hypothesis would be that, in such a situation (in which SmrB interposes itself at the interface between the two stalled ribosomes), the RNase R could in any case reach and bind the stalled ribosome in a “wait-and-see” situation, on the collided one, for the non-stop mRNA once it will be ejected by tmRNA-SmpB complex. In this way, the ribonuclease is able to degrade the defective mRNA, abruptly preventing other ribosome stalling within the bacterial cell. The second possibility is that, in this context, the RNase R interacts with other areas on the ribosomal surface. These hypotheses are now being tested in the laboratory, through several ongoing experiments in which we try to produce disomes in presence of both tmRNA-SmpB and the RNase R.

At the same time, we decided to observe at high-resolution the complex formed by the disomes in presence of tmRNA and SmpB in order to get more information regarding the *trans*-transaltional process, describe more completely the entire mechanisms and try to characterize new molecular interaction essential to its successful completion. The images have been acquired in Heidelberg at the end of August 2022 and they are now being processed and analyzed in the laboratory.

2.5 Conclusion and perspectives

The key mechanism of *trans*-translation has been well characterized by our previous study in which we shed light on the molecular basis of the process. However, not all the components involved have been characterized and described. For that reason we focused our attention on the characterization of the RNase R, the protein responsible for the non-stop mRNA degradation.

First of all, we asked whether the protein was able to recognize and bind a stalled ribosome. As previously suggested, the RNase R efficiently binds the 30S subunit, even in the 70S context. The binding site, localized at the base of the beak, near the proteins uS2, uS3, uS4 and uS5, differs from the one used by the RNase R to degrade the non-processive ribosomes. Indeed, a recent study by Wilson lab was able to solve the structure of the RNase R degrading a 30S rRNA in *B. subtilis* (unpublished results). In that case, the RNase R binds between the head and the body of the 30S, at the upstream end of the mRNA exit channel, and interacts with uS7, uS11 and bS18. The binding site clearly differs from what we observed, suggesting that the RNase R can bind different sites at the surface of the ribosome depending of the task at hand. Then, we simultaneously tried to observe the tmRNA-SmpB complex and the RNase R on stalled ribosome. However, what we demonstrate is that the *trans*-translation tmRNA-SmpB complex and RNase R compete for the same binding site at the mRNA entry channel. We also acquired high-resolution images of the RNase R on a stalled ribosome. However, the complex appears to be extremely dynamical and we could not obtain sufficient resolution to shed light on the molecular interactions underlying the binding of the protein. The observed competition led us to inquire if the RNase R plays its role in concert with tmRNA-SmpB but on a system made of multiple ribosomes. To answer this question we purified collided disomes and demonstrate that the tmRNA-SmpB complex can take charge of the ribosome stalled at the end of the non-stop mRNA. These encouraging results have lead us to acquire high-resolution images of this complex and the data are being processed. Our preliminary reconstruction also reveals that the collided disomes obtained from non-stop mRNA are similar to the one obtained using arresting peptides. Although the RNase R wasn’t present in this complex, its putative binding site, at surface of the mRNA entry channel of the collided ribosome, is not easily accessible but corresponds to the one occupied by the SmrB splitting factor (Saito et al., 2022).

Altogether these results suggest the RNase R could interact elsewhere on the stalled ribosomes, awaiting to degrade the defective mRNA. Further studies are ongoing to challenge these hypotheses.

Section 3:

Structural insights into the binding of bS1 protein to the ribosome.

3.1 Context of study

The two main actors of *trans*-translation are tmRNA and SmpB but several other "secondary" actors are also needed for this rescue mechanism to take place. As mentioned previously, alanyl-tRNA synthetase is required for tmRNA activation, EF-Tu is necessary for ribosome binding, RNase R is needed for degradation of non-stop RNAs, and the degradation of proteins tagged by tmRNAs is accomplished by three energy-dependent proteases, ClpXP, ClpAP, FtsH as well as Tsp, a periplasmic energy-independent protease. The number of tmRNA molecules per *E. coli* cell is roughly 5% of the total number of ribosomes, and tmRNA rescues 1 ribosome every 250 translation events (Moore et al., 2005). To ensure the efficiency of this process, the tmRNA-SmpB complex needs to quickly recognize and bind the stalled ribosome. Among the many factors involved in *trans*-translation, the bS1 protein has been shown to be needed for the binding of tmRNA to ribosomes (Wower et al., 2000; Karzai and Sauer, 2001; Bordeau and Felden, 2002; Saguy et al., 2007). Although the exact role and mode of action of the bS1 protein during *trans*-translation is not entirely clear, several studies have reported that this protein plays a key role in protecting tmRNA from an eventual cytoplasmic degradation, as well as promoting the resumption of translation at the tmRNA's ORF, in particular through the interaction *via* the domain 4 (McGinnes and Sauer, 2004). In addition, changes in the expression level of bS1 strongly reduce the rate of binding to tmRNA, normally characterized by an apparent binding constant ranging from 10 to 100 mM (Wower et al., 2000; Bordeau and Felden, 2002; McGinness and Sauer, 2004; Okada et al., 2004).

Despite its importance, not only in *trans*-translation but also and especially during canonical translation initiation, bS1 lacks a high-resolution structure, either by crystallography or cryo-EM. In addition, the only available structural characterizations of the protein have been done on hibernating ribosomes or through chimeric protein formation necessary for its stabilization (Byrgazov et al., 2014; Beckert et al., 2018).

In the course of this Ph.D., we tried to structurally characterize the role of the bS1 protein during *trans*-translation. From the analysis of density maps derived from the study of Guyomar, D'Urso, and coworkers, a number of classes were identified in which both the tmRNA-SmpB complex and the bS1 protein were present on the ribosome.

The bS1 protein was observed during the pre-accommodation and accommodation of the tmRNA, but not during the translocation step, and no direct interaction between the tmRNA-SmpB and bS1 could be observed. Moreover, although the amount of signal related to the bS1 protein was rather low, the bS1 protein was clearly bound to the uS2 protein above the E-site but in a somehow different conformation than the one previously described. We concluded that the observed conformation of bS1 was related to the presence of the SD – anti-SD base pairing and not to the tmRNA-SmpB complex (the ejection of the mRNA from the ribosome during the translocation of tmRNA-SmpB, explaining why the density corresponding to bS1 could not be observed during this and the following *trans*-translation steps).

We, therefore, started from a simpler system with which we tried to characterize for the first time the bS1 protein on an elongation competent ribosome (70S with a SD-containing mRNA and fMet-tRNA), just before the beginning of translation. This study led to some very interesting results that on the one hand confirmed what had already been said in previous works while, on the other hand, revealed new interesting details that allowed us to expand the knowledge related to this protein. This work represents the content of the next paragraph and is currently under review in Nucleic Acid Research the journal.

3.2 Article: *"Structural insights into the binding of bS1 to the ribosome"* (under review)

Structural insights into the binding of bS1 to the ribosome

Gaetano D'Urso[1], Sophie Chat[1], Reynald Gillet[1*], and Emmanuel Giudice[1*]

[1]Univ. Rennes, CNRS, Institut de Génétique et Développement de Rennes (IGDR) UMR 6290, 35000 Rennes, France.

[*]Correspondance to: reynald.gillet@univ-rennes1.fr and emmanuel.giudice@univ-rennes1.fr

ABSTRACT

The multidomain ribosomal protein bS1 is the biggest and the most flexible and dynamic protein in the 30S small subunit. Despite being essential for mRNA recruitment and its primary role in the accommodation of the start codon within the decoding centre, there has not yet been a high-resolution description of its structure. Here, we present a 3D atomic model of OB1 and OB2, bS1's first two N-terminal domains, bound to an elongation-competent 70S ribosome. Our structure reveals that, as previously reported, bS1 is anchored both by a π-stacking to the 30S subunit and via a salt bridge with the Zn^{2+} pocket of uS1. These contacts are further stabilized by other interactions with additional residues on OB1. Our model also shows a new conformation of OB2, interacting with the Shine-Dalgarno portion of the mRNA. This study confirms that OB1 plays an anchoring role, but also highlights a novel function for OB2, which is directly involved in the modulation and support of mRNA binding and accommodation on the ribosome.

Keywords: *bS1, cryo-EM, Ribosome, translation*

INTRODUCTION

The flow of genetic information from DNA to functional proteins is achieved through the translation of mRNA molecules by ribosomes. The initiation of this translation process is the rate-limiting step for protein synthesis (1). In prokaryotes, the recognition of the first codon by P-site fMet-tRNA^{fMet} relies on mRNA binding to the small ribosomal subunit, 30S (2). This process is driven by the interaction between the AG-rich ribosome-binding site of the mRNA's 5′ untranslated region (5′ UTR) known as the Shine–Dalgarno (SD) sequence (3), and its counterpart, the CU-rich anti-SD sequence (aSD) at the 3′ end of 16S rRNA (4). The duplex formed by the two RNA molecules proceeds through various base-pairing interactions, ensuring that the 30S initiation complex (30S IC) is formed in such a way that the "start" codon of the open reading frame (usually an AUG) is correctly placed at the P site (5, 6). This interaction between the SD and the aSD is sufficient for most mRNAs to initiate translation. However, some natural mRNAs have weak SD sequences, none at all, or structural motifs in the 5′ UTR upstream from the coding portion, and these will all impede interactions with the 16S rRNA (7, 8, 9). In such cases, other factors are required to form the translation initiation complex.

The ribosomal protein bS1 is a single-stranded RNA-binding protein which is conserved in all Gram-negative bacteria. More distant "S1 proteins", generally formed of fewer domains, have also been identified in Gram-positive bacteria (10). With a length in solution of approximately 230 Å (11), it is the largest and most acidic protein that interacts, although in a weak and reversible way, with the small subunits of bacterial ribosomes (12). It is instrumental not just during the late steps of canonical translation initiation, but also in facilitating the binding of the small subunit to the mRNA SD portion (13, 14). The structure of bS1 contains six consecutive domains connected by loops of 10–15 residues which provide the flexibility essential for accomplishing its principal function, that of recruiting mRNA

transcripts on the ribosome (15, 16). Each bS1 domain, or oligonucleotide/oligosaccharide—binding (OB)-fold domain, consists of approximately 70 amino acids folded into a β-barrel. The barrel is composed of five antiparallel β-strands arranged into a Greek key topology, and one α-helix, which closes the bottom (15). From a functional point of view, the first two N-terminal domains (OB1 and OB2) do not have detectable RNA–binding activity, and they seem to be mostly involved in binding ribosomes (10, 15, 16, 17, 18, 19, 20). More specifically, the protein's first 106 amino acids are sufficient to ensure the contact with the 30S subunit by means of an interaction with the protein uS2 (10, 15, 16, 17, 18, 19, 20, 21). However, because OB2 is located near the 16S helix h26 and the 5′-end of mRNA, it has also been suggested that it is involved in mRNA interaction on the ribosome (20). In contrast, the uS1 C-terminal portion (formed by domains OB3 to OB6) is essential for RNA binding (13, 16, 22, 23, 24).

Besides its primary role in translation initiation, the bS1 protein is also involved in many other important cellular mechanisms. For instance, bS1, EF-Tu, EF-Ts are the essential host-derived subunits of Q-Beta-replicase (QBR), an enzyme that directly replicates RNA from the genomic RNA positive–strand in *Escherichia coli* (25, 26, 27). The OB1 and OB2 domains are essential for establishing interactions between these three protein partners during formation of the QBR, while OB3 is required for the efficient recognition and synthesis of the negative-strand RNA (25, 26, 27). In addition, bS1 is a potent activator of transcriptional cycling, affecting the transcriptional activity of the RNA polymerase (28). The protein is also involved in *trans*-translation, where it binds tmRNA (29, 30, 31, 32, 33), as well as intervening to protect single-stranded RNAs from degradation by RNase E (34).

Although the bS1 protein is obviously of primary importance, there has been no high-resolution structure, a description that is essential to better understand its participation in various molecular mechanisms. To address this, we present here a cryo-EM structure at an

overall resolution of 3.42 Å, showing the N-terminal portion of bS1 interacting with a 70S elongation-competent (70S EC) complex. This new atomic model reveals a previously unseen conformation of the protein, with the OB2 domain interacting with the SD portion of the mRNA. This highlights the fact that OB2 has an RNA-binding role when bS1 is already bound to the 30S subunit (Figure 1). Our study provides new insights into the role of bS1's N-terminal domains during the initial steps of translation, improving our knowledge of the mechanisms underlying the protein's functions.

MATERIAL AND METHODS

Ribosome purification

Ribosomes were purified from E. coli MG1655. When the culture reached an OD_{600} of 0.8, cells were pelleted, resuspended in FP buffer (20 mM Tris-HCl pH 7.5, 50 mM MgOAc, 100 mM NH_4Cl, 0.5 mM EDTA and 1 mM DTT) and lysed in a French press. The lysate was then clarified by centrifugation at 20,000 × g for 45 min at 4 °C. Next, the supernatant was layered 1:1 (v:v) over a high-salt sucrose cushion buffer (10 mM Tris- HCl pH 7.5, 10 mM MgOAc, 500 mM NH_4Cl, 0.5 mM EDTA, 1.1 M sucrose and 1 mM DTT). After ultracentrifugation at 92,000 × g for 20 h at 4 °C, the resulting ribosome pellets were resuspended in 1 mL of 'Ribo_A' buffer (10 mM Tris-HCl pH 7.5, 10 mM $MgCl_2$, 50 mM NH_4Cl, 0.5 mM EDTA and 1 mM DTT). To isolate the 70S ribosomes from 30S and 50S ribosomal subunits, the ribosomes were centrifuged at 95,000 × g for 18 h at 4 °C through a 10–45% (w/w) linear sucrose gradient in Ribo_A buffer. Gradients were fractionated before determining the A_{260} absorbance profiles. Fractions corresponding to the 70S peak were mixed and diluted in Ribo_A buffer for a final ultracentrifugation at 92,000 × g for 20 h at 4 °C. The ribosomal pellets were resuspended in Ribo_A buffer, and flash frozen and stored at −80 °C.

Sample preparation and cryo-EM data collection

To prepare the 70S EC complex, 25 pmol of fMet-tRNA^{fMet} (ICNA0219915410; VWR) was first refolded for 2 min at 80 °C in "Buffer I" (10 mM HEPES-KOH pH 7.5, 25 mM $MgCl_2$, 25 mM, and 20 mM NH_4Cl). This was followed by a second incubation at room temperature for 30 min. Purified 70S ribosomes (12.5 pmol) were incubated for 20 min at 37 °C in "Buffer-III" (10 mM MgOAc, 10 mM NH_4Cl, 50 mM KCl, 5 mM HEPES-KOH pH 7.5, and 1 mM DTT) with 25 pmol of cspA mRNA and 25 pmol of the folded fMet-tRNA^{fMet}. The cspA mRNAs contained the Shine-Dalgarno sequence and a linker to place the AUG codon into the P site: GG GCU UAA GUA UAA GGA GGA AAA AAU AUG CCA CAG GGA. After adjusting concentrations to 160 nM in Buffer-III, samples were directly applied to glow-discharged holey carbon films (Quantifoil 3.5/1). These grids were flash-frozen in liquid ethane using an FEI Vitrobot Mark III. They were then imaged at the IECB Structural Biophysical Chemistry Platform using a 200 kV Talos Arctica cryo-TEM (Thermo Fisher Scientific) equipped with a field emission gun. SerialEM software was used to automatically record 6,381 movies under low-dose conditions with a Gatan K2 direct electron detector with a defocus range of 0.4-2.0 µm and a pixel size of 0.9291 Å.

Image processing

The initial steps of single particle analysis were done using cryoSPARC (version 2.15.0) (35). Movies were motion-corrected using Patch Motion, and Patch CTF was used for contrast transfer function (CTF) estimation. Particles were manually picked from 18 micrographs using cryoSPARC. To generate an initial model for template picking, the resulting 476 particles were subjected to a first run of 2D classification into eight distinct classes. Of these, six classes (a total of 401 particles) were selected and used as templates to pick particles in the entire dataset of 6381 micrographs. The selected particles were inspected, extracted from

the micrographs, and then underwent two rounds of 2D classification (200 classes each). We retained 294820 particles that were used to generate an initial *ab initio* model, and then refined with the legacy version of homogeneous refinement in cryoSparc. The micrographs and particle coordinates were transferred to RELION (version 3.1 beta) (36). Movies were once again corrected for the effects of drift and beam-induced motion using MotionCor2 software (37). CTF parameters were re-estimated using Gctf software (38). A first 3D auto-refinement was performed to reconstruct a density map of the ribosome using the cryoSparc homogeneous refinement map as an initial model. The heterogeneity of the dataset was then assessed using a 3D classification into 12 classes, which separates the 50S subunit (Classes 10, 12), junk particles (Class 8), ribosomes in ratcheted conformations (Classes 7, 11), and canonical ribosomes with feeble and noisy densities attributed to the bS1 protein (Classes 1, 2, 3, 4, 5, 6, 9; 175859 particles). Overall, this unbiased and unfocused classification process did not uncover a well-resolved conformation for bS1, but it did allow us to minimize ribosomal heterogeneity resulting from different subunit conformations as well as filtering out "junk particles" from the entire dataset. To further focus in on bS1 and limit the classification to the ribosomal portions known to interact with that protein, we used UCSF Chimera (39) to create a spherical mask with a radius of 50 Å. We then subtracted the ribosomal signal and performed a 3D classification with six classes, without alignment on the region of interest. The particles corresponding to bS1 were selected (Classes 1, 3, 4, 6; 141003 particles), reverted to the original one and subjected to a second round of 3D classification with signal subtraction and using a tighter spherical mask of 40 Å. The dataset was split into six classes, and class number 5 (containing 33,572 particles) was selected and reverted to the original images. After refinement, the resulting map still displayed heterogeneity. To further limit this, a final 3D classification (3 classes) was done with the 70S signals removed using a mask created with the Segger volume data partition extension (40) of Chimera. From the resulting

classification, we selected 16,381 particles (Class 3). The dataset was reverted to the original and 3D-refined. The particles were then CTF refined and polished. Finally, we reconstructed the map, which was then post-processed with a solvent mask to produce an overall resolution of 3.42 Å (Supp. Fig. 2A).

Model reconstruction

To build and refine an atomic model of bS1, the high-resolution cryo-EM map was further processed using the CCP-EM software suite (version 1.5.0) (41). First, the small bS1 density was isolated from the entire map using the Segger tool of Chimera. The protein coordinates were extracted from the 6BU8 PDB file (20) and rigid-body fitted into the bS1 volume. The map was converted into the MTZ format, and the model underwent two consecutive RIBFIND runs (42) to identify rigid body elements after calculating the spatial proximities between the protein's secondary structures. To optimize the fit to the experimental volume, the previously-calculated rigid-body domain information was entered into Flex-EM (43). The model was then refined against the electron density with REFMAC5 software (44) using its jelly-body restraints option. The resulting density map showed regions at different resolutions – mostly because the images are centred on the ribosome so peripheral zones are blurry, but also because of the higher flexibility of certain molecular components. These factors lead to a falloff in amplitude, resulting in the poor density contrast which is typical of the most dynamic portions of molecular complexes. We used LocScale (45) to compensate for the loss of information on the protein, enhance the interpretability of the bS1 volume, and to facilitate the fitting of the atomic model. This program uses prior information from the refined bS1 coordinates to improve the contrast of cryo-EM maps, and we down-weighted the ribosomal signal in order to focus in on the zone corresponding to bS1. The entire map was then used to rigid-body fit the atomic model of the complex in Chimera, and the atomic model was

manually adjusted in Coot (46). A final round of PHENIX (version 1.18.2) (47) real-space refinement (48) allowed us to improve the fitting of the coordinates against the sharpened volume. Once the model was refined, atomic model geometry, density fit, and FSC curves were calculated using the PHENIX cryo-EM comprehensive validation tool. All figures shown here were created with Chimera.

RESULTS

bS1 forms a highly dynamic complex with the ribosome

The protein bS1 is the ‘mRNA-catching arm of the ribosome. Formed by six highly flexible OB-fold domains, and attached to the ribosomal small subunit through its N-terminal domain, bS1 acts as a highly flexible lasso to capture mRNA molecules. While the protein’s activity is crucial for translation initiation, its high flexibility make it a challenging subject for structural biology. For our investigations, we therefore used image analysis protocols to focus in on a particular region of a big complex, such as the ribosome (see Material and Methods). This targeted approach has proven to be quite successful for separating different ribosomal conformations and for improving model resolution, especially when it comes to highly dynamic regions (49). Our structure consists of a 70S ribosome in complex with a short mRNA, a P-site tRNA, an E-site tRNA, and the first two domains of bS1, OB1 and OB2 (Figure 1).

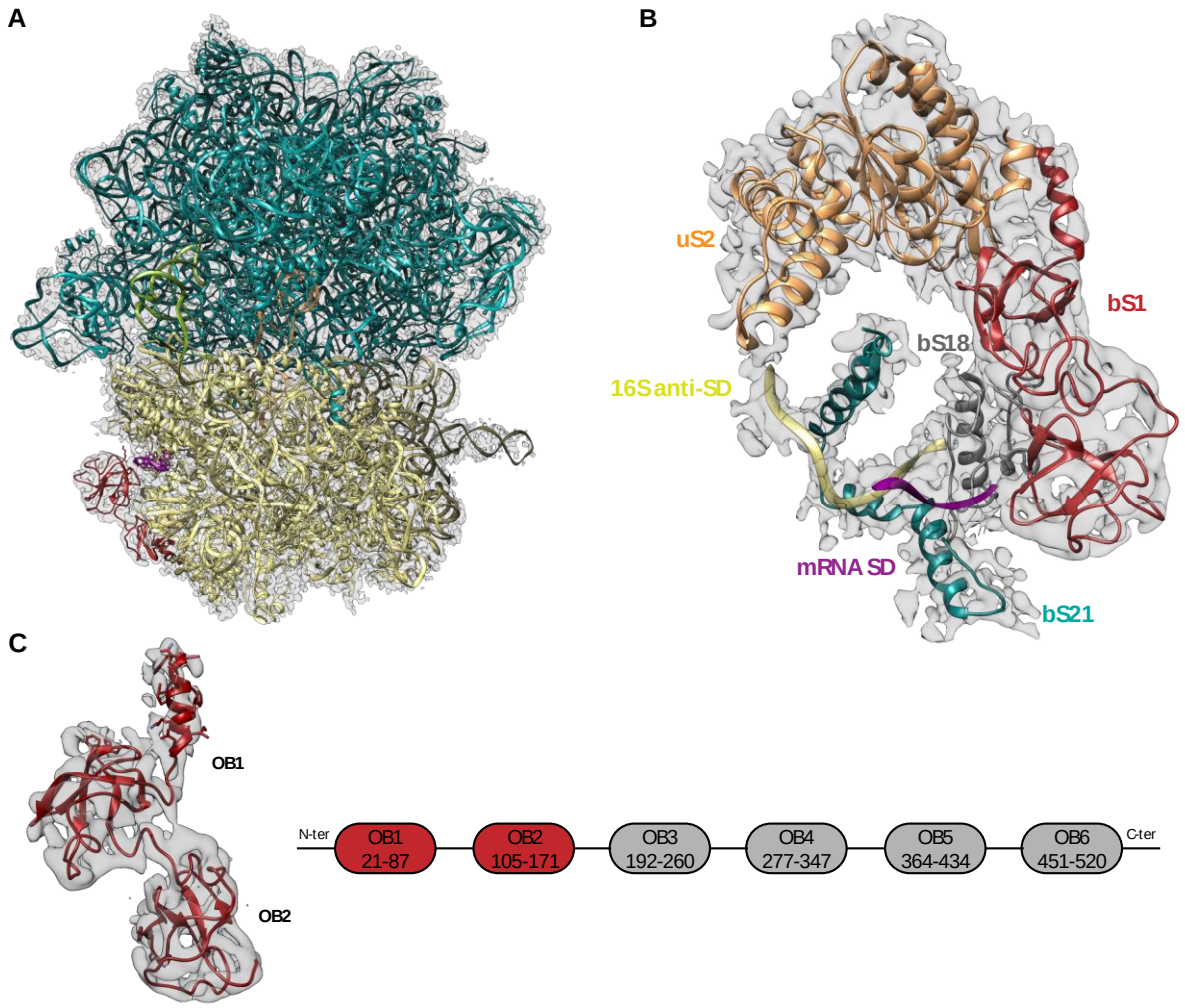

Figure 1: Structure of the elongation competent ribosome in complex with bS1.
A *- Atomic model of the translating* E. coli *ribosome in complex with the first two N-terminal domains of bS1, OB1 and OB2. The 50S subunit is aquamarine, 30S is khaki, P-site tRNA is orange, E-site tRNA is light green, the mRNA Shine-Dalgarno (SD) sequence is purple, and bS1 is red.* ***B*** *- Focus on the bS1 binding site, with uS2 orange, 16S anti-SD khaki, bS21 aquamarine, bS18 grey, SD purple, and bS1 red.* ***C*** *– Secondary structure and atomic model of OB1 and OB2. In the secondary structure, the domains present in our model are highlighted in red.*

Consistent with previous reports, bS1 binds at the mRNA exit channel, in the narrow cleft between the 30S head and platform (Figures 1A, B). The mRNA exit channel is formed by uS2, bS18, bS21, and the 3′ end of the 16S rRNA needed for the stabilization of the mRNA through the SD–aSD base pairing (Figure 1B). The mRNA contains the SD portion at its 5′-end, and is properly paired with the 16S aSD sequence. The tRNA in the P site is paired with the AUG starting codon, and this interaction is essential for the correct formation of the

complex. Our complex looks therefore like an elongation-competent 70S (70S EC) (49), although a second tRNA is observed in the E-site, presumably due to the excess of tRNA used during the *in vitro* complex formation. Translation initiation is driven and controlled by the three initiation factors IF1, IF2, and IF3. These ensure that the 70S initiation complex (70S IC) matures into a 70S EC complex whose P site contains an $fMetRNA^{fMet}$ properly paired with the mRNA start codon (49). During translation initiation, bS1 facilitates the recruitment and correct positioning of the mRNA, giving life to a ribosome which is ready to translate (19). This description fits well with the present structure, which contains bS1 still bound to the small subunit of a 70S EC. Only the first two bS1 N-terminal domains, the most stable portions of the protein, were sufficiently resolved to allow reconstruction (Figure 1C), as the rest of the protein elements are extremely flexible and dynamic. However, this new model still allows us to understand how these two bS1 domains interact with the 70S EC and help bring and stabilize the mRNAs waiting to be translated.

bS1 requires unique interactions to anchor the small subunit of the 70S EC

In agreement with previous studies (19, 20), we found that the bS1 N-terminal domain binds to the cleft between the head and the platform, in a zone consisting of uS2, uS18, and bS21 residues as well as helix h26 and the 3′-end of the 16S rRNA. The volume obtained from single particle analysis shows not only the bS21 OB1 and OB2 domains, but also the mRNA SD portion paired to the 16S aSD (Figure 1B). Unfortunately, no other densities are present for the 5′ UTR sequence upstream from these six nucleotides, nor for the other bS21 domains (OB3 through OB6). The major anchoring point for bS1 on the *E. coli* ribosome is the uS2 protein (50, 51). The OB1 N-terminal helix is the most well-resolved element, confirming its conformational stability and its role in binding the entire protein to the ribosomal platform. As already seen in other bS1 structural studies (19, 20), the OB1 N-

terminal helix binds the uS2 protein *via* a classical π-stacking between the Phe5 and Phe9 residues of bS1 and the Phe32 of uS2 (Figure 2A). In addition to these previously described interactions, however, we saw other electrostatic interactions: bS1, Gln7, and Glu10 interact with uS2, Met6, and Arg7, respectively, and this is probably important for the global stability of OB1 on the ribosome (Figure 2A).

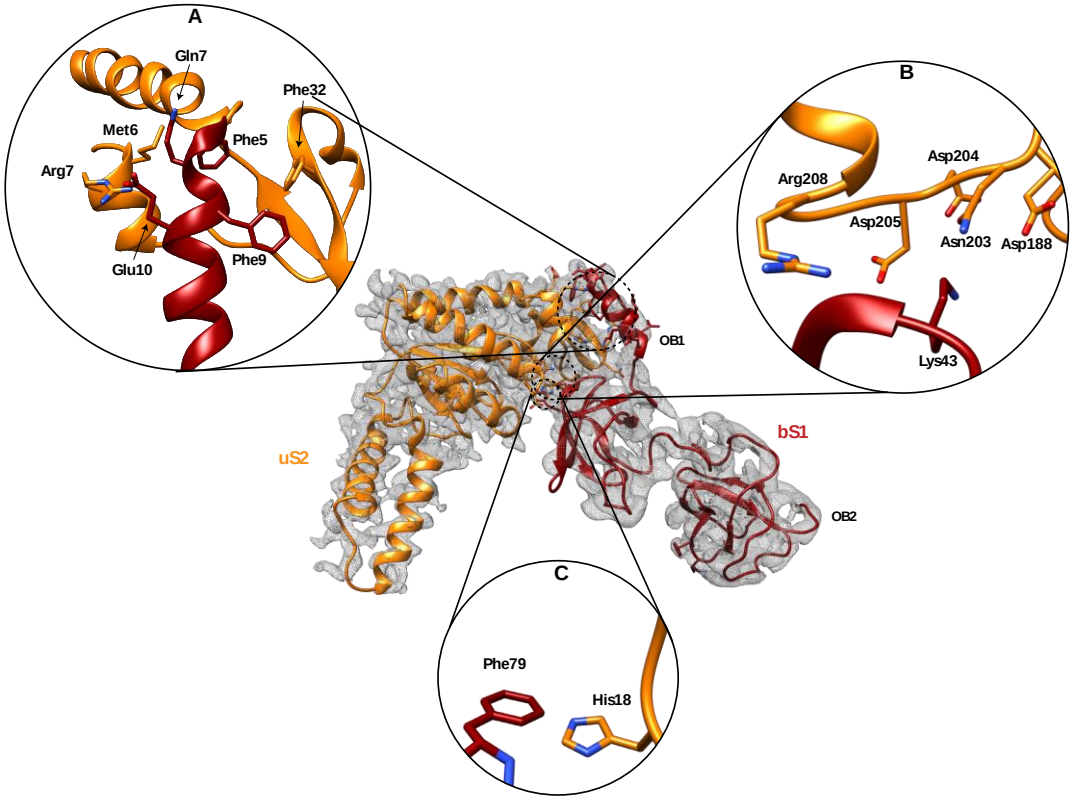

Figure 2: bS1 interaction with uS2.
A *- Interactions between uS2 (orange) and the OB1 N-terminal helix of bS1 (red).* ***B*** *– Interaction between loop 2 in bS1 (red) and the* Zn^{2+}*-binding pocket of uS2 (orange).* ***C*** *– Close-up of the novel stacking between bS1 Phe79 and uS2 His18 residues.*

The extreme tip of bS1's loop 2 packs on two uS2 α-helices, and this allows the insertion of Lys43 into a zinc-binding pocket formed by Asp188, Asn203, Asp204, and Asp205 (Figure 2B) (19, 20). The uS2 Arg208 points in the opposite direction as the bS1 Asp39 residue, and the salt bridges described by Byrgazov *et al.* (2015) were not observed in our structure. However, in a previously unseen interaction, the aromatic rings of bS1 Phe79 and uS2 His18

were involved in a classical π-stacking in our structure (Figure 2C), another novel interaction contributing to the overall stability of OB1 on the ribosome. This confirms the roles of both uS2 and bS1's OB1 domain for ensuring the temporary stable interaction essential for bS1 to correctly position the mRNA. Taken together, these observations prove that it is not only Phe5, Phe9, and Lys43 residues, but also Gln7, Glu10, and Phe79 who participate in binding bS1 to uS2. Therefore, during the early steps of protein synthesis, it is the entire OB1 that stabilizes bS1 at the 30S surface, while the other domains remain inherently free and flexible.

The bS21 protein is involved in bS1 stabilization on the ribosome

The protein bS21 is the smallest (70 amino-acids) and most basic protein in the small ribosomal (30S) subunit of bacteria (52, 53). It assumes a particular conformation in the cleft between the head and the platform of 30S, thus participating in the formation of the mRNA exit channel (53). Together with bS1, bS21 is required for the initial steps of protein synthesis, favouring the base-pairing between 16S rRNA and the SD portion of mRNA (53, 54). In agreement with the studies cited here, we saw that bS21 participates in the base-pairing between 16S and mRNA by directly interacting with the SD sequence *via* two arginines (Arg17 and Arg21) positioned at the protein's N-terminal region (Figure 3B). The C-terminal end of bS21 protrudes towards the 30S platform in a previously unseen hinge function between bS1 OB1 and the 16S rRNA (Figure 3A). Indeed, our structure reveals that the Arg67 and Arg69 residues in bS21 point in two opposite directions, with Arg67 interacting with bS1 Gly78, and Arg69 contacting nucleotide G1099 of the 16S rRNA (Figure 3A). This conformation allows bS21 to act as a second anchoring point for bS1, certainly strengthening its binding with the ribosome. These observations confirm the role of bS21 in translation initiation not only *via* its promotion of base-pairing between the SD and aSD sequences, but also by acting as a bridge to reinforce the binding of the bS1 OB1 to 16S rRNA.

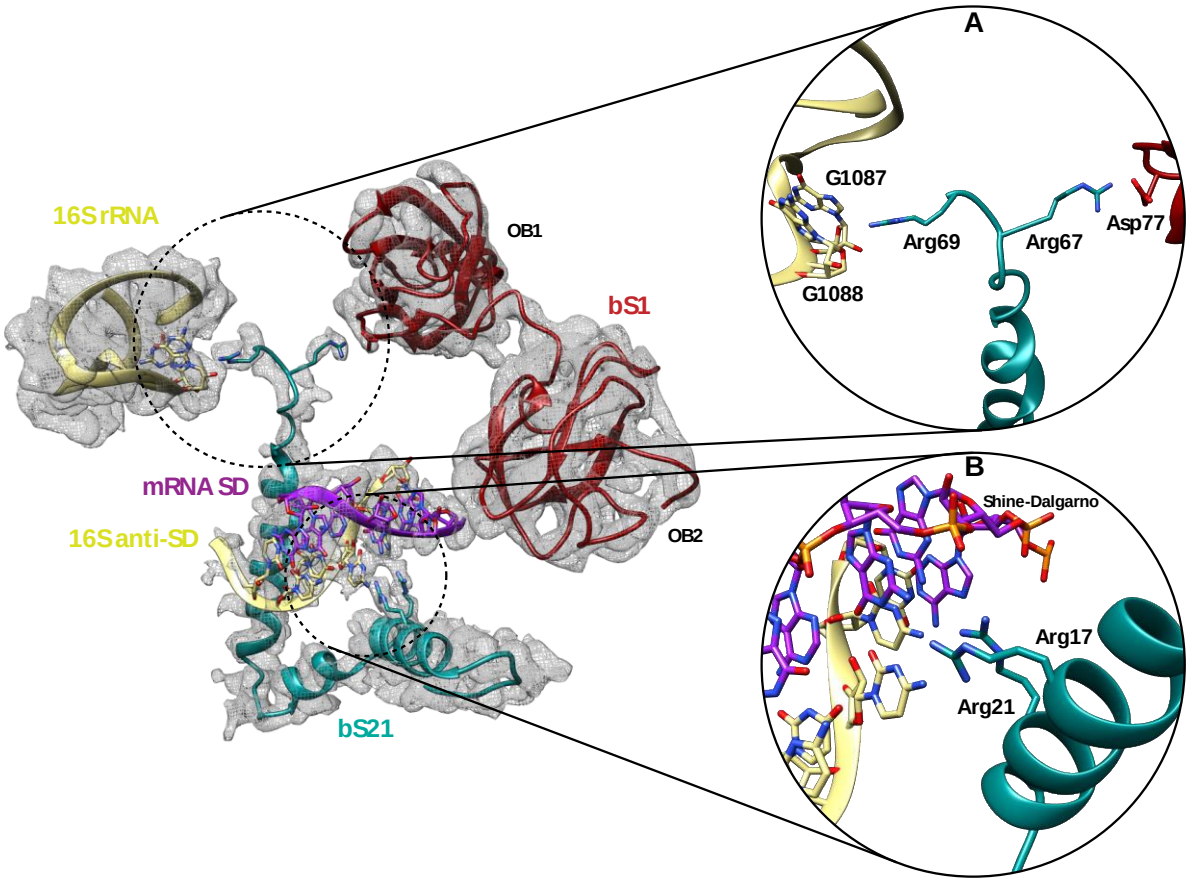

Figure 3: bS1 OB1 interactions with bS21. ***A*** *– The ribosomal protein bS21 shows a novel hinge activity between the 16S rRNA (khaki) and OB1 (red), the first N-terminal domain of bS1.* ***B*** *– Close-up showing the interaction between bS21 (aquamarine) and the Shine-Dalgarno (SD) portion of mRNA (purple).*

OB2 stabilizes the base-pairing between the SD and anti-SD sequences

Our new data also allowed us to reconstruct the OB2 domain, yielding in fundamental insights into how bS1 interacts with its partners. The OB2 domain flanks the mRNA exit channel, in close vicinity to the SD-aSD helix (Figure 4). The α-helix connecting OB1 to OB2 is mostly unfolded, which explains the partial rotation of OB2 as well as why the domain appears in a totally different conformation than in previously described structures (Supp. Fig. 3) (16, 20, 55). Here, the aromatic rings of two phenylalanine residues, Phe120 and Phe130, form a binding pocket with Lys117, welcoming the first nucleotides of the mRNA SD segment (Figure 4). This triad of residues captures the mRNA in a pincer movement, suggesting that OB2 also plays a role in stabilizing the SD-aSD interaction. This particular

conformation corroborates previous observations that bS1 requires a particular orientation of its first three OB domains to bind RNA molecules and unfold structured messenger RNA, and that deletion of OB1 and OB2 not only decreases the binding rates of bS1 to the ribosome, but also damages its ability to interact with mRNA (19, 24). Indeed, the new positioning of OB2 and the presence of the Lys117-Phe120-Phe130 binding pocket might provide an explanation for why the bS1 N-terminal domains are not only needed to anchor the protein to the ribosome, but also for stabilizing and correctly placing the mRNAs there, and thus for allowing the 30S initiation complex to be formed.

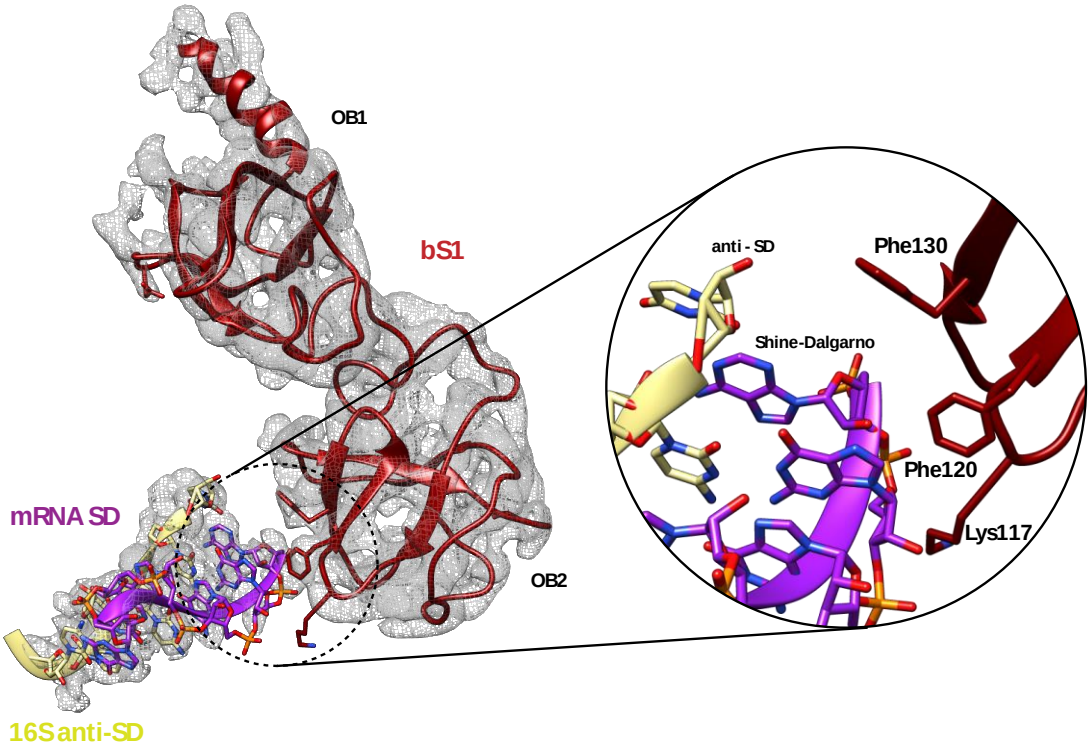

Figure 4: bS1 OB2 interactions with the mRNA exit channel. *– Close-up showing the interactions between the bS1 OB2 pocket (red) and the Shine–Dalgarno (SD) portion of the mRNA (purple).*

On the OB2 domain, the conformation of the pocket suggests that it can work as a groove to stabilize mRNA while the base pairing with the SD is being formed. Unlike other structural studies of bS1 (16, 19, 20) stating that most of the interactions around the mRNA exit channel are with OB3, we actually found that during the formation of the 70S EC complex, bS1 places its OB2 domain into the cleft of the 30S subunit. This suggests that OB2 is involved in

correctly positioning the mRNA into the 30S late initiation complex as well as in stabilizing the SD-aSD base-pairing. With the exception of bS18 and uS2, no interactions between OB2 and other ribosomal proteins were observed.

DISCUSSION

Translation initiation is the rate-limiting step in protein synthesis. It depends mostly on the presence of recruitment signals in the 5′ UTR leader region, as well as several protein factors, which assist in forming the 70S EC (49, 56). The ribosomal protein bS1 is one of these agents, helping mRNAs to reach the ribosome and then ensuring their proper accommodation into the decoding channel even in the absence of a 5′ UTR or proper SD sequence (24, 57). Two distinctive features of bS1 are its flexibility and dynamicity, but this means that we still lack a full-length atomic description of the protein. The detailed model we present here consists of the first two N-terminal domains of bS1 in complex with a 70S EC ribosome charged with an mRNA, and an fMet-tRNA^{fMet}. The in-depth classification of the particles in our cryo-EM dataset uncovered a completely unique conformational rearrangement of bS1 that had not been observed previously. Due to the presence of the SD-aSD pairing, our structure reveals a more detailed interaction between the two first domains of bS1 and the 70S EC. The other four domains of the protein are not stable enough to be modelled, and their description may require the presence of a longer and structured 5′ UTR region.

The N-terminal segment of the OB1 domain is folded into an α-helix which mediates its interaction with uS2 via a well-conserved and well-described π-stacking involving bS1 Phe5 to Phe9 and uS2 Phe32 residues (Figure 2A) (19, 20). The high stability of the N-terminal portion ensured by this hydrophobic interaction is also reinforced by electrostatic interactions described here for the first time as a result of improved resolution. In particular, bS1 Gln7 and

Glu10 interact with uS2 Met6 and Arg7, respectively (Figure 2A). In perfect agreement with previous findings, the bS1 Lys43 residue found on the extremity of loop 2 is inserted into the uS2 Zn^{2+}-binding pocket (Figure 2B) (19, 20). Based on previous knowledge of the Zn^{2+}-binding function of uS2 and on crystallographic results from earlier structural studies, we are able here to confirm the positioning of Lys43 within this pocket formed by uS2 Asp188, Asn203, Asp204, and Asp205 (19, 58). The residues involved in forming the pocket are conserved among different species, underlining the importance of the Zn^{2+} ion for stabilizing the uS2 structure and correctly positioning bS1 (19). The most novel element that completes the ribosome interaction picture is the presence of a stacking between bS1 Phe79 and uS2 His18 (Figure 2C). This interaction is certain to further stabilize bS1 at the surface of the ribosome.

In addition, our study shows that an important role in the ribosome-bS1 interaction is also played by the protein bS21, whose ability to interact with bS1 itself was previously observed by NMR (16). Our high-resolution structure allows for a clearer description of these interactions, and clarifies the role of bS21 during translation initiation. Acting as a three-way bridge, the C-terminal portion of bS21 mediates the interaction between the bS1 OB1 domain and 16S rRNA via two arginines (Figure 3A). The N-terminal extremity of bS21 also makes contact with the 3′-end of the 16S rRNA, creating an elegant three–point contact system which further anchors bS1 to the ribosomal platform (Figure 3B). In the course of our analysis, we also uncovered a new binding pocket in the OB2 domain (Figure 4). This previously unseen binding site is formed by Lys117, Phe120, and Phe130, and it surrounds the first nucleotides of the Shine-Dalgarno sequence of the mRNA (Figure 4). In comparing our model with that of Loveland and Korostelev (2018; PDB 6BU8), we see that the residues involved in forming this pocket point in the opposite direction. We are therefore describing a different bS1 conformation in which the OB2 domain rotates thanks to a partial misfolding of

the helix connecting OB1 to OB2, thus further emphasizing the protein's intrinsic dynamicity (Supp. Fig. 3). The partial loss of the α-helical conformation allows the protein to position the OB2 domain residues exactly upstream from the mRNA SD element. Interestingly, a ConSurf (59) analysis of bS1 (Supp. Fig. 3) using a sample of 150 sequences (the homologues) reveals that Phe120, Phe130, and Lys117 present high conservation scores. This analysis reinforces the idea that these residues have a specific function, as they recur systematically in different species.

Until now, it was thought that the first two OB domains of bS1 were involved only in anchoring the protein to the ribosomal platform, with the other domains intervening in the capture, binding, and unfolding of leaderless or structured mRNAs. However, our data shows that OB2 also interacts with the 5′-end of the SD through the formation of a characteristic pocket in which the mRNA nucleotides are accommodated. This new role for OB2 is supported by 3D density maps published by Loveland and Korostelev showing some bS1 conformations with OB-fold domains checking the mRNA exit channel, with the OB2 near the 5′-end of the mRNA. During translation initiation, this pocket could act as clamp to stabilize Watson-Crick SD-aSD interactions. Our atomic model presented features a 70S subunit in the elongation-competent state wherein the association of the two subunits around an fMet-tRNA^{fMet} produces a ribosome that is ready to translate the mRNA. At this stage, bS1 still binds both the ribosome and the initial region of the mRNA. This particular conformation of the second domain of bS1 can be explained by the topological rearrangement occuring after RNA molecules are bound, which in turn causes a global reorganization of the protein on the ribosome *via* other interactions involving OB1, OB2, uS2, and uS18, as described previously (18, 19). Collectively, these interactions facilitate the correct positioning of the mRNA, and might also facilitate the transition from the 30S initiation complex to the elongation-competent 70S.

To conclude, the results presented here broaden the collective knowledge of the functionality of one of the most flexible ribosomal proteins. They emphasize the functional versatility of the OB2 domain, and highlight several new interactions essential for the stability of bS1 during translation initiation. Together with the contacts previously described in other studies (19, 20), our results emphasize the importance of new accessory interactions between bS1 and uS2. We also demonstrate that bS21 is essential in the binding between bS1 the 30S small ribosomal subunit, acting as a three-way clamp indirectly connecting OB1 to the 16S. In particular, we clarify the role of this protein's OB2 domain by describing a previously unseen conformation allowing it to interact directly with the SD portion of mRNA. In this way, the OB2 domain actively participates in the formation of the SD-aSD pairing, giving life to the 30S initiation complex.

Author Contributions

Performed research: G.D., S.C.; analyzed data: G.D., E.G., designed research: E.G., R.G., wrote the paper: G.D. with contributions from all the authors. R.G. and E.G. supervised the study. All authors have given approval to the final version of the manuscript.

ACKNOWLEDGMENTS

This work was supported by the Agence Nationale pour la Recherche under the frame of the Joint JPI-EC-AMR Project named "Ribotarget - Development of novel ribosome-targeting antibiotics". Gaetano D'Urso is supported by JPIAMR and Région Bretagne for PhD financial support. The authors gratefully acknowledge the facilities of the Microscopy Rennes Imaging Center (Mric) and the facilities and expertise of the Structural Biophysico-Chemistry platform

(BPCS) at the IECB (CNRS UMS3033, Inserm US001, Bordeaux University. The authors also are particularly grateful to Juliana Berland for insightful comments on the manuscript.

REFERENCES

1. Shah P, Ding Y, Niemczyk M, Kudla G, Plotkin JB. Rate-limiting steps in yeast protein translation. Cell. 2013 Jun 20;153(7):1589-601. doi: 10.1016/j.cell.2013.05.049.

2. Laursen BS, Sørensen HP, Mortensen KK, Sperling-Petersen HU. Initiation of protein synthesis in bacteria. Microbiol Mol Biol Rev. 2005 Mar;69(1):101-23. doi: 10.1128/MMBR.69.1.101-123.2005.

3. Shine J, Dalgarno L. The 3'-terminal sequence of Escherichia coli 16S ribosomal RNA: complementarity to nonsense triplets and ribosome binding sites. Proc Natl Acad Sci U S A. 1974 Apr;71(4):1342-6. doi: 10.1073/pnas.71.4.1342.

4. Wen JD, Kuo ST, Chou HD. The diversity of Shine-Dalgarno sequences sheds light on the evolution of translation initiation. RNA Biol. 2021 Nov;18(11):1489-1500. doi: 10.1080/15476286.2020.1861406.

5. Yusupova GZ, Yusupov MM, Cate JH, Noller HF. The path of messenger RNA through the ribosome. Cell. 2001 Jul 27;106(2):233-41. doi: 10.1016/s0092-8674(01)00435-4.

6. Yusupova G, Jenner L, Rees B, Moras D, Yusupov M. Structural basis for messenger RNA movement on the ribosome. Nature. 2006 Nov 16;444(7117):391-4. doi: 10.1038/nature05281.

7. Marzi S, Myasnikov AG, Serganov A, Ehresmann C, Romby P, Yusupov M, Klaholz BP. Structured mRNAs regulate translation initiation by binding to the platform of the ribosome. Cell. 2007 Sep 21;130(6):1019-31. doi: 10.1016/j.cell.2007.07.008.

8. Breaker RR. Riboswitches and the RNA world. Cold Spring Harb Perspect Biol. 2012 Feb 1;4(2):a003566. doi: 10.1101/cshperspect.a003566.

9. Kortmann J, Narberhaus F. Bacterial RNA thermometers: molecular zippers and switches. Nat Rev Microbiol. 2012 Mar 16;10(4):255-65. doi: 10.1038/nrmicro2730.

10. Salah P, Bisaglia M, Aliprandi P, Uzan M, Sizun C, Bontems F. Probing the relationship between Gram-negative and Gram-positive S1 proteins by sequence analysis. Nucleic Acids Res. 2009 Sep;37(16):5578-88. doi: 10.1093/nar/gkp547.

11. Subramanian AR. Structure and functions of ribosomal protein S1. Prog Nucleic Acid Res Mol Biol. 1983;28:101-42. doi: 10.1016/s0079-6603(08)60085-9. PMID: 6348874.

12. Sykes MT, Williamson JR. A complex assembly landscape for the 30S ribosomal subunit. Annu Rev Biophys. 2009;38:197-215. doi: 10.1146/annurev.biophys.050708.133615.

13. Boni IV, Isaeva DM, Musychenko ML, Tzareva NV. Ribosome-messenger recognition: mRNA target sites for ribosomal protein S1. Nucleic Acids Res. 1991 Jan 11;19(1):155-62. doi: 10.1093/nar/19.1.155.

14. Tzareva NV, Makhno VI, Boni IV. Ribosome-messenger recognition in the absence of the Shine-Dalgarno interactions. FEBS Lett. 1994 Jan 10;337(2):189-94. doi: 10.1016/0014-5793(94)80271-8.

15. Bycroft M, Hubbard TJ, Proctor M, Freund SM, Murzin AG. The solution structure of the S1 RNA binding domain: a member of an ancient nucleic acid-binding fold. Cell. 1997 Jan 24;88(2):235-42. doi: 10.1016/s0092-8674(00)81844-9.

16. Lauber MA, Rappsilber J, Reilly JP. Dynamics of ribosomal protein S1 on a bacterial ribosome with cross-linking and mass spectrometry. Mol Cell Proteomics. 2012 Dec;11(12):1965-76. doi: 10.1074/mcp.M112.019562.

17. McGinness KE, Sauer RT. Ribosomal protein S1 binds mRNA and tmRNA similarly but plays distinct roles in translation of these molecules. Proc Natl Acad Sci U S A. 2004 Sep 14;101(37):13454-9. doi: 10.1073/pnas.0405521101.

18. Aliprandi P, Sizun C, Perez J, Mareuil F, Caputo S, Leroy JL, Odaert B, Laalami S, Uzan M, Bontems F. S1 ribosomal protein functions in translation initiation and ribonuclease RegB activation are mediated by similar RNA-protein interactions: an NMR and SAXS analysis. J Biol Chem. 2008 May 9;283(19):13289-301. doi: 10.1074/jbc.M707111200.

19. Byrgazov K, Grishkovskaya I, Arenz S, Coudevylle N, Temmel H, Wilson DN, Djinovic-Carugo K, Moll I. Structural basis for the interaction of protein S1 with the Escherichia coli ribosome. Nucleic Acids Res. 2015 Jan;43(1):661-73. doi: 10.1093/nar/gku1314.

20. Loveland AB, Korostelev AA. Structural dynamics of protein S1 on the 70S ribosome visualized by ensemble cryo-EM. Methods. 2018 Mar 15;137:55-66. doi: 10.1016/j.ymeth.2017.12.004.

21. Byrgazov K, Manoharadas S, Kaberdina AC, Vesper O, Moll I. Direct interaction of the N-terminal domain of ribosomal protein S1 with protein S2 in Escherichia coli. PLoS One. 2012;7(3):e32702. doi: 10.1371/journal.pone.0032702.

22. Tedin K, Resch A, Bläsi U. Requirements for ribosomal protein S1 for translation initiation of mRNAs with and without a 5' leader sequence. Mol Microbiol. 1997 Jul;25(1):189-99. doi: 10.1046/j.1365-2958.1997.4421810.x.

23. Qu X, Lancaster L, Noller HF, Bustamante C, Tinoco I Jr. Ribosomal protein S1 unwinds double-stranded RNA in multiple steps. Proc Natl Acad Sci U S A. 2012 Sep 4;109(36):14458-63. doi: 10.1073/pnas.1208950109.

24. Duval M, Korepanov A, Fuchsbauer O, Fechter P, Haller A, Fabbretti A, Choulier L, Micura R, Klaholz BP, Romby P, Springer M, Marzi S. Escherichia coli ribosomal protein S1 unfolds structured mRNAs onto the ribosome for active translation initiation. PLoS Biol. 2013 Dec;11(12):e1001731. doi: 10.1371/journal.pbio.1001731.

25. Vasilyev NN, Kutlubaeva ZS, Ugarov VI, Chetverina HV, Chetverin AB. Ribosomal protein S1 functions as a termination factor in RNA synthesis by Qβ phage replicase. Nat Commun. 2013;4:1781. doi: 10.1038/ncomms2807.

26. Takeshita D, Yamashita S, Tomita K. Molecular insights into replication initiation by Qβ replicase using ribosomal protein S1. Nucleic Acids Res. 2014;42(16):10809-22. doi: 10.1093/nar/gku745.

27. Gytz H, Mohr D, Seweryn P, Yoshimura Y, Kutlubaeva Z, Dolman F, Chelchessa B, Chetverin AB, Mulder FA, Brodersen DE, Knudsen CR. Structural basis for RNA-genome recognition during bacteriophage Qβ replication. Nucleic Acids Res. 2015 Dec 15;43(22):10893-906. doi: 10.1093/nar/gkv1212.

28. Sukhodolets MV, Garges S, Adhya S. Ribosomal protein S1 promotes transcriptional cycling. RNA. 2006 Aug;12(8):1505-13. doi: 10.1261/rna.2321606.

29. Karzai AW, Roche ED, Sauer RT. The SsrA-SmpB system for protein tagging, directed degradation and ribosome rescue. Nat Struct Biol. 2000 Jun;7(6):449-55. doi: 10.1038/75843.

30. Wower IK, Zwieb CW, Guven SA, Wower J. Binding and cross-linking of tmRNA to ribosomal protein S1, on and off the Escherichia coli ribosome. EMBO J. 2000 Dec 1;19(23):6612-21. doi: 10.1093/emboj/19.23.6612.

31. Bordeau V, Felden B. Ribosomal protein S1 induces a conformational change of tmRNA; more than one protein S1 per molecule of tmRNA.. *Biochimie*, Elsevier, 2002, 84 (8), pp.723-9. Doi:10.1016/S0300-9084(02)01442-6

32. Saguy M, Gillet R, Skorski P, Hermann-Le Denmat S, Felden B. Ribosomal protein S1 influences trans-translation in vitro and in vivo. Nucleic Acids Res. 2007;35(7):2368-76. doi: 10.1093/nar/gkm100.

33. Gillet R, Kaur S, Li W, Hallier M, Felden B, Frank J. Scaffolding as an organizing principle in trans-translation. The roles of small protein B and ribosomal protein S1. J Biol Chem. 2007 Mar 2;282(9):6356-63. doi: 10.1074/jbc.M609658200.

34. Kaberdin VR, Bläsi U. Translation initiation and the fate of bacterial mRNAs. FEMS Microbiol Rev. 2006 Nov;30(6):967-79. doi: 10.1111/j.1574-6976.2006.00043.x.

35. Punjani A, Rubinstein JL, Fleet DJ, Brubaker MA. cryoSPARC: algorithms for rapid unsupervised cryo-EM structure determination. Nat Methods. 2017 Mar;14(3):290-296. doi: 10.1038/nmeth.4169

36. Scheres SH. RELION: implementation of a Bayesian approach to cryo-EM structure determination. J Struct Biol. 2012 Dec;180(3):519-30. doi: 10.1016/j.jsb.2012.09.006.

37. Zheng SQ, Palovcak E, Armache JP, Verba KA, Cheng Y, Agard DA. MotionCor2: anisotropic correction of beam-induced motion for improved cryo-electron microscopy. Nat Methods. 2017 Apr;14(4):331-332. doi: 10.1038/nmeth.4193.

38. Zhang K. Gctf: Real-time CTF determination and correction. J Struct Biol. 2016 Jan;193(1):1-12. doi: 10.1016/j.jsb.2015.11.003. Epub 2015 Nov 19. PMID: 26592709; PMCID: PMC4711343.

39. Pettersen EF, Goddard TD, Huang CC, Couch GS, Greenblatt DM, Meng EC, Ferrin TE. UCSF Chimera--a visualization system for exploratory research and analysis. J Comput Chem. 2004 Oct;25(13):1605-12. doi: 10.1002/jcc.20084.

40. Pintilie GD, Zhang J, Goddard TD, Chiu W, Gossard DC. Quantitative analysis of cryo-EM density map segmentation by watershed and scale-space filtering, and fitting of structures by alignment to regions. J Struct Biol. 2010 Jun;170(3):427-38. doi: 10.1016/j.jsb.2010.03.007.

41. Burnley T, Palmer CM, Winn M. Recent developments in the CCP-EM software suite. Acta Crystallogr D Struct Biol. 2017 Jun 1;73(Pt 6):469-477. doi: 10.1107/S2059798317007859.

42. Pandurangan AP, Topf M. RIBFIND: a web server for identifying rigid bodies in protein structures and to aid flexible fitting into cryo EM maps. Bioinformatics. 2012 Sep 15;28(18):2391-3. doi: 10.1093/bioinformatics/bts446.

43. Topf M, Lasker K, Webb B, Wolfson H, Chiu W, Sali A. Protein structure fitting and refinement guided by cryo-EM density. Structure. 2008 Feb;16(2):295-307. doi: 10.1016/j.str.2007.11.016.

44. Murshudov GN, Skubák P, Lebedev AA, Pannu NS, Steiner RA, Nicholls RA, Winn MD, Long F, Vagin AA. REFMAC5 for the refinement of macromolecular crystal structures. Acta Crystallogr D Biol Crystallogr. 2011 Apr;67(Pt 4):355-67. doi: 10.1107/S0907444911001314.

45. Jakobi AJ, Wilmanns M, Sachse C. Model-based local density sharpening of cryo-EM maps. Elife. 2017 Oct 23;6:e27131. doi: 10.7554/eLife.27131. PMID: 29058676; PMCID: PMC5679758.

46. Emsley P, Cowtan K. Coot: model-building tools for molecular graphics. Acta Crystallogr D Biol Crystallogr. 2004 Dec;60(Pt 12 Pt 1):2126-32. doi: 10.1107/S0907444904019158.

47. Liebschner D, Afonine PV, Baker ML, Bunkóczi G, Chen VB, Croll TI, Hintze B, Hung LW, Jain S, McCoy AJ, Moriarty NW, Oeffner RD, Poon BK, Prisant MG, Read RJ, Richardson JS, Richardson DC, Sammito MD, Sobolev OV, Stockwell DH, Terwilliger TC, Urzhumtsev AG, Videau LL, Williams CJ, Adams PD. Macromolecular structure determination using X-rays, neutrons and electrons: recent developments in Phenix. Acta Crystallogr D Struct Biol. 2019 Oct 1;75(Pt 10):861-877. doi: 10.1107/S2059798319011471.

48. Afonine PV, Poon BK, Read RJ, Sobolev OV, Terwilliger TC, Urzhumtsev A, Adams PD. Real-space refinement in PHENIX for cryo-EM and crystallography. Acta Crystallogr D Struct Biol. 2018 Jun 1;74(Pt 6):531-544. doi: 10.1107/S2059798318006551.

49. Kaledhonkar S, Fu Z, Caban K, Li W, Chen B, Sun M, Gonzalez RL Jr, Frank J. Late steps in bacterial translation initiation visualized using time-resolved cryo-EM. Nature. 2019 Jun;570(7761):400-404. doi: 10.1038/s41586-019-1249-5.

50. Ahmed T, Shi J, Bhushan S. Unique localization of the plastid-specific ribosomal proteins in the chloroplast ribosome small subunit provides mechanistic insights into the chloroplastic translation. Nucleic Acids Res. 2017 Aug 21;45(14):8581-8595. doi: 10.1093/nar/gkx499.

51. Desai N, Brown A, Amunts A, Ramakrishnan V. The structure of the yeast mitochondrial ribosome. Science. 2017 Feb 3;355(6324):528-531. doi: 10.1126/science.aal2415.

52. Vandekerckhove J, Rombauts W, Peeters B, Wittmann-Liebold B. Determination of the complete amino acid sequence of protein S21 from Escherichia coli ribosomes. Hoppe Seylers Z Physiol Chem. 1975 Dec;356(12):1955-76. doi: 10.1515/bchm2.1975.356.2.1955.

53. Van Duin J, Wijnands R. The function of ribosomal protein S21 in protein synthesis. Eur J Biochem. 1981 Sep 1;118(3):615-9. doi: 10.1111/j.1432-1033.1981.tb05563.x.

54. Held, W.A., Nomura, M. & Hershey, J.W.B. Ribosomal protein S21 is required for full activity in the initiation of protein synthesis. *Molec. Gen. Genet.* **128,** 11–22 (1974). https://doi.org/10.1007/BF00267291

55. Beckert B, Turk M, Czech A, Berninghausen O, Beckmann R, Ignatova Z, Plitzko JM, Wilson DN. Structure of a hibernating 100S ribosome reveals an inactive conformation of the ribosomal protein S1. Nat Microbiol. 2018 Oct;3(10):1115-1121. doi: 10.1038/s41564-018-0237-0.

56. Jenner LB, Demeshkina N, Yusupova G, Yusupov M. Structural aspects of messenger RNA reading frame maintenance by the ribosome. Nat Struct Mol Biol. 2010 May;17(5):555-60. doi: 10.1038/nsmb.1790.

57. Gualerzi CO, Pon CL. Initiation of mRNA translation in bacteria: structural and dynamic aspects. Cell Mol Life Sci. 2015 Nov;72(22):4341-67. doi: 10.1007/s00018-015-2010-3.

58. Katayama A, Tsujii A, Wada A, Nishino T, Ishihama A. Systematic search for zinc-binding proteins in Escherichia coli. Eur J Biochem. 2002 May;269(9):2403-13. doi: 10.1046/j.1432-1033.2002.02900.x.

59. Ashkenazy H, Abadi S, Martz E, Chay O, Mayrose I, Pupko T, Ben-Tal N. ConSurf 2016: an improved methodology to estimate and visualize evolutionary conservation in macromolecules. Nucleic Acids Res. 2016 Jul 8;44(W1):W344-50. doi: 10.1093/nar/gkw408.

SUPPLEMENTARY INFORMATION

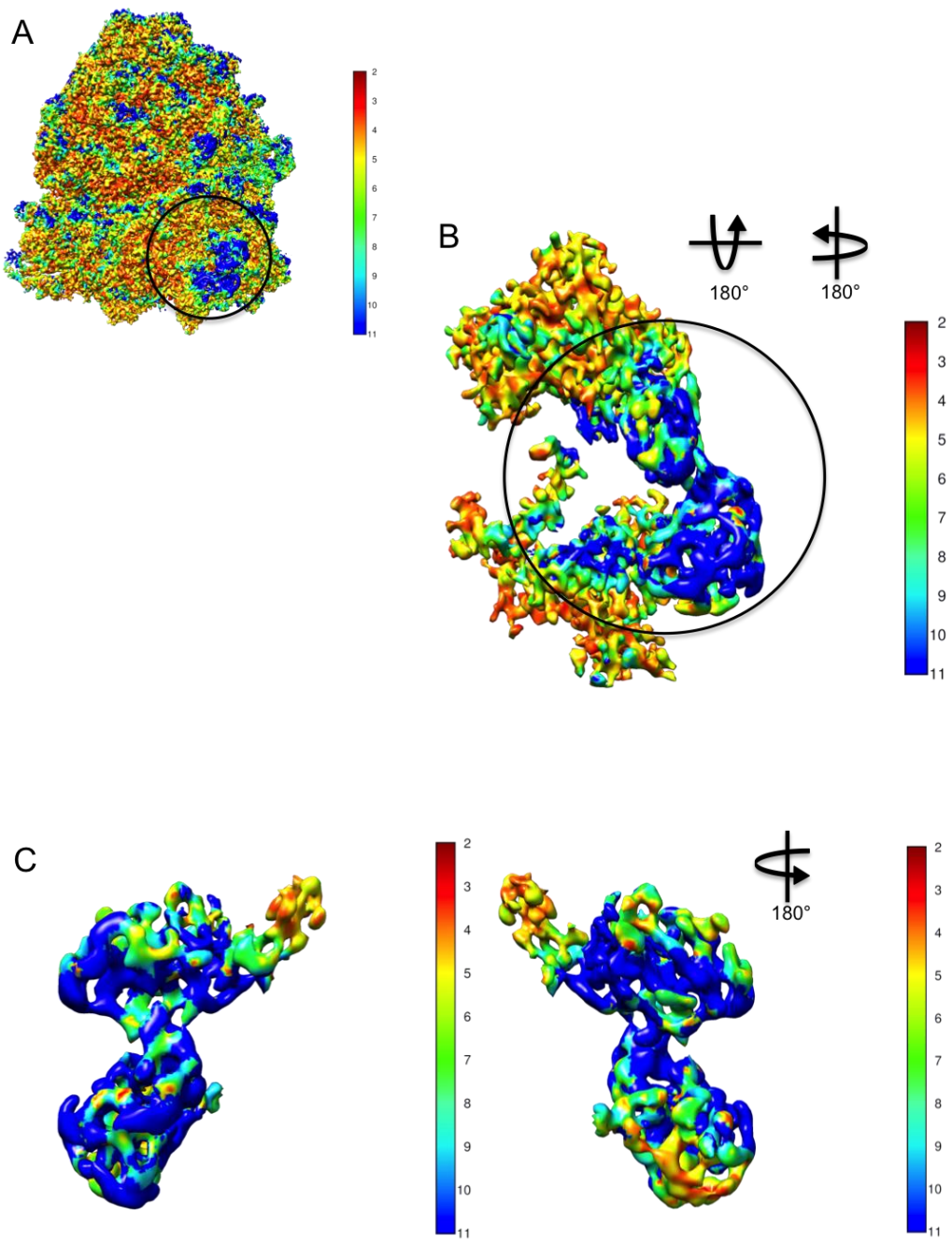

Supplementary Figure 1: cryo-EM map of the ribosome-bound bS1 protein. *A – Local-resolution map of the translating ribosome in complex with bS1 N-terminal domains. B – Focus on the bS1 binding site at the mRNA exit channel. C – Local-resolution map of bS1 N-terminal domains for the side that faces the external surface (left) and that which faces the ribosome (right).*

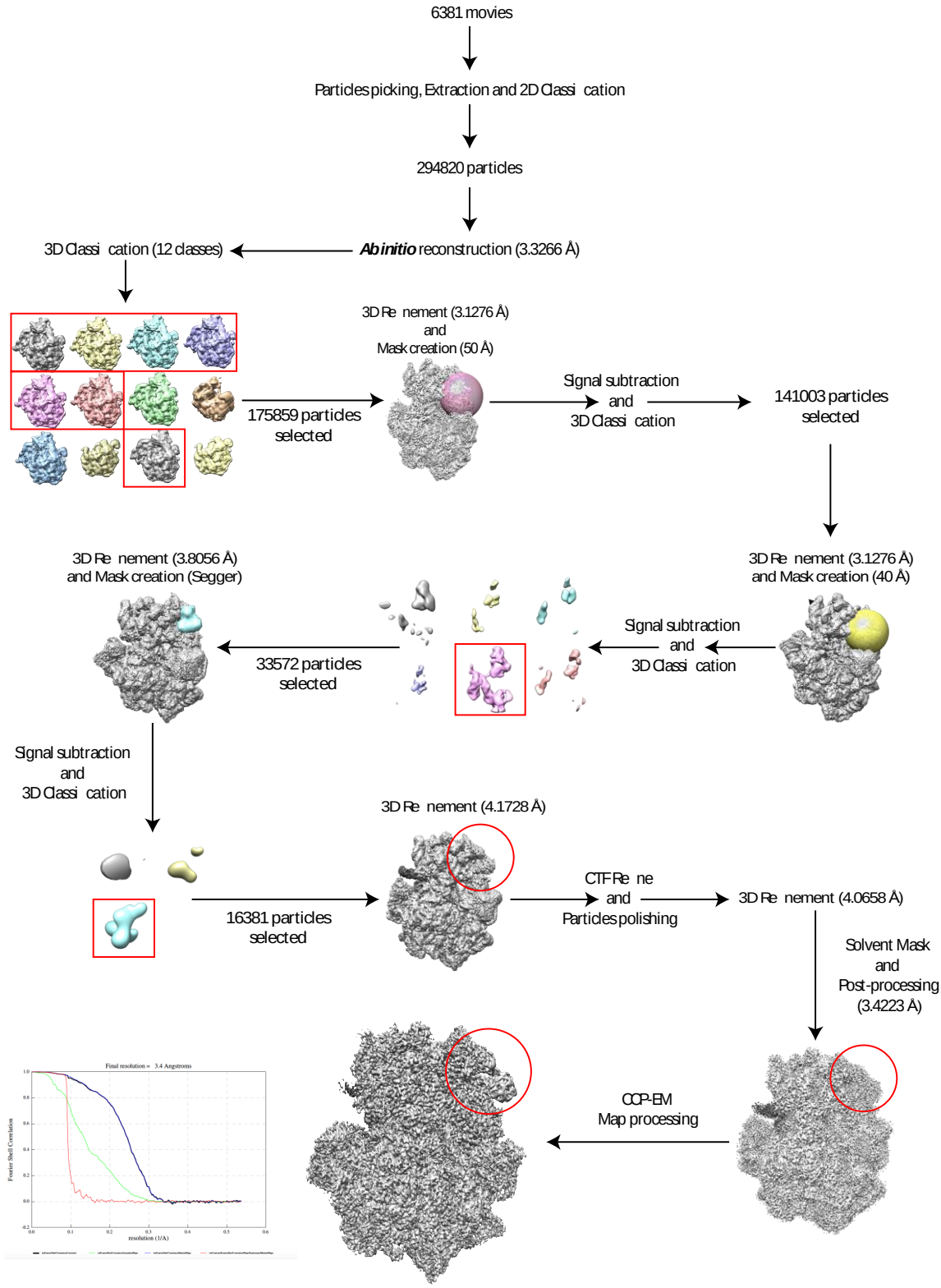

Supplementary Figure 2: Image analysis protocol. *Workflow adopted during the image analysis in order to obtain the final cryo-EM map*

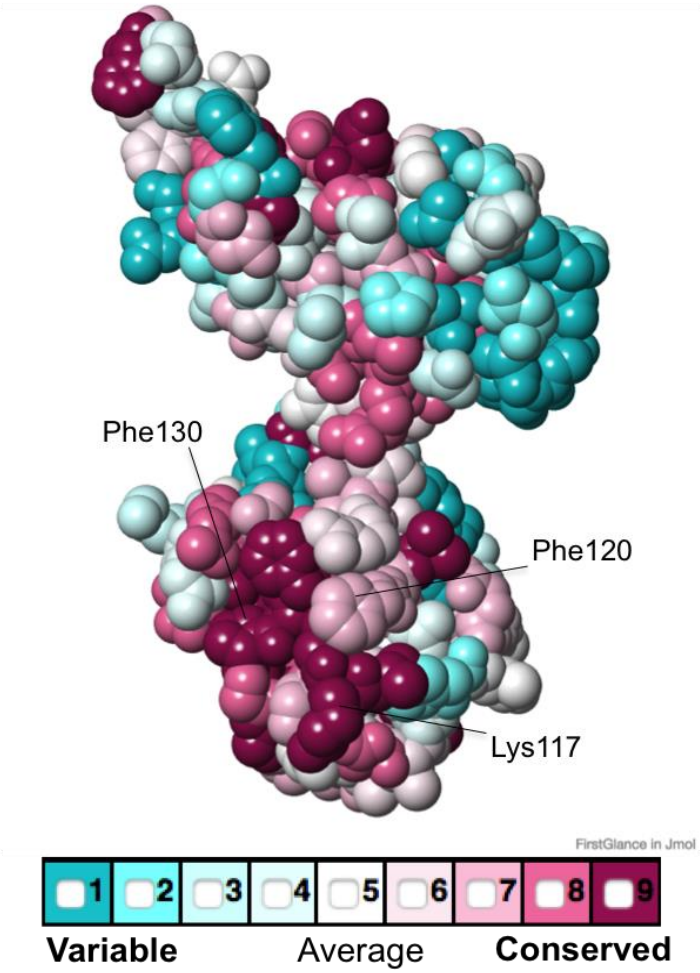

Supplementary Figure 3: Sequence analysis between bS1 and its homologues. *Analysis of the conservation scores of the residues forming the first two N-terminal domains of bS1. The scores are calculated based on the sequence alignments of 150 bS1 homologues, and range from low (blue) to high (purple).*

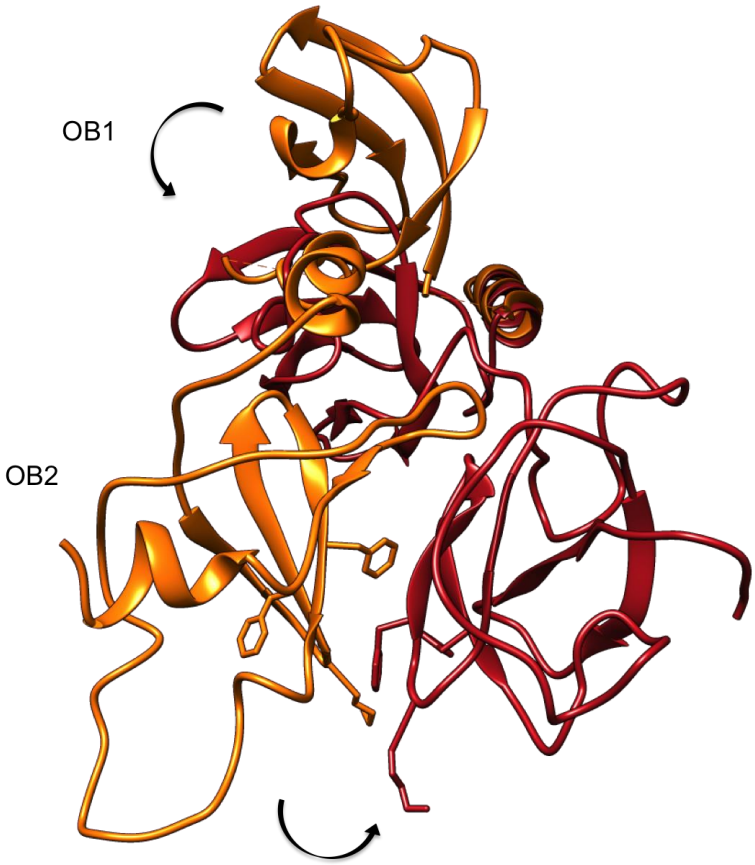

Supplementary Figure 4: Atomic model comparison between our model and a previous bS1 structure. *Comparison between the new conformation described in our bS1 model (red) and the conformation reported in previous structural studies (PDB file 6BU8, orange).*

3.3 Conclusion and perspectives

The work conducted has allowed us to expand the knowledge related to the bS1 protein, one of the fundamental promoters of the initiation of canonical translation, as well as of the initial stages of *trans*-translation.

The results derived from this study are necessary to amplify an increasingly complete scenario related to the role of this protein, which, given its importance in the course of protein synthesis and, apparentely, during *trans*-translation. On one hand, although we confirmed the role of OB1 domain in stabilizing the anchoring with the ribosomal platform, on the other hand, interesting new observations have been made for OB2. Contrary to what might have been thougth, this domain turns out to be involved in interacting with the mRNA by stabilizing and strengthening the SD – anti-SD interaction. Based on that, further studies are needed to enable a better understanding of its functioning during not only canonical transaltion but also during *trans*-translation, to better understand the interaction between the protein and the tmRNA-SmpB complex. Any further findings, in our case especially during the process of *trans*-translation, may help us to enrich the knowledge related to this mechanism that represents one of the most important target against which to develop molecules with antibacterial activity.

V – GENERAL CONCLUSION

V GENERAL CONCLUSION

To address the growing and increasingly problem of antibiotic resistance, mechanisms rescuing stalled ribosomes during translation of defective mRNAs have been recently proposed as new targets to develop antimicrobial compounds. Indeed, they are often essential for bacterial cell viability and they are very different in eukaryotes. For this reason, in the course of this Ph.D., we focused on the study of the main rescue system present in bacteria, known as *trans*-translation, and we applied ourselves to understand its dynamics through the characterization of the different actors that are participating in this complex ballet. First, we studied the different conformations assumed by the tmRNA-SmpB complex during the different steps of the mechanism, trying to glimpse at new interesting molecular interactions underlying the whole process. Obtaining four high-resolution structures characterizing different steps of *trans*-translation allowed us to better understand how this bacterial life-saving machine functions. In particular, we shed light on how the complex formed by tmRNA-SmpB recognizes and enters a stalled ribosome, how it selects the correct resume codon present within the MLD, and how it moves within the ribosome, from the A site to the P site. Among the various contacts that occur between the two partners, it is worth noting the insertion of the tmRNA G19 base within a hydrophobic pocket formed by three leucines at positions 90, 91, 91 on the body of SmpB, the maintenance of which is essential for the smooth performance of *trans*-translation since it has been observed that the G19C mutation induces a loss of rescue activity (Hanawa-Suetsugu et al., 2002). This interaction may therefore represent a potential target against which to develop new molecules with anti - *trans*-translational activity. However, it remains to be understood how the mechanism evolves once the tmRNA arrives within the E site, exits the ribosome, and canonical translation resumes on the ORF placed within the tmRNA MLD portion. In addition, the third major player involved in this mechanism, represented by RNase R, remains to be characterized. During this work we were able to visualize, both biochemically and structurally, for the first time RNase R bound to a stalled ribosome. Biochemical evidences assured us of strong binding between the protein and the ribosomal platform, while structural analysis confirmed that this interaction takes place exactly at the level of the mRNA entry channel, where the H5 helix and the second pseudoknot of tmRNA are usually located. In this regard, several tests have been

carried out to study the behavior of both RNase R and the tmRNA-SmpB complex simultaneously during *trans*-translation in presence of a stalled ribosome on a non-stop messenger. These evidences have led to the conclusion that RNase R and parts of the tmRNA have the same binding site at the surface of the ribosome SSU. Moreover, the interaction between the ribosome and tmRNA-SmpB turns out to be much stronger than the one occurring between RNase R and the ribosome. The high-resolution study of RNase R did not allow us to describe the molecular interactions underlying its binding to the ribosome because of an intrinsic dynamicity and flexibility that was highly difficult to account for during image analysis. However, our preliminary results, which clearly suggest a competition between the tmRNA-SmpB complex and RNase R for the same stalled ribosome, lead us to initiate a new step in the research work. In fact, relying on the literature from which we know that both players intervene simultaneously during *trans*-translation, and, at the same time, on the scientific evidence developed in our laboratory, we hypothesized that the two actors intervene simultaneously during the process, acting, however, on two different ribosomes stalled on the same defective messenger. To verify this hypothesis we obtained the first reconstructions of disomes undergoing *trans*-translation. Looking at the latest work on an additional rescue factor during the protein synthesis, called SmrB (Saito et al., 2022), the RNase R probably interacts differently from what we have observed previously on single-stalled ribosomes. In this case, the mRNA entrance channel at the interface between the two collided ribosomes is partially occupied by SmrB causing competition for the binding to this area. Thus, we can assume a new binding site for the RNase R involving a waiting phase during which is bound in a different zone of the ribosome before intervening in defective messenger degradation. This question is still open and we are still working on it. On the other hand, the disomes in complex with tmRNA-SmpB are going to be analyzed at high-resolution in order to get a new and a more complete description of the entire process at the molecular level.

In the course of our studies, we also got interested in an additional functional element essential during canonical translation, as well as of primary importance during *trans*-translation: the bS1 protein. As shown in previous studies (Saguy et al., 2007), bS1 turns out to be essential for the mRNA-like activity of tmRNA. In fact, it has been hypothesized that bS1 prevents degradation of tmRNA before it reaches the ribosome or helps tmRNA itself to correctly position its ORF within the decoding

center. (Saguy et al., 2007). To this end, we obtained the first cryo-EM structure of the first two domains of bS1 (OB1 and OB2) bound to an elongation competent (EC) ribosome, the three other domains being too flexible to be properly resolved. In addition, to confirming what was already known, we were able to observe a completely new function related to the OB2 domain, which appears to directly interact with the Shine-Dalgarno portion of the messenger end. These results complete and increase the knowledge regarding the mechanism of action of the protein during the early stages of translation, thereby opening the doors toward a clearer understanding of its function. The results obtained in this study will have to be followed by other efforts with the aim of clarifying the role of this protein during the canonical mechanism of translation, as well as during *trans*-translation.

Many questions are left unanswered and new studies are needed along the lines of those addressed during this doctoral work. To conclude, as we have seen, *trans*-translation is an appealing target for new antibiotics given its importance for the survival of numerous bacterial species and, at the same time, its absence in eukaryotic organisms. The molecular and structural studies of the different partners, which are contributing to this rescue mechanism, give a more complete description of how the process takes place, emphasizing especially the main differences with canonical translation. The thoroughness of this work has enabled us, thus, to find out regions that could serve as a specific target to inhibit *trans*-translation and develop a new class of antibiotics. Any study in this direction will lay the groundwork in fighting against antibiotic resistance.

IV - BIBLIOGRAPHY

Abo, T., Ueda, K., Sunohara, T., Ogawa, K., and Aiba, H. (2002). SsrA-mediated protein tagging in the presence of miscoding drugs and its physiological role in Escherichia coli. Genes Cells **7**, 629**–**638.

Achenbach, J., and Nierhaus, K.H. (2015). The mechanics of ribosomal translocation. Biochimie 114, 80**–**89.

Adrian, M., Dubochet, J., Lepault, J., and McDowall, A.D. (1984). Cryo-electron microscopy of viruses. *Nature* **308,** 32–36.

Alberts, B., Johnson, A., Lewis, J., Raff, M., Roberts, K., and Walter, P. (2002). Molecular Biology of the Cell. 4th edition. New York: Garland Science.

Almgren, M., Edwards, K., and Gustafsson, J. (1996). Cryotransmission electron microscopy of thin vitrified samples. Current Opinion in Colloid & Interface Science, Vol 1, Issue 2, pp 270-278.

Andrade, J. M., Cairrão, F., and Arraiano, C. M. (2006). RNase R affects gene expression in stationary phase: regulation of ompA. *Molecular microbiology*, *60*(1), 219-228.

Arraiano, C. M., Andrade, J. M., Domingues, S., Guinote, I. B., Malecki, M., Matos, R. G., Moreira, R.N., Pobre, V., Reis, F.P., Saramaga, M., Silva, I.J., and Viegas, S. C. (2010). The critical role of RNA processing and degradation in the control of gene expression. *FEMS microbiology reviews*, *34*(5), 883-923.

Awano, N., Rajagopal, V., Arbing, M., Patel, S., Hunt, J., Inouye, M., and Phadtare, S. (2010). Escherichia coli RNase R has dual activities, helicase and RNase. *Journal of bacteriology*, *192*(5), 1344-1352.

Bai, X.C., McMullan, G., and Scheres, S.H. (2015). How cryo-EM is revolutionizing structural biology. Trends Biochem Sci. 40(1):49-57.

Ban, N., Nissen, P., Hansen, J., Moore, P.B., and Steitz, T. (2000). The Complete Atomic Strucutre of the Large Ribosomal Subunit at 2.4 Å Resolution. Science, vol 289, Issue 5481, pp. 905-920.

Ban, N., Beckmann, R., Cate, J.H., Dinman, J.D., Dragon, F., Ellis, S.R., Lafontaine, D.L., Lindahl, L., Liljas, A., Lipton, J.M., et al. (2014). A new system for naming ribosomal proteins. Curr Opin Struct Biol 24, 165**–**169.

Barends, S., Kraal, B., and van Wezel, G.P (2011). The tmRNA-tagging mechanism and the control of gene expression: a review. Wiley Interdiscip Rev RNA. Mar-Apr;2(2):233-46.

Bellare, J.R., Davis, H.T., Scrive, L.E., and Talmon, Y. (1988). Controlled environment vitrification system: An improved sample preparation technique. J. of Electron Microscopy Technique, Vol 10, Issue 1, pp 87-111.

Ben-Shem, A., Garreau De Loubresse, N., Melnikov, S., Jenner, L., Yusupova, G., and Yusupov, M. (2011). The Structure of the Eukaryotic Ribosome at 3.0 Å Resolution. Science, Vol 334, Issue 6062, pp. 1524-1529.

Berchtold, H., Reshetnikova, L., Reiser, C., Schirmer, N., Sprinzl, M., and `hilgenfeld, R. (1993). Crystal structure of active elongation factor Tu reveals major domain rearrangements. *Nature* **365,** 126–132.

Betts, J.C., Lukey, P.T., Robb, L.C., McAdam, R.A., and Duncan, K. (2002). Evaluation of a nutrient starvation model of Mycobacterium tuberculosis persistence by gene and protein expression profiling. Mol Microbiol. 43(3):717-31.

Blaha, G., Stanley, R.E., and Steitz, T.A. (2009). Formation of the First Peptide Bond: The Structure of EF-P Bound to the 70S Ribosome. Science 325, 966**–**970.

Blanchard, S., Gonzalez, R., Kim, H., Chu, S., and Puglisi, J.D. (2004). tRNA selection and kinetic proofreading in translation. *Nat Struct Mol Biol* **11,** 1008–1014

Bordeau, V., and Felden, B. (2002). Ribosomal protein S1 induces a conformational change of tmRNA; more than one protein S1 per molecule of tmRNA. *Biochimie*, *84*(8), 723-729.

Bordes, P., Cirinesi, A. M., Ummels, R., Sala, A., Sakr, S., Bitter, W., and Genevaux, P. (2011). SecB-like chaperone controls a toxin–antitoxin stress-responsive system in Mycobacterium tuberculosis. *Proceedings of the National Academy of Sciences*, *108*(20), 8438-8443.

Bordes, P., Sala, A. J., Ayala, S., Texier, P., Slama, N., Cirinesi, A. M., Guillet, V., Mourey, L., and Genevaux, P. (2016). Chaperone addiction of toxin–antitoxin systems. *Nature communications*, *7*(1), 1-12.

Booth, D.S., Avila-Sakar, A., and Cheng, Y. (2011). Visualizing proteins and macromolecular complexes by negative stain EM: from grid preparation to image acquisition. J. Vis. Exp.58:3227.

Bornemann, T., Holtkamp, W., and Wintermeyer, W. (2014). Interplay between trigger factor and other protein biogenesis factors on the ribosome. Nature Communications **5**, 4180.

Bracewell, R.N. (2000). The Fourier Transform and Its Applications. McGraw-Hill, Boston.

Brock, J.E., Pourshahian, S., Giliberti, J., Limbach, P.A., and Janssen, G.R. (2008). Ribosomes bind leaderless mRNA in Escherichia coli through recognition of their 5′-terminal AUG. RNA 14, 2159–2169.

Burnett, B.J., Altman, R.B., Ferrao, R., Alejo, J.L., Kaur, N., Kanji, J., and Blanchard, S.C. (2013). Elongation Factor Ts Directly Facilitates the Formation and Disassembly of the Escherichia coli Elongation Factor Tu·GTP·Aminoacyl-tRNA Ternary Complex. J Biol Chem 288, 13917**–**13928.

Buskirk, A.R., and Green, R. (2013). Getting Past Polyproline Pauses. Science 339, 38–39.

Caban, K., Pavlov, M., Ehrenberg, M., and Gonzalez, R.L. (2017). A conformational switch in initiation factor 2 controls the fidelity of translation initiation in bacteria. Nat Commun **8**, 1475.

Cairrao, F*.,* Cruz, A*.,* Mori, H*., and* Arraiano, C.M. *(*2003*)* Cold shock induction of RNase R and its role in the maturation of the quality control mediator SsrA/tmRNA*.* Mol Microbiol 50*:* 1349–1360*.*

Campos-Silva, R., D'Urso, G., Delalande, O., Giudice, E., Macedo, A.J., Gillet, R. (2022). *Trans*-Translation Is an Appealing Target for the Development of New Antimicrobial Compounds. *Microorganisms*, *10*, 3

Carter, A.P., Clemons, W.M., Brodersen, D.E., Morgan-Warren, R.J., Wimberly, B.T., and Ramakrishnan, V. (2000). Functional insights from the structure of the 30S ribosomal subunit and its interactions with antibiotics. Nature 407(6802):340-8.

Castanié-Cornet, M.-P., Bruel, N., and Genevaux, P. (2014). Chaperone networking facilitates protein targeting to the bacterial cytoplasmic membrane. Biochim. Biophys. Acta 1843, 1442**–**1456.

Cerullo, F., Filbeck, S., Patil, P.R., Hung, H.C., Xu, H., Vonberger, J., Hofer, F.W., Schmitt, J., Kramer, G., Bukau, B., Hofmann, K., Pfeffer, S., Joazeiro, C.AP. (2022). Bacterial Ribosome Collision Sensing by a MutS DNA Repair ATPase Paralogue. Nature 603(7901):509-514.

Chadani, Y., Ito, K., Kutsukake, K., and Abo, T. (2012). ArfA recruits release factor 2 to rescue stalled ribosomes by peptidyl-tRNA hydrolysis in Escherichia coli. Mol. Microbiol. 86, 37**–**50.

Chadani, Y., Matsumoto, E., Aso, H., Wada, T., Kutsukake, K., Sutou, S., and Abo, T. (2011). trans-translation-mediated tight regulation of the expression of the alternative ribosome-rescue factor ArfA in Escherichia coli. Genes Genet. Syst. 86, 151**–**163.

Chadani, Y., Ono, K., Ozawa, S.-I., Takahashi, Y., Takai, K., Nanamiya, H., Tozawa, Y., Kutsukake, K., and Abo, T. (2010). Ribosome rescue by Escherichia coli ArfA (YhdL) in the absence of trans-translation system. Mol. Microbiol. 78, 796**–**808.

Chen, C., and Deutscher, M.P. (2010). RNase R is a highly unstable protein regulated by growth phase and stress. *Rna*, *16*(4), 667-672.

Cheng, Z. F., and Deutscher, M. P. (2005). An important role for RNase R in mRNA decay. *Molecular cell*, *17*(2), 313-318.

Cheng, Z.F., and Deutscher, M.P. (2002). Purification and Characterization of the Eschericia coli Exoribonuclease RNase R. JBC, Vol 277, Issue 24, pp 21624-21629.

Cheng, Y., Grigorieff, N., Penczek, P.A., and Walz, T. (2015). A primer to single-particle cryo-electron microscopy. *Cell* **161**, 438–449.

Chu, L.Y., Hsieh, T.J., Golzarroshan, B., Chen, Y.P., Agrawal, S., Yuan, H.S. (2017). Structural insights into RNA unwinding and degradation by RNase R. Nucleic Acids Res. 45(20):12015-12024.

Condon, C. *(*2007*).* Maturation and degradation of RNA in bacteria*.* Curr Opin Microbiol 10*:* 271–278*.*

Connell, S., Topf, M., Qin, Y. Wilson, D.N., Mielke, T., Fucini, P., Nierhaus, K.H., and Spahn, C.M.T. (2008). A new tRNA intermediate revealed on the ribosome during EF4-mediated back-translocation. *Nat Struct Mol Biol* **15,** 910–915

Correll, C.C., Munishkin, A., Chan, Y.L., Ren, Z., Wool, I.G., and Steitz, T. (1998). Crystal structure of the ribosomal RNA domain essential for binding elongation factors. PNAS, 95 (23) 13436-13441.

Crowe-McAuliffe, C., Takada, H., Murina, V., Polte, C., Kasvandik, S., Tenson, T., Ignatova, Z., Atkinson, G.C., Wilson, D.N., and Hauryliuk, V. (2021). Structural Basis for Bacterial Ribosome-Associated Quality Control by RqcH and RqcP. Mol Cell. 7;81(1):115-126.e.7.

Crowther, R.A., DeRosier, D.J., and Klug, A. (1970). The reconstruction of a three-dimensional strucutre from projections and its application to electron microscopy. Proceedings of the Royal Society A, Vol 317, Issue 15330.

D'Urso, G., Guyomar, C., Chat, S., Giudice, E., and Gillet, R. (2022). Insights into the ribosomal trans-translation rescue system: lessons from recent structural studies. FEBS J. https://doi.org/10.1111/febs.16349.

Demo, G., Svidritskiy, E., Madireddy, R., Diaz-Avalos, R., Grant, T., Grigorieff, N., Sousa, D., and Korostelev, A.A. (2017). Mechanism of ribosome rescue by ArfA and RF2.

Deutscher, M.P., and Li, Z. (2000). Exoribonucleases and their multiple roles in RNA metabolism. Progress in Nucleic Acid Research and Molecular Biology, Vol 66, pp 67-105.

Diaconu, M., Kothe, U., Schlünzen, F., Fischer, N., Harms, J.M., Tonevitsky, A.G., Stark, H., Rodnina, M.V., and Wahl, M.C. (2005). Structural basis for the function of the ribosomal L7/12 stalk in factor binding and GTPase activation. Cell 121, 991**–** 1004.

Domingues, S., Moreira, R. N., Andrade, J. M., Dos Santos, R. F., Bárria, C., Viegas, S. C., and Arraiano, C. M. (2015). The role of RNase R in trans-translation and ribosomal quality control. *Biochimie*, *114*, 113-118.

Dubochet, J., and McDowall, A.W. (1981. Vitrification of pure water electron

microscopy. J. of Microscopy, Vol 124, Pt. 3, pp RP3-RP4.

Dubochet, J., Chang, J.J., Freeman, R., Leapult, J., and McDowall, A.W. (1982b). Frozen aqueous suspensios. Ultramicroscopy, Vol 10, Issues 1-2, pp 55-61.

Dubochet, J., Lepault,J., Freeman, R., Berriman, J.A., and Homo, J.C. (1982b). Electron microscopy of frozen water and aqueous solutions. J. of Microscopy, Vol 128, Issue 3, pp 219-237.

Dunkle, J.A., and Cate, J.H.D. (2010). Ribosome Structure and Dynamics During Translocation and Termination. Annu. Rev. Biophys. 39, 227–244.

Faruqi, A.R., and Henderson, R. (2007). Electric detectros for electron microscopy. Current Opinion in Structural Biology, Vol 17, Issue 5, pp 549-555.

Fey, P.D., Endres, J.L., Yajjala, V.K., Widhelm, T.J., Boissy, R.J., Bose, J.L., and Bayles, K.W. (2013). A genetic resource for rapid and comprehensive phenotype screening of nonessential Staphylococcus aureus genes. mBio 4(1):e00537-12.

Filbeck, S., Cerullo, F., Paternoga, H., Tsaprailis, G., Joazeiro, C.A.P., and Pfeffer, S. (2021). Mimicry of Canonical Translation Elongation Underlines Alanine Tail Synthesis in RQC. Mol Cell. 81, 104.e6-114.e6.

Fischer, N., Neumann, P., Konevega, A.L., Bock, L.V., Ficner, R., Rodnina, M.V., and Stark, H. (2015). Structure of the E. coli ribosome–EF-Tu complex at <3 Å resolution by Cs-corrected cryo-EM. Nature 520, 567–570.
Frank, J. (1996). Three-Dimensional Electron Microscopy of Macromolecular Assemblies. Academic Press, San Diego, pp 12–53.

Fivian-Hughes, A. S., and Davis, E. O. (2010). Analyzing the regulatory role of the HigA antitoxin within Mycobacterium tuberculosis. *Journal of bacteriology*, *192*(17), 4348-4356.

Frischmayer, P.A., van Hoof, A., O'Donnel, K., Guerrerio, A.L., Parker, R., and Dietz, H.C. (2002). An mRNA Surveillance Mechanism That Eliminates Transcripts Lacking Termination Codons. Science, Vol 295, Issue 5563, pp. 2258-2261.

Gagnon, M.G., Seetharaman, S.V., Bulkley, D., and Steitz, T.A. (2012). Structural basis for the rescue of stalled ribosomes: structure of YaeJ bound to the ribosome. Science 335, 1370–1372.

Gamow G. (1954). Possible Relation between Deoxyribonucleic Acid and Protein Structures. Nature 173, 318.

Gan, L., Chen, S., and Jensen, G.J. (2008). Molecular organization of Gram-negative peptidoglycan. Proc Natl Acad Sci U S A 105, 18953-18957.

Gao, N., Zavialov, A.V., Li, W., Sengupta, J., Valle, M., Gursky, R.P., Ehrenberg, M., and Frank, J. (2005). Mechanism for the Disassembly of the Posttermination Complex Inferred from Cryo-EM Studies. Molecular Cell Vol 18, Issue 6, pp 663-674.

Garrett, R.A., and Grishman, C. (2009). Biochemestry (4th ed.). Cengage Learning Services.

Garrett, R.A., and Rodriguez-Fonseca, C. (1996). Ribosomal RNA: Structure, Evolution, Processing and Function in Protein Biosynthesis. CRC Press, Boca Raton, FL, pp. 327-335.

Garza-Sánchez, F., Shoji, S., Fredrick, K., and Hayes, C.S. (2009). RNase II is important for A-site mRNA cleavage during ribosome pausing. Mol. Microbiol. 73, 882**–**897.

Garza-Sanchez, F., Schaub, R.E., Janssen, B.D., and Hayes, C.S. (2011). tmRNA regulates synthesis of the ArfA ribosome rescue factor. Molecular microbiology, Vol 80, Issue 5, pp 1204-1219.

Ge, Z., Mehta, P., Richards, J., and Karzai, A.W. (2010). Non-stop mRNA decay initiates at the ribosome. *Molecular microbiology*, *78*(5), 1159-1170.

Giudice, E., and Gillet, R. (2013). The task force that rescues stalled ribosomes in bacteria. Trends Biochem. Sci. 38, 403**–**411.

Giudice, E., Macé, K., and Gillet, R. (2014). Trans-translation exposed: understanding the structures and functions of tmRNA-SmpB. *Frontiers in microbiology*, *5*, 113.

Goeders, N., and Van Melderen, L. (2014). Toxin-antitoxin systems as multilevel interaction systems. *Toxins*, *6*(1), 304-324.

Grigorieff, N. (2007). FREALIGN: High-resolution refinement of single particle strucutres. J. of Struct. Biol. Vol 157, Issue 1, pp 117-125.

Gualerzi, C.O., and Pon, C.L. (2015). Initiation of mRNA translation in bacteria: structural and dynamic aspects. Cell Mol Life Sci. Nov;72(22):4341-67.

Guillet, V., Bordes, P., Bon, C., Marcoux, J., Gervais, V., Sala, A. J., Dos Reis, S., Slama, N., Mares-Mejia, I., Cirinesi, A.M., Maveyraud, L., Genevaux, P., and Mourey, L. (2019). Structural insights into chaperone addiction of toxin-antitoxin systems. *Nature communications*, *10*(1), 1-15.

Guydosh, N. R., and Green, R. (2014). Dom34 rescues ribosomes in 3′ untranslated regions. *Cell*, *156*(5), 950-962.

Guydosh, N.R., and Green, R. (2017). Translation of poly(A) tails leads to precise mRNA cleavage. RNA. May;23(5):749-761.

Guyomar, C., D'Urso, G., Chat, S., Giudice, E., and Gillet, R. (2021). Structures of tmRNA and SmpB as they transit through the ribosome. *Nat Commun* **12,** 4909.

Handa, Y., Inaho, N., and Nameki, N. (2011). YaeJ is a novel ribosome-associated protein in *Escherichia coli* that can hydrolyze peptidyl-tRNA on stalled ribosomes. *Nucleic Acids Res.* 39 1739–1748 10.1093.

Harms, A., Brodersen, D. E., Mitarai, N., and Gerdes, K. (2018). Toxins, targets, and triggers: an overview of toxin-antitoxin biology. *Molecular cell*, *70*(5), 768-784.

Harms, J., Schluenzen, F., Zarivach, R., Bashan, A., Gat, S., Agmon, I., Bartels, H., Franceschi, F., and Yonath, A. (2001) High resolution structure of the large ribosomal subunit from a mesophilic eubacterium. Cell. 107(5):679-88.

Hayes, C.S., and Keiler, K.C. (2010). Beyond ribosome rescue: tmRNA and co-translational processes. FEBS Letters, Vol 584, Issue 2, pp 413-419.

Hayes, C.S., and Sauer, R.T. (2003a). Cleavage of the A site mRNA codon during ribosome pausing provides a mechanism for translational quality control. Mol. Cell 12, 903–911.

Hayes, C.S., Bose, B., and Sauer, R.T. (2002). Stop codons preceded by rare arginine codons are efficient determinants of SsrA tagging in Escherichia coli. Proc. Natl. Acad. Sci. U.S.A. 99, 3440–3445.

Hecht, A., Glasgow, J., Jaschke, P.R., Bawazer, L.A., Munson, M.S., Cochran, J.R., Endy, D., and Salit, M. (2017). Measurements of translation initiation from all 64 codons in E. coli. Nucleic Acids Res 45, 3615–3626.

Himeno, H., Nameki, N., Kurita, D., Muto, A., and Abo, T. (2015). Ribosome resuce systems in bacteria. Biochimie Vol 114, pp 102-112.

Holtkamp, W., Wintermeyer, W., and Rodnina, M.V. (2014). Synchronous tRNA movements during translocation on the ribosome are orchestrated by elongation factor G and GTP hydrolysis. Bioessays 36, 908–918.

Horan, L.H., and Noller, H.F. (2007). Intersubunit movement is required for ribosomal translocation. Proc. Natl. Acad. Sci. U.S.A. 104, 4881–4885.

Hossain, S.T, Malhotra, A., and Deutscher, M.P. (2015). The Helicase Activity of Ribonuclease R Is Essential for Efficient Nuclease Activity. J Biol Chem. 290(25):15697-15706.

Huang, C., Wolfgang, M.C., Withey, J., Koomey, M., and Friedman, D.I. (2000). Charged tmRNA but not tmRNA-mediated proteolysis is essential for Neisseria gonorrhoeae viability. EMBO J 19, 1098–1107.

Hummels, K.R., and Kearns, D.D. (2020). Translation elongation factor P (EF-P), *FEMS Microbiology Reviews*, Volume 44, Issue 2, Pages 208–218.

Huter, P., Müller, C., Arenz, S., Beckert, B., and Wilson, D.N. (2017a). Structural Basis for Ribosome Rescue in Bacteria. Trends in Biochemical Sciences 42, 669–680.

Huter, P., Müller, C., Beckert, B., Arenz, S., Berninghausen, O., Beckmann, R., and Wilson, D.N. (2017b). Structural basis for ArfA–RF2-mediated translation termination on mRNAs lacking stop codons. Nature 541, 546–549.

Ikeuchi, K., Tesina, P., Matsuo, Y., Sugiyama, T., Cheng, J., Saeki, Y., Tanaka, K., Becker, T., Beckmann, R., and Inada, T. (2019). Collided ribosomes form a unique structural interface to induce Hel2-driven quality control pathways. EMBO J. Mar 1;38(5):e100276.

Inada, T. (2020). Quality controls induced by aberrant translation. Nucleic Acid Research, Vol 48, Issue 3, pp 1084-1096.

Ingolia, N. T., Hussmann, J. A., and Weissman, J. S. (2019). Ribosome profiling: global views of translation. *Cold Spring Harbor perspectives in biology*, *11*(5), a032698.

Jacob, A. I., Köhrer, C., Davies, B. W., RajBhandary, U. L., and Walker, G. C. (2013). Conserved bacterial RNase YbeY plays key roles in 70S ribosome quality control and 16S rRNA maturation. *Molecular cell*, *49*(3), 427-438.

James, N.R., Brown, A., Gordiyenko, Y., and Ramakrishnan, V. (2016). Translational termination without a stop codon. Science 354, 1437–1440.

Jenner, L., Demeshkina, N., Yusupova, G., and Yusupov, M. (2010). Structural rearrangements of the ribosome at the tRNA proofreading step. Nat. Struct. Mol. Biol. 17, 1072-1078.

Karzai, A. W., and Sauer, R. T. (2001). Protein factors associated with the SsrA· SmpB tagging and ribosome rescue complex. *Proceedings of the National Academy of Sciences*, *98*(6), 3040-3044.

Kastner, B., Fischer, N., Golas, M., Sander, B., Dube, P., Boehringer, D., Hartmuth, K., Decket, J., Hauer, F., Wolf, E., Uchtenhagen, H., Urlaub, H., Herzog, F., Peters, J.M., Poerschke, D., Luhrmann, R., and Stark, H. (2008). GraFix: sample preparation for single-particle electron cryomicroscopy. *Nat Methods* **5,** 53–55

Keiler, K. (2015). Mechanisms of ribosome rescue in bacteria. *Nat Rev Microbiol* **13,** 285–297

Keiler, K. and Shapiro, L. (2003). tmRNa Is Required for Correct Timing of DNA Replication in Caulobacter crescentus. J. of Bacteriology, Vol 185, No. 2.

Kingery, D.A., Pfund, E., Voorhees, R.M., Okuda, K., Wohlgemuth, I., Kitchen, D.E., Rodnina, M.V., and Strobel, S.A. (2008). An Uncharged Amine in the Transition State of the Ribosomal Peptidyl Transfer Reaction. Chemistry & Biology, Volume 15, Issue 5, 2008, pp. 493-500, ISSN 1074-5521.

Klinge, S., Voigts-Hoffmann, F., Leibundgut, M., Arapgaus, S., and Ban, N. (2011). Crystal Structure of the Eukaryotic 60S Ribosomal Subunit in Complex with Initiation

Factor 6. Science, Vol 334, Issue 6058, pp. 941-948.

Kogure, H., Handa, Y., Nagata, M., Kanai, N., Güntert, P., Kubota K., and Nameki, N. (2014). Identification of residues required for stalled-ribosome rescue in the codon-independent release factor YaeJ. *Nucleic Acids Res.* 42 3152–3163 10.1093.

Komoda, T.M., Sato, N.S., Phelps, S.S., Namba, N., Joseph, S., and Suzuki, T. (2006). The A-site Finger in 23S rRNA Acts as a Functional Attenuator for Translocation. J. of Biological Chemistry 281(43):32303-9.

Korostelev, A.A. (2011). Structural aspects of translation termination on the ribosome. RNA 17, 1409–1421.

Korostelev, A., Asahara, H., Lancaster, L., and Noller, H.F. (2008). Crystal strucutre of a translation termination complex formed with release factor RF2. PNAS 105 (50) 19684-19689.

Korostelev, A., Laurberg, M., and Noller, H.F. (2009). Multistart simulated annealing refinement of the crystal structure of the 70S ribosome. PNAS 106 (43) 18195-18200.

Koutmou, K.S., McDonald, M.E., Brunelle, J.L., and Green, R. (2014). RF3:GTP promotes rapid dissociation of the class 1 termination factor. RNA 20, 609–620.

Kramer, G., Boehringer, D., Ban, N., and Bukau, B. (2009). The ribosome as a platform for co-translational processing, folding and targeting of newly synthesized proteins. Nat. Struct. Mol. Bio. 16, 589-597.

Kurita, D., Miller, M.R., Muto, A., Buskirk, A.R., and Himeno, H. (2014). Rejection of tmRNA-SmpB after GTP hydrolysis by EF-Tu on ribosomes stalled on intact mRNA. RNA, 20:1706-1714.

Kurita, D., Muto, A., and Himeno, H. (2011). tRNA/mRNA Mimicry by tmRNA and SmpB in Trans-Translation. Journal of Nucleic Acids, Vol 2011, ID 130581.

Lang, K., Erlacher, M., Wilson, D.N., Micura, R., and Polacek, N. (2008). The role of 23S ribosomal RNA residue A2451 in peptide bond synthesis revealed by atomic mutagenesis. Chem. Biol. 15, 485–492.

Laurberg, M., Asahara, H., Korostelev, A., Zhu, J., Trakhanov, S., and Noller, H.F. (2008). Structural basis for translation termination on the 70S ribosome. Nature 454, 852–857.

Lareau, L. F., Hite, D. H., Hogan, G. J., and Brown, P. O. (2014). Distinct stages of the translation elongation cycle revealed by sequencing ribosome-protected mRNA fragments. *elife*, *3*.

Lepault, J., Booy, F.P., and Dubochet, J. (1983). Electron microscopy of frozen biological samples. J. of Microscopy, Vol 129, Issue 1, pp 89-102.

Lepault 1982

Lepper, S., Merkel, M., Sartori, A., Cyrklaff, M., and Frischknecht, F. (2010). Rapid quantification of the effects of blotting for correlation of light and cryo-light microscopy images. J Microsc. 238(1):21-6.

Li, Z., and Deutscher, M.P. (2004). Exoribonucleases and Endoribonucleases. ASM Journals, Vol 1, No.1.

Li, Z.Z., Lam, C.H., Yu, T., and You, J.Q. (2013). Detector-induced backaction on the counting statistics of a double quantum dot. *Sci Rep* **3,** 3026

Li, X., Mooney, P., Zheng, S., Booth, C.R., Braunfeld, M.B., Gubbens, S., Agard, D.A., and Cheng, Y. (2013). Electron counting and beam-induced motion correction enable near-atomic-resolution single-particle cryo-EM. Nat Methods. 10:584–590.

Li, G.W., Oh, E., and Weissman, J.S. (2012). The anti-Shine-Dalgarno sequence drives translational pausing and codon choice in bacteria. Nature 484, 538**–**541.

Li, X., Yagi, M., Morita, T., and Aiba, H. (2008). Cleavage of mRNAs and role of tmRNA system under amino acid starvation in Escherichia coli. Mol. Microbiol. 68, 462**–**473.

Liang, W., and Deutscher, M. P. (2010). A Novel Mechanism for Ribonuclease Regulation: TRANSFER-MESSENGER RNA (tmRNA) AND ITS ASSOCIATED PROTEIN SmpB REGULATE THE STABILITY OF RNase R*[S]. *Journal of biological chemistry*, *285*(38), 29054-29058.

Liang, W., and Deutscher, M.P. (2012). Post-translational modification of RNase R is regulated by stress-dependent reduction in the acetylating enzyme Pka (YfiQ). *Rna*, *18*(1), 37-41.

Liang, W., and Deutscher, M.P. (2013). Ribosomes regulate the stability and action of the exoribonuclease RNase R. *Journal of Biological Chemistry*, *288*(48), 34791-34798.

Lightowlers, R.N., Rozanska, A., and Chrzanowska-Lightowlers, Z.M. (2014). Mitochondrial protein synthesis: Figuring the fundamentals, complexities and complications, of mammalian mitochondrial translation. FEBS Lett 588, 2496**–**2503.

Liu, Q., and Fredrick, K. (2013). Contribution of intersubunit bridges to the energy barrier of ribosomal translocation. Nucleic Acids Res. 41, 565**–**574.

Liu, Q., and Fredrick, K. (2016). Intersubunit bridges of the bacterial ribosome. J Mol Biol 428, 2146**–**2164.

Loh, P.G., and Song, H. (2010). Structural and mechanistic insights into translation termination. Current Opinion in Structural Biology 20, 98**–**103.

Luirink, J., and Sinning, I (2004). SRP-mediated protein targeting: structure and function revisited. Biochim Biophys Acta. Nov 11;1694(1-3):17-35.

Lytvynenko, I., Paternoga, H., Thrun, A., Balke, A., Muller, T.A., Chiang, C.H., Nagler, K., Tsaprailis, G., Anders, S., Bischofs, I., Maupin-Furlow, J.A., Spahn, C.M.T., and Joazeiro, C.A.P. (2019). Alanine Tails Signal Proteolysis in Bacterail Ribosome-Associated Quality Control. Cell 27;178(1):76-90.e22.

Ma, C., Kurita, D., Li, N., Chen, Y., Himeno, H., and Gao, N. (2017). Mechanistic insights into the alternative translation termination by ArfA and RF2. Nature 541, 550**–**553.

Maguire, B.A., and Zimmermann, R.A. (2001). The Ribosome in Focus. Cell 104, 813–816.

Malecki, M., Bárria, C., and Arraiano, C.M. (2014). Characterization of the RNase R association with ribosomes. *BMC microbiology*, *14*(1), 1-9.

Mann, B., van Opijnen, T., Wang, J., Obert, C., Wang, Y.D., Carter, R., McGoldrick, D.J., Ridout, G., Camilli, A., Toumanen, E.I., and Rosch, J.W. (2012). Control of Virulence bt Small RNAs in Streptococcus pneumoniae. J. Plos Pathogens https://doi.org/10.1371/journal.ppat.1002788.

Matsuo, Y., Ikeuchi, K., Saeki, Y., Iwasaki, S., Schmidt, C., Udagawa, T., Sato, F., Tsuchiya, H., Becker, T., Tanaka, K., Ingolia, N.T., Beckmann, R., and Inada, T. (2017). Ubiquitination of stalled ribosome triggers ribosome-associated quality control. *Nature communications*, *8*(1), 1-14.

McGinness, K. E., and Sauer, R. T. (2004). Ribosomal protein S1 binds mRNA and tmRNA similarly but plays distinct roles in translation of these molecules. *Proceedings of the National Academy of Sciences*, *101*(37), 13454-13459.

Melnikov, S., Ben-Shem, A., Garreau de Loubresse, N., Jenner, L., Yusupova, G., and Yusupov, M. (2012). One core, two shells: bacterial and eukaryotic ribosomes. Nat. Struct. Mol. Biol. 19, 560**–**567.

Mindell, J.A., and Grigorieff, N. (2003). Accurate determination of local defocus and specimen tilt in electron microscopy. J. of Struct. Biol. Vol 142, Issue 3, pp 334-347.

Moll, I., Hirokawa, G., Kiel, M.C., Kaji, A., and Bläsi, U. (2004). Translation initiation with 70S ribosomes: an alternative pathway for leaderless mRNAs, *Nucleic Acids Research*, Vol 32, Issue 11, 1, pp. 3354–3363.

Muller, C., Crowe-McAuliffe, C., and Wilson, D.N. (2021). Ribosome Rescue Pathways in Bacteria. Front. Microbiol. 12:652980.

Munavar, H., Zhou, Y.N., Gottesman, S. (2005). Analysis of the Escherichia coli Alp Phenotype: Heat Shock Induction in ssrA Mutants. J. of Bacteriology, Vol 187, No. 14.

Nissen, P., Kjeldgaard, M., Thirup, S., Polekhina, G., Reshetnikova, L., Clark, B.F.C., and Nyborg, J. (1995). Crystal Structure of the Ternary Complex of Phe-tRNA^{Phe}, EF-Tu, and a GTP Analog. Science Vol 270, Issue 5241, pp. 1464-1472.

Nissen, P., Hansen, J., Ban, N., Moore, P.B., and Steitz, T.A. (2000). The Structural Basis of Ribosome Activity in Peptide Bond Synthesis. Science 289, 920**–**930.

Nogales, E. (2016). The development of cryo-EM into a mainstream structural biology technique. *Nat Methods* **13,** 24–27.

Noller, H.F., Lancaster, L., Mohan, S., and Zhou, J. (2017). Ribosome structural dynamics in translocation: yet another functional role for ribosomal RNA. Q. Rev. Biophys. 50, e12.

Ogle, J.M., and Ramakrishnan, V. (2005). Structural insights into translational fidelity. Annu Rev Biochem. 2005;74:129-77.

Ohi, M., Li, Y., Cheng, Y.*,* and Walz, T. (2004). Negative staining and image classification — powerful tools in modern electron microscopy. *Biol. Proced. Online* **6,** 23–34

Okada, T., Wower, I. K., Wower, J., Zwieb, C. W., and Kimura, M. (2004). Contribution of the second OB fold of ribosomal protein S1 from Escherichia coli to the recognition of TmRNA. *Bioscience, biotechnology, and biochemistry*, *68*(11), 2319-2325.

Olson, A. N., and Dinman, J. D. (2020). Two Ribosomes Are Better Than One... Sometimes. *Molecular Cell*, *79*(4), 541-543.

Pallesen, J., Hashem, Y., Korkmaz, G., Koripella, R.K., Huang, C., Ehrenberg, M., Sanyal, S., and Frank, J. (2013). Cryo-EM visualization of the ribosome in termination complex with apo-RF3 and RF1 eLife 2:e00411.

Pan, D., Kirillov, S.V., and Cooperman, B.S. (2007) Kinetically Competent Intermediates in the Translocation Step of Protein Synthesis. Molecular Cell, Vol 25, Issue 4, pp. 519-529, ISSN 1097-2765.

Personne, Y., and Parish, T. (2014). Mycobacterium tubercolosis possesses an unusual tmRNA rescue system. Tubercolosis, Vol 94, Issue 1, pp 34-42.

Peske, F., Kuhlenkoetter, S., Rodnina, M.V., and Wintermeyer, W. (2014). Timing of GTP binding and hydrolysis by translation termination factor RF3. Nucleic Acids Res 42, 1812–1820.

Poulsen, H.E., Specht, E., Broedbaek, K., Henriksen, T., Ellervik, C., Mandrup-Poulsen, T., Tonnesen, M., Nielsen, P.E., Andersen, H.U., and Weimann, A. (2012). RNA modifications by oxidation: A novel disease mechanism? Free Radical Biology and Medicine 52, 1353**–**1361.

Punjani, A., Rubinstein, J., Fleet, D., and Brubaker, M.A. (2017). cryoSPARC:

algorithms for rapid unsupervised cryo-EM structure determination. *Nat Methods* **14,** 290–296

Purusharth, R. I., Madhuri, B., and Ray, M. K. (2007). Exoribonuclease R in Pseudomonas syringae is essential for growth at low temperature and plays a novel role in the 3′ end processing of 16 and 5 S ribosomal RNA. *Journal of Biological Chemistry*, *282*(22), 16267-16277.

Qin, P., Yu, D., Zuo, X., and Cornish, P.V. (2014). Structured mRNA induces the ribosome into a hyper-rotated state. EMBO Rep. 15, 185**–**190.

Qin, Y., Polacek, N., Vesper, O., Staub, E., Einfeldt, E., Wilson, D.N., and Nierhaus, K.H. (2006). The Highly Conserved LepA Isa Ribosomal Elongation Factor that Back-Translocates the Ribosome. Cell, Vol 127, Issue 4, pp 721-733.

Rajendran, V., Kalita, P., Shukla, H., Kumar, A., and Tripathi, T. (2018). Aminoacyl tRNA synthetases: Structure, function, and drug discovery. International Journal of Biological Macromolecules 111, 400**–**414.

Ramadoss, N.S., Alumasa, J.N., Cheng, L., Wang, Y., Li, S., Chambers, B.S., Chang, H., Chatterjee, A.K., Brinker, A., Engels, I.H., et al. (2013). Small molecule inhibitors of transtranslation have broad-spectrum antibiotic activity. Proc Natl Acad Sci U S A 110, 10282–10287.

Ramage, H. R., Connolly, L. E., and Cox, J. S. (2009). Comprehensive functional analysis of Mycobacterium tuberculosis toxin-antitoxin systems: implications for pathogenesis, stress responses, and evolution. *PLoS genetics*, *5*(12), e1000767.

Richards, J., Mehta, P., and Karzai, A. W. (2006). RNase R degrades non-stop mRNAs selectively in an SmpB-tmRNA-dependent manner. *Molecular microbiology*, *62*(6), 1700-1712.

Roche, E.D., and Sauer, R.T. (2002). Identification of endogenous SsrA-tagged proteins reveals tagging at positions corresponding to stop codons. J Biol Chem. Jul 27;276(30):28509-15.

Rodnina, M.V. (2018). Translation in Prokaryotes. CSH Perspectives in Biology, doi: 10.1101/cshperspect.a032664.

Rodnina, M.V. (2013). The ribosome as a vertile catalyst: reactions at the peptidyl transferase center. Current Opinion in Structural Biology 23, 595**–**602.

Rodnina, M.V., and Wintermeyer, W. (2016). Protein Elongation, Co-translational Folding and Targeting. J. Mol. Biol. 428, 2165**–**2185.

Rozov, A., Wolff, P., Grosjean, H., Yusupov, M., Yusupova, G., and Westhof, E. (2010). Tautomeric G•U pairs within the molecular ribosomal grip and fidelity of decoding in bacteria. Nucleic Acids Res; 46(14):7425-7435.

Rubinstein, J.L, and Brubaker, M.A. (2015). Alignment of cryo-EM movies of individual particles by optimization of image translations. J Struct Biol. 192(2):188-95.

Saguy, M., Gillet, R., Skorski, P., Hermann-Le Denmat, S., and Felden, B. (2007). Ribosomal protein S1 influences trans-translation in vitro and in vivo. *Nucleic acids research*, *35*(7), 2368-2376.

Saito, K., Kratzat, H., Campbell, A., Buschauer, R., Burroughs, A.M., Berninghausen, O., Aravind, L., Green, R., Beckmann, R., and Buskirk, A.R. (2022). Ribosome collisions induce mRNA cleavage and ribosome rescue in bacteria. *Nature*, 603, 503-508.

Sala, A., Bordes, P., and Genevaux, P. (2014). Multiple toxin-antitoxin systems in Mycobacterium tuberculosis. *Toxins*, *6*(3), 1002-1020.

Sala, A. J., Bordes, P., Ayala, S., Slama, N., Tranier, S., Coddeville, M., Cirinesi, A.M., Castanié-Cornet, P., Mourey, L., and Genevaux, P. (2017). Directed evolution of SecB chaperones toward toxin-antitoxin systems. *Proceedings of the National Academy of Sciences*, *114*(47), 12584-12589.

Sander, B., Golas, M.M., Stark, H. (2005). Advantages of CCD detectors for de novo three-dimensional structure determination in single-particle electron microscopy. J. Struct. Biol., 151, pp 92-105.

Saramago, M., Bárria, C., Dos Santos, R. F., Silva, I. J., Pobre, V., Domingues, S., Andrade, J.M., Viegas, S.C., and Arraiano, C. M. (2014). The role of RNases in the regulation of small RNAs. *Current opinion in microbiology*, *18*, 105-115.

Satpati, P., and Aqvist, J. (2014). Why base tautomerization does not cause errors in mRNA decoding on the ribosome. Nucleic Acid Research, Vol 42, Issue 20, pp. 12876-12884.

Satterthwait A.C., and Jencks, W.P. (1974). The Mechanism of the Aminolysis of Acetate Esters. J. of the American Chamical Society 96:22.

Scheres, S.H. (2012). RELION: Implementation of a Bayesian approach to cryo-EM structure determination. J. of Struct. Biol. Vol 180, Issue 3, pp 519-530.

Scheres, S.H. (2014). Beam-induced motion correction for sub-megadalton cryo-EM particles. Elife. 3:e03665.

Schmeing, T.M., and Ramakrishnan, V. (2009). What recent ribosome structures haverevealed about the mechanism of translation. Nature 461, 1234–1242.

Schmeing, T.M., Huang, K.S., Strobel, S.A., and Steitz, T.A. (2005). An induced-fit mechanism to promote peptide bond formation and exclude hydrolysis of peptidyl-tRNA. Nature 438, 520–524.

Schuwirth, B.S., Borovinskaya, M.A., Hau, C.W., Zhang, W., Vila-Sanjurjo, A., Holton, J.M., and Cate, J.H.D. (2005). Structures of the Bacterial Ribosome at 3.5 Å

Resolution. Science 310, 827–834.

Seidelt, B., Innis, C.A., Wilson, D.N., Gartmann, M., Armache, J.P., Villa, E., Trabuco, L.G., Becker, T., Mielke, T., Schulten, K., Steitz, T.A., and Beckmann, R. (2009). Structural Insights into Nascent Polypeptide Chain-Mediated Transaltional Stalling. Science, Vol 326, Issue 5958, pp. 1412-1415.

Seila, A.C., Okuda, K., Nunez, S., Seila, A.F., and Strobel, S.A. (2005). Kinetic Isotope Effect Analysis of the Ribosomal Peptidyl Transferase Reaction. Biochemistry 44, 10, 4018-4027.

Semenkov, Y., Rodnina, M. and Wintermeyer, W. Energetic contribution of tRNA hybrid state formation to translocation catalysis on the ribosome. *Nat Struct Mol Biol* **7,** 1027–1031

Sharma, H., Adio, S., Senyushkina, T., Belardinelli, R., Peske, F., and Rodnina, M.V. (2016). Kinetics of Spontaneous and EF-G-Accelerated Rotation of Ribosomal Subunits. Cell Rep 16, 2187–2196.

Sharma, P.K., Xiang, Y., Kato, M., and Warshel, A. (2005) What Are the Roles of Substrate-Assisted Catalysis and Proximity Effects in Peptide Bond Formation by the Ribosome?. Biochemistry 44, 34, 11307-11314.

Shi, X., and Joseph, S. (2016). Mechanism of Translation Termination: RF1 Dissociation Follows Dissociation of RF3 from the Ribosome. Biochemistry 55, 45, 6344-6354.

Shimizu, Y. (2012). ArfA recruits RF2 into stalled ribosomes. J. Mol. Biol. 423, 624–631.

Shin, J.H., and Price, C.W. (2007). The ssrA-SmpB Ribosome Rescue System Is Important for Growth of Bacillus subtilis at Low and High Temperatures. J. of Bacteriology, Vol 189, No. 10.

Shine, J., and Dalgarno, L. (1974). The 3'-terminal sequence of Escherichia coli 16S ribosomal RNA: complementarity to nonsense triplets and ribosome binding sites. Proc. Natl. Acad. Sci. U.S.A. 71, 1342–1346.

Sievers, A., Beringer, M., Rodnina, M.V., and Wolfenden, R., (2004) The ribosome as an entropy trap. PNAS 101 (21) 7897-7901.

Spahn, C.M., Gomez-Lorenzo, M.G., Grassucci, R.A., Jørgensen, R., Andersen, G.R., Beckmann, R., Penczek, P.A., Ballesta, J.P., and Frank, J. (2004) Domain movements of elongation factor eEF2 and the eukaryotic 80S ribosome facilitate tRNA translocation. EMBO J. Mar 10;23(5):1008-19.

Stark, H., Rodnina, M., Rinke-Appel, J., Brimacombe, R., Wintermeyer, W., and van Heel, M. (1997). Visualization of elongation factor Tu on the *Escherichia coli* ribosome. *Nature* **389,** 403–406.

Stewart, G.R., Wernisch, L., Stabler, R., Mangan, J.A., Hinds, J., Laing, K.G., Young, D.B., and Butcher, P.D. (2002). Dissection of the heat-shock response in *Mycobacterium tuberculosis* using mutants and microarrays. Microbiology. 148:3129–3138.

Strader M.B., Hervey W. J. T., Costantino N., Fujigaki S., Chen C. Y., Akal-Strader A., Ihunnah, C.A., Makusky, A.J., Court, D.L., Markey, S.P., and Kowalak, J.A. (2013). A coordinated proteomic approach for identifying proteins that interact with the *E. coli* ribosomal protein S12. J. Proteome Res. 12, 1289–1299 10.1021/pr3009435

Svetlanov, A., Puri, N., Mena, P., Koller, A., Karzai, A.W. (2012). Francisella tularensis tmRNA system mutants are vulnerable to stress, avirulent in mice, and provide effective immune protection. Molecular biology, Vol 85, Issue 1, pp. 122-141.

Szewczak, A. A., and Moore, P. B. (1995). The sarcin/ricin loop, a modular RNA. *Journal of molecular biology*, *247*(1), 81-98.

Tang, G., Peng, L., Baldwin, P.R., Mann, D.S., Jiang, W., Rees, I., and Ludtke, S.J. (2007). EMAN2: An extensible image processing suite for electron microscopy. J. of Struct. Biol. Vol 157, Issue 1, pp 38-46.

Thibonnier, M., Thiberge, J.M., and De Reuse, H. (2008). Trans-Translation in Helicobacter pylori: Essentiality of Ribosome Rescue and Requirement of Protein Tagging for Stress Resistance and Competence. J. Plosone, https://doi.org/10.1371/journal.pone.0003810

Thompson, R.F., Walker, M., Siebert, C.A., Muench, S.P., and Ranson, N.A. (2016). An introduction to sample preparation and imaging bt cryo-electron microscopy for structural biology. Methods, Vol 100, pp 3-15.

Thon, F. (1966). Notien : Zur Defokussierungsabhängigkeit des Phasenkontrastes bei der elektronenmikroskopischen Abbildung. Der Gruyter Vol 21, Issue 4, pp 476-478.

Tissieres, A., and Watson, J.D. (1958). Ribonucleoprotein particles from Escherichia coli. Nature. 182(4638):778-80.

Udagawa, T., Shimizu, Y., and Ueda, T. (2004). Evidence for the translation initiation of leaderless mRNAs by the intact 70 S ribosome without its dissociation into subunits in eubacteria. J. Biol. Chem. 279, 8539–8546.

Udagawa, T., Seki, M., Okuyama, T., Adachi, S., Natsume, T., Noguchi, T., Matsuzawa, A., and Inada, T. (2021). Failure to Degrade CAT-Tailed Proteins Disrupts Neuronal Morphogenesis and Cell Survival. Cell Rep. 5;34(1):108599.

Ude, S., Lassak, J., Starosta, A.L., Kraxenberger, T., Wilson, D.N., and Jung, K. (2013). Translation Elongation Factor EF-P Alleviates Ribosome Stalling at Polyproline Stretches. Science 339, 82–85.

Ueda, K., Yamamoto, Y., Ogawa, K., Abo, T., Inokuchi, H., and Aiba, H. (2002). Bacterial SsrA system plays a role in coping with unwanted translational readthrough caused by suppressor tRNAs. Genes Cells **7**, 509**–**519.

Valle, M., Gillet, R., Kaur, S., Henne, A., Ramakrishnan, V., and Frank, J. (2003). Visualizing tmRNA entry into a stalled ribosome. Science 300, 127**–**130.

Valle, M., Sengupta, J., Swami, N.K., Grassucci, R.A., Burkhardt, N., Nierhaus, K.H., Agrawal, R.K., and Frank, J. (2002). Cryo-EM reveals an active role for aminoacyl-tRNA in the accommodation process. EMBO J. 21: 3557-3567.

van Heel, M. (1987). Angular reconstruction: A posteriori assignment of projection directions for 3D reconstruction. Ultramicroscopy, Vol 21, Issue 2, pp 111-123.

van Hoof, A., Frischmayer, P.A., A.L., Dietz, H.C, and Parker, R. (2002). Exosome-Mediated Recognition and Degradation of mRNAs Lacking a Termination Codon. Science, Vol 295, Issue 5563, pp. 2262-2264.

Venkataraman, K., Guja, K. E., Garcia-Diaz, M., and Karzai, A. W. (2014). Non-stop mRNA decay: a special attribute of trans-translation mediated ribosome rescue. *Frontiers in microbiology*, *5*, 93.

Vincent, H. A., and Deutscher, M.P. (2009). The roles of individual domains of RNase R in substrate binding and exoribonuclease activity: the nuclease domain is sufficient for digestion of structured RNA. *Journal of Biological Chemistry*, *284*(1), 486-494.

Vogel, R., Provencher, S., von Bonsdorff, C.H., Adrain, M. and Dubochet, J. (1986). Envelope structure of Semliki Forest virus reconstructed from cryo-electron micrographs. *Nature* **320,** 533–535

Voorhees, R.M., and Ramakrishnan, V. (2013). Structural Basis of the Translational Elongation Cycle. Annu. Rev. Biochem. 82, 203**–**236.

Voss, N.R., Gerstein, M., Steitz, T.A., and Moore, P.B. (2006). The geometry of the ribosomal polypeptide exit tunnel. J. Mol. Biol. 360, 893**–**906.

Walker, S.E., Shoji, S., Pan, D., and Fredrick, K. (2008). Role of hybrid tRNA-binding states in ribosomal translocation. PNAS 105 (27) 9192-9197.

Watson, J., and Crick, F. (1953). Molecular Structure of Nucleic Acids: A Structure for Deoxyribose Nucleic Acid. Nature 171, 737-738.

Weixlbaumer, A., Jin, H., Neubauer, C., Voorhees, R., Petry, S., Kelley, A.C., and Ramakrishnan, V. (2008). Insights into Translational Termination from the Strucutre of RF2 Bound to the Ribosome. Science Vol 322, Issue 5903, pp 953-956.

Wellner, K., Czech, A., Ignatova, Z., Betat, H., and Mörl, M. (2018). Examining tRNA 3′-ends in Escherichia coli: teamwork between CCA-adding enzyme, RNase T, and RNase R. *RNA*, *24*(3), 361-370.

Wendrich, T.M., Blaha, G., Wilson, D.N., Marahiel, M.A., and Nierhaus, K.H. (2002). Dissection of the mechanism for the stringent factor RelA. Mol. Cell 10, 779**–**788.

Wieden, H.J., Wintermeyer, W., and Rodnina, M. (2001). A Common Structural Motif in Elongation Factor Ts and Ribosomal Protein L7/12 May Be Involved in the Interaction with Elongation Factor Tu. *J Mol Evol* **52,** 129–136

William, D.B., and Carter, C.B. (2009). Transmission Electron Microscopy. Springer Science & Business Media, Vol 2.

Wimberly, B.T., Brodersen, D.E., Jr, W.M.C., Morgan-Warren, R.J., Carter, A.P., Vonrhein, C., Hartsch, T., and Ramakrishnan, V. (2000). Structure of the 30S ribosomal subunit. Nature 407, 327**–**339.

Wower, I. K., Zwieb, C. W., Guven, S. A., and Wower, J. (2000). Binding and cross-linking of tmRNA to ribosomal protein S1, on and off the Escherichia coli ribosome. *The EMBO journal*, *19*(23), 6612-6621.

Yamaguchi, Y., Park, J. H., and Inouye, M. (2011). Toxin-antitoxin systems in bacteria and archaea. *Annual review of genetics*, *45*(1), 61-79.

Yamamoto, H., Wittek, D., Gupta, R., Qin, B., Ueda, T., Krause, R., Yamamoto, K., Albrecht, R., Pech, M., and Nierhaus, K.H. (2016). 70S-scanning initiation is a novel and frequent initiation mode of ribosomal translation in bacteria. Proc Natl Acad Sci U S A 113, E1180**–**E1189.

Yusupov, M.M., Yusupova, G.Z., Baucom, A., Lieberman, K., Earnest, T.N., Cate, J.H.D., and Noller, H.F. (2001). Crystal Structure of the Ribosome at 5.5 Å Resolution. Science 292, 883**–**896.

Yusupova, G., Jenner, L., Rees, B., Moras, D., and Yusupov M.M. (2006). Structural basis for messenger RNA movement on the ribosome. Nature 444, 391-394.

Zavialov, A.V., Buckingham, R.H., and Ehrenberg, M. (2001). A Post-termination Ribosomal Complex Is the Guanine Nucleotide Exchange Factor for Peptide Release Factor RF3. Cell 107, 115–124.

Zavialov, A.V., Mora, L., Buckingham, R.H., and Ehrenberg, M. (2002). Release of Peptide Promoted by the GGQ Motif of Class 1 Release Factors Regulates the GTPas Activity of RF3. Molecular Cell 10, 789–798.

Zeng, F., and Jin, H. (2018). Conformation of methylated GGQ in the Peptidyl Transferase Center during Translation Termination. *Sci Rep* 8, 2349.

Zeng, F., Chen, Y., Remis, J., Shekhar, M., Phillips, J.C., Tajkhorshid, E., and Jin, H. (2017). Structural basis of co-translational quality control by ArfA and RF2 bound to ribosome. Nature 541, 554–557.

Zuo, Y., and Deutscher, M.P. (2001). Exoribonuclease superfamilies: structural analysis and phylogenetic distribution. Nucleic Acid Reasearch, Vol 29, Issue 5, pp 1017-1026.

Annex

Structural study of TAC RNase toxin of *Mycobacterium tubercolosis*

1 Context of study

In collaboration with the team of Pierre Genevaux (LMGM/CBI CNRS - Université de Toulouse), we studied the mechanism of action of the TAC tripartite complex and, in particular, its toxin known as HigB1, a *Mycobacterium tubercolosis* toxin. The increasing occurrence of multi-drug resistant *Mycobacterium tubrcolosis* strains has greatly heightened the need for the development of new antimicrobial molecules and new strategies of treatment. Such a study required the use of several cross-disciplinary skills including that of our team, which was involved in the structural characterization (through cryo-EM) of the toxin within the *Mycobacterium tuberculosis* ribosome, in order to understand its catalytic mechanism since it may represent a new target for future antimicrobial molecules.

2 HigB1 toxin and its tripartite TAC complex

The *Mycobacterium tubercolosis* (*Mtb*) bacterium is the causative agent of tubercolosis and it represents one of the major health problems accounting for over 1.5 million deaths per year. In addition to its lethality, a further peculiarity of *Mtb* is that about the 4% of its genome encodes for a particular system called toxin-antitoxin (TA) system (Sala et al., 2014). Although their cellular function remains largely unknown, many of these systems are involved in stress response including heat-shock, DNA damage, drug exposure, etc., suggesting that some of these TA systems can contribute to *Mtb* physiology and virulence. (Betts et al., 2002; Stewart et al., 2002; Ramage et al., 2009; Fivian-Huges and Davis, 2010; Sala et al., 2014). In particular, *Mtb* shows a particular TA system called toxin-antitoxin-chaperone (TAC) system (Figure 44), which is composed by the HigB1 toxin that belongs to the RelE/ParE toxin superfamily, which covers both ribosome-dependent mRNA endoribonuclease that inhibits translation and toxins targeting the DNA gyrase to block DNA replication, an HTH-Xre antitoxin and a SecB-like chaperone (Yamaguchi et al., 2011; Bordes et al., 2016; Guillet et al., 2019). Under normal growth condtions, the antitoxin-bound toxinis inactive and the bacteria grows normally. Under certain stress conditions, the antitoxin is less stable and is rapidly degraded by proteases, freeing in this way the toxin. The toxin is now capable of targeting essential cellular

process, leading to growth inhibition and ultimately cell death (Goeders and Van Melderen, 2014; Harms et al., 2018). The TA pair of TAC is tightly controlled by the Sec-like chaperone through direct interactions with the antitoxin (Bordes et al., 2011). In particular, SecB chaperone specifically binds the antitoxin to facilitate its folding, stabilize its structure and ensure the subsequent toxin inhibition (Bordes et al., 2011; Bordes et al., 2016; Sala et al., 2017). To date, there is no available structural and functional data confirming this works and nothing is known about the function, the targets specificty and the mechanism of action of the HigB1 toxin.

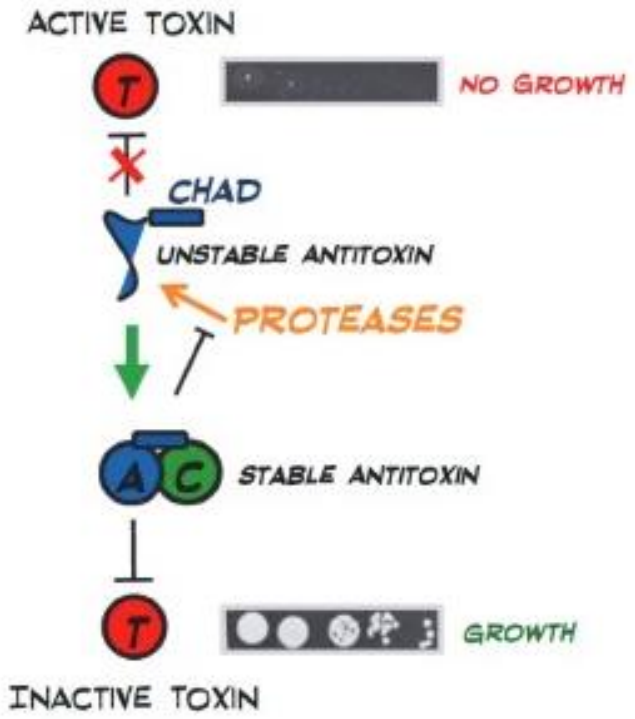

Figure 44: Inhibition of the TAC toxin (T) relies on the stabilization of the antitoxin (A) by its dedicated chaperone (C), which prevents its aggregation and degradation.

In this work, we have shown that the HigB1 TAC toxin cleaves a specific codon in mRNA targets on a wide range of transcriptomes *in vivo*. Thanks to the cryo-EM structure of the ribosome-bound TAC toxin in presence of native *Mtb* cspA mRNA, we have revealed the specific mechanism by which HigB1 interacts with the ribosome and the P-site tRNA to cleave the CCA codon present in the mRNA target.

3 Cryo-EM structure of HigB1 toxin of *Mycobacterium tuberculosis*

nature COMMUNICATIONS

ARTICLE

https://doi.org/10.1038/s41467-022-30373-w OPEN

Check for updates

Substrate recognition and cryo-EM structure of the ribosome-bound TAC toxin of *Mycobacterium tuberculosis*

Moise Mansour[1,6], Emmanuel Giudice[2,6], Xibing Xu[1], Hatice Akarsu[3,5], Patricia Bordes[1], Valérie Guillet[4], Donna-Joe Bigot[1,4], Nawel Slama[1], Gaetano D'urso[2], Sophie Chat[2], Peter Redder[1], Laurent Falquet[3], Lionel Mourey[4], Reynald Gillet[2✉] & Pierre Genevaux[1✉]

Toxins of toxin-antitoxin systems use diverse mechanisms to control bacterial growth. Here, we focus on the deleterious toxin of the atypical tripartite toxin-antitoxin-chaperone (TAC) system of *Mycobacterium tuberculosis*, whose inhibition requires the concerted action of the antitoxin and its dedicated SecB-like chaperone. We show that the TAC toxin is a bona fide ribonuclease and identify exact cleavage sites in mRNA targets on a transcriptome-wide scale in vivo. mRNA cleavage by the toxin occurs after the second nucleotide of the ribosomal A-site codon during translation, with a strong preference for CCA codons in vivo. Finally, we report the cryo-EM structure of the ribosome-bound TAC toxin in the presence of native *M. tuberculosis* cspA mRNA, revealing the specific mechanism by which the TAC toxin interacts with the ribosome and the tRNA in the P-site to cleave its mRNA target.

[1] Laboratoire de Microbiologie et de Génétique Moléculaires, Centre de Biologie Intégrative (CBI), Université de Toulouse, CNRS, UPS, Toulouse, France. [2] Institut de Génétique et Développement de Rennes (IGDR), UMR6290, Université de Rennes, CNRS, Rennes, France. [3] Department of Biology, University of Fribourg & Swiss Institute of Bioinformatics, Fribourg, Switzerland. [4] Institut de Pharmacologie et de Biologie Structurale, IPBS, Université de Toulouse, CNRS, UPS, Toulouse, France. [5] Present address: Institute of Veterinary Bacteriology, University of Bern, Bern, Switzerland. [6] These authors contributed equally: Moise Mansour, Emmanuel Giudice. ✉email: reynald.gillet@univ-rennes1.fr; pierre.genevaux@univ-tlse3.fr

Toxin–antitoxins (TA) are two-component systems composed of a poisonous toxin and a counteracting antitoxin[1–3]. Toxins generally employ very diverse and elegant strategies to inhibit bacterial growth, mainly targeting essential processes or structures, including translation, replication, or membranes[2,4–12]. Although the specific conditions that lead to toxin activation in vivo remain largely unknown[13], TA systems have been involved in the maintenance of chromosomes, plasmids, or other genetic mobile elements, in the defense against phage infection through a process known as abortive infection and in some cases, in antibiotic persistence in vivo in infectious models and in bacterial virulence[14–20].

Mycobacterium tuberculosis, the bacterium responsible for human tuberculosis, encodes for more than 86 TA systems, covering large sets of conserved TA families, including VapBC (50 pairs), MazEF/PemIK (11), MenTA (4), HigBA (3), RelBE (3), ParDE (2), Res-Xre (2), DarTG (1), PezAT (1), and RHH-GNAT (1), as well as other less conserved or uncharacterized TA pairs[21,22]. Many *M. tuberculosis* toxins inhibit bacterial growth when overexpressed and TA operons are often induced under relevant stresses, including hypoxia, macrophage engulfment, or antibiotics[23,24]. This suggests that stress-activated toxins could potentially modulate the growth of *M. tuberculosis* and contribute to its success as a major human pathogen[22,24]. Yet, except for *ΔvapC22*, *ΔvapBC3/4/11* and *ΔmazF3/6/9* mutants that were shown to be impaired in host infection, almost nothing is known about the role of TA modules in the biology of *M. tuberculosis*[25–27].

Rv1955-Rv1956 (HigBA^{TAC}, also named HigBA1), Rv2022c-Rv2021c (HigBA2), and Rv3182-Rv3183 (HigBA3) were originally annotated as HigBA-like TA pairs due to their less common inverted genetic organization, i.e., the toxin encoded first, similar to the HigBA (host inhibition of growth) module found on the Rts1 plasmid of *Proteus vulgaris*[28]. Such a module was shown to contain a RNase toxin (HigB) that possesses a similar fold as the RelE[29] toxin of *Escherichia coli* and a HTH-Xre DNA-binding domain containing antitoxin (HigA) (Fig. 1a, b). The HigBA^{TAC} pair is part of the atypical tripartite TAC (toxin–antitoxin–chaperone) system in which efficient inhibition of the HigB^{TAC} toxin (also named HigB1) by the antitoxin (HigA^{TAC}, also named HigA1) relies on the molecular chaperone Rv1957 (SecB^{TA}) encoded as the third gene of the *TAC* (*higB-higA-Rv1957*) operon[30,31]. The TAC chaperone, which is homologous to the export chaperone SecB of *E. coli*[32,33], specifically interacts with the C-terminal chaperone-addiction region of the antitoxin to prevent its aggregation and degradation, and to facilitate subsequent inhibition of the toxin by the antitoxin[34–36]. Although transcription of *TAC* is induced under relevant stresses for *M. tuberculosis*, including nutritional starvation, hypoxia, antibiotics treatment, and drug-induced persistence[22,23,37–39], very little is known about its possible involvement in *M. tuberculosis* physiology and virulence[40]. Deletion of the HigA^{TAC} antitoxin is lethal, possibly due to the synthesis of free active toxin[39]. Accordingly, overexpression of the HigB^{TAC} is toxic in *M. tuberculosis*, *Mycobacterium smegmatis*, *Mycobacterium marinum*, and *E. coli*[30,35,41], and was shown to affect the abundance of a subset of transcripts related to iron and zinc homeostasis[41]. In contrast with the TAC system, nearly nothing is known about the putative function and activity of HigBA2 and HigBA3, except that ectopic expression of the HigB3 toxin does not affect *M. smegmatis* growth and that neither *higA2* nor *higA3* are essential for *M. tuberculosis*[23,42].

In this work, we investigate the in vivo targets and the molecular mechanism of HigB-like toxins of *M. tuberculosis*, mainly focusing on the TAC toxin. We find that among the three toxins, only HigB^{TAC} exhibits robust toxicity and efficiently inhibits translation. In addition, we show that HigB^{TAC} functions as a bona fide RNase that specifically cleaves mRNA after the second nucleotide of A-site codons (mainly CCA codons) during translation. Finally, we solve both the X-ray structure of HigB^{TAC} alone and the cryo-EM structure of the ribosome-bound HigB^{TAC} in the presence of its native *M. tuberculosis cspA* mRNA. The specific mechanism by which HigB^{TAC} interacts with the ribosome and the tRNA at the P-site to cleave its mRNA target is discussed.

Results

HigB^{TAC}, but not HigB2 and HigB3, is toxic and inhibits protein synthesis. In order to assess the toxicity of the three *M. tuberculosis* HigB-like toxins in comparable expression systems, the toxins were cloned and expressed in *M. smegmatis* under the control of an anhydrotetracycline (ATc) inducible promoter on an integrative plasmid. *M. smegmatis* does not have endogenous HigA antitoxin, which is very convenient to study the impact of solitary HigB toxins. Under these conditions, we found that the expression of HigB^{TAC} induces a robust toxic phenotype (Fig. 1c). In addition, alanine substitution of residue K95 of HigB^{TAC}, which possibly corresponds to the active site residue R81 of *E. coli* RelE[29], fully inhibited toxicity in vivo in *M. smegmatis* (Fig. 1c and Supplementary Fig. 1a). This strongly suggests that HigB^{TAC} toxicity was due to its putative RNase activity. Note that the K95A substitution that leads to the inactive toxin was used as non-toxic HigB^{TAC} control for further in vivo and in vitro analysis. In contrast, no toxicity was observed for HigB2 or HigB3 under the same conditions. In a similar manner, no toxicity was observed when these toxins were expressed in *M. smegmatis* from a high copy number plasmid under the control of an acetamide-inducible promoter (Supplementary Fig. 1a) or in *E. coli* following expression from an arabinose-inducible promoter (Supplementary Fig. 1b). In addition, expression of HigB toxins could only be detected on SDS-PAGE when expressed from the strong T7 promoter of pET-vector in *E. coli*. In this case, both HigB2 and HigB3 toxins showed higher expression levels than HigB^{TAC} (Supplementary Fig. 1c). The lack of toxicity of HigB2 and HigB3 is further supported by the fact that their respective antitoxins are not essential for *M. tuberculosis* growth[42].

To further investigate the difference in growth inhibition observed between the three toxins, the impact of purified HigB^{TAC}, HigB^{TAC}[K95A], HigB2, or HigB3 on protein synthesis was monitored in vitro by following the expression of the model protein GFP in a coupled transcription/translation assay[34]. In agreement with the toxicity data, HigB^{TAC} efficiently blocked GFP synthesis while HigB2, HigB3, and the HigB^{TAC}[K95A] mutant did not (Fig. 1d). Note that, at a high concentration of toxins (i.e., 20 times higher than the one at which HigB^{TAC} wild-type efficiently inhibits translation), we do observe a decrease in GFP synthesis in the presence of HigB2, HigB3, or HigB^{TAC}[K95A]. In contrast, the addition of unrelated proteins at the same concentration did not show such a marked effect on GFP synthesis (Supplementary Fig. 1d). This suggests that these toxins might have a lower affinity for the ribosome or be catalytically inactive but still able to interact with the ribosome and/or the mRNA, and somehow interfere with translation under our in vitro conditions.

Genome-wide identification of toxin targets and cleavage preference. A nEMOTE (nonphosphorylated exact mapping of transcriptome ends) approach was used to identify HigB toxin substrates and recognition sequences in vivo for further in vitro characterization. This qualitative method, which allows the exact mapping of 5'-OH cleaved sites in mRNA in vivo on a transcriptome-wide scale

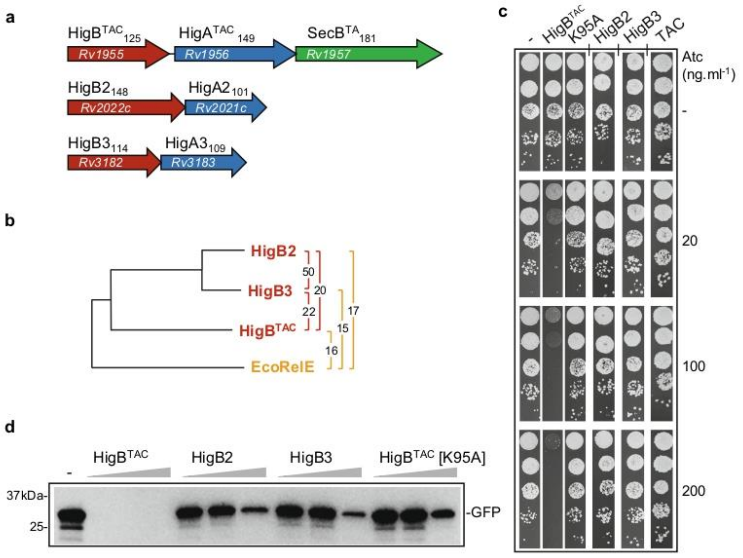

Fig. 1 Impact of HigB toxins on growth and protein synthesis. a Schematic representation of the three HigBA-like systems of *M. tuberculosis*. Toxins are shown in red, antitoxins in blue and the chaperone of the TAC system ($SecB^{TA}$) in green. The amino acid length of each protein is given as a subscript and the locus tag for each gene within color arrows. **b** Phylogenetic tree of *M. tuberculosis* HigB toxins (red) and *E. coli* RelE (orange). The percentage of sequence identity between pairs of toxins is shown on the right (colored brackets). **c** Expression of HigB toxins in vivo. *M. smegmatis* transformed with pGMC-vector (-), $HigB^{TAC}$, $HigB^{TAC}$ [K95A], HigB2 or HigB3 or TAC (HigB/HigA/SecB)^{TAC} were serial diluted and spotted on LB agar plates supplemented with or without Atc inducer at the indicated concentration. Plates were incubated for 3 days at 37 °C. **d** In vitro transcription/translation reactions assessing the synthesis of GFP protein in the absence (-) or presence of increasing concentrations of HigB toxins, (0.3, 3, and 6 μM). Samples were separated by SDS-PAGE and revealed by western blot using an anti-GFP antibody. Representative results of three independent experiments are shown.

has been successfully used in *Caulobacter crescentus* and *Staphylococcus aureus*[43–45]. The nEMOTE analyzes were performed with $HigB^{TAC}$, $HigB^{TAC}$[K95A] as negative control, HigB2, and HigB3 expressed in both *M. smegmatis* WT and *ΔrnJ*. The *ΔrnJ* mutant does not produce ribonuclease J and was used to minimize degradation of cleaved toxin targets and thus potentially increase the robustness of the signal of the preferred cleavage sites[46]. Although HigB2 and HigB3 were not toxic, we hypothesized that they might still exhibit some weak RNase activity. Expression of the toxins was induced with ATc for 3 hours (or additionally for 24 hours in the case of HigB2 and HigB3) at mid-log phase, whereupon total RNAs were extracted and analyzed with nEMOTE (see "Methods"). Cleavage sites for each condition are presented in Supplementary Data 1 and the identified target genes are summarized in Fig. 2a and Supplementary Fig. 2a. For this analysis, we considered that a cleavage site for a given toxin should be found at least seven times in one condition and at least in two out of the six replicates to be counted as a bona fide target site in vivo (see Bioinformatic analysis in the Methods section). Remarkably, ectopic expression of $HigB^{TAC}$ led to the identification of 24 unique cleavage sites located within 22 different RNA targets (Fig. 2a). Eight of these cleaved coding regions of essential proteins are conserved in *M. tuberculosis* and affect different cellular processes, including translation, replication, protein folding, and metabolism (Supplementary Fig. 2a). Additionally, four cleavage sites were identified in previously non-annotated transcripts (named nat1 to nat4). We found a strong overlap among the identified target sites from the WT and *ΔrnJ* mutant, with 15 out of 24 found in both strains. Strikingly, all the cleavages identified in annotated open reading frames occurred between the second and the third nucleotide of the codons, suggesting that $HigB^{TAC}$ might preferentially cleave mRNA during translation. Alignment of all the sequences flanking the cleavage sites revealed a clear preference for CCA codons (encoding a proline), with cleavage occurring between the C and A nucleotides (Fig. 2b and Supplementary Fig. 2b). In sharp contrast, expression of $HigB^{TAC}$[K95A] only led to a single potential hit in a non-annotated transcript (nat5) that appeared with low frequency (22 cuts in 2 replicates), which could be a false positive caused by the background noise or a very weak RNase activity (Supplementary Fig. 2a, c). Similarly, only 3 and 1 hits were identified for HigB2 and HigB3, respectively. Such hits were only detected after prolonged exposure to the toxins (24 h instead of 3 h in the case of $HigB^{TAC}$) in the wild-type strain and with a low frequency (Supplementary Data 1 and Supplementary Fig. 2c). These data are in line with the lack of toxicity observed in vivo.

Ribosome dependence and cleavage preference by TAC toxin in vitro. The nEMOTE data highlighted several potential substrates of $HigB^{TAC}$, including the frequently cleaved *cspA* and *groES* transcripts, whose cleavage sites are conserved in both *M. smegmatis* and *M. tuberculosis* (Fig. 2a and Supplementary Fig. 2a). In agreement with the in vivo data, we found that both *cspA* and *groES* of *M. tuberculosis* were also bona fide $HigB^{TAC}$ substrates in vitro, as judged by $HigB^{TAC}$ ability to inhibit *M. tuberculosis* CspA (Fig. 3a) and GroES (Supplementary Fig. 3a) synthesis by *E. coli* ribosomes. The *cspA* mRNA, which has only one $HigB^{TAC}$ cleavage site in its sequence, i.e., a CCA codon at the amino acid position 2, was selected as a model substrate transcript to further study $HigB^{TAC}$

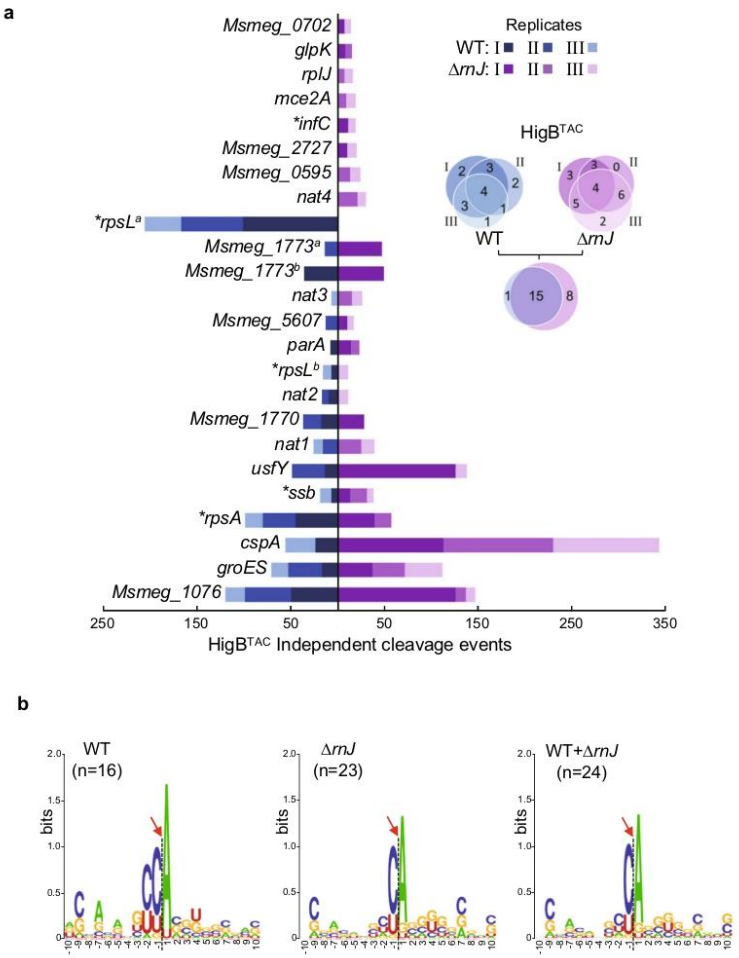

Fig. 2 HigB^{TAC} targets and recognition sequences in vivo. a HigB^{TAC} targets identified in vivo by nEMOTE following 3 h expression in *M. smegmatis* WT (on the left; shade of blue; replicates I, II, and III) and Δ*rnJ* (on the right; shade of violet; replicates I, II, and III). Target overlaps between the replicates and between the strains are represented by Venn diagrams. Bar length represents the number of independently observed cleavage events for each unique target site (*x* axis). The name of the gene of the cleaved mRNA is given on the left. The number of cleavages identified in each replicate for the WT (shade of blue; replicates I, II, and III) and the Δ*rnJ* mutant (shade of violet; replicates I, II, and III) is shown using the indicated color code. (*) indicates essential genes in both *M. smegmatis* and *M. tuberculosis*. **b** HigB^{TAC} preferred sequence motif. Logoplots showing HigB^{TAC} preferred motif obtained with the unique cleavage sequences identified for the WT ($n = 16$), the Δ*rnJ* mutant ($n = 23$) or both WT + Δ*rnJ* ($n = 24$). The *x* axis represents the 10 nucleotides upstream and downstream of the cleavage site that is located by the position between −1 and 1 (red arrow and dash line), and the default label for the *y* axis is bits.

mode of action and motif preference in vitro. To confirm that inhibition of CspA synthesis was reflecting *cspA* mRNA cleavage, we performed primer extension experiments to monitor *cspA* transcript during translation in the cell-free coupled transcription/translation system (Supplementary Fig. 3b) and showed that *cspA* transcripts were indeed cleaved by HigB^{TAC} (Fig. 3b) and not by the inactive HigB^{TAC}[K95A] substitution (Supplementary Fig. 3c). Remarkably, we found that *cspA* cleavage by HigB^{TAC} occurred only in the presence of the ribosome (Fig. 3b) and that out of frame CCA motifs in *cspA* (OOF1 and OOF2) were not recognized by HigB^{TAC}, demonstrating that mRNA cleavage by the TAC toxin is ribosome-dependent. Furthermore, although the CCA codon at the second position was the most robustly processed by HigB^{TAC}, we found that relocating CCA codon along the *cspA* transcript (with the native CCA at position 2 replaced by CCG also encoding a proline) results in cleavage at the new CCA sites, indicating that HigB^{TAC} is capable of cleaving mRNA during translation elongation (Supplementary Fig. 4). This is in agreement with the nEMOTE data that identified HigB^{TAC} cleavages along different transcripts (Supplementary Fig. 2a).

The in vivo nEMOTE data strongly suggest that HigB^{TAC} cleaves between the second and the third nucleotide within codons,

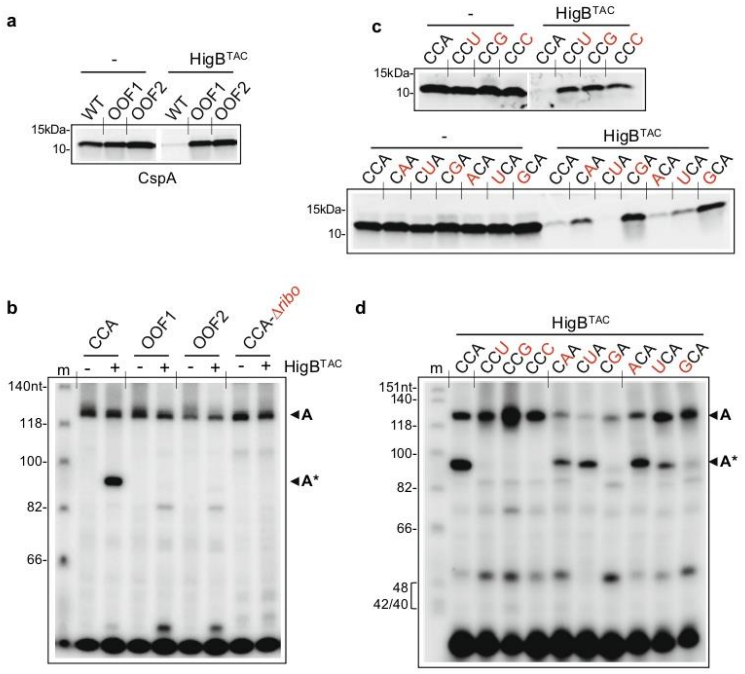

Fig. 3 HigB^{TAC} cleaves *cspA* mRNA at CCA codon during translation in vitro. a HigB^{TAC} inhibits synthesis of CspA wild-type (WT with codon CCA at Pro2) but not of CspA with +1 (OOF1) and +2 (OOF2) out of frame CCA motifs. CspA WT, OOF1, and OOF2 were independently expressed in a cell-free translation system with or without HigB^{TAC} (1.5 μM) as described in Fig. 1d. CspA translation products were labeled with [^{35}S]methionine and reactions were performed for 1 h 30 min at 37 °C. After translation, samples were separated on SDS–PAGE and visualized by phosphorimager. **b** Cleavage of *cspA* wild-type is ribosome-dependent. *cspA* wild-type (CCA), OOF1, and OOF2 were independently expressed in a cell-free translation system for 2 h with or without HigB^{TAC} (1.5 μM). RNA was extracted and subjected to a primer extension with [^{32}P]-labeled *cspA* primer. In parallel, *cspA* mRNA was incubated for the same time with or without HigB^{TAC} (1.5 μM) in the absence of ribosomes (CCA-Δ*ribo*), and also used for primer extension. The obtained labeled cDNAs were separated on denaturing urea-polyacrylamide gel and revealed by autoradiography. Arrows show the uncleaved (A, 126 nt) and cleaved (A*, 95 nt) *cspA*, and (m) stands for molecular ladder. Mutations in the CCA codon prevent both inhibition of CspA synthesis (**c**) and cleavage (**d**) of *cspA* by HigB^{TAC} in vitro. *cspA* wild type (CCA) and its mutant derivatives (mutations depicted in red) were independently expressed in a cell-free translation system with or without HigB^{TAC} (1.5 μM) and analyzed as described in panel (**a**) for CspA protein synthesis and in panel (**b**) for *cspA* cleavage. Representative results of triplicate experiments are shown.

with a preference for adenosine at the third position and with CCA codons being the most represented targets (Supplementary Fig. 2b). We next engineered mutations at each position of the CCA codon of *cspA* and tested them for translation inhibition and cleavage by HigB^{TAC} in vitro (Fig. 3c, d and Supplementary Fig. 3d, e). Strikingly, our data show that the adenosine at the third position is indeed critical for cleavage by HigB^{TAC}, as all of the mutations at this position efficiently prevented both inhibition of protein synthesis and cleavage by the toxin. In contrast, cytosines at the first and second positions were generally less sensitive to certain mutations. Indeed, while both positions were severely impacted when mutated for guanine, other mutations led to a more minor (i.e., UCA and CAA) or no (i.e., ACA and CUA) detectable impact. These data are in strong agreement with the cleavage sites identified in vivo on a transcriptome-wide scale (Supplementary Fig. 2a) and demonstrate that the TAC toxin shows substantial substrate preference.

Overall structures of isolated and 70S ribosome-bound HigB^{TAC}. We solved the structure of HigB^{TAC}[K95A] in complex with the *E. coli* 70 S ribosome, fMet-tRNA^{fMet} and native *M. tuberculosis cspA* mRNA by single-particle cryo-EM, with an average resolution of 3.64 Å (Fig. 4a and Supplementary Fig. 5a–d). Note that exploitable cryo-EM data were obtained only when a high concentration of inactive toxin over ribosomes was used in the presence of full-length *cspA* mRNA (100 toxins for 1 ribosome, 2 tRNAs and 2 mRNAs; see "Methods" section). Interestingly, while the sample presented a certain heterogeneity with 70 S in classical or ratcheted conformation and with tRNA in the P- and/or E-site, the toxin was only observed on non-ratcheted ribosome with a tRNA in the P-site. This suggests that binding of the toxin to the ribosome relies on the presence of a tRNA in the P-site and that the toxin might be rapidly released upon ratcheting. Overall, our cryo-EM structure shows that HigB^{TAC} occupies the ribosomal A-site and makes interactions with the 16S (h18, h30-31, h34, and h44) and the 23S (H69) rRNA, as well as with the P-site tRNA^{fMet}, the ribosomal protein uS13 and *cspA* mRNA (Fig. 4a, c). The fMet-tRNA^{fMet} is bound to the AUG initiation codon in the P-site and the CCA codon (Pro 2) of *cspA* lies in the A site, in the vicinity of the toxin, which is in agreement with the in vivo and in vitro cleavages obtained at this position.

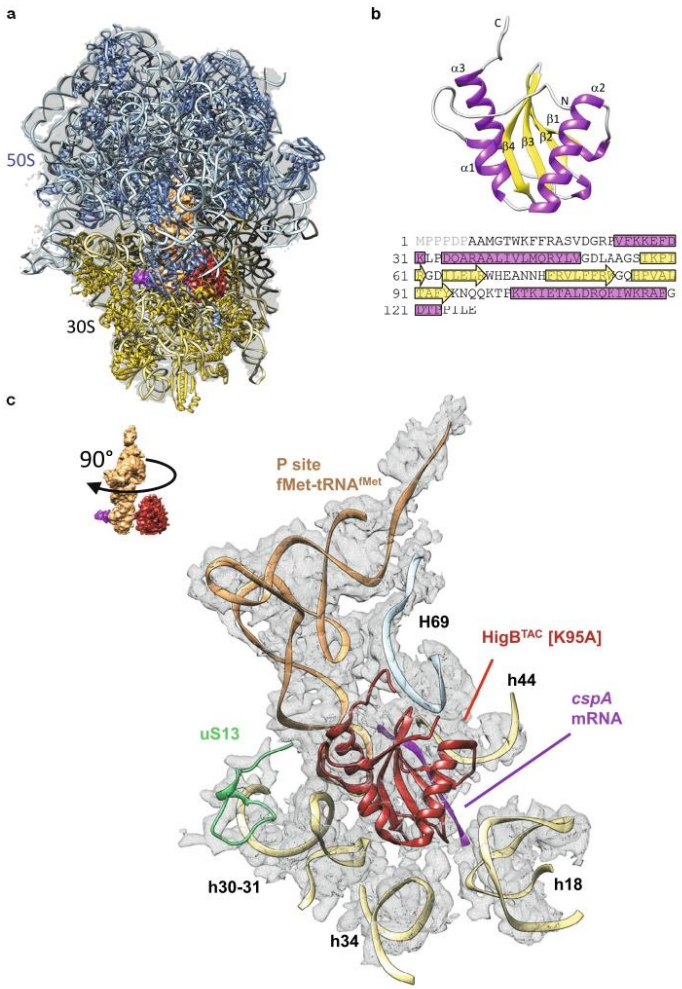

Fig. 4 Structure of the ribosome-associated TAC toxin with its native *cspA* substrate. a Electron density map of the complex (transparent gray), showing HigB^{TAC} [K95A] (red), its target *cspA* mRNA (purple), fMet-tRNA^{fMet} (orange), and the atomic models for the 50S (blue) and 30S (yellow) ribosomal subunits. **b** Crystal structure of HigB^{TAC} [K95A]. The N-terminus, C-terminus, and the secondary structure elements are indicated. The sequence of the toxin is shown underneath with the secondary structure element highlighted (α-helix in pink, β-strand in yellow). The first six residues (light gray) are not visible in the crystal structure. **c** Close-up of the interactions between HigB^{TAC} [K95A], the *cspA* mRNA, and the translating ribosome, rotated by 90° with respect to the structure in **a**. The HigB^{TAC} [K95A] is red; the P-site fMet-tRNA^{fMet} is orange; the *cspA* mRNA is purple; the uS13 ribosomal protein is green; the 16S rRNA is light yellow; the 23S rRNA is light blue; and the cryo-electron density map is a gray mesh. For clarity, 16S and 23S α-helices are labeled.

In parallel, the crystal structure of isolated monomeric HigB^{TAC}[K95A] was obtained at a 1.9 Å resolution and used to compare possible conformational changes that may occur upon association with the ribosome (Fig. 4b and Supplementary Fig. 5e, f). HigB^{TAC} has a similar compact fold as other RelE homologs, with four antiparallel β-strands flanked by three α-helices[29,47,48]. In contrast with *E. coli* RelE[29] or *P. vulgaris* HigB[49], HigB^{TAC} possesses a long C-terminal helix α3 (Fig. 4b and Supplementary Fig 6). Such long C-terminal helix is found in other closely related Gp49-like toxins, including *S. pneumoniae* HigB[47] and *V. cholera* HigB2[48]. Both cryo-EM and crystal structures of HigB^{TAC}[K95A] were very similar, with an rmsd value of 1.9 Å, indicating that little conformational changes occur upon binding to the ribosome, except for the loop between β2 and β3 (residues 68 to 75), α1 and α2 (residues 31 to 35), β4 and α3 (residues 95 to 101), and the beginning of β1 (residues 54 to 56) that fold to interact with the 16S rRNA decoding site and the target mRNA. Notably, these regions include most of the proposed catalytic

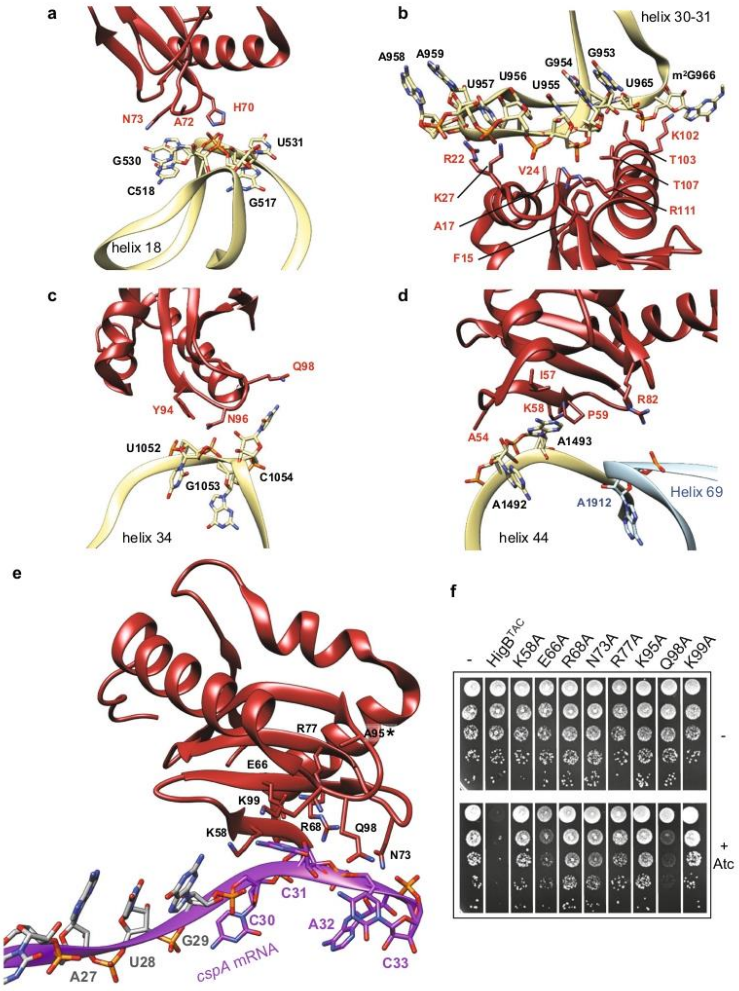

Fig. 5 HigB^{TAC} interactions with the ribosome and with *cspA* mRNA. Interaction between HigB^{TAC} [K95A] and: **a** helix 18 of 16S rRNA; **b** the region delimited by helices 30 and 31 of 16S rRNA; **c** helix 34 of 16S rRNA; and **d** helix 44 of 16S rRNA and helix 69 of 23S mRNA. **e** Interactions between the HigB^{TAC} [K95A] catalytic site and the CCA codon of the *cspA* mRNA. In all figures, HigB^{TAC} [K95A] is red, the *cspA* mRNA is purple, the 16S rRNA is light yellow, and the 23S rRNA is light blue. Residues and nucleotides within 4 Å of each other are indicated. **f** *M. smegmatis* transformed with pGMC-vector (−), HigB^{TAC} wild-type or its mutant derivatives were serial diluted, spotted on LB streptomycin agar plates with or without anhydrotetracycline (Atc ng/mL) inducer and incubated 3 days at 37 °C. Representative results of three independent experiments are shown.

residues of HigB^{TAC} (i.e., E66, R68, N73, K95, F93, Q98, and K99), suggesting that such differences could have some functional significance.

HigB^{TAC} interaction with 16S and 23S rRNA. The 16S rRNA appears as the main contact site for HigB^{TAC} on the ribosome (Fig. 5a–d). The interface engages more than twenty amino acid residues of HigB^{TAC}, covering a large surface of the toxin and interacting with the regions of the rRNA that include helices h18, h30-31, h34, h32, and h44 (Supplementary Fig. 7). Such interactions are very similar to the ones observed for *E. coli* RelE and YoeB, and *P. vulgaris* HigB toxins[29,50,51]. A comparison of contact areas between rRNA and known ribosome-bound toxins is detailed in Supplementary Fig. 7. The main contact of HigB^{TAC} with the 16S rRNA involves amino acid residues of its N-terminal region and of helices α1 and α3, as well as nucleotides at the junction between rRNA helices h30 and h31 (Fig. 5b). Using a cut-off distance of 3 Å, we considered that important residues include K27 that interacts with the O4 of U957 and R22 and R111 that are within hydrogen-bonding distance of the phosphate groups of A959 and U955, respectively. These residues may

provide key interaction for the correct positioning of HigB^{TAC} into the A site. Important interactions are also provided by histidine 70 (located between β2 and β3), which contacts the phosphate group of C518 (Fig. 5a), and by residue N96 (located between β4 and α3) with G1053 (Fig. 5c). In addition, HigB^{TAC} interacts with the decoding center, with residues A72 and N73 (located in the loop between β2 and β3) both interacting with G530 (Fig. 5a), and residues I57, K58, and P59 of β1 contacting A1493 (Fig. 5d). As a result, A1493 adopts an intermediate state between its fully flipped position observed during cognate mRNA-tRNA pairing and its position inside h44 observed when the A-site is vacant. A1492 remains mostly inside h44 while G530 is in a *syn* conformation, like in vacant 30S subunits. Together these results are consistent with what was previously observed for the pre-cleavage complex of *P. vulgaris* HigB on the ribosome[52] but differ from what was described for (i) RelE[29], where A1492 replaces A1493 outside of h44 and (ii) YoeB[53], where both A1492 and A1493 are fully flipped out (Supplementary Fig. 7). No major contact was found between HigB^{TAC} and the 50S subunit, except residue R82, which sits within a 4 Å distance of residue A1912 of H69 (Fig. 5d).

HigB^{TAC} catalytic site and interaction with *cspA* mRNA. In agreement with the in vivo and in vitro data, the CCA motif of native *cspA* transcript is directly facing HigB^{TAC} in the ribosomal A-site. While the HigB^{TAC}:*cspA* interface has an estimated local resolution of 3.3 Å, the densities are not very well defined and we were not able to rigorously orientate the nucleobases of C30 and A32, suggesting that interaction between the toxin and the CCA motif might be dynamic, at least in the case of HigB^{TAC}[K95A]. Yet, we could identify with confidence several key features of *cspA* and HigB^{TAC} interaction (Fig. 5e). Residues K58, E66, R68, N73, R77, Q98, and K99 are within a 4 Å distance of *cspA* mRNA nucleotides C30, C31, A32 (CCA codon) and C33. Together with the mutated residue K95, these residues may form the catalytic pocket of HigB^{TAC} that pulls the mRNA from its canonical position in the A-site, and surround the nucleotide C31. Based on available structures, residues R68, R77, and K95 of HigB^{TAC} may correspond to the K54, R61, and R81 catalytic residues in RelE, and to R68, R73, and K92 in HigB from *S. pneumoniae* (Supplementary Fig. 6). In addition, residue K58 possibly corresponds to residues K57 in *P. vulgaris* HigB and K49 in YoeB that interact with the second nucleotide of the A-site mRNA codon[49]. Residue E66 in HigB^{TAC} is conserved in *S. pneumoniae* HigB (residue E66) where it was proposed to be part of the catalytic site[47]. Alanine substitution of this residue partially inhibits HigB^{TAC} activity in vivo (Fig. 5f and Supplementary Fig. 8), suggesting that E66 could indeed contribute to catalysis[49,51]. Amino acid F93 in HigB^{TAC} corresponds to core residues F90 in *S. pneumoniae* HigB and Y82 in *V. cholerae* HigB2[48]. While Y82 was proposed to be involved in mRNA positioning[48], F93 is not in close contact with the mRNA in our structure. However, its current orientation suggests that it could be required to correctly position the proposed catalytic residues. More work will be needed to clarify the role of this residue. As observed for K95A, alanine substitutions of the positively charged residues K58, R68, R77, and K99 inhibited HigB^{TAC} toxicity (Fig. 5f and Supplementary Fig. 8), highlighting their importance for HigB^{TAC} activity in vivo. In addition, the N73A substitution had a strong effect on HigB^{TAC} toxicity, while Q98A showed only a mild effect (Fig. 5f). Both Q98 and N73 point towards the adenosine at the third position of the CCA codon, which is critical for the mRNA recognition by HigB^{TAC} (Fig. 3d). Remarkably, while N73 has no detectable equivalent in closely related toxins of *S. pneumoniae* and *V. cholerae*[47,48], it could have a similar role as residue N71 of *P. vulgaris* HigB, which is in the vicinity of the third nucleotide of the A-site codon and contributes to the toxin sequence specificity[49]. Although *P. vulgaris* HigB was proposed to select for adenosine at the 3rd position of the A-site codon through a *trans* Watson–Crick–Hoogsteen interaction with 16S rRNA C1054[52], our structure did not reveal any base pairing between the *cspA* mRNA and C1054.

HigB^{TAC} α3 interacts with P-site fMet-tRNA^{fMet} and S13 ribosomal protein. The HigB^{TAC} long C-terminal α3 (Figs. 4 and 6a) is found in HigB of *S. pneumoniae* and HigB2 of *V. cholera*, but not in *E. coli* RelE, YoeB, and *P. vulgaris* HigB (Fig. 6b and Supplementary Figs. 6 and 9). Our cryo-EM structure reveals that upon binding to the ribosome, one exposed face of α3 lies along the P-site fMet-tRNA^{fMet}. As a result, HigB^{TAC} is more deeply embedded in the A site than any other ribosome-dependent toxin described so far. Noticeably, positively charged residues K113 and R117 interact with the tRNA nucleotides G30 and C29, and R117 is also in close contact with residue I116 in the C-terminal tail of the ribosomal protein uS13 (Fig. 6a). This suggests that these residues may play an important role for HigB^{TAC} activity. Accordingly, single alanine substitution of either K113 or R117 affected HigB^{TAC} toxicity both in *M. smegmatis* and in *E. coli*, with K113A showing the strongest inhibitory effect (Fig. 6c and Supplementary Fig. 8). In contrast, alanine substitutions of the exposed negatively charged residues E106 and D110 of α3 did not inhibit HigB^{TAC} toxicity. In addition to α3, interaction with the P-site fMet-tRNA^{fMet} is also reinforced by residue R61, located at the end of strand β1, which lies within hydrogen bonding distances of the phosphate group between the fMet-tRNA^{fMet} nucleotides A36 and U37. Finally, we purified HigB^{TAC} [R61A] and HigB^{TAC} [K113A] and tested their activity in vitro. Our data show that indeed both mutations abolished HigB^{TAC} ability to inhibit CspA synthesis and severely affect *cspA* mRNA cleavage in vitro (Fig. 6d, e). Together these data suggest that the interactions between HigB^{TAC} and the P-site tRNA are critical for the toxin activity.

Discussion

This work shows that the TAC toxin is a bona fide ribosome-dependent RNase that binds the ribosome A-site to cleave its mRNA target and inhibit protein synthesis. Such activity is in agreement with its robust toxicity observed in all the bacterial hosts tested so far[22,23,30,41]. In contrast with HigB^{TAC}, no toxicity was detected when HigB2 and HigB3 were expressed in *M. smegmatis* or in *E. coli*. This suggests that both proteins could have a lower affinity for the ribosome or have lost their toxic RNase activity. Although we cannot exclude that these proteins might still be active RNases and toxic when expressed in *M. tuberculosis* in the absence of their endogenous antitoxins, the lack of toxicity of both toxins is supported by the fact that several key active residues of HigB^{TAC} (and of other closely related RelE-like toxins) are missing in both HigB2 and HigB3, including residues K58, N73, F93 and K99 of the catalytic center, and the newly identified K113 and R117 residues of the long C-terminal helix α3 contacting the initiator tRNA (Supplementary Fig. 10a). In support of this, the structure of HigB^{TAC} clearly differs from the alpha-fold models of HigB2 and HigB3 in particular in the two loops between β2-β3 and β4-α3, which contain most of the catalytic residues (Supplementary Fig. 10b). Moreover, the long C-terminal helix α3 of both HigB2 and HigB3, which corresponds to the α3 of HigB^{TAC}, is negatively charged and may thus not be able to interact with the P-site tRNA (Supplementary Fig. 10c). HigB2 and HigB3 also lack the large positive patch that allows the binding of HigB^{TAC} to the 16S rRNA (Supplementary Fig. 10c)

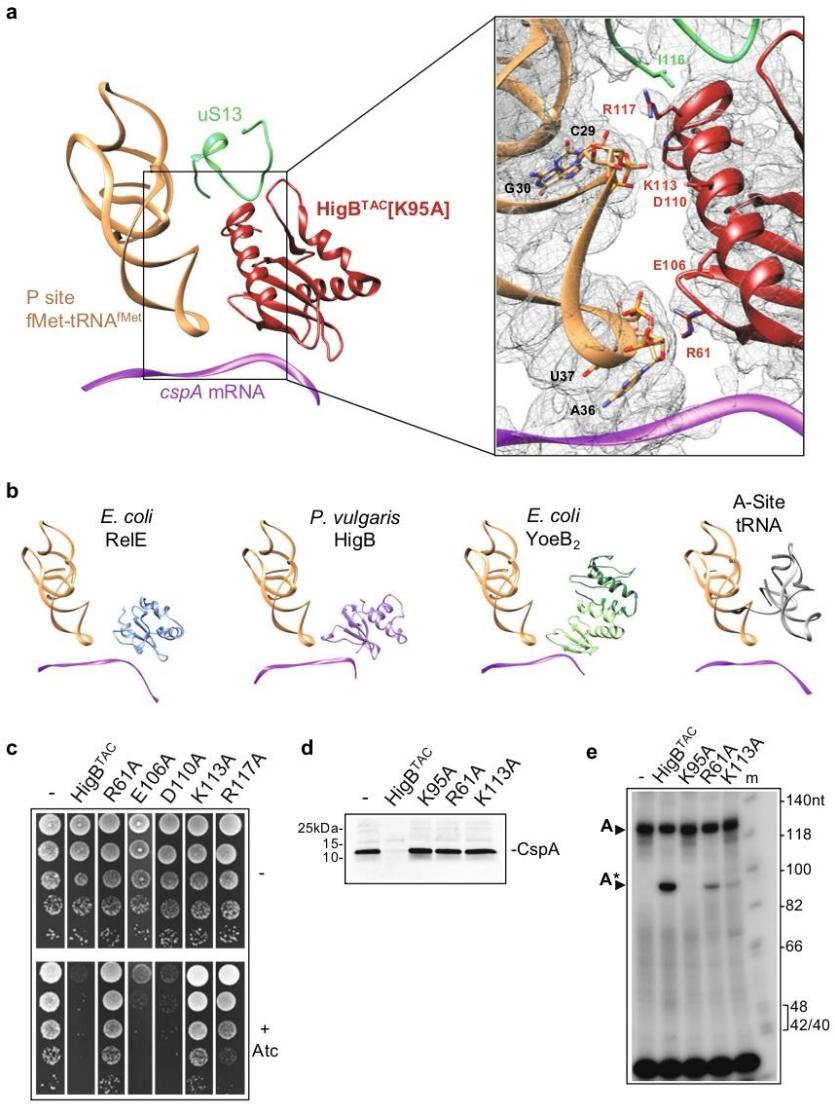

Fig. 6 The C-terminal extension of the TAC toxin interacts with P-site fMet-tRNA^{fMet} and is critical for its function. a Contrary to other ribosome-dependent toxins, HigB^{TAC} strongly interacts with the P-site tRNA and ribosomal protein S13 (uS13). Left, Overview of the contacts between HigB^{TAC} [K95A], the P-site fMet-tRNA^{fMet}, uS13, and the *cspA* mRNA. Right, Close up of the interactions observed between the third α-helix of HigB^{TAC} [K95A], the P-site fMet-tRNA^{fMet}, and uS13. Residues and nucleotides within 4 Å of each other are indicated, and the cryo-electron density map is displayed as a gray mesh. **b** Known toxins observed in pre-cleavage state with their respective mRNA targets and the P-site tRNA are shown here with a canonical translation reference. The structures are aligned on the P-site tRNA and presented in the same orientation as in **a**. Shown are (left to right): *E. coli* RelE [R45A-R81A] (PDB 4V7J); *Proteus vulgaris* HigB (PDB 4ZSN); *E. coli* YoeB dimer (PDB 4V8X); and a cognate tRNA observed in the A-site during canonical translation (PDB 7K00). As above, the P-site tRNA is orange and the mRNA is purple. **c** Positively charged residues of HigB^{TAC} helix α3 in contact with P-site tRNA are important for its function. *M. smegmatis* transformed with pGMC-vector (-), HigB^{TAC} wild-type or its mutant derivatives (Alanine substitution of residue R61, E106, D110, K113, or R117) were serial diluted, spotted on LB streptomycin agar plates with or without anhydrotetracycline (Atc ng/mL) inducer and incubated 3 days at 37 °C. Alanine substitution in R61 and K113 affects HigB^{TAC} inhibition of CspA synthesis (**d**) and cleavage (**e**) in vitro. CspA was expressed in a cell-free translation system with or without HigB^{TAC} wild-type, R61A, or K113A substitution, and analyzed as described in Fig. 3a for CspA protein synthesis and Fig. 3b for *cspA* cleavage. HigB^{TAC} [K95A] is shown as inactive control. Arrows show the uncleaved (A, 126 nt) and cleaved (A*, 95 nt) *cspA*. Representative results of three independent experiments are shown.

and the hydrophobic pocket shown to host the mRNA is less well defined (Supplementary Fig. 10d). Together these results suggest that HigB2 and HigB3 may neither be able to efficiently bind translating ribosomes nor be active as RNases. Remarkably, a substantial number of *M. tuberculosis* toxins appeared to be non-toxic[4,21–23]. Despite the limited number of conditions tested so far (i.e., mainly expressed in *M. smegmatis* or *E. coli*), these data suggest that selection for less harmful toxin mutants might have occurred in order to limit possible growth disadvantages (or growth inhibition) conferred by an uncontrolled expression of toxins from newly acquired TA genes (or even antitoxin-less toxin genes) via horizontal gene transfer[22,30,54]. In support of this, transposon insertion in at least 10 toxin encoding genes appeared to confer some growth advantages to *M. tuberculosis*[42]. In the case of HigB toxins, the fact that the RelE-like toxin is encoded first in the TA operon could somehow strengthen such a selection for less toxic mutant, as inhibition of newly synthesized toxin by the downstream antitoxin must be well tuned in order to ensure that de novo synthesized toxin is rapidly and efficiently inhibited. Intriguingly, the sole HigB of *M. tuberculosis* that remains active in our conditions is the toxin of the TAC system, in which inhibition of the toxin is performed by the concerted action of the antitoxin and its dedicated chaperone encoded from the same operon[33,34,36].

Activated HigB^{TAC} might randomly scan translating ribosomes until it finds its preferred codon sequences at the ribosomal A-site[29,52]. Our in vivo nEMOTE approach provides a robust identification of the codon sequences recognized by HigB^{TAC}, which was further supported in vitro using *cspA* mRNA as a model substrate. It shows that HigB^{TAC} cleaves between the second and the third nucleotide of A-site codons, with the CCA codon encoding a proline being the most represented in vivo (1365 out of the 2037 cleavages identified). CCA is a relatively rare codon in *M. smegmatis* (0.3%) and *M. tuberculosis* (0.6%), but is present in 51 and 75% of their coding sequences, respectively. Although less represented, codons ACA, UCA, UUA or CUA (coding for threonine, serine, leucine, and leucine, respectively) are also well recognized and cleaved by the toxin in vivo and/or in vitro. Overall, HigB^{TAC} appears to have a strong preference for adenosine at the third position, as found for *P. vulgaris* HigB[52,55], with the first and second position also contributing to specificity, although less significantly. Therefore, HigB^{TAC} cleaves irrespectively of the codon family and has the ability to target a large set of mRNAs as long as they are being translated. Despite a robust identification of the preferred motifs, nEMOTE only identified a few annotated mRNA transcripts that are cleaved following HigB^{TAC} expression (18 in total). Four of them encode essential proteins in *M. smegmatis* (seven in *M. tuberculosis*), suggesting that cleavage of such mRNA targets may contribute to the growth inhibition or cell death induced by this toxin. Although the relatively small number of mRNA targets identified could reflect that only a few types of RNA molecules are cleaved, it is more likely that only a fraction of each RNA species is cleaved. In this case, nEMOTE would consistently detect frequent cleavages in abundant RNAs, while cleavages of low-abundance RNAs (and rare cleavages of abundant RNAs) would only be detected in some RNA samples but at the level of background noise in others[44]. An estimation of transcripts abundance in *M. smegmatis* indicates that all the HigB^{TAC} mRNA targets identified in this work have an average, or above average, abundance in vivo when compared to all the annotated transcripts, suggesting that indeed only well-represented transcripts could be identified with confidence (Supplementary Fig. 11). Nevertheless, these data are in agreement with a model in which active HigB^{TAC} would preferentially target highly translated mRNAs, allowing a rapid inhibition of protein synthesis[49]. Whether such activity would provide a pool of free ribosomes that would ensure bacterial growth once normal conditions resume is not known.

Despite similar fold, ribosome-dependent RelE-like toxins are poorly related in sequences, even for their catalytic site[29,49,51,53], and exhibit important differences in codon preference. Indeed, *V. cholerae* HigB1 was shown to preferentially cleave AAA, ACU, GCG, and GCA, whereas AAA, ACU, AAU, CUG, GUG and GCG are cleaved in vivo by *Vc*HigB2[56]. Other studies revealed that *P. vulgaris* HigB cleaves AAA in vivo[55] and adenosine rich codons in vitro[52], *E. coli* YoeB cleaves AUG, UAA, CUG, GCG and GCU in vitro[53] and YafQ cleaves AAA in vivo[57]. The *E. coli* RelE, which exhibits little specificity in vivo, was shown to preferentially cleaves codons with purines at positions 2 and 3 of the A-site codon[29,58]. Finally, a recent work performed in vivo in *E. coli* with multiple RNase toxins showed that both RelE and HigB favor guanosine after the cleavage site and YoeB adenosine before the cleavage site within codons[59]. Although the conditions and organisms used to test toxin activities were generally different (comparison should thus be taken with caution), these data suggest relatively few overlaps with HigB^{TAC}, especially in vivo where none of the four most represented codons targeted by HigB^{TAC} were identified as preferred targets for the other toxins (except for RelE that shows little specificity in vivo). Besides, the AAA codon, which is efficiently recognized by most of the toxins described above was not identified in our in vivo work and was only poorly cleaved by HigB^{TAC} in vitro when compared to CCA or other preferred codons (Supplementary Fig. 3c). This further highlights the remarkable reservoir of substrate preferences found among RelE-like toxins so far.

We found that 3 out of the 10 annotated transcripts of *M. smegmatis* that are recognized by HigB^{TAC} are cleaved at a CCA codon located at position 2, just after the initiation codon (i.e., *cspA*, *rpsA*, and *rpsL*). Together these 3 transcripts account for about 37% (761/2037) of all the cleavage events detected in vivo. Yet, while more than half of all the annotated coding sequences in *M. smegmatis* or *M. tuberculosis* contain at least one CCA (see above), only 0.84 and 1.4% have a CCA at this position, respectively. These data indicate that despite the fact that cleavage can occur all along a targeted mRNA, there is a preference for HigB^{TAC} to cleave a CCA at the second position, both in vivo and in vitro. Translation initiation could thus offer a window of opportunity for the toxin to reach the A-site, as previously proposed[50]. Indeed, a comparison of the ribosome-bound HigB^{TAC} with the structure of the ribosomal initiation complexes (IC) shows that HigB^{TAC} cannot bind the 30S-IC when IF1 is present[60]. However, HigB^{TAC} could easily accommodate into the late 70S-IC, even if IF2 is still present (Supplementary Fig. 12). Noticeably, crucial contact between the long C-terminal helix α3 of HigB^{TAC} and the P-site fMet-tRNA described in this work would still be possible, even if the fMet-tRNA is in P/I conformation. The fact that initiation is by far the slowest step of translation[61,62] and that the presence of IF2 prevents tRNAs from accessing the A-site and competing with the toxin, suggests that HigB^{TAC} would have more chances to recognize and cleave at the CCA adjacent to the initiation codon than at other codons further down the sequence. Such a mechanism would contribute to the efficient and rapid inhibition of protein synthesis and the resulting growth inhibition caused by HigB^{TAC}. Whether the specific contacts found between the HigB^{TAC} C-terminal extension and the fMet-tRNA facilitate such a process remains unknown. Further work is warranted to address such a possible scenario.

Methods

Bacterial strains and culture conditions. *E. coli* strains W3110[34], MG1655(ATCC 700926), BL21(λDE3) (Novagen), BL21 AI(λDE3) (Novagen), *M. smegmatis* mc^2155 (strain ATCC 700084) and mc^2155 *rnj102* (*Δrnj*)[46] were previously

described. DNA cloning experiments were carried out in *E. coli* DH5α (NEB) or Stellar (Clontech). *E. coli* strains were grown in Luria Bertani medium (LB) and supplemented with streptomycin (25 µg/mL), ampicillin (50 µg/mL), or kanamycin (50 µg/mL) as required. *M. smegmatis* strains were grown in LB medium supplemented when necessary with streptomycin (25 µg/mL) or kanamycin (50 µg/mL), and Tween80 (0.05%) to minimize cell aggregation in liquid culture.

Western blot analysis. Whole-cell extracts were performed as described[35]. Briefly, 1 ml aliquots of the cell cultures were collected at 5000 x g and resuspended in 1× SDS loading buffer (1/4th volume of the initial OD_{600}). Western blots monitoring GFP or Strep-tagged GroES in vitro synthesis using the PURE system with or without $HigB^{TAC}$ toxin were performed by loading 10 µL of PURE reaction with 1× SDS loading buffer. Proteins were then separated on Mini-Protein TGX gels (Bio-Rad) by SDS-PAGE and transferred to polyvinylidene difluoride membranes (Bio-Rad) using the Trans-Blot® TurboTM transfer system (Bio-Rad). Membranes were blocked for 1 h at room temperature in 5% (w/v) nonfat dry milk in PBS containing 0.05% (v/v) Tween 20. Primary antibodies used in this study were anti-$HigB^{TAC}$ antibody (dilution 1:1000)[30], anti-GFP (Invitrogen, 1:3000), StrepMAB-Classic horseradish peroxidase (HRP; Iba Life Sciences, 1:30,000), and anti-His6-HRP (Invitrogen, 1:1000). HRP-conjugated mouse IgG (Promega, 1:2500) was used as a secondary antibody. Blots were developed by chemiluminescence using Clarity Western ECL substrate (Bio-Rad) with the ChemidocTM Touch imaging system (Bio-Rad) and analyzed with the Image Lab software (Bio-Rad).

RNA isolation for the nEMOTE procedure. Total RNA was isolated from *M. smegmatis* strains WT/Δ*rnJ* that were transformed by electroporation with pGMC-toxins and grown to mid-exponential phase. Independent cultures of each strain were launched on different days and with different batches of the medium. When 10 mL cultures reached an OD_{600} of 0.4, anhydrotetracycline was added to a final concentration of 100 ng/mL to induce toxins for 3 or 24 h. After induction, 1 mL of culture was serial diluted on a LB agar plate supplemented with streptomycin and with or without ATc to check the activity of the toxins and the presence of potential suppressor before RNA extraction. Plates were stored at 37 °C for 3 days. Cells were pelleted by centrifugation at 2800 × *g* for 10 min at 4 °C and the supernatants were removed. Then, 1 mL of cold ethanol/acetone (1:1, v/v) was immediately added to the pellets to protect the RNA (note that these pellets could be kept at −80 °C). Next, the mix ethanol/acetone was removed and a mix of 700 µL of buffer RLT (RNeasy® Mini Kit. QIAGEN) + 10 µL β-mercaptoethanol was added to resuspend the pellet. For each sample, 25–50 mg acid-washed glass beads (500 µm diameter Sigma Aldrich) were weighed in a 2 mL Safe-Lock tube. The cells were broken using a BeadBeater (Bertin Technologies Precellys 24) 1 min ON–1 min OFF–1 min ON. The lysed cells were centrifuged at 15,800 × *g* at 4 °C for 10 min. The supernatants were transferred in a new RNase-free Eppendorf tubes. Then, 70% Ethanol v/v is added to the supernatants, mixed, and transferred to the provided column (RNeasy® Mini Kit. QIAGEN). Finally, purification of total RNA using the RNeasy® Mini Kit was completed according to the manufacturer's guidelines. RNA quality was verified with an Agilent 2100 BioAnalyzer (Genotoul platform in Toulouse).

nEMOTE library preparation. The protocol for nEMOTE was carried out as described[43], with slightly modified primers (Supplementary Table 3). Briefly, 8 µg of RNA were incubated with XRN-1 (NEB) for 4 h to digest mono-phosphorylated RNA. Then the RNA was split into two pools, one pool of RNA was both phosphorylated with polynucleotide kinase (NEB) and ligated to Rp8 oligo, the control pool of RNA was only ligated to Rp8. The Rp8 oligo that we ligate to the 5'OH ends of the RNA contains a unique molecular identifier (a series of random nucleotides), which allows us to tag each ligation event with its own unique barcode. Reverse transcription was performed using DRNA primer and ProtoScript II RT enzyme (NEB). Finally, PCR amplification was performed with barcode primers and Illumina adaptator A and B primer using Q5 Polymerase Hot-Start (NEB).

Bioinformatics analyses. Raw sequencing reads were first filtered and trimmed using the emoteStepI method from a Perl program called EMOTE-conv[63]. The trimmed reads are mapped against the *M. smegmatis* genome (NC_008596.1) with bowtie (version 1.2)[64], using the parameters -a --best –strata -v 1. The obtained alignment file is submitted to the emoteStepII step from EMOTE-conv in order to compute an annotated coverage table corresponding to the number of reads per position per EMOTE barcode. The unique molecular identifier that was included in the Rp8 oligo allows us to detect when the cDNA from a single ligated RNA molecule is represented by one or more different illumina reads (this is possible due to the PCR amplification in the library preparations). Thus, all identical reads with the same unique molecular identifier are only counted as a single RNA cleavage event. Downstream analysis and plots are performed in R (version 3.4.4, running under Ubuntu 14.04.6). We set a very conservative cut-off for what was considered a true toxin-dependent cleavage event: The genomic positions where the 5' OH-ends of at least 7 independent RNA molecules were detected for at least one test sample (toxin + PNK) and where no 5'OH-ends were detected in all three negative control samples (toxin-PNK, vector+PNK, and vector-PNK). The putative cut-site motif is plotted with the R package ggseqlogo (version 0.1).

The evolutionary history between *M. tuberculosis* $HigB^{TAC}$, HigB2, HigB3, and *E. coli* RelE was inferred using the maximum likelihood method. Protein sequences were aligned by PROMALS3D and the tree was generated by MEGA11. The tree with the highest log likelihood (−1228.63) is presented in Fig. 1b. The tree is drawn to scale, with branch length representing the number of substitutions per site.

***M. smegmatis* gene expression**. To generate the violin plot showing *M. smegmatis* gene expression in transcripts per million the following procedure was applied. The data from *M. smegmatis* wild-type mRNA sequenced with Illumina[65] consists of 2 replicates: Replicate 1 (112309244 SE reads of 51 bp) and Replicate 2 (126869005 SE reads of 51 bp). After Trimmomatic cleaning, the cleaned reads, replicate 1 (24637386 SE reads), replicate 2 (67623219 SE reads), were remapped to the reference genome of *M. smegmatis* MC^2155 (CP000480) with bwa and converted to sorted bam with Samtools. Since no differential analysis was possible with two replicates of the same condition, we decided to calculate the TPM (transcripts per million) for all genes of both replicates and compare them by their mean values. The TPM and read counts were obtained from the bam and TPMCalculator[66].

Cell-free transcription–translation system in vitro. Cell-free transcription/translation-coupled in vitro assay using the PURE system (NEB) was carried out as described[34]. Briefly, DNA of *cspA* (*Rv3648c*) 204 bp, *gfp* 717 bp, or *groES* (*Rv3418c*) 303 bp were amplified by PCR using primers containing T7 promoter and terminator and added at a final concentration of 20 ng/µL to the PURE system with or without toxins (1.5 µM). Protein synthesis was performed at 37 °C for 1 h 30 min in the presence of 0.6 µCi/µL of ^{35}S-methionine. Samples were then separated by SDS/PAGE on 4–20% Mini-Protean TGX gels (Bio-Rad) for 1 h 15 min at 100 V. Gels were fixed in 10% acetic acid/40% methanol (v/v) for 30 min and proteins were visualized using a Typhoon phosphorimager (GE Healthcare) and Multigauge software (Fuji).

Primer extension. For *cspA* RNA extracts without ribosome, DNA fragment of *cspA* containing T7 promoter and terminator (forward primers CspA_CCA_Fw, CspA_CCT_Fw/CspA_CCG_Fw/CspA_CCC_Fw, CspA_CAA_Fw/CspA_CTA_Fw/CspA_CGA_Fw, CspA_ACA_Fw/CspA_TCA_Fw/CspA_GCA_Fw, CspA_codon 7_Fw, OOF1_Fw, OOF2_Fw, or CspA_AAA_Fw, and the reverse primer CspA_term_Rv listed in Supplementary Table 3), as prepared for the cell-free transcription–translation system in vitro, was transcribed using 40 unit of T7 RNA polymerase (Promega) with or without $HigB^{TAC}$ (1.5 µM) for 2 h at 37 °C. RNA was subsequently extracted with TRI Reagent (MRC) and chloroform. For *cspA* RNA extracts with the ribosome, the DNA fragment of *cspA* containing T7 promoter and terminator was added to the cell-free transcription–translation system as described above, except that ^{35}S-Methionine was not included. After 2 h at 37 °C, RNA was extracted with TRI Reagent (MRC) and chloroform. For the reverse transcription, up to 2 µg of purified *cspA* RNA, 0.05 µM ^{32}P-labeled *cspA* primer (primer RT CspA P32 PAGE 1, except in Supplementary Fig. 4b; Supplementary Table 3 where primer RT CspA P32 PAGE 2 was used in order to obtain longer *cspA* fragments that included the P17 and P22 region) and 1 mM dNTPs were mixed in a 10 µL volume, incubated at 65 °C for 5 min, and chilled on ice for 1 min. Finally, 10 µL 2× buffer (mix 4 µL 5× ProtoScript II RT (NEB), 2 µL 0.1 M DTT, 8 units RNasin® Plus Ribonuclease Inhibitor (Promega), 200 units of ProtoScript II RT Enzyme (NEB) in 10 µL) were mixed and incubated at 48 °C for 1 h. cDNA was mixed with RNA loading dye, loaded on a 6% Polyacrylamide gel containing 7 M urea, separated at 300 V for 1 h 15 min, and revealed by autoradiography using Typhoon phosphorimager (GE Healthcare) and Multigauge (Fuji Film). Note that ^{32}P labeling of the primer was performed using PNK (10 u, Thermofisher) at 37 °C for 1 h in the presence of the primer RT CspA P32 PAGE 1 or 2 (0.5 µM final concentration) and 2,5µCi/µL of ^{32}P. The labeled primer was purified with Bio-Spin® 6 Columns (Biorad).

Protein purification. Purification of $HigB^{TAC}$, its mutant derivatives, HigB2, and HigB3 with a C-terminal His_6 tag was performed as follows. About 50 fresh colonies of *E. coli* BL21 AI transformed with pET20b-toxin derivatives were pooled and grown in 1 liter (or 250 mL for $HigB^{TAC}$ inactive mutants) of LB ampicillin supplemented with glucose (0.2% w/v) at 37 °C until OD_{600} reaches 0.5-0.7. Cell cultures were centrifuged at 6000 × *g* for 10 min, resuspended in LB ampicillin supplemented with 0.2% of L-arabinose to induce toxin expression, and incubated overnight at 22 °C. Cells were centrifuged and lysis was performed by resuspending the pellets in 20 mL of lysis buffer (25 mM equimolar solution of Na_2HPO_4/NaH_2PO_4; 200 mM NaCl; 20 mM imidazole pH 8.0) supplemented with one EDTA-free Protease Inhibitor tablets (Roche) and benzonase 500 unit (Sigma-Aldrich) followed by lysis in a cell disruptor at 1.5 bar (One shot model, constant systems Ltd). Intact cells were removed by centrifugation at 30,000 × *g* for 30 min at 4 °C. After washing the Ni-NTA column 3 times with the wash buffer, the supernatant was applied to the column for 30 min. Finally, the protein was eluted with Elution buffer (25 mM equimolar solution of Na_2HPO_4/NaH_2PO_4; 200 mM NaCl; 250 mM imidazole, pH 8.0). Proteins were dialyzed with the exchange buffer (25 mM equimolar solution of Na_2HPO_4/NaH_2PO_4; 200 mM NaCl; 10% (w/v) glycerol; pH 8.0) using PD-10 MiniTrap (GE-life science) and concentrated if

needed with Vivaspin (5 kDa pore size. Sartorius) and stock at −80 °C. For X-ray crystallography analysis, fresh colonies of pET15b-*Mtb*-HigB^{TAC}[K95A] transformed in *E. coli* BL21 (DE3) were pooled in 20 mL LB broth supplemented with ampicillin (100 µg/mL) and grown overnight at 37 °C. Cultures were carried out by inoculating 1 L of LB broth (+ampicillin 100 µg/mL) with 15 mL of pre-culture at 37 °C at 180 rpm. Heterologous protein expression was induced by adding 1 mM IPTG when OD_{600} reached ~0.5. Cells were allowed to grow for 4 h at 37 °C. The pelleted cells were suspended in 80 mL of buffer A (25 mM Na_2HPO_4/NaH_2PO_4, 200 mM NaCl, pH 7.0) supplemented with 20 mM imidazole, 0.2 mM PMSF, 0.5 mg/mL lysozyme and lysed using 4 cycles of cell disruptor (EmulsiFlex-C5, Avestin) at about 10,000 psi prior to centrifugation at 25,000 × *g* for 30 min at 4 °C. The supernatant was applied to a 1-mL HisTrap^{TM} HP column (Cytiva) equilibrated with buffer A containing 20 mM imidazole. After extensive washing with 30 mM and 60 mM imidazole in buffer A, the recombinant protein was eluted with buffer A supplemented with 150 mM imidazole. The eluted protein was dialyzed twice against 1 L of buffer A without imidazole under magnetic stirring at 4 °C and the His_6-tag was then cleaved with 0.1 U of thrombin per mg of protein in the presence of 10X cleavage buffer (200 mM Tris-HCl, 1.5 M NaCl, 25 mM $CaCl_2$, pH 8.4) overnight at 12 °C under rotary agitation. The cleaved protein was injected into a 1-mL HisTrapTM HP column (Cytiva) equilibrated with buffer A supplemented with 20 mM imidazole and recovered from the flow-through, then concentrated using a Vivaspin 5 centrifugal concentrator (Sartorius) to about 7 mg/mL, prior to injection into a HiLoad 16/60 Superdex 75 (GE Healthcare) pre-equilibrated with 20 mM MES, 200 mM, NaCl pH 6.5 (buffer B). MenT3^{K189} was purified as described[4] and Bovine Serum Albumin (BSA) was purchased from Sigma (ref.A3059).

Crystallization and crystal structure determination. Purified HigB^{TAC}[K95A] was concentrated to 28.6 mg/mL in buffer B and crystallized at 12 °C in 30% (w/w) PEG 4,000, 0.2 M ammonium acetate, 0.1 M sodium acetate, pH 4.6. The volume ratio between the purified toxin and crystallization solutions was 200:100 (nL). Crystals were directly flash-frozen in liquid nitrogen. Datasets were collected on beamline MASSIF-3 (ID30-A3) at the European Synchrotron Radiation Facility (ESRF, Grenoble, France). All data were indexed, integrated, and scaled using XDS version Jan 31, 2020, and the CCP4 v7.0.078 software suite was used for subsequent crystallographic calculations[67]. The structure was solved by molecular replacement using PHASER v2.8.3[68] and a structure-based homology model derived from the structure of *S. pneumoniae* HigB (PDB 6AF4). The search model was truncated to a polyalanine and all loops were removed to avoid model bias. Iterative cycles of manual model building in COOT v0.9.6[69] and refinement procedures using REFMAC v5.8.0258[70] were applied until convergence. Details of data collection, cell parameters, processing, and refinement statistics are presented in Supplementary Table 1.

Sample preparation for cryo-EM. For the cryo-EM complex, ribosomes were purified from *E. coli* MG1655. When the culture reached an OD_{600} of 0.8, cells were pelleted, resuspended in FP buffer (20 mM Tris-HCl pH 7.5, 50 mM MgOAc, 100 mM NH_4Cl, 0.5 mM EDTA, and 1 mM DTT) and lysed in a French press. The lysate was then clarified by centrifugation at 20,000 × *g* for 45 min at 4 °C. Next, the supernatant was layered 1:1 (v:v) over a high-salt sucrose cushion buffer (10 mM Tris-HCl pH 7.5, 10 mM MgOAc, 500 mM NH_4Cl, 0.5 mM EDTA, 1.1 M sucrose and 1 mM DTT). After ultracentrifugation at 92,000 × *g* for 20 h at 4 °C, the resulting ribosome pellets were resuspended in 1 mL of 'Ribo_A' buffer (10 mM Tris-HCl pH 7.5, 10 mM $MgCl_2$, 50 mM NH_4Cl, 0.5 mM EDTA and 1 mM DTT). To isolate the 70 S ribosomes from 30 S and 50 S ribosomal subunits, the ribosomes were centrifuged at 95,000 × *g* for 18 h at 4 °C through a 10–45% (w/w) linear sucrose gradient in Ribo_A buffer. Gradients were fractionated before determining the A_{260} absorbance profiles. Fractions corresponding to the 70S peak were mixed and diluted in Ribo_A buffer for final ultracentrifugation at 92,000 × *g* for 20 h at 4 °C. The ribosomal pellets were resuspended in Ribo_A buffer, and flash frozen and stored at −80 °C.

To prepare the complex, 25 pmol of fMet-tRNA^{fMet} (VWR, Ref. ICNA0219915410) was first refolded for 2 min at 80 °C in "Buffer I" (10 mM HEPES-KOH pH 7.5, 25 mM $MgCl_2$, 25 mM, and 20 mM NH_4Cl), and this was followed by a second incubation at room temperature for 30 min. Next, purified 70 S ribosomes (12.5 pmol) were incubated at 37 °C for 15 min in "Buffer-III" (10 mM MgOAc, 10 mM NH_4Cl, 50 mM KCl, 5 mM HEPES-KOH pH 7.5, and 1 mM DTT) with 25 pmol of *cspA* mRNA and 25 pmol of the folded fMet-tRNA^{fMet}. Finally, 1250 pmol of HigB^{TAC} [K95A] toxin were added, and this was incubated at 37 °C for 5 min. After adjusting concentrations to 160 nM in buffer-III, samples were directly applied to glow-discharge holey carbon films (Quantifoil 3.5/1 µm). These grids were flash-frozen in liquid ethane using a Vitrobot Mark III (FEI).

Cryo-EM data collection. The frozen grids were then transferred to the Structural Biophysical Chemistry Platform of the IECB, where they were imaged using a Talos Arctica cryo-TEM (Thermo Fisher Scientific) operating at 200 kV and equipped with a field-emission gun. SerialEM v3.8 software was used to automatically record 6381 movies under low-dose conditions on a K2 direct electron detector (Gatan) with a defocus range of 0.4–2.0 µm and at a final pixel size of 0.9291 Å.

Image processing. Movies were corrected for the effects of drift and beam-induced motion using MotionCor2 v1.0.6 software[71]. Contrast transfer function (CTF) parameters were estimated using Gctf v1.18 software[72]. Electron micrographs showing signs of drift or astigmatism were discarded, resulting in a dataset of 5178 movies. Particles were semi-automatically selected in Cryosparc v2.12[73] and subjected to two rounds of 2D classification in order to remove defective particles. This resulted in the selection of 284,820 particles. All subsequent data processing was performed using RELION v3.1.3[74]. An initial three-dimensional (3D) auto-refinement using a large soft circular mask (diameter 380 Å) produced a reconstruction at a resolution of 3.33 Å. The pixel size was then re-estimated by comparison to the atomic model of the *E. coli* mature 70S subunit (PDB ID 4YBB), and adjusted to 0.893 Å/pixel. To improve the homogeneity, the datasets were then sorted into 12 subsets using the 3D-classification function. This resulted in the following grouping: 70S ribosomes (7 classes containing 175,859 particles); ratcheted ribosomes (2 classes and 39,752 particles); the 50S ribosomal subunit (2 classes and 51,812 particles); and poorly resolved particles (1 class of 27,397 particles). The particles which were clearly homogenous 70S or ratcheted ribosomes were further processed separately using the same protocol. This was followed by a second round of 3D auto-refinement using the same parameters, resulting in reconstructions with resolutions of 3.4 Å (for the 70S) and 4.21 Å (for the ratcheted ribosomes). We then subtracted the ribosome signal from the datasets by using a soft mask generated from the previous refinement run (voxel values of 0 inside, 1 outside, extended by 6 pixels, and a soft edge of 6 pixels). The subtracted datasets were then sorted by 3D classification without alignment, using a tight soft spherical mask with a diameter of 200 Å. We tested various combinations in order to split the datasets into as many 3D classes as possible while still keeping the groups homogeneous; however, the HigB^{TAC} [K95A] toxin could not be found in the dataset with the ratcheted ribosomes. The dataset containing the 70S ribosomes was separated into eight classes, with one containing HigB^{TAC} [K95A]. The 42,261 particles corresponding to that class were then selected and reverted to their original content, before the subtraction of the ribosome signal. A third round of 3D auto-refinement resulted in a 3.8-Å map of the ribosome containing the CspA mRNA, an fMet-tRNA^{fMet}, and HigB^{TAC} [K95A]. To ensure that a homogeneous class was indeed obtained, 3D classification with signal subtraction was again performed, this time using a soft mask with a diameter of 80 Å to focus on the toxin. This dataset was split into four classes, with one class of 13,877 particles containing the toxin. Once again, we reverted to the original non-subtracted particles and reconstructed a new map at a resolution of 4.85 Å. After CTF refinement and particle polishing, the 'shiny' particles were subjected to a final round of 3D auto-refinement and post-processing. This resulted in a consensus map with an overall resolution of 3.11 Å as per RELION's gold-standard Fourier shell correlation (FSC) calculation[75]. To take into account the internal flexibility of the ribosome, we also performed a multibody refinement[76]. The ribosome was separated into the large 50S subunit, the body of the small 30S subunit, and the 30S head. HigB^{TAC} [K95A] and CspA mRNA were only included in the two 30 S fragments, while the tRNA was included in all three sections. Masks corresponding to these sections were made from a 30-Å low-pass filtered version of the consensus map, with soft edges of 12 Å in order to define the solvent region boundary and to ensure that all the sections overlapped. The multibody maps were then fitted and resampled on the consensus map using UCSF-Chimera v1.13.1[77]. Finally, the four maps were sharpened using Phenix v1.18.2[78], their local resolutions estimated using Resmap v1.1.4, and map quality was assessed using Phenix mtriage[79].

Model building and refinement. UCSF-Chimera v1.13.1[77] was used to rigid-body fit the cryo-EM structure of the *E. coli* ribosome at a resolution of 2 Å (PDB 7K00) into our maps, with each protein and RNA treated separately. Our crystal structure of *M. tuberculosis* HigB^{TAC} [K95A] toxin (PDB code 7AWK) was then fitted in the remaining portion of the map. The different molecules were manually adjusted in their respective multi-body maps using COOT v0.9.5. Special attention was paid to the toxin, the tRNAfMet, and the CspA mRNA, and their models were compared with the different multibody maps. The final atomic model was further improved by real-space refinement against the consensus maps using Phenix v1.18.2. Outliers were then again manually corrected in COOT and the model was refined a second time in Phenix. Once the structure was complete, Mg2+ ions were manually added in COOT using the "unmodelled blobs" function and a threshold of 5.5 RMSD. The model quality was evaluated with MolProbity v4.5.1[80]. The remaining analysis and the illustrations were done using UCSF-Chimera v1.13.1[77]. Details of data collection, processing, and refinement statistics are presented in Supplementary Table 2, and a schematic representation of the cryo-EM single-particle reconstruction workflow is in Supplementary Fig. 13. Note that full scan blots and source data can be found in the Source Data file and in the Supplementary Information file.

Reporting summary. Further information on research design is available in the Nature Research Reporting Summary linked to this article.

Data availability

The data that support this study are available from the corresponding author upon reasonable request. The electron density maps and structure models are deposited in the

EMDB and PDB under the following accession codes, respectively: 7AWK for the crystal structure of the *M. Tuberculosis* HigB^{TAC} [K95A] toxin alone; and EMD-12261 and 7NBU for the toxin and its target mRNA on the translating *E. coli* ribosome. The nEMOTE sequencing data have been deposited in Zenodo [https://doi.org/10.5281/zenodo.6397033]. Source data are provided with this paper.

Received: 4 February 2022; Accepted: 27 April 2022;
Published online: 12 May 2022

References

1. Page, R. & Peti, W. Toxin-antitoxin systems in bacterial growth arrest and persistence. *Nat. Chem. Biol.* **12**, 208–214 (2016).
2. Harms, A., Brodersen, D. E., Mitarai, N. & Gerdes, K. Toxins, targets, and triggers: an overview of toxin-antitoxin biology. *Mol. Cell* **70**, 768–784 (2018).
3. Wang, X., Yao, J., Sun, Y.-C. & Wood, T. K. Type VII toxin/antitoxin classification system for antitoxins that enzymatically neutralize toxins. *Trends Microbiol.* **29**, 388–393 (2021).
4. Cai, Y. et al. A nucleotidyltransferase toxin inhibits growth of *Mycobacterium tuberculosis* through inactivation of tRNA acceptor stems. *Sci. Adv.* **6**, eabb6651 (2020).
5. Yao, J. et al. Novel polyadenylylation-dependent neutralization mechanism of the HEPN/MNT toxin/antitoxin system. *Nucleic Acids Res.* **48**, 11054–11067 (2020).
6. Songailiene, I. et al. HEPN-MNT toxin-antitoxin system: the HEPN ribonuclease is neutralized by OligoAMPylation. *Mol. Cell* **80**, 955–970.e7 (2020).
7. Freire, D. M. et al. An NAD+ phosphorylase toxin triggers *Mycobacterium tuberculosis* cell death. *Mol. Cell* https://doi.org/10.1016/j.molcel.2019.01.028 (2019).
8. Jurėnas, D., Van Melderen, L. & Garcia-Pino, A. Mechanism of regulation and neutralization of the AtaR-AtaT toxin-antitoxin system. *Nat. Chem. Biol.* **15**, 285–294 (2019).
9. Cintrón, M. et al. Accurate target identification for *Mycobacterium tuberculosis* endoribonuclease toxins requires expression in their native host. *Sci. Rep.* **9**, 5949 (2019).
10. Li, M. et al. Toxin-antitoxin RNA pairs safeguard CRISPR-Cas systems. *Science* **372**, eabe5601 (2021).
11. Wilcox, B. et al. *Escherichia coli* ItaT is a type II toxin that inhibits translation by acetylating isoleucyl-tRNAIle. *Nucleic Acids Res.* **46**, 7873–7885 (2018).
12. Wilmaerts, D. et al. HokB monomerization and membrane repolarization control persister awakening. *Mol. Cell* **75**, 1031.e4–1042.e4 (2019).
13. LeRoux, M., Culviner, P. H., Liu, Y. J., Littlehale, M. L. & Laub, M. T. Stress can induce transcription of toxin-antitoxin systems without activating toxin. *Mol. Cell* **79**, 280.e8–292.e8 (2020).
14. Pecota, D. C. & Wood, T. K. Exclusion of T4 phage by the hok/sok killer locus from plasmid R1. *J. Bacteriol.* **178**, 2044–2050 (1996).
15. Guegler, C. K. & Laub, M. T. Shutoff of host transcription triggers a toxin-antitoxin system to cleave phage RNA and abort infection. *Mol Cell* https://doi.org/10.1016/j.molcel.2021.03.027 (2021).
16. Helaine, S. et al. Internalization of Salmonella by macrophages induces formation of nonreplicating persisters. *Science* **343**, 204–208 (2014).
17. Fraikin, N., Goormaghtigh, F. & Van Melderen, L. Type II toxin-antitoxin systems: evolution and revolutions. *J. Bacteriol.* https://doi.org/10.1128/JB.00763-19 (2020).
18. Norton, J. P. & Mulvey, M. A. Toxin-antitoxin systems are important for niche-specific colonization and stress resistance of uropathogenic *Escherichia coli*. *PLoS Pathog.* **8**, e1002954 (2012).
19. Jurėnas, D., Fraikin, N., Goormaghtigh, F. & Van Melderen, L. Biology and evolution of bacterial toxin–antitoxin systems. *Nat. Rev. Microbiol.* https://doi.org/10.1038/s41579-021-00661-1 (2022).
20. Dedrick, R. M. et al. Prophage-mediated defence against viral attack and viral counter-defence. *Nat. Microbiol.* **2**, 16251 (2017).
21. Akarsu, H. et al. TASmania: a bacterial toxin-antitoxin systems database. *PLoS Comput. Biol.* **15**, e1006946 (2019).
22. Sala, A., Bordes, P. & Genevaux, P. Multiple toxin-antitoxin systems in *Mycobacterium tuberculosis*. *Toxins* **6**, 1002–1020 (2014).
23. Ramage, H. R., Connolly, L. E. & Cox, J. S. Comprehensive functional analysis of *Mycobacterium tuberculosis* toxin-antitoxin systems: implications for pathogenesis, stress responses, and evolution. *PLoS Genet.* **5**, e1000767 (2009).
24. Keren, I., Minami, S., Rubin, E. & Lewis, K. Characterization and transcriptome analysis of *Mycobacterium tuberculosis* persisters. *mBio* **2**, e00100–e00111 (2011).
25. Agarwal, S. et al. VapBC22 toxin-antitoxin system from *Mycobacterium tuberculosis* is required for pathogenesis and modulation of host immune response. *Sci. Adv.* **6**, eaba6944 (2020).
26. Deep, A. et al. Structural, functional and biological insights into the role of *Mycobacterium tuberculosis* VapBC11 toxin-antitoxin system: targeting a tRNase to tackle mycobacterial adaptation. *Nucleic Acids Res.* **46**, 11639–11655 (2018).
27. Tiwari, P. et al. MazF ribonucleases promote *Mycobacterium tuberculosis* drug tolerance and virulence in guinea pigs. *Nat. Commun.* **6**, 6059 (2015).
28. Tian, Q. B., Hayashi, T., Murata, T. & Terawaki, Y. Gene product identification and promoter analysis of hig locus of plasmid Rts1. *Biochem. Biophys. Res. Commun.* **225**, 679–684 (1996).
29. Neubauer, C. et al. The structural basis for mRNA recognition and cleavage by the ribosome-dependent endonuclease ReIE. *Cell* **139**, 1084–1095 (2009).
30. Bordes, P. et al. SecB-like chaperone controls a toxin-antitoxin stress-responsive system in Mycobacterium tuberculosis. *Proc. Natl Acad. Sci. USA* **108**, 8438–8443 (2011).
31. Sala, A., Calderon, V., Bordes, P. & Genevaux, P. TAC from *Mycobacterium tuberculosis*: a paradigm for stress-responsive toxin-antitoxin systems controlled by SecB-like chaperones. *Cell Stress Chaperones* **18**, 129–135 (2013).
32. Sala, A., Bordes, P. & Genevaux, P. Multitasking SecB chaperones in bacteria. *Front. Microbiol.* **5**, 666 (2014).
33. Sala, A. J. et al. Directed evolution of SecB chaperones toward toxin-antitoxin systems. *Proc. Natl Acad. Sci. USA* **114**, 12584–12589 (2017).
34. Bordes, P. et al. Chaperone addiction of toxin-antitoxin systems. *Nat. Commun.* **7**, 13339 (2016).
35. Texier, P. et al. ClpXP-mediated degradation of the TAC antitoxin is neutralized by the SecB-like chaperone in *Mycobacterium tuberculosis*. *J. Mol. Biol.* **433**, 166815 (2021).
36. Guillet, V. et al. Structural insights into chaperone addiction of toxin-antitoxin systems. *Nat. Commun.* **10**, 782 (2019).
37. Rustad, T. R., Harrell, M. I., Liao, R. L. & Sherman, D. R. The enduring hypoxic response of *Mycobacterium tuberculosis*. *PLoS ONE* **3**, e1502 (2008).
38. Betts, J. C., Lukey, P. T., Robb, L. C., Mcadam, R. A. & Duncan, K. Evaluation of a nutrient starvation model of *Mycobacterium tuberculosis* persistence by gene and protein expression profiling. *Mol. Microbiol.* **43**, 717–731 (2002).
39. Fivian-Hughes, A. S. & Davis, E. O. Analyzing the regulatory role of the HigA antitoxin within *Mycobacterium tuberculosis*. *J. Bacteriol.* **192**, 4348–4356 (2010).
40. Sharma, A. et al. HigB1 toxin in *Mycobacterium tuberculosis* is upregulated during stress and required to establish infection in guinea pigs. *Front Microbiol* **12**, 748890 (2021).
41. Schuessler, D. L. et al. Induced ectopic expression of HigB toxin in *Mycobacterium tuberculosis* results in growth inhibition, reduced abundance of a subset of mRNAs and cleavage of tmRNA. *Mol. Microbiol.* **90**, 195–207 (2013).
42. DeJesus, M. A. et al. Comprehensive essentiality analysis of the *Mycobacterium tuberculosis* genome via saturating transposon mutagenesis. *mBio* https://doi.org/10.1128/mBio.02133-16 (2017).
43. Redder, P. Mapping 5′-ends and their phosphorylation state with EMOTE, TSS-EMOTE, and nEMOTE. *Methods Enzymol.* **612**, 361–391 (2018).
44. Kirkpatrick, C. L. et al. Growth control switch by a DNA-damage-inducible toxin-antitoxin system in *Caulobacter crescentus*. *Nat. Microbiol.* **1**, 16008 (2016).
45. Sierra, R. et al. Insights into the global effect on *Staphylococcus aureus* growth arrest by induction of the endoribonuclease MazF toxin. *Nucleic Acids Res.* **48**, 8545–8561 (2020).
46. Taverniti, V., Forti, F., Ghisotti, D. & Putzer, H. *Mycobacterium smegmatis* RNase J is a 5′-3′ exo-/endoribonuclease and both RNase J and RNase E are involved in ribosomal RNA maturation. *Mol. Microbiol.* **82**, 1260–1276 (2011).
47. Kang, S.-M. et al. Structure-based design of peptides that trigger *Streptococcus pneumoniae* cell death. *FEBS J.* **288**, 1546–1564 (2021).
48. Hadži, S. et al. Ribosome-dependent *Vibrio cholerae* mRNAse HigB2 is regulated by a β-strand sliding mechanism. *Nucleic Acids Res.* **45**, 4972–4983 (2017).
49. Schureck, M. A., Repack, A., Miles, S. J., Marquez, J. & Dunham, C. M. Mechanism of endonuclease cleavage by the HigB toxin. *Nucleic Acids Res.* **44**, 7944–7953 (2016).
50. Schureck, M. A., Maehigashi, T., Miles, S. J., Marquez, J. & Dunham, C. M. mRNA bound to the 30S subunit is a HigB toxin substrate. *RNA* **22**, 1261–1270 (2016).
51. Feng, S. et al. YoeB-ribosome structure: a canonical RNase that requires the ribosome for its specific activity. *Nucleic Acids Res.* **41**, 9549–9556 (2013).
52. Schureck, M. A., Dunkle, J. A., Maehigashi, T., Miles, S. J. & Dunham, C. M. Defining the mRNA recognition signature of a bacterial toxin protein. *Proc. Natl Acad. Sci. USA* **112**, 13862–13867 (2015).
53. Pavelich, I. J. et al. Monomeric YoeB toxin retains RNase activity but adopts an obligate dimeric form for thermal stability. *Nucleic Acids Res.* **47**, 10400–10413 (2019).

54. Fernandez-Garcia, L., Kim, J.-S., Tomas, M. & Wood, T. K. Toxins of toxin/antitoxin systems are inactivated primarily through promoter mutations. *J. Appl. Microbiol.* **127**, 1859–1868 (2019).
55. Hurley, J. M. & Woychik, N. A. Bacterial toxin HigB associates with ribosomes and mediates translation-dependent mRNA cleavage at A-rich sites. *J. Biol. Chem.* **284**, 18605–18613 (2009).
56. Christensen-Dalsgaard, M. & Gerdes, K. Two higBA loci in the Vibrio cholerae superintegron encode mRNA cleaving enzymes and can stabilize plasmids. *Mol. Microbiol.* **62**, 397–411 (2006).
57. Prysak, M. H. et al. Bacterial toxin YafQ is an endoribonuclease that associates with the ribosome and blocks translation elongation through sequence-specific and frame-dependent mRNA cleavage. *Mol. Microbiol.* **71**, 1071–1087 (2009).
58. Hurley, J. M., Cruz, J. W., Ouyang, M. & Woychik, N. A. Bacterial toxin RelE mediates frequent codon-independent mRNA cleavage from the 5' end of coding regions in vivo. *J. Biol. Chem.* **286**, 14770–14778 (2011).
59. Culviner, P. H., Nocedal, I., Fortune, S. M. & Laub, M. T. Global analysis of the specificities and targets of endoribonucleases from *Escherichia coli* toxin-antitoxin systems. *mBio* https://doi.org/10.1128/mBio.02012-21 (2021).
60. Kaledhonkar, S. et al. Late steps in bacterial translation initiation visualized using time-resolved cryo-EM. *Nature* **570**, 400–404 (2019).
61. Dykeman, E. C. A stochastic model for simulating ribosome kinetics in vivo. *PLoS Comput. Biol.* **16**, e1007618 (2020).
62. Milón, P. & Rodnina, M. V. Kinetic control of translation initiation in bacteria. *Crit. Rev. Biochem. Mol. Biol.* **47**, 334–348 (2012).
63. Yasrebi, H. & Redder, P. EMOTE-conv: a computational pipeline to convert exact mapping of transcriptome ends (EMOTE) data to the lists of quantified genomic positions correlated to related genomic information. *J. Appl. Bioinformatics Comput. Biol.* https://doi.org/10.4172/2329-9533.1000118 (2016).
64. Langmead, B., Schatz, M. C., Lin, J., Pop, M. & Salzberg, S. L. Searching for SNPs with cloud computing. *Genome Biol.* **10**, R134 (2009).
65. Shell, S. S. et al. Leaderless transcripts and small proteins are common features of the Mycobacterial translational landscape. *PLoS Genet.* **11**, e1005641 (2015).
66. Alvarez, R. V., Li, S., Landsman, D. & Ovcharenko, I. SNPDelScore: combining multiple methods to score deleterious effects of noncoding mutations in the human genome. *Bioinformatics* **34**, 289–291 (2018).
67. Collaborative Computational Project, Number 4. The CCP4 suite: programs for protein crystallography. *Acta Crystallogr. D Biol. Crystallogr.* **50**, 760–763 (1994).
68. McCoy, A. J. et al. Phaser crystallographic software. *J. Appl. Crystallogr.* **40**, 658–674 (2007).
69. Emsley, P., Lohkamp, B., Scott, W. G. & Cowtan, K. Features and development of Coot. *Acta Crystallogr. D Biol. Crystallogr.* **66**, 486–501 (2010).
70. Murshudov, G. N. et al. REFMAC5 for the refinement of macromolecular crystal structures. *Acta Crystallogr. D Biol. Crystallogr.* **67**, 355–367 (2011).
71. Zheng, S. Q. et al. MotionCor2: anisotropic correction of beam-induced motion for improved cryo-electron microscopy. *Nat. Methods* **14**, 331–332 (2017).
72. Zhang, K. Gctf: Real-time CTF determination and correction. *J. Struct. Biol.* **193**, 1–12 (2016).
73. Punjani, A., Rubinstein, J. L., Fleet, D. J. & Brubaker, M. A. cryoSPARC: algorithms for rapid unsupervised cryo-EM structure determination. *Nat. Methods* **14**, 290–296 (2017).
74. Zivanov, J. et al. New tools for automated high-resolution cryo-EM structure determination in RELION-3. *Elife* **7**, e42166 (2018).
75. Scheres, S. H. W. & Chen, S. Prevention of overfitting in cryo-EM structure determination. *Nat. Methods* **9**, 853–854 (2012).
76. Nakane, T. & Scheres, S. H. W. Multi-body refinement of Cryo-EM images in RELION. *Methods Mol. Biol.* **2215**, 145–160 (2021).
77. Pettersen, E. F. et al. UCSF Chimera–a visualization system for exploratory research and analysis. *J. Comput. Chem.* **25**, 1605–1612 (2004).
78. Afonine, P. V. et al. Real-space refinement in PHENIX for cryo-EM and crystallography. *Acta Crystallogr. D Struct. Biol.* **74**, 531–544 (2018).
79. Kucukelbir, A., Sigworth, F. J. & Tagare, H. D. Quantifying the local resolution of cryo-EM density maps. *Nat. Methods* **11**, 63–65 (2014).
80. Williams, C. J. et al. MolProbity: more and better reference data for improved all-atom structure validation. *Protein Sci.* **27**, 293–315 (2018).

Acknowledgements

We thank Pauline Texier et Michele Coddeville for plasmid gifts and for their assistance during the course of this study, and Patrick Viollier for useful advice. We also thank Israel Mares-Mejía for his help with toxin purification. This work has benefited from the facilities of the Microscopy Rennes Imaging Center (Mric) and from the facilities and expertise of the Structural Biophysico-Chemistry platform (BPCS) at the IECB (CNRS UMS3033, Inserm US001, Bordeaux University. We thank the scientific staff of the European Synchrotron Radiation Facility (Grenoble, France). We thank the staff of beamline MASSIF-3 (ID30-A3) at the European Synchrotron Radiation Facility where the crystallographic experiments were conducted. The crystallization and macro-molecular crystallography equipment used in this study are part of the Integrated Screening Platform of Toulouse (PICT, IPBS, IBiSA). We also thank the iGE3 genomics platform at the University of Geneva. This work was supported by Agence Nationale de la Recherche (ANR-19-CE12-0026) to P.G., R.G., and L.M, Programme d'Investisse-ments d'Avenir (ANR-20-PAMR-0005) to P.G., by the National Natural Science Foun-dation of China (32000021) to X.X., by Fondation pour la Recherche Médicale (FDT201805005796) to M.M., and by the Swiss National Science Foundation (CRSII3_160703) to P.G. and L.F.

Author contributions

Performed research: M.M., E.G., X.X., P.B., V.G., D.-J.B., N.S., S.C.; analyzed data: M.M., E.G., X.X., H.A., P.B., V.G., D.-J.B., N.S., G.D., S.C., P.R., L.F., L.M., R.G., P.G.; designed research: M.M., E.G., X.X., P.B., V.G., D.-J.B., N.S., S.C., P.R., L.F., L.M., R.G., P.G.; wrote the paper: M.M., E.G., and P.G. with contributions from all the authors. R.G. and P.G. supervised the study.

Competing interests

The authors declare no competing interests.

Additional information

Supplementary information The online version contains supplementary material available at https://doi.org/10.1038/s41467-022-30373-w.

Correspondence and requests for materials should be addressed to Reynald Gillet or Pierre Genevaux.

Peer review information *Nature Communications* thanks the anonymous reviewers for their contribution to the peer review of this work. Peer reviewer reports are available.

Reprints and permission information is available at http://www.nature.com/reprints

Publisher's note Springer Nature remains neutral with regard to jurisdictional claims in published maps and institutional affiliations.

SUPPLEMENTARY INFORMATION FILE

Substrate recognition and cryo-EM structure of the ribosome-bound TAC toxin of *Mycobacterium tuberculosis*

Moise Mansour, Emmanuel Giudice, Xibing Xu, Hatice Akarsu, Patricia Bordes, Valérie Guillet, Donna-Joe Bigot, Nawel Slama, Gaetano D'urso, Sophie Chat, Peter Redder, Laurent Falquet, Lionel Mourey, Reynald Gillet, Pierre Genevaux

This PDF file includes:

Supplementary Methods: Plasmid constructs

Supplementary Fig. 1 to 13

Supplementary Table 1 to 3

Uncropped scans

Other Supplementary Materials for this manuscript include the following:

Supplementary Data 1 contains nEMOTE data as a separate excel file

Supplementary Methods

Plasmid constructs

Plasmids pMPMK6[1], pET-20b (Novagen), pET-20b-HigB^{TAC} and pET-20b-HigB^{TAC}[K95A][2] pBAD33[3], pK6-HigB^{TAC} [4], pK6-GFP[5], pSE380ΔNcoI[6], pLAM12[7], pGMC[8] and pGMC-TAC[2] have been described.

All the primers used in this study are listed in **Supplementary Table 3**. To construct plasmids pGMC-HigB^{TAC}, pGMC-HigB2 and pGMC-HigB3, *higB^{TAC}* (Rv1955; 378pb), *higB2* (Rv2022c; 444pb) and *higB3* (Rv3182; 345pb) were PCR amplified from *M. tuberculosis* H37Rv genomic DNA using primers HigB1_pGMC_Fw and HigB1_pGMC_Rv, HigB2_pGMC_Fw and HigB2_pGMC_Rv or HigB3_pGMC_Fw and HigB3_pGMC_Rv, respectively. Compared to the first genome annotation, a shorter and more accurate version of *higB2* based on the analysis of available RNAseq and ribosome profiling data for *M. tuberculosis* (https://www.wadsworth.org/research/scientific-resources/interactive-genomics) was used in our experiments. In this case, HigB2 protein sequence is 148 amino acid long, starting at the sequence MSYPEEYH. PCR fragments were cloned into the pGMC plasmid linearized using pGMC_Infusion_Fw and pGMC_Infusion_Rv primers with the In-Fusion PCR cloning system. R68A, R77A and K95A substitutions in pGMC-HigB^{TAC} were obtained by QuickChange site directed mutagenesis using pGMC-HigB^{TAC} as DNA template and primers HigB1_R68A_pGMC_Fw and HigB1_R68A_pGMC_Rv, HigB1_R77A_pGMC_Fw and HigB1_R77A_pGMC_Rv or HigB1_K95A_pGMC_Fw and HigB1_K95A_pGMC_Rv respectively. K58A, E66A, N73A, Q98A, K99A, R61A, E106A, D110A, K113A and R117A substitutions in pGMC-HigB^{TAC} were constructed by InFusion using pK6-HigB^{TAC} alanine mutations as template and with primers HigB1_pGMC_Fw and HigB1_pGMC_Rv.

To construct pLAM12-HigB2 and pLAM12-HigB3, PCR fragments of *higB2*, *higB3* were subcloned from, pGMC-HigB2 or pGMC-HigB3 using primers HigB2_pLAM_Fw and

HigB2_pLAM_Rv, and HigB3_pLAM_Fw and HigB3_pLAM_Rv, respectively, and cloned by In-Fusion PCR cloning system into pLAM12 vector linearized with primers pLAM_Infusion_Fw and pLAM_Infusion_Rv. To construct pLAM12-HigB^{TAC} and pLAM12- HigB^{TAC}[K95A], *higB^{TAC}* PCR fragments were subcloned from *M. tuberculosis* H37Rv genomic DNA using primers HigB1_pLAM_Fw and HigB1_pLAM_Rv and cloned by In-Fusion PCR cloning system into pLAM12 vector linearized using primers pLAM_Infusion_Fw and pLAM_Infusion_Rv. K95A substitution was obtained by QuickChange site directed mutagenesis using pLAM-HigB^{TAC} as DNA template and primers HigB1_K95A_pLAM_Fw and HigB1_K95A_pLAM_Rv.

For pET20b-HigB2 and -HigB3, *higB2* and *higB3* PCR fragment were subcloned from pGMC-*Mtb*-HigB2 and pGMC-*Mtb*-HigB3 using primers higB2_infusion_20b_for and higB2_infusion_20b_rev, and HigB3_ infusion_20b_for and HigB3_ infusion_20b_rev, respectively, and cloned by In-Fusion into pET20b vector linearized using primer pET20b_Infusion_Fw and pET20b_Infusion_Rv. To construct pET20b-HigB^{TAC} with K61A, and K113A substitutions in pET20b-HigB^{TAC}, the corresponding alleles were PCR amplified from pK6-HigB^{TAC} plasmids using primers HigB1-pET20b-NdeI-Fw and HigB1-pET20b-XhoI-Rv, and cloned as an NdeI/XhoI fragment into pET20b vector. For pET15b-HigB^{TAC}-K95Aopt, PCR fragment using primers HigB1opt_NdeI_Fw and HigB1opt_BamHI_Rv, and pET20b-HigB^{TAC} K95A as template was cloned as an NdeI/BamHI fragment into pET15b vector digested with the same enzymes.

To construct plasmid pSE380ΔNcoI-CspA, the *cspA* gene (204 bp) was PCR amplified from *M. tuberculosis* H37Rv genomic DNA using primers CspA_IF_Fw and CspA_IF_Rv, and cloned by In-Fusion PCR cloning system into pSE380ΔNcoI linearized using primers pSE_Infusion_Fw and pSE_Infusion_Rv. Plasmids pSE-CspA with CCA codons at position 12, 17, 22, 27, 39, 44, 49 and 54, and with the CCA at position Pro2

replaced by CCG codon were obtained by QuickChange site directed mutagenesis using pSE-*Mtb*-CspA as template with the primers CspA_codon 12_Fw and CspA_codon 12_Rv, CspA_codon 17_Fw and CspA_codon 17_Rv, CspA_codon 22_Fw and CspA_codon 22_Rv, CspA_codon 27_Fw and CspA_codon 27_Rv, CspA_codon 39_Fw and CspA_codon 39_Rv, CspA_codon 44_Fw and CspA_codon 44_Rv, CspA_codon 49_Fw and CspA_codon 49_Rv, CspA_codon 54_Fw and CspA_codon 54_Rv, respectively. For plasmid pSE380ΔNcoI-GroES with a c-terminal Strep Tag, the *groES* gene (303bp) was amplified from *M. tuberculosis* H37Rv genomic DNA using primers GroES_IF_Fw and GroES-strep_IF_Rv, and cloned by In-Fusion PCR cloning system into linearized pSE380ΔNcoI.

To construct pBAD33-HigB^{TAC}, EcoRV/SphI digested *higB* from pK6-HigB^{TAC} was ligated into pBAD33 digested with the same enzymes. For plasmids pBAD33-HigB2 and -HigB3, *higB2* and *higB3* were PCR amplified from *M. tuberculo*sis H37Rv genome using primers HigB2_pBAD33_Fw and HigB2_pBAD33_Rv, or HigB3_pBAD33_Fw and HigB3_pBAD33_Rv, respectively, and cloned by In-Fusion into pBAD33 vector linearized with pBAD33_Infusion_Fw/ pBAD33_Infusion_Rv. HigB^{TAC} alanine substitutions in pK6-HigB^{TAC} plasmid were obtained by quickchange mutagenesis using appropriate primers (**Supplementary Table 3**). All the plasmids were sequence-verified.

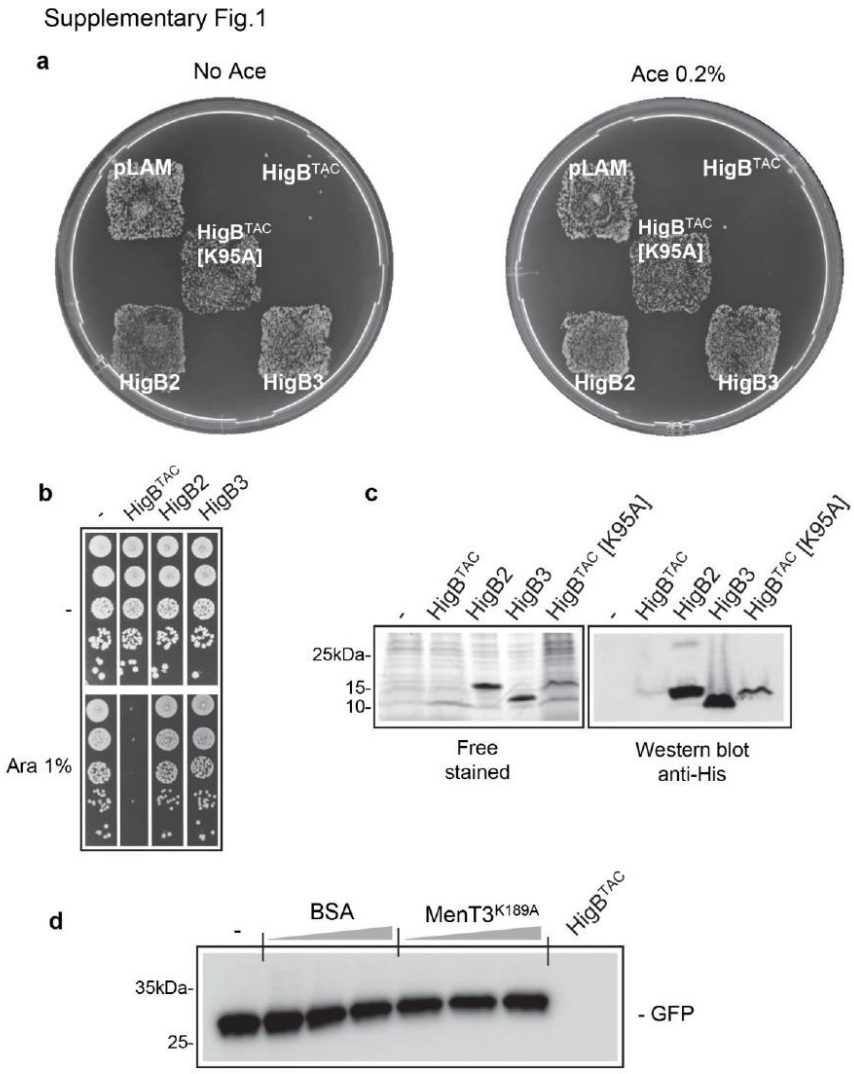

Supplementary Fig. 1: HigB^{TAC}, but not HigB2 and HigB3, impacts *M. smegmatis* and *E. coli* growth. **a** Cultures of *M. smegmatis* transformed with pLAM-vector, HigB^{TAC}, HigB^{TAC} [K95A], HigB2 or HigB3 were plated on LB kanamycin agar plates with or without acetamide (Ace) inducer at the indicated concentration. Plates were incubated 3 days at 37

°C. Representative results of two independent experiments are shown. **b** Cultures of *E. coli* transformed with pBAD33-vector (-), $HigB^{TAC}$, HigB2 or HigB3 were serial diluted and spotted on LB agar plates in the absence or presence of 1% arabinose inducer (Ara). Plates were incubated overnight at 37 °C. Representative results of three independent experiments are shown. **c** Steady state levels of His-tagged $HigB^{TAC}$, $HigB^{TAC}$ [K95A], HigB2 and HigB3 in pET20b expressed in BL21AI in the presence of 0.2% arabinose inducer overnight at 25 °C. Free stained SDS-PAGE of whole cell extracts (left) and the corresponding western blot using anti-His antibodies (right) are shown. Note that the signal obtained for HigB2 by western blot with anti-His antibodies was very strong when compared to the other two toxins. Therefore, the whole cell extract of the HigB2 sample was diluted 50 fold for the western blot. Representative results of two independent experiments are shown. **d** *In vitro* transcription/translation reactions assessing the synthesis of GFP protein in the absence (-) or presence of increasing concentrations of BSA or MenT3[K189A] (0.3, 3 and 6 μM). Samples were separated by SDS-PAGE and revealed by western blot using an anti-GFP antibody. Representative results of three independent experiments are shown.

a Supplementary Fig.2

toxins	genes	position (codon)	motif	genomic position	cleavages/ replicates	Mtb: transcript/ cleavage site	essentiality Msmeg/Mtb	functional annotation
HigB^{TAC}	*MSMEG_1076*	23/91	CC/A	+1141497	267/6	-/-	-/NA	Hypothetical protein
	groES	8/100	CC/A	+1671201	183/6	+/+	-/+	Protein folding
	cspA	2/67	CC/A	-6230161	399/5	+/+	-/-	RNA chaperone
	rpsA	2/479	CC/A	-3904814	156/5	+/-	+/+	Translation
	ssb	36/165	AC/A	-6942744	57/5	+/-	+/+	Replication
	usfY	14/99	CC/A	+1858535	187/4	-/-	-/ NA	LPS metabolic process
	nat1	NA	UU/A	-5862601	65/4	NA/NA	NA	NA
	MSMEG_1770	6/80	UC/A	-1859100	65/4	-/-	NA	Hypothetical protein
	nat2	NA	UU/A	+354	28/3	NA/NA	NA	NA
	rpsL^{b}	74/124	CU/U	+1498523	27/3	+/-	+/+	Translation
	parA	300/323	UC/A	-6981819	31/3	+/-	-/+	Replication
	MSMEG_5607	53/82	CC/A	+5693295	30/3	-/-	-/ NA	Hypothetical protein
	nat3	NA	UG/A	+5184433	33/3	NA/NA	NA	NA
	MSMEG_1773^{b}	42/340	CC/A	-1861165	85/2	-/-	-/ NA	Hypothetical protein
	MSMEG_1773^{a}	19/340	AU/A	-1861234	61/2	-/-	-/ NA	Hypothetical protein
	rpsL^{a}	2/124	CC/A	+1498307	206/3	+/+	+/+	Translation
	nat4	NA	AC/A	-5862595	30/2	NA/NA	NA	NA
	MSMEG_0595	25/245	GC/A	+673478	24/2	-/-	-/ NA	Hypothetical protein
	MSMEG_2727	206/273	CC/A	-2795804	20/2	-/-	-/ NA	Hypothetical protein
	infC	201/206	CC/A	-3861748	19/2	+/-	+/+	Translation
	mce2A	392/404	GU/G	+5884998	19/2	-/-	-/ NA	Virulence, adaptation
	rplJ	140/175	AU/G	+1459087	16/2	+/+	-/+	Translation
	glpK	15/505	AC/A	+6803807	15/2	-/-	-/ NA	Metabolism
	MSMEG_0702	261/310	UC/A	-790771	14/2	-/-	-/ NA	Hypothetical protein
HigB^{TAC}K95A	nat5	NA	UU/G	+307135	22/2	NA/NA	NA	NA
HigB2 (24h)	*cdd*	34/128	GAC/GAC	+1766889	60/2	+/-	-/-	Metabolism
	yajC	28/107	GCC/ATG	+3022816	43/2	+/+	-/-	Secretion
	nat6	NA	UC/C	+6371128	42/2	NA/NA	NA	NA
HigB3 (24h)	*yajC*	28/107	GCC/ATG	+3022816	22/2	+/+	-/-	Secretion

b

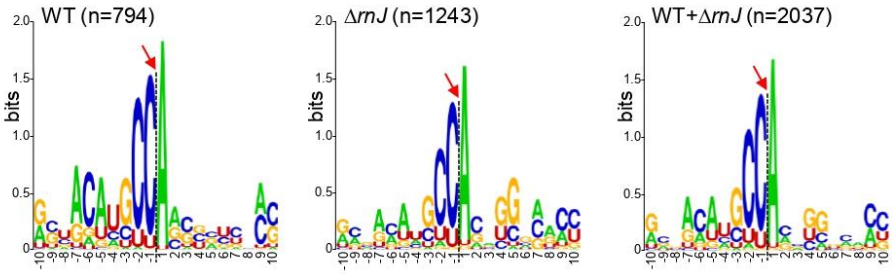

c

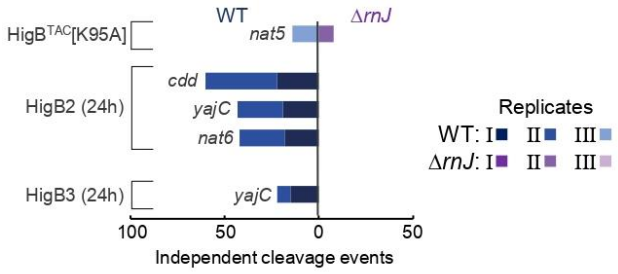

Supplementary Fig. 2: Cleavage sites and overview of the targets identified. a General information about the cleavage sites identified in this work. "NA" stands for not available or non-applicable. The gene names or the locus tags are indicated when available. Names nat1 to nat6 stand for previously *n*on-*a*nnotated *t*ranscripts that have been found by RNAseq and ribosome profiling of the *M. smegmatis* genome available at https://www.wadsworth.org/research/scientific-resources/interactive-genomics. The position of the cleaved codons is given as codon position per total number of codons of the transcript. The cleaved codon sequence is indicated as "motif" and the bar slash shows where cleavage occurs. The position of the first nucleotide after cleavage in *M. smegmatis* genome is given in the "genomic position" column. The number of total detected cleaved RNA molecules (cleavages) for each transcript and the number of replicates in which such cleavages were identified (replicates) are shown. The presence (+) or absence (-) of homologous transcript (transcript) and conserved sequence motif (cleavage site) in *M. tuberculosis* (Mtb) is also shown. Essentiality of the identified genes in *M. smegmatis* (Msmeg; DOI: 10.1038/s41598-019-47905-y) or in *M. tuberculosis* (Mtb; doi: 10.1128/mBio.02133-16) is depicted a (+) essential or (-) non-essential. Functional annotation of conserved genes is based on information available on the Universal Protein Knowledgebase (UniProtKB). **b** Logoplots generated following alignment of all HigB^{TAC} target sequences identified for the WT (n=794), the Δ*rnJ* mutant (n=1243) or both WT + Δ*rnJ* (n=2037). The *x* axis represents the 10 nucleotides upstream and downstream of the cleavage site that is located by the position between -1 and 1 (red arrow and dash line), and default label for the *y* axis is bits (https://weblogo.berkeley.edu/logo.cgi). **c** Cleavages identified *in vivo* by nEMOTE for the inactive HigB^{TAC} [K95A] after 3 hours and for HigB2 and HigB3 after 24 hours of expression in *M. smegmatis* WT (blue bars on the left) and Δ*rnJ* (violet bars on the right) as shown in **Fig. 2a**. The name of the cleaved mRNA is given in line with each bar. The number of cleavages identified in each replicate for the WT (shade of blue; replicates I, II and III) and the Δ*rnJ* mutant (shade of violet; replicates I, II and III) is shown within each bar using the indicated color code. Bar height represents the number of independently observed cleavage events for each unique target site.

Supplementary Fig. 3

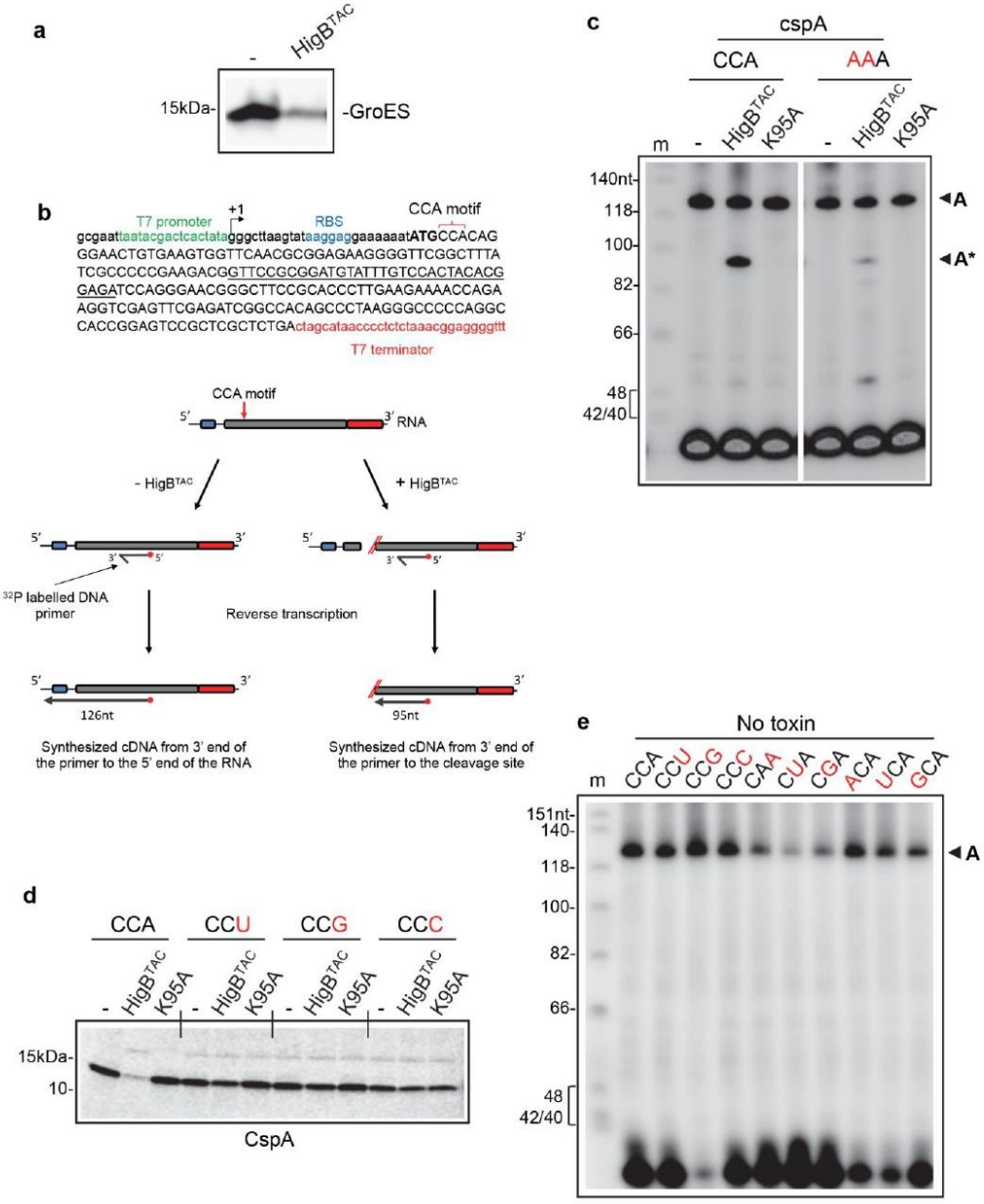

Supplementary Fig. 3: *Mtb*-GroES synthesis inhibition and *cspA* cleavage *in vitro*. **a** Strep-tagged *M. tuberculosis* GroES was expressed in a cell-free translation system with or without HigB^{TAC}. Reactions were performed for 1 h 30 min at 37 °C. After translation,

samples were separated on SDS–PAGE and visualized by western blot using an anti-Streptag II antibody. **b** Schematic representation of the primer extension experiment using cspA as template.. The nucleotide sequence of *cspA* is shown with the initiation codon in bold. The T7 promoter and terminator sequences are shown in green and red, respectively, and the ribosome binding site in blue. The labeled reverse DNA primer used for reverse transcription is underlined. Cleavage of the *cspA* mRNA in the CCA motif will lead to the synthesis of a 95nt cDNA. No cleavage will lead to the synthesis of a 126nt cDNA. **c** *cspA* cleavage by $HigB^{TAC}$ wild-type or its non-toxic K95A derivative. *cspA* wild-type (CCA) or AAA mutant (AAA replaces CCA of Pro 2 codon) were independently expressed in a cell-free translation system for 2 h with or without $HigB^{TAC}$ (1.5 µM). RNA were extracted and subjected to a primer extension with [^{32}P]-labeled *cspA* primer. Labeled cDNAs were separated on denaturing urea-polyacrylamide gel and revealed by autoradiography. Arrows show the uncleaved (A, 126 nt) and cleaved (A*, 95 nt) *cspA*. (m) stands for molecular ladder. Representative results of three independent experiments are shown. **d** Mutations in the CCA codon prevent inhibition of synthesis of *cspA* by $HigB^{TAC}$ *in vitro*. *cspA* wild type (CCA) and its mutant derivatives (mutations depicted in red) were independently expressed in a cell-free translation system with or without 1.5 µM of $HigB^{TAC}$ (or $HigB^{TAC}$ [K95A] inactive mutant as control) and analyzed as described in **Fig. 3a**. Representative results of triplicate experiments are shown. **e** Control without toxin for primer extension experiments shown in **Fig. 3d**. A representative gel of two independent experiments is shown.

Supplementary Fig.4

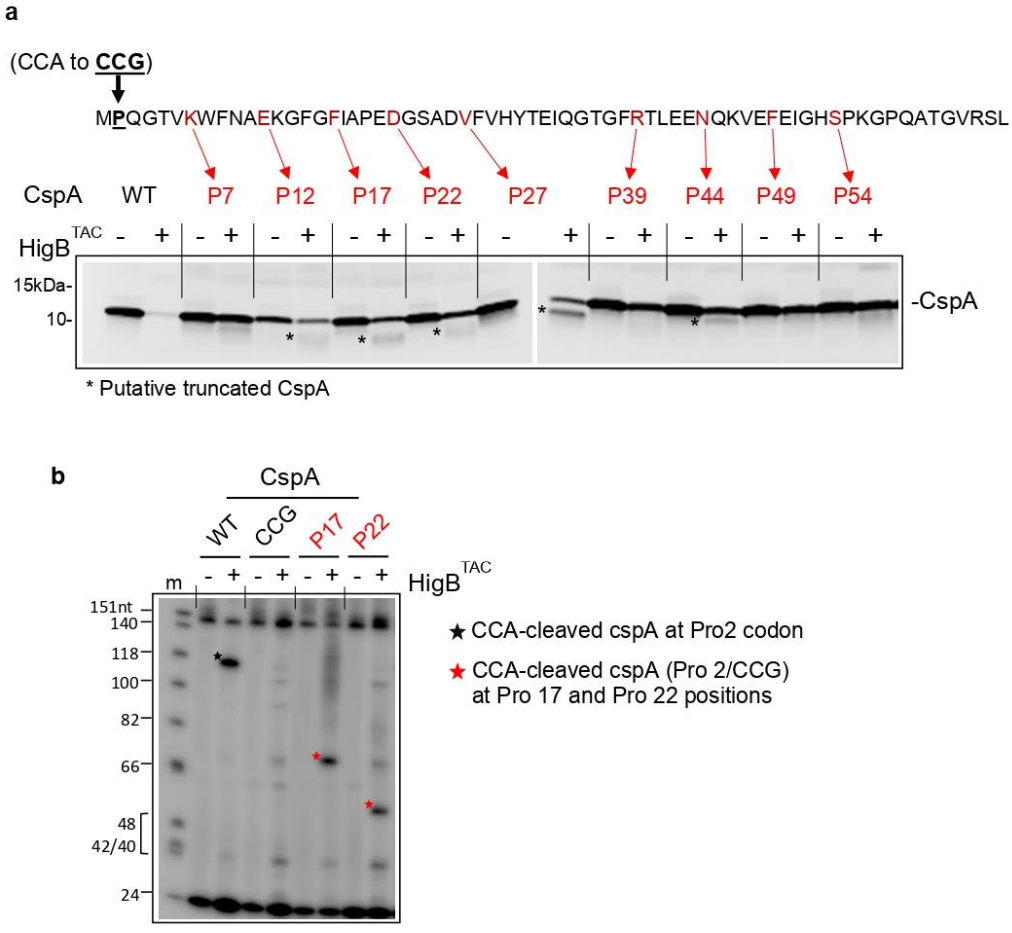

Supplementary Fig. 4: HigB^{TAC} can cleave along the mRNA during translation. a Inhibition of CspA synthesis with displaced Pro CCA codons along the *cspA* transcript. The amino acid sequence of CspA is shown on top, with each position independently substituted by a Pro (CCA codon) depicted in red. In these cases, the native Pro CCA codon is replaced by Pro CCG, which is not detectably cleaved by HigB^{TAC} (**Fig. 3c and d**). The asterisk indicates the putative truncated CspA. CspA WT, and its derivatives (P7 to P54) were independently expressed in a cell-free translation system with or without HigB^{TAC} (1.5 μM). CspA translation products were labelled with [^{35}S]methionine and reactions were performed for 1 h 30 min at 37 °C. After translation, samples were separated on SDS–PAGE and visualized by phosphorimager. **b** Cleavage of *cspA* and its P17 and P22 derivatives. *cspA*

(WT), P17 and P22 were independently expressed in a cell-free translation system for 2 h with or without $HigB^{TAC}$ (1.5 µM). RNAs were extracted and subjected to a primer extension with [^{32}P]-labeled *cspA* primer. The obtained labeled cDNAs were separated on denaturing urea-polyacrylamide gel and revealed by autoradiography. The black star shows the expectedly cleaved *cspA* wild-type product and red stars shows the shorter *cspA* cleavage products obtained when cleavage occurs at the newly positioned CCA codons (P17 at 72 nt and P22 at 57 nt). Representative results of three independent experiments are shown.

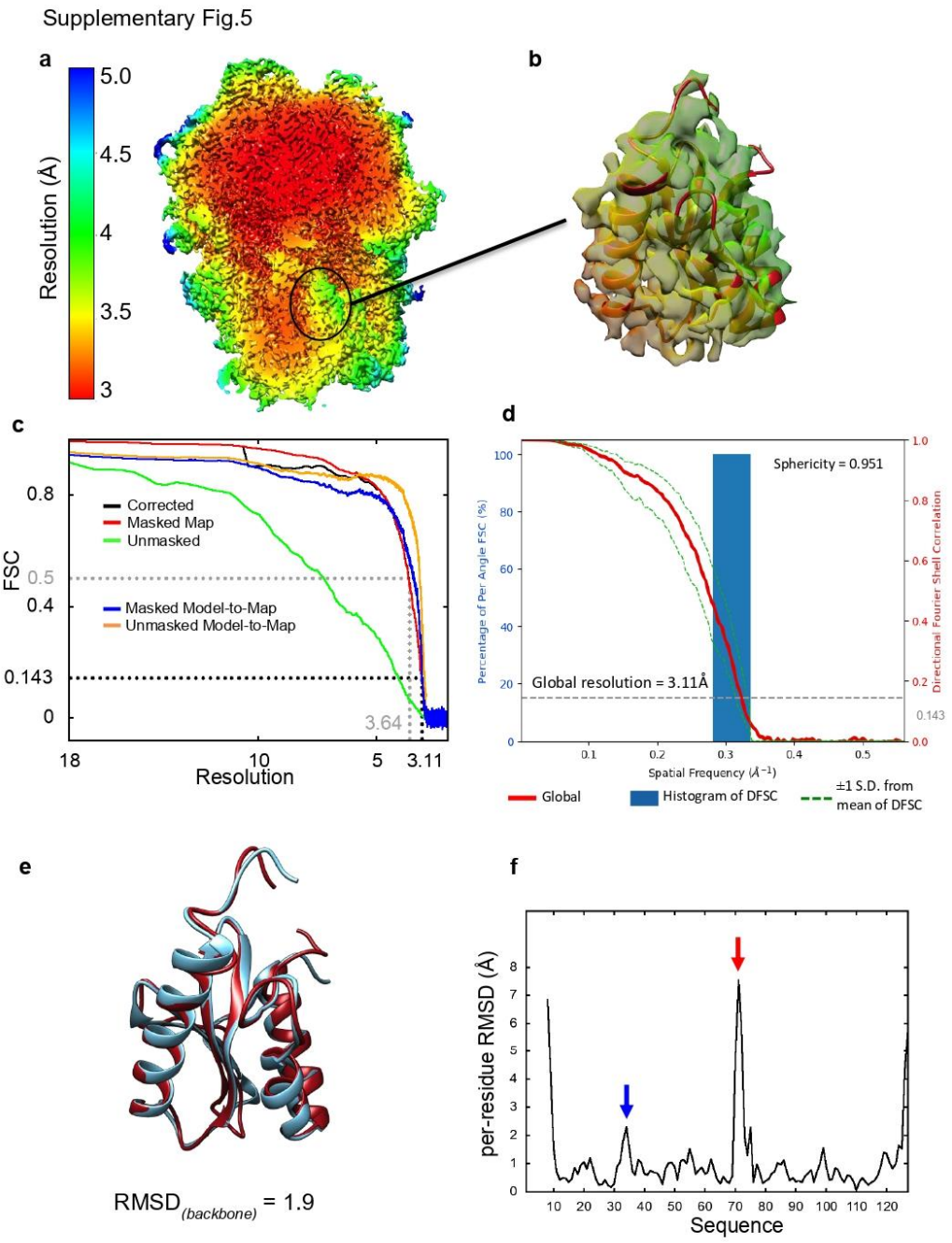

Supplementary Fig. 5: Evaluation of the quality of the map and models. a Sliced view of the consensus-sharpened density map colored according to the local resolutions computed

with Resmap (see color key). **b** Same, but a close-up to show the local resolution of $HigB^{TAC}$ [K95A]. **c** Fourier shell correlation (FSC) curves calculated between the unmasked, masked, or solvent-corrected half-maps, and between the atomic model and the unmasked or masked consensus-sharpened maps. Dashed lines indicate *FSC* = 0.143 (black) and 0.5 (grey). The corresponding resolutions calculated for the solvent-corrected half-maps are also indicated. **d** Directional 3DFFSC plot showing the global half-map FSC (solid red line), the spread of directional resolution values defined by ±1σ from the mean (dotted green lines, left axis) and a histogram of 100 such values evenly sampled over the 3D FSC (blue bars, right axis). **e** Superimposition of the atomic coordinates of $HigB^{TAC}$ [K95A] alone (our crystal structure, blue) and observed on a translating ribosome (our cryo-EM model, red). The root-mean-square deviation (RMSD) calculated for the backbone atoms is indicated. **f** Average per-residue RMSD calculated between the two $HigB^{TAC}$ [K95A] structures. With the exception of the extremities, the two structures mostly differ in the region between the first and second alpha helices (blue arrow), and between the second and third beta strand (red arrow).

Supplementary Fig. 6

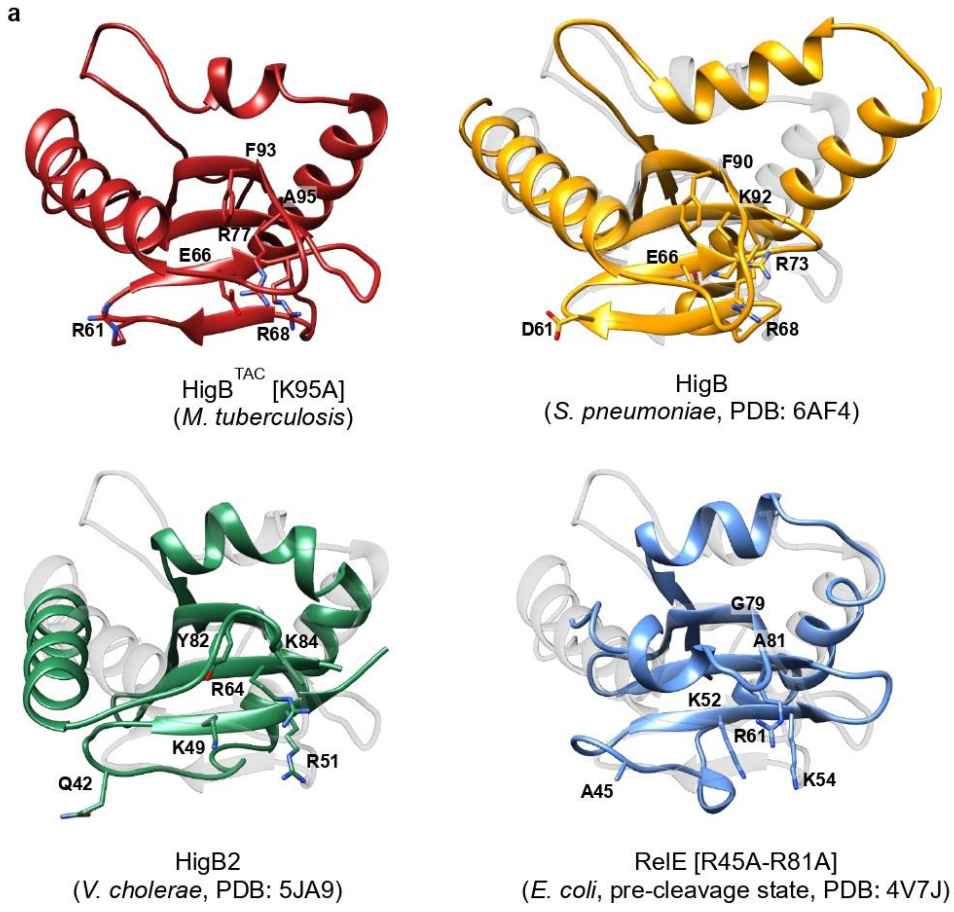

b

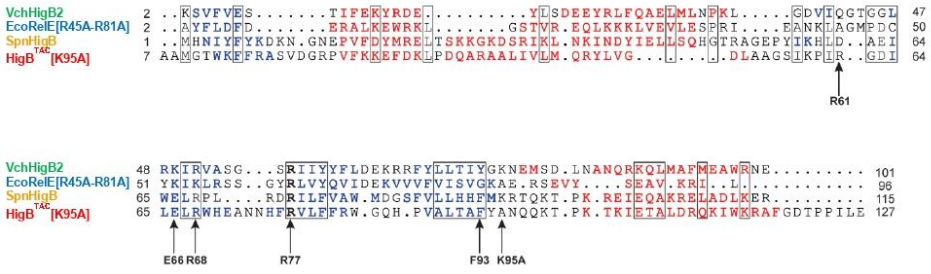

Supplementary Fig. 6: Comparison of the catalytic sites of ribosome-dependent toxins. a Structure showing the proposed catalytic-site residues in HigB^{TAC} [K95A], *S. pneumoniae*

HigB (PDB 6AF4), *V. cholera* HigB2 (PDB 5JA9), and in *E. coli* RelE [R45A-R81A] (PDB 4V7J). All the structure were aligned on $HigB^{TAC}$ [K95A] using UCSF chimera and, for comparison, the structure of $HigB^{TAC}$ [K95A] (transparent white) is superimposed to the other toxins. **b** Structure-derived protein sequence alignments obtained using PROMALS3D and submitted to ESPript 3.0 for amino acid similarity analysis. Conserved residues are indicated in bold. Residues with high similarity are shown in a black frame. Residues in red and blue correspond to α-helix and β-strand, respectively. Residues that are part of the catalytic center are indicated with arrows.

Supplementary Fig. 7

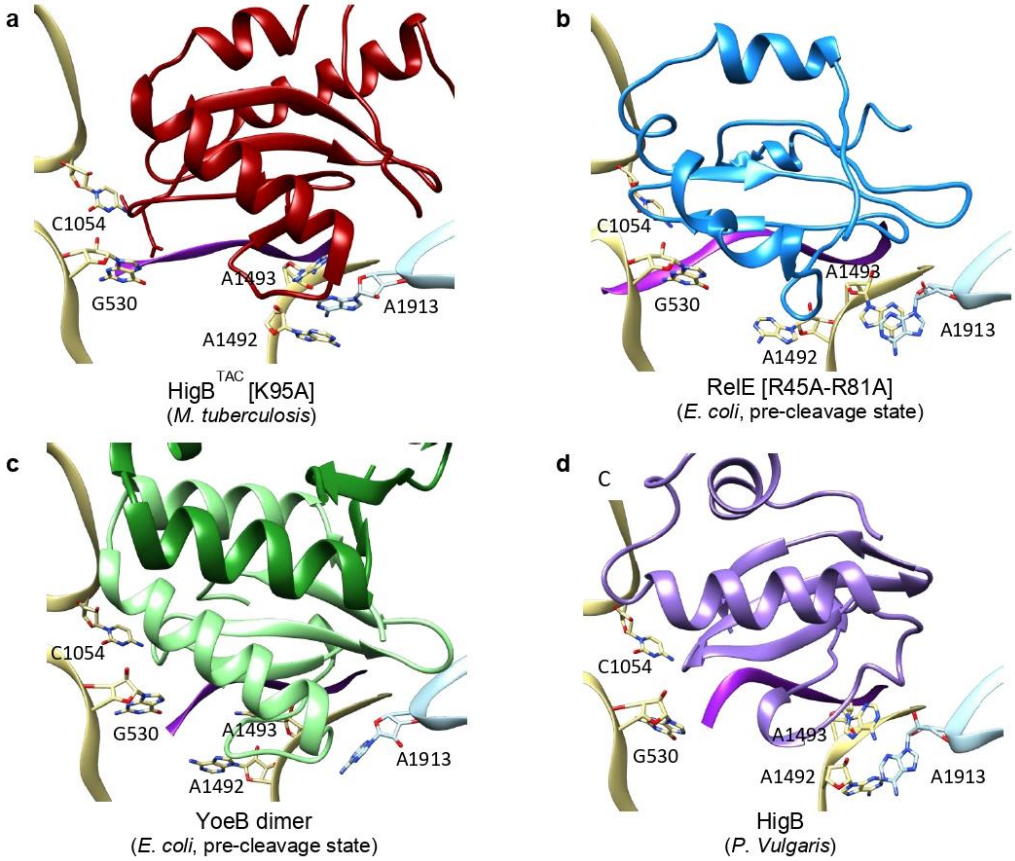

e

Contacts		HigB^{TAC} [K95A]	RelE [R45A-R81A]	YoeB dimer	HigB
fMet-tRNA^{fMet}		C29-G30, A36-U37			A35-U36
CspA mRNA		C30-C33	(A2M)20-A22	G18-A22	G18-(A2M)21
23S rRNA	H69	A1912	A1913	A1913-U1915	
16S rRNA	h18	G517-C518, G530-U531	U516-C519, G530-A532	G517-A520, G530-U531	G517, C519, G530-U531
	h30-31	G953-A959, U965-m^{2}G966	U955, U957, A959-U960	U955-A959	G954, U957, U960-U961
	h34	U1052-C1054	G1050-A1055, G1198, C1208	C1054	G1050-C1054, C1208-C1209
	h32				C1214
	h44	A1492-A1493	A1492-G1494	A1492-U1495	A1493
uS13		R117			
uS12			S50	T44, P48, S50-L52	T44, S50, A51

Supplementary Fig. 7: Effect of toxins on the decoding site and summary of all the contacts made by toxins with the ribosome, their target mRNAs, and eventually with P-site tRNA. Contact of decoding site residues with **a** $HigB^{TAC}$ [K95A], **b** *E. coli* RelE [R45A-R81A] (PDB 4V7J), **c** *E. coli* YoeB dimer (PDB 4V8X), and **d** *P. vulgaris* HigB (PDB 4ZSN). The four structures are aligned on the 16S rRNA using UCSF chimera. The mRNA is purple, the 16S rRNA is light yellow, the 23S rRNA is light blue, the ribosomal proteins uS12 and uS13 are gold and lime green, respectively. Nucleotides within 4 Å of the toxin are shown. **e** Table summarizing all the interactions found between known toxins with the ribosome, their target mRNAs, and eventually with P-site tRNA.

Supplementary Fig. 8

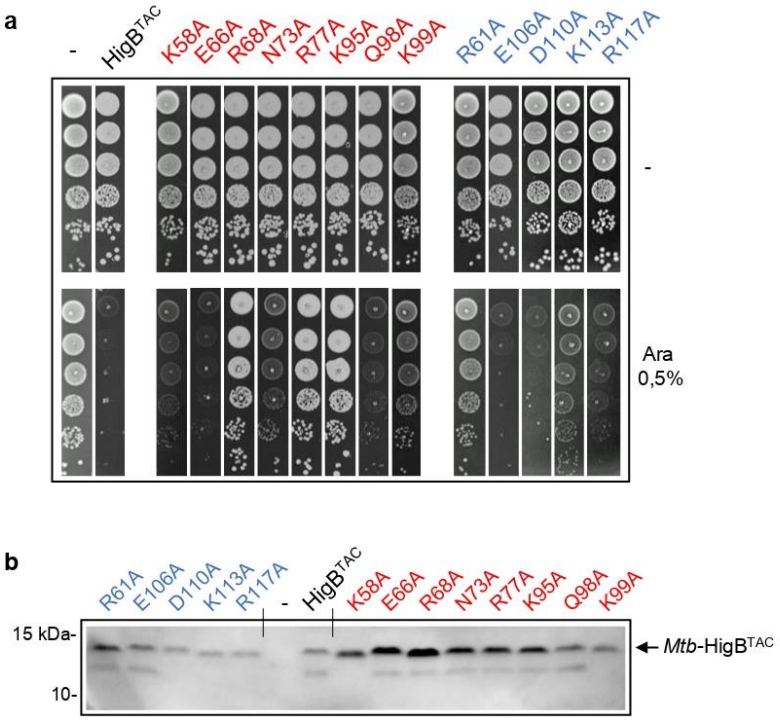

Supplementary Fig. 8: Toxicity of HigB^{TAC} derivatives in *E. coli*. **a** *E. coli* W3110 strain transformed with pMPMK6-vector, HigB^{TAC} wild-type or its mutant derivatives (Alanine substitution of residue K58, E66, R68, N73, R77, K95, Q98, K99, R61, E106, D110, K113 or R117) were serial diluted, spotted on LB kanamycin agar plates with or without arabinose (0.5%) inducer and incubated 1 day at 37°C. **b** Western blot showing HigB^{TAC} steady state expression level following a 3h induction in the presence of 0.5% arabinose. Representative results of two independent experiments are shown.

Supplementary Fig. 9

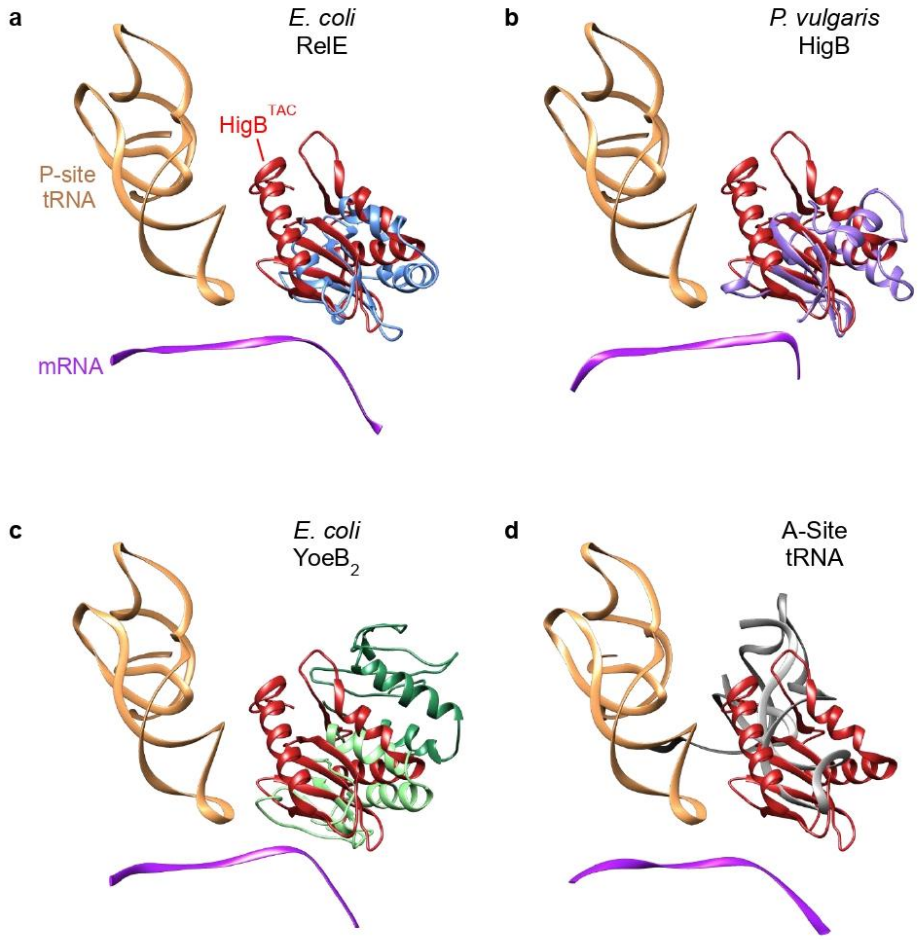

Supplementary Fig. 9: Structural comparison between HigB^{TAC}[K95A] and known toxins observed in pre-cleavage state with their respective mRNA targets and the P-site tRNA. a *E. coli* RelE[R45A_R81A] (PDB code 4V7J), **b** *P. vulgaris* HigB (PDB 4ZSN), **c** *E. coli* YoeB dimer (PDB 4V8X), and **d** a cognate tRNA observed in the A-site during canonical translation (PDB 7K00). The structures were all aligned, using UCSF chimera, on the P-site tRNA of the ribosome-associated TAC toxin. For clarity reason only the HigB^{TAC}[K95A] (in red) is shown superimposed to the other structures.

Supplementary Fig. 10

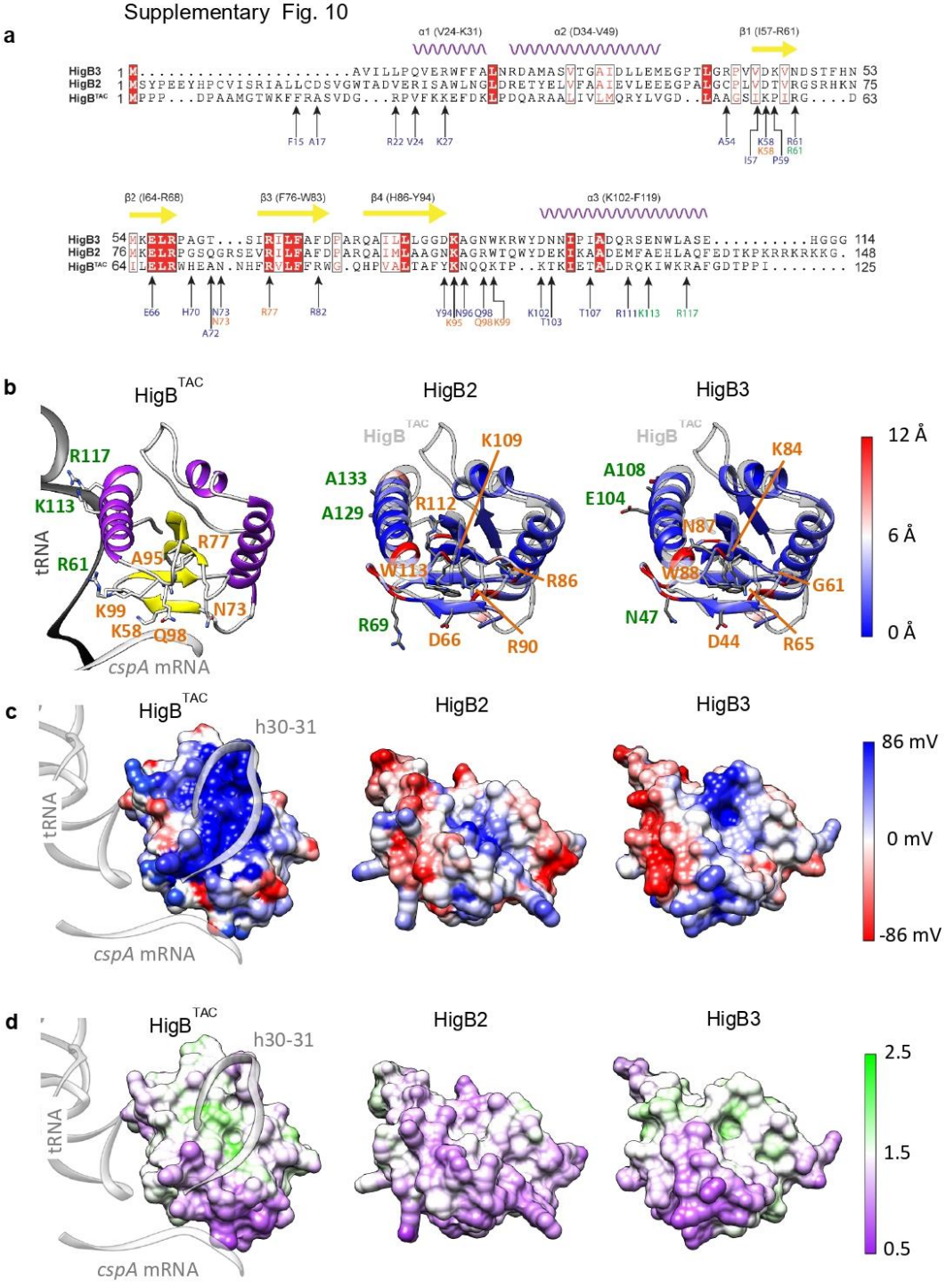

Supplementary Fig. 10: Comparison of *M. tuberculosis* HigB toxins. a Alignment of HigB toxins was performed using PROMALS3D and submit to ESPript 3.0 for amino acid similarity analysis. Conserved residues are shown in red background and blue frame. Residues with high similarity are shown in red and black frame. Symbols above sequence alignment correspond to the secondary structure of $HigB^{TAC}$ with α-helix and β- sheet colored in purple and yellow respectively. Residues that are within 3Å of the 16S and 23S are shown in blue, and those within 3Å of fMet-$tRNA^{fMet}$ in green. Residues located in the catalytic center and in contact with *cspA* mRNA are shown in orange. **b** Comparison between our cryo-EM structure of $HigB^{TAC}$ [K95A] mutant and the AlphaFold[9] models of *M. tuberculosis* HigB2 and HigB3. The three proteins are aligned with STAMP[10]. $HigB^{TAC}$ is colored based on its secondary structure (purple for the helices and yellow for the strands) and the position of the P-site tRNA, and CspA mRNA are indicated. HigB2 and HigB3 are colored based on the per-residue RMSD with $HigB^{TAC}$ from blue (low RMSD) to red (High RMSD) and for comparison, the structure of $HigB^{TAC}$ [K95A] (transparent white) is superimposed to the two other toxins. Residues located in the catalytic center or in contact with fMet-$tRNA^{fMet}$ as well as their equivalent in HigB2 and HigB3 are shown. **c** Electrostatic surface potential calculated with Protein-sol[11]. The proteins are colour-coded from negatively charge (red) to positively charge (blue) and the range of potential given here is in the range of what is expected for electrostatic interactions at the protein surface. The position of the P-site tRNA, CspA mRNA, and the junction between 16S rRNA helices 30 and 31 are also indicated. **d** Same as **c** but for hydrophobicity. The proteins are color-coded by patch NPP ratio from polar (purple) to more hydrophobic (green).

Supplementary Fig. 11

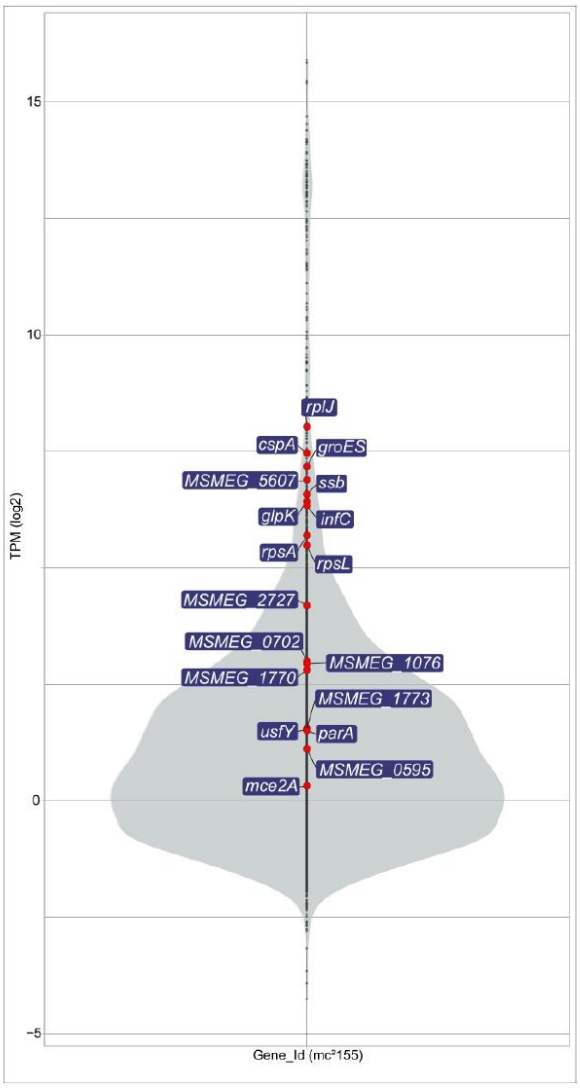

Supplementary Fig. 11: *M. smegmatis* mRNA expression. Violin plot showing the distribution of the intensity of expression in *M. smegmatis* obtained from available transcriptomic data. The x-axis represents the total genes of *M. smegmatis* with the transcripts cleaved by $HigB^{TAC}$ highlighted with red dots and on the y-axis the representation of gene expression in transcripts per million (TPM). Violin Plot was generated with ggplot in RStudio.

Supplementary Fig. 12

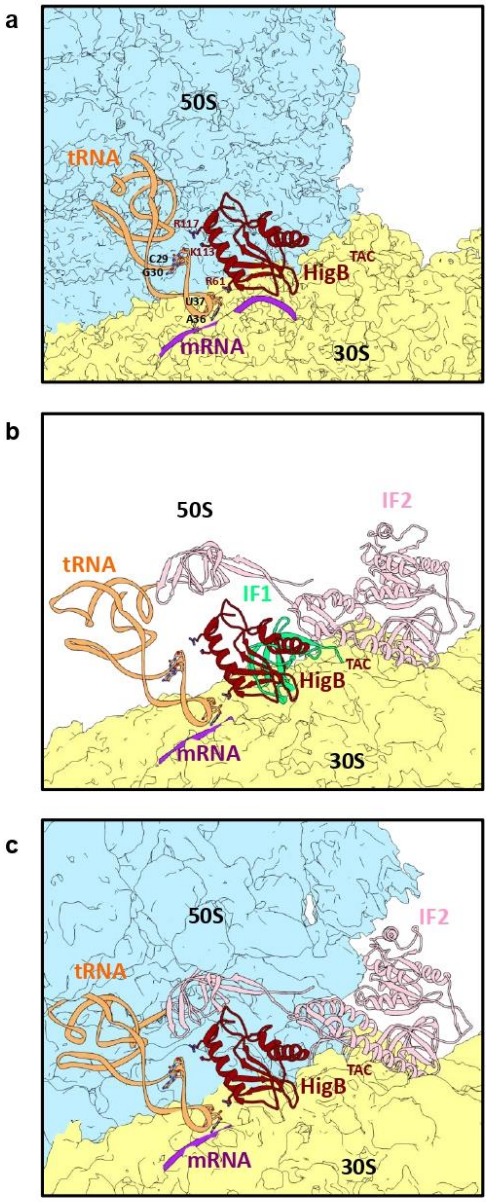

Supplementary Fig. 12: HigB^{TAC} potentially targets the late steps of the translation initiation. **a** Close-up view of the ribosome-associated HigB^{TAC} with its native *cspA* substrate. **b** Structural comparison between the 30S initiation complex (PDB 6O7K, EMD-0643) and the ribosome-associated HigB^{TAC} shows that IF1 and the toxin are mutually exclusive. **c** Structural comparison between the 70S initiation complex (PDB 6O9K, EMD-0662) and the ribosome-associated HigB^{TAC}. The presence of IF2 stabilizes the ribosome in a semi-rotated state and the fMet-tRNA^{fMet} in its P/I configuration. This prevents the tRNA-EF-Tu complex to bind the ribosome but does not impede HigB^{TAC} to access the A-site and interact with the P-Site tRNA. The structures are aligned on the 16S rRNA. HigB^{TAC} is red, the mRNA is purple, the fMet-tRNA^{fMet} is orange, IF1 is green, IF2 is pink and the electron density maps of the 50S and 30S ribosomal subunits are blue and yellow respectively. HigB^{TAC} residues R61, K113 and R117 and the fMet-tRNA^{fMet} nucleotides C29, G30, A36, and U37 are also shown to highlight that HigB^{TAC} can contact the fMet-tRNA^{fMet}, even if it is in the P/I configuration.

Supplementary Fig. 13

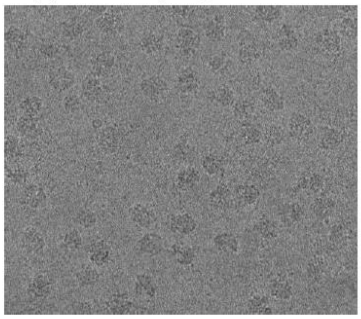

6,381 micrographs

Motion Correction (MotionCor2_v1.0.6)
CTF estimation (Gctf_v1.18)

5,178 micrographs selected

Particle Picking (cryoSPARC v2.12)
2D Classification

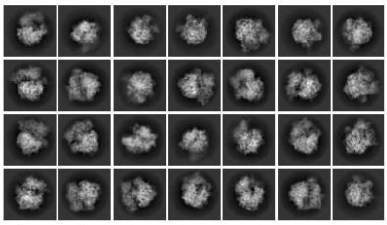

294,820 particles selected

3D Auto-Refine
(Relion v3.1.3)

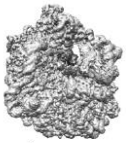

3.33Å

Pixel reassessment
0.893 Å/pix

3D Classification
12 classes

70S
7 classes
175,859

Ratcheted
2 classes
39,752

50S
2 classes
51,812

Bad
1 class
27,397

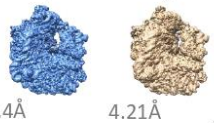

3.4Å 4.21Å

3D Classification with signal subtraction of the ribosome
8 classes

1 class
42,261

No Toxin

Return to original images
3D Auto-Refine

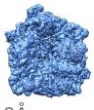

3.8Å

3D Classification with signal subtraction of the ribosome and spherical mask on HigB^{TAC}, 4 classes

1 class
13,877

Return to original images
3D Auto-Refine

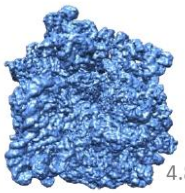

4.85Å

CTF Refinement ,
Polishing,
3D Auto-Refine,
Post-processing with
pixel = 0.893 Å

3.11Å

Multibody refinement
and Post-processing

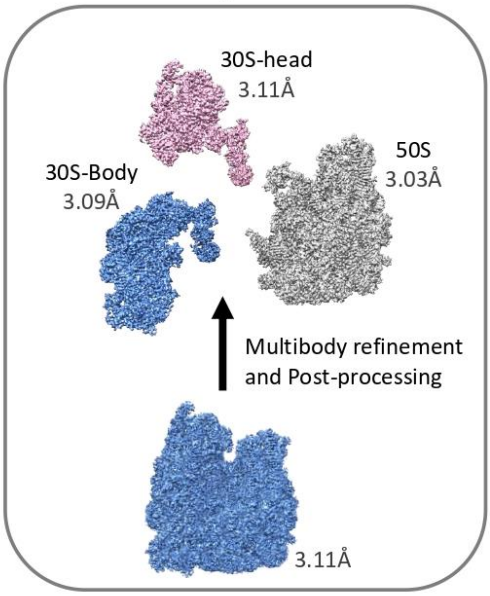

30S-head
3.11Å

30S-Body
3.09Å

50S
3.03Å

Sharpening and Model buiding
(Phenix v1.18.2 + coot v0.9.5)

25

Supplementary Fig. 13: Schematic representation of the cryo-EM single-particle reconstruction workflow.

Supplementary Table 1.

Crystallographic data collection and refinement statistics ([a]Values in brackets are for the highest-resolution shell and [b]Asymmetric unit)

Data set	*Mtb*-HigB1^{K95A}
PDB code	7AWK
Data collection	
Beamline	ESRF MASSIF-3
Space group	$P2_12_12$
Unit cell *a*, *b*, *c* (Å) [α, β, γ (°)] for *P*1	43.98, 82.05, 38.05
Resolution range (Å)[a]	41.03 – 1.91 (1.95 – 1.91)
No. of unique reflections	11,202 (739)
Completeness (%)	98.9 (92.7)
Redundancy	6.7 (6.4)
$\langle I/\sigma(I)\rangle$	9.2 (1.3)
R_{meas} (%)	12.0 (131.8)
CC1/2	0.991 (0.602)
Wilson B factor (Å^2)	36.6
Refinement	
No. of reflections (work / test)	10,632 (560)
R_{work} / R_{free}	0.212 / 0.273
No. of molecules/AU[b]	1
No. of non-hydrogen atoms	1,049
Protein	984
Ligands	0
Ions	0
Water molecules	65
RMS deviations	
Bond lengths (Å)	0.013
Bond angles (°)	1.833
Ramachandran plot (%)	
Most favored	97.5
Allowed / disallowed	2.5 / 0
Average B-factors (Å^2)	40.6
Protein	40.4
Solvent	44.5

Supplementary Table 2.

Cryo-EM data collection and refinement statistics.

EMDB code	(EMD-12261)
PDB code	(PDB 7NBU)
Data collection and processing	
Magnification	105k
Voltage (kV)	200
Electron exposure (e–/Å^2)	35
Defocus range (μm)	-0.4 to -2
Pixel size (Å)	0.9291 (fitted to 0.893)
Symmetry imposed	None
Micrographs collected (no.)	6,381
Micrographs used (no.)	6,381
Initial particle images (no.)	294,820
Final particle images (no.)	13,877
Map resolution (Å)	
FSC threshold : 0.143	3.11
FSC threshold : 0.5	3.64
Map resolution range (Å)	2.9-7
Refinement	
Initial models used (PDB code)	7K00 and 7AWK
Model resolution (Å)	
FSC threshold: 0.143	2.9
Map sharpening	
B factor (Å^2)	26.58
Model composition	
Non-hydrogen atoms	144,943
Protein residues	5,719
Nucleotide	4,648
Ligands	317
B factors mean (Å^2)	
Protein	87.67
Nucleotide	97.17
Ligand	61.85
RMS deviations	
Bond lengths (Å)	0.007
Bond angles (°)	0.772
Validation	
MolProbity score	1.93
Clashscore	10.28
Poor rotamers (%)	0.09
Ramachandran plot	
Favored (%)	94.03
Allowed (%)	5.78
Disallowed (%)	0.20

Supplementary Table 3. Primers list

Primer name	Sequence (5'-3')
Toxins cloning in pGMC	
pGMC_Infusion_Fw	CAACTTTATTATACATAGTTGATAATTC
pGMC_Infusion_Rv	GGGCAGCCTGTCTTCCTC
HigB1_pGMC_Fw	GAAGACAGGCTGCCCATGCCGCCCCCTGATCCAGCCGCCATG
HigB1_pGMC_Rv	TGTATAATAAAGTTGTTAGATCGGTGGGGTGTCGCCGAAG
HigB2_pGMC_Fw	GAAGACAGGCTGCCCATGTCTTACCCGGAGGAATATCACCCTTG
HigB2_pGMC_Rv	TGTATAATAAAGTTGTTACCCTTTCTTGCGCTTGCGCCTC
HigB3_pGMC_Fw	GAAGACAGGCTGCCCATGGCCGTGATCCTGCTCCCGCAG
HigB3_pGMC_Rv	TGTATAATAAAGTTGTTATCCACCTCCGTGCTCGCTC
HigB1_R68A_pGMC_Fw	GACATTCTGGAGTTGGCCTGGCATGAGGCGAAC
HigB1_R68A_pGMC_Rv	GTTCGCCTCATGCCAGGCCAACTCCAGAATGTC
HigB1_R77A_pGMC_Fw	GCGAACAACCACTTCGCCGTACTGTTCTTCCGC
HigB1_R77A_pGMC_Rv	GCGGAAGAACAGTACGGCGAAGTGGTTGTTCGC
HigB1_K95A_pGMC_Fw	CTGACAGCGTTCTACGCCAACCAGCAGAAGACTC
HigB1_K95A_pGMC_Rv	GAGTCTTCTGCTGGTTGGCGTAGAACGCTGTCAG
Toxins cloning in pLAM	
pLAM_Infusion_Fw	GAATTCGAAGCTTATCGATG
pLAM_Infusion_Rv	CATATGTGGACTCCCTTTC
HigB1_pLAM_Fw	GGGAGTCCACATATGCCGCCCCCTGATCCAGCCGCCATG
HigB1_pLAM_Rv	ATAAGCTTCGAATTCTCAGATCGGTGGGGTGTCGCCGAAG
HigB1_K95A_pLAM_Fw	CTGACAGCGTTCTACGCCAACCAGCAGAAGACTC
HigB1_K95A_pLAM_Rv	GAGTCTTCTGCTGGTTGGCGTAGAACGCTGTCAG
HigB2_pLAM_Fw	GGGAGTCCACATATGTCTTACCCGGAGGAATATCACCCTTG
HigB2_pLAM_Rv	ATAAGCTTCGAATTCTTACCCTTTCTTGCGCTTGC
HigB3_pLAM_Fw	GGGAGTCCACATATGGCCGTGATCCTGCTCCCGCAG
HigB3_pLAM_Rv	ATAAGCTTCGAATTCTCATCCACCTCCGTGCTCGC
Toxins cloning in pBAD33	
pBAD33_Infusion_Fw	GGCTGTTTTGGCGGATGAGAGAAGATTTTCAGC
pBAD33_Infusion_Rv	CGAGACAACCTCCTGCTAGCCCAAAAAAACGGGTATGGA
HigB2_pBAD33_Fw	CAGGAGGTTGTCTCGATGtcttacccggaggaata
HigB2_pBAD33_Rv	TCCGCCAAAACAGCCTTACCCTTTCTTGCGCTTG
HigB3_pBAD33_Fw	CAGGAGGTTGTCTCGATGGCCGTGATCCTGCTCCCG
HigB3_pBAD33_Rv	TCCGCCAAAACAGCCTCATCCACCTCCGTGCTCGCTCGCC
nEMOTE primers	
Rp8	5'**Bio**CGGCACCAACCGAGGVVVVVVVVACAGA V (A or C or G)
D6A	CTCTTTCCCTACACGACGCTCTTCCGATCTNTACACGGCACCAACCGAGG
D6B	CTCTTTCCCTACACGACGCTCTTCCGATCTNGTATCGGCACCAACCGAGG
D6C	CTCTTTCCCTACACGACGCTCTTCCGATCTNCGTCCGGCACCAACCGAGG
D6D	CTCTTTCCCTACACGACGCTCTTCCGATCTNAAGTCGGCACCAACCGAGG
D6E	CTCTTTCCCTACACGACGCTCTTCCGATCTNACACCGGCACCAACCGAGG

D6F	CTCTTTCCCTACACGACGCTCTTCCGATCTNGGTACGGCACCAACCGAGG
D6H	CTCTTTCCCTACACGACGCTCTTCCGATCTNTCGGCGGCACCAACCGAGG
D6I	CTCTTTCCCTACACGACGCTCTTCCGATCTNCAAGCGGCACCAACCGAGG
D6J	CTCTTTCCCTACACGACGCTCTTCCGATCTNTTGACGGCACCAACCGAGG
D6K	CTCTTTCCCTACACGACGCTCTTCCGATCTNGCTGCGGCACCAACCGAGG
D6L	CTCTTTCCCTACACGACGCTCTTCCGATCTNCCGACGGCACCAACCGAGG
D6M	CTCTTTCCCTACACGACGCTCTTCCGATCTNCTCGCGGCACCAACCGAGG
D6N	CTCTTTCCCTACACGACGCTCTTCCGATCTNAGGACGGCACCAACCGAGG
D6O	CTCTTTCCCTACACGACGCTCTTCCGATCTNATTGCGGCACCAACCGAGG
D6P	CTCTTTCCCTACACGACGCTCTTCCGATCTNGACGCGGCACCAACCGAGG
D6Q	CTCTTTCCCTACACGACGCTCTTCCGATCTNTGTTCGGCACCAACCGAGG
DRNA	GGCATTCCTGCTGAACCGCTCTTCCGATCTNNNNNNNNNA
Adaptator A	AATGATACGGCGACCACCGAGATCTACACTCTTTCCCTACACGACG
Adaptator B	CAAGCAGAAGACGGCATACGAGATCGGTCTCGGCATTCCTGCTGAACCGC

Toxin cloning in pET vector

pET20b_Infusion_Fw	ATGTATATCTCCTTCTTAAAG
pET20b_Infusion_Rv	CACCACCACCACCACCACTG
higB2_infusion_20b_for	GAAGGAGATATACATATGtcttacccggaggaatatc
higB2_infusion_20b_rev	GTGGTGGTGGTGGTGCCCTTTCTTGCGCTTGCGCC
HigB3_ infusion_20b_for	GAAGGAGATATACATaTGGCCGTGATCCTGCTCCCG
HigB3_ infusion_20b_rev	GTGGTGGTGGTGGTGTCCACCTCCGTGCTCGCTCGCC
HigB1_pET20b_NdeI_Fw	Texier *et al* 2021
HigB1_pET20b_XhoI_Rv	Texier *et al* 2021
HigB1opt_NdeI_Fw	ATACATATGCCGCCGCCGGACCCGGCAG
HigB1opt_BamHI_Rv	TTTGGATCCTTACTCGAGGATCGGCGGGGTATCACC

PURE with cspA

pSE_Infusion_Fw	CCGGTTGTTAACGTTAGCCGG
pSE_Infusion_Rv	GCTGGAATTCTCCTGTGTGAAATTG
CspA_IF_Fw	CAGGAGAATTCCAGCATGCCACAGGGAACTGTGAAG
CspA_IF_Rv	AACGTTAACAACCGGTCATTTTTCGAACTGCGGGTGGCTCCAGCTACCCCCGAGCG AGCGGACTCCGGTGGCC
CspA_CCA_Fw	GCGAATTAATACGACTCACTATAGGGCTTAAGTATAAGGAGGAAAAAATATGCCAC AGGGAACTGTGAAG
CspA_term_Rv	AAACCCCTCCGTTTAGAGAGGGGTTATGCTAGTCAGAGGGAGCGGACTCCGGTGG CCTG
CspA_CCT_Fw	GCGAATTAATACGACTCACTATAGGGCTTAAGTATAAGGAGGAAAAAATATGCCTC AGGGAACTGTGAAG
CspA_CCG_Fw	GCGAATTAATACGACTCACTATAGGGCTTAAGTATAAGGAGGAAAAAATATGCCGC AGGGAACTGTGAAG
CspA_CCC_Fw	GCGAATTAATACGACTCACTATAGGGCTTAAGTATAAGGAGGAAAAAATATGCCCC AGGGAACTGTGAAG

CspA_CAA_Fw	GCGAATTAATACGACTCACTATAGGGCTTAAGTATAAGGAGGAAAAAATATGCAAC AGGGAACTGTGAAG
CspA_CTA_Fw	GCGAATTAATACGACTCACTATAGGGCTTAAGTATAAGGAGGAAAAAATATGCTAC AGGGAACTGTGAAG
CspA_CGA_Fw	GCGAATTAATACGACTCACTATAGGGCTTAAGTATAAGGAGGAAAAAATATGCGA CAGGGAACTGTGAAG
CspA_ACA_Fw	GCGAATTAATACGACTCACTATAGGGCTTAAGTATAAGGAGGAAAAAATATGACAC AGGGAACTGTGAAG
CspA_TCA_Fw	GCGAATTAATACGACTCACTATAGGGCTTAAGTATAAGGAGGAAAAAATATGTCAC AGGGAACTGTGAAG
CspA_GCA_Fw	GCGAATTAATACGACTCACTATAGGGCTTAAGTATAAGGAGGAAAAAATATGGCA CAGGGAACTGTGAAG
CspA_codon 7_Fw	GCGAATTAATACGACTCACTATAGGGCTTAAGTATAAGGAGGAAAAAATATGCCGC AGGGAACTGTGCCA
CspA_codon 12_Fw	AAGTGGTTCAACGCGCCAAAGGGGTTCGGCTTT
CspA_codon 12_Rv	AAAGCCGAACCCCTTTGGCGCGTTGAACCACTT
CspA_codon 17_Fw	GAGAAGGGGTTCGGCCCAATCGCCCCCGAAGAC
CspA_codon 17_Rv	GTCTTCGGGGGCGATTGGGCCGAACCCCTTCTC
CspA_codon 22_Fw	TTTATCGCCCCCGAACCAGGTTCCGCGGATGTA
CspA_codon 22_Rv	TACATCCGCGGAACCTGGTTCGGGGGCGATAAA
CspA_codon 27_Fw	GACGGTTCCGCGGATCCATTTGTCCACTACACG
CspA_codon 27_Rv	CGTGTAGTGGACAAATGGATCCGCGGAACCGTC
CspA_codon 39_Fw	ATCCAGGGAACGGGCCCACGCACCCTTGAAGAA
CspA_codon 39_Rv	TTCTTCAAGGGTGCGTGGGCCCGTTCCCTGGAT
CspA_codon 44_Fw	TTCCGCACCCTTGAACCAAACCAGAAGGTCGAG
CspA_codon 44_Rv	CTCGACCTTCTGGTTTGGTTCAAGGGTGCGGAA
CspA_codon 49_Fw	GAAAACCAGAAGGTCCCATTCGAGATCGGCCAC
CspA_codon 49_Rv	GTGGCCGATCTCGAATGGGACCTTCTGGTTTTC
CspA_codon 54_Fw	GAGTTCGAGATCGGCCCAAGCCCTAAGGGCCCC
CspA_codon 54_Rv	GGGGCCCTTAGGGCTTGGGCCGATCTCGAACTC
OOF1_Fw	GCGAATTAATACGACTCACTATAGGGCTTAAGTATAAGGAGGAAAAAATATGACCA AGGGAACTGTGAAG
OOF2_Fw	GCGAATTAATACGACTCACTATAGGGCTTAAGTATAAGGAGGAAAAAATATGCACC AGGGAACTGTGAAG
CspA_AAA_Fw	GCGAATTAATACGACTCACTATAGGGCTTAAGTATAAGGAGGAAAAAATATGAAA CAGGGAACTGTGAAG
RT_CspA_P32_PAGE_1	TCTCCGTGTAGTGGACAAATACATCCGCGGAAC
RT_CspA_P32_PAGE_2	GTGCGGAAGCCCGTTCCCTGGATCTC
PURE with gfp	
FPUREGfpT7	(Bordes et al., 2016)[5]
RPUREGfpT7	(Bordes et al., 2016)[5]
PURE with groES	
GroES_IF_Fw	CAGGAGAATTCCAGCATGGCGAAGGTGAACATCAAG
GroES-strep_IF_Rv	AACGTTAACAACCGGTCATTTTTCGAACTGCGGGTGGCTCCAGCTACCCCCCTTGGA AACGACGGCCAG

GroES_T7_Fw	GCGAATTAATACGACTCACTATAGGGCTTAAGTATAAGGAGGAAAAAATATGGCG AAGGTGAACATCAAGCCACTCGAGGAC
GroES-strepterm_Rv	AAACCCCTCCGTTTAGAGAGGGGTTATGCTAGTCATTTTTCGAACTGCGGGTGGC

Supplementary Data 1. Data file (separate excel data file): nEMOTE data

Supplementary References

1. Mayer, M. P. A new set of useful cloning and expression vectors derived from pBlueScript. *Gene* **163**, 41–46 (1995).
2. Texier, P. *et al.* ClpXP-mediated Degradation of the TAC Antitoxin is Neutralized by the SecB-like Chaperone in Mycobacterium tuberculosis. *Journal of Molecular Biology* **433**, 166815 (2021).
3. Guzman, L. M., Belin, D., Carson, M. J. & Beckwith, J. Tight regulation, modulation, and high-level expression by vectors containing the arabinose PBAD promoter. *J.Bacteriol.* **177**, 4121–4130 (1995).
4. Bordes, P. *et al.* SecB-like chaperone controls a toxin-antitoxin stress-responsive system in Mycobacterium tuberculosis. *Proceedings of the National Academy of Sciences of the United States of America* **108**, 8438–43 (2011).
5. Bordes, P. *et al.* Chaperone addiction of toxin-antitoxin systems. *Nat Commun* **7**, 13339 (2016).
6. Genevaux, P. *et al.* In vivo analysis of the overlapping functions of DnaK and trigger factor. *EMBO Rep.* **5**, 195–200 (2004).
7. van Kessel, J. C. & Hatfull, G. F. Recombineering in Mycobacterium tuberculosis. *Nat. Methods* **4**, 147–152 (2007).
8. Blumenthal, A., Trujillo, C., Ehrt, S. & Schnappinger, D. Simultaneous Analysis of Multiple Mycobacterium tuberculosis Knockdown Mutants In Vitro and In Vivo. *PLOS ONE* **5**, e15667 (2010).
9. Jumper, J. *et al.* Highly accurate protein structure prediction with AlphaFold. *Nature* **596**, 583–589 (2021).
10. Russell, R. B. & Barton, G. J. Multiple protein sequence alignment from tertiary structure comparison: assignment of global and residue confidence levels. *Proteins* **14**, 309–323 (1992).
11. Hebditch, M. & Warwicker, J. Web-based display of protein surface and pH-dependent properties for assessing the developability of biotherapeutics. *Sci Rep* **9**, 1969 (2019).

Supplementary uncropped scans:

Supplementary Fig.1c

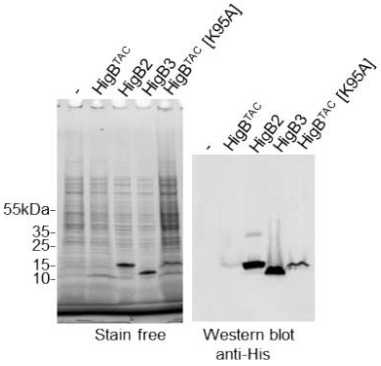

Supplementary Fig.1d

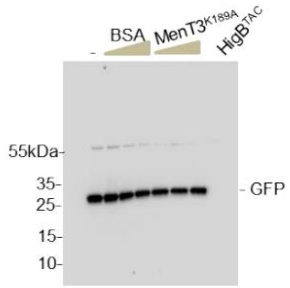

Supplementary Fig.3a

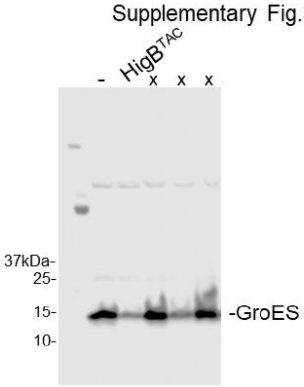

Supplementary Fig.3c

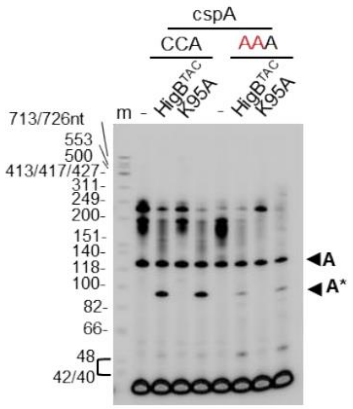

Supplementary Fig.3d

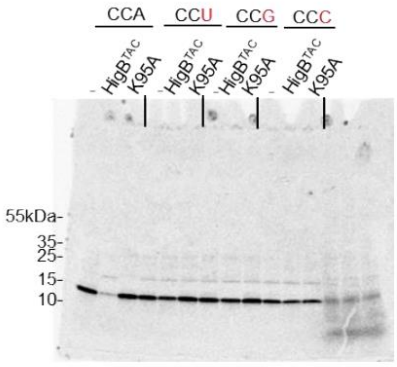

Supplementary Fig.3e

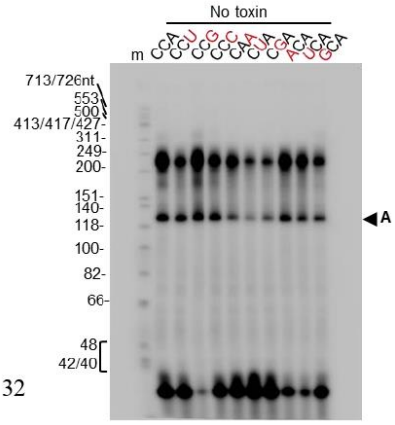

Supplementary Fig.4a

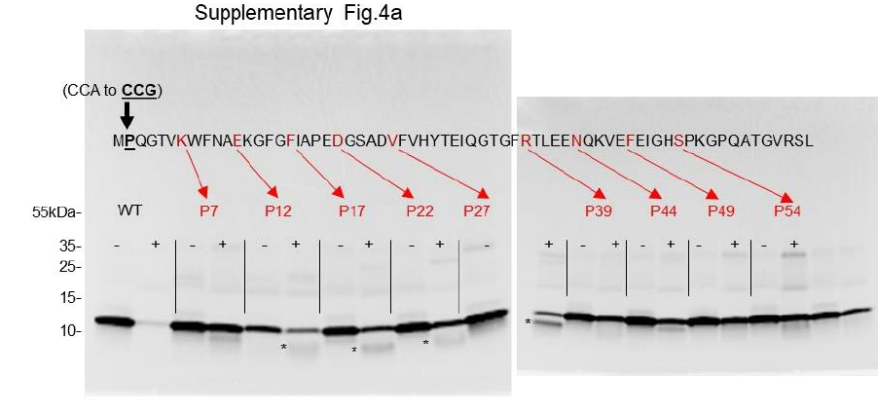

Supplementary Fig.4b

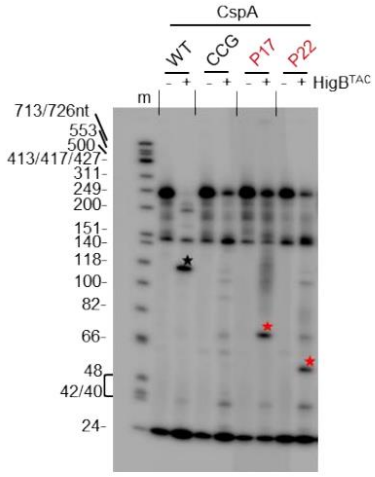

Supplementary Fig 8b

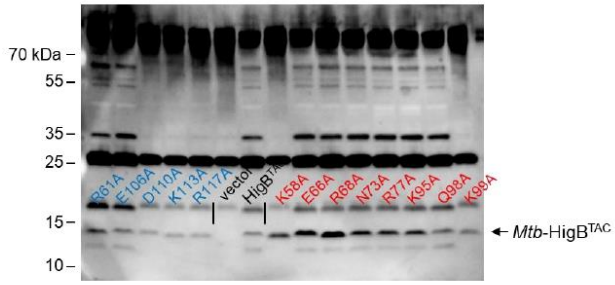

Mots-clés : Cryo-EM - trans-traduction - ARNt - SmpB - RNase R - bS1

Le présent travail effectué au cours de cette thèse se concentre sur le mécanisme le plus important impliqué dans le contrôle de la qualité de la synthèse des protéines bactériennes, appelé trans-traduction. La trans-traduction est essentielle pour la survie des cellules bactériennes car elle permet le sauvetage des ribosomes bloqués sur l'ARNm non-stop pendant la traduction, permettant leur recyclage avec la dégradation simultanée du messager défectueux et la dégradation de la chaîne polypeptidique naissante non fonctionnelle. L'importance biologique du sauvetage des complexes de traduction " non-stop " est soulignée par le fait que trois mécanismes différents ont évolué chez plusieurs espèces bactériennes pour assurer la survie cellulair. Parmi eux, le plus important est la trans-translation dont les composants centraux, essentiels pour orchestrer ce ballet sophistiqué, sont l'ARN messager de transfert (ARNtm) et son partenaire la petite protéine de base B (SmpB). Ce complexe, avec d'autres facteurs de traduction, assure l'éjection de l'ARNm aberrant, le marquage du polypeptide tronqué et le recyclage des ribosomes. Nous décrivons, les acteurs impliqués dans ce processus, le détail moléculaire du mécanisme tel que déduit de nos récentes études. L'ARN transfert-messager (ARNtm) est une molécule d'ARN chimérique capable de jouer à la fois le rôle d'un ARNt et d'un ARNm. Son partenaire est la petite protéine basique B (SmpB), qui est essentielle pour la liaison au ribosome, le positionnement correct du codon de reprise et l'expulsion de l'ARNm non-stop du ribosome.

Dans a première section de ce manuscrit, nous expliquons l'étude structurale, par cryo-EM, du processus de trans-traduction qui nous a permis de reconstruire quatre structures atomiques à haute résolution du ribosome dans quatre différentes étapes consécutives de ce mécanisme (pré-accommodation, accommodation, translocation et post-translocation). Pour chacune de ces étapes, nous avons reconstruit un modèle atomique à haute résolution, et même identifié un intermédiaire conformationnel supplémentaire de l'étape de translocation. Ensemble, ces structures éclairent le transit du complexe ARNt-SmpB au sein d'un ribosome bloqué sur un ARNm non-stop, depuis leur arrivée avec le facteur d'élongation-thermo instable (EF-Tu) jusqu'au positionnement du domaine analogue au transfert (TLD) de l'ARNt au sein du site P. En outre, notre description quasi atomique du processus nous a permis d'identifier les éléments saillants à la base de son fonctionnement, de

décrire les changements de conformation du ribosome et de comprendre pourquoi la trans-translation n'interfère pas avec la traduction canonique. Étant donné que la trans-translation est vitale pour de nombreuses bactéries, qu'elle est nécessaire à la virulence d'autres espèces et qu'elle est absente des eucaryotes, elle constitue une nouvelle cible prometteuse pour le développement de nouveaux composés antimicrobiens. À ce titre, nos résultats contribueront également à la conception d'inhibiteurs de trans-translation basée sur la structure.

Dans la deuxième partie du travail, nous avons concentré notre attention sur la caractérisation structurelle d'un troisième composant impliqué dans la trans-traduction, connu sous le nom de RNase R. La RNase R est une ribonucléase essentielle pour la dégradation de l'ARNm non-stop.

Pour caractériser le troisième acteur majeur impliqué dans la trans-translation, c'est-à-dire la RNase R, nous avons d'abord cherché à étudier sa capacité à reconnaître et à lier les ribosomes bloqués sur les ARNm non-stop. Le complexe obtenu par cryo-EM a mis en évidence la présence d'une protubérance chevauchant la tête et le corps de la petite sous-unité près des protéines uS3, uS4 et uS5, où est localisé le canal d'entrée de l'ARNm. Comme la présence de la RNase R ancrée aux ribosomes bloqués a été confirmée par SDS PAGE, nous avons conclu que la protubérance observée était la RNAse R. Bien que le résultat soit à une résolution plutôt basse, il était suffisant pour noter que la RNase R se lie au ribosome sur la même région que l'hélice H5 de l'ARNtm et le pseudoknot PK2 pendant la trans-translation. Ce résultat suggère qu'une forte compétition pourrait exister entre la RNase R et le complexe ARNtm-SmpB pour lier un ribosome bloqué au cours de la trans-translation, contrairement à ce qui a été montré par des études précédentes démontrant que le recrutement de la RNase R dépend de l'activité du complexe ARNt-SmpB ou de SmpB seul. En tenant compte des résultats préliminaires obtenus à partir de l'observation du premier complexe, l'étape suivante a consisté à étudier le comportement de la protéine simultanément avec l'ARNtm et la SmpB. Pour ce faire, nous avons ajouté le ARNtm-SmpB au complexe avec la RNAse R. De la comparaison des résultats, on peut observer que dans les deux cas, la masse correspondant à la RNAse R est absente, alors que la densité correspondant au complexe ARNtm-SmpB peut être facilement reconnue. D'après ce que nous avons vu, l'addition d'ARNtm et de SmpB a induit un déplacement de la

RNase R précédemment liée qui était bien ancrée au ribosome. Cela montre clairement que les deux acteurs se lient à la surface 30S près du canal d'entrée de l'ARNm mais l'affinité de l'ARNtm-SmpB est beaucoup plus forte au point qu'elle peut éjecter la RNase R de son site de liaison. Sur cette base, la seule hypothèse que nous avons pu formuler est que la RNase R et l'ARNtm-SmpB arrivent simultanément pendant la trans-translation, exerçant leur activité sur deux ribosomes distincts mais consécutifs, bloqués sur le même ARNm non-stop. Pour tester cette hypothèse, l'étape suivante a consisté à étudier la RNase R, l'ARNtm et la SmpB sur un système plus complexe, formé par deux ribosomes calés sur le même ARNm non-stop. Tout d'abord, nous avons vérifié la capacité du complexe ARNt-SmpB à reconnaître et à se lier aux disomes bloqués, sans RNase R. D'après la reconstruction 3D résultante, nous pouvons voir la présence du complexe ARNtm-SmpB dans le site A du ribosome bloqué. Le ribosome heurté est en rotation par rapport au ribosome bloqué, les deux SSU sont en contact l'un avec l'autre et la conformation des disomes que nous observons ne correspond à aucune forme d'hibernation. Les données expérimentales que nous avons obtenues ont également été comparées à celles issues d'un travail récent de Saito et ses collaborateurs (Saito et al., 2022) dans lequel ils ont mis en lumière l'activité du facteur SmrB, impliqué dans la détection et le sauvetage de la collision des ribosomes suite au décrochage. Sur la base de ce que nous avons observé lors de notre précédente étude de la RNase R, il apparaît que, si la protéine se lie au ribosome entré en collision, elle sera placée à peu près au niveau du site de liaison de SmrB, dont l'activité est de cliver le brin d'ARNm défectueux à l'interface entre les deux ribosomes décrochés afin de les libérer et de favoriser la trans-translation. L'ensemble de ces résultats suggère que la RNase R pourrait interagir ailleurs sur les ribosomes bloqués, en attendant de dégrader l'ARNm défectueux. D'autres études sont en cours pour remettre en question ces hypothèses.

Pour assurer l'efficacité de ce processus, le complexe ARNtm-SmpB doit rapidement reconnaître et lier le ribosome bloqué. Parmi les nombreux facteurs impliqués dans la trans-translation, la protéine bS1 s'est avérée nécessaire pour la liaison de l'ARNtm aux ribosomes. Bien que le rôle exact et le mode d'action de la protéine bS1 pendant la trans-translation ne soient pas entièrement clairs, plusieurs études ont rapporté que cette protéine joue

un rôle clé dans la protection de l'ARNtm contre une éventuelle dégradation cytoplasmique, ainsi que dans la promotion de la reprise de la traduction au niveau de l'ORF de l'ARNtm. De plus, des changements dans le niveau d'expression de bS1 réduisent fortement le taux de liaison à l'ARNtm. Malgré son importance, non seulement dans la trans-translation mais aussi et surtout lors de l'initiation canonique de la traduction, bS1 manque d'une structure à haute résolution, que ce soit par cristallographie ou par cryo-EM.
Au cours de ce doctorat, nous avons tenté de caractériser structurellement le rôle de la protéine bS1 lors de la trans-translation. À partir de l'analyse des cartes de densité issues de l'étude de Guyomar, D'Urso et de leurs collègues, un certain nombre de classes ont été identifiées dans lesquelles le complexe ARNtm-SmpB et la protéine bS1 étaient tous deux présents sur le ribosome. De plus, bien que la quantité de signal liée à la protéine bS1 soit plutôt faible, la protéine bS1 était clairement liée à la protéine uS2 au-dessus du site E mais dans une conformation différente de celle décrite précédemment. Nous avons conclu que la conformation observée de bS1 était liée à la présence de l'appariement de bases SD - anti-SD et non au complexe ARNtm-SmpB. Nous sommes donc partis d'un système plus simple avec lequel nous avons essayé de caractériser pour la première fois la protéine bS1 sur un ribosome compétent pour l'élongation. Jusqu'à présent, on pensait que les deux premiers domaines OB de bS1 n'étaient impliqués que dans l'ancrage de la protéine à la plateforme ribosomique, les autres domaines intervenant dans la capture, la liaison et le dépliage des ARNm sans leader ou structurés. Cependant, nos données montrent que OB2 interagit également avec l'extrémité 5′ du SD par la formation d'une poche caractéristique dans laquelle sont logés les nucléotides de l'ARNm. Ce nouveau rôle pour OB2 est soutenu par les cartes de densité 3D publiées par Loveland et Korostelev montrant certaines conformations de bS1 avec des domaines de plis OB vérifiant le canal de sortie de l'ARNm, avec l'OB2 près de l'extrémité 5′ de l'ARNm. Pendant l'initiation de la traduction, cette poche pourrait agir comme une pince pour stabiliser les interactions Watson-Crick SD-aSD. En conclusion, les résultats présentés ici élargissent la connaissance collective de la fonctionnalité de l'une des protéines ribosomales les plus flexibles. Ils soulignent la polyvalence fonctionnelle du domaine OB2, et mettent en évidence plusieurs nouvelles interactions essentielles pour la stabilité de bS1 pendant l'initiation de la traduction.

UNIVERSITÉ DE RENNES 1

Titre : Caractérisation structurale du mécanisme de sauvetage de la synthèse des protéines chez les bactéries

Mots clés : Cryo-MET – *trans*-traduction – ARNtm – SmpB – RNase R – bS1

Résumé : Le travail effectué se concentre sur un mécanisme biologique impliqué dans le contrôle de la qualité de la synthèse des protéines bactériennes, appelé *trans*-traduction.
Ce processus est crucial dans le sauvetage des ribosomes bloqués sur l'ARNm non-stop, permettant leur libération avec la dégradation simultanée du peptide incomplet ainsi que de l'ARNm défectueux. Les deux principaux acteurs impliqués dans la *trans*-traduction sont l'ARN messager de transfert (ARNtm) et la petite protéine B (SmpB). Le premier chapitre du manuscrit se concentre sur l'étude structurale, par cryo-TEM, à la suite de quoi nous avons obtenu quatre structures atomiques du ribosome bloqué lors de la *trans*-traduction, chacune délimitant une étape spécifique: pré-accommodation, accommodation, translocation et post-translocation.
Dans le deuxième chapitre, nous avons tenté de caractériser un troisième facteur impliqué dans la *trans*-traduction, la RNase R. Cette ribonucléase est essentielle dans la dégradation de l'ARNm non-stop. Une sorte de compétition pour le site de liaison ribosomique avec l'ARNtm a été observée, et par conséquent cette étude a été étendue pour étudier le mécanisme de sauvetage sur les disomes. Dans le troisième chapitre, nous avons décrit une nouvelle particularité d'une des principales protéines ribosomales connue sous le nom de bS1. Cette protéine est cruciale dans les premières étapes de la traduction Nous avons observé un des domaines connus pour interagir avec le ribosome impliqué dans la stabilisation de l'interaction S.D - anti-S.D, essentielle pour le positionnement correct de l'ARNm au sein du ribosome.

Title : Structural characterization of the rescue mechanism of proteins synthesis in bacteria

Keywords : Cryo-EM – *trans*-translation – tmRNA – SmpB – RNase R – bS1

Abstract : The work carried out in the course of this PhD and reported withi the manuscript is focused on a biological mechanism involved in the quality control fo the bacterial protein synthesis, called *trans*-transaltion.
This process is crucial in the rescue of stalled ribosomes on non-stop mRNA, allowing their release with simultaneous degradation of the incomplete peptide as well as the defective mRNA. The two main actors involved in trans-translation are the transfer-messenger RNA (tmRNA) and the small protein B (SmpB).
The first chapter of the manuscript is focused on the structural study, by cryo-EM, following which we obtained four atomic structures of the stalled ribosome during *trans*-translation, each of which delineating a specific step that we can summarise as pre-accommodation, accommodation, translocation and post-translocation.
In the second chapter, we undertook a study focusing on the characterisation of a third factor involved in the *trans*-translation process, known as RNase R. This ribonuclease is essential in the degradation of non-stop mRNA. A kind of competition for the ribosome binding site of RNase R with tmRNA was observed, and consequently this study was extended to investigate the mechanism of rescue on disomes.
In the third and final chapter, we described a new peculiarity concerning one of the main ribosomal proteins known as bS1. This protein is crucial in the early stages of translation due to its ability to interact with both the ribosome and the messenger. In this study, we observed one of the domains known to interact with the ribosome involved in stabilising the S.D - anti-S.D interaction, essential for the correct positioning of mRNA within the ribosome.